Finite Element Analysis of Curl Development in the Selective Laser Sintering Process

Naim Musa Jamal

A Thesis submitted in accordance with the requirements of

Doctor of Philosophy

The University of Leeds
Department of Mechanical Engineering

September 2001

The candidate confirms that the work submitted is his own and that appropriate credit has been given where reference has been made to the work of others.

Acknowledgements

First, I must thank the sponsors of this project; the University of Leeds and the Mechanical Engineering Department. I would also like to thank the Keyworth Institute of Manufacturing and Information Systems for giving me the opportunity to work as a CAD engineer in their rapid prototyping and tooling group during the period of this research. That was made possible through Dr. Kenny Dalgarno, the supervisor of this work, whom I would like to thank for his guidance, support and help in the duration of this project.

I would also like to thank Professor Tom Childs for the valuable discussions we had during the conduct of this research. I am always grateful for the enormous help, assistance and advice of Mr Andrew Marsden, Keyworth institute.

I am so grateful to my colleague Majed Haiba for his continuous encouragement, help and advice, and for putting up with my complaining, particularly during the writing up of this thesis, when things looked bleak. I would also like to express my gratitude to Mr R.M. Martin and D. Readman in the vehicle dynamics laboratory.

Many thanks are due to Mr N. Tyres, IRC-Polymer, school of chemistry, and to Dr P. Hine, IRC-polymer, school of physics.

Finally, I would like to dedicate this thesis to my parents for their endless support and motivation during the period of this research.

Abstract

Selective laser sintering (SLS) is a rapid prototyping process, which operates by using a laser to locally heat an area within a layer of powder material, causing it to fuse together, creating a thin cross-section of solid material. 3D shapes are built by repeatedly depositing a layer of fresh powder on top of the cross-section and then locally heating it, causing it to fuse together and to the layer beneath. However, during SLS processing, temperature differences that exist in different regions of the fabricated parts lead to uneven shrinkages. The shrinkages cause surfaces in the part, which are intended to be flat, to exhibit a curved profile; a phenomenon termed curl. The development of curl is highly influenced by the SLS machine parameters selected in fabrication. The production of geometrically acceptable parts involves numerous fabrication trials before the optimum machine parameters can be found. The procedure can be time consuming and expensive.

The aim of the work presented in this thesis was to develop finite element models for the purpose of predicting curl in SLS fabricated polycarbonate parts. The ultimate goal was to use the models to estimate the optimum SLS machine parameters for the physical fabrication of geometrically acceptable parts, produced in any material, and therefore avoid the costly and time consuming process of using SLS machines for experimental purposes.

The prediction of curl was made through heat transfer and stress finite element models that were both coupled using the sequentially coupled thermal-stress analysis technique. Experimental work was carried out to measure material properties used as input to the models and to validate results predicted. The sensitivity of curl predicted to assumptions considered in the heat and stress models was introduced, and the assumptions highly influencing the accuracy of curl predictions were identified.

Table of Contents

List of Notations

A	Cross-sectional area
a	Radius of the solid particles in powder bed.
a_1, a_2	thickness of layers
B	Deformation parameter of the particle
b	width of part
C_1, C_2	WLF constants
C_p	Specific heat
C_{pi}	Specific heat of component i
D	Nominal laser beam spot diameter.
D_p	Average diameter of packing
D'	Actual diameter of laser beam spot at different positions on part bed.
E	Elastic modulus
E_{br}	total radiation energy emitted from a black body
ED	Energy density
E_r	total radiation energy emitted from the surface
F	Force
f	Conversion factor for estimating energy density
F_R	view factor
G	$(U.D)/2\alpha_d$
$g_r(t)$	Ratio of modulus at instant t during relaxation to modulus prior to relaxation
g_i	Prony series parameter
h	thickness of part
h_c	Convection heat transfer coefficient
h_{rs}	Heat transfer coefficient for radiation, solid to solid
h_{rv}	Heat transfer coefficient for radiation, void to void
I	Laser Intensity.
I_A	Area moment of inertia
$I_\circ$	Maximum laser intensity at centre of laser beam spot
k	Thermal conductivity
k_g	Thermal conductivity of gas
k_R	Radiation thermal conductivity
k_e^o	Effective thermal conductivity of the powder bed

k_s	Thermal conductivity of solid
L	length of a scanned line.
l	length of part
$log(a_T)$	WLF horizontal shift
l_p	Effective length between adjacent particle centres
l_s	Effective length of solid relating to thermal conduction of powder bed
l_v	Effective thickness of the fluid film
M	Bending moment
m	Ratio of the thickness of the top layer to thickness of bottom layer in two-layer part
m_s	mass
N	Number of particles in powder bed
n	Ratio of the modulus of the top layer to modulus of bottom layer in two-layer part
P	Fill laser power.
Q	Heat
q_o	Heat flux
r	Radial distance from the centre of laser beam spot.
R	Radius of curvature
RS	Roller speed
S	Scan spacing.
t	Time
T	Temperature
t_d	Delay period between successive radiation scans.
T_{env}	Temperature of environment
T_g	Glass transition temperature
T_s	Reference temperature in WLF approximation
T_{sur}	Temperature of surrounding walls
U	Laser beam velocity in direction of scanning
V_l	velocity of laser beam in direction perpendicular to the scanning direction
u_θ	Rotational component of node about its local y-axis co-ordinate
u_z	Translational component of a node in the defined z-direction
u_x	Translational component of a node in the defined x-direction
V	Volume
V_T	Volume of the solid figure bounding the cubical powder bed arrangement
α	Coefficient of thermal expansion
α_d	Thermal diffusivity
α_p	Angle identifying position of laser spot on part bed.

α_R	Absorptivity
β	l_p / D_p
Δl	Change in length
ΔT	Change in temperature
δ	Phase lag of the strain response to an applied stress in viscoelastic polymers
δ_d	Deflection
ε	Strain
ε_v	Void fraction
ϕ	Flattened surface fraction of a particle in contact with another particle
γ	l_s / D_p
η	Viscosity
φ	l_v / D_p
ρ	Physical density
ρ_R	Reflectivity
ω_i	Weight fraction of component *i*
ω_r	Characteristic radius
$\in$	Emissivity
σ	Stress
σ_R	Stefan-Boltzmann constant (5.67×10^{-8} W/m^2·K^4)
$\sigma_{thermal}$	Thermal stresses
τ	Dwell Period
τ_R	Transmissivity
τ_M	Relaxation time constant

Chapter 1

Introduction

1.1 Introduction

The selective laser sintering (SLS) process is one of a number of mature rapid prototyping (RP) technologies, which allows geometrical and functional prototypes to be made directly from a three-dimensional (3D) computer aided design (CAD) model. The process operates by using a laser to locally heat an area within a layer of powder material, causing it to fuse together, creating a thin cross-section of solid material. 3D shapes are built by repeatedly depositing a layer of fresh powder on top of the cross-section and then locally heating it, causing it to fuse together and to the layer beneath.

However, during the SLS process, temperature differences that exist in different regions of the fabricated parts lead to uneven shrinkages. The uneven shrinkages cause surfaces in the part, which are intended to be flat, to exhibit a curved profile; a phenomenon termed curl. The development of curl is highly influenced by the SLS machine parameters selected in fabrication. Often the successful production of geometrically acceptable parts involves numerous fabrication trials before the optimum machine parameters can be found. The procedure can be tedious, time consuming and expensive.

The purpose of the work presented in this thesis is to develop a finite element model that can predict curl in SLS fabricated parts. The ultimate goal of the model is to avoid the need, in the long term, of using the SLS machine for experimental fabrication for the purpose of estimating the optimum machine parameters. The optimal parameters estimated by the model can be applied to physically produce geometrically accurate parts, which can considerably reduce the time and cost of operating the machine for experimental purposes.

1.2 Organisation of Thesis

Chapter 2 reviews the building strategies of common rapid prototyping processes with emphasis given to describe the process specific to this work, selective laser sintering. As the material examined in this work is polycarbonate, which is a thermoplastic polymer, a number of physical properties of thermoplastics used as input to the finite element models are also described in this chapter. Additionally, some previous studies in curl are reviewed. In chapter 3, SLS fabrication of polycarbonate specimens and the method of measuring their curled profiles are introduced. The measurements are performed to guide the development of the finite element models and to verify the accuracy of results predicted. Chapter 4 presents simple analytical heat transfer and stress models. The models are used to help understand the material properties required as input to the heat and stress finite element models. In addition, the methods available in coupling heat transfer and stress models in the finite element package used (ABAQUS) are introduced. Furthermore, implementation of the most suitable method in coupling simple heat and stress finite element models (first version of model development) for the purpose of predicting curl is described. Chapter 5 presents the experimental work carried out to measure a number of material properties used as input to further developed heat and stress models. Chapter 6 describes the second and third versions of the heat and stress finite element models along with results predicted. The aim of the second version of the models was to improve simulation of the SLS process, whilst implementing the experimentally measured material properties. The third version of the models further improved simulation of thermal effects occurring during SLS processing, in an attempt to enhance curl predicted by the previous version of the models. In chapter 7, the sensitivity of curl predicted to assumptions considered in the heat and stress models is given. The assumptions highly influencing the accuracy of curl predicted were also identified. The chapter also presents the conclusions drawn from the sensitivity study and recommendations for future model developments.

Chapter 2

Literature Review

2.1 Introduction

Rapid Prototyping (RP) denotes a class of processes that can automatically fabricate physical models from three-dimensional CAD data. Such models have various applications. They serve as exceptional visual aids for sharing ideas with associates and customers. Additionally, prototypes can be employed for design testing, fit and functional reviews. Besides prototypes, RP processes are utilised to make tooling, referred to as Rapid Tooling, or creating production-quality parts, called Rapid Manufacturing. RP processes have also been termed Solid Freeform Fabrication, Computer Automated Manufacturing and Layered Manufacturing. These processes begin with a three-dimensional computer solid model of the part. The data is then sent to an Automatic Process Planner. This decomposes the model into a number of thin slices. Each slice resembles a planar cross-section of the object with a small, but finite thickness. The information is then sent to an Automatic Fabrication machine. Every slice in the CAD model is physically deposited, during fabrication, and is fused to the previous one to produce an object sequentially. The main stages of a RP process are illustrated in Figure 2.1.

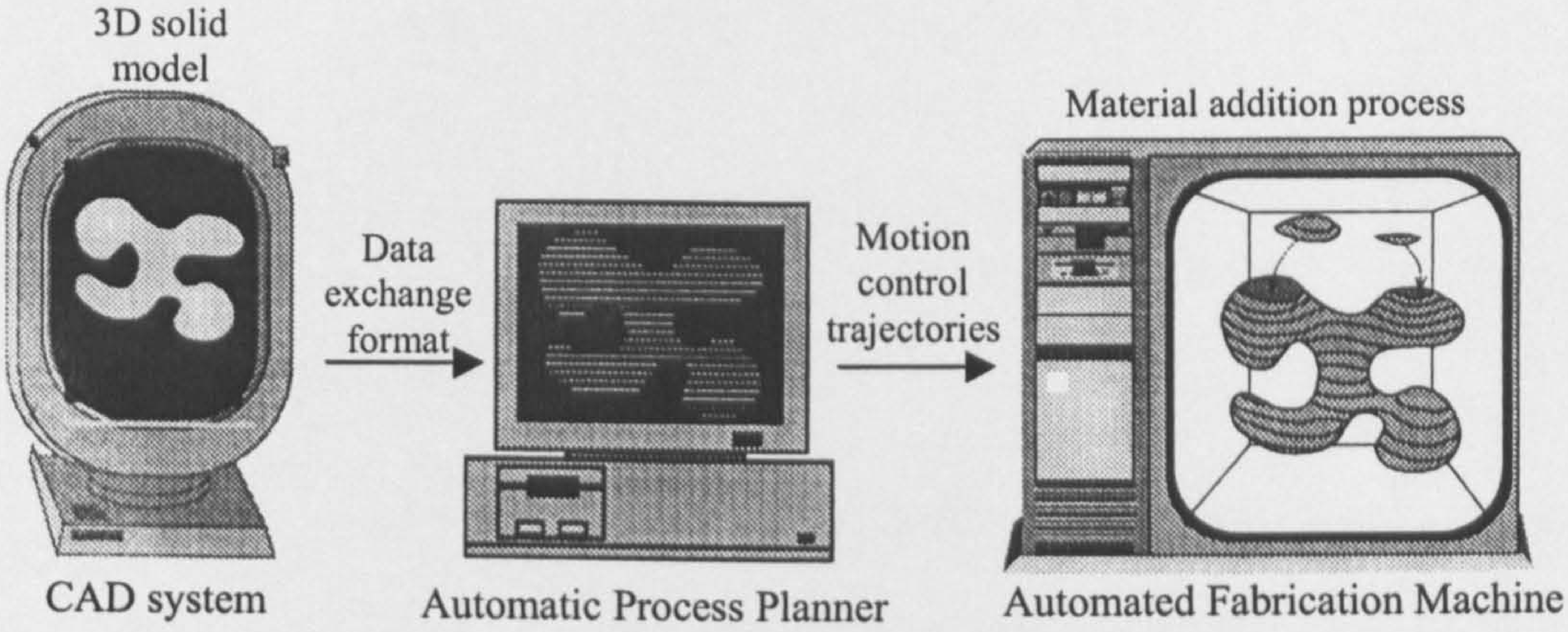

Figure 2.1 Rapid Prototyping build process. From [1].

A major advantage of RP over conventional manufacturing is shorter production times. Most prototypes require from three to seventy two hours to build depending on the size of the object. This can seem slow but is generally much faster than the weeks or months required to produce complex-featured prototypes using conventional manufacturing methods [2]. Moreover, the additive layered nature of RP allows it to create objects with complicated internal features, which cannot be manufactured directly using the most advanced Computer Numerical Control (CNC) machines.

Most conventional machining processes such as milling, drilling etc. are subtractive processes. These involve the removal of unwanted material from a solid block. In general, complex tooling and tool path planning need to be designed and constructed prior to producing a complex object. Furthermore, sophisticated fixturing techniques and reorientation of complex objects are required during the fabrication process. In contrast, RP builds parts by adding material layer by layer, and thus does not involve reorientation and fixturing problems. When the bottom layer is attached to a platform, the part is produced without any reorientation or refixturing needed during manufacturing.

The following sections have a number of goals. Firstly, a brief description of common RP processes and their building strategies is presented. In addition, an effort is made to describe the RP process specific to this study, Selective Laser Sintering (SLS). This process has an advantage over some other RP processes in that it can use a wide variety of materials to make parts. A number of these materials and their applications are mentioned. The physical properties of thermoplastic polymers, and in particular amorphous polymers, are given emphasis because of their importance later in this study. Additionally, some of the common problems found in parts produced in SLS are introduced. Then a description of previous studies of distortion in SLS is given.

2.2 Common RP Processes and Building Strategies

In following sections, a brief description of the most common RP processes and their building strategies is provided. The materials used in fabricating parts using these processes are also mentioned. In addition, a description of the major advantages and disadvantages of these processes is provided.

2.2.1 Stereolithography

Stereolithography (SLA) was the first RP process to be developed and offered commercially. Building of parts in SLA takes place on a platform that is positioned inside a vat of photo-curable resin (see Figure 2.2). The initial position of the platform is at the top surface of the resin. The platform is then lowered the intended thickness of the first layer of the part. An ultraviolet laser next draws the layer structure on the surface of the resin allowing the scanned resin to polymerise and solidify. The build process then pauses for the surface of the resin to level. The process is continued until the part is completely fabricated [3].

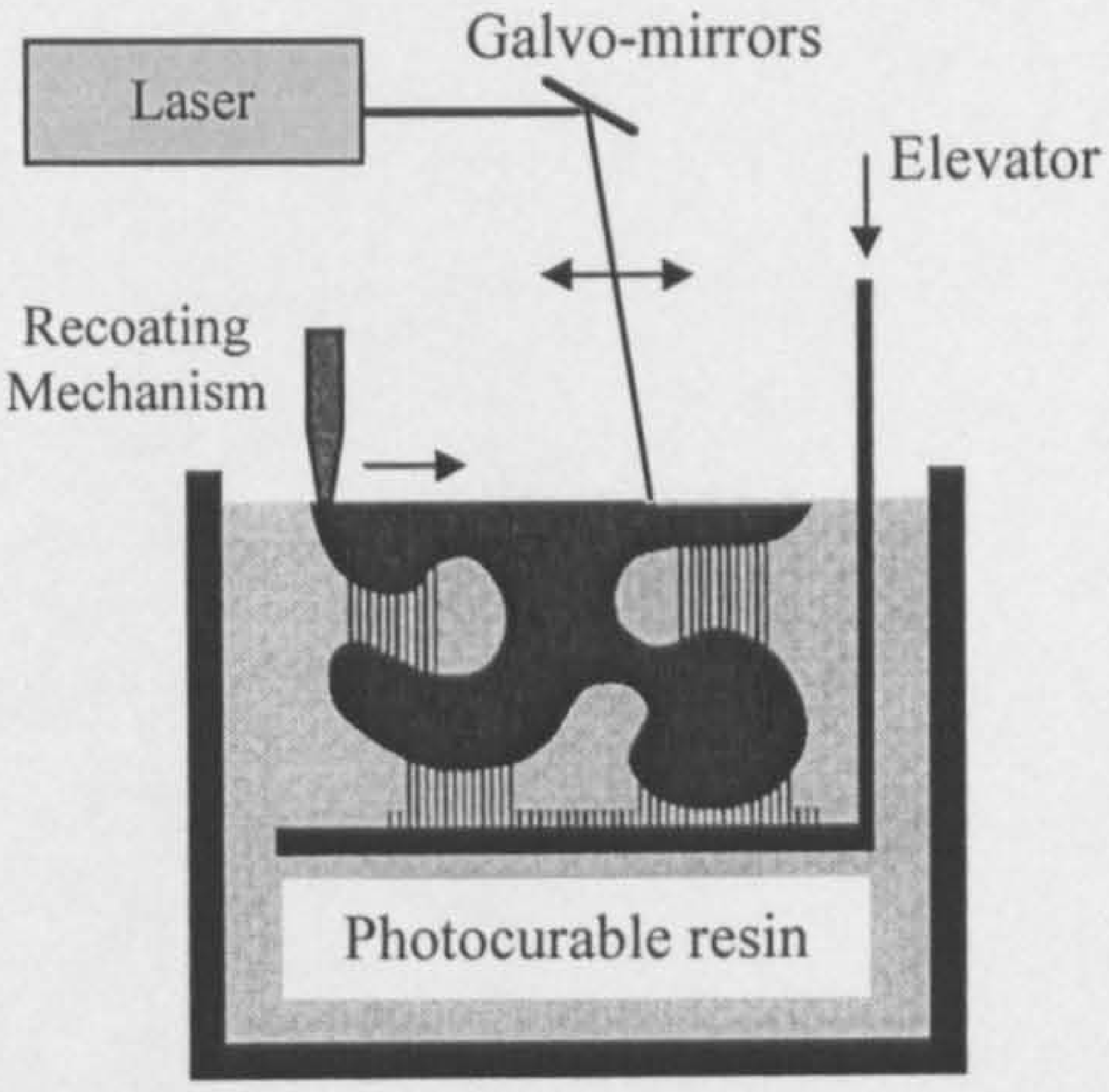

Figure 2.2 Schematic view of the SLA process. From [1].

Any overhangs in parts produced in SLA require support structures. The support structures prevent swaying and deformation of the overhangs in the liquid environment. The supports are removed after the part is completely fabricated. However, in the manual removal of supports, tolerance deviation results from the removal of too little support or too much of the part. Additionally, accessibility to support structures can be a concern. In the condition that a fabricated part has internal cavities with little or no accesses, the supports in these cavities are not removed.

2.2.2 Three Dimensional Printing

Three-dimensional printing (3DP) was developed at M.I.T and was first licensed to Soligen Technologies Inc. The process uses powder-based materials such as metals and ceramics to fabricate parts. Building of parts takes place in a flask fitted with a piston, as schematically illustrated in Figure 2.3. A hopper supplies the powder, which is then spread and levelled by a roller. Binding material is then deposited by a print head where the solid section is required. The piston then lowers the work piece and the roller spreads the next layer of powder. The process is repeated until the part is completely built. Any overhangs in the part do not require the design and fabrication of support structures, as overhangs are supported during the build by the surrounding unbound powder [3].

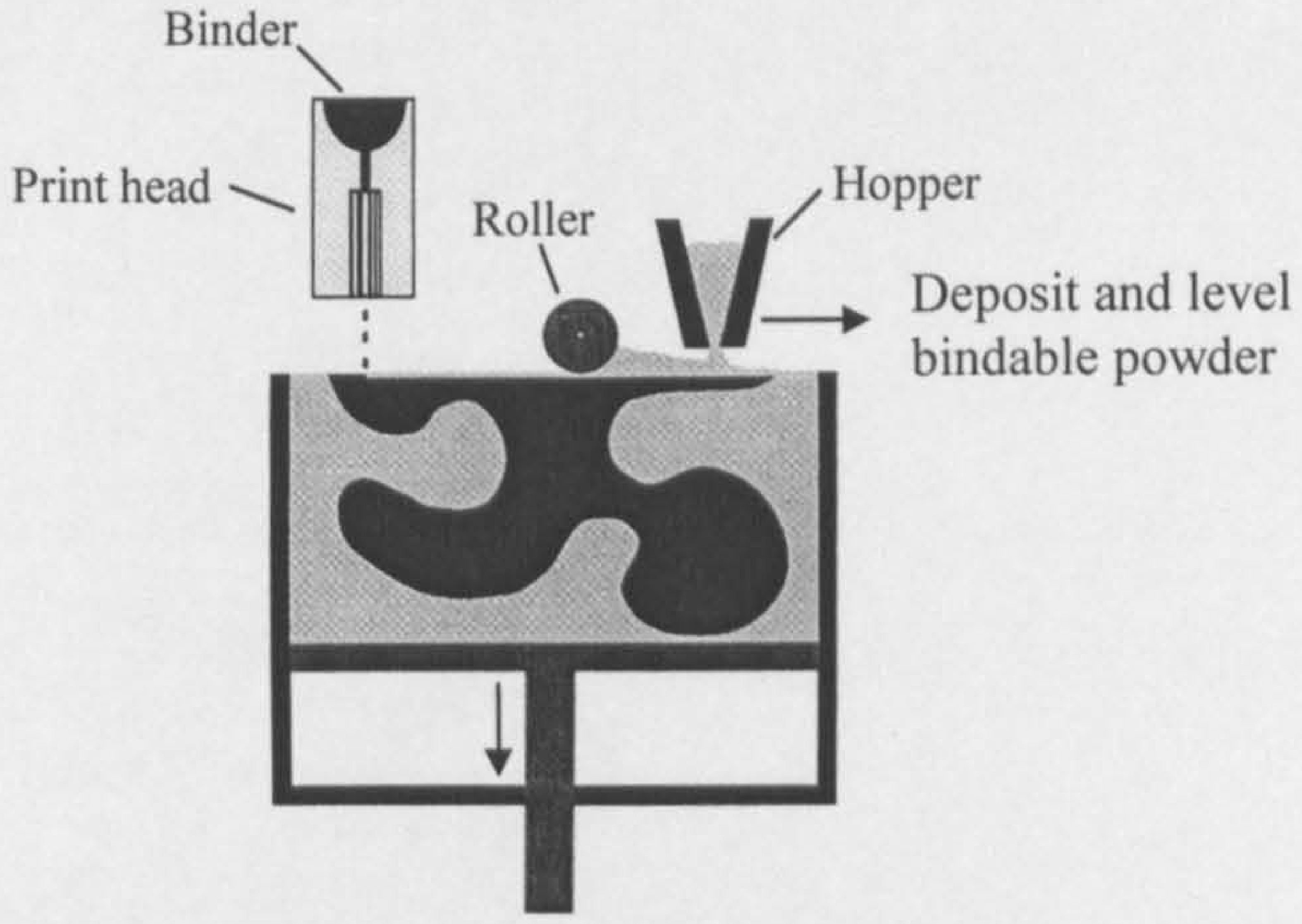

Figure 2.3 Schematic view of the 3DP process. From [1].

2.2.3 Laminated Object Manufacturing

Laminated object manufacturing (LOM) is developed and marketed by Helisys. The process uses thin layers of paper, polymer or composites to form parts. The sheets are coated with heat-sensitive adhesives, which allows layer by layer bonding with hot roller compression. The building process takes place on a platform, which moves vertically under computer control. The material sheets are supplied from one end of the machine and taken up to the opposite end, as schematically illustrated in Figure 2.4. A laser beam, controlled by a CAD system, is used to cut the cross-sectional profile of each layer of the part. The laser then cuts any material that is not part of the model into a crosshatch pattern; a process called cubing, for later removal when fabrication of the part is completed. The crosshatches act as external support for part overhangs during the building process. One of the major advantages of LOM over other RP processes is the accuracy of parts produced. That is because the parts can be generated from very fine layers of material. In addition, dimensional distortions developed in a part due to thermal stresses generated as a result of lamination can be minimised by using a low thermal-expansion material [4].

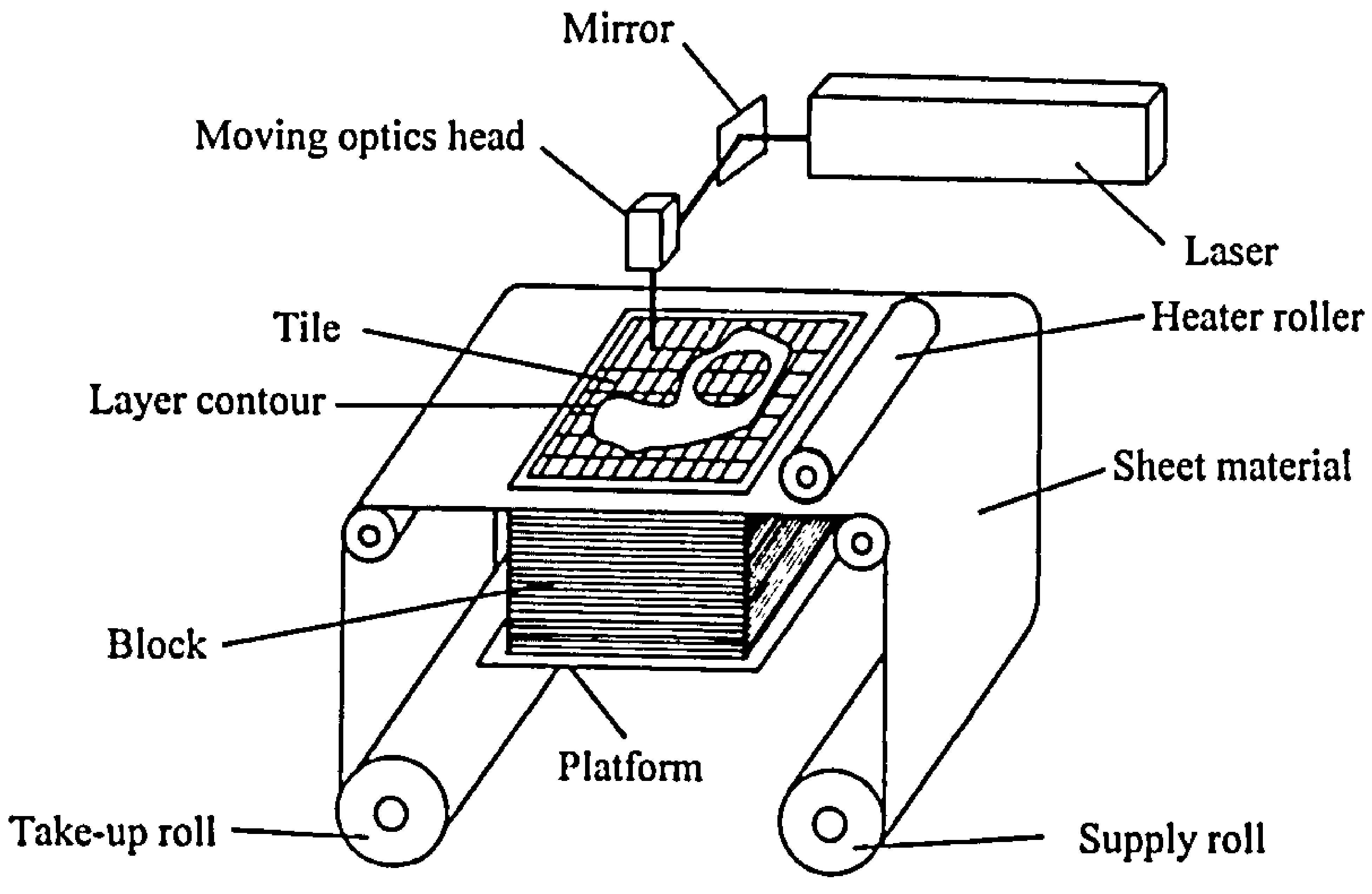

Figure 2.4 Schematic view of the LOM process. From [4].

However, as the majority of the material supporting the part is scrapped after building, the cost of such waste can be significant. In addition, the material or adhesive could fail under the application of load, causing delamination of the produced part. Thus, LOM fabricated parts have limited applications as functional prototypes and are mainly used in a range of moulding operations and as visual aids in the design process.

2.2.4 Fused Deposition Modelling

Fused Deposition Modelling (FDM), schematically illustrated in Figure 2.5, was developed and is marketed by Stratasys. The process uses filament thermoplastics or wax to produce parts. The material is fed into a head where it is heated to one degree above its solidification point. The melt is then extruded tracing out the CAD cross-sectional layer information. The material is deposited in layer form on a fixtureless foundation supported by a moving piston. Each added layer bonds to the previous one as a result of thermal fusion. However, as the solidification rate of the deposited material is high, it is necessary to ensure that the material is delivered at an optimal temperature. In addition, the build needs to be maintained at a temperature just below the solidification point to ensure proper adhesion between subsequently added layers [4].

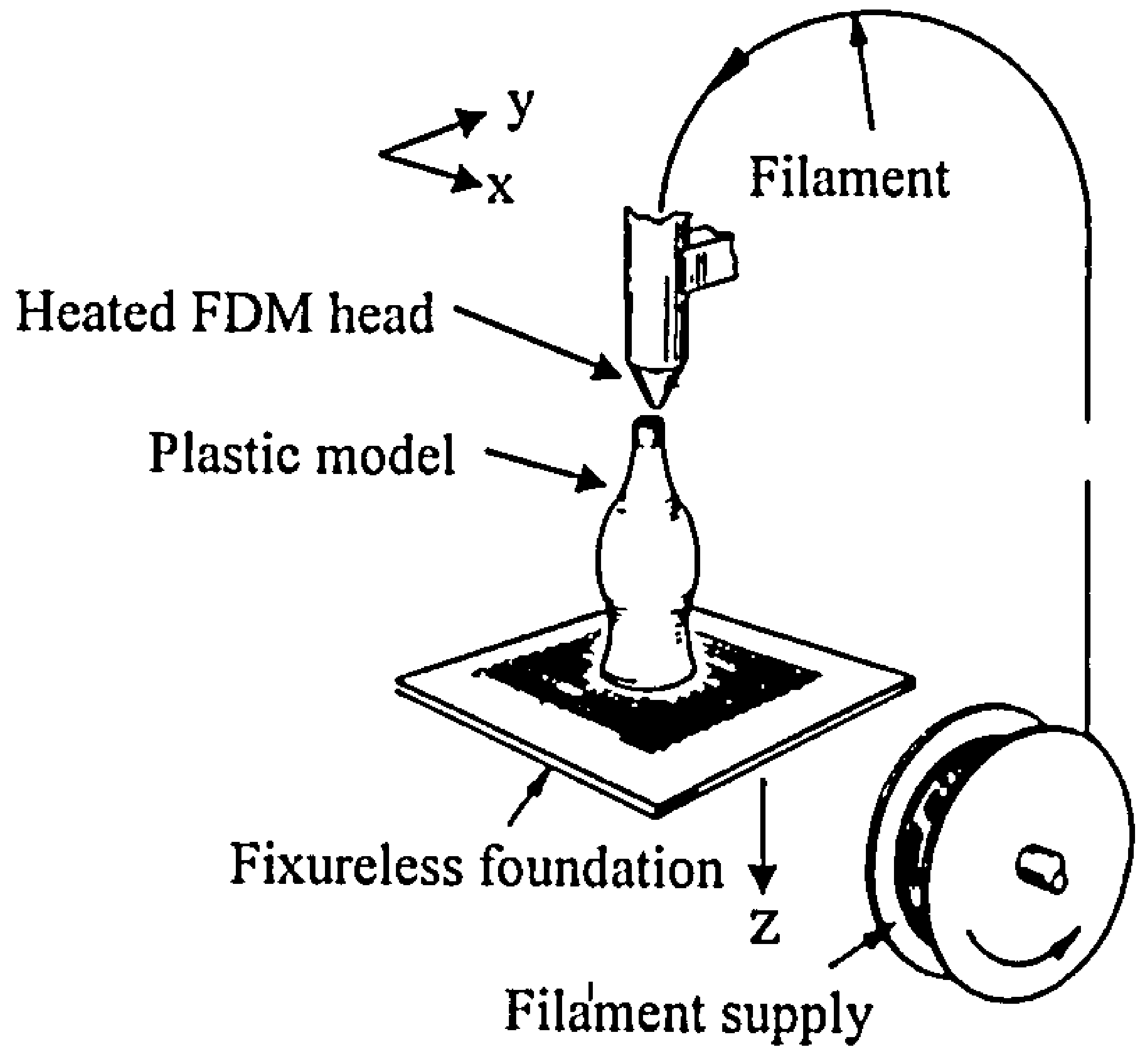

Figure 2.5 Schematic view of the FDM process. From [4].

Parts with overhanging features require support structures. The support structures can be made from the same material as that of the part or from a different material. In the latter case, the structures have a weaker bond with the part and can be easily removed. The structures can be also made from a material of a different colour for easier identification.

Parts formed in FDM can be used in investment casting applications, where the fabricated patterns may be dipped directly into a ceramic slurry to produce the ceramic shells. Parts produced in FDM can also be employed in conceptual modelling, fit and functional applications [3].

One of the advantages of FDM is that there is no waste material during or after part fabrication. In addition, there is no worry of possible exposure to toxic chemicals, lasers, or a liquid polymer bath. Additionally, the material used in the process can be changed rather quickly. However, the accuracy of the parts produced is restricted as the filament material has a diameter of 1.27mm [5].

2.2.5 Selective Laser Sintering

Selective Laser Sintering (SLS) was originally developed at the University of Texas at Austin and was licensed to DTM Corporation. Similar to other rapid prototyping processes, a three-dimensional computer representation of the part is first generated using CAD software or a computer tomography imaging scanning process. The SLS process fabricates parts by fusing powder-based material with the heat of an infrared laser beam. The powder is supplied by powder feed cartridges, which is then spread evenly over the build region by a roller. The build region is supported by a movable piston as illustrated in Figure 2.6.

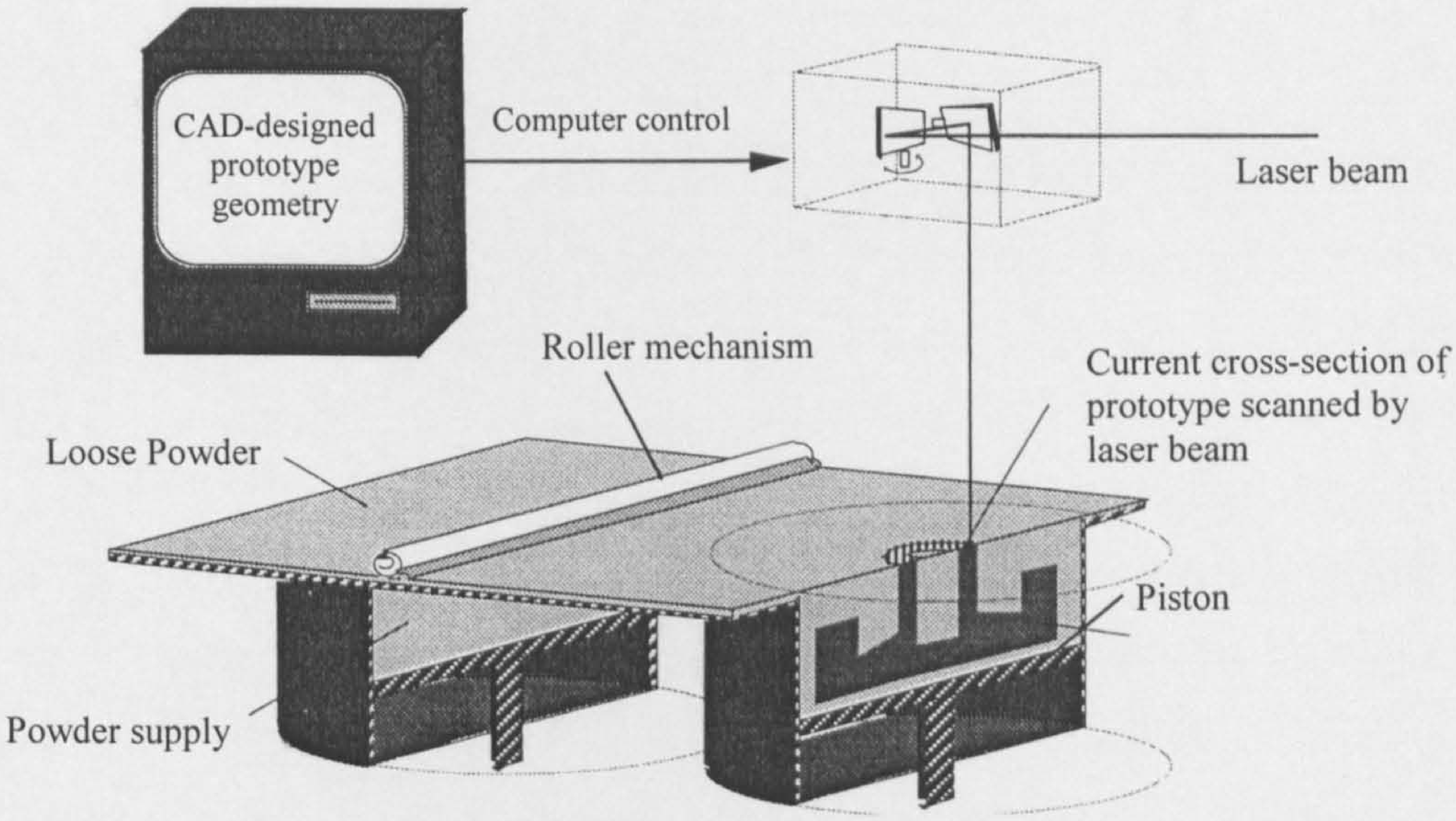

Figure 2.6 Schematic view of the SLS process. From [1].

The process starts by spreading layers of powder onto the piston to form the powder bed. The piston then lowers a distance equal to the thickness of the first layer of the sliced CAD model (see Figure 2.1). That is followed by the roller spreading a layer of powder. A pattern that matches the cross-section of the first CAD layer is next traced by the laser on the powder surface, causing the powder particles to bind to one another to form the first solid layer of the part. The piston then lowers for the next layer of powder to be added, and the process continues until the part is completely fabricated. Any overhangs in the part are supported during fabrication by the surrounding unbound powder. In the context of this thesis, the powder bed together with the fabricated layers and their surrounding powder are termed the part bed.

The SLS machine uses a CO_2 laser with a power of up to 50W and an emission wavelength of 10.6μm. The laser beam is directed onto the surface of the powder by two mirrors (see Figure 2.6), one rotating faster than the other. Each mirror is actuated by a galvanometer, and is rotated about an axis perpendicular to that of the other mirror. The faster rotating mirror draws continuous straight scans on the surface of the powder. The rotation of the other mirror causes an offset in the laser beam position for other parallel scans to be created (see Figure 2.7). In SLS, the part bed is encapsulated in a process chamber, which is supplied with nitrogen to create an inert atmosphere to eliminate the possibility of powder ignition and explosion.

The SLS process depends on many parameters, a number of which influence the quality of parts produced. The parameters include the laser scanning strategy controls, powder layering mechanism and heater controls. In the following, the parameters are described, as they are often referred to in following chapters.

2.2.5.1 Laser Scanning Strategy Controls

In SLS, the laser beam raster scans the surface of the powder during sintering, i.e. the laser beam travels along the x-direction at different y-positions as schematically illustrated in Figure 2.7. The scanning parameters that influence the intensity and method of energy delivered to the surface of the powder are the laser spot diameter (D), fill laser power (P), laser beam velocity (U), scan spacing (S) and the vector length (L) of the scans. These parameters are explained in following sections.

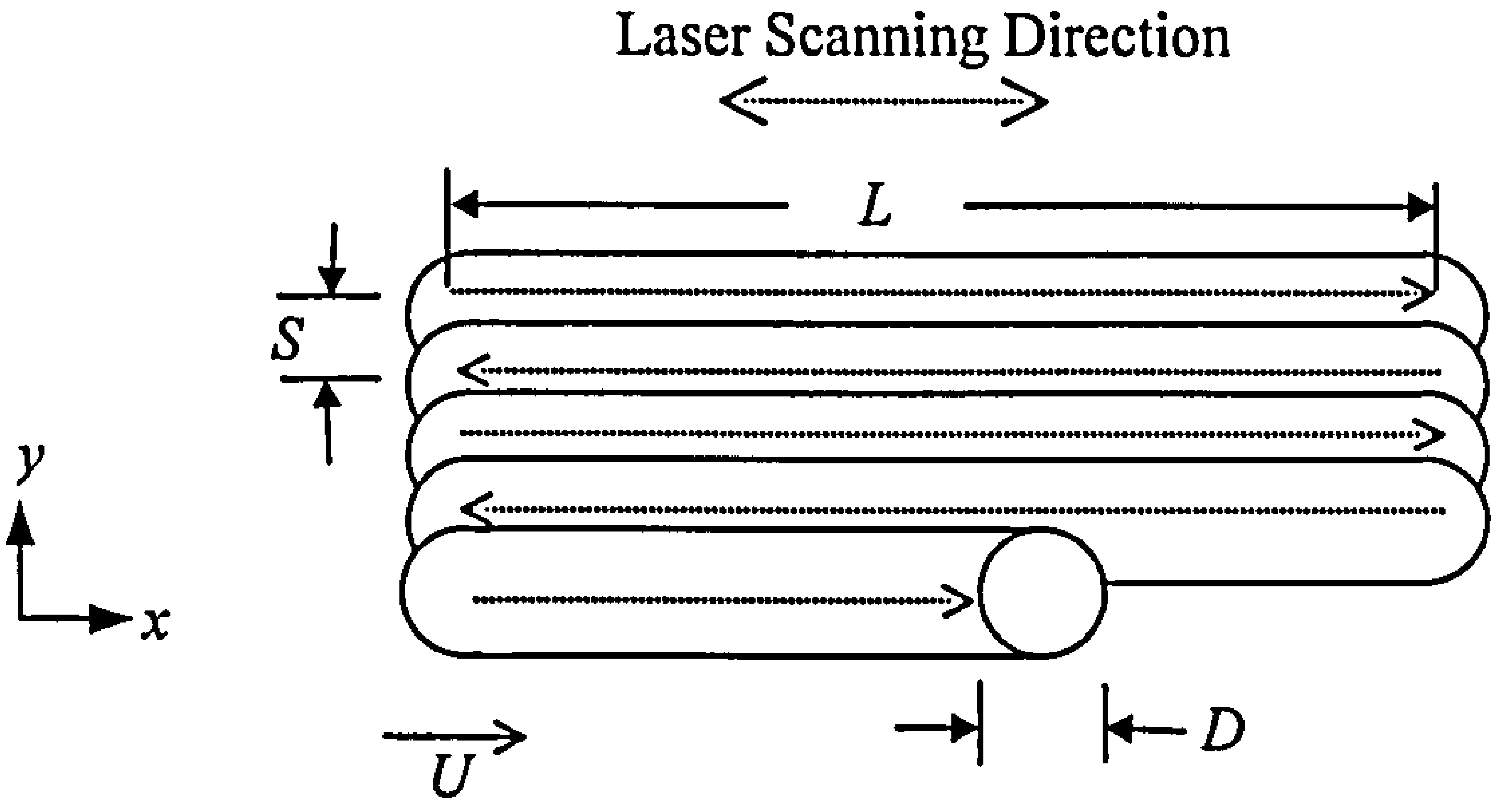

Figure 2.7 The SLS Scanning Strategy.

2.2.5.1.1 Laser Beam Diameter

The DTM Sinterstation 2000, used in Leeds University, has a laser beam diameter equal to 0.4mm. This parameter is fixed by the design of the SLS machine. However, it has been reported that the laser spot changes in diameter at different positions on the surface of the powder [6]. Referring to Figure 2.8, the laser spot has the best focus and the smallest diameter (D) when α_p = zero. An increase in the angle α_p allows the laser spot diameter to increase to $D' = D/\cos\alpha_p$. However, the increase in diameter was predicted to be very small; approximately 5.7% at the maximum value of α_p (19°), and thus its effect is normally neglected.

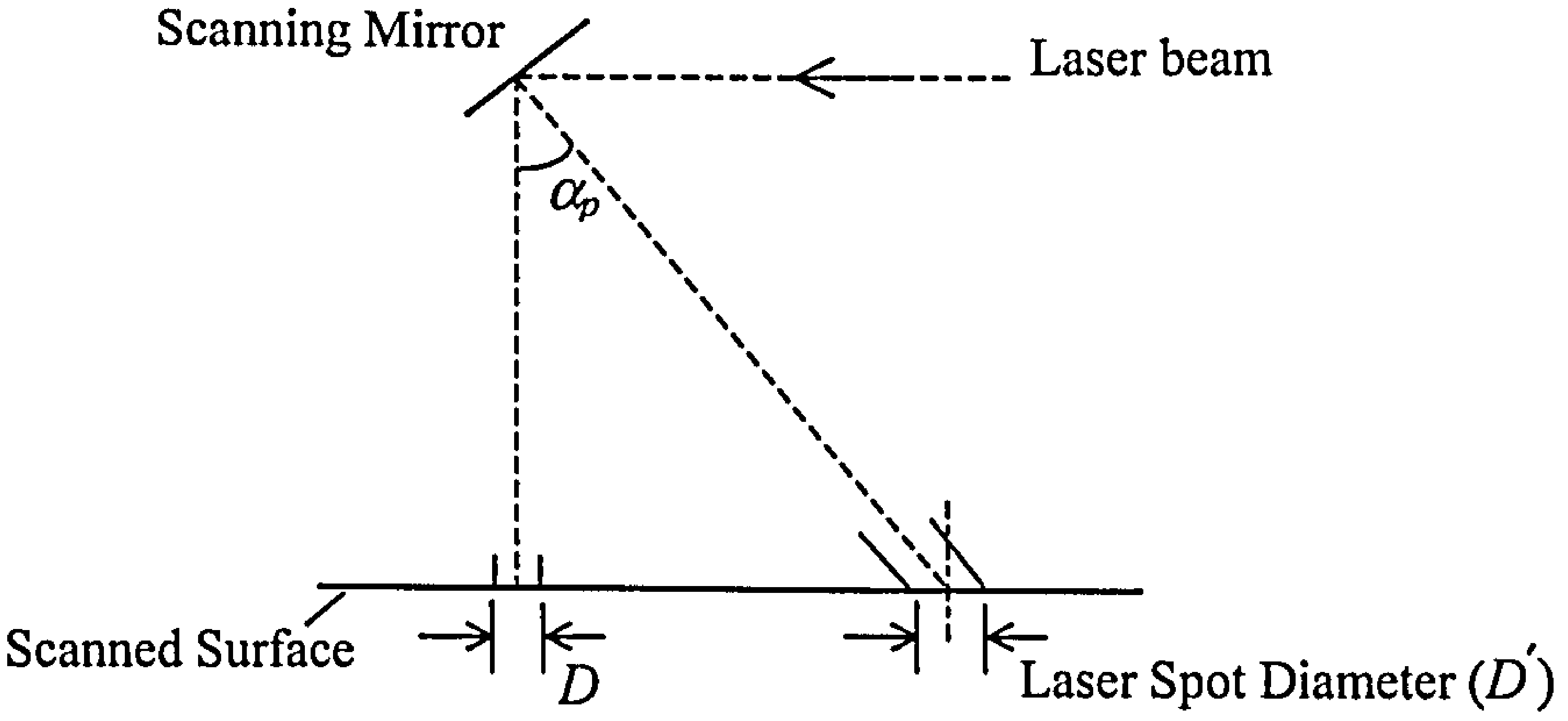

Figure 2.8 Changes in laser spot diameter at different positions on part bed

2.2.5.1.2 Fill Laser Power

The fill laser power is an adjustable SLS machine parameter. It refers to the power available from the laser beam over the part bed surface. The laser intensity, I, (irradiance), i.e. the laser power incident on a unit area (W/m^2), was found to follow a Gaussian profile [7], schematically illustrated in Figure 2.9. The Intensity Gaussian function has a peak at the centre of the laser beam spot (r = 0) that drops monotonically as the radial distance (r) from the centre increases. The value of (r) at which the beam intensity decreases to $1/e^2 \approx 0.135$ of its maximum value at the centre (I) is termed the characteristic radius (ω_f). The circle of the radius ω_f was reported to carry 86% of the total laser power [8].

The fill laser power is an important SLS parameter that is set according to the material used in fabrication. The aim of the laser application is to heat the powder to a temperature that exceeds its melting point to allow bonding between adjacent powder particles to occur. The machine operator therefore generally fabricates test parts, produced at various laser powers, to determine the optimum laser power for the material used. If the laser power applied is insufficient, fabricated parts lack strength or delaminate. Conversely, if the laser power applied is excessive, large thermal penetration into the powder bed occurs, which may result in small details on downward facing surfaces to lack definition.

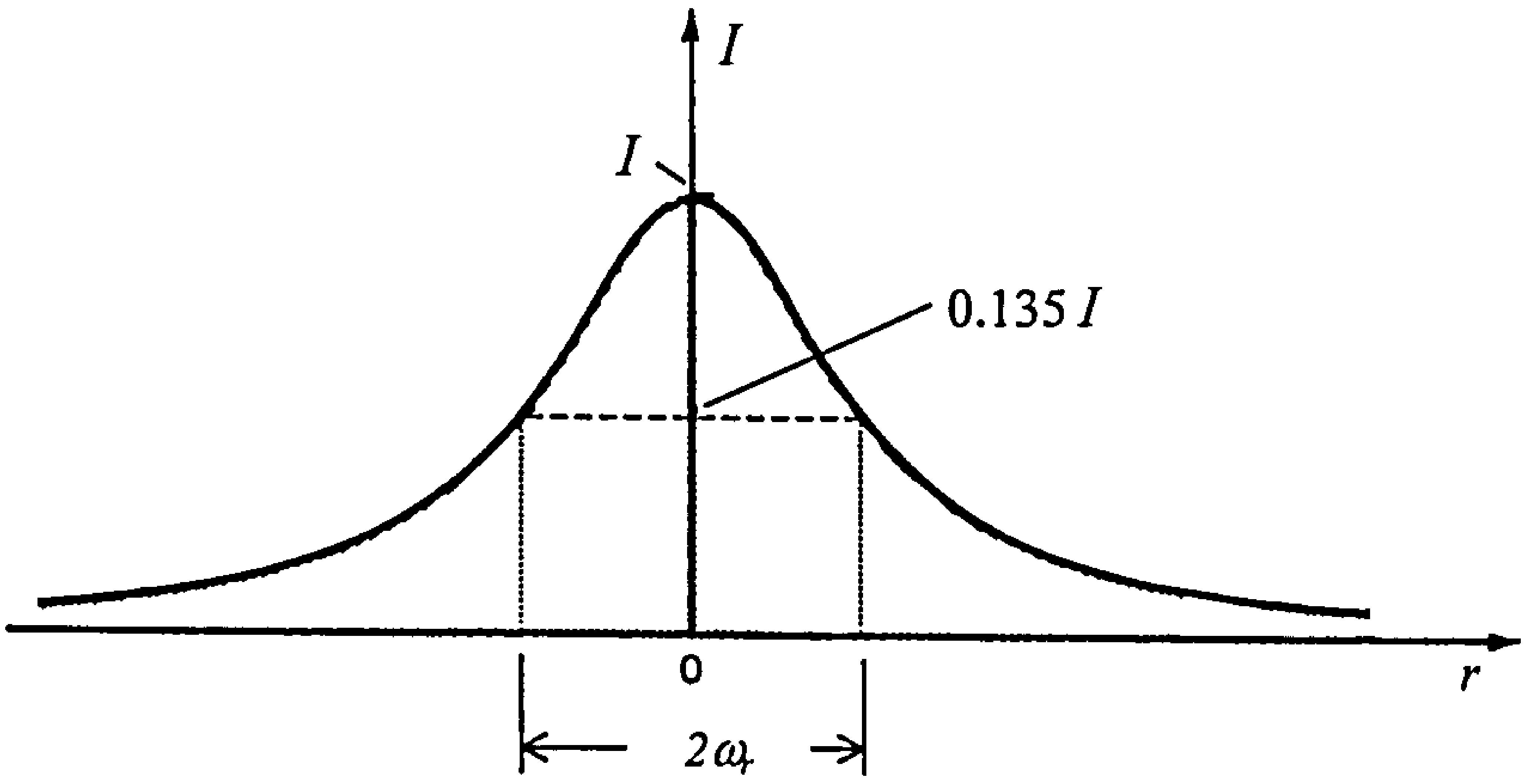

Figure 2.9 Gaussian profile of the incident laser intensity

2.2.5.1.3 Laser Beam Velocity

The laser beam velocity U is an adjustable machine parameter, which denotes the speed of the laser beam in the direction of scanning, i.e. along the x-direction in Figure 2.7. The parameter is important as it influences the period that a spot on the part bed is exposed to the laser beam effect. That period (τ) can be expressed in terms of the diameter of the laser beam (D) and its velocity (U) as follows [9],

$$\tau = \frac{D}{U} \qquad \text{2-1}$$

However, the speed of the laser beam is not constant. Due to the inertia of the mirrors and the motor, the scanner mirrors require an initial period before constant velocity can be achieved. This causes the beginning of a scanned line to be overexposed to the laser. Avoiding that phenomenon can be performed by controlling the On/Off timing of the laser. The Fill Laser On parameter allows a deliberate delay in turning on the laser during acceleration of the scanner mirrors at the beginning of the line segment. Moreover, as a result of the initial ramping process, the scanning mirrors require additional time to reach the end of the (intended) scanned line. That can be compensated by setting a delay in turning off the laser until the intended length of the line segment is completely scanned [10]. Following sintering of a line, the scanner mirrors are usually allowed a brief time to stabilise before starting to scan the next line. The length of that period can be adjusted by setting the Fill scan delay parameter. However, considering a long delay may result in an increase in processing time. Alternatively, a very short delay, if not long enough for the mirrors to stabilise, causes the following scanned line not to be straight [11].

2.2.5.1.4 Scan Spacing and Vector Length

The distance (*S*) between two neighbouring parallel scanned lines is termed the scan spacing (see Figure 2.7). This parameter is set by the machine operator and it influences the number of exposures seen by a point on the surface being sintered. The value of *S* should not be set to exceed the diameter of the laser beam, otherwise neighbouring scanned lines would not be (properly) bonded together. The length of a scanned line (*L*) is determined, however, by the geometry of the scanned area (see Figure 2.7). This parameter influences the delay period t_d between successive radiation scans, which can be expressed in terms of *L* and the laser speed *U* as follows [9],

$$t_d = \frac{L}{U} \qquad 2\text{-}2$$

The relationship between the process parameters aforementioned and the energy transferred to the part bed surface is shown in Figure 2.10 [9].

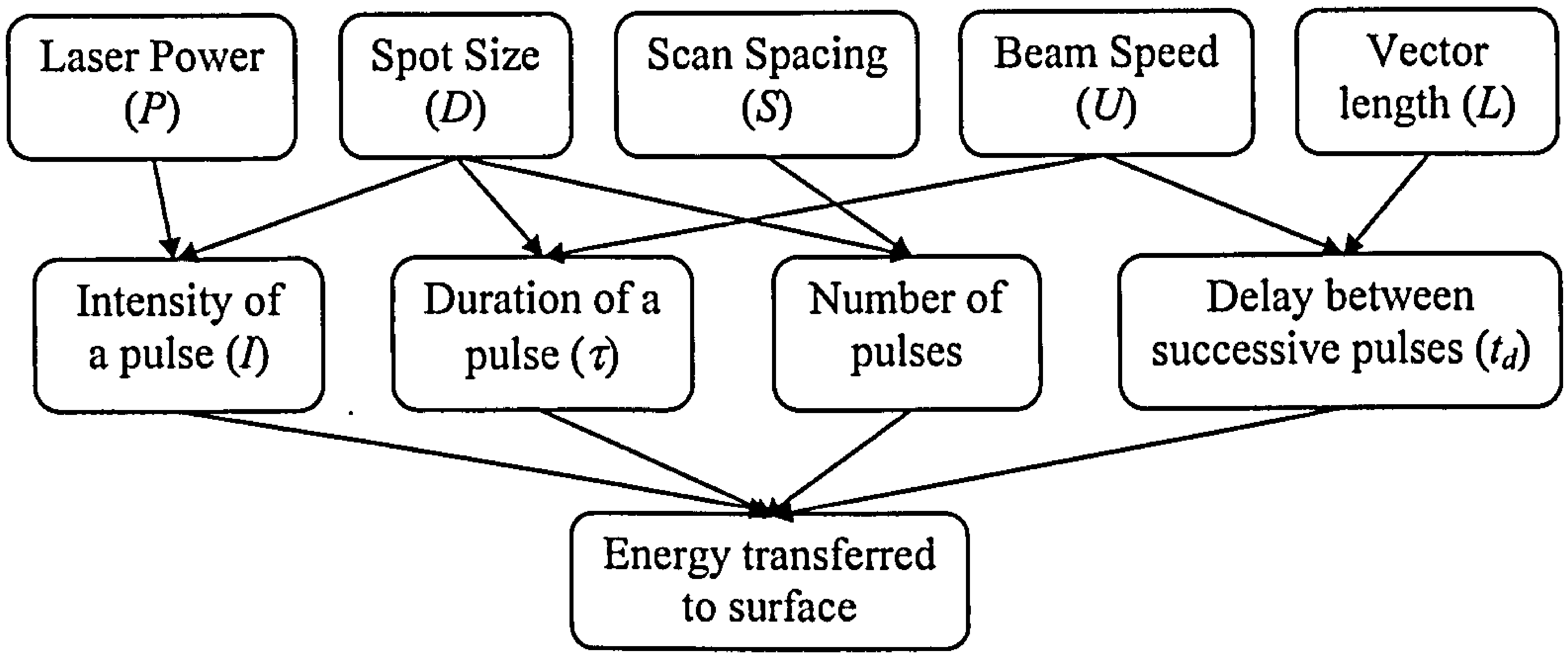

Figure 2.10 Influence of process parameters on energy transferred to surface of part bed. From [9].

2.2.5.2 Powder Layering Mechanism

The powder layering mechanism is made primarily of a roller, which is used to transport and level powder from one of the feed cartridges onto the build region. The roller counter rotates as it moves horizontally, i.e. the powder at the gap between the roller and the trailing edge of the powder mound is ejected towards the leading edge of the mound (see Figure 2.11). That allows the powder to be spread without transmitting shear stresses to the previously built-up layers [12]. The roller transverse speed is an adjustable machine parameter. If the roller speed is set too slow, the processing time increases. Conversely, setting the roller speed relatively high may result in the powder being pushed in front of the roller [11].

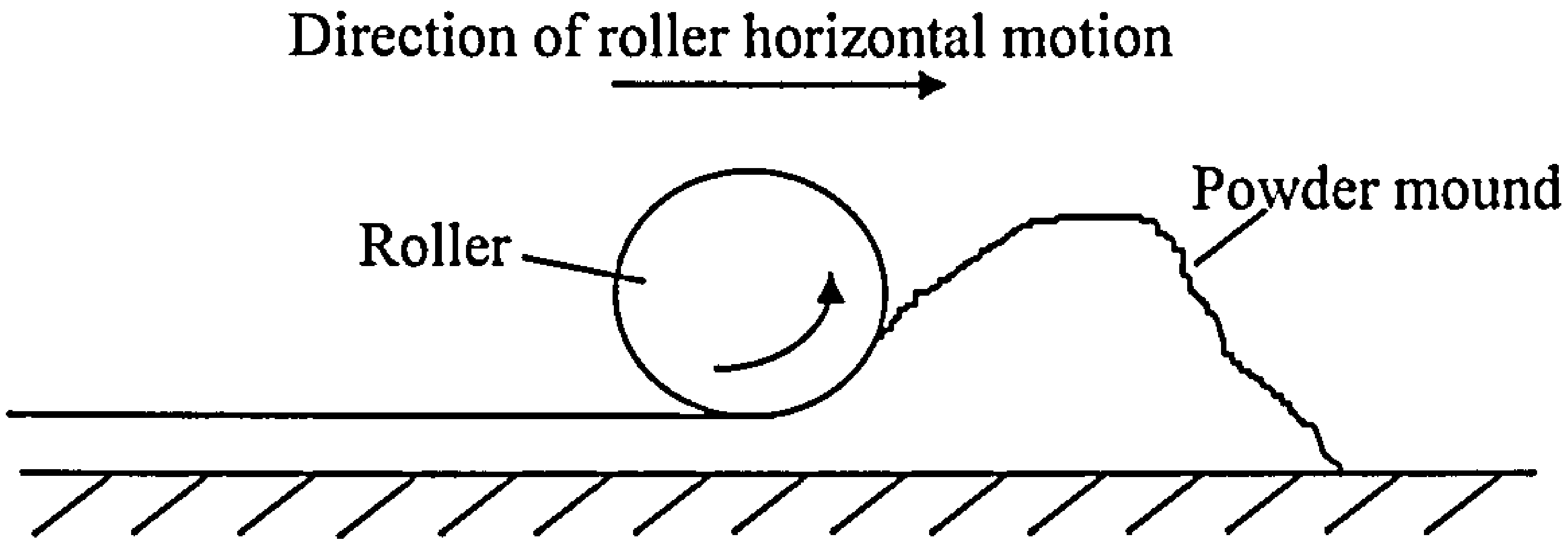

Figure 2.11 Levelling device in Selective Laser Sintering

The thickness of a layer is an adjustable machine parameter, which is controlled by the movement of the part piston. The default layer thickness set by DTM is 0.127mm, but can range from 0.076mm to 0.508mm [11]. An increase in the layer thickness reduces the production time but can also reduce the dimensional accuracy of fabricated parts with angled or curved surfaces. The reason being that these surfaces are approximated in SLS as stair-stepped surfaces as schematically illustrated in Figure 2.12.

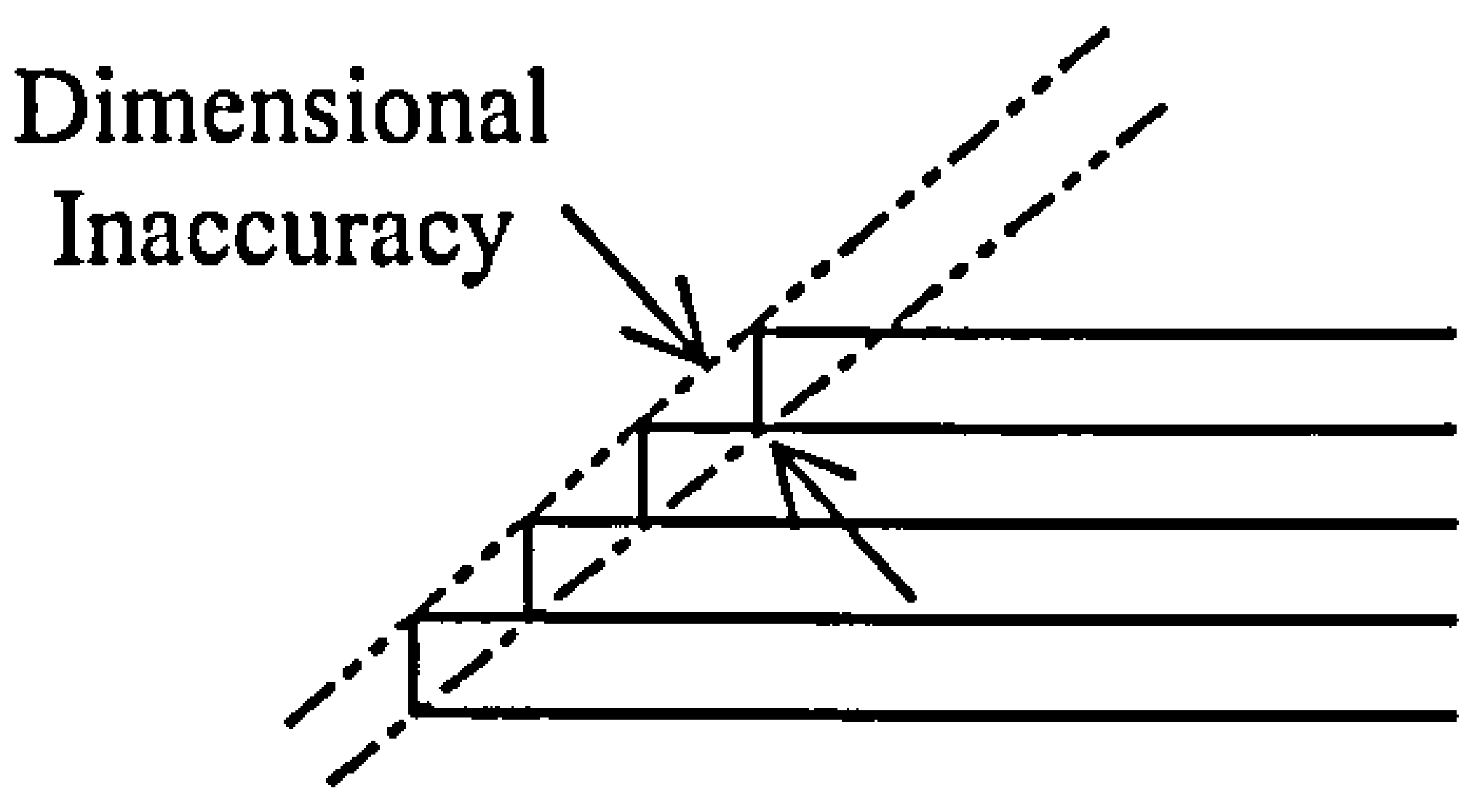

Figure 2.12.The dimensional inaccuracy developed due to stair steps when an angle sided surface is manufactured.

The SLS machine contains two powder-feed cartridges positioned on both sides of the part cylinder, as schematically shown in Figure 2.13. The powder in each feed cartridge is supported by a feed piston. After a layer is scanned by the laser, the part piston is lowered and a feed piston is raised. The roller then spreads the powder from the raised feed cartridge onto the build region. Excess powder transported across the part bed is deposited into an overflow cartridge.

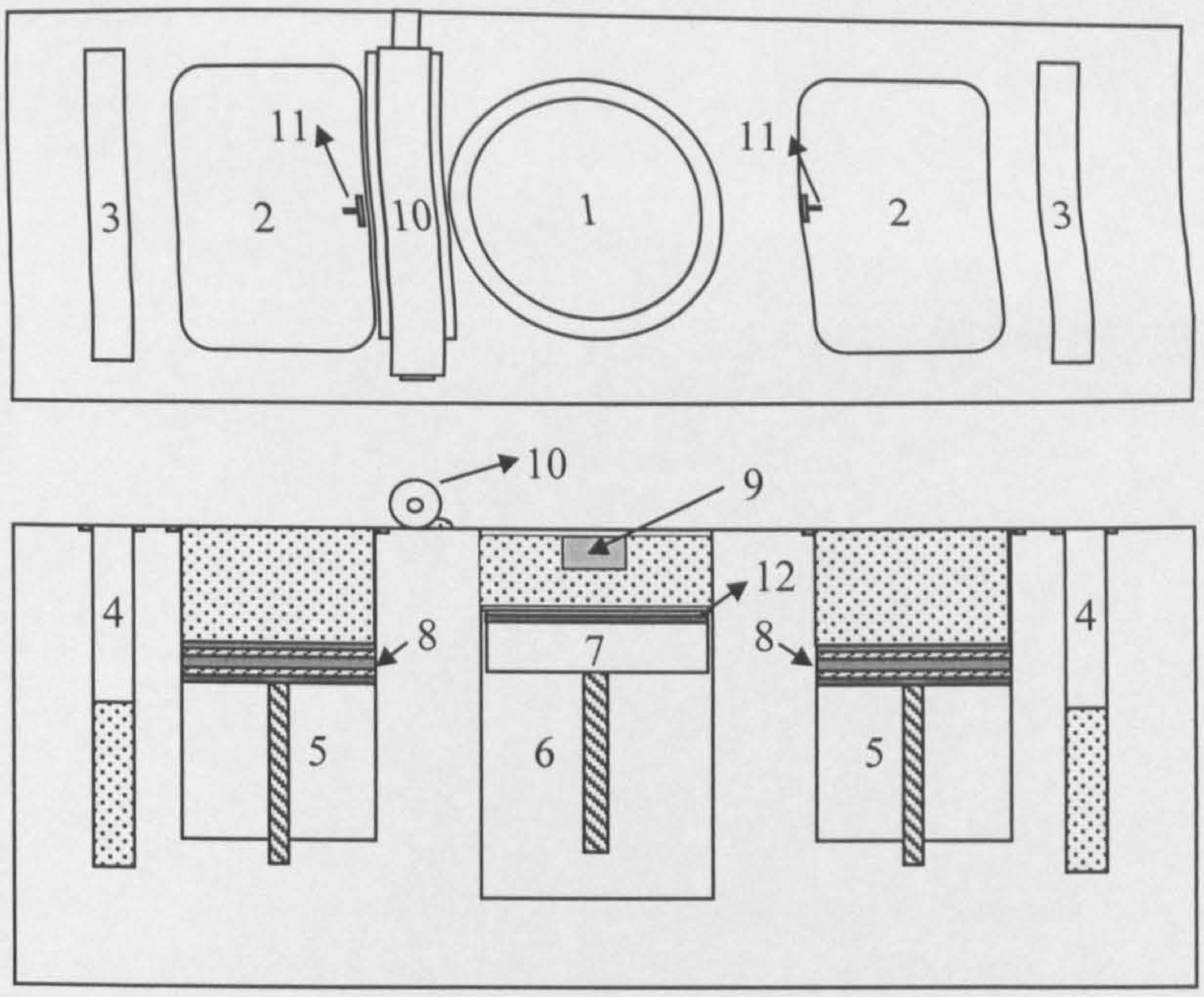

(1) Part bed.
(2) Powder feed cartridge opening.
(3) Overflow cartridge openings
(4) Overflow cartridges
(5) Powder feed cartridges
(6) Part cylinder
(7) Part piston
(8) Feed Piston
(9) Sintered layers
(10) Roller
(11) Thermocouples
(12) Part Piston heater

Figure 2.13 Internal view of the DTM Sinterstation 2000 machine

2.2.5.3 The Heater Control

The SLS machine uses three heaters to maintain and control the temperatures of the powder during the process. One heater is placed above the build area, termed the part heater, and a feed heater is positioned above each of the two powder-feed cartridges. The temperature at the top surface of the part bed is regularly monitored by an infrared (IR) heat sensor, whereas thermocouples measure the temperature at the top surface of the powder in the feed cartridges (see Figure 2.13). The heaters automatically switch on and off to maintain and regulate the measured temperature to the temperature set by the operator.

The SLS process consists of three stages; "warmup", "build" and "cooldown". In the "warmup" stage, the powder in the feed cartridges is initially heated to an initial set point temperature. No powder is spread by the roller during the initial heating of the powder. The first layer is then spread onto the part piston and is heated by the part heater. Subsequent layers are added with the temperature of the powder in the feed cartridges and that of added layers raised to the feed-heater and part heater set points.

In the "build" stage, the system maintains the temperature of the powder at the feed-heater and part heater set points. The set points are adjusted by the SLS machine operator according to the material used in fabrication. The feed heater set point generally represents the highest possible temperature at which the powder can flow freely when spread by the roller. The part heater set point is a temperature generally adjusted just below the glass transition temperature of amorphous polymers, or the melting temperature of crystalline polymers. The temperature is set to reduce additional laser energy needed to heat the powder to the fusing temperature.

In the "cooldown" stage, the heaters are switched off and the part bed is allowed to cool in the process chamber.

2.2.5.4 General Problems in SLS produced parts

Many SLS process parameters highly influence the quality of parts produced. DTM specifies default values for all process parameters according to the material used in fabrication. The operator can modify the process variables to change some of the physical properties of a fabricated part to suit application. However, many of the effects of process variables interact with one another, and a change in a process parameter may require alteration of the other parameters. It is therefore required to optimise the process parameters in an attempt to eliminate or at least reduce as many defects and geometrical inaccuracies as possible that may arise in fabricated parts. Common geometrical inaccuracies include bonus Z and curl and are introduced in following sections.

2.2.5.4.1 Bonus Z

Bonus Z is a phenomenon identified when the thickness of the fabricated part (in the *z*-direction) is larger than its intended thickness (see Figure 2.14). It occurs due to additional material being sintered early in the build as a result of the large thermal penetration into the part bed. As a corrective measure, DTM recommends reducing the laser power during fabrication of the first few layers of the part [13].

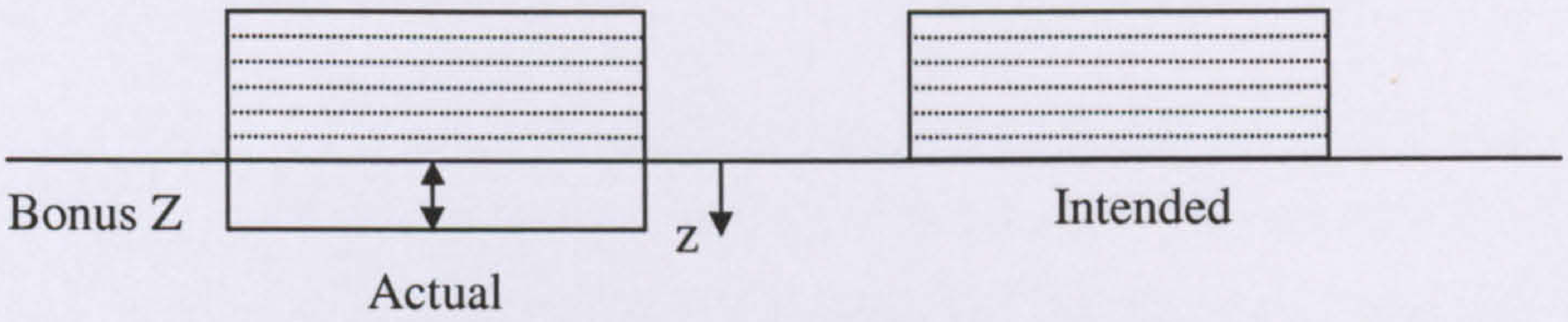

Figure 2.14 A schematic view of Bonus Z

2.2.5.4.2 Curl

Curl is identified when the downward facing surfaces of a part, intended to be flat, exhibit a curved profile close to their free edges. The fabricated part may also become thinner (in the *z*-direction) in the curled regions (see Figure 2.15). Curl is attributed to uneven shrinkages that generate in different regions of the build. It develops during the SLS "build" stage and may also develop during the "cooldown" stage.

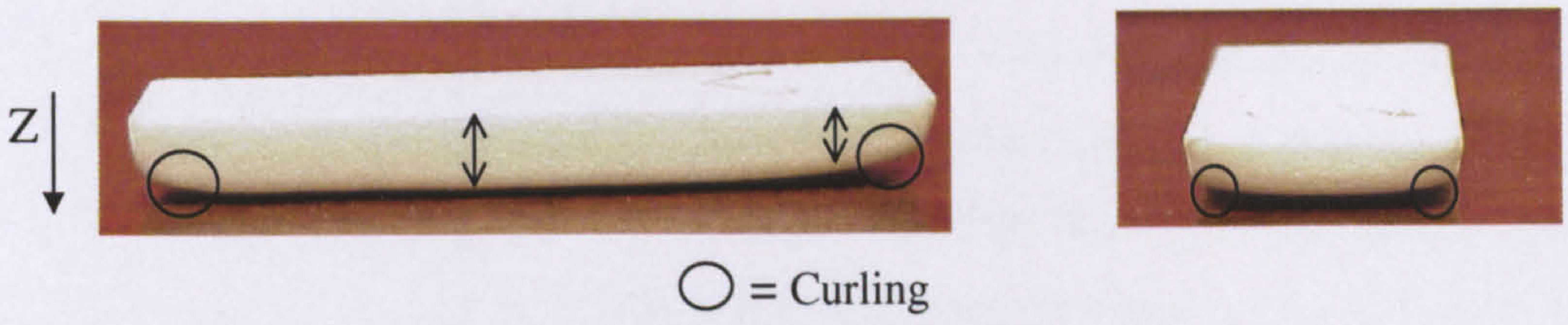

Figure 2.15 Curl developed in an SLS fabricated polycarbonate part

In the "build" stage, curl is seen to develop following addition of fresh powder on the top surface of a recently sintered layer. If the feed-heater set points are extremely low, the upper regions of the recently sintered layer will experience a large drop in temperature after powder addition. This is expected to result in the upper most regions of the layer to experience more shrinkage than other regions in the build, causing the build to curl (see Figure 2.16). However, severe curling may result in the build to shift as the roller passes over. In this condition, it becomes essential to terminate the process.

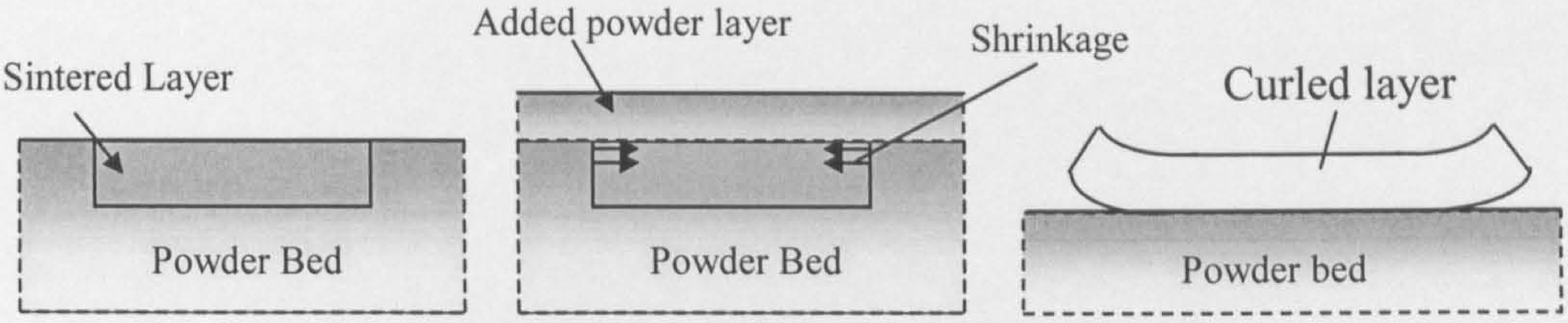

Figure 2.16 Curling developed when fresh powder is added on top of a recently sintered layer

As a corrective measure for curl, DTM recommends the feed powder to be heated to the highest possible temperature, yet ensuring that the powder can flow freely when spread by the roller. Additionally, increasing the powder bed temperature may reduce the heat transfer from the build to the powder bed. This may decrease the differential shrinkages that may arise in the build during processing, causing curl to reduce. However, if the temperature of the powder bed is greatly increased, the support powder can fuse making part breakout difficult or even impossible.

Curl may also develop due to excessive cooling rates that take place in a part following its fabrication, i.e. during the "cooldown" stage. That occurs when the heaters are switched off or if the sintered part is removed from the chamber prematurely.

Curl can also be reduced in parts made of amorphous polymers (such as polycarbonate) by using bases. A base is a lightly sintered material, which is normally made of three or four layers, and constructed directly below all downward facing surfaces of the part [14]. The base bonds to the first layer of the part when the layer is sintered. Bases are made strong to constrain shrinkage of the first layer and maintain its flatness. However, they should also be weak enough to be removed without causing damage to the part [1].

Curl was also reported to vary according to the position of the part in the part bed [15]. Typically, the part piston and cylinder wall surfaces are cooler than the sintered parts and their surrounding powder. Therefore, parts placed close to these surfaces were seen to experience more curl than in other positions in the part bed due to the heterogeneous cooling taking place within the part [1]. However, the temperature of the part piston can be raised by activating the part piston heater. In regions distant from the part piston and cylinder wall, temperature gradients in the part can be reduced by percolating gas through the porous powder bed; a practice termed downdraft. The temperature at the top surface of the part bed, which is heated by the part heater, is high compared to other regions in the bed. As the gas is drawn through, cooling of the build in the bed is retarded by actively supplying heat to the part and the bed.

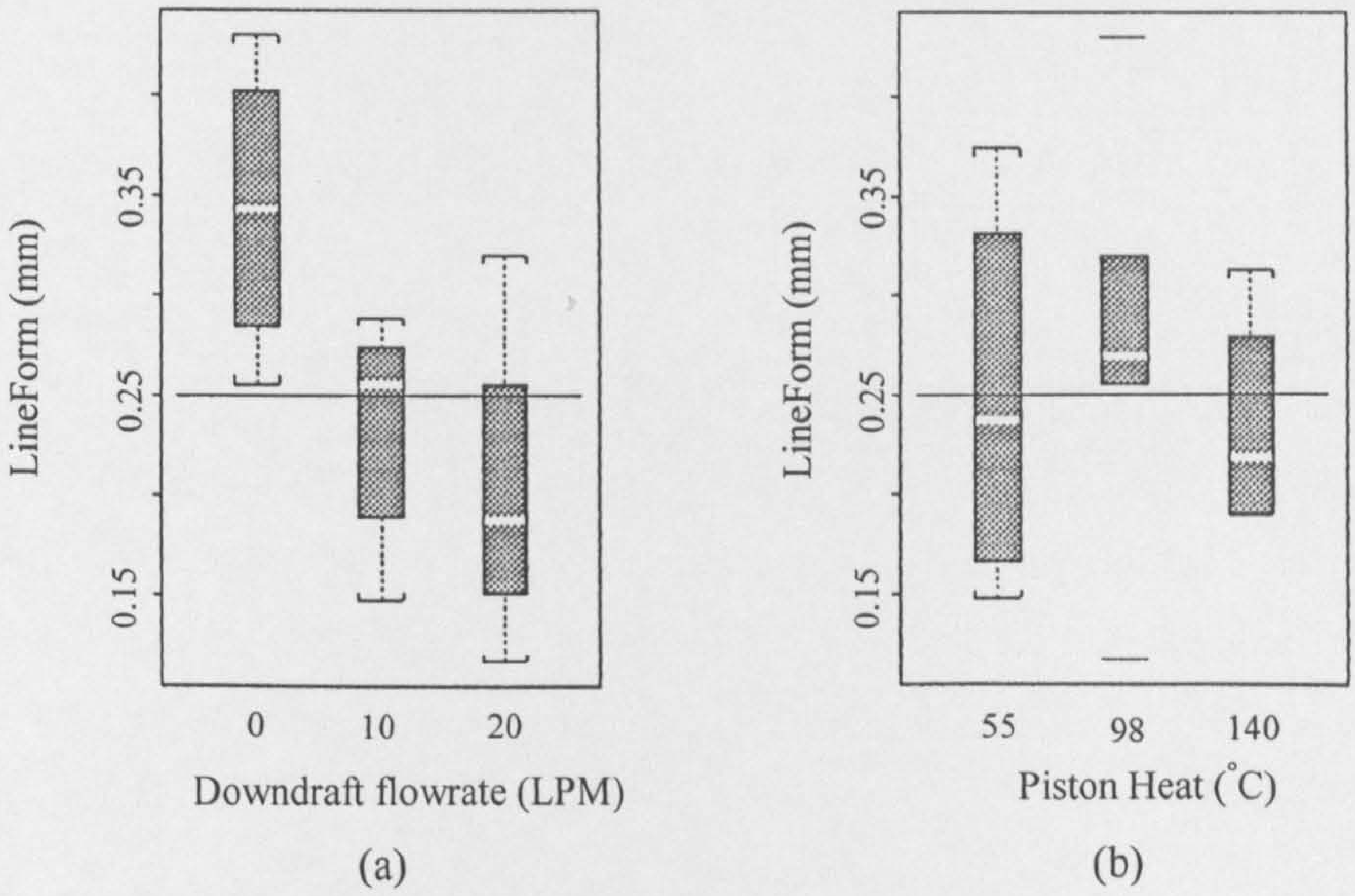

Figure 2.17 Effect of downdraft flow rate and piston heater temperature on the Lineform of a two-layer SLS fabricated nylon part. From [15].

In a previous study [15], the effects of the part piston temperature and the downdraft flow rate on curling of two-layer nylon parts were examined. The parts were 185mm long and 135mm wide, fabricated approximately 40mm from the part piston surface. Part curling was characterised in the study by measuring the line form, which is taken as the deviation of the bottom surface of the parts from a theoretical flat plane. Results obtained in the study are illustrated in Figures 2.17*a* and *b*. The upper and lower brackets in the figures symbolise 5% of the data whereas the box represents 50% of the data. The data in Figure 2.17*b* showed that an increase in the piston temperature had an insignificant effect on curl, when the fabricated parts were positioned at the distance of 40mm from the piston surface. That was attributed to the excellent insulating properties of the nylon powder. Conversely, the impact of downdraft on curl was apparent; the higher the downdraft flow rate was the less curl became (see Figure 2.17*a*).

2.2.5.5 Materials Used in SLS and Their Applications

The SLS process is not limited to a specific class of materials. In theory, a wide range of powder-based thermoplastics, composites, ceramics and metals can be used to produce parts in SLS. The main types of materials used in the process include the following:

- Wax (LWX2010): This is typically used in SLS to create wax patterns, which are then employed in investment casting to produce metal prototypes and cast tooling [16]. The wax powder particles are spherical and have an average diameter of 105 micrometers [17].

- Nylon: The SLS process uses two types of nylon products; LN4010 which has a mean particle size of 120 micrometers, and LNF5000 which has a mean size of 50 micrometers [17]. The particle shape of both products is substantially spherical. Nylon is used in SLS to create models and prototypes that can perform in a demanding environment. The parts produced are durable and offer substantial heat and chemical resistance. The fine particle sized nylon produces parts with improved small feature details and edge definitions, which becomes apparent when complex parts are fabricated.

- Metals: Metal parts in SLS are currently produced through an indirect sintering process. The metal powder is coated with a thermoplastic binder. During processing, the laser only melts the polymer coating. This causes polymer necks to develop between the particles, and a solid mass, termed a green part, is produced. The part is then post-processed in an oven where the polymer coating is removed and the steel powder is sintered [17]. However, as the green part is not fully dense, large shrinkages may happen during post-processing. That can be reduced by infiltrating the part with copper or bronze resulting in a fully dense part. The process is mainly employed in creation of mould cavities and core inserts for Rapid tooling [16].

- Polycarbonate (LPC3000): The SLS polycarbonate particles are irregular in shape and have a mean diameter of 90 micrometers. The produced parts have an interconnected pore structure and hold moderate strength and durability. They are very easy to finish and are used to create concept and functional models. If required, the mechanical properties and surface appearance can be improved by infiltrating the parts with an epoxy resin [17]. The SLS polycarbonate parts are also used in investment casting of metal prototypes. The porous structure of the polycarbonate parts allows them not to sufficiently expand to cause ceramic shell cracking. In contrast, fully dense parts are not suitable for investment casting due to their large expansion during the polymer removal process. Polycarbonate patterns are more durable and less temperature sensitive than wax patterns, which facilitates handling and shipping of the parts.

2.3 Material Properties

The work presented in this thesis focuses on polycarbonate parts produced in SLS. In the process, the polymer goes through extreme changes in temperatures. These changes in temperature result in changes in the physical properties of the polymer. In following sections, a brief description of some of these physical properties is given. In addition, an effort is made to show how such properties are influenced when the temperature of the polymer is changed.

Polymers include a large class of materials such as plastics, rubbers and adhesives. The process in which polymers are produced is known as polymerisation. In the process, small molecules, termed monomers, join together to create a polymer chain [18]. If only one type of monomer is used in the polymer formation, the resulting molecule is called a homopolymer. However, superior properties can be obtained if different types of monomers are employed in the polymer formation. In this case, the resulting molecule is termed a copolymer [19]. Polyethylene is the most common and simply structured homopolymer. The monomer used in forming polyethylene is ethylene, which is a gas and has the formula C_2H_4. The polymer chain consists of a backbone of carbon atoms, whereby each carbon atom is bonded to two hydrogen atoms, as illustrated in Figure 2.18.

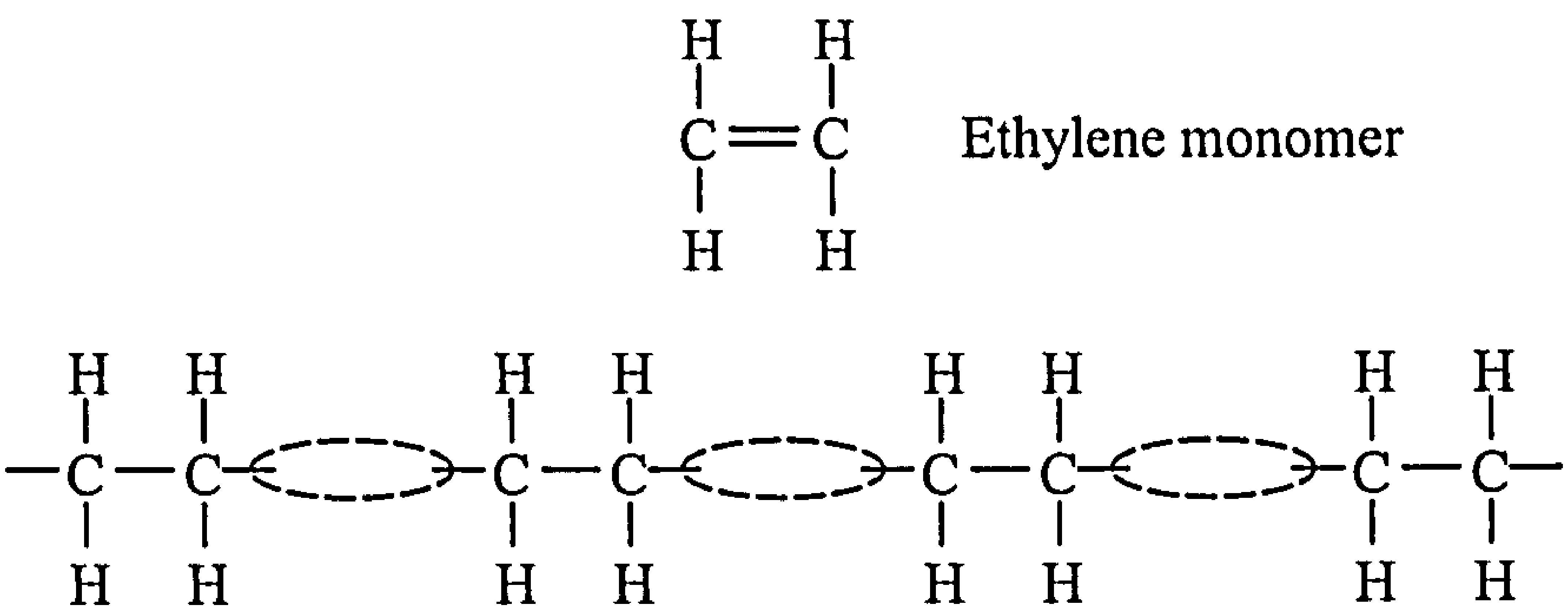

Figure 2.18 The chemical structure of polyethylene

An example of a copolymer is polycarbonate bis-phenol A. The polymer chain is made of repeated units of methyl and phenyl groups [20]. The chemical structure of polycarbonate bis-phenol A is shown in Figure 2.19*a*. In the figure, the methyl group is denoted CH_3, while the phenyl groups are symbolised by the two six-sided structures. The phenyl groups have the formula C_6H_5, and their chemical structure is illustrated in Figure 2.19*b*.

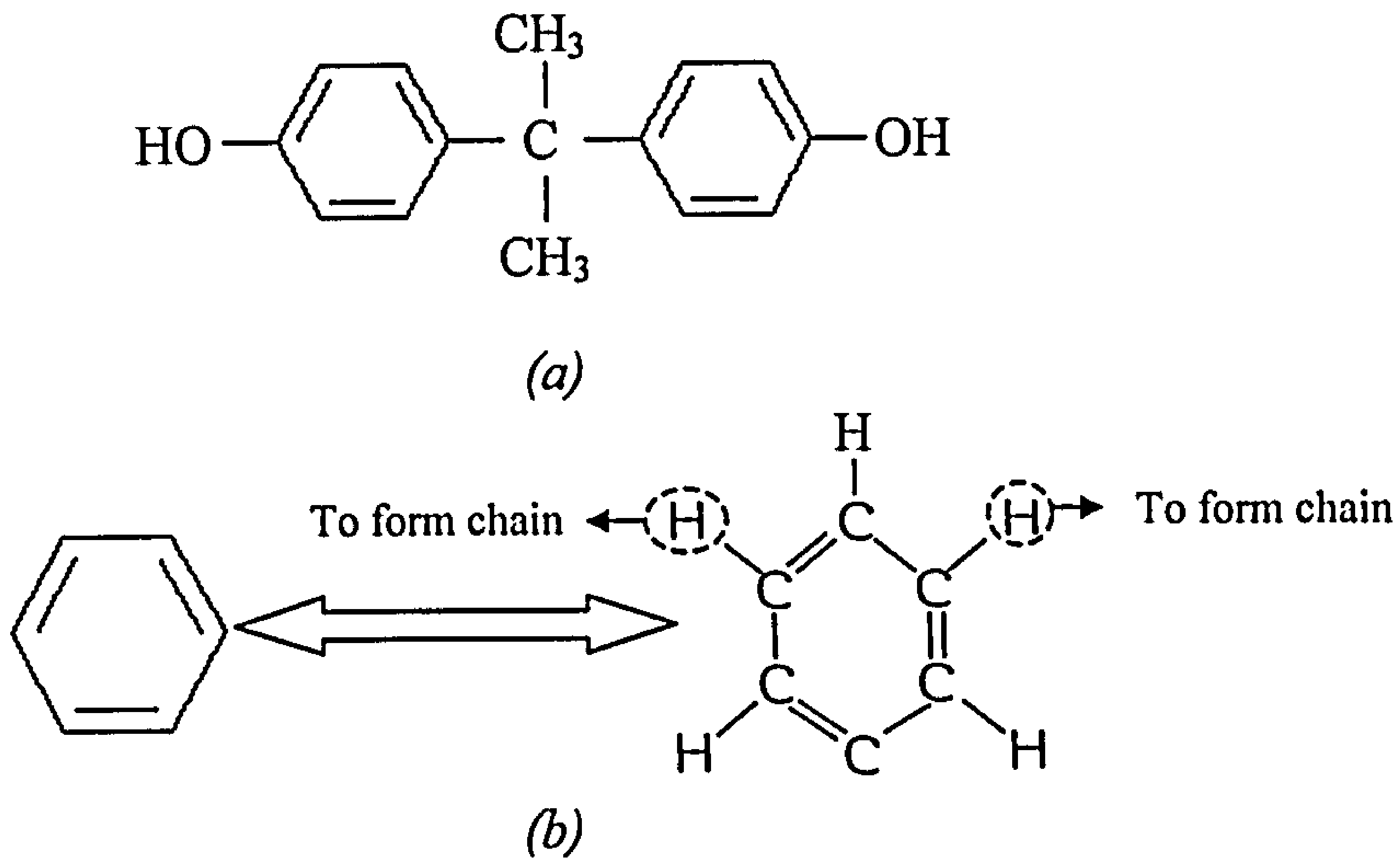

Figure 2.19 (a) The chemical structure of polycarbonate bis-phenol A (b) The chemical representation of a phenyl group structure.

The presence of the phenyl and the two methyl side groups in the molecular chain has a large influence on the properties of the polymer. The high attractions between these groups in the polymer chains contribute to the lack of mobility of the individual molecules. This results in the polymer having a high melting point and a relatively high viscosity when melted. The high stiffness of the chains also prevents polycarbonate from developing a crystalline structure, causing the polymer to exhibit an amorphous molecular formation.

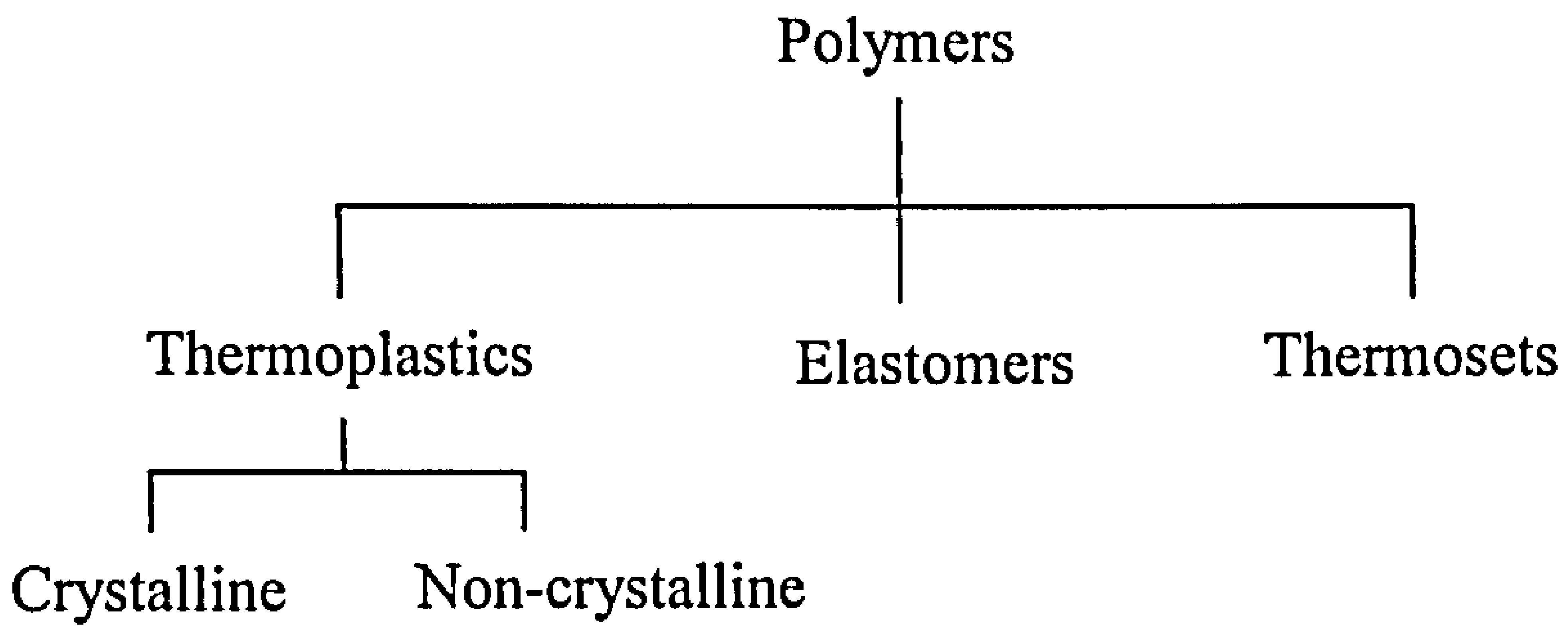

Figure 2.20 Classification of polymers

Polymers are classified according to their properties into three main categories; thermoplastics, thermosets and elastomers. Additionally, thermoplastics are separated into crystalline and non-crystalline (amorphous) polymers [19]. The classification of polymers is outlined in Figure 2.20.

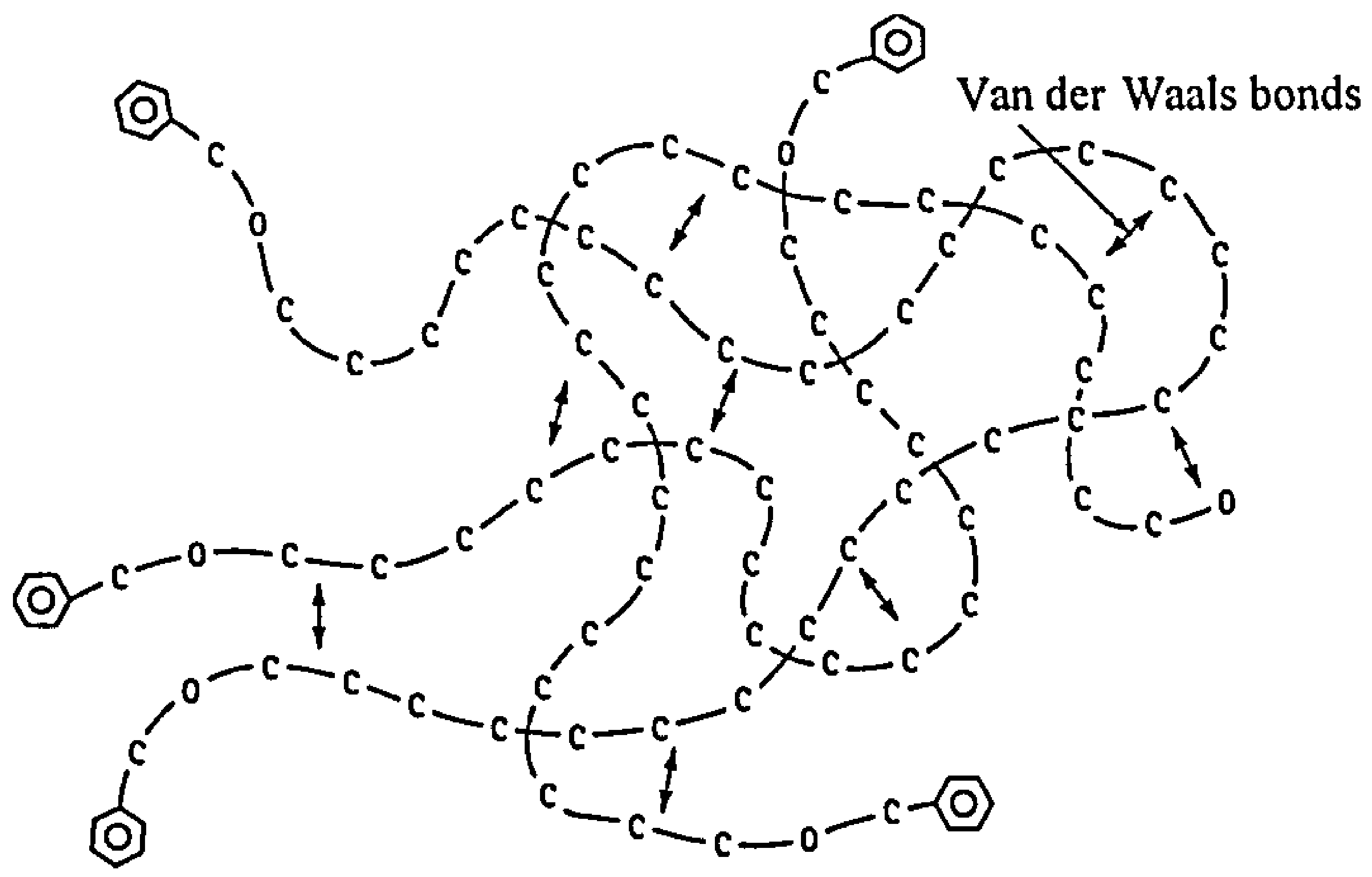

Figure 2.21 Thermoplastic polymer: chains held loosely together by van der Waal bonds and mechanical entanglement. From [21].

Thermoplastics can be melted upon the application of heat. Although bonding within the coiled chains is covalent, the polymer chains are held to one another by weak secondary bonding, Van der Waals bonds, and by entanglements [21] (see Figure 2.21). At and above the melting temperature, bonding between the twisted chains is weak. This result in the chains passing one another upon the application of force, causing the polymer to flow. In this state, the strength and modulus of elasticity of the polymer are almost zero, and the polymer is suitable for forming.

Below the melting point, many thermoplastics partially crystallise, i.e. the coiled polymer chains in the liquid state rearrange into a more orderly close packed structure (see Figure 2.22). Polyethylene is a polymer that shows a high degree of crystalline order when cooled. As polymers that have crystalline regions also consist of some amorphous zones, they are often termed semi-crystalline polymers.

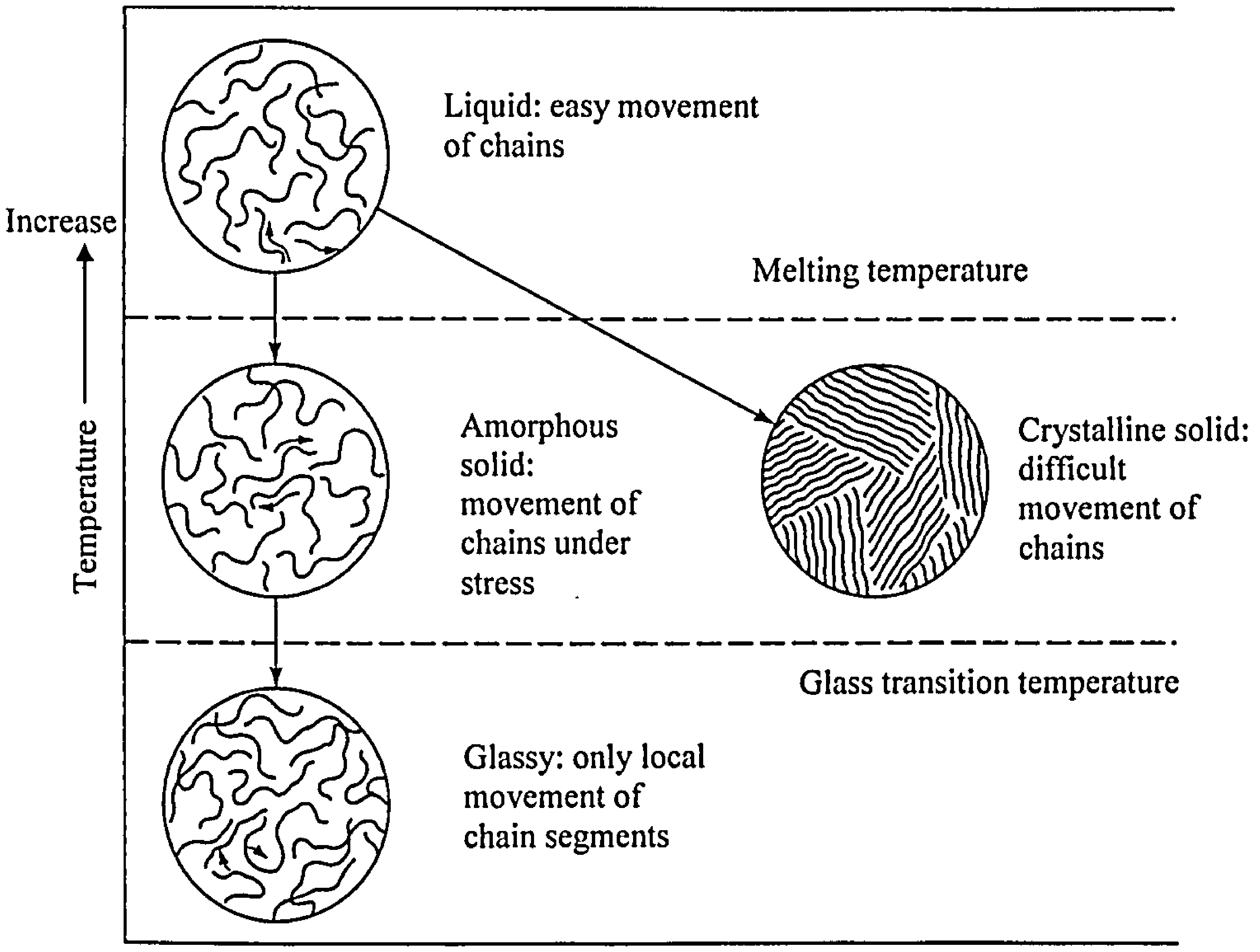

Figure 2.22 The effect of temperature on the structure and behaviour of thermoplastic polymers. From [21].

In contrast, non-crystalline polymer chains remain twisted at temperatures below the melting point and the polymer continues to have an amorphous structure. At temperatures just below the melting point, the polymer behaves in a rubbery manner, and bonding between the polymer chains is weak. Permanent deformation occurs when load is applied on the polymer and then removed. However, bonding between the polymer chains becomes stronger as the temperature is further reduced. Below a temperature, termed the glass transition temperature T_g, the polymer becomes hard, and a large increase in the elastic modulus occurs. The change in the structure of an amorphous polymer with temperature is shown in Figure 2.22.

Elastomers, however, can stretch to enormous extensions without permanent change in shape. That is due to the cross-links that exist between the polymer chains. Upon the application of load, the molecules slide past each other, but the cross-links prevent permanent flow, and the molecules spring back to their original position when the load is removed.

Thermosetting polymers are composed of long chains of molecules that are strongly cross-linked to one another. In general, these polymers are more rigid, but are more brittle than thermoplastics. The presence of cross-links in both thermosetting and elastomer polymers implies that melting does not occurs, and these polymers degrade instead [21]. The general structures of both elastomer and thermosetting polymers are shown in Figure 2.23.

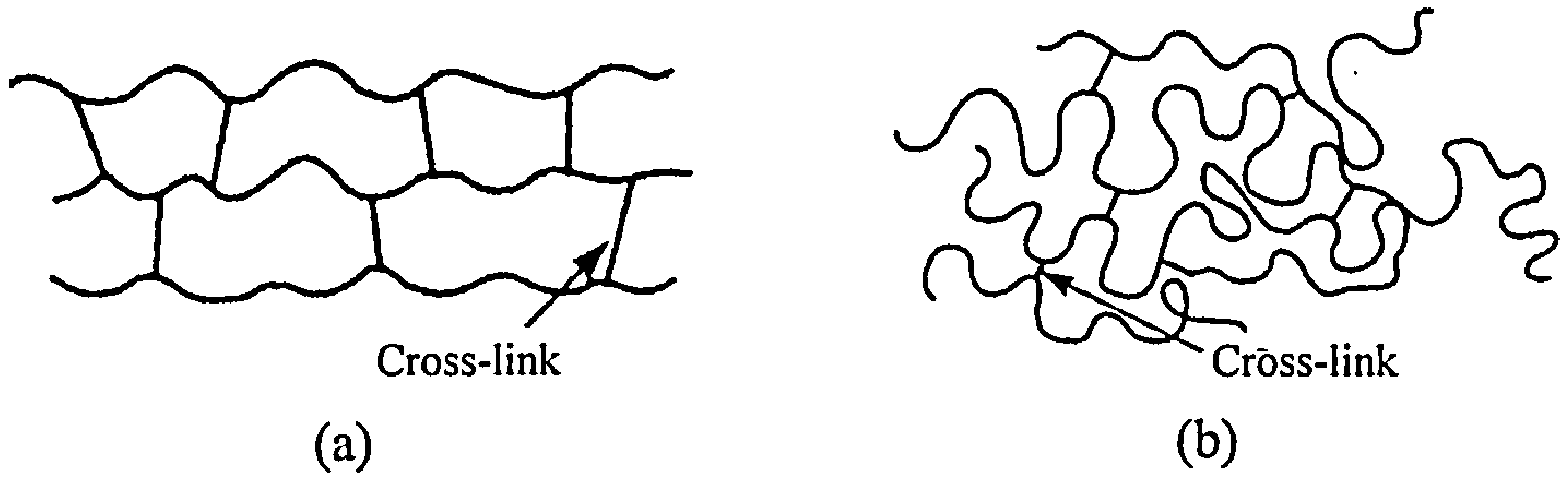

Figure 2.23 (a) Thermosetting structure (b) Elastomer structure

2.3.1 Viscoelastic Polymers

As polycarbonate, which is the subject of this study, is an amorphous polymer, the focus in following sections is to describe a number of physical properties related to amorphous polymers. Amorphous polymers have a unique feature in their mechanical behaviour in that their response to an applied load or strain depends on the rate and time period of application. This dependency is not observed in the behaviour of elastic solids. Elastic solids at low strains obey Hook's law, whereby the stress is proportional to the strain but is independent on the rate of loading. Conversely, the behaviour of fluids is completely time-dependent. Their behaviour at low strains can be expressed by Newton's law, whereby the stress is proportional to the strain rate but is independent of the strain. The behaviour of amorphous polymers is somewhere between that of elastic solids and liquids. At low temperatures and at high strain rates the polymer behaves like an elastic solid. However, at high temperatures and (or) low strain rates, the polymer behaves in a viscous manner and flows like a liquid. Amorphous polymers are hence termed viscoelastic polymers as they show both viscous and elastic types of behaviour [22].

It has now been established that temperature and time influence the behaviour of amorphous polymers. To gain a better understanding of how these two factors contribute to the behaviour of the polymer, each will be individually discussed. Following on from that, their combined effects will be explained.

2.3.1.1 Temperature Dependent Behaviour of Viscoelastic Polymers

Amorphous polymers show a large change in their properties when their temperature is changed. As the polymer is heated, it changes from a glassy state to a soft rubbery state. The effect of the change in temperature on the elastic modulus of an amorphous polymer is schematically illustrated in Figure 2.24. At low temperatures, below the glass transition temperature (T_g), the polymer is in a glassy state. As the temperature is increased whilst still below T_g, the polymer goes through a number of secondary transitions in which a slight decrease in the modulus is exhibited [23]. However, a primary transition takes place at T_g, and a large drop in the modulus takes place. In most references, T_g is generally reported as a single temperature value. However, it practically represents a range of temperatures in the range of $T_g \pm (5\text{-}10^{\circ}C)$ [24]. This temperature range is termed the glass transition region.

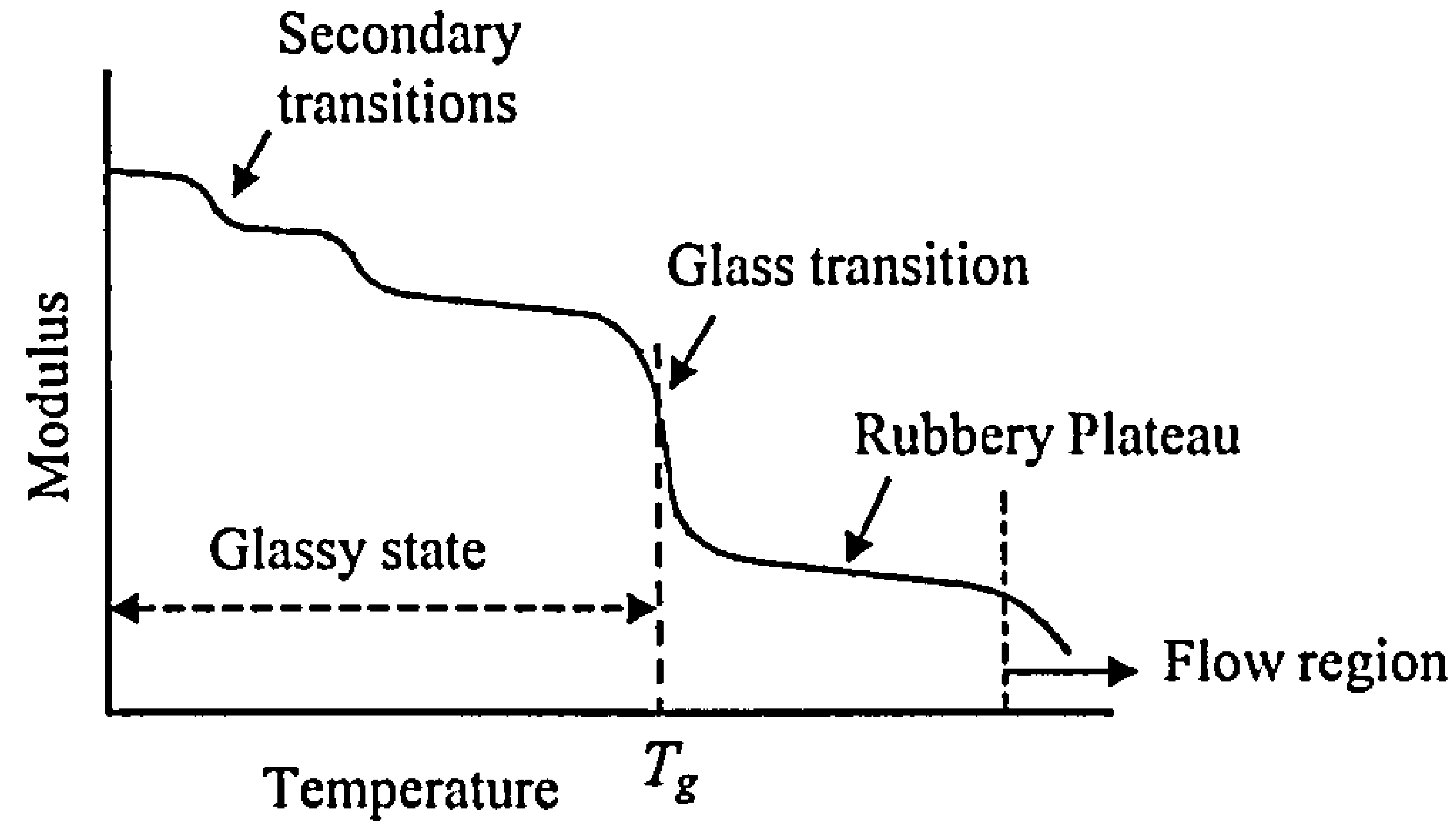

Figure 2.24 Modulus variation with temperature of a typical amorphous polymer.

Figure 2.25 shows the load-elongation curves of an amorphous polymer, stretched at identical strain rates, but at four different temperatures. At temperatures well below T_g, as demonstrated by curve (A), the polymer behaves as a brittle solid; the load rises almost linearly with respect to elongation, and fracture takes place at strains as low as 10%. At higher temperatures, but still below T_g, illustrated by curve (B), the polymer behaves as a ductile material; a yield point can be identified before fracture. At slightly higher temperatures, but still maintained below T_g, as shown by curve (C), a yield point can still be noticed and necking occurs with a decrease in the load. A further increase in the applied strain causes the load to fall to a constant level and strains of the order of 300-1000% can be observed. That is ultimately followed by an increase in the load and fracture finally occurs. However, at temperatures above T_g, as demonstrated by curve (D), the polymer behaves like a rubber. The load rises to the breaking point with a sigmoidal relationship with respect to elongation and rupture occurs at very high strains [23].

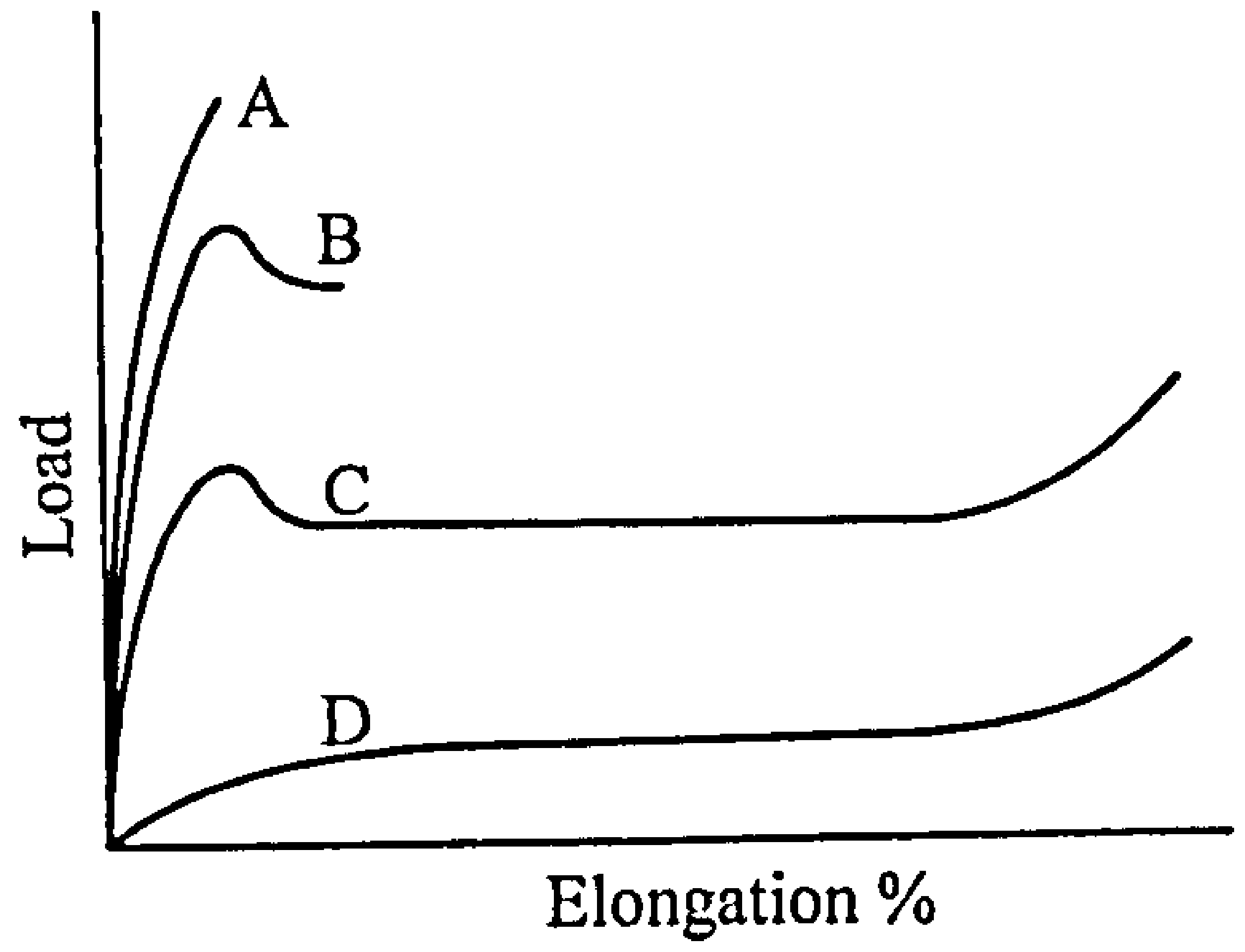

Figure 2.25 Load-elongation curves of a polymer stretched at different temperatures. Curve A, brittle fracture; curve B, ductile failure; curve C, necking; curve D, rubber-like behaviour. From [23].

2.3.1.2 Time Dependent Behaviour of viscoelastic polymers

A method generally used to study the influence of time on the behaviour of a polymer is a creep test. In the test, a polymer specimen is subjected to a constant load, over a long period of time, and at a constant temperature, and the change in elongation with time is recorded.

While the polymer specimen is loaded in a creep test, it experiences both elastic and plastic deformations. When the load is removed, the specimen is left with a measurable amount of elongation. If the specimen is reloaded in the same previous way, and then unloaded, the specimen would undergo even a higher elongation than that exhibited prior to the second loading. This is due to the failure of the polymer to return to its normal structure and stress distribution, immediately after the first loading is released. However, if the specimen is allowed sufficient time between the two loadings, the elongation from the first and second loadings will be the same, under identical testing conditions [23].

Several mechanical models were developed to explain the time-dependent behaviour of viscoelastic polymers. The models consist of two basic components; a spring element to describe the elastic behaviour of the polymer and a dashpot filled with a Newtonian fluid to describe its time-dependent response. An example of a simple mechanical model is shown in Figure 2.26 [18]. The model will be used here to describe the strain-time relationship, illustrated in Figure 2.27, of an amorphous polymer in a creep test. The corresponding stress-time relationship is displayed in Figure 2.28.

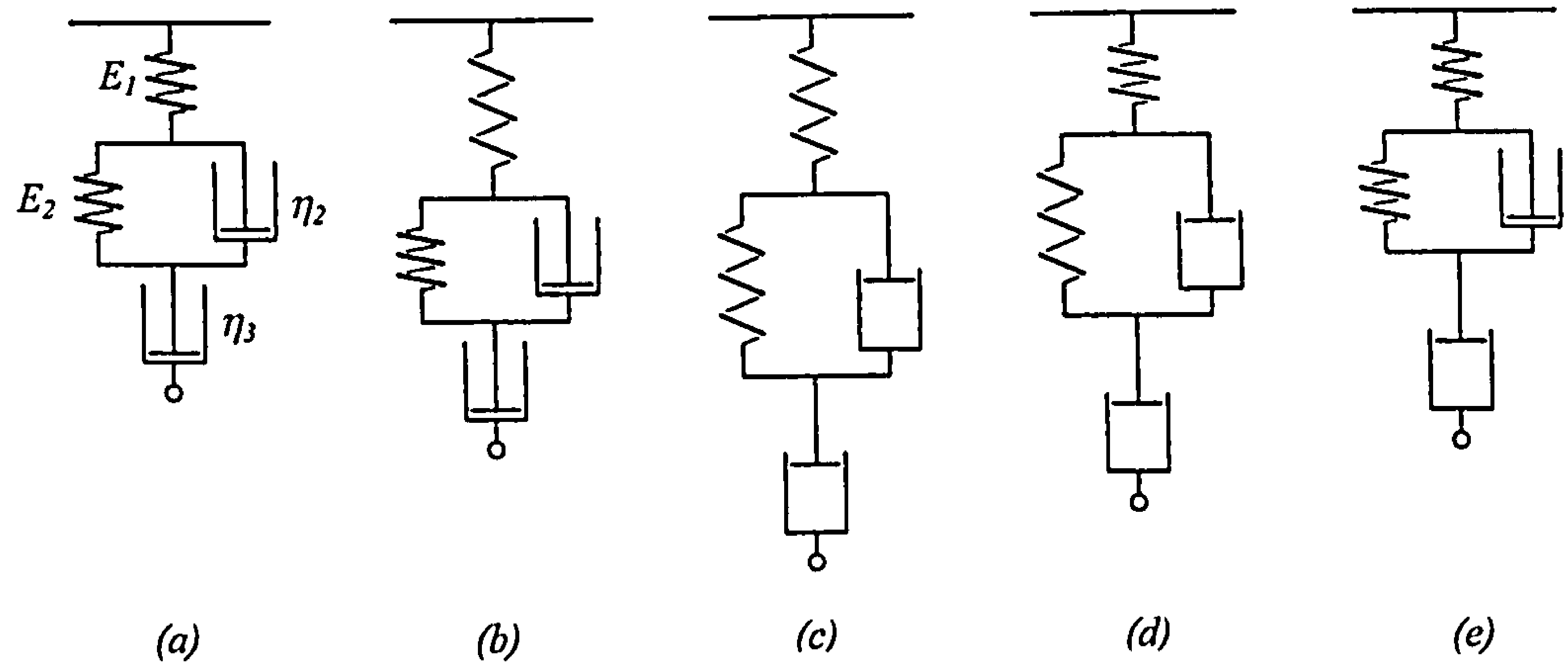

Figure 2.26 A mechanical model used in interpretation of the strain-time curve of a polymer in a creep test, illustrated in Figure 2.27. From [18].

First, it is essential to examine the strain response (ε) to a constant stress (σ), for each of the spring and dashpot elements individually. For the elastic element, the strain is instantaneous upon the application of load, and is time-independent. Considering (E) to denote the modulus of the elastic element, the strain can be expressed in terms of the stress as $\varepsilon = (1/E)\sigma$. Conversely, for the dashpot, the strain is linear with time, and can be expressed in terms of the viscosity (η) as $d\varepsilon/dt = (1/\eta)\sigma$ [28].

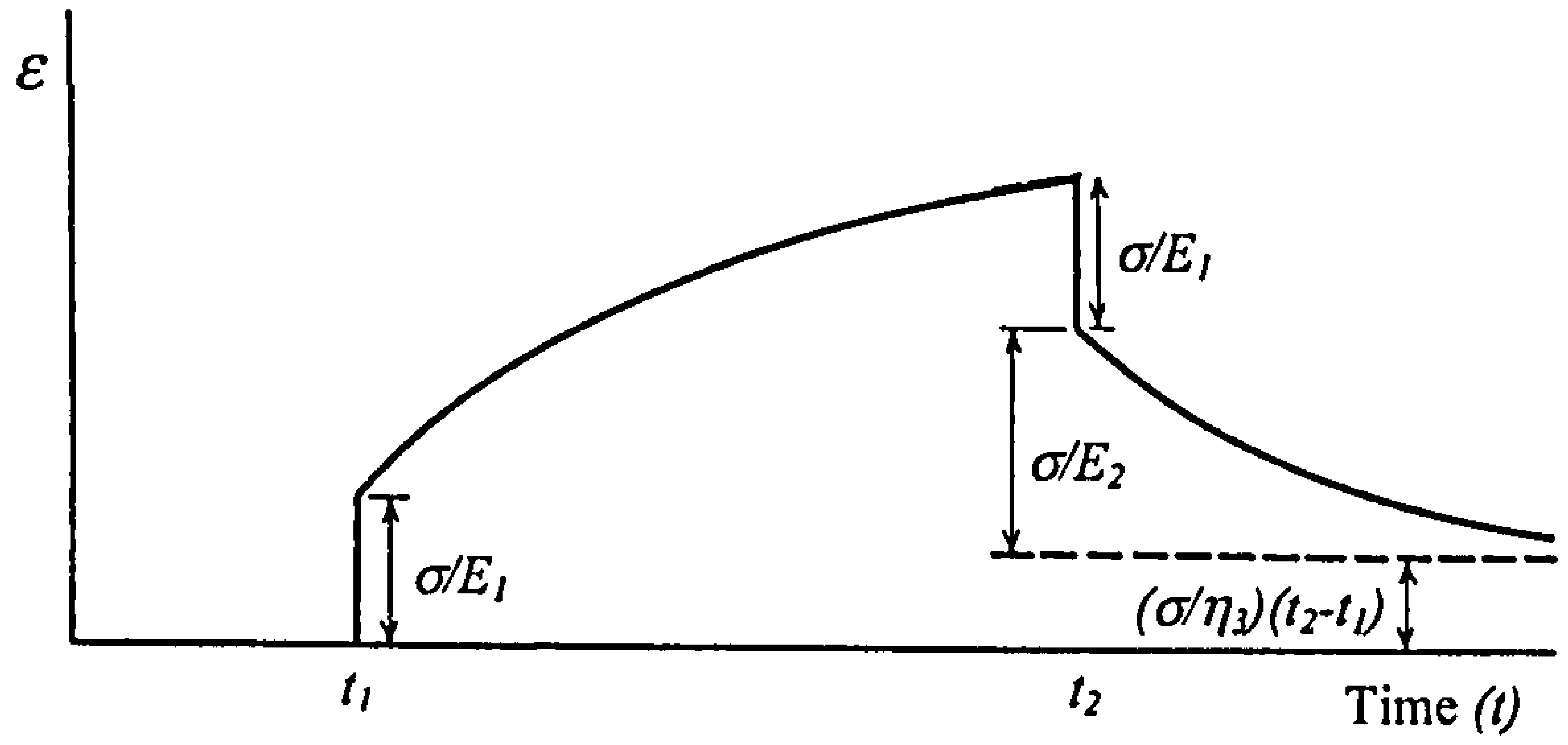

Figure 2.27 Strain-time relationship for a generalised mechanical model in a creep test combining elasticity, viscoelasticity, and flow [18]

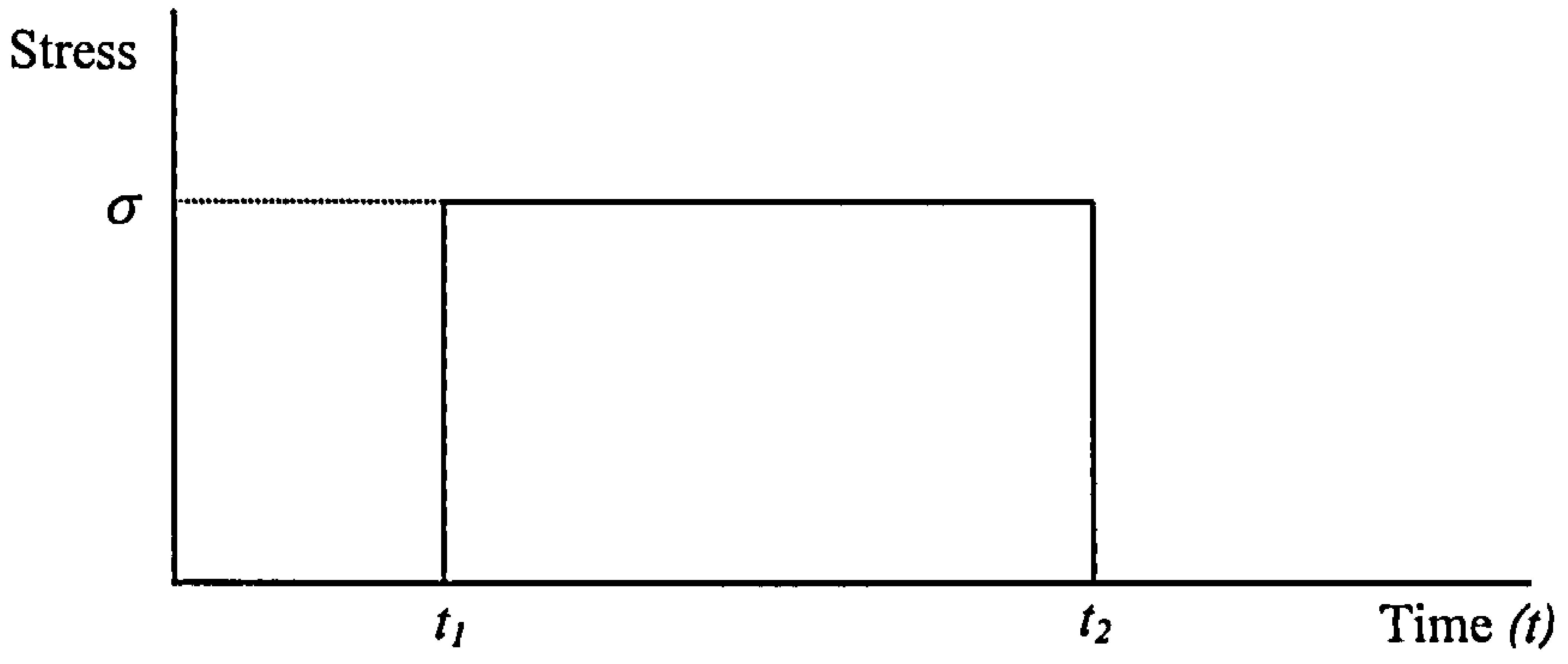

Figure 2.28 Stress-time relationship in a creep test.

When the mechanical model, illustrated in Figure 2.26, is loaded at time t_1, so that the stress experienced is (σ) (see Figure 2.28), the model undergoes an immediate strain equal to σ/E_1 (see Figure 2.27). This behaviour is termed the *immediate* elastic response of the polymer, and is reflected in the model by the extension of the spring with modulus E_1 (see Figure 2.26*b*). The viscoelastic response then follows, which is shown in Figure 2.26*c* by extension of the spring and the dashpot elements that are in parallel. In that period, the dashpot acts as a damping resistance to the establishment of equilibrium in the spring. However, these two components reach equilibrium, after a period, when their strain approaches σ/E_2. As the response of the elastic element with modulus E_2 is not immediate, it is termed the *delayed* elastic modulus. That is then proceeded by a viscous strain at the rate of (σ/η_3), and is characterised in the model by the extension of the dashpot with viscosity η_3, as illustrated in Figure 2.26*c*. On the removal of the load at time t_2 (see Figure 2.28), the elastic element with modulus E_1 relaxes immediately as shown in Figure 2.26*(d)*. This is then followed slowly by the viscoelastic response, which is the response of the elastic element and dashpot that are in parallel, but the viscous flow with viscosity η_3 is never recovered (see Figure 2.26*e*).

Figure 2.29 shows the typical change in the elastic modulus of an amorphous polymer during a creep test, with the temperature of the polymer held constant. At short experimental times, the polymer is in a glassy state, and the modulus is generally in the order of 10^9N/m^2, and is time-independent. At very long experimental times, the polymer is in a rubbery state, and the modulus is usually in the order of 10^5N/m^2, and is also time-independent. However, at intermediate times, the polymer is in a viscoelastic state. In that state, the modulus lies in between the glassy elastic modulus and that at the rubbery state, and is time-dependent. If the polymer is left for an extremely long period to creep, the polymer becomes viscous, and flow happens [23].

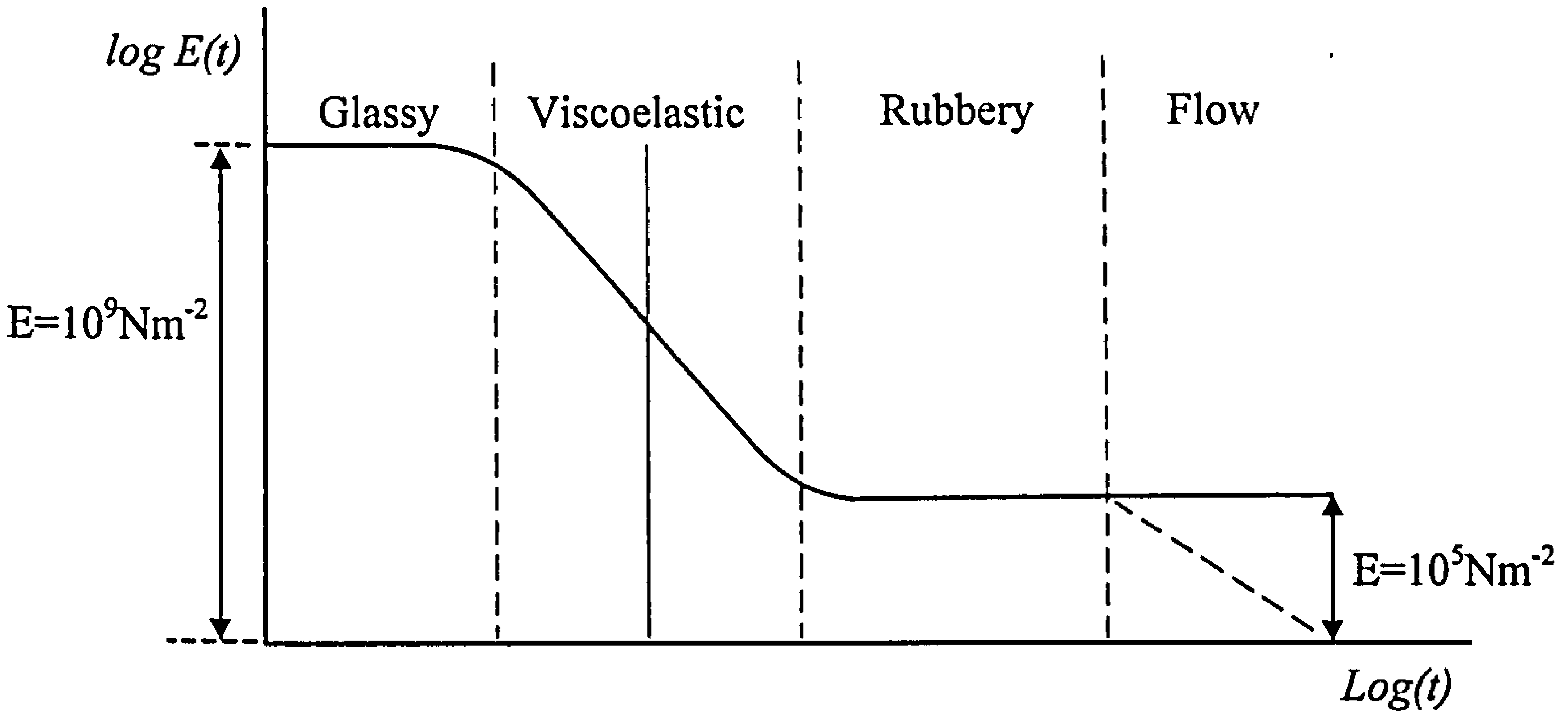

Figure 2.29 Schematic illustration of changes in the modulus of an amorphous polymer with time in a creep or a stress relaxation test.

Another method usually employed to examine the time-dependent response of a polymer is a stress relaxation test. In the test, the polymer is subjected to a constant strain, and the decay in the load required to maintain that constant strain is recorded over a long period of time. Figure 2.30 schematically illustrates the decay in stress with time in a stress relaxation test. In the test, the elastic modulus of the polymer goes through similar transitions to those experienced during a creep test, schematically illustrated in Figure 2.29 [23].

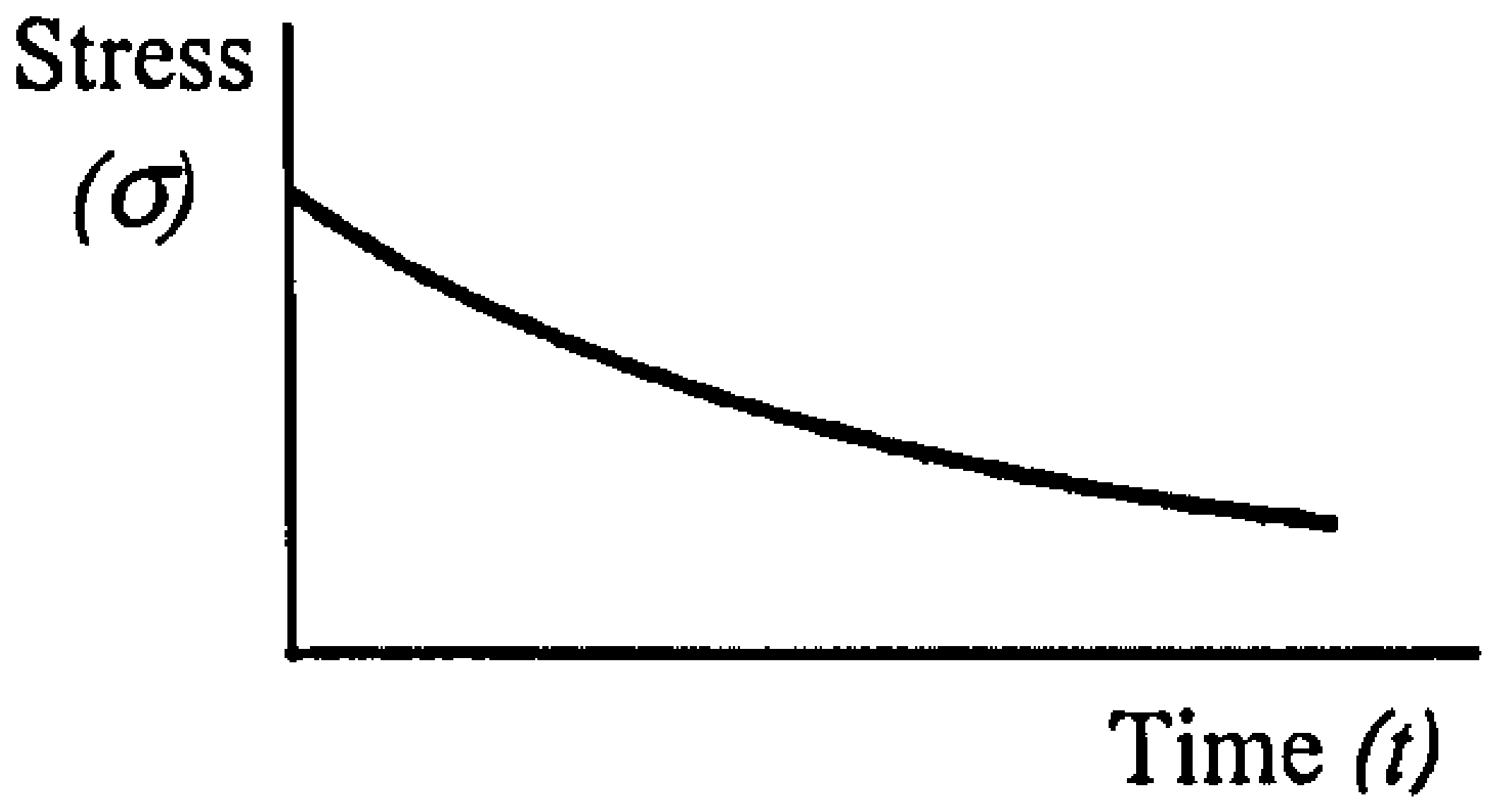

Figure 2.30 Schematic illustration of the decay in stress with time in a stress relaxation test.

The previous sections described the individual influences of temperature and time on the behaviour of an amorphous polymer. However, the effect of the temperature on the time-dependent response of the polymer has not yet been demonstrated. In the following section, a description of that effect is provided.

2.3.1.3 Time-Temperature Superposition and the (WLF) Approximation

It has been established in Section 2.3.1.1 that the polymer at extremely high temperatures is in a rubbery state. In that state, the behaviour of the polymer is time-independent (see Figure 2.29). Additionally, the polymer at low temperatures is in a glassy state, and its behaviour at short experimental times is also time-independent. However, in the glass transition region (see Figure 2.24), the time-dependent behaviour of the polymer is highly influenced by changes in temperature. The higher the temperature of the polymer, the shorter the period it takes the polymer to transform from an elastic to a rubbery state and vice versa [24].

Typical stress relaxation or creep (modulus-log(*time*)) curves obtained at temperatures T_s, T_1 and T_2, where $T_s > T_1 > T_2$ are schematically illustrated in Figure 2.31. The curves shown in the figure are similar in shape, but are horizontally shifted parallel to the logarithmic time scale. Additionally, it was recognised that if one (modulus-log(*time*)) curve at a particular reference temperature is known, for example at T_s, the (modulus-log(*time*)) curves at the other temperatures can be estimated by applying a horizontal shift $log(a_T)$ on the logarithmic time scale [23]. This remarkable observation was established largely by the work of Williams, Landel and Ferry, and they proposed $log(a_T)$ to be expressed in the form,

$$\log(a_T) = \frac{-C_1(T-T_s)}{C_2+(T-T_s)} \qquad 2\text{-}3$$

where T_s is the reference temperature, C_1 and C_2 are the William Landel and Ferry (WLF) constants (calculated at that reference temperature), and T is the temperature at which the (modulus-log (time)) curve is required. The equation, which was originally developed empirically, is termed the WLF equation. It was found to be generally expressible for most amorphous polymers over the temperature range $T = T_s \pm 50^\circ\mathrm{C}$ [23].

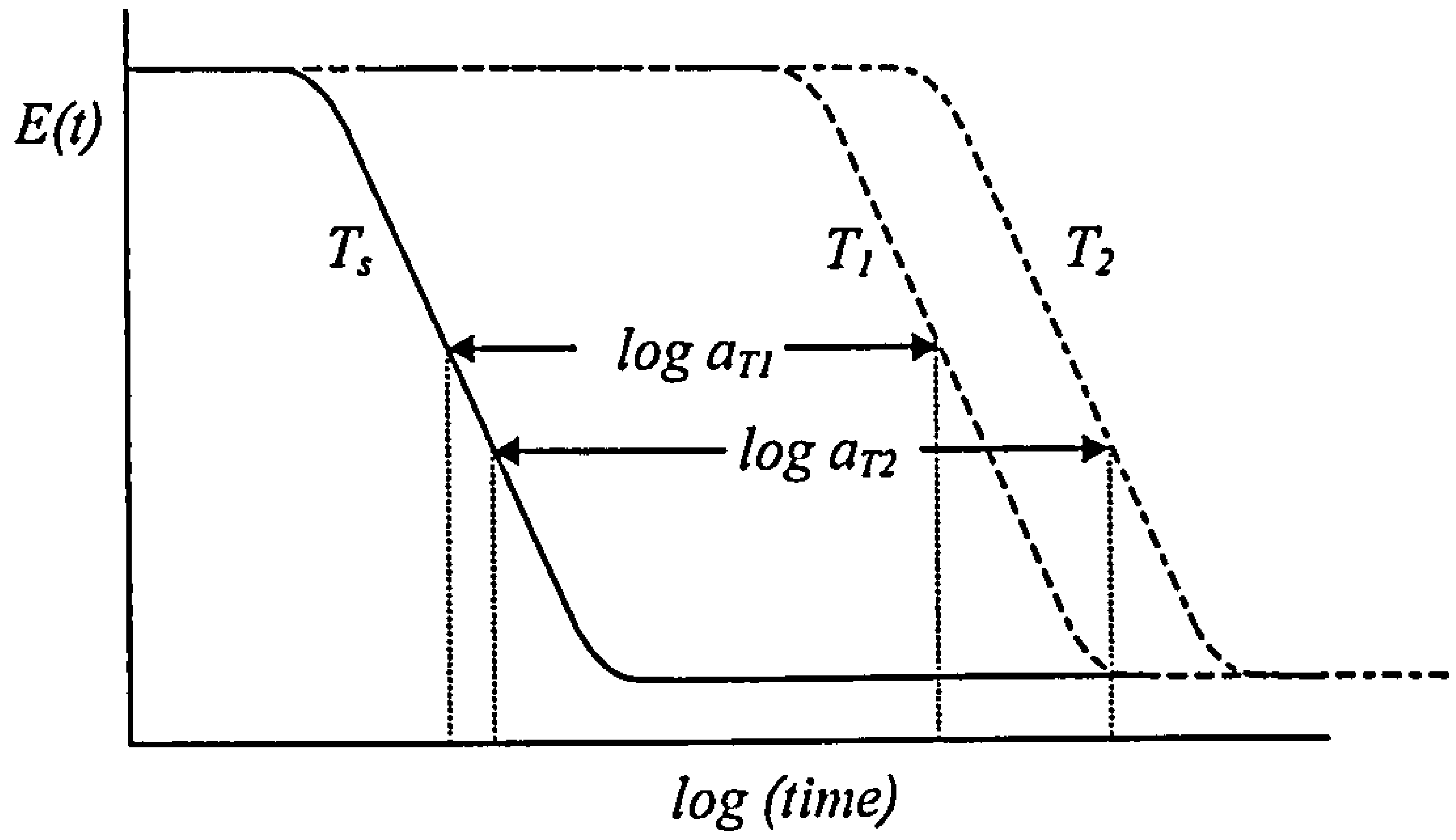

Figure 2.31 Schematic diagram illustrating the creep or stress relaxation (modulus-log(*time*)) curves obtained at three different temperatures T_s, T_1 and T_2, where $T_s > T_1 > T_2$

2.3.2 Thermal Conductivity

The thermal conductivity k is a physical property of a material. It is a measure of the rate at which heat is transferred through a body. The instantaneous rate at which heat flows undirectionally through an object can be expressed by the Fourier's law of heat conduction as follows,

$$\frac{dQ}{dt} = -kA\frac{dT}{dx} \qquad 2\text{-}4$$

where dQ/dt is the heat transfer rate along the x direction, A is the cross sectional area taken at right angles to the direction of the heat flow and dT/dx is the temperature gradient along the path of heat flow.

Thermal energy is conducted in polymeric materials by the vibration and molecular motion of polymer chains. The thermal conductivity of polymers is understood to be anisotropic [24]. The reason being that heat transferring along the backbone primary bond encounters less scattering than that transmitted from chain to chain along the secondary bonds. Consequently, an increase in the degree of polymerisation and the existence of extensive cross-links can allow higher thermal conductivity [21].

Amorphous polymers have a low thermal conductivity compared to other polymers. In amorphous polymers, heat transfer may take the backbone path, but the loosely packed structure minimises the points at which the polymer chains contact one another. As the temperature of the polymer increases, the atoms gain thermal energy and vibrate. The vibration of each atom is then transferred to surrounding atoms. This causes rapid heat transfer, exhibited in an increase in the thermal conductivity, provided that the temperature of the polymer is below T_g. At the glass transition temperature, the conductivity reaches a maximum value. However, at temperatures above T_g, bonding between the polymer chains becomes weak, and thus scattering of the thermal energy is more pronounced, exhibited in a decrease in the thermal conductivity [21].

However, a polymer powder bed conducts heat far less readily than a homogenous solid of the same material. This is due to the interstitial spaces that exist in the powder bed, which is not the case in solids. In addition, the powder particles contact one another over a small area and at a few contact points. The conductivity of a powder bed is therefore highly influenced by the degree of compaction [25].

Several models were developed to formulate a mathematical expression for the effective thermal conductivity of a powder bed. Yagi and Kunii [26] studied the influence of both temperature and packing characteristics of the powder bed on the effective thermal conductivity. They considered in their study seven heat transfer modes to take place in a powder bed. The modes that are not affected by the flow of gas through the interstitial spaces in the powder bed were identified as follows (see Figure 2.32),

1. Thermal conduction through solid particles.

2. Thermal conduction through the contact surfaces of particles.
3. Radiant heat transfer between particle surfaces.
4. Radiant heat transfer between neighbouring voids.

In addition, the heat transfer mechanisms that are influenced by the flow of gas through the interstitial spaces in the powder bed were identified as (see Figure 2.32),

5. Thermal conduction through the gas film near the contact surface.
6. Heat transfer by convection, solid-gas-solid.
7. Heat transfer by lateral mixing of the gas.

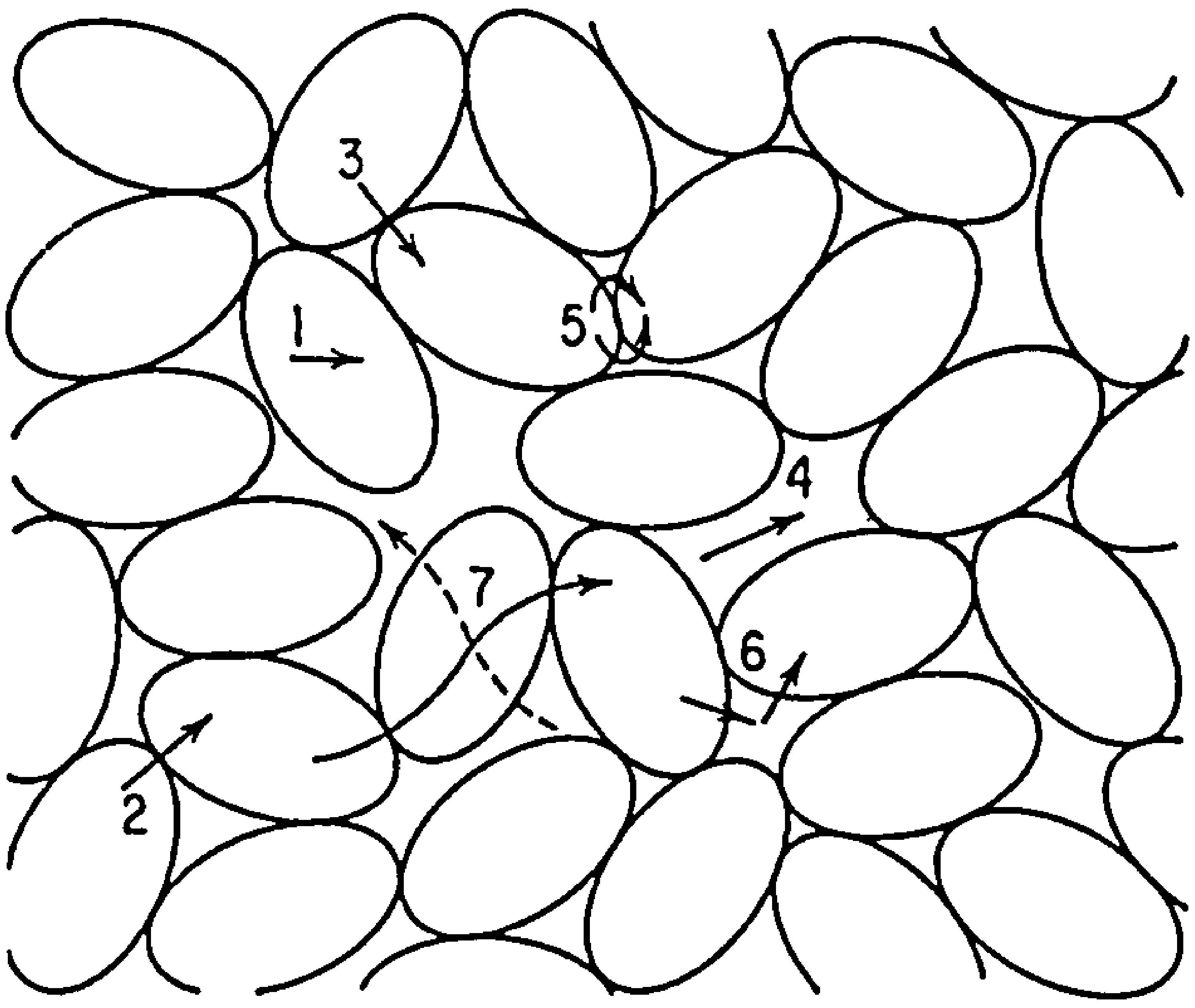

Figure 2.32 Illustration of the heat transfer mechanisms in a packed bed. (1) Heat transfer through solid (2) Heat transfer through the contact surface of solid (3) Radiation heat transfer between surfaces of solid (4) Radiation heat transfer between adjacent voids (5) Heat transfer through the gas film near the contact surface (6) Heat transfer by convection, solid-gas-solid, (7) Heat transfer by lateral mixing of gas. From [25].

A mathematical description of the heat transfer model required the summation of the flow of heat through the various paths in the powder bed, proportioned according to their relative importance. As the conductivity of most gases is considerably lower than the conductivity of solids, the dominant resistance to heat flow in a powder bed is that of the gas. In a situation where the gas is motionless, or when Reynolds number is small, the dominant heat transfer mechanisms taking place are mechanisms 1, 2, 3, 4, and 5 (see Figure 2.32). However, when Reynolds number is large, mechanism 7 controls the heat transfer in any packed bed. Mechanism 6, however, was found to be less important than the other mechanisms, at all values of Reynolds number, and its effect was therefore neglected. Conversely, mechanisms 1 to 4 were considered to be of importance when vacuum occupies the voids within the powder bed [26].

The packing of particles in a powder bed was described in the Yagi-Kunii model by the parameters β, γ, φ. Parameter β is defined as the ratio of the average length between the centres of two neighbouring solids in the direction of the heat flow (l_p) to the mean diameter of the packing D_p. The parameter γ is defined as the effective length of the solid relating to thermal conduction (l_s) divided by the mean diameter of the solid (D_p). For simplicity, both factors β and γ can be taken as unity [26]. The factor φ is the ratio of the effective thickness of the fluid film through which heat is conducted (l_v) to the average diameter of the packing material (D_p).

The general equation derived for the effective thermal conductivity of a powder bed (k_e^o), with motionless gas filling the voids, was expressed by the Yagi-Kunii model as follows,

$$\frac{k_e^o}{k_g} = \frac{\beta(1-\varepsilon_v)}{\gamma\left(\frac{k_g}{k_s}\right) + \frac{1}{(1/\varphi) + \left(D_p h_{rs} / k_g\right)}} + \varepsilon_v \beta \frac{D_p h_{rv}}{k_g} \qquad 2\text{-}5$$

where k_g and k_s are the thermal conductivities of the gas and solid respectively and ε_v is the void fraction of the powder bed. In addition, the parameters h_{rs} and h_{rv}, denoted in Equation 2-5, represent the radiation heat transfer coefficients from solid to solid (mechanism 3), and from void to void (mechanism 4) respectively, and are expressed in Kcal/m^2-hr-K as follows [26],

$$h_{rs} = 0.1952\left(\frac{\in}{2-\in}\right)\left(\frac{T}{100}\right)^3 \qquad 2\text{-}6$$

$$h_{rv} = \frac{0.1952}{\left(1+\left(\dfrac{\varepsilon_v(1-\in)}{2\in(1-\varepsilon_v)}\right)\right)}\left(\frac{T}{100}\right)^3 \qquad \text{2-7}$$

where $\in$ is the emissivity of the solid surface, and T is the temperature in Kelvin. At low temperatures, the effect of radiation within the powder bed becomes unimportant, and the effective thermal conductivity of the powder bed can be simplified as [26],

$$k_e^\circ = \frac{k_s(1-\varepsilon_v)}{(1+\varphi k_s/k_g)} \qquad \text{2-8}$$

Additional models [27, 28] were also formulated to predict the effective thermal conductivity of a powder bed at high temperatures. Sih et al. [27] developed the following expression for the effective thermal conductivity (k_e^o),

$$\frac{k_e^\circ}{k_g} = (1-\sqrt{1-\varepsilon_v})(1+\frac{\varepsilon_v k_R}{k_g})$$

$$+\sqrt{1-\varepsilon_v}\left[(1-\phi)\left(\frac{2}{1-\dfrac{Bk_g}{k_s}}\left(\frac{B}{\left(1-\dfrac{Bk_g}{k_s}\right)^2}\left(1-\frac{k_g}{k_s}\right)\ln\frac{k_s}{Bk_g}-\frac{B+1}{2}-\frac{B-1}{1-\dfrac{Bk_g}{k_s}}\right)\right)+\frac{k_R}{k_g}+\phi\frac{k_s}{k_g}\right] \qquad \text{2-9}$$

where B is the deformation parameter of the particle; when $B=1$, the particle has a spherical shape and $B \to \infty$ when the particle surface is that of a cylinder. The parameter ϕ denotes the flattened surface fraction of a particle in contact with another particle, i.e. $\phi=0$ when the particles are not in contact and $\phi=1$ when the particles are in complete contact. The term k_R refers to the radiation thermal conductivity and is expressed as follows,

$$k_R = 4F_R\sigma_R T^3 D_p \qquad \text{2-10}$$

where σ_R is the Stefan-Boltzman constant $[5.67\times10^{-8}\mathrm{W/m^2.K^4}]$ and F_R is the view factor, defined as the fraction of radiation leaving a surface and intersecting another surface [28].

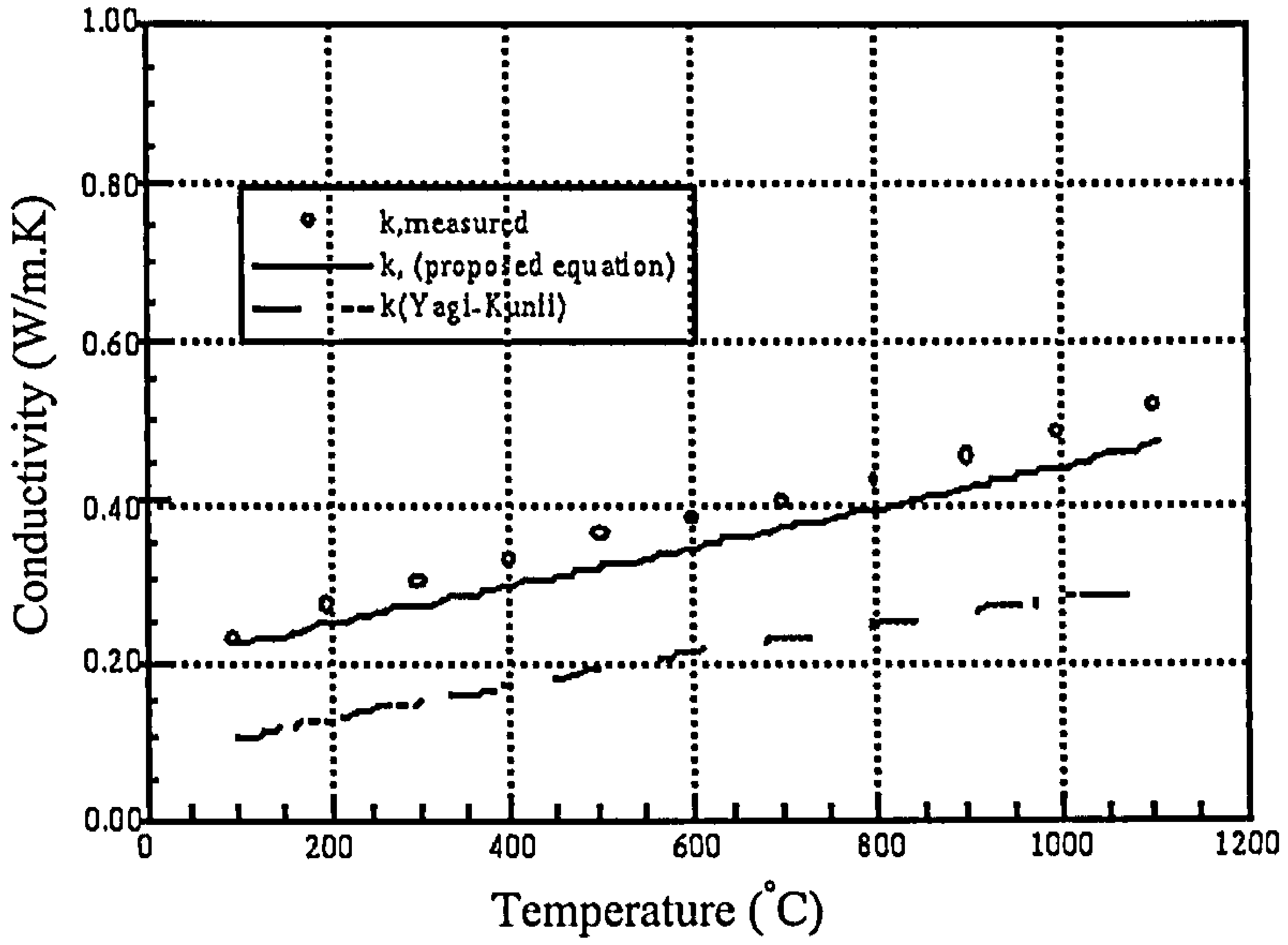

Figure 2.33 Sih and Yagi-Kunii predictions of the effective thermal conductivity of an alumina powder bed (ε_v=0.71) drawn alongside the experimentally measured data. From [28].

Figure 2.33 shows the Sih and Yagi-Kunii predictions of the effective thermal conductivity of an alumina powder bed drawn alongside the experimentally measured data [28]. The figure shows that the prediction of the Sih model was more accurate, for this specific type of material, than the Yagi-Kunii model.

2.3.3 Specific Heat

The specific heat (C_p) is the amount of heat required to increase the temperature of a unit mass by one degree. It is expressed in the form,

$$C_p = \frac{dQ}{dT} \qquad \text{2-11}$$

where dT is the change in temperature experienced by a unit mass of the material when subjected to a quantity of heat dQ. There are no theoretical expressions for the specific heat of amorphous polymers [24]. However, experimental observations showed the specific heat of amorphous polymers to increase as the temperature is increased, below and above the glass transition region. In the glass transition region, a step change in the specific heat is exhibited [24]. Based on experimental measurements [7], the specific heat of polycarbonate is expressed in both the glassy and rubbery states as follows,

$$C_p(glass) = 0.262 + 9.768 \times 10^{-4} T \text{ Cal/(g}^\circ\text{C)} \qquad T < 145\,^\circ\text{C} \tag{2-12}$$

$$C_p(rubber) = 0.371 + 5.438 \times 10^{-4} T \text{ Cal/(g}^\circ\text{C)} \qquad 145\,^\circ\text{C} \le \text{T} < 300\,^\circ\text{C} \tag{2-13}$$

For a powder bed, the specific heat is written as follows [1],

$$C_p = \sum_n \omega_i C_{pi} \tag{2-14}$$

where ω_i and C_{pi} are the weight fraction and specific heat of component i, respectively [1]. The powder bed is made of two types of components; solid particles and the gas filling the interstitial spaces that exist in the powder bed. As the weight fraction of the gas is one thousand times less than that of the solid, the product $\omega_i C_{pi}$ for the gas is extremely small when compared to that of the solid [1]. Thus, the gas has very little influence on the overall specific heat of the powder bed, and the specific heat of a powder bed can considered to be that of a solid particle [1].

2.3.4 Density

The mechanical and physical properties of an SLS fabricated part were found to be highly related to its density. Emphasis was therefore given to investigate the factors that influence the density. One of the methods employed in increasing the density of fabricated parts is by increasing the density of the powder bed, prior to SLS processing. The powder bed density, however, is influenced by the density of the solid particles and their packing. The latter is a function of the particle size, particle size distribution and particles shape [1].

An optimal packing density of a powder bed could be achieved if the voids among the largest particles in the bed are filled with smaller particles, which are in turn filled with smaller particles and so forth. In principle, spherical uniform particles can be packed in different arrangements such as the cubical and the orthorhombic arrangements, schematically illustrated in Figure 2.34.

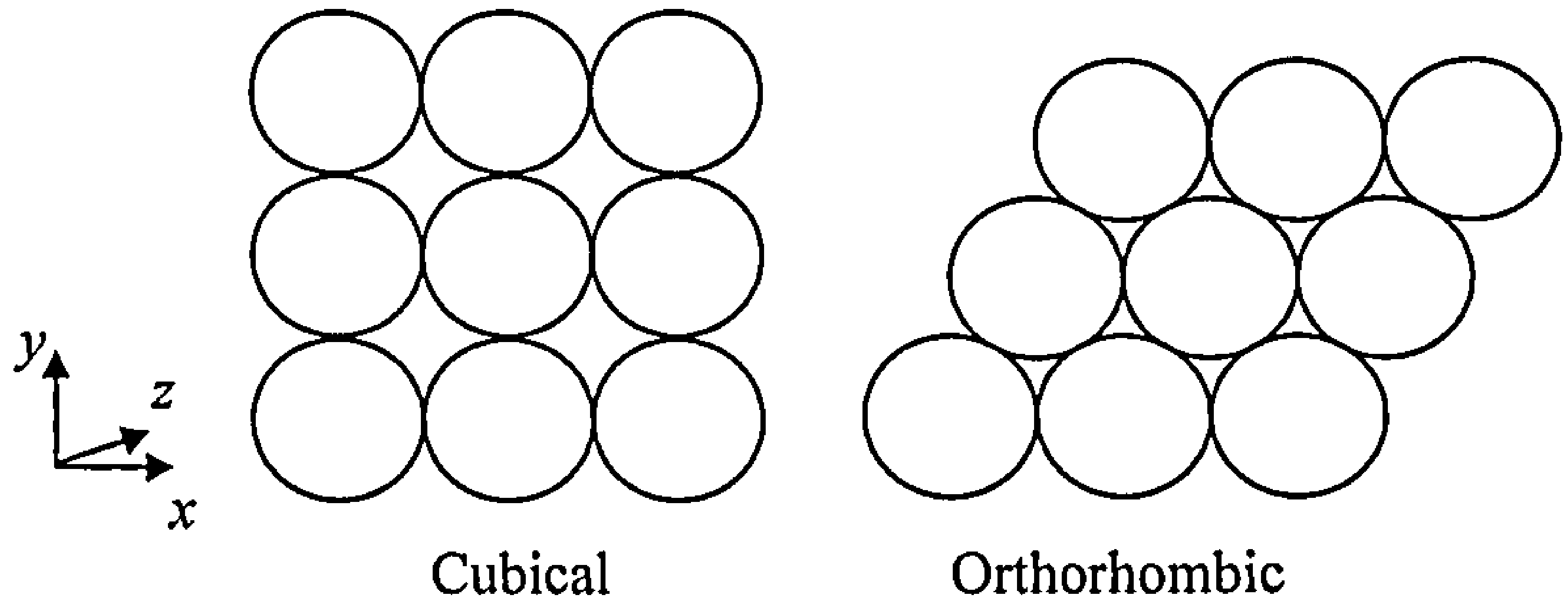

Figure 2.34 The cubical and orthorhombic arrangements of uniform spherical particles

If the radius of the solid particles forming a cubical arrangement is denoted *a*, the volume of the solid spheres *V* in the powder bed can be expressed as,

$$V = \frac{4}{3}\pi a^3 N_x N_y N_z \qquad \text{2-15}$$

where N_x, N_y, N_z are the number of spheres along the *x*, *y*, and *z* axes respectively (see Figure 2.34). In addition, the volume V_T of the solid figure bounding the cubical arrangement powder bed can be written as,

$$V_T = 2aN_x \times 2aN_y \times 2aN_z \qquad \text{2-16}$$

Therefore, the volume of the void space as a percentage of the total volume occupied by the arrangement of the spheres is $[(8a^3 - (4/3)\pi a^3)/8a^3] = 47.6\%$, or the spheres occupy only 53.4% of the total volume of the powder bed. In a similar way, the percentage void volume of the orthorhombic packed bed can be found to be 39.5%. The cubical packing is unstable and does not occur in nature, whereas the orthorhombic is the most likely arrangement to exist in uniform-sized sphere beds [25].

However, the actual packing of a powder bed is more represented by systems of particles containing two, three and more sizes of components. This arrangement is shown in Figure 2.35 for the powder used in SLS to produce polycarbonate parts; Laserite Polycarbonate compound LPC-3000 [29]. The powder particles have an irregular shape with particle sizes ranging from 30 to 180μm.

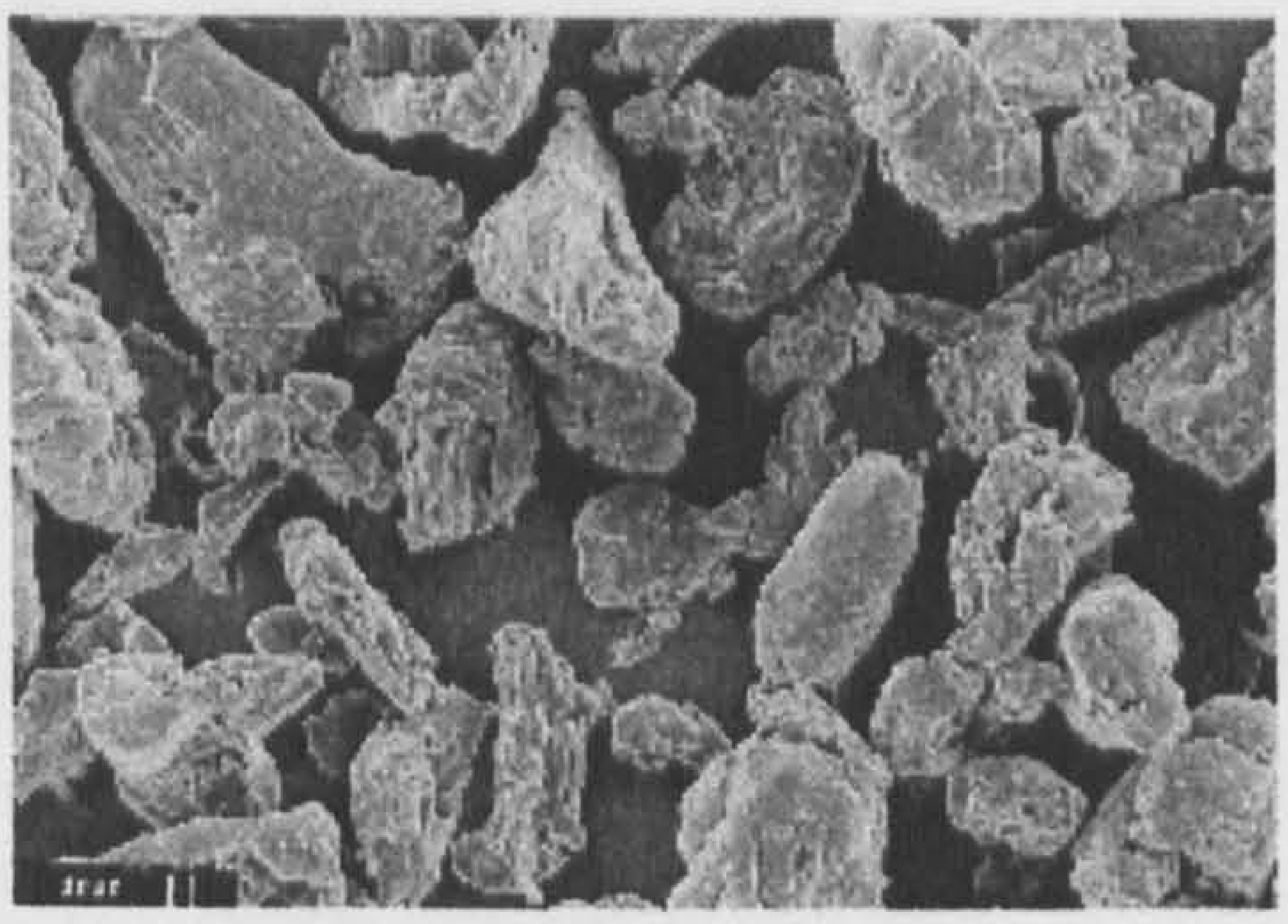

Figure 2.35 Microscopic image of Laserite Polycarbonate compound LPC-3000. From [29].

It is expected that the smaller the diameters of the finest particles, the denser is the bed, which is due to the finest particles filling more of the interstitial spaces among the coarse particles. A method used to produce highly dense packing was reported by Orr [25]. Initially, the large powder particles are placed into a container and vibrated to minimum porosity. The finest components are then added and vibrated until maximum density is achieved and so on. However, it was reported that less dense packing is achieved when the different sized powder components are first mixed and then vibrated [25].

The bulk density of a powder structure can be estimated using two basic methods, aerated and tapped. The aerated bulk density is determined by allowing the powder to settle first when poured into a container, whereas the 'tapped or 'packed' density is estimated following tapping or vibrating the aerated sample [30]. In general, the density of SLS powder beds is closer to the poured density than the tapped density [1]. At Leeds, the SLS powder bed density is determined by building hollow cylinders with closed bases. The cylinders are then carefully removed from the powder bed containing within them the unsintered powder. The density of the powder is then estimated from its weight divided by the volume it had occupied in the fabricated cylinder [31].

In SLS, a part is formed when the solid particles, in contact with each other in the powder bed, coalesce at elevated temperatures. This process is termed sintering. It is accompanied by a decrease in the volume of the pore spaces between the particles, and thus reduction in the total surface area and volume of the sintered powder bed occurs. This phenomenon involves viscous flow between adjacent particles, and its rate is therefore greatly affected by the local temperature. Sintering proceeds in two distinct stages. First, interfaces and bridges between adjacent particles are developed with very little change in density (see Figure 2.36). This is then followed by a stage of densification in which inter-particle cavities are significantly reduced or eliminated.

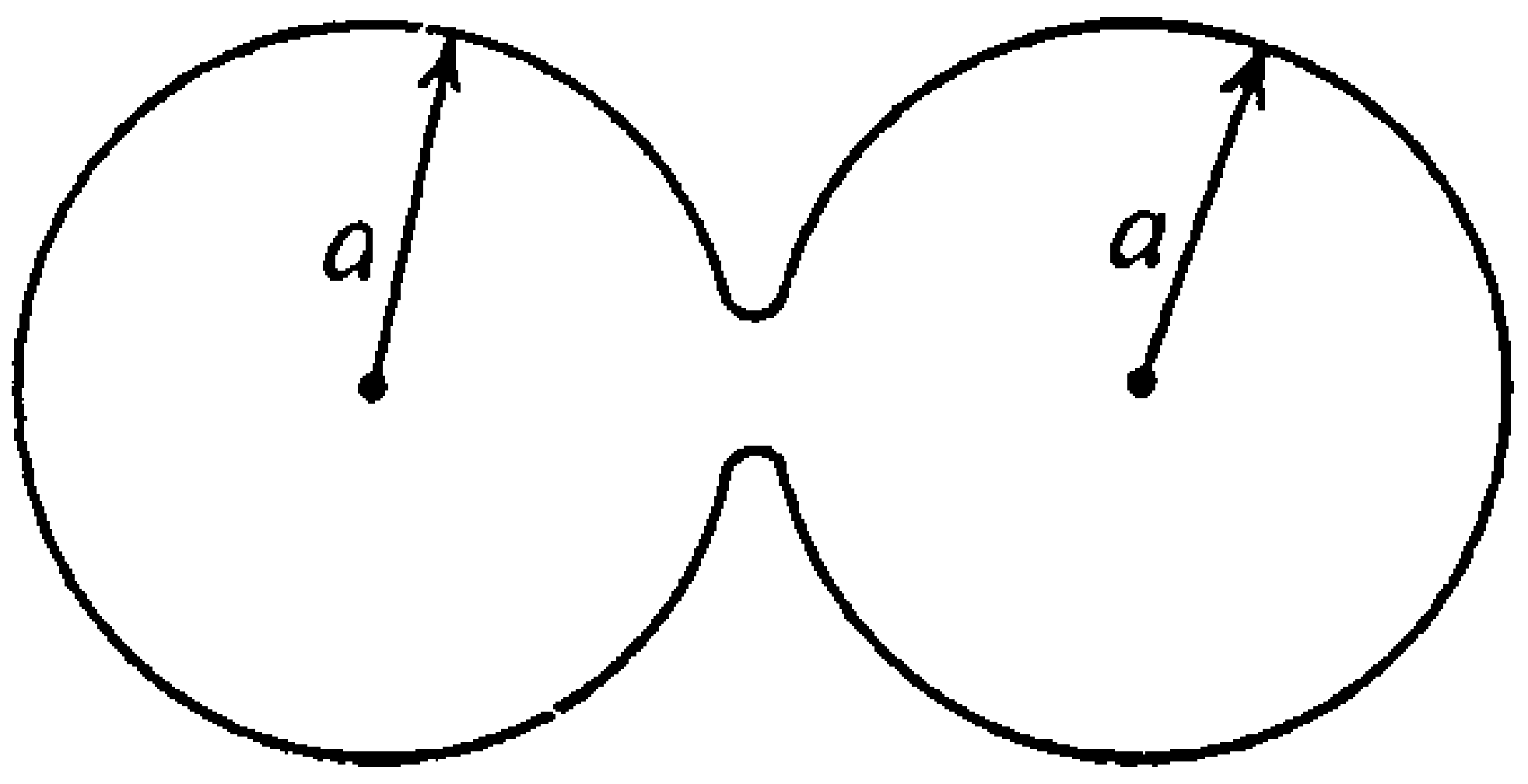

Figure 2.36 Schematic view of the first stage of sintering

A number of researchers studied the effect of various SLS process parameters on the density of fabricated parts. Generally, the density was found to increase with the increase in the fill laser power *P*, but was seen to reduce with increasing the laser beam speed *U* and the scan spacing *S*. The SLS process parameters *P*, *U* and *S* are combined into a single parameter termed the energy density (*ED*) which is defined as [1],

$$ED = \frac{P.f}{U.S} \qquad 2\text{-}17$$

where f is a conversion factor [29]. Ho et al. [29] studied the effects of varying *ED* on the microstructure and the physical density of SLS fabricated polycarbonate parts. The energy density was varied by setting different values for the fill laser power *P* whilst maintaining the other parameters constant; scan spacing and laser speed at 0.2mm and 861mm/sec respectively. The powder layer thickness was 0.13mm and the part heater set point was adjusted at 145°C during the "build" stage in SLS.

The microstructure of the top surface of a polycarbonate specimen built at *ED* equal to 0.036J/mm^2 is illustrated in Figure 2.37*a*. In the figure, the particles are only slightly fused at the points of contact, and individual particles and voids in between can be easily identified. A cryogenically fractured cross-section of the specimen is shown in Figure 2.37*b*. Similar to the top surface, individual particles and voids can be also seen along the depth of the specimen.

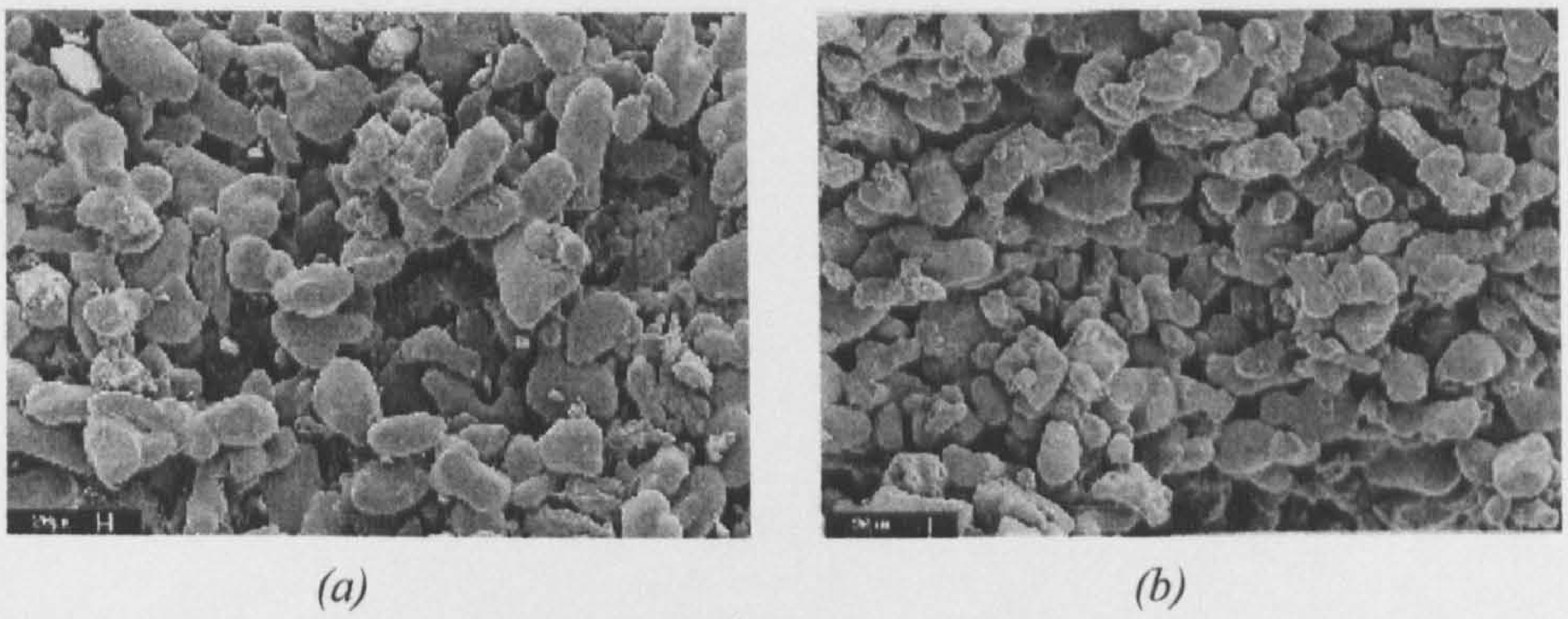

Figure 2.37 (a) Microscopic image of top surface of a polycarbonate specimen built at *ED* equal to 0.036J/mm^2 (b) Microscopic image of the fractured cross-section of the specimen. From [29]

The microscopic image of the top surface of a polycarbonate part fabricated at *ED* equal to 0.07J/mm^2 is shown in Figure 2.38*a*. The presence of voids at the surface is less apparent than that exhibited in the previous case (see Figure 2.37*a*). This is likely to be caused by the flow of material, which facilitated better fusion of the polymer particles. However, a number of peaks at the surface, (A) and (B) were noticed. That was thought to be due to the presence of some unmelted particles underneath the sintered surface of the layer.

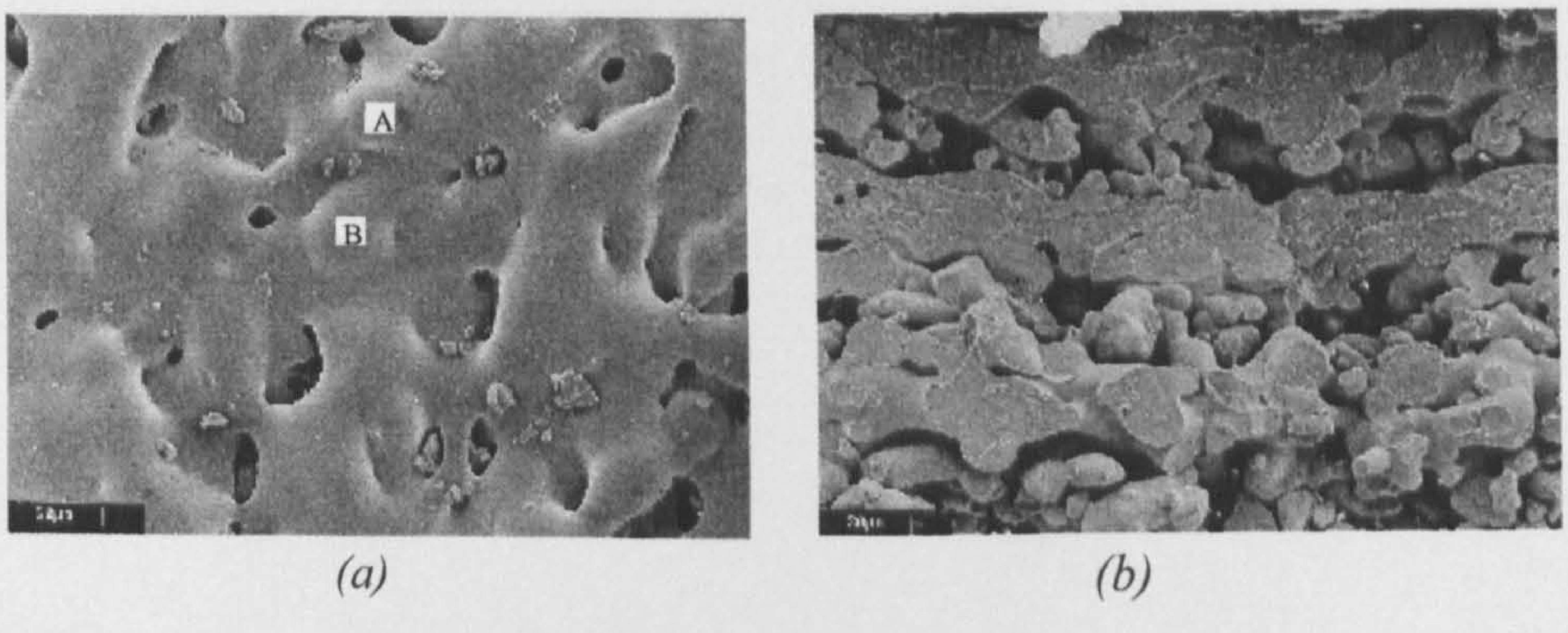

Figure 2.38 (a) Microscopic image of the top surface of a polycarbonate specimen sintered at *ED* equal to 0.07J/mm^2 (b) Microscopic image of the fractured cross-section of the same specimen. From [29].

A microscopic image of the fractured cross-section of the specimen is shown in Figure 2.38*b*. The existence of voids between two well-defined layers can be clearly noticed. This is possibly due to the energy density not being high enough to cause complete melting at a larger depth than the nominal thickness of a layer, resulting in slight fusion between subsequently sintered layers.

The microscopic image of the top surface of a specimen sintered at *ED* equal to 0.094J/mm^2 is illustrated in Figure 2.39*a*. In the figure, the presence of peaks at the surface was less apparent and the number of holes at the surface decreased. The fractured cross-sectional view of the specimen, illustrated in Figure 2.39*b*, showed a more compact structure, and the boundaries of the layers forming the specimen were less identifiable.

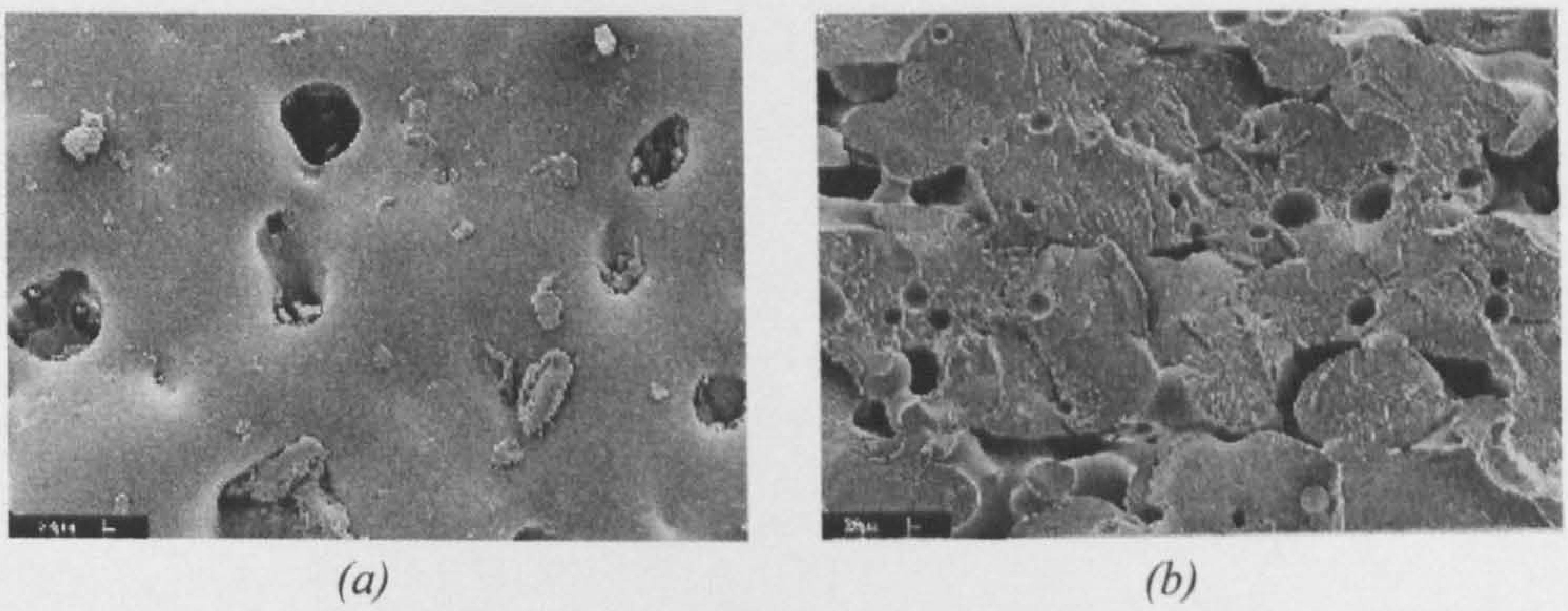
(a) *(b)*

Figure 2.39 (a) Microscopic image of the top surface of a polycarbonate specimen built at *ED* equal to 0.094J/mm^2 (b) Microscopic image of the fractured cross section of the same specimen. From [29]

As the energy density was further increased, smoke was observed when components were sintered. That phenomenon was believed to be a sign of degradation. Degradation is expected to be most severe in SLS on the layer surface, where the polymer is in direct contact with the laser beam. However, degradation is also believed to take place at a deeper section in the sintered layer. That happens as the smoke and gases generated escape from the sintered surface, allowing the laser beam to penetrate through the gaps between the polymer particles. However, if the gaps are sealed off rapidly due to efficient melting, gases generated could be trapped. This results in large voids to exist within the fabricated layer. Figure 2.40 shows a microscopic image of a fractured cross-section of a polycarbonate specimen fabricated at *ED* equal to 0.12J/mm^2, where voids are clearly identifiable.

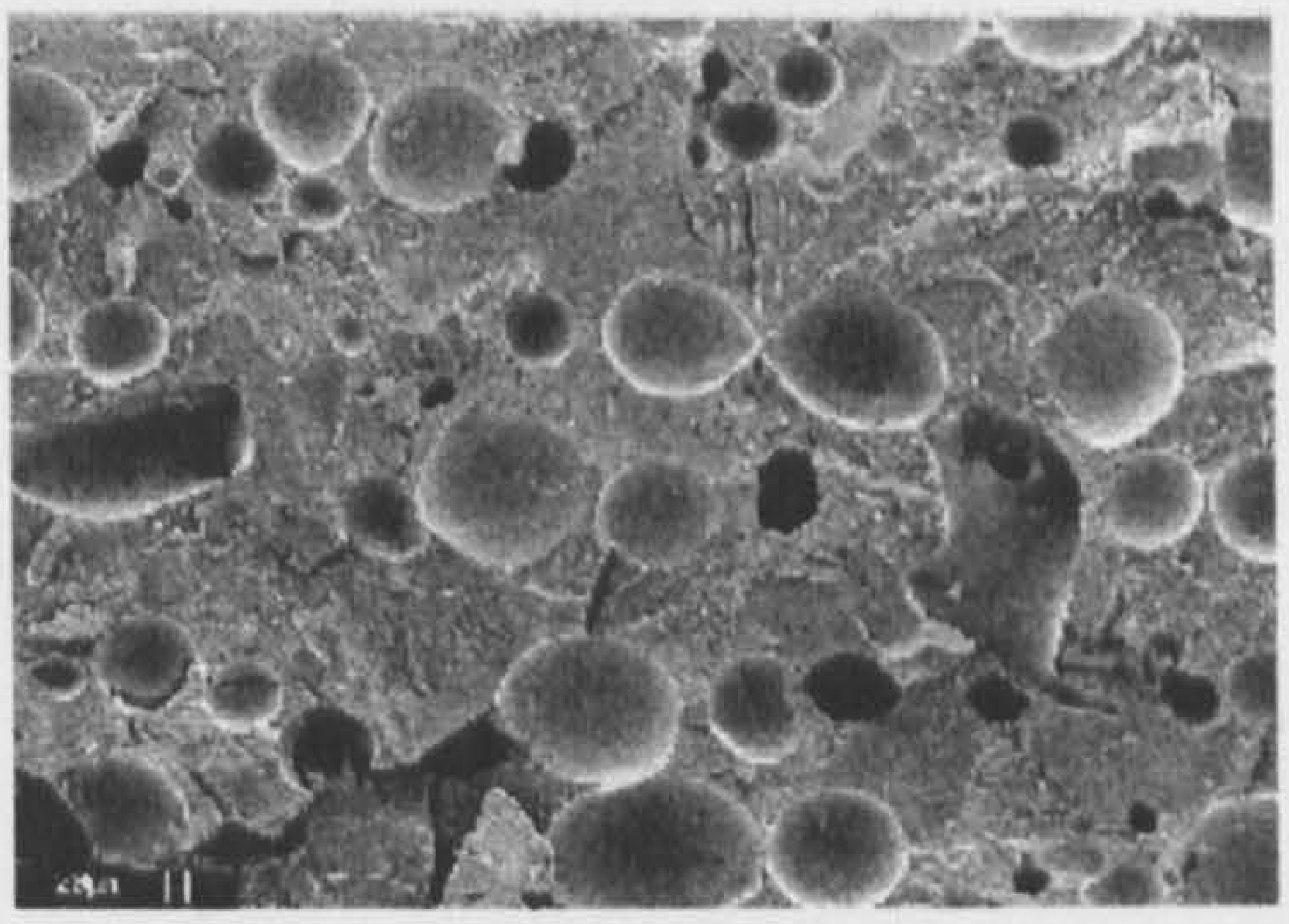

Figure 2.40 Microscopic image of the fractured cross section of a specimen sintered at *ED* equal to 0.12J/mm^2. From [29]

Ho et al. [29] also measured the apparent density of the polycarbonate specimens, fabricated at the energy densities aforementioned. Results obtained are shown in Figure 2.41. In the figure, the maximum density (1056kg/m^3) of the components was obtained at $ED \approx 0.09$J/mm^2. However, the density is seen to reduce as the *ED* was further increased, which also agrees with the microscopic images shown in Figure 2.40.

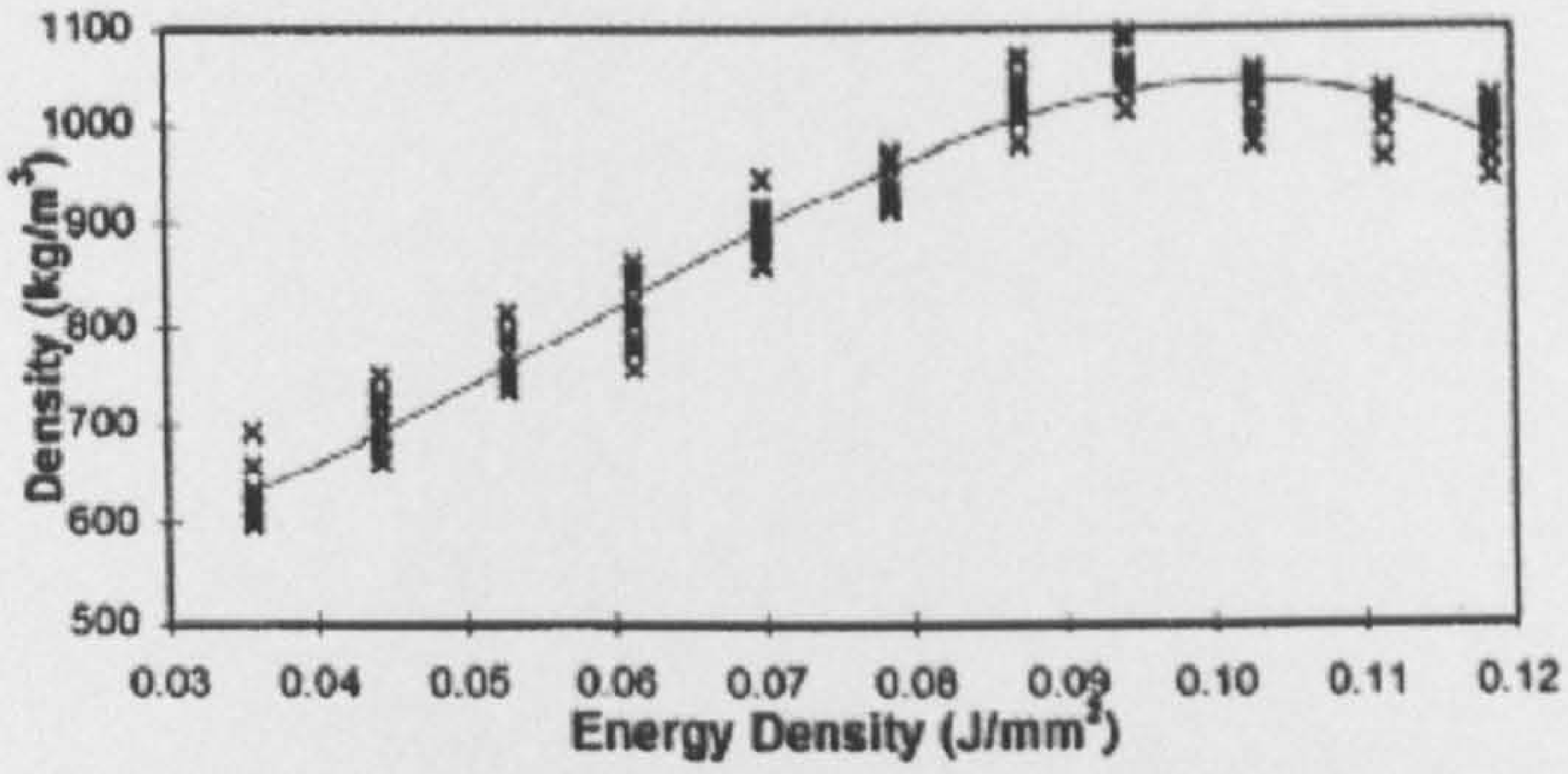

Figure 2.41 Variation in the physical density of SLS fabricated polycarbonate with variation in energy density. From [29].

2.3.5 Radiation Properties

Thermal radiation is one of several mechanisms of heat transfer. It is emitted in the form of electromagnetic waves and thus it does not require the presence of a material medium. Conversely, heat transfer through convection and conduction require the presence of a material medium. All materials emit and receive thermal radiation at a rate primarily dependent on their temperature. Its effectiveness is determined by the radiation properties of the material, which include the emissivity, absorptivity, transmissivity and reflectivity. In the following sections, a description of these properties is provided.

2.3.5.1 Surface Emissivity

In theory, a blackbody is considered to be an ideal emitter of radiation, in the sense that no surface can emit more radiation than a blackbody at the same temperature. It is therefore convenient to choose the blackbody as a reference in describing emission from a real surface. The emissivity $\in$, which is a surface property, is defined as the ratio of the radiation emitted by the surface to the radiation emitted by a black body at the same temperature, and is expressed as follows,

$$\in(T) = \frac{E_r(T)}{E_{br}(T)} \qquad 2\text{-}18$$

where $E_r(T)$ is the total energy emitted from the surface and $E_{br}(T)$ is the total energy emitted from a black body at the same surface temperature. Additionally, $E_{br}(T)$ is defined as a function of the absolute temperature of the surface, T(K), and the Stefan-Boltzmann constant ($\sigma_R = 5.67\times10^{-8}$ W/m^2·K^4) as follows,

$$E_{br}(T) = \sigma_R \cdot T^4 \qquad 2\text{-}19$$

2.3.5.2 Absorptivity, Reflectivity and Transmissivity

When radiation energy strikes a material surface, a fraction of the incident energy (I) is reflected, termed the reflectivity, ρ_R, a fraction is absorbed, termed the absorptivity α_R and a fraction is transmitted termed the transmissivity τ_R (see Figure 2.42). From an energy balance point of view, it follows that the summation of ρ_R, τ_R and α_R is unity.

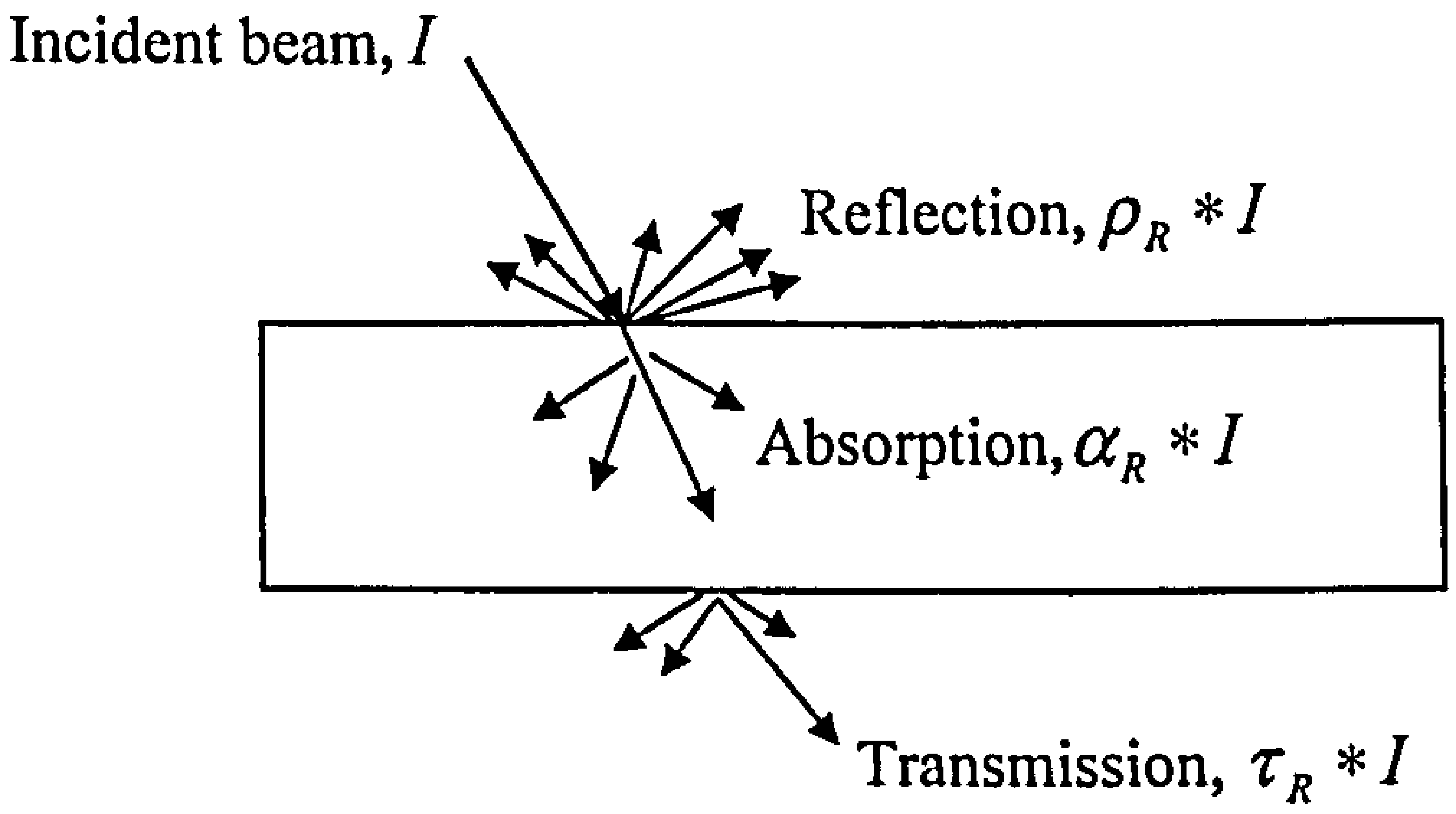

Figure 2.42 Schematic view of the reflection, absorption and transmission of an incident beam

In a previous study [7], the emissivity of SLS polycarbonate powder was experimentally measured using an integrating sphere, schematically illustrated in Figure 2.43. The polycarbonate powder sample was placed in a holder positioned at the bottom of the sphere, and a laser beam was then projected normal to the sample (see Figure 2.43). The amount of radiation reflected from the sample was measured as a voltage signal with a photodetector. The measurements gave a reflectivity (ρ_R) of the polycarbonate powder equal to 5%. As transmission of infrared radiation through polycarbonate is very poor, the assumption made in the study was that the transmissivity (τ_R) of polycarbonate is equal to zero. A radiation balance implies that the sum of ρ_R, τ_R and α_R is equal to unity, and thus the absorptivity (α_R) is equal to 95%. Additionally, at thermal equilibrium, the emissivity ($\in$) and absorptivity (α_R) are the same, and thus the emissivity of the polycarbonate powder was assumed to be 0.95 [7]. The measurements were also performed on SLS fabricated polycarbonate samples. However, results obtained for the fabricated samples did not significantly vary from those measured for the powder samples.

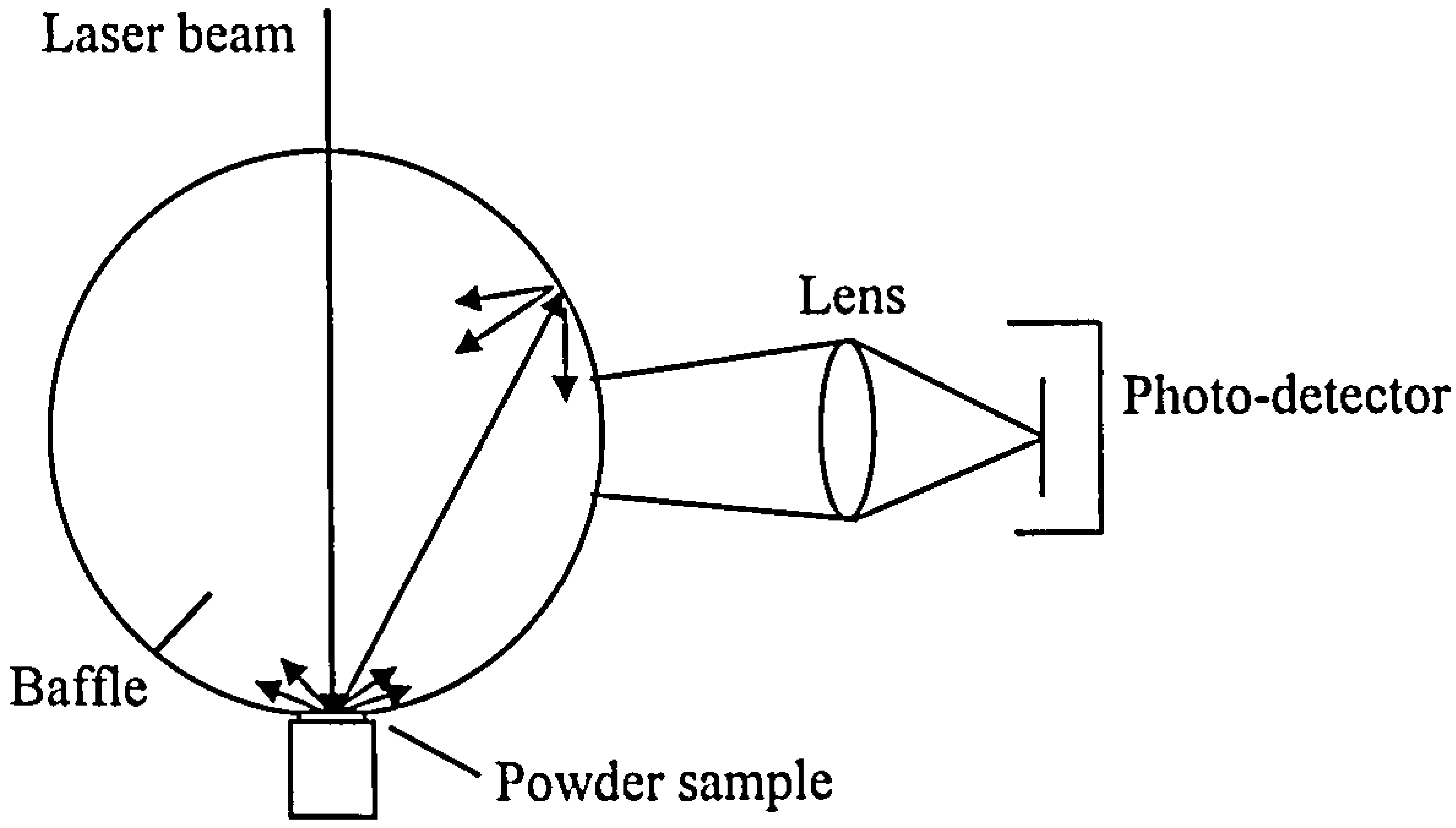

Figure 2.43 Schematic illustration of an integrating sphere

2.3.6 Thermal Expansion

In general, an object expands when heated and contracts when cooled. The change in the length of a body Δl due to variation in temperature ΔT can be expressed in terms of the initial length l of the body and the linear coefficient of thermal expansion α as follows,

$$\Delta l = \alpha \times l_o \times \Delta T \qquad 2\text{-}20$$

Equation 2-20 can be used to determine the dimensional changes of a body due to variation in its temperature provided that the body is able to uniformly expand or contract freely with no residual stresses produced. However, if the body is restrained from moving, dimensional changes may not be possible and stresses develop. These stresses are termed thermal stresses $\sigma_{thermal}$ and can be written in terms of the expansion coefficient α and elastic modulus E as follows [32],

$$\sigma_{thermal} = \alpha \cdot E \cdot \Delta T \qquad 2\text{-}21$$

In general, thermal expansion is related to the strength of the atomic bonds within a material. Strong atomic bonding results in slight separation of the atoms, when the temperature is elevated, resulting in a low coefficient of thermal expansion. In amorphous polymers, thermal expansion does not only depend on the bonding within the polymer chains, which is covalent, but is also highly influenced by the strength of the secondary bonding holding the polymer chains together. At the glass transition temperature T_g, the secondary bonds become extremely weak, allowing a large number of the polymer chains to rotate and translate freely. That is exhibited by an abrupt rise in the specific volume at T_g, as schematically illustrated in Figure 2.44.

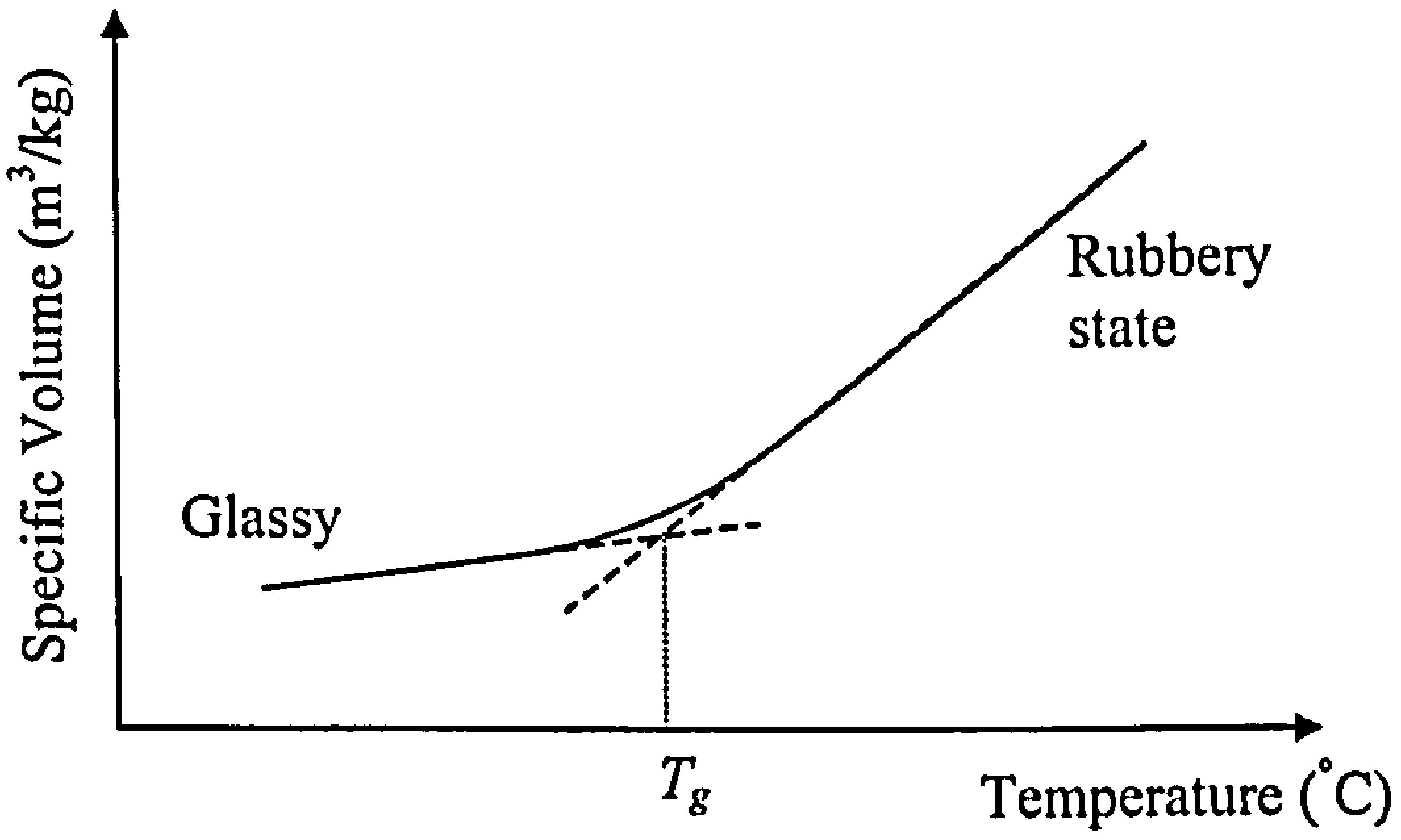

Figure 2.44 Schematic diagram showing the variation in specific volume with temperature for a typical amorphous polymer.

The linear coefficient of thermal expansion of solid polycarbonate is reported to equal 68×10^{-6}1/°C [33]. However, in a previous study [7], the value of the expansion coefficient of solid polycarbonate was found too small to explain the expansion of a polycarbonate powder bed. Additionally, the expansion of a polycarbonate powder bed was too large to be described by the expansion of trapped gases in the bed. The considerable expansion of the powder bed was attributed in the study to the change in the shape of the powder particles from oblate to a spherical shape. That was also supported by microscopic images that showed such a change in particle shape for a polycarbonate powder bed heated above T_g. However, re-introducing the previously heated powder to an oven, and heating it in the same way showed no expansion of the bed during heating, which proved that the bed expansion effect is irreversible [7].

2.4 Previous studies of curl in SLS

The ability of the SLS process to produce dimensionally accurate parts is essential to its overall acceptance in the market place. However, for a given material, the accuracy of a part is highly influenced by the SLS machine parameters selected in fabrication. Often the successful production of geometrically acceptable parts involves numerous fabrication trials before the optimum machine parameters can be found.

Curl and shrinkage are probably the largest causes of inaccuracy in SLS. If shrinkage within the part is uniform, the problem can be solved by simply scaling the part's CAD model geometry to compensate for shrinkage. Unfortunately, shrinkage is not uniform, and part curling can occur. The problem has been investigated by many researchers. Their objective has been to eliminate (or at least reduce) the curling effect in SLS fabricated parts. Some research work approached the problem experimentally by studying the effects of the machine parameters on curl (see Section 2.2.5.4.2). Others have used a numerical approach such as the finite element modelling. These numerical models are very powerful in understanding the stages of curl development during the SLS process. Additionally, this approach avoids the need, in the long term, for experimental fabrication for the purpose of finding the optimum SLS machine parameters. The optimum parameters found from the numerical models can be applied to physically produce geometrically acceptable parts, which can considerably reduce the time and cost of operating the SLS machine for experimental purposes.

In the following sections, a number of previous studies in curl are presented. The studies that have examined curl through experimental measurements are first introduced. Then, a description of previous studies that have used the finite element modelling approach in an attempt to understand the development of curl is given.

2.4.1 Experimental Studies of Curl

Previous experimental work was carried out to examine the variation in the profile of the curled bottom surfaces of SLS fabricated polycarbonate blocks with variation in thickness of the blocks [34]. The blocks, fabricated for the purpose of the study, were 90×26mm in area and 1, 2, 3, 5, 10, 20 and 50 layers in thickness, where the nominal thickness of a layer was equal to 0.125mm. The laser power (*P*), laser speed (*U*) and scan spacing (*S*) selected in fabrication of the blocks were 10W, 1189mm/s and 0.15mm respectively. In the "build" stage of SLS processing, the part heater set point was set at 154°C. In addition, there were no bases constructed below the downward facing surfaces of the blocks (see Section 2.2.5.4.2).

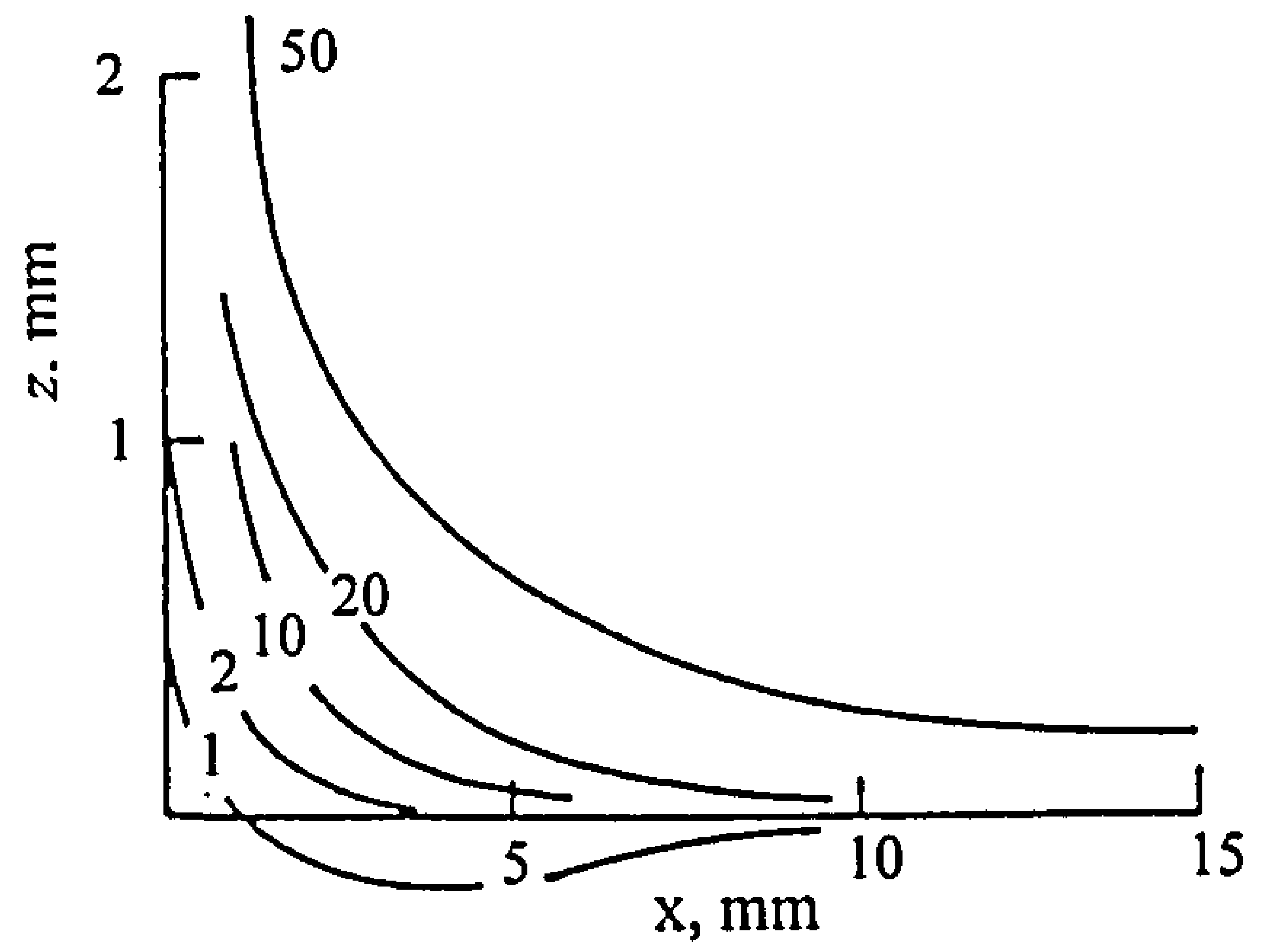

Figure 2.45 Measured profiles of the bottom surfaces of SLS fabricated polycarbonate parts 2, 10, 20 and 50 layers in thickness. From [34].

The bottom surface of each of the fabricated blocks was then traced using a stylus profilometer. The profiles measured are shown in Figure 2.45, where the part co-ordinate system is illustrated in Figure 2.46. The edge profile of the one-layer thick part is seen in Figure 2.45 to exhibit a downward curl. That was reported to be artificially caused by placing the thin (very flexible) upward curling layer upside down on a flat surface, as its profile was measured [34].

The slopes of the measured profiles (*dz/dx*) were then estimated, where a linear variation in slope pointed to a circular profile. The results obtained suggested that the measured profiles could be approximated to two circular arcs. The first arc, denoted in Figure 2.46 (region *I*), was seen to exist in the region extending 2.5mm from the edge of bottom surfaces of the parts. The second circular arc, denoted (region *II*), extend from the end of region *I* towards the centre of the part (see Figure 2.46). Further investigation revealed that the length of region (*I*) and its radius (10mm) were independent on the thickness of the blocks. However, the length of region (*II*) and its radius were found to increase with the increase in thickness, but stopped growing as the thickness of the blocks exceeded 20 layers.

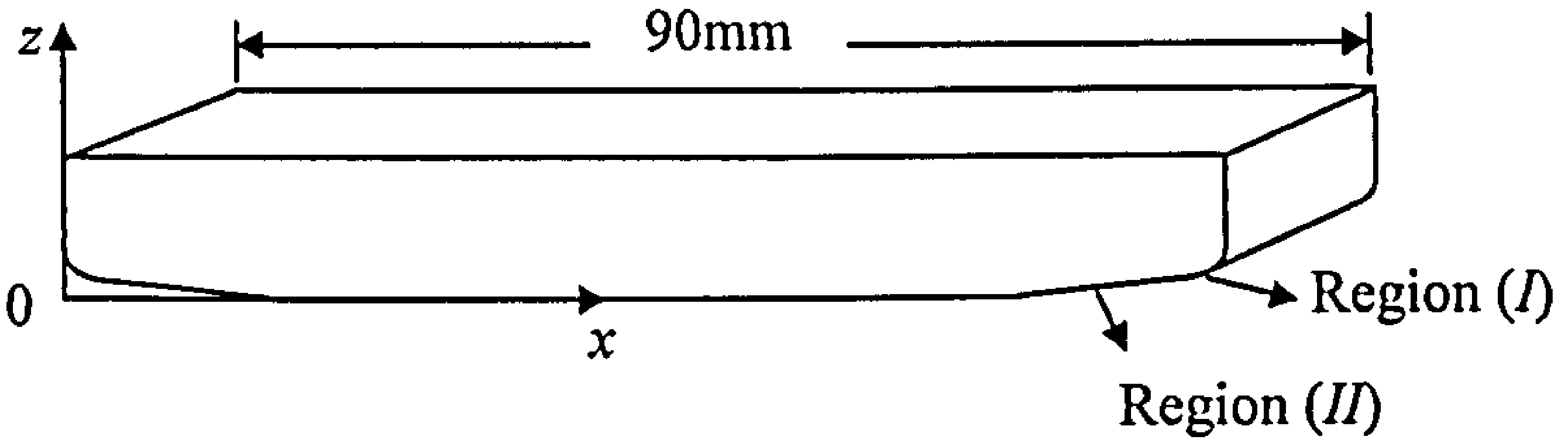

Figure 2.46 Schematic illustration of the curled regions (*I*) and (*II*) seen at the bottom surfaces of SLS fabricated polycarbonate parts.

The work also examined the influence of bases on the curl profile of the bottom surfaces of 50-layer thick polycarbonate blocks. The blocks were fabricated using the SLS machine parameters aforementioned. The bases, however, were sintered at laser power (*P*) and laser speed (*U*) equal to 10W and 1189mm/s respectively, but at scan spacings (*S*) that ranged from 0.15 to 0.63mm. The results showed that the radius of region (*I*) was unchanged with the use of bases. However, the radius of region (*II*) was found to depend on [*P/(U.S)*] used in building the base. The study revealed that the base had no restraining effect on curl at [*P/(U.S)*] less than 0.015J/mm^2. As [*P/(U.S)*] was increased, the radius of that region also increased. However, above [*P/(U.S)*] equal to 0.03J/mm^2, the base had no additional restraining effect on curl.

In the study [34], attempts were made to investigate the causes of curl. Initially, an analytical density model was developed to predict the edge shape of a single SLS fabricated polycarbonate layer. The curved density contours predicted by the model were seen to correspond to a corner of radius 0.5 to 1mm, which was approximately one tenth the radius obtained based on the experimentally measured profiles. Thus, the density model failed to explain the curvature seen close to the edges of the part.

The authors then attempted to examine the effect of thermal shrinkages that arise following cooling of a melt layer (recently sintered layer) on curl. An analytical model was developed for that purpose consisting of a viscoelastic model to represent the cooling (melt) layer bonded to an elastic substrate representing the previously sintered layers. The analytical model predicted significant strains to develop once the temperature of the melt layer reduced below 190°C. Additionally, the model showed that an increase in the cooling rate of the layer resulted in larger strains. These cooling rates were expected to be the highest closest to the edges of the layer, which (according to the authors) may have resulted in the distinct curl seen at the edges of the bottom surface of the part.

2.4.2 Finite Element Modelling of Curl

In this section, a number of previous studies that used the finite element approach to examine curl development in the SLS process are introduced. Dalgarno et al. [35] developed a finite element model to predict curl in SLS fabricated polycarbonate parts. The approach taken within the work reported was to model part build by adding layers of elements to represent addition of material to a part, and introducing compressive strains as the layers are added. Figure 2.47 schematically shows the finite element mesh used within the analysis. The mesh represents a block 90×26mm in area and 10 layers in thickness (see Figure 2.48). The thickness of each layer forming the ten-layer part was defined in the analysis based on experimental measurements. In the model, all the layers with exception of the first and second layers were given a thickness of 0.125mm, which was the default thickness within the manufacture of a ten-layer part. The first layer of the part was given a thickness of 0.66mm, whereas the second layer was given a thickness of 0.25mm. The additional thickness of these layers was reported to be a result of bonus Z (see Section 2.2.5.4.1).

The analysed ten-layer part was symmetrical about the *y-z* plane (see Figure 2.48), and thus only half of the part was modelled. Additionally, it was reported that a 2D analysis was used as it was the distortion along the 90mm length of the part that was of interest [35]. The elements used in the mesh were four noded coupled thermal-displacement plane stress elements. Coupled elements allowed compressive strains to be introduced to the layers as they were built by artificially lowering their temperature within the mesh. The powder bed was modelled as a rigid surface. It was reported that the surface is unlikely to be rigid. However, as the powder bed was assumed not to experience elevated temperatures during the SLS process (compared to the part), the bed is likely to be stiff relative to the part.

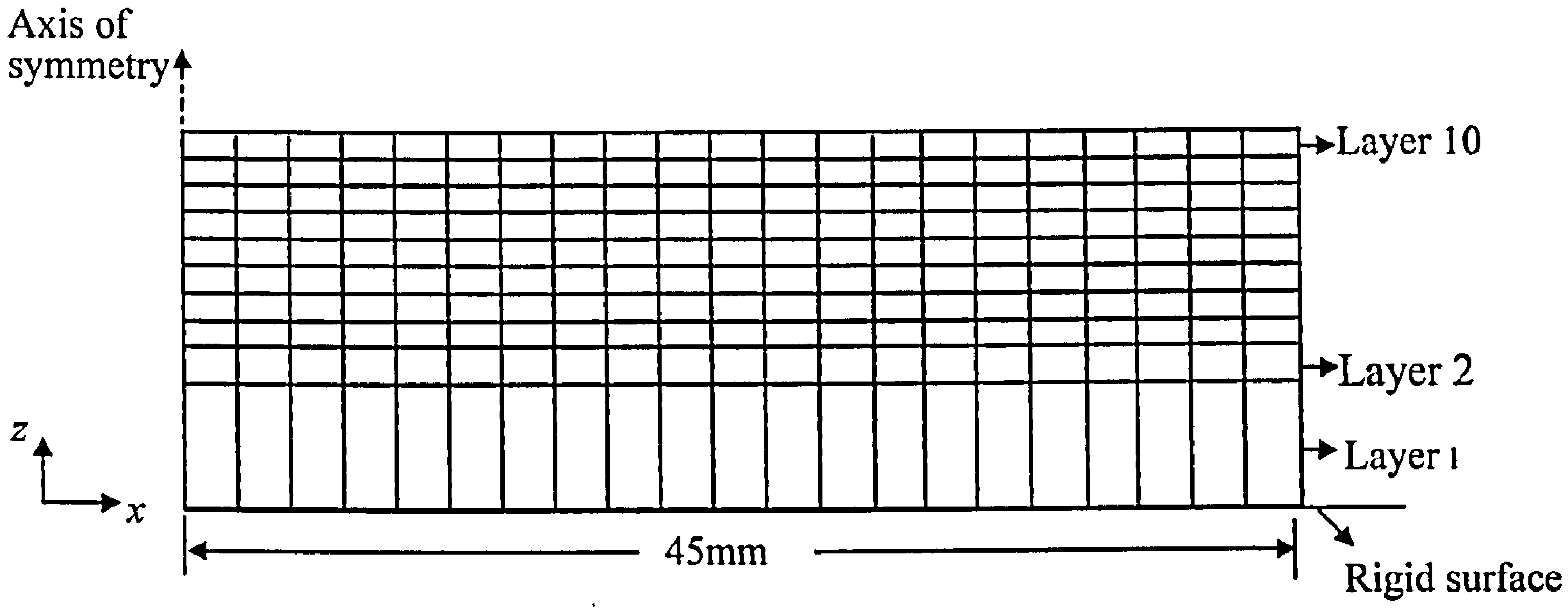

Figure 2.47 Schematic illustration of the 2D finite element mesh used in the curl analysis performed by Dalgarno et al. [35].

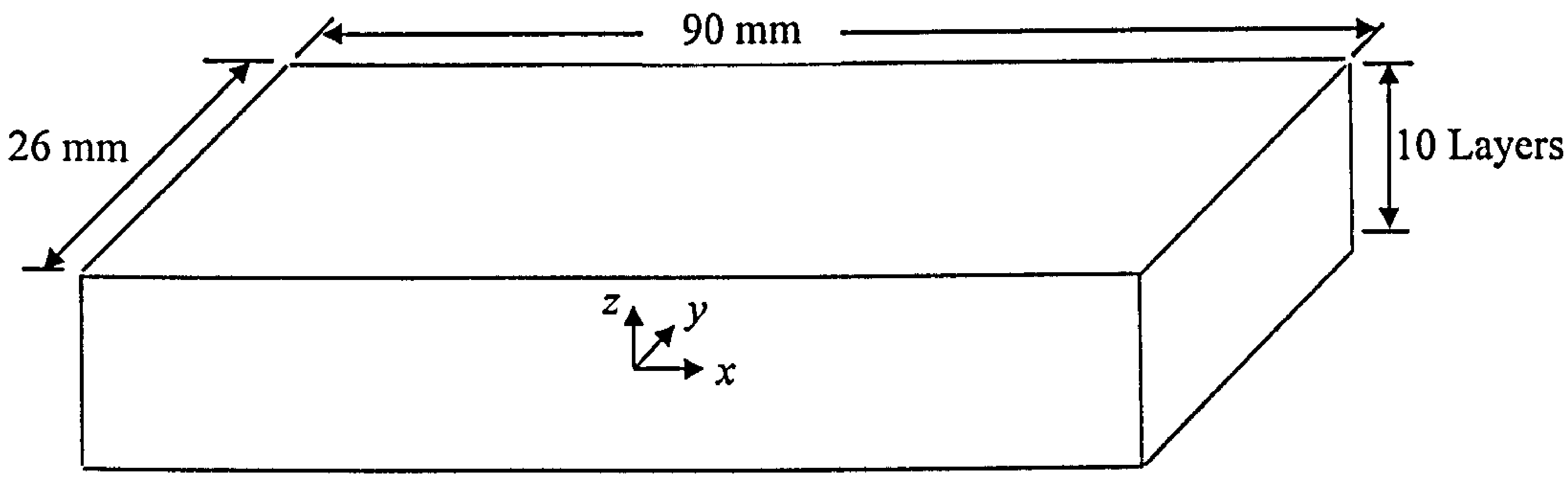

Figure 2.48 Schematic diagram of the 10-layer part modelled in the finite element analysis performed by Dalgarno et al. [35].

Based on experimental measurements, elements representing the part were given a density of 700kg/m^3. However, the elastic modulus, Poisson's ratio and expansion coefficient were given assumed values equal to 50MPa, 0.4 and $2\times10^{-6}C^{-1}$ respectively. The interaction between the part and powder bed was modelled with an assumed coefficient of friction of 1. That value was selected to reflect that real surfaces would be quite rough, giving high resistance to relative motion.

The first step of the analysis was to remove the layers from two to ten, following their initial definition. In the step, the first layer of the part was analysed. The only boundary condition applied was to enforce symmetry; the nodes along the axis of symmetry were constrained not to move in the *x*-direction (see Figure 2.47). A gravity load was applied to the elements active in the model. The compressive strain (2.6×10^{-4}) was then imposed on the layer by artificially reducing its temperature. After the first layer was loaded in this way, elements making up the second layer were introduced, and the gravity load and compressive strain applied to them, with this procedure repeated until all ten layers of the part were introduced and loaded.

Measured displacement in the z-direction, 3.25mm from the part edge of a two-layer part.	0.025mm
Finite element predicted displacement in the z-direction, 3.25mm from the part edge of a two-layer part.	0.011mm
Measured displacement in the z-direction, 5.5mm from the part edge of a ten-layer part.	0.05mm
Finite element predicted displacement in the z-direction, 5.5mm from the part edge of a ten-layer part.	0.052mm

Table 2-1 Comparison between the finite element prediction of curl and the experimental measurements. From [35].

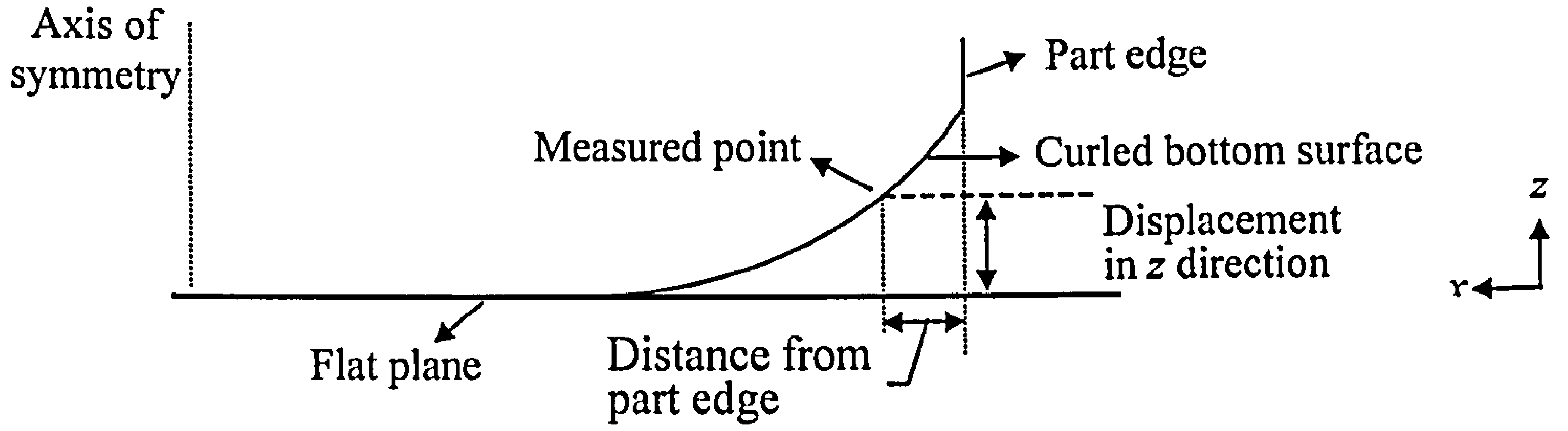

Figure 2.49 Schematic diagram of a curled bottom surface of a part, clarifying the terms denoted in Table 2-1.

Using the above-mentioned method, a separate analysis was also carried out to predict curl of a two-layer part, 90×26mm in area. Table 2-1 shows the finite element model predictions compared to measurements of distortion performed on two and ten-layer parts of the same geometry. Figure 2.49 shows a schematic diagram of the curled bottom surface of a part, presented here to clarify the terms denoted in Table 2-1. It was reported that the results suggest that the combination of gravity loads, compressive strain introduced within the layers as they are manufactured and the interaction between the powder bed and the part all lead to the development of curl.

Jamal [36] further developed the previously described finite element models by considering fewer assumptions with regard to the material properties of polycarbonate. In the model, the elastic modulus was defined based on experimental measurements. Additionally, the viscoelastic behaviour of polycarbonate was taken into account in the analysis. The analysis was initially performed on a part, 90×26mm in area and 10 layers in thickness. The finite element mesh generated for the analysis was that used in the previous model developed by Dalgarno et al. [35], schematically illustrated in Figure 2.47. Additionally, the thickness of each layer forming the part and element type used in the mesh were identical to those defined in the previous finite element model. Material properties defined in the analysis were those assigned in the previous model with the exception of the elastic modulus. The elastic modulus was considered in the analysis to be constant, equal to 319.4MPa. The modulus was determined from tensile test measurements performed on an SLS fabricated polycarbonate part at 100°C. The time-temperature dependent behaviour of the polymer was also considered in the analysis. The model required as input the stress relaxation data experimentally obtained at a reference temperature along with the WLF constants estimated at that reference temperature (see Section 2.3.1.3). The reference temperature specified in the model was 100°C. The stress relaxation data experimentally obtained at 100°C were defined in the form of ($g_R(t) = E(t)/E$) against the relaxation time (t), where $E(t)$ is the modulus at relaxation time (t), and E is the instantaneous modulus obtained from the tensile test measurements performed at 100°C.

Relaxation time t (sec)	$E(t)$ MPa	$g_R(t) = E(t)/E$
0	319.4	1
33.33	293.02	0.9174
146.6	277.85	0.8699
2000	254.88	0.798

Table 2-2 Selected stress relaxation data experimentally obtained at 100°C. From [36].

The data of $g_R(t)$ against the relaxation time (t), reported in the study, are summarised in Table 2-2. Stress relaxation tests were also carried out at 120°C and 140°C in order to estimate the WLF constants (C_1 and C_2) at the reference temperature (100°C). The values reported for C_1 and C_2 were 2.778 and 7.389 respectively.

Similar to the previous model, elements representing the layers from two to ten of the part were deactivated in the first step of the analysis. A boundary condition was then applied to enforce symmetry of the first layer. A gravity load was also applied to all active elements in the mesh. Compressive strain was introduced to the layer by reducing its temperature from 190°C to 150°C. The temperature 190°C was selected as it was reported in a previous study [34] (see section 2.4.1) to be the temperature below which considerable thermal strains develop in a recently sintered polycarbonate layer. The temperature 150°C is generally selected as the set point at which the part heater maintains the top surface of the part bed during the "build" stage of SLS fabrication of polycarbonate parts. After the first layer was loaded in this way, elements making up the second layer were introduced, and the gravity load and compressive strain applied to them, with this procedure repeated until all ten layers of the part were introduced and loaded. Using the same method, analysis was performed to predict curl of a two-layer part.

The effect of the time-temperature dependent response of polycarbonate on curl was investigated by selecting different periods to represent the time it took the recently added layers to reduce in temperature from 190°C to 150°C. The cooling periods selected were 0.01 seconds and 30 seconds. Table 2-3 shows the finite element model predictions compared with measurements of distortion reported by Dalgarno et al. [35]. The terms denoted in the table are clarified in Figure 2.49. The results suggested that the time-temperature dependent response of the polymer had a significant effect on curl.

Results	Experimental measurement	Finite element results	
		Cooling in 0.01 seconds	Cooling in 30 seconds
Displacement in the z-direction, 3.25mm from the part edge of a two-layer part.	0.025 mm	0.019 mm	0.012 mm
Displacement in the z-direction, 3.25mm from the part edge of a ten-layer part.	0.05 mm	0.0456 mm	0.036 mm

Table 2-3 Comparison between the finite element predictions of curl and the experimentally obtained measurements. From [36].

The studies reported in Section 2.4 suggested a number of factors that influence the development of curl in SLS fabricated polycarbonate parts. The experimental study [34] showed the profile of the curled bottom surface of a part to be highly influenced by the thickness of the part. The study also suggested that the use of bases can reduce the curling effect, but cannot completely eliminate it. However, the numerical models developed in the study did not identify the exact reasons for curl development, particularly in the region close to the edges of the bottom surface of a part (Region *I* in Figure 2.46).

However, the finite element models developed by Dalgarno et al. [35] suggested a number of factors that influence the development of curl. These are thermal shrinkages generated in each layer forming the part, gravity load and friction between the part and powder bed. The finite element models by Jamal [36] suggested that the cooling rate of a recently sintered layer has a high effect on the development of curl; the higher the cooling rate, the larger the curl developed and vice versa. However, the models did not produce accurate prediction of curl, which presumably is due to the large number of assumptions the models comprised. For example, material properties defined in the models were mainly assumed. Additionally, temperature reductions specified in the analyses to each layer of the part were based on hypotheses, and were not defined on the basis of experimental measurements, analytical investigations or numerical models. While the curl models reported can give an indication of the some of the factors influencing curl, they remain extremely basic in nature. Moreover, the models do not provide a real understanding of the underlying problem with relation to the SLS machine parameters. Consequently, further work is required to develop a finite element model that is capable of accurately predicting curl in SLS fabricated parts. This requires proper simulation of the SLS process with the use of the least assumptions with regard to material properties.

Chapter 3

Experimental Investigation of Curl

3.1 Introduction

The subject of this chapter is to describe the SLS fabrication of ten-layer polycarbonate specimens and to introduce the method employed in measuring the profiles of their curled surfaces. The measured profiles, presented in this chapter, were employed in guiding the development of the finite element models, created to predict curl, and to validate results obtained.

3.2 Geometry of Parts and SLS Parameters Used in Manufacturing

In this section, the geometry of the polycarbonate specimens and the SLS machine parameters used in their fabrication are introduced. The five specimens separately SLS fabricated were polycarbonate blocks 90×26mm in area and 10 layers in thickness. The nominal thickness of each layer was 0.127mm. As previously reported, the SLS process consists of three stages; "warmup", "build" and "cooldown". In the following, a description of these stages in fabrication of the ten-layer parts is given.

In the "warmup" stage, layers of powder were deposited onto the part piston. The overall thickness of the powder spread in that stage was approximately 15.24mm. That was then followed by the "build" stage, wherein the temperature of the powder in the feed cartridges was maintained at 80°C. Layers of powder were spread by the roller, with the part heater raising the temperature of the top surface of the added layer to 150°C, prior to sintering taking place. Each of the blocks were separately fabricated, at the centre of the part bed, in an arrangement schematically illustrated in Figure 3.1. The SLS machine parameters selected in fabrication, i.e. laser power (*P*), laser speed (*U*) and scan spacing (*S*) were 11W, 1188.87mm/s and 0.25mm respectively. There were no bases manufactured underneath the ten-layer parts.

Additionally, the piston heater and downdraft were deactivated during processing. After the last (tenth) layer of a block was sintered, the heaters were switched off, indicating the start of the "cooldown" stage. In that stage, the process chamber door cannot be unlocked as long as the temperature measured by the IR sensor was above 100°C. The IR sensor readings represent the temperature at the top surface of the part bed at a location distant from the top surface of the last sintered layer.

After the temperature measured by the IR sensor reached 100°C, the process chamber door was unlocked. The part piston then raised the part bed and a plastic hollow cylinder, with an internal diameter slightly larger than that of the part bed, was positioned to support the side wall of the part bed previously supported by the (part piston) cylinder wall. Once the part bed was completely raised, a metallic tray was slid underneath the part bed and the hollow cylinder. The tray with the part bed and the plastic hollow cylinder (supporting the bed side wall) on its top surface was then placed on the breakout station for the fabricated part to cool naturally to room temperature. The fabricated part was then cleaned in the breakout station for the curl measurements to be performed.

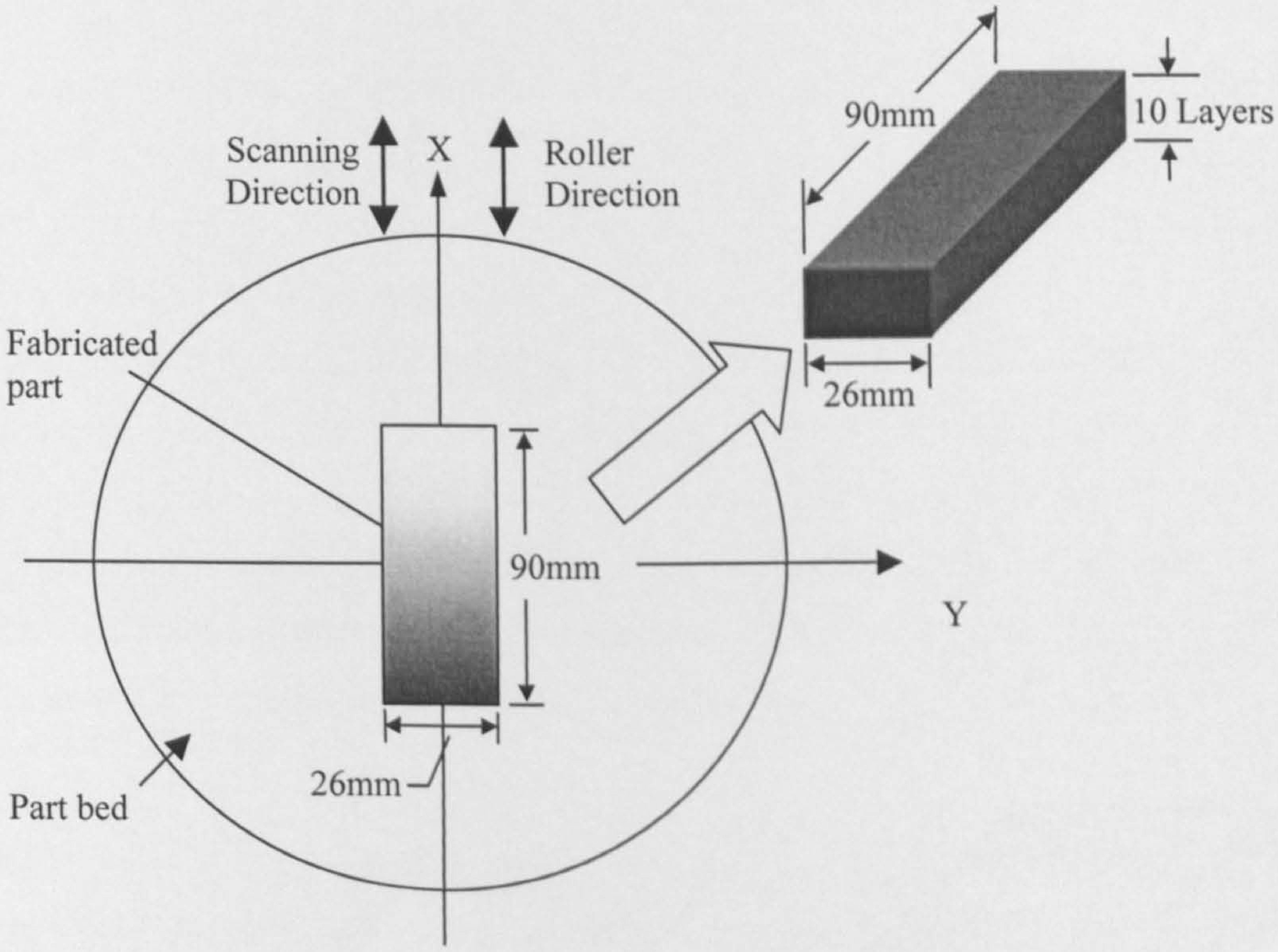

Figure 3.1 Schematic diagram showing the position of the modelled ten-layer part in the part bed during fabrication.

3.3 Procedure for measuring Curl

The curl was examined by experimentally measuring the profiles of the (90×26mm) upward and downward facing surfaces of the fabricated blocks. The measurements were performed using a non-contacting laser displacement meter; an Anritsu KL133B (see Figure 3.2). The meter estimates the vertical distance of a point on a body from a flat reference plane. The laser beam is projected from a sensor head onto the point to be measured. From the reflection of the laser beam back to the sensor head, a sensor-processing unit estimates the vertical distance between the point of measurement and the sensor head. The distance between the sensor head and the reference plane is also measured. Using these distances, the distance between the point of measurement and the reference flat plane is calculated, and is shown on an LCD display, illustrated in Figure 3.2.

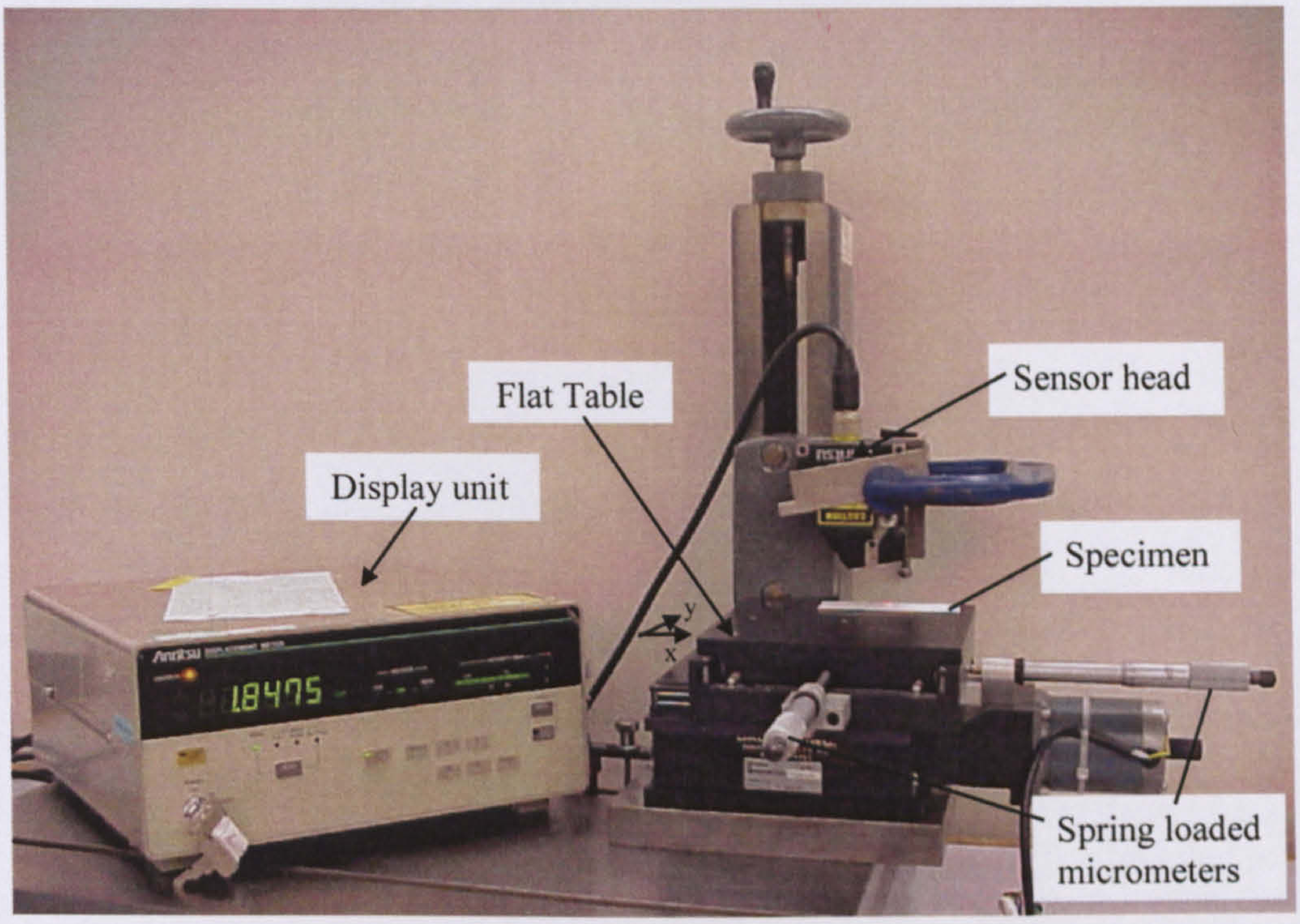

Figure 3.2 Curl measurement using the non-contacting laser displacement meter; Anritsu KL133B.

The specimen for which curl is to be measured was first placed with its top surface facing downwards onto a flat table, as schematically shown in Figure 3.3. The table is taken as the reference for measurements. The table is driven in the *x* and y directions by spring loaded micrometers, illustrated in Figure 3.2. The sensor head shown in the figure does not move; the profile of the bottom surface of the part was traced by the laser beam by the movement of the flat table.

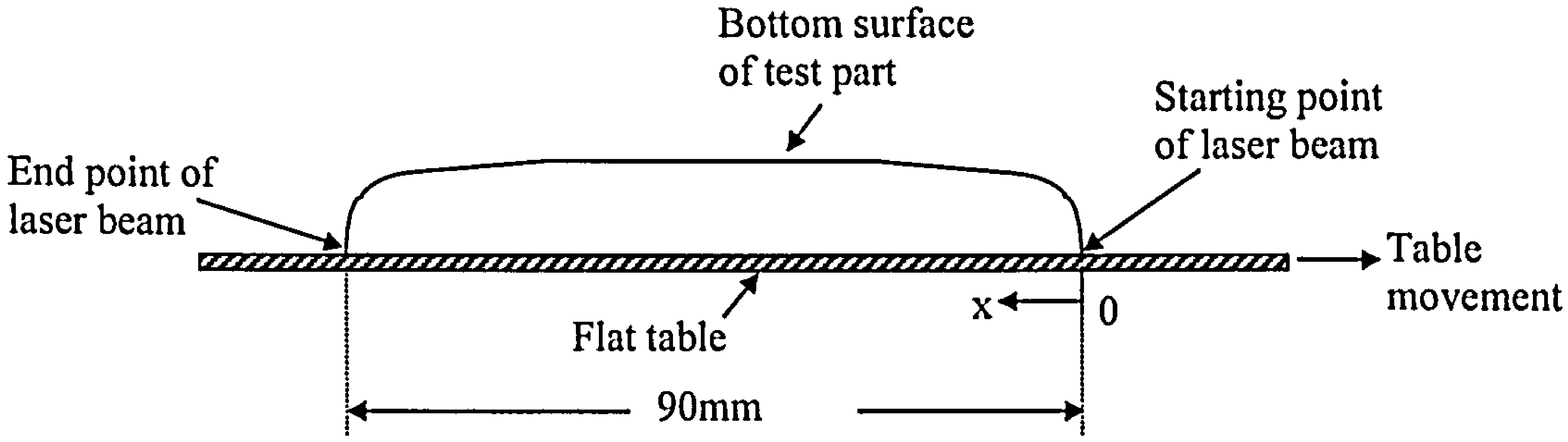

Figure 3.3 Schematic diagram showing the method used in measuring the profile of the curled bottom surface of the modelled ten-layer part.

In the test, the laser beam traces in the x-direction (shown in Figures 3.1 and 3.3) along the bottom surface of the part; starting from one edge where the part makes contact with the flat table, and working along to the same position on the opposite edge. The measurements were taken along the 10mm distance closest to both edges at 0.25mm increments. These are the regions where curl of the bottom surface was most evident. The measurements were then taken every 1mm along the rest of the traced path. Several measurements, parallel to this path, were then performed to test the repeatability of the results. It is essential, for accurate measurements, that the paths traced by the laser beam are distant from the curl occurring at the edges that run parallel to these paths. In a similar way, the profiles of the top surfaces of the specimens were measured. However, the specimens were placed with their bottom surfaces facing downwards onto the flat table, as schematically shown in Figure 3.4.

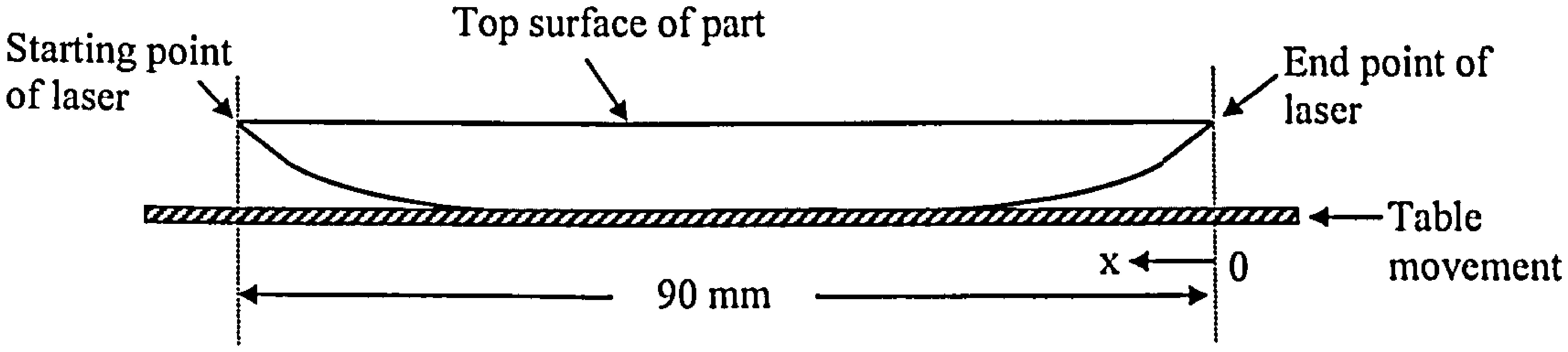

Figure 3.4 Schematic illustration of the method used to measure the profile of the top surface of the modelled ten-layer part.

3.4 Results

The measured profiles of the top and bottom surfaces of the fabricated ten-layer parts are illustrated in Figure 3.5. In the figure, the profile of the bottom surface of the part is seen to deviate from being flat at a distance of approximately 20mm from both edges of the surface, which indicates the existence of curl in that region. However, the curled regions at the top surface of the part are exhibited along a distance of approximately 7mm from both edges of the surface.

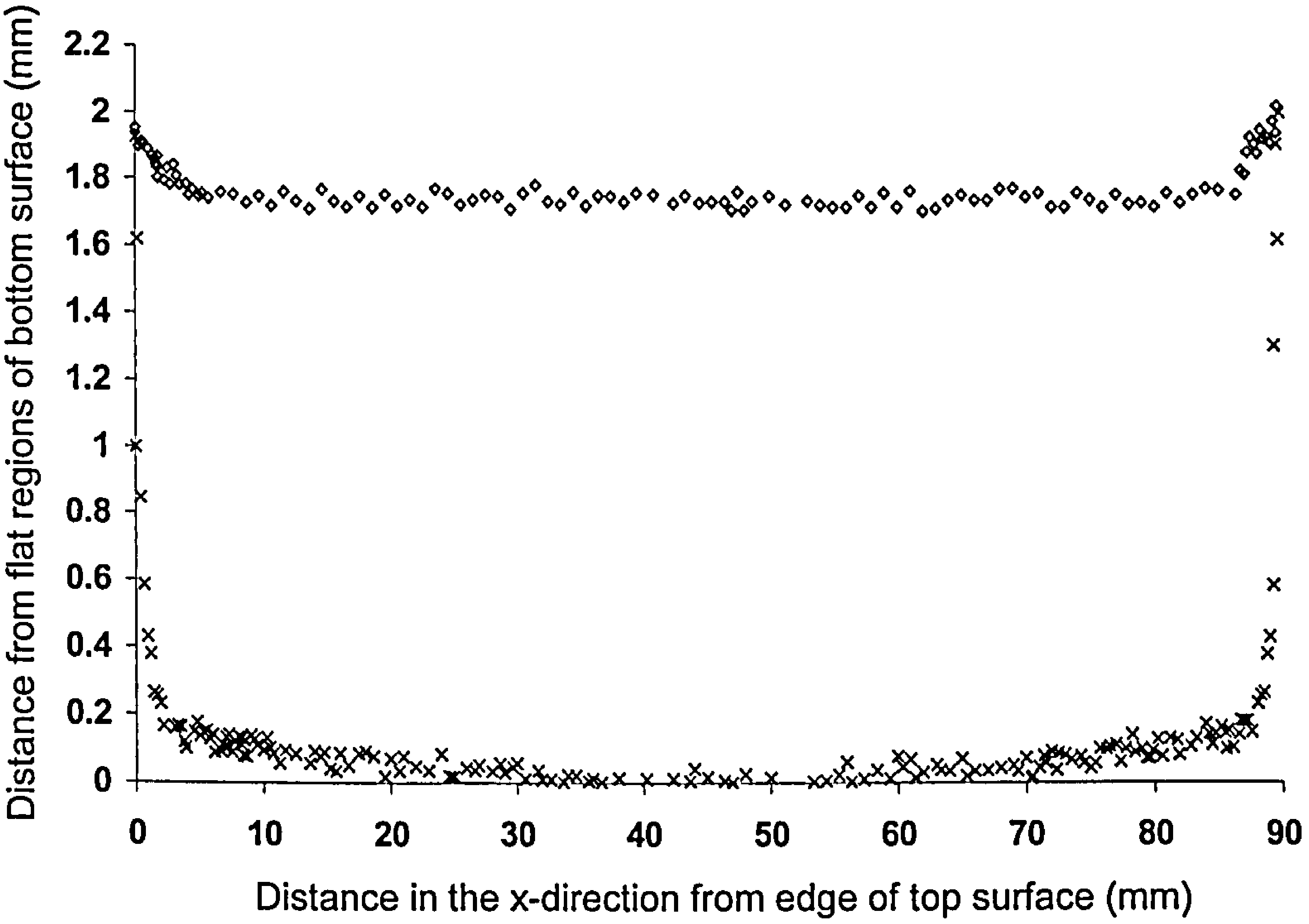

× Measured profile of bottom surface of part ◇ Measured profile of top surface of part

Figure 3.5 Experimentally measured profiles of the top and bottom surfaces of the SLS fabricated ten-layer parts.

Chapter 4

Initial Development of Thermal-Stress Analyses

4.1 Introduction

Curling of a selectively laser sintered part occurs due to non-uniform thermal shrinkages that arise at different regions within the part during processing [1]. Hence, identifying the amount of shrinkage experienced by each layer during processing is of paramount importance for an accurate prediction of curl to be achieved. In the finite element models reported in Section 2.4.2, part build was simulated by adding layers of elements to represent addition of layers in SLS. Thermal shrinkage was introduced to each layer after it had been activated by artificially reducing its temperature. However, temperature reductions specified for each layer in these models were based on hypotheses. In addition, material properties of polycarbonate were mainly assumed and were not based on experimental measurements. The considerable number of assumptions the models comprised was expected to be the main cause of their inaccurate prediction of curl. Nevertheless, the early work by Dalgarno et al. [35] (see Section 2.4.2) had developed a basic understanding of the fundamental theory required to create a curling model. Based on that work, the finite element model by Jamal [36] had identified the high influence of the viscoelastic behaviour on the development of curl in polycarbonate parts produced in SLS. The purpose of this study is to develop the most recent finite element model [36] to a stage where accurate prediction of curl can be obtained.

During the period of this research, model development had gone through a number of stages. Each of these stages attempted to improve functionality and accuracy over the previous. In this chapter, the general method selected for model development is introduced. The first version of the curling model developed considering this method is then described. The results predicted are next presented, and a comparison between these results and the experimental measurements of curl reported in the previous chapter is provided.

4.2 Description of General Method for Model Development

The method undertaken in model development was mainly focused on two aspects; improving definition of material properties and specifying temperature changes expected to reflect those experienced during SLS processing. In the former, experimental work was carried out to obtain better material property data. In the latter, heat transfer finite element models were developed to predict temperature changes experienced by each layer forming a build during processing. The results of the heat transfer analysis were then transferred to a finite element stress model. Based on temperatures estimated by the heat transfer analysis, the stress model calculates thermal strains developed in each layer forming the part and a prediction of curl is obtained.

In following sections, simple analytical heat and stress models are presented. These models are mainly used to help identify material properties required as an input to the heat and stress finite element models. Next, the techniques available for coupling heat and stress analyses in the finite element package employed (ABAQUS) are introduced, and the technique most suitable for this study is selected.

4.3 Analytical Heat Transfer Model

In solving the heat transfer problem in SLS, one must account for the heat transfer modes the powder bed is subjected to during sintering. As the laser beams scans the surface of the powder bed, a fraction of the incident laser energy is reflected from the surface and the rest of the energy is absorbed. Furthermore, part of the absorbed energy is conducted into the powder bed, while the remainder is lost from the top surface of the sintered powder through convection and radiation. The heat transfer modes expected to occur during processing in SLS are illustrated in Figure 4.1.

In principle, estimation of temperature changes in a powder bed requires solving of a three-dimensional, non-linear, heat transfer problem. The energy conducted into the powder bed can be described by the general heat conduction equation as follows [9,24],

$$\rho C_p \frac{\partial T}{\partial t} = \frac{\partial}{\partial x}\left[k\frac{\partial T}{\partial x}\right] + \frac{\partial}{\partial y}\left[k\frac{\partial T}{\partial y}\right] + \frac{\partial}{\partial z}\left[k\frac{\partial T}{\partial z}\right] \qquad 4\text{-}1$$

where ρ is the density, C_p is the specific heat and k is the conductivity. The symbols T and t, however, denote the temperature and time respectively. The term on the left of Equation 4-1 represents the rate of change in the internal energy per volume whereas the term on the right signifies the three dimensional net conduction into the powder bed.

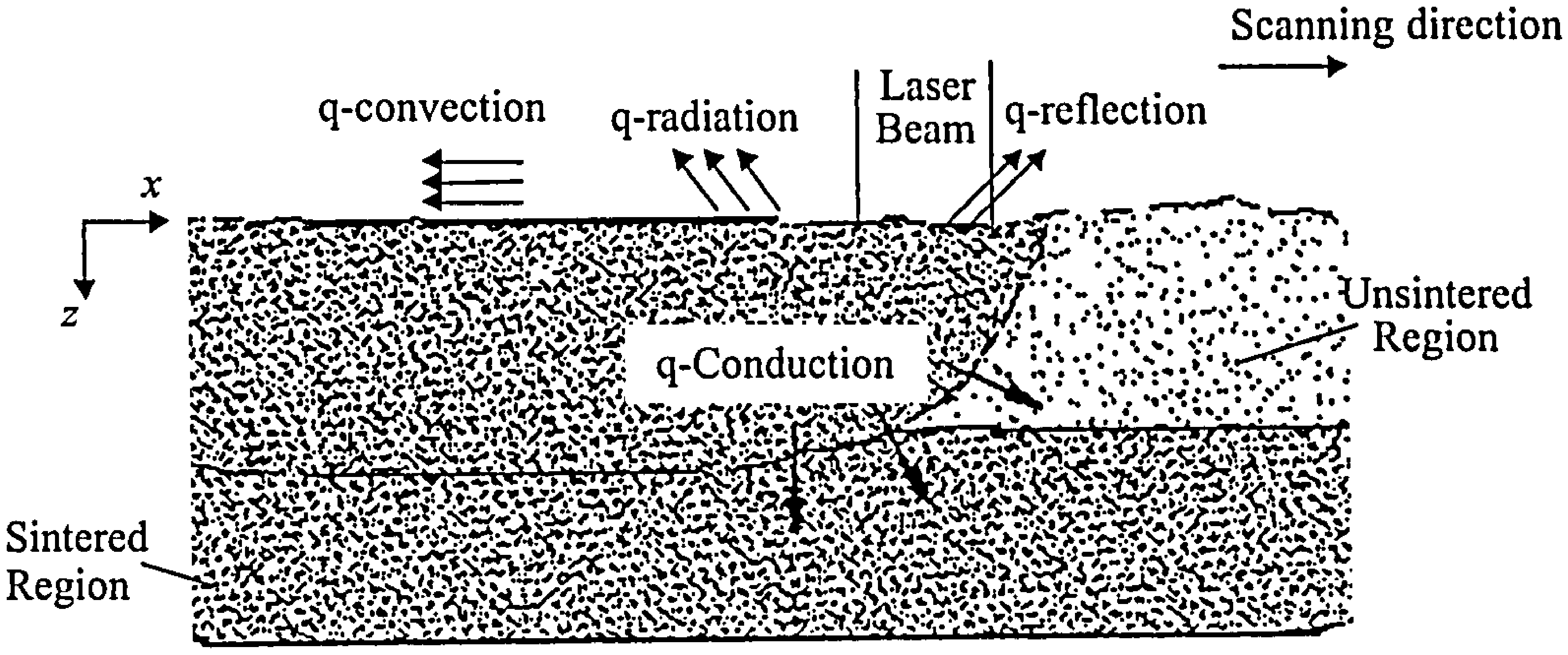

Figure 4.1 Illustration of the heat transfer modes in effect during sintering of a powder bed. Reproduced from [9].

The heat lost from the top surface of the sintered area through convection and radiation can be taken into account by applying the following boundary condition [9],

$$-k\left.\frac{\partial T}{\partial z}\right|_{z=0} = \epsilon\, \sigma_R\left(T_{z=0}^4 - T_{sur}^4\right) + h_c\left(T_{z=0} - T_{env}\right) \qquad 4\text{-}2$$

where σ_R is the Stefan-Boltzmann constant (5.67×10^{-8}W/m$^2\cdot$K^4), ϵ is the emissivity of the surface, h_c is the convection heat transfer coefficient, T_{sur} is the temperature of the surroundings and T_{env} is the temperature of the environment.

Equations 4-1 and 4-2 display the material properties required as an input for solving the heat transfer problem in SLS. These are the density (ρ), specific heat (C_p), thermal conductivity (k) and the emissivity (ϵ).

4.4 Analytical Stress Model

In this section, an analytical stress model that examines curling of a two-layer part is presented. The development of this model is based on previous studies that investigated curling of a bimetallic strip [37,38]. Due to the mismatch between the coefficients of thermal expansion of the metallic layers forming the strip, uniform cooling resulted in non-uniform thermal shrinkages to arise causing the strip to curl.

Curling of SLS fabricated parts, however, is believed to occur as a fresh layer of powder is added on the top surface of a recently sintered layer [39]. Powder addition results in large reduction in the temperature of the recently sintered layer causing it to shrink and the build to curl. Figure 4.2 shows a schematic diagram of the two-layer part analysed. The top layer in this figure represents the recently sintered layer, while that at the bottom signifies the previously sintered layer underneath. In the analysis, non-uniform shrinkage is introduced to the part by reducing the temperature of the top layer from T_l to T_f to reflect the effect of powder addition on its top surface. However, for simplicity the temperature of the bottom layer was assumed to remain constant.

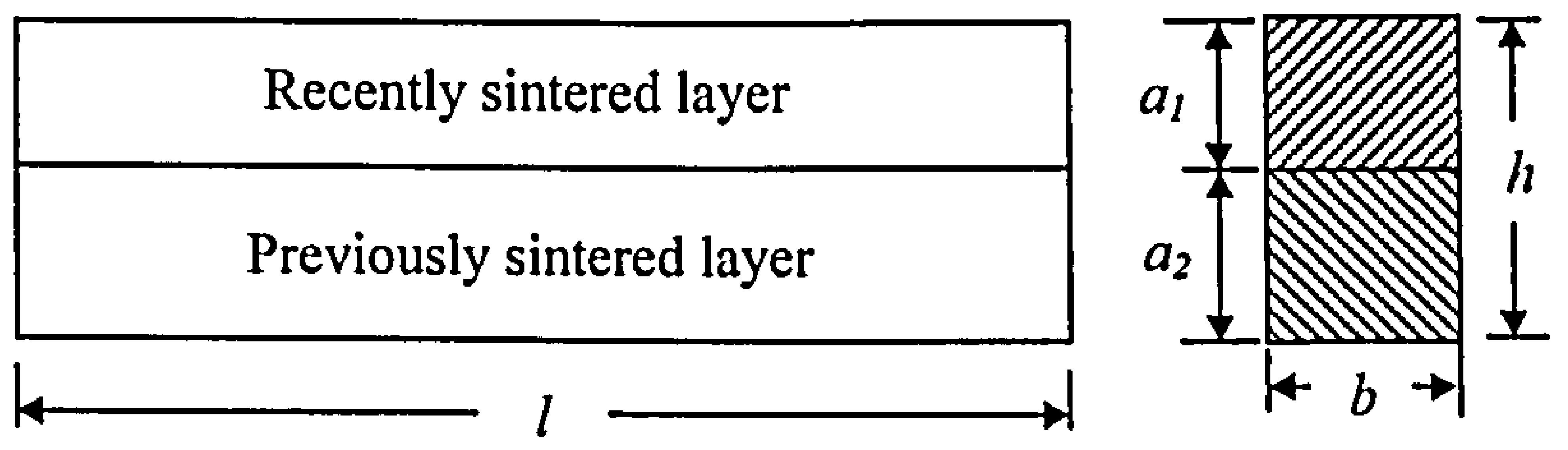

Figure 4.2 A schematic diagram of a two-layer part

The coefficients of thermal expansion of the top and bottom layers are considered to be equal, and are referred to as α. In addition, since the modulus of polycarbonate is highly dependent on temperature, the top and bottom layers are assigned different modulus terms; E_1 and E_2 respectively. However, to simplify the analysis, material properties given for each layer are regarded not to vary with temperature or with the cooling rate. The thicknesses of the top and bottom layers are denoted a_1 and a_2 respectively, whereas the width of both layers is termed (b) and is considered to be equal to unity. In the analysis, the weight of each layer is not taken into account.

Additionally, friction between the bottom surface of the part and the powder bed is not considered.

In the condition where the top and bottom layers are not bonded together (see Figure 4.3*a*), reduction in the temperature of the top layer causes the layer to contract freely with no thermal stresses developing. Conversely, the bottom layer would not experience any thermal strains given that its temperature remains constant. However, provided that both layers are bonded together, shrinkage of the top layer would be impeded causing thermal stresses to arise in the layer. The forces at the bearing surface that act against compressive thermal strains in the top layer are termed F_1 in Figure 4.3*b*. Additionally, shrinkage of the top layer causes the bottom layer to strain. The forces at the bearing surface resulting in the bottom layer to strain are denoted as F_2 (see Figure 4.3*b*). All forces acting over the section of the top layer can be represented by axial tensile forces F_1 and bending moments M_1, where $M_1=F_1a_1/2$. For the bottom layer, all forces acting over its section can be represented by compressive forces F_2 and bending moments M_2, where $M_2=F_2a_2/2$ (see Figure 4.3*c*).

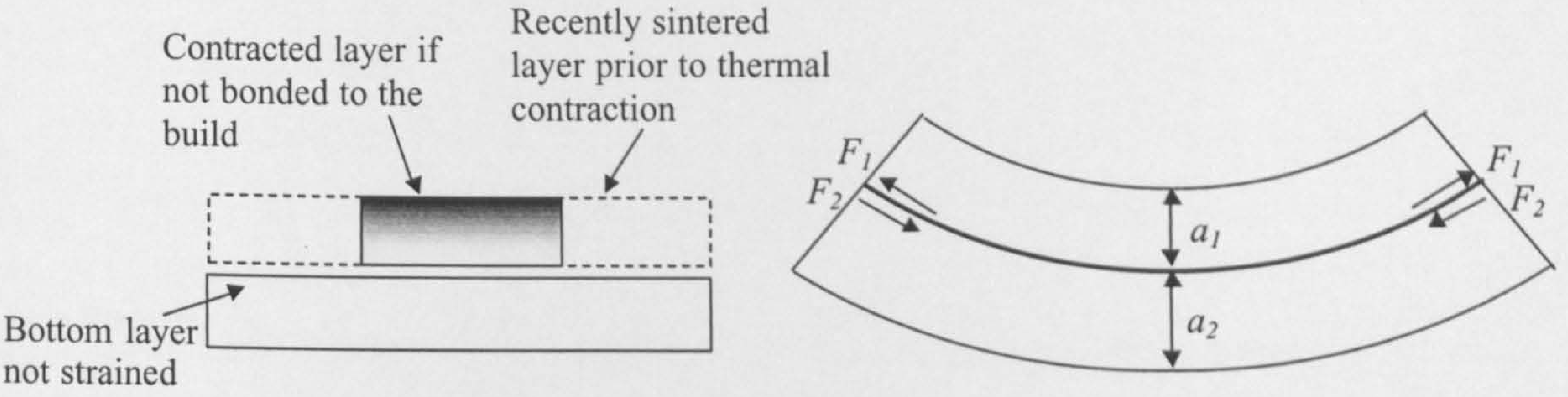

(a) Shrinkage of top layer when not attached to bottom layer

(b) Forces generating at the bearing surface of attached layers due to the shrinkage of the top layer

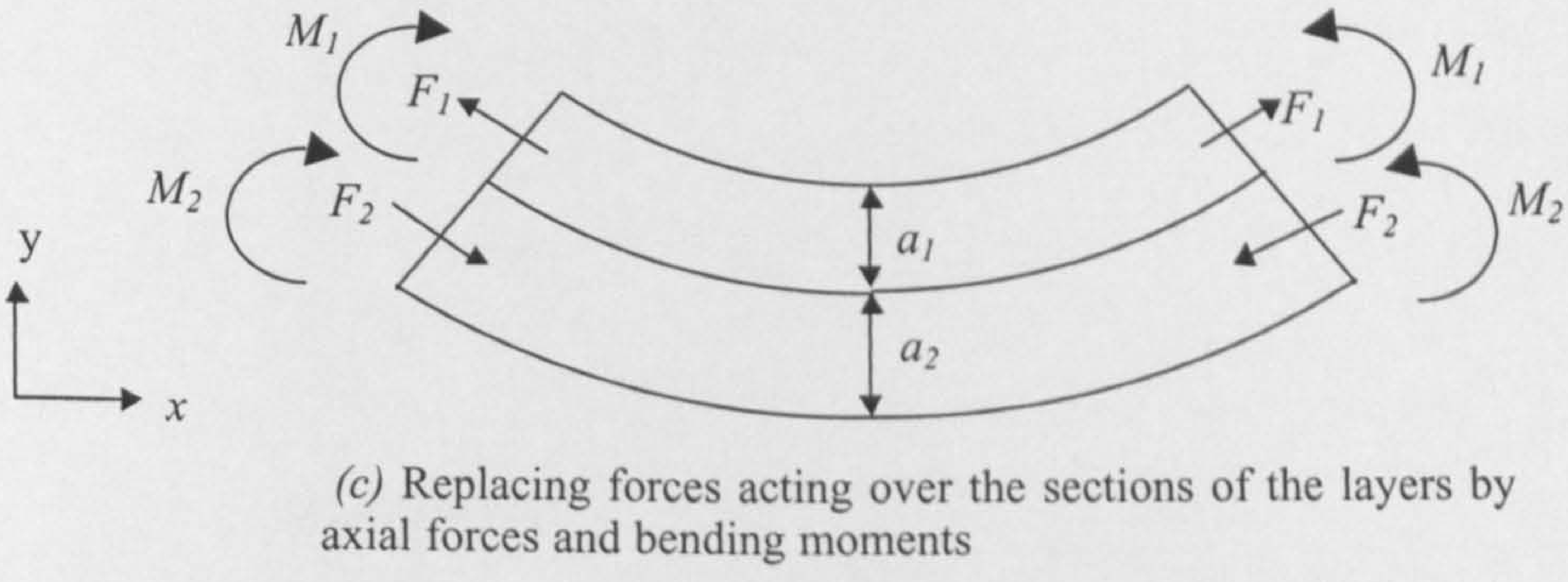

(c) Replacing forces acting over the sections of the layers by axial forces and bending moments

Figure 4.3 Deformation of two-layer part due to shrinkage of top layer

Since there are no external forces acting on the part, all forces acting over any cross section of the part must be in equilibrium, therefore,

$$F_1 = F_2 = F \qquad 4\text{-}3$$

$$M_1 + M_2 = \frac{Fh}{2} \qquad 4\text{-}4$$

where h is the thickness of the part (see Figure 4.2). The bending moments M_1 and M_2 can also be written in terms of the radius of curvature of the two-layer part R as follows [32],

$$M_1 = \frac{E_1 I_{A1}}{R} \qquad 4\text{-}5$$

$$M_2 = \frac{E_2 I_{A2}}{R} \qquad 4\text{-}6$$

where I_{A1} and I_{A2} are the moments of inertia of the cross sectional areas of the top and bottom layers respectively. Substituting the expressions of M_1 and M_2 (Equations 4-5 and 4-6) into Equation 4-4 gives,

$$\frac{Fh}{2} = \frac{E_1 I_{A1} + E_2 I_{A2}}{R} \qquad 4\text{-}7$$

The force F can therefore be expressed in terms of R as follows,

$$F = \frac{2}{h}\left[\frac{E_1 I_{A1} + E_2 I_{A2}}{R}\right] \qquad 4\text{-}8$$

Another equation that relates F to R can be obtained from the consideration of deformation. On the bearing surface, the unit elongation along the x direction (see Figure 4.3) of the top and bottom layers must be equal, then,

$$\alpha(T_f - T_1) + \frac{F}{a_1 E_1} + \frac{a_1}{2R} = -\frac{F}{a_2 E_2} - \frac{a_2}{2R} \qquad 4\text{-}9$$

The radius of curvature can then be found by substituting the expression of *F* in Equation 4-8 into Equation 4-9 giving,

$$\frac{1}{R}=\frac{\alpha(T_1-T_f)}{\frac{h}{2}+\frac{2\left[E_1I_{A1}+E_2I_{A2}\right]}{h}\left[\frac{1}{a_1E_1}+\frac{1}{a_2E_2}\right]} \tag{4-10}$$

Assuming that,

$$\frac{a_1}{a_2}=m, \qquad \frac{E_1}{E_2}=n \tag{4-11}$$

and bearing in mind that

$$I_{A1}=\frac{ba_1^3}{12}=\frac{a_1^3}{12}, \qquad I_{A2}=\frac{ba_2^3}{12}=\frac{a_2^3}{12} \tag{4-12}$$

Equation 4-10 can be written as follows,

$$\frac{1}{R}=\frac{6\alpha(T_1-T_f)(1+m)^2}{h\left(3(1+m)^2+(1+mn)\left(m^2+\frac{1}{mn}\right)\right)} \tag{4-13}$$

Having known the radius of curvature *R*, the deflection δ_d of the part can be estimated. Assuming that the deflection δ_d is small in comparison with the radius of curvature *R*, and denoting *l* to be the length of the part, the following equations can be derived (see Figure 4.4),

$$R^2=(R-\delta_d)^2+\left(\frac{l}{2}\right)^2 \tag{4-14}$$

which gives,

$$\frac{l^2}{4}\approx\delta_d(2R-\delta_d) \tag{4-15}$$

$$\delta_d \approx \frac{l^2}{8R} \tag{4-16}$$

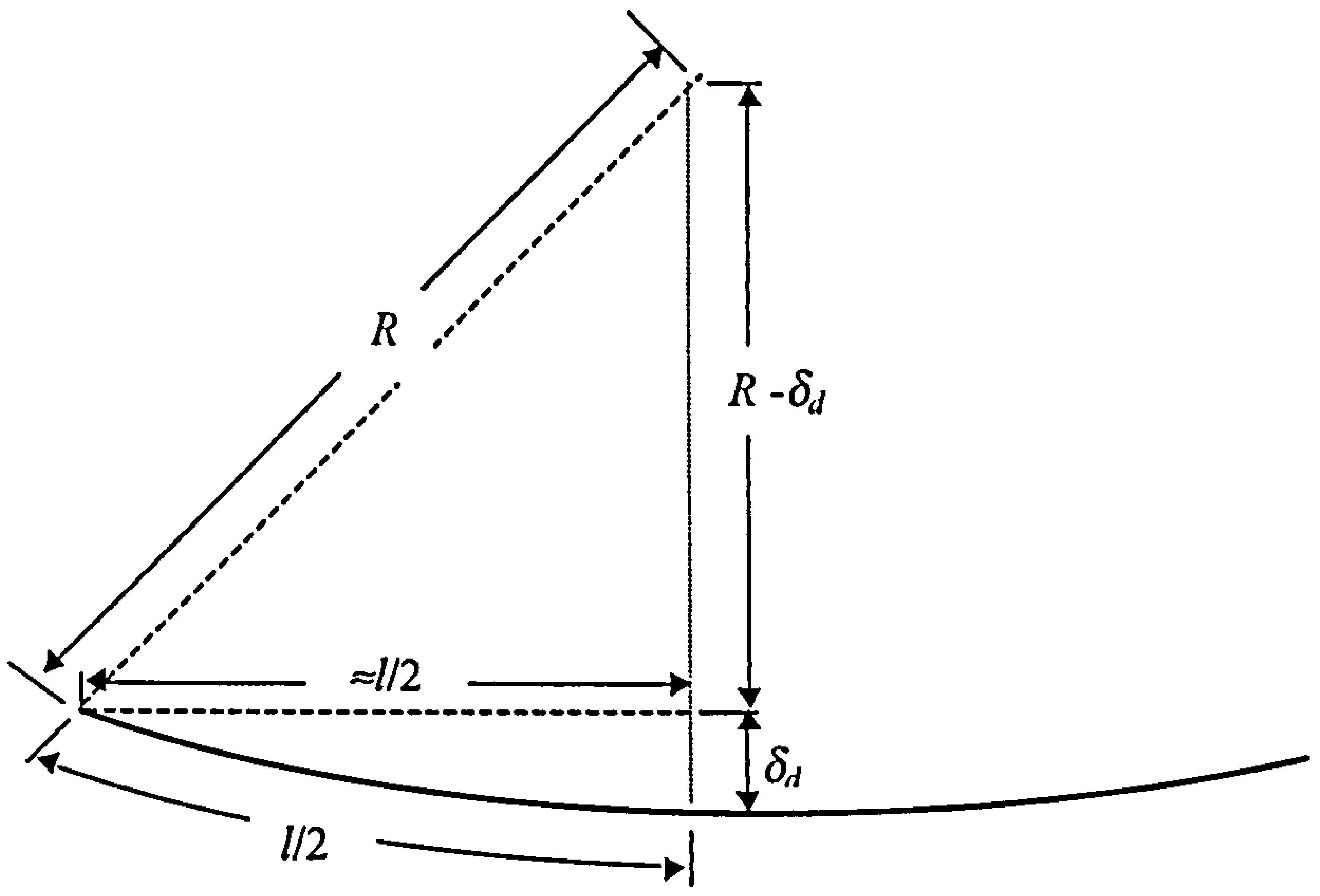

Figure 4.4 Relationship between the radius of curvature R and deflection δ_d.

Equations 4-13 and 4-16 can provide an understanding on some of the factors that affect curling of SLS fabricated parts. These equations imply that the deflection δ_d of a two-layer part is proportional to the shrinkage experienced by the top layer due to the reduction in its temperature and to l^2, but is inversely proportional to the thickness (h). Additionally, the top layer while being sintered could have temperatures that exceed 400°C [7]. At such high temperatures, polycarbonate is in a viscous state and has a very low modulus that is close to zero, i.e. $n \approx 0$. In this condition, the reduction in the temperature of the top layer whilst in that state does not produce any curl. However, as the temperature of the sintered layer reduces below the glass transition temperature, a considerable increase in the modulus of the top layer would be observed (see Figure 2.24). Assuming that the thicknesses of the top and bottom layers are equal i.e. $a_1 = a_2$ which implies that $m = 1$, Equation 4-13 can be written as follows,

$$\frac{1}{R} = \frac{24\alpha(T_1 - T_f)}{h(14 + n + 1/n)} \tag{4-17}$$

Thus, the maximum deflection δ_d can be expressed as (see Equation 4-16),

$$\delta_d \approx \frac{3\alpha(T_1 - T_f)l^2}{h(14 + n + 1/n)} \qquad 4\text{-}18$$

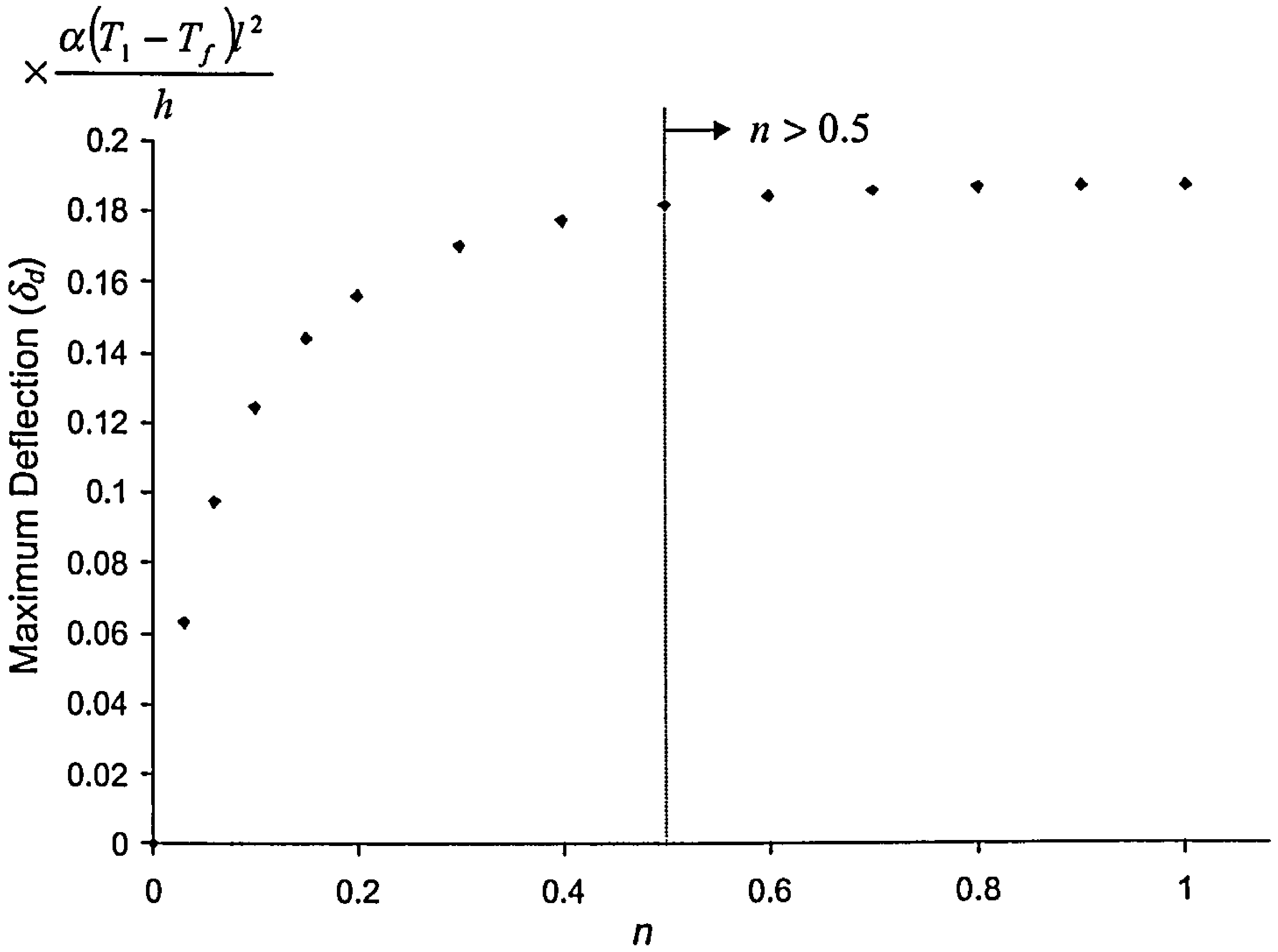

Figure 4.5 Relationship between the maximum deflection δ_d and n, m = 1.0.

Figure 4.5 illustrates a graphical representation of Equation 4-18 showing the relationship between the maximum deflection δ_d and the magnitude of the ratio $n = E_1/E_2$, where $E_1 \le E_2$. It can be seen that provided $n < 0.5$ an increase in the magnitude of (n) produces a noticeable rise in the maximum deflection of the part. However, for $n > 0.5$, the effect of the increase in (n) on the maximum deflection becomes less evident. For example, the difference in the maximum deflection between the case where n = 0.1 and n = 0.2 is approximately 20%, whereas the difference in the maximum deflection for n = 0.5 and n = 1.0 is only approximately 3%. The conclusion is that curling of a part is highly dependent on changes in modulus during the cooling of a recently sintered layer from the melt, where (n) attains values smaller than 0.5. As the temperature of the layers forming the part reduce below the glass transition, for example during the "cooldown" stage in SLS, the modulus becomes less susceptible to changes in temperature. In this condition, n is expected to be larger than 0.5 and changes in the modulus would not produce any substantial effect on the deformation of the part. Curl in the "cooldown" stage is therefore mainly expected to be produced by the non-uniform shrinkages that arise through changes in temperature of the layers.

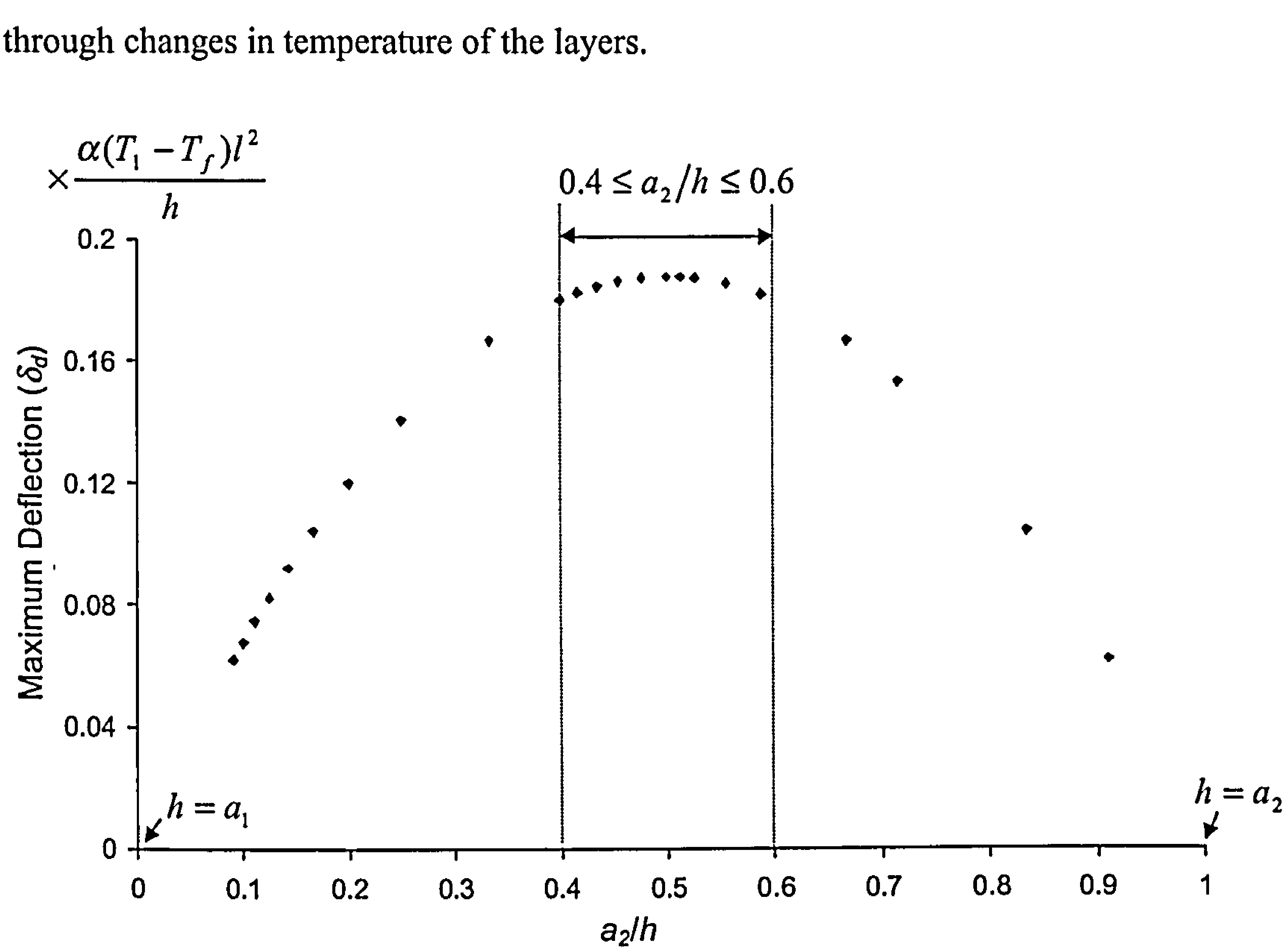

Figure 4.6 Relationship between the maximum deflection δ_d and a_2/h, $n = 1.0$.

Equation 4-13 also implies that the deflection of the part is dependent on the magnitude of the ratio $m = a_1/a_2$ while maintaining h constant. In the simplest condition where the ratio $n = 1$, the maximum deflection δ_d can be expressed as (see Equations 4-13 and 4-16),

$$\delta_d \approx \frac{3\alpha(T_1 - T_f)(1+m)^2 l^2}{4h\left(3(1+m)^2 + (1+m)\left(m^2 + \frac{1}{m}\right)\right)} \qquad \text{4-19}$$

A graphical representation of this equation is illustrated in Figure 4.6. For an easier understanding of the effect of the ratio m on δ_d, the maximum deflection of the part δ_d is plotted against the ratio a_2/h where $h = a_1 + a_2$ and,

$$\frac{a_2}{h} = \frac{1}{1+m} \qquad 4\text{-}20$$

Figure 4.6 shows that the deflection δ_d is zero when the part is only made of one layer, i.e. $h = a_1$ or $h = a_2$. When $h = a_1$, the (top) layer shrinks freely without producing any thermal stresses, provided that temperatures change uniformly in the layer. In addition, Figure 4.6 shows that the maximum deflection of the part δ_d is achieved at $a_2/h = 0.5$ (the thicknesses of both layers are equal $a_1 = a_2$) and deviates from that maximum deflection by less than 4% in the range $0.4 \le a_2/h \le 0.6$. However, for $a_2/h < 0.4$ or $a_2/h > 0.6$ a noticeable decrease in δ_d is seen. The results can provide a general insight on the choice of layer thicknesses for the purpose of reducing curl during the "cooldown" stage in SLS where $n \approx 1.0$.

The mathematical model developed is employed in estimating the deflection of a two-layer part produced in SLS. The results from the model are compared to curl measurements reported by Dalgarno et al. [35] and are presented in Table 2-1 for a two-layer part. The two-layer part analysed by Dalgarno et al. [35] was 90×26mm in area. The thickness of the bottom layer (a_2) was 0.66mm and that of the top layer (a_1) was 0.25mm. For simplicity, the viscoelastic behaviour of polycarbonate is not taken into account in the analysis; the modulus is independent on both time and temperature effects. Based on experimental measurements, the modulus of polycarbonate (E_1 and E_2) is considered to be 319.4MPa [36]. The coefficient of thermal expansion α is taken as $2\times10^{-6}\ ^{\circ}C^{-1}$ [35]. Additionally, thermal strains and stresses are regarded to develop in a melt layer only once its temperature reduced below 190°C [34].

In the analysis, SLS fabrication of a two-layer part is simulated. The temperature of the first (bottom) layer is expected to reach 400°C during sintering [7]. The temperature is then assumed to reduce homogeneously in the layer to 150°C prior to adding the second layer. Homogenous reduction in temperature causes the layer to shrink freely with no thermal stresses developing; no curl occurs during the cooling of this layer. The second layer is next added in its powder form at 150°C and then sintered, exceeding temperatures equal to 400°C. The reduction in temperature of this layer from 190°C to 150°C causes the layer to shrink and the part to curl. This is followed by the "cooldown" stage in SLS. During that stage, the temperature of the part is assumed to reduce homogeneously from 150°C to room temperature. In this situation, the two-layer part contracts uniformly without producing any additional curl. Combining both Equations 4-10 and 4-16, the final deflection of the part can be estimated as follows,

$$\delta_d = \frac{\alpha(T_1 - T_f)l^2}{4h + \frac{16[E_1 I_{A1} + E_2 I_{A2}]}{h}\left[\frac{1}{a_1 E_1} + \frac{1}{a_2 E_2}\right]} \qquad 4\text{-}21$$

As the deflection was experimentally measured 3.25mm away from the 90mm edge of the two-layer part (see Table 2-1), the length l is substituted in Equation 4-21 with 83.5mm. The moments of inertia of the cross sectional areas of the top and bottom layers I_{A1} and I_{A2} are calculated using Equation 4-12 with b = 26mm. Additionally, the temperatures T_1 and T_f are considered 190°C and 150°C respectively. The deflection estimated using Equation 4-21 is approximately 0.15mm, which is 6 times the value measured experimentally (0.025mm). The inaccurate prediction of deflection is thought to be a result of the considerable number of assumptions the model comprised. For example, the weight of layers forming the part is expected to influence the development of curl. As the weight acts downwards, it is believed that it opposes curl which rises upwards. Nevertheless, the effect of weight is dependent on the modulus of elasticity, as Hooke's law implies. A decrease in the modulus causes an increase in strains that result from weight, allowing less curl to generate. Then again, the modulus of polycarbonate is highly dependent on the temperature and cooling rate. A proper prediction of their effects on the modulus would therefore require a viscoelastic model to be developed (see Section 2.3.1.2). Conversely, other factors not taken into account in the model are expected to further give rise to curl. For instance, part of the heat absorbed during sintering of the top layer is conducted to the layer underneath. Consequently, as the top layer contracts, expansion of the bottom layer is believed to occur. Deflection of the part would then be dependent on the difference in strain of the two layers. Therefore, identifying changes in temperature occurring simultaneously in both layers is essential for an accurate prediction of curl. In addition, friction between the bottom surface of the part and the powder bed is expected to oppose relative motion, which may influence the development of curl. Combining all of these factors into a mathematical model would make the analysis extremely complicated, compelling us to resort to the finite element technique as a method of solution. Nevertheless, the model presented in this section has identified the most essential material properties required as an input for solving the curl problem in SLS. These are the modulus of elasticity and the coefficient of thermal expansion of each layer forming the part. The model has also emphasised the paramount need for developing a proper heat transfer model for an accurate prediction of curl to be obtained.

4.5 Thermal-Stress Analysis Procedures

There are two methods in ABAQUS in which heat transfer and stress analyses can be coupled; indirect method and the direct method. The former is generally expressed as sequentially coupled thermal-stress analysis, whereas the latter is commonly termed fully coupled thermal-stress analysis. In this section, both methods are investigated and the one more suitable for solving the curl problem in SLS is selected.

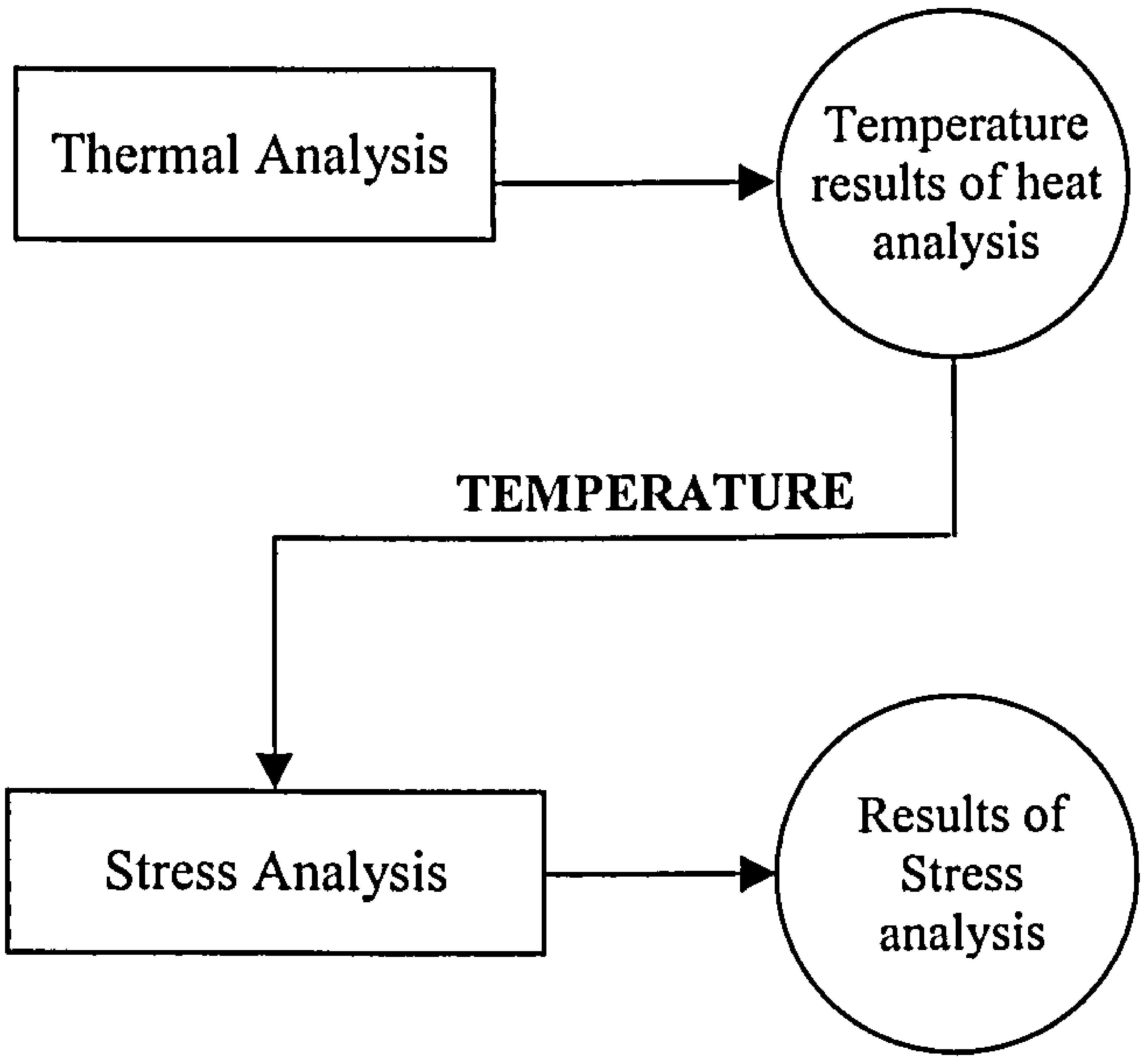

Figure 4.7 Flow chart showing the sequentially coupled thermal-stress procedure.

Sequentially coupled thermal-stress analysis is performed when the stress analysis solution is dependent on the temperature results of the heat analysis, but there is no inverse dependency. This type of analysis is carried out by first solving the pure heat transfer problem. The temperature results are saved as a binary format file. The temperatures are then read into a stress model as a predefined field. The (TEMPERATURE) command in ABAQUS is the link between the two analyses: it reads specified temperature results from the heat model and applies them as loads in the stress analysis. Figure 4.7 shows the data flow for a sequentially coupled thermal-stress analysis.

The interface requires that node numbers are the same for corresponding nodes in the heat transfer analysis mesh and the stress analysis mesh. Elements in the heat model that represent non-structural parts in the stress model can be omitted in the stress analysis mesh. In this situation, when the temperature results file is read during the stress analysis, temperatures at nodes that are not in the stress mesh are ignored. In thermal analysis, the material properties defined should have thermal properties, such as conductivity, whereas mechanical properties, for example elasticity, are defined in the stress analysis.

Fully coupled thermal stress analysis, however, involves solving the heat and stress analysis simultaneously rather than sequentially. This type of analysis is used when the solution of the heat transfer analysis strongly affects the solution of the stress analysis, and that of the stress analysis strongly affects the solution of the heat transfer analysis. The analysis requires the use of elements that have temperature and displacement nodal degrees of freedom. In addition, material properties in a fully coupled thermal-stress analysis should have both thermal and mechanical properties.

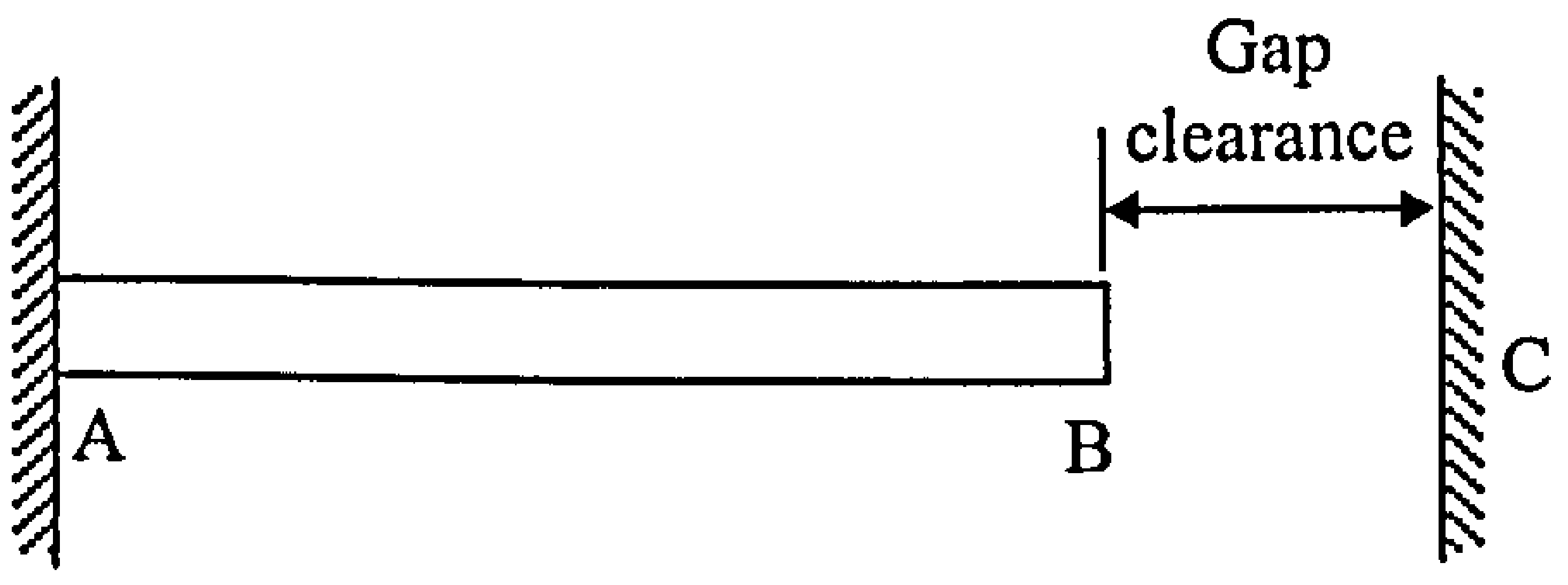

Figure 4.8 A schematic diagram of a conductive rod: fully coupled thermal-stress analysis problem.

The following example describes a problem that requires solution using fully coupled thermal-stress analysis. The model is shown in Figure 4.8: a conductive rod fixed at one end, A, and free at the other end, B. Between the free end and the adjacent fixed wall, C, exists a gap through which heat is conducted. The heat transfer coefficient of the gap increases as the clearance decreases. Heat transfers from point A to point C causing an increase in the temperature of the beam. This increase in temperature results in the beam to expand and the gap clearance to decrease, raising the heat transfer coefficient of the gap. As a consequence, the heat solution affects the stress solution, which in turn affects the heat solution and so forth. A flow chart that illustrates the fully coupled thermal-stress analysis procedure is shown in Figure 4.9.

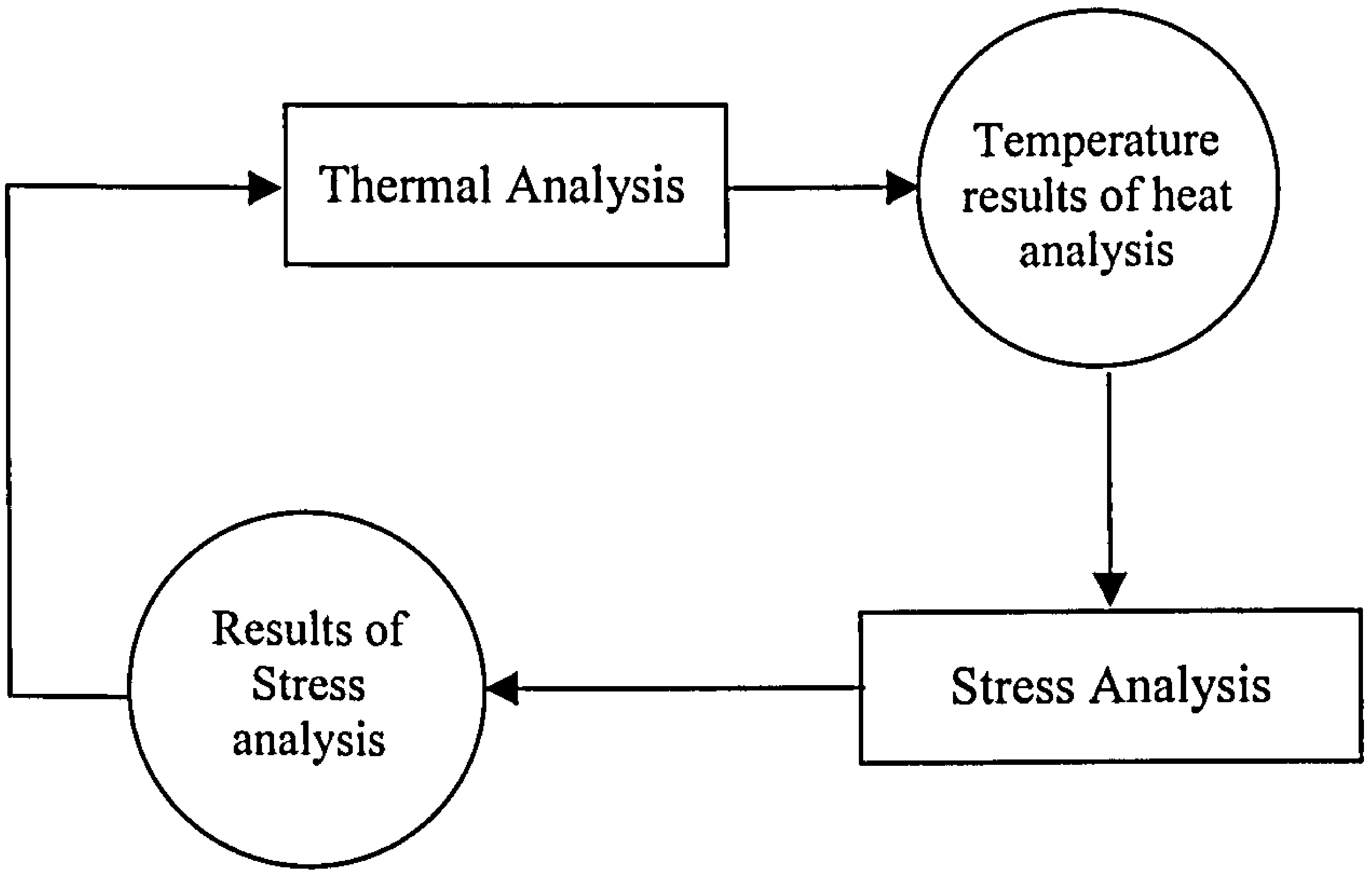

Figure 4.9 Flow chart showing the fully coupled thermal-stress analysis procedure.

The major differences between fully coupled thermal-stress analysis and sequentially coupled thermal-stress analysis have now been established. In the following, the suitability of these analyses for solving the curl problem in SLS is assessed. The criteria supported in selecting the most appropriate method for solving is its capability in simulating effects acting on a part during SLS processing and the simplicity of the models developed. To give a better understanding of these criteria, the stages of building a two-layer part in SLS is first described. The possibility of using fully and sequentially coupled thermal-stress analyses to simulate these stages is next investigated.

The SLS process starts by spreading layers of powder on the part piston to form the powder bed. The laser beam is then directed onto the surface of the powder. A fraction of the energy absorbed by the surface is lost through convection and radiation, while the remainder is conducted into the powder bed to produce the first layer of the part. At this stage, the heat transfer analysis mesh would comprise elements representing the powder bed and the sintered layer. The laser effect can be simulated by heat flux applied on the top surface of elements symbolising the layer to be sintered. In addition, boundary conditions could be specified on that surface for the effects of radiation and convection to be considered (see Equation 4-2). The variation in thermal material properties with temperature could also be defined based on experimental measurements or the results of previously developed material models such as the Yagi-Kunii model (see Section 2.3.2).

In fully coupled thermal-stress analysis, the same mesh is used for the heat and stress analysis. The stress analysis simultaneously uses temperatures predicted by the heat transfer analysis to estimate the deformation of the modelled powder bed and first layer of the part. However, in the SLS process, the sintered part is not actually bonded to the powder bed. Consequently, deformation of the powder bed is not expected to substantially influence curl which is believed to occur as a result of non-uniform deflection of bonded layers forming the sintered part (see Section 4.4). Hence, representing the powder bed would make solving the stress analysis more expensive due to the additional computational resources required, with no significant effect expected on curl results.

In addition, mechanical properties of the powder bed have to be defined when using fully coupled thermal-stress analysis. For polycarbonate powder beds, mechanical material property data (to our knowledge) are not available. Additionally, mechanical properties of powder beds are expected to differ from those of a sintered (continuous) polycarbonate structure; powder beds are made of loose, discrete particles. For example, compression testing does not give an indication of the modulus of elasticity of powder beds [30]. This is because forces applied in the test are also required to overcome friction arising between surfaces of neighbouring particles for deformation of the bed to occur. Due to the lack of mechanical property data of polycarbonate powder beds and the complexity in analysing its mechanical behaviour, the use of sequentially coupled thermal-stress analysis can enormously simplify solving the problem.

In sequentially coupled thermal-stress analysis, the stress analysis mesh does not need to be identical to the heat transfer analysis mesh. Hence, a mesh representing the powder bed in SLS may be included in the heat transfer analysis mesh while omitted in the stress analysis mesh. In this situation, thermal effects of the powder bed on the deformation of the sintered part are only considered. Nevertheless, similar to previous curling models (see Section 2.4.2), the top surface of the powder underneath the sintered part can be simulated as a rigid surface in the stress analysis. Additionally, friction between that surface and the bottom surface of the sintered part can also be taken into account. Thus, the sequentially coupled thermal-stress analysis appears to be a more applicable method for solving the curl problem than the fully coupled thermal-stress analysis. Figure 4.10 shows the heat transfer analysis mesh and the corresponding stress analysis mesh when sequentially coupled thermal-stress analysis are employed.

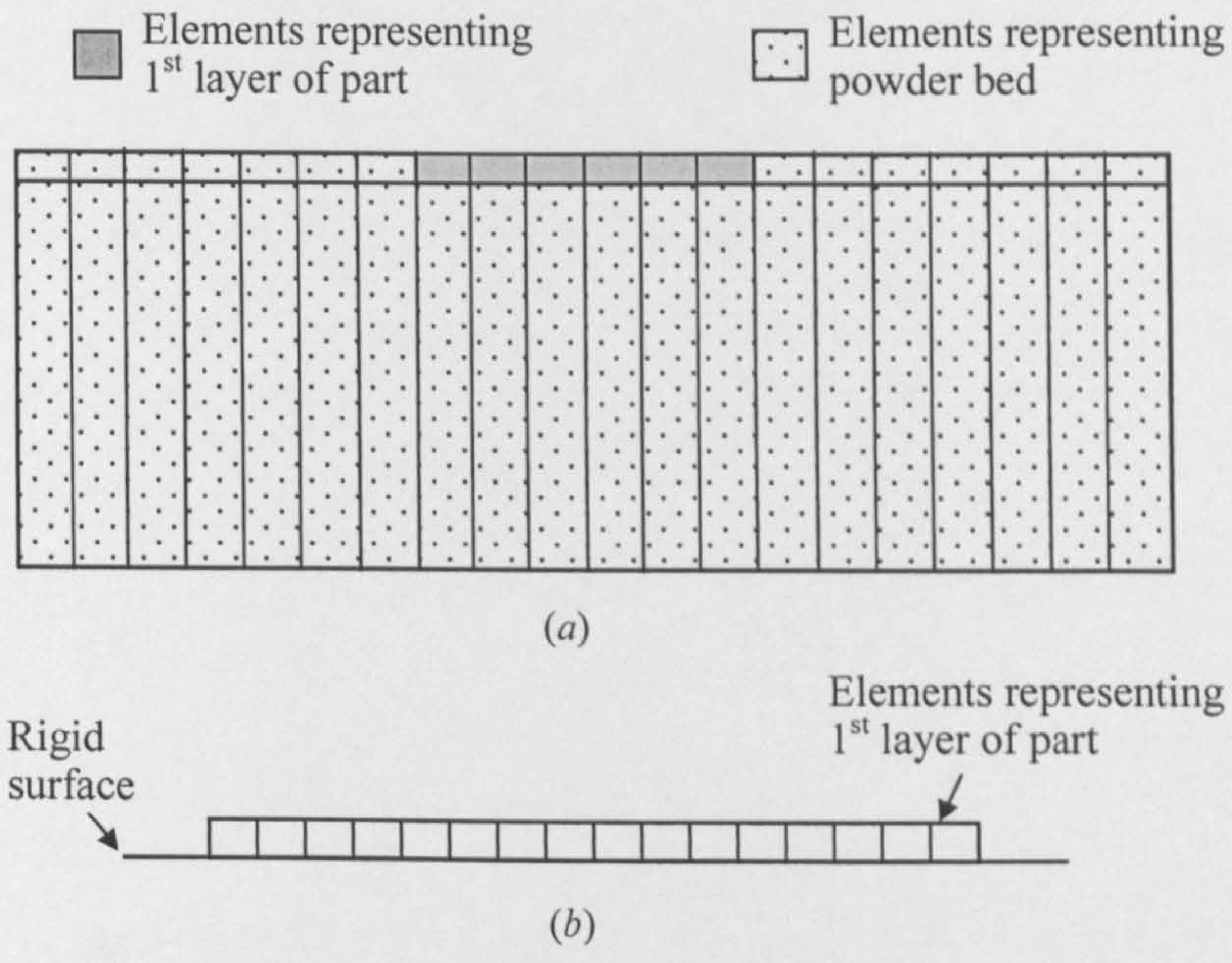

Figure 4.10 (*a*) Schematic diagram of the pure heat transfer analysis mesh after the first layer of the part is added and sintered. (*b*) Corresponding stress analysis mesh when sequentially coupled thermal-stress analysis is used.

The suitability of using fully and sequentially coupled thermal-stress analyses in simulating effects occurring during sintering of the first layer will additionally be investigated. The initial temperature of the layer (prior to its sintering) in a typical polycarbonate build is approximately 150°C. During the application of the laser beam, the temperature of the layer is understood to exceed 400°C [7] and then reduce as the effect of the laser is removed. Figure 4.11 (*a*) illustrates temperature changes expected to arise in the first layer during its sintering and prior to adding the second layer in its powder form.

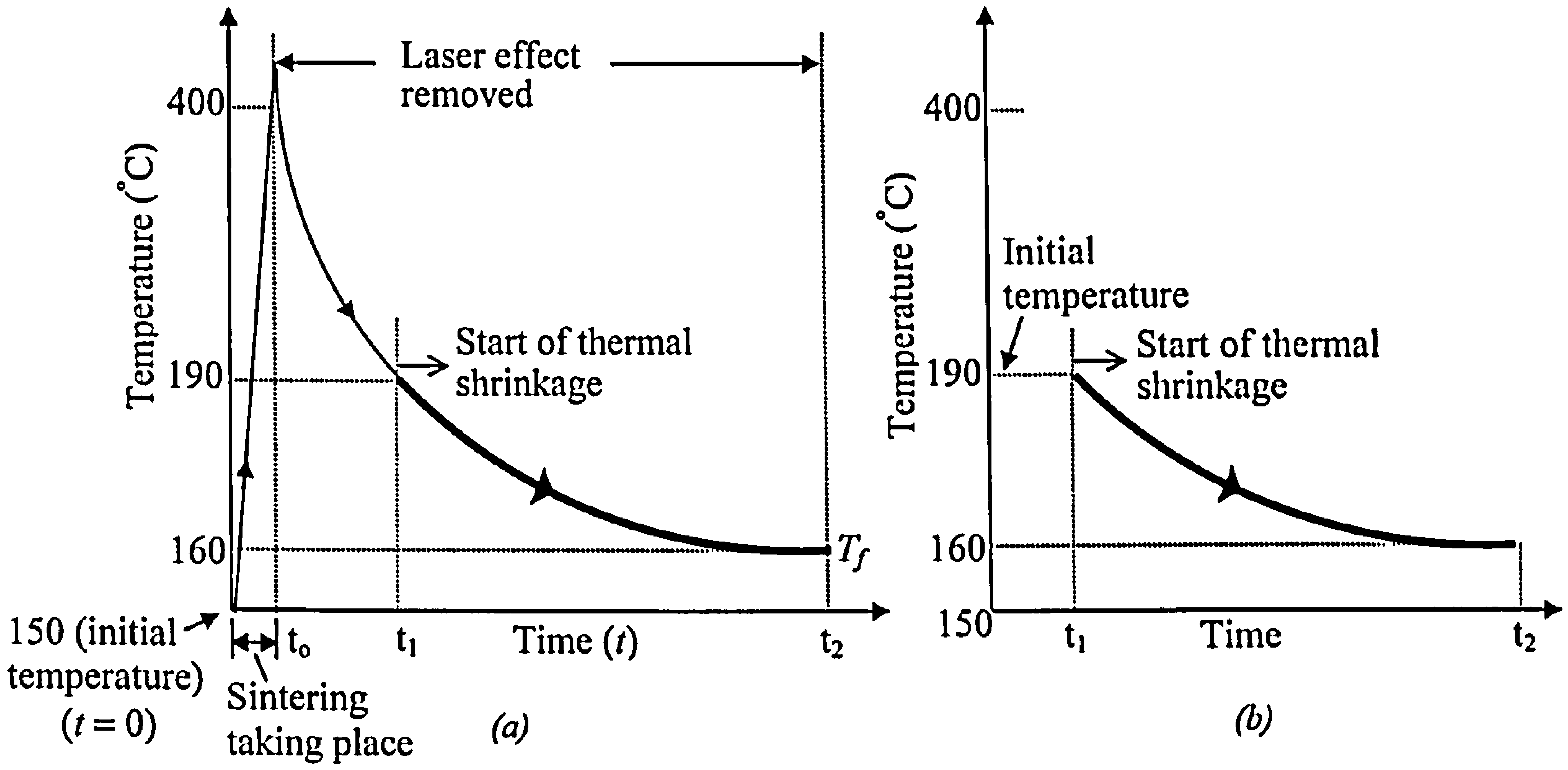

Figure 4.11 (a) Schematic representation of the temperature history expected to be predicted by the heat transfer analysis during and following sintering. (*b*) Temperature history read by the stress analysis in sequentially coupled thermal-stress analysis.

In fully coupled thermal-stress analysis, the initial temperature specified in the heat transfer analysis is identical to that given for the stress analysis (150°C). Thermal strains develop in the layer (estimated by the stress analysis) as temperatures predicted by the thermal analysis deviate from the initial temperature specified. If the temperature calculated by the heat transfer analysis at an instant is denoted T_f and the initial temperature specified is 150°C, then strain estimated by the stress analysis would be $\alpha(T_f-150)$, where α is the coefficient of thermal expansion. However during sintering, a layer of powder undergoes reduction in volume (see Section 2.3.4). Thus, using the expression $\alpha(T_f-150)$ to determine dimensional changes of the layer while it is being sintered is inapplicable since it would predict the layer to expand. In this situation, dimensional changes are estimated using viscous sintering models such as the MacKenzie and Shuttleworth model, which takes into consideration the effects of melt viscosity and surface tension [1]. Nevertheless, thermal shrinkages accountable for curl are expected to generate once the temperature of the melt layer reduces below 190°C [34]. Therefore, simulating effects in the stress analysis occurring on a layer of powder during its sintering and then its cooling from the melt state (whilst above 190°C) is bound to overcomplicate the analysis. This complication is inevitable when fully coupled thermal-stress analysis is employed as temperatures read by the stress analysis are those simultaneously calculated by the heat transfer analysis.

In sequentially coupled thermal-stress analysis, the user can specify in the stress analysis a particular temperature history data to be read from the heat transfer analysis. Additionally, the initial temperature given for the stress analysis does not need to be identical to that defined in the heat transfer analysis. These features in sequentially coupled thermal-stress analysis most certainly simplify solving the curl problem. Assuming that temperature changes occurring in the layer as predicted by the heat transfer analysis are those illustrated in Figure 4.11 (*a*). In the stress analysis, thermal shrinkage can be introduced to the layer by defining the initial temperature to be 190°C and specifying the temperature history to be read from the heat transfer analysis that in the period from t_1 to t_2 (see Figure 4.11 *b*). In that period, the layer would have a sintered (continuous) structure of which mechanical material properties can be provided.

The following stage in the SLS process is the addition of the second layer in its powder state on the top surface of the first (sintered) layer. Considering that the added layer is at a temperature less than that of the layer previously sintered, powder addition is expected to reduce the temperature of the upper most regions of the sintered layer causing it to curl. In contrast, weight of the added powder (acting downwards) is expected to oppose curl which rises upwards. In the following discussion, the suitability of using fully and sequentially coupled thermal-stress analysis in simulating effects taking place through this stage of the SLS process is assessed.

For an estimation of thermal effects of the added layer of powder on temperatures in the sintered layer, elements representing the added layer have to be activated in the heat transfer analysis mesh. In fully coupled thermal-stress analysis, the elements are activated for both the heat and stress analysis. Nevertheless, the added layer of powder is not actually bonded to the sintered layer underneath. Thus, deformation of the layer of powder, assuming it occurs due to changes in its temperature, is unlikely to influence curl of the sintered layer. As a consequence, activation of the added layer in the stress analysis in an attempt to simulate this stage of the SLS process is not feasible. Furthermore, in agreement with the view concerning the powder bed, mechanical properties of the added layer are also not available.

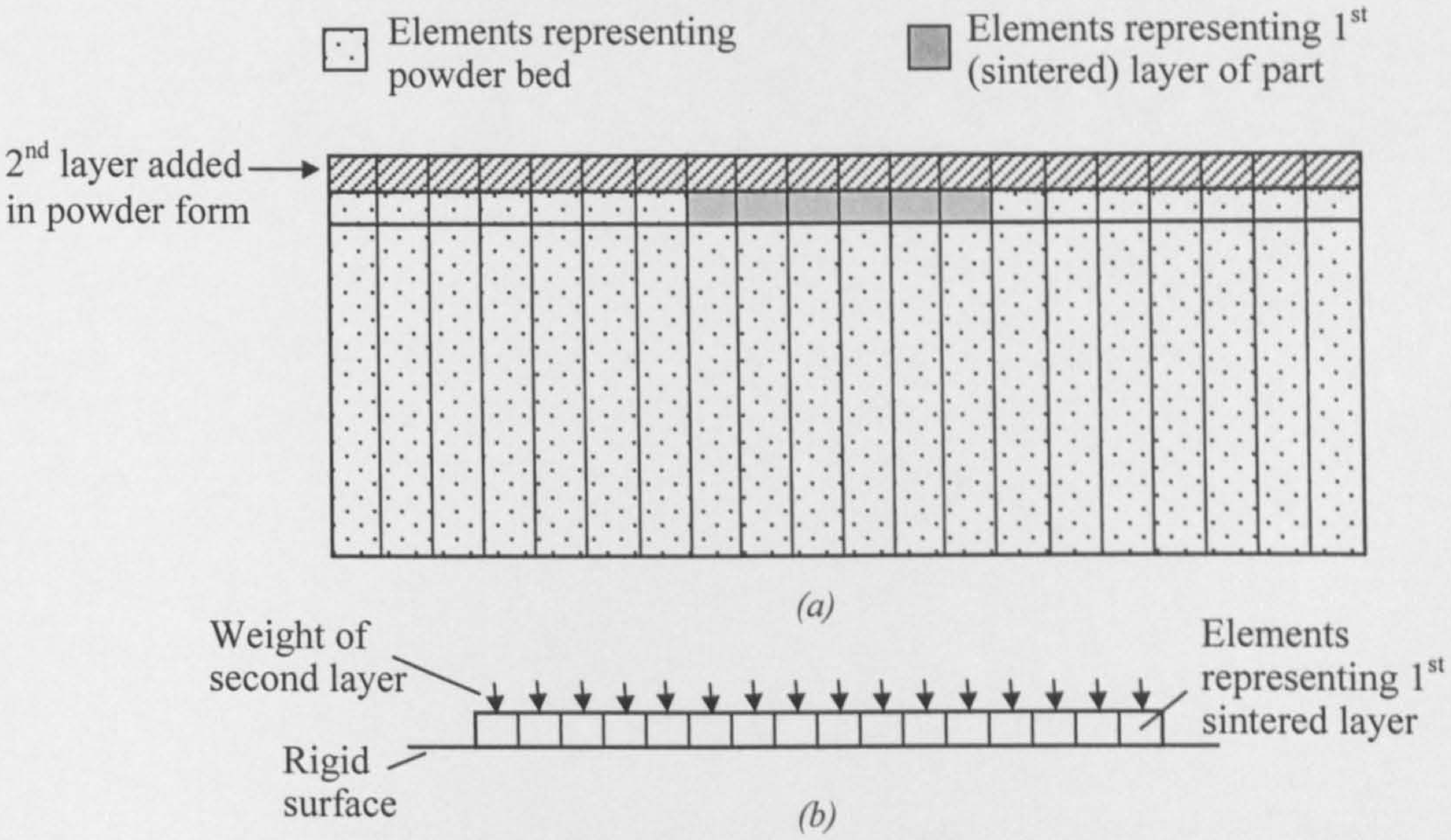

Figure 4.12 (*a*) Schematic illustration of the heat transfer analysis mesh when the second layer is added in its powder form (*b*) Corresponding stress analysis mesh using sequentially coupled thermal-stress analysis.

Sequentially coupled thermal-stress analysis, however, signifies a better approach in that elements representing the second layer of powder can be activated in the heat transfer analysis mesh but do not have to be activated in the corresponding stress analysis mesh. Therefore, temperatures considered in the stress analysis are only at nodes of active elements in the stress analysis mesh. In this situation, the thermal effect of adding the layer of powder on curling of the previously sintered layer can be estimated in the stress analysis. In addition, the weight of the layer of powder can also be simulated in the stress analysis by load applied on the top surface of the sintered layer. Figure 4.12 shows the heat transfer analysis mesh and the corresponding stress analysis mesh when sequentially coupled thermal-stress analysis is used to simulate this stage in SLS.

The following stage in SLS is sintering of the recently added layer of powder (second layer). Temperature changes expected in the layer during this stage are as illustrated in Figure 4.11 (*a*). For the same reasons reported earlier where sintering of the first layer was examined, the use of sequentially coupled thermal-stress analysis is a better choice than using fully coupled thermal-stress analysis. In the former, as the temperature of the second layer reduces below 190°C after it had been sintered, the load previously applied on the top surface of the first layer is removed and the second layer is activated in the stress analysis mesh. Further description of this stage is deferred till later in this chapter. The heat transfer analysis mesh and the stress analysis mesh when sequentially coupled thermal-stress analysis is used to simulated this stage in SLS is shown in Figure 4.13.

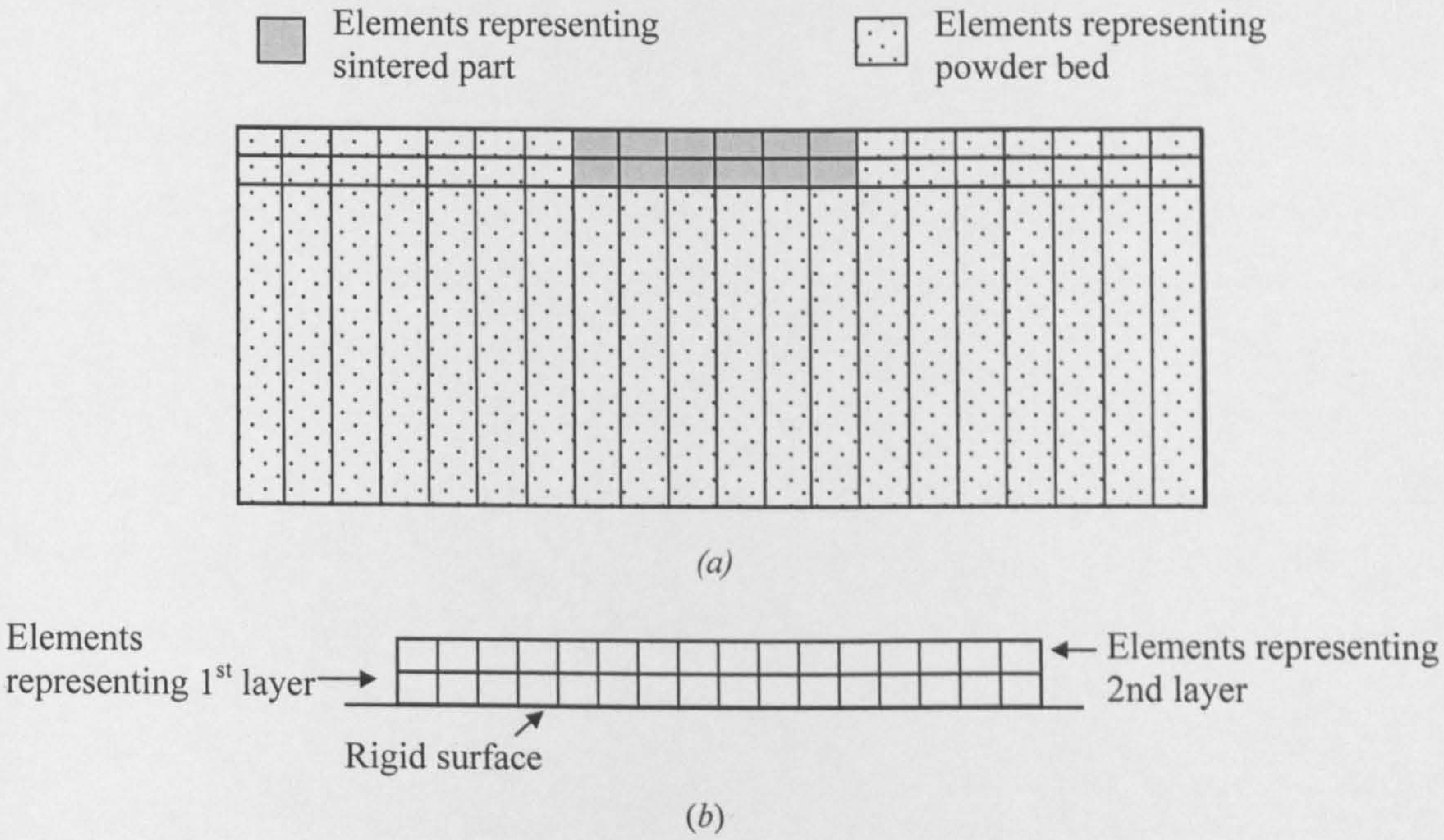

Figure 4.13 (*a*) Schematic illustration of the heat transfer analysis mesh during and after the second layer is sintered (*b*) Corresponding stress analysis mesh during the cooling of the sintered second layer when sequentially coupled thermal-stress analysis are used.

The overall conclusion is that sequentially coupled thermal-stress analysis is more appropriate for solving the curl problem in SLS than fully coupled thermal-stress analysis. Therefore, the sequentially coupled thermal-stress approach is used in the present work. However, one major drawback of using this method is that the heat transfer solution is independent of part deformations predicted by the stress analysis. The heat transfer analysis, for example, considers the entire bottom surface of the part to be in contact with the powder underneath at all times. However, as curling of the part occurs, regions of the bottom surface would no longer be contacting the powder. In this situation, heat transfer from these regions could take place through convection and radiation rather than by conduction to the powder underneath as considered in the heat transfer analysis.

The main focus in the following sections is to demonstrate how sequentially coupled thermal-stress analysis can be employed in ABAQUS to predict curl of a ten-layer part. For that purpose, a heat transfer model which simulates building of the part in SLS is first developed. A stress model that reads temperatures predicted by the thermal model is additionally generated. In the following sections, both models are described. The deflection results from the stress analysis are then compared with experimental measurements of curl reported in the previous chapter.

4.6 Heat Transfer Model

The subject of this section is to provide a description of the first version developed for the heat transfer finite element model. The main goal of the model was to predict temperature changes occurring in a ten-layer part during SLS fabrication. The model (as in all finite element models) consisted of several different blocks of information that together described the physical problem to be analysed and the results to be obtained. The information the model comprised define the geometry of the structure to be modelled, its material properties, loads and boundary conditions applied, sequence of events for simulation and the output requests. These are detailed in the following sections.

4.6.1 Geometry

It has been established in Section 4.5 that a proper heat transfer finite element mesh should comprise elements representing the sintered part and the powder bed. Therefore, the geometries of the part and powder bed had to be defined. In the model, attempts were made to simulate building of the ten-layer polycarbonate parts that curl measurements, reported in Chapter 3, had been performed on. Prior to the building of these parts, layers of powder with nominal thickness of 0.127mm were spread on the part piston. The overall thickness of these layers was approximately 15.24mm with diameter identical to the diameter of the part piston, 330mm (see Figure 4.14). The sintered parts, however, were 90×26mm in area. The thicknesses of layers forming the part were defined in the model based on thickness measurements reported by Dalgarno et al. [35] (see Section 2.4.2). These measurements showed that each layer of a ten-layer polycarbonate part had a thickness of 0.125mm except for the first two layers. The thickness of the first layer was 0.66mm and that of the second was 0.25mm.

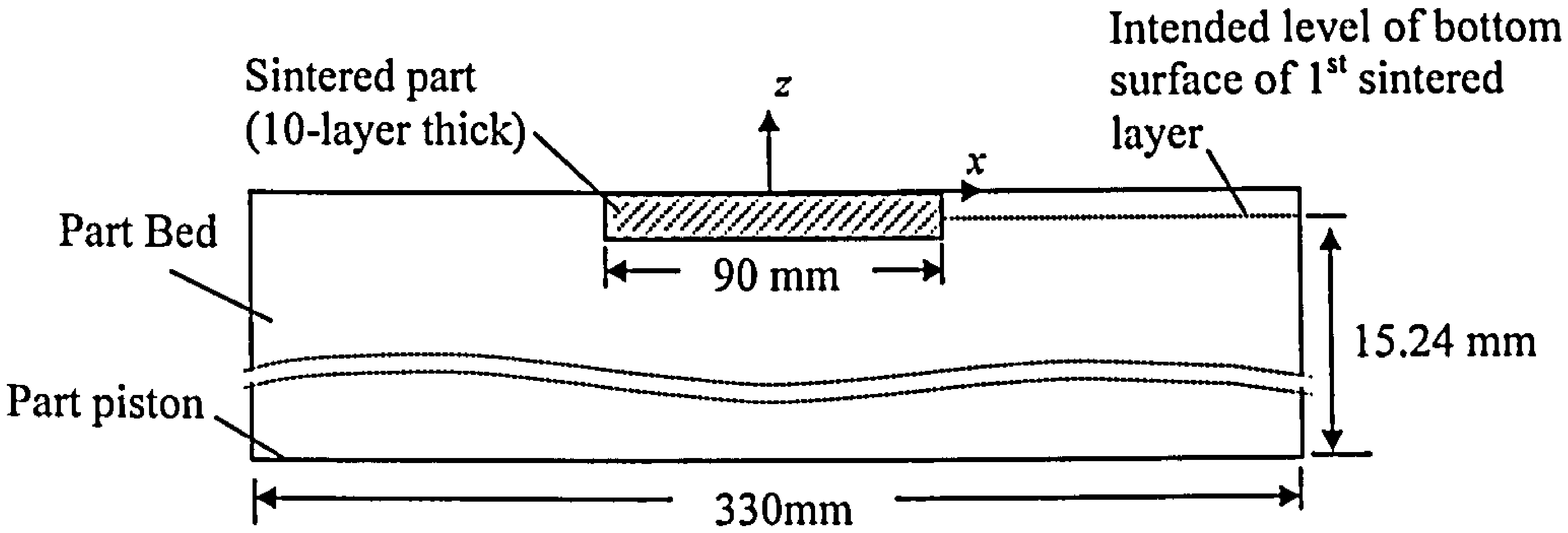

Figure 4.14 Schematic diagram showing dimensions of the powder bed.

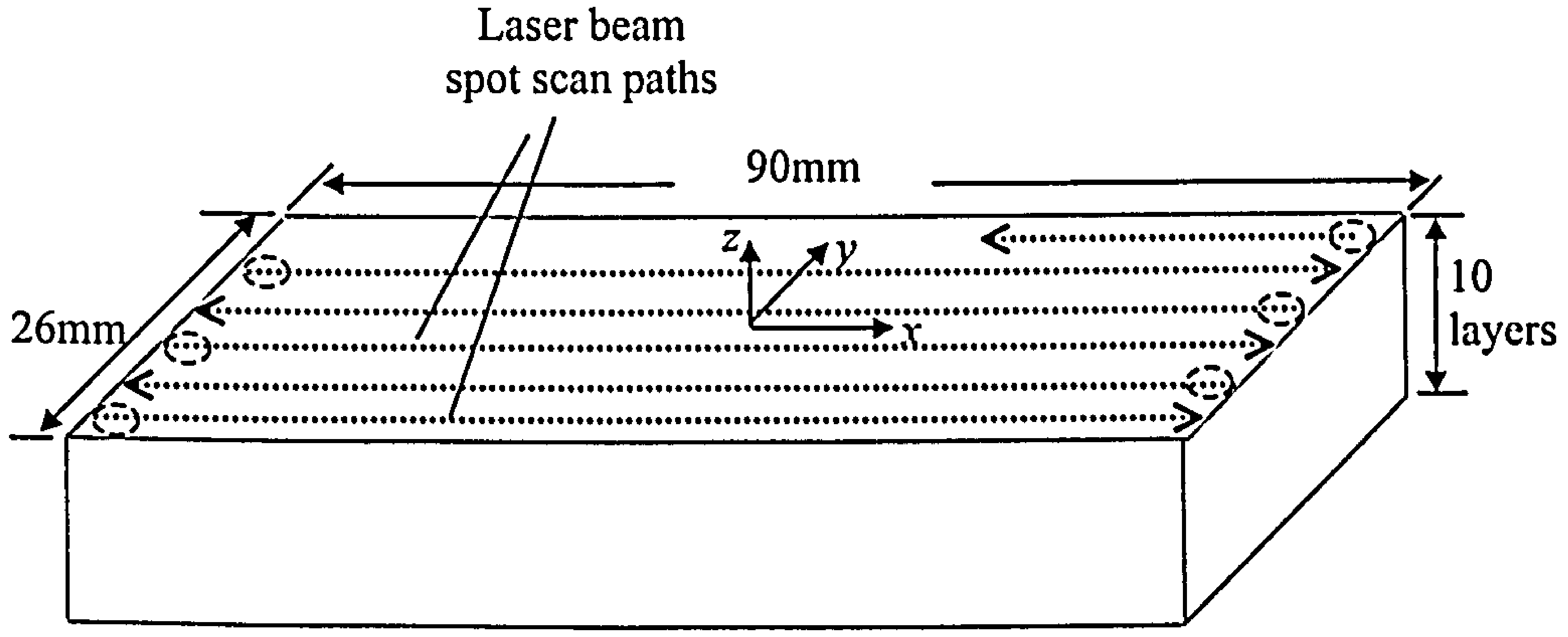

Figure 4.15 Three-dimensional representation of the part analysed with its top layer being sintered.

Figure 4.15 shows a three-dimensional (3D) representation of the ten-layer part while its top layer is being sintered. As the laser scans the surface of the layer, conduction of heat into the powder is expected to take place in the x, y and z directions (see Figure 4.15). Consequently, one may assume that a 3D thermal model would be required to capture temperature changes occurring in these directions.

Additionally, a 3D model can facilitate simulation of the raster scanning pattern of the laser beam spot; its travelling along the x direction at various y positions (see Figure 4.15). However, representing the entire structures of the powder bed and sintered part using 3D elements can entail long computational time and huge disk space for solving the analysis. The aim therefore is to define a simplified mesh that can produce accurate results at a reasonable cost.

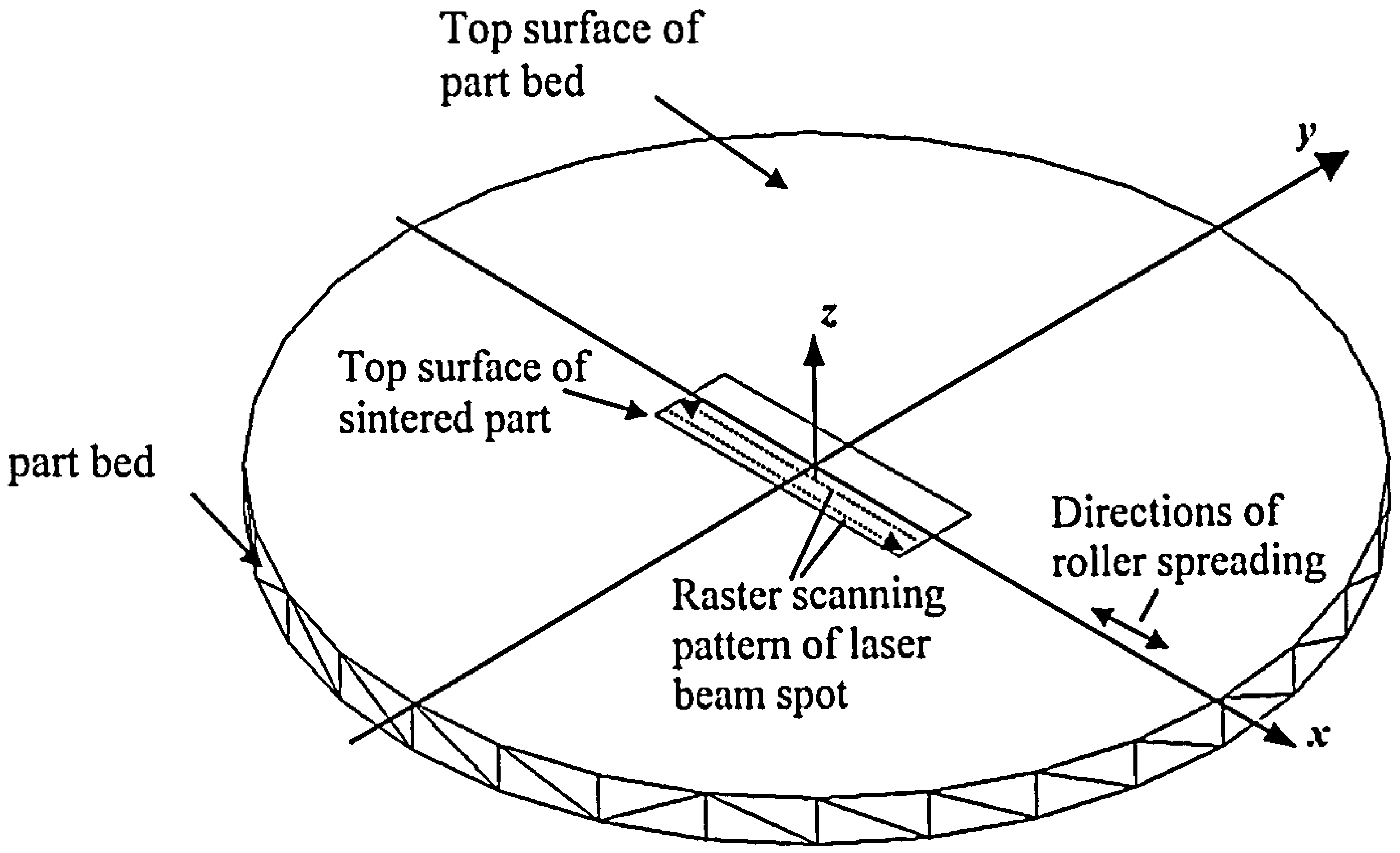

Figure 4.16 3D schematic diagram showing the position of sintered part with respect to the part bed.

One method of simplifying a mesh is to make use of symmetry provided that the analysed structure is made of repeated segments. Each of the ten-layer parts (to be modelled) when SLS fabricated were positioned at the centre of the powder bed in an arrangement illustrated in Figures 4.14 and 4.16. In that condition, the part bed and sintered part were geometrically (mirror) symmetrical about the y-z and x-z planes (see Figure 4.16). However, due to the raster scanning pattern of the laser beam, the effect of the laser beam (thermal load) was not symmetrical about these planes. Thus, modelling only the repeated segment of the structure with using symmetrical thermal boundary conditions as a simplifying measure is not applicable. In the following discussion, alternative (approximate) methods in simulating the raster scanning pattern of the laser beam are explored. The goal is to attempt to simplify the heat transfer analysis mesh without causing a substantial reduction in the accuracy of results.

In a previous study by Festa et al. [40], a two-dimensional (2D) heat transfer mathematical model was developed. The purpose of the model was to estimate temperature distributions in a semi-infinite body as its surface was scanned by a moving laser beam. In the model, the effect of the laser beam was represented by a uniform heat flux (q) with width D (denoting the diameter of the laser beam), moving at a constant speed U (see Figure 4.17*a*). During the motion of the laser beam, conduction of heat into the body in both the x and z directions was considered. However, convection and radiation from the surface of the body was not taken into account in the analysis.

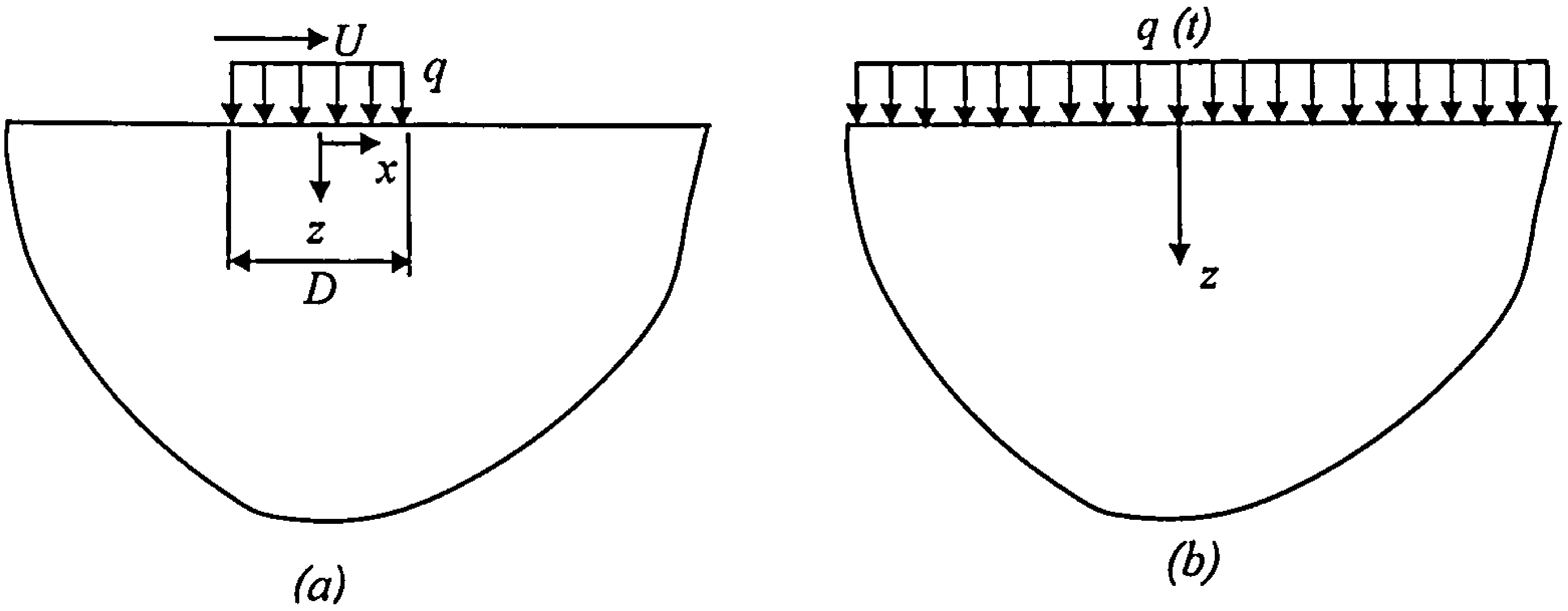

Figure 4.17 (a) Semi-infinite body heated over the surface by a moving heat source D wide. (b) Semi-infinite body heated over the surface with a uniform heat flux for a finite period of time.

The model was then simplified through representing the effect of the moving heat source by a stationary uniform heat flux (q), simultaneously applied over the entire surface of the body for a finite period of time (see Figure 4.17*b*). That period, termed the dwell time τ, was expressed as $\tau = D/U$. It denoted the time a particular point on the surface of the body was exposed to the moving heat flux. In this model, conduction of heat was considered to take place only in the z direction. However, similar to the previous model, the effects of convection and radiation were not taken into account in the analysis. Comparing the temperature distributions in the body estimated using both models found the results to differ by less than 5%, provided that a parameter G was greater than 3.9, where G was defined by [1],

$$G = \frac{U.D}{2\alpha_d} \qquad \text{4-22}$$

where α_d is the thermal diffusivity of the material being sintered, and can be expressed in terms of the density ρ, specific heat C_p and conductivity k as $\alpha_d = k/(\rho.C_p)$.

The polycarbonate ten-layer parts (to be modelled) were sintered in SLS while the laser beam spot was travelling in the x-direction at a speed of 1188.87mm/s (see Figure 4.15). The laser beam diameter in SLS is 0.4 mm, and thermal diffusivity α_d of polycarbonate is approximately $1.28\times10^{-7}m^2/sec$ [24]. Substituting these values into Equation 4-22 gives a value of G (in the x-direction) of 3715, which is greater than 3.9. Thus, according to Festa et al. [40], simulating the moving effect of the laser beam as it scans a vector line in the x direction (see Figure 4.18*a*) is no longer an extreme necessity. That can be approximated to an equivalent, stationary heat flux, simultaneously applied over the entire line for the dwell period τ (see Figure 4.18*b*).

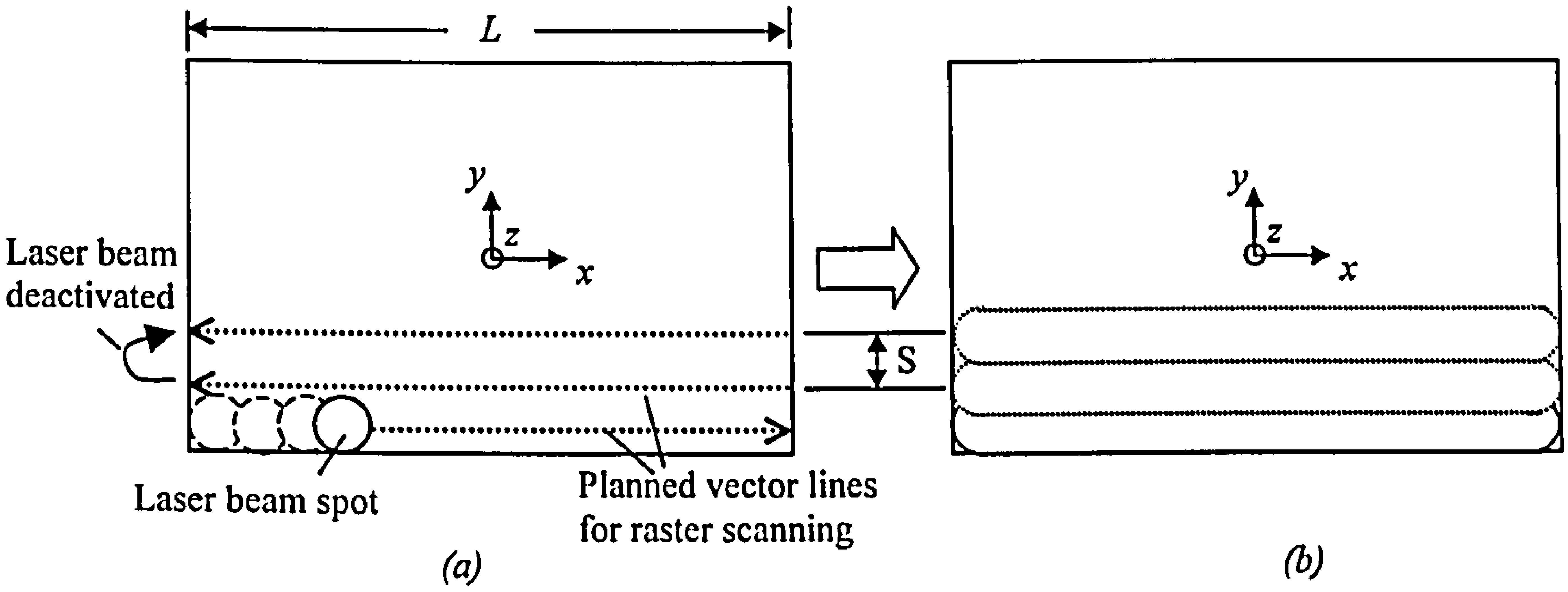

Figure 4.18 (a) Actual raster scanning pattern in SLS, arrows represent planned movement of laser beam spot during sintering (*b*) Simplification based on Festa et al. [40]: uniform heat flux applied simultaneously along the x direction (for dwell period τ) at various y positions.

Temperature profiles predicted using this approximation are expected to differ slightly (by less than 5%) from those estimated if a moving heat source was simulated. That is mainly due to the poor thermal diffusivity of polycarbonate and the high speed of the laser beam causing temperature gradients in the x direction to be extremely small. The main advantage of this approximation that application of the laser beam, in this case, would be symmetrical about the y-z plane (see Figure 4.16

and Figure 4.18*b*). Therefore, only half of the powder bed and the sintered part structures (repeated about the *y-z* plane) need to be modelled with thermal boundary conditions being applied.

Once SLS scanning of a vector line is completed, the laser beam is automatically deactivated before starting to scan the following vector line, i.e. the laser beam does not sinter along the *y* direction (see Figure 4.18*a*). The period the laser beam is deactivated between successive scan lines is extremely small (approximately 3ms) [10]. Due to the poor thermal diffusivity of polycarbonate, temperature changes occurring in the processed powder during that period (with the laser beam deactivated) are assumed to be negligible. Hence, a number of previous SLS thermal models [31, 41, 42] had simulated the raster scanning pattern as a strip heat source of width D (laser beam diameter) moving steadily in the *y* direction at speed V_l (see Figure 4.19*a*). The laser beam movement seen in the *y-z* plane is illustrated in Figure 4.19*b*.

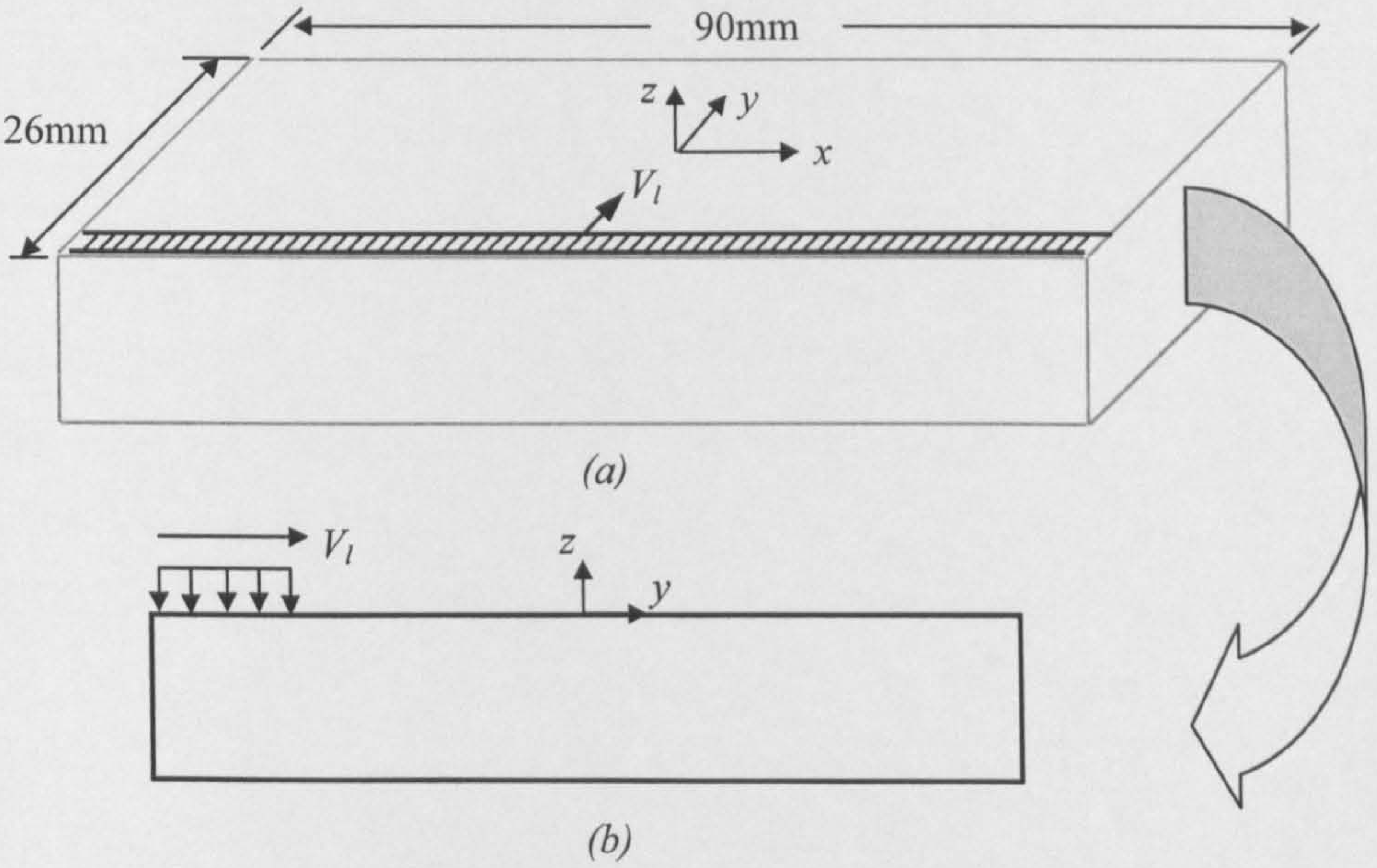

Figure 4.19 (*a*) 3D representation of the part with the laser beam represented as a strip source moving along the *y* direction. (*b*) *y-z* plane view of the strip source

Referring to Figure 4.19*b*, Equation 4-22 can be applied to evaluate the value of G in the *y* direction. However, the velocity (V_l) of the laser strip along that direction has to be first estimated. That velocity is expressed by [41],

$$V_l = S(U/L) \quad \text{4-23}$$

where U is the speed of the laser beam in the x direction, L is the length of a scan vector line (90mm) and S is the scan spacing (see Figure 4.18*a*). The scan spacing selected in fabricating the ten-layer parts to be modelled was 0.25mm. Substituting the estimated value of V_l into Equation 4-22 gives G in the y direction as 10.32, which is also greater than 3.9. Consequently, simulating the effect of the raster scanning pattern of the laser beam can be approximated to an equivalent, stationary heat flux, simultaneously applied over the entire area to be sintered for the dwell period τ. The advantage of this approximation that heat flux applied in this way is symmetrical about the y-z and x-z planes (see Figure 4.16). Thus, only a repeated quarter of the sintered part and powder bed structures need to be modelled with thermal boundary conditions being applied (see Figure 4.20).

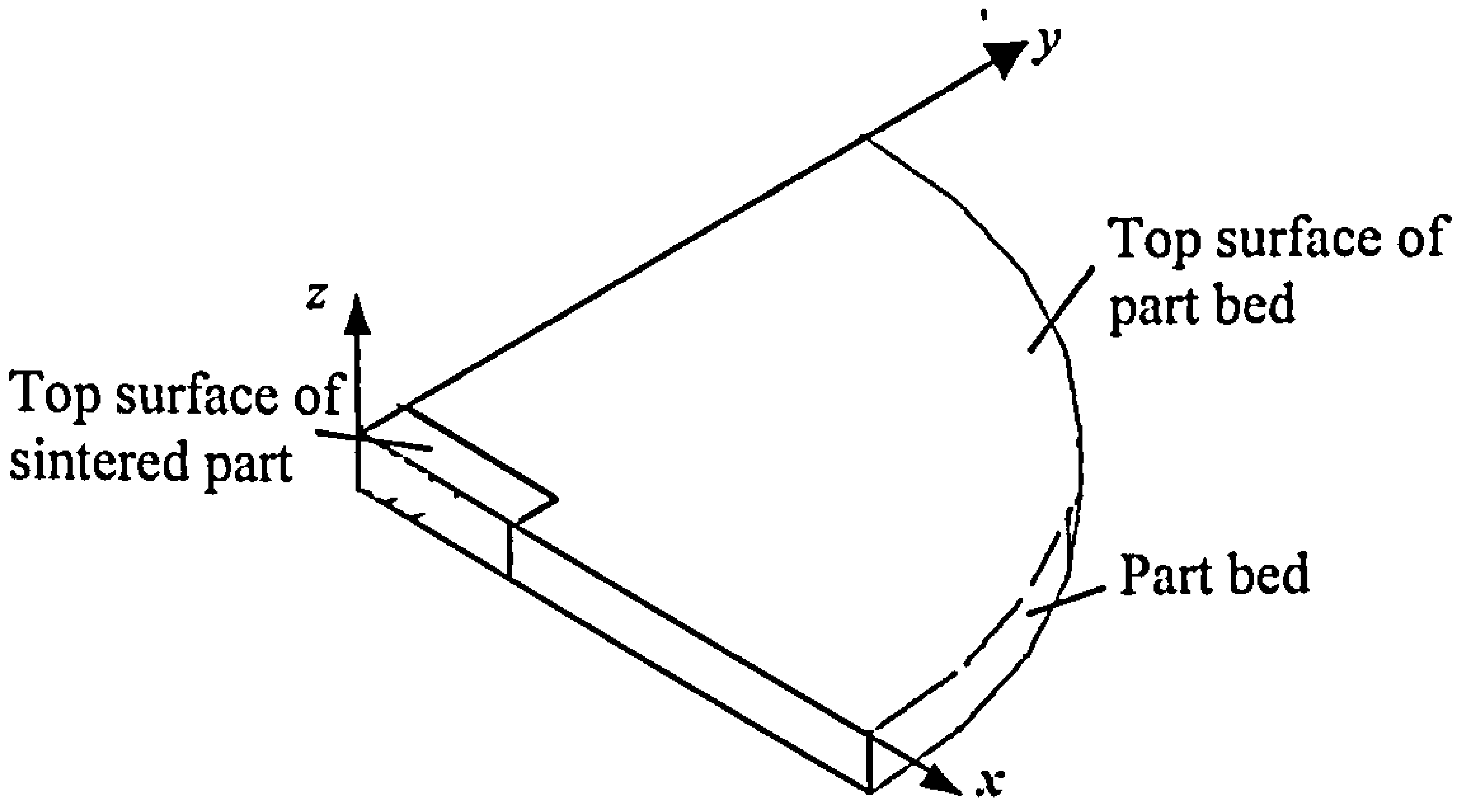

Figure 4.20 Three-dimensional representation of quarter the structures of the powder bed and the sintered part.

As a layer of powder is sintered, it transforms to a molten state with temperatures extremely exceeding those of its surrounding powder. Therefore, heat transfer from the sintered layer to the surrounding powder would be highly expected. However, sintering of the layer is accompanied by decrease in its volume (see Section 2.3.4). Consequently, a diminutive gap between the side walls of the sintered layer and the surrounding powder is assumed to develop. The gap is believed to further develop as temperatures of the sintered layer reduce and thermal shrinkages begin to generate. As the conductivity of the gas filling the gap is considerably lower than the conductivity of solid powder particles, the existence of the gap is expected to resist heat flow from the side walls of the sintered layer to the surrounding powder. In addition, heat transfer rate is proportional to temperature differences along the path of heat flow (see Equation 2-4). The build up of heat in the gap is expected to raise the temperature of the gas, thus reducing the rate of heat loss from the side walls of the layer. Therefore, in the first version of the heat transfer model, the powder surrounding the side walls of the sintered layer was assumed to have an insignificant effect on temperatures of the layer, and thus was not considered in the analysis. In addition, for simplicity of the analysis, powder surrounding the portion of the powder bed underneath the part was also not taken into account.

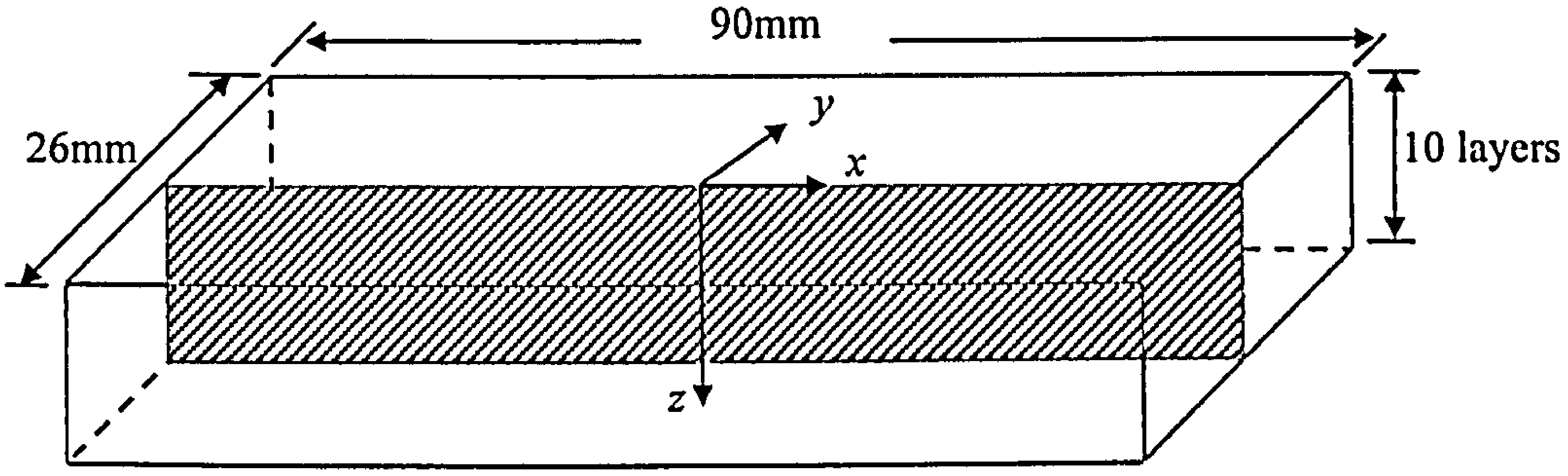

Figure 4.21 Three dimensional representation of the part showing the region where curl deformation is investigated.

In the present work, the curl deformation investigated is that occurring in the *x*-*z* plane at the mid point of the part in the *y* direction (the hatched region shown in Figure 4.21). Hence, emphasis was given to estimate temperature profiles occurring in that region during SLS fabrication of the modelled ten-layer parts. The simplification of not taking into account thermal effects of the surrounding powder with heat flux simultaneously applied over the entire surface to be sintered implies that temperatures only vary in the *z* direction. In this condition, a one-dimensional (1D) model would be sufficient to capture temperature changes occurring in that direction. However, a 2D heat transfer analysis mesh was developed in correspondence with the 2D mesh generated for the stress analysis, as will be explained later.

Figure 4.22*a* shows the 2D finite element mesh generated for the heat transfer analysis. In the mesh, the ten-layer sintered part and the portion of the powder bed underneath that part are only represented. The elements used in the mesh are of the type four noded heat transfer linear quadrilateral, denoted in ABAQUS (DC2D4).

The overall thickness of the powder directly underneath the part was 14.707 mm (see Figures 4.14 and 4.23). The first and second layers of the part had thicknesses equal to 0.66mm and 0.25mm respectively, while the thickness of layers from three to ten was 0.125mm [35]. In generating the finite element mesh, emphasis was made to ensure that the aspect ratio of elements (ratio of the length of the largest side of the element to the shortest) did not exceed a value of 5. An aspect ratio above this value can lead to the shape of elements being excessively distorted giving errors in the temperature results obtained. Thus, the powder bed was represented using a 5×72 element mesh (see Figure 4.22*a*). Each layer of the sintered part, however, was represented using a 1×72 mesh as shown in Figure 4.22*b*.

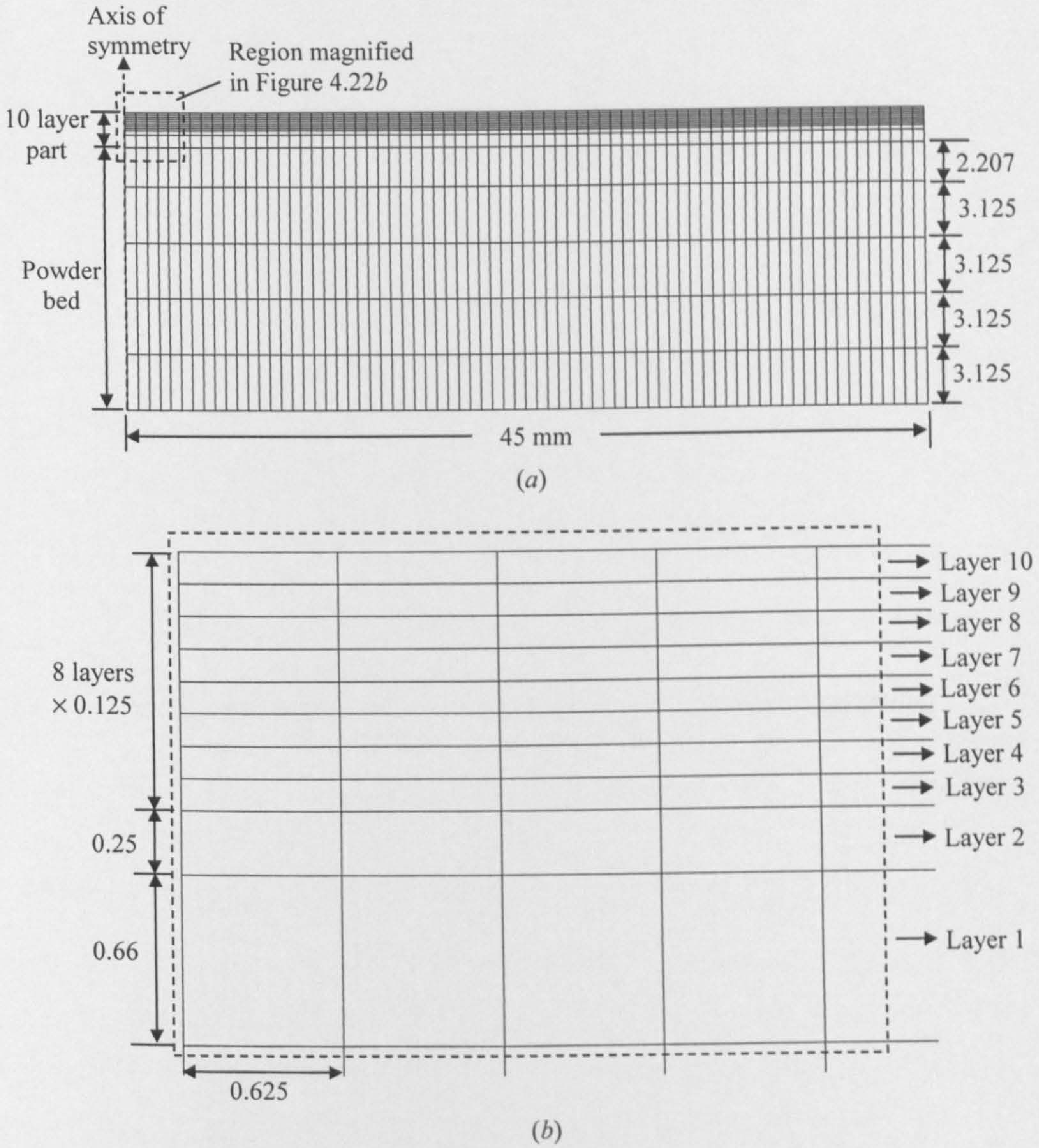

Figure 4.22 (*a*) First version of 2D heat transfer analysis mesh. (*b*) magnified view showing dimensions of elements forming a region of the part mesh. (All dimensions are in mm)

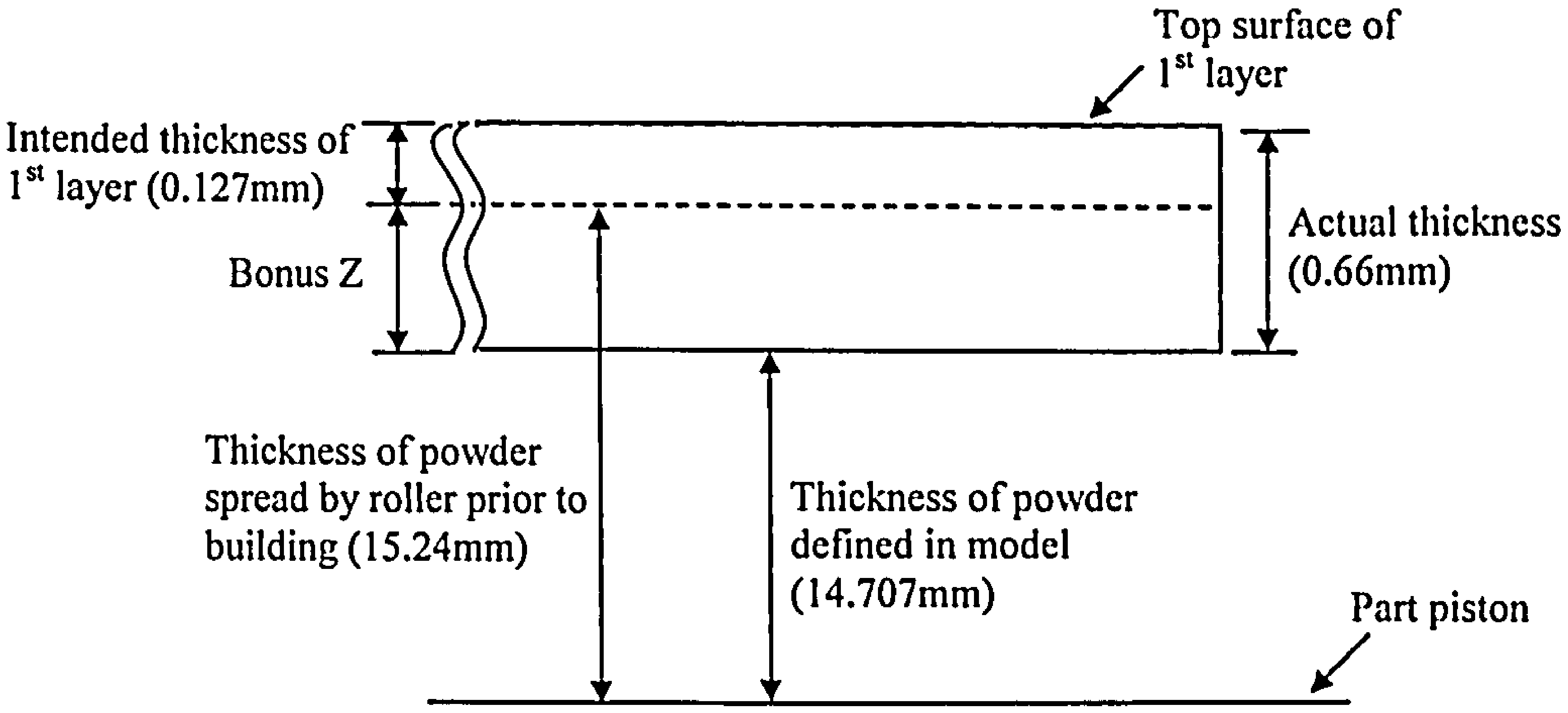

Figure 4.23 Schematic diagram showing the method used to calculate thickness of powder underneath the part to be defined in the model. (not to scale).

4.6.2 Material Properties Defined in Heat Model

Thermal material properties required as input to the heat transfer analysis were identified in Section 4.3. These properties are the density (ρ), specific heat (C_p) and thermal conductivity (k). Additionally, definition of emissivity ϵ is essential if thermal radiation boundary conditions are to be applied (see Equation 4-2). The heat transfer analysis mesh shown in Figure 4.22 consisted of elements representing the sintered part and a section of the powder bed (underneath the part). Consequently, thermal material properties of both of these structures had to be defined in the model.

However, in defining thermal properties of layers forming the fabricated part, one must remember that these layers were initially in powder form prior to sintering taking place. Thus, in principle, elements representing these layers have to be initially assigned thermal properties of polycarbonate powder structures. Based on temperature history data predicted during sintering, these properties then should be allowed to simultaneously transform to those corresponding to polycarbonate sintered formations. Based on previous experimental measurements, the density of SLS polycarbonate powder (beds) was estimated to be equal to 485kg/m^3 [31]. This value was defined in the model for all elements representing the powder bed in the heat transfer analysis mesh (see Figure 4.22*a*). However, the finite element package employed (ABAQUS) does not support changes in density with temperature, i.e. it considers the density defined for an element to be constant regardless of any temperature changes predicted throughout the analysis [43]. Therefore, for simplicity, elements representing the sintered part were assigned a constant density value equal to the density of SLS polycarbonate fabricated parts. Based on previous experimental measurements reported by Dalgarno et al. [35], that density was defined in the model equal to 700kg/m^3.

The specific heat was measured experimentally by Nelson et al. [7] during the heating of an SLS polycarbonate powder sample. The reported relationships between the specific heat and temperature are described in Equations 2-12 and 2-13. As the specific heat of powder beds and sintered solids are approximately identical (see Section 2.3.3), these equations were also used to calculate changes in specific heat with temperature for the sintered part. These changes were defined in the model in tabulated form (specific heat against temperature) and were assigned (identical) to all elements in the heat transfer analysis mesh. In addition, based on previous experimental measurements [7], the emissivity was defined in the model equal to 0.95.

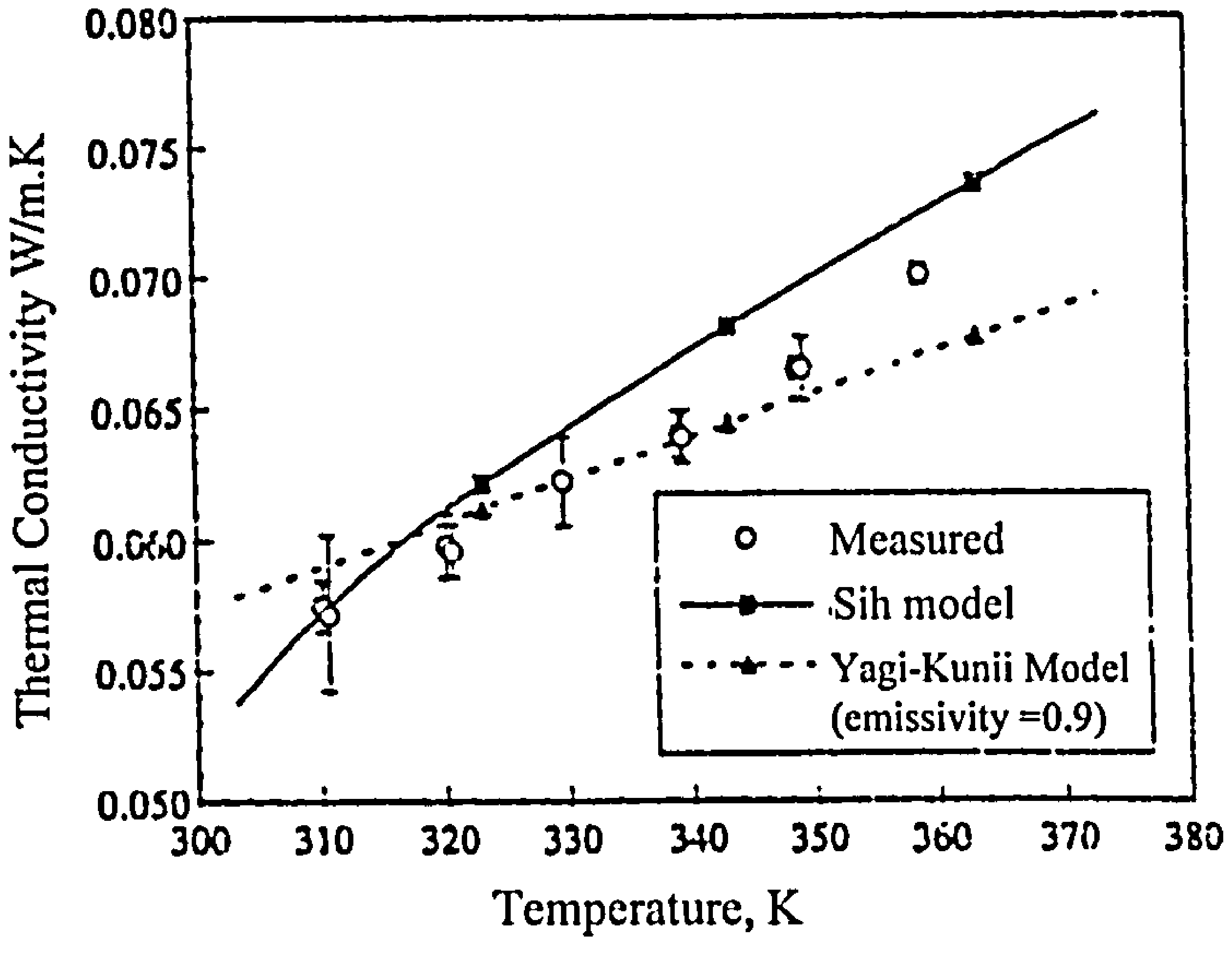

Figure 4.24 Thermal conductivity results of both Sih and Yagi-Kunii compared with experimental measurements performed on polycarbonate powder with porosity 0.5. From [44].

Experimentally obtained thermal conductivity data of polycarbonate (to our knowledge) are not available over the entire temperature range expected in SLS fabrication. The alternative approach was, therefore, to rely on previously developed mathematical models for the definition of thermal conductivity of polycarbonate in the heat transfer model. In Section 2.3.2, the Yagi-Kunii and Sih models were described. These models attempted to weigh the relative contributions to the conductivity of powder beds by conduction in solid particles, in gas filling the voids between the solid particles and by interparticle radiation. In a previous study [44], predictions of the Yagi-Kunii and Sih models were compared with conductivity measurements performed on polycarbonate powder with porosity equal to 0.54 over the temperature range from 27°C to 107°C (see Figure 4.24).

The conclusion was that the high temperature form of Yagi-Kunii model is more accurate in predicting thermal conductivity of polycarbonate beds than the Sih model. Accordingly, the Yagi-Kunii model (Equation 2-5) was implemented in this work. A simplification of the model can be made by taking β and γ in Equation 2-5 to be equal to unity [26], resulting in,

$$\frac{k_e^o}{k_g}=\frac{(1-\varepsilon_v)}{\left(\frac{k_g}{k_s}\right)+\frac{1}{(1/\varphi)+\left(D_p h_{rs}/k_g\right)}}+\in\frac{D_p h_{rv}}{k_g} \qquad 4\text{-}24$$

where parameters denoted in Equation 4-24 are described in Section 2.3.2. Based on previous experimental measurements [7], the parameter φ was expressed in terms of the void fraction (ε_v) of polycarbonate as,

$$\varphi=0.02\times 10^{2(\varepsilon_v-0.3)} \qquad 4\text{-}25$$

The dominant resistance to heat transfer in a powder bed is that of the gas filling interstitial spaces [1]. In a low density (highly porous) medium, powder particles contact one another over a small area, and at few contact points. In that condition, conductivity of the powder bed is low. However, as sintering occurs and bridges between adjacent particles develop, both the density and thermal conductivity increase. The effect of density on the thermal conductivity of powder beds is taken into account in the Yagi-Kunii model (see Equation 4-24) through the parameters φ and ε_v. The void fraction ε_v, however, of material with density ρ can be calculated as follows,

$$\varepsilon_v = \frac{(\rho_{solid} - \rho)}{\rho_{solid}} \qquad 4\text{-}26$$

where ρ_{solid} denotes the density of solid polycarbonate with zero void fraction (1200kg/m^3) [45].

The high temperature form of the Yagi-Kunii model (see Equation 4-24) was used to calculate the thermal conductivity of both the powder bed and the (porous) sintered part. However, the assumption considered in calculating void ratios using Equation 4-26 was that densities of the powder and sintered solid are constant and independent of temperature variations, i.e. changes in density occurring during sintering were not considered. Thus, the void fraction of sintered polycarbonate was estimated by substituting ρ in Equation 4-26 with the density reported for the sintered part (700kg/m^3) [35], and therefore the void fraction of the sintered part was equal to 0.417. This value was used in Equation 4-24 for the calculation of the conductivity of the sintered part. Similarly, the void fraction of the powder was calculated by substituting ρ in Equation 4-26 with the density of the powder (485kg/m^3). This gave a value of the void fraction of the powder bed equal to 0.596, which was used in Equation 4-24 for calculating the thermal conductivity of the powder.

The Yagi-Kunii model also requires the diameter of particles forming the powder bed, denoted in Equation 4-24 as D_p. Polycarbonate powder particles used in SLS fabrication have an irregular shape with a mean diameter equal to 90μm [45]. However, that diameter was reported to be for the as-received polycarbonate powder. Microscopic images showed polycarbonate powder particles to change in shape from oblate to spherical when heated above T_g [7] (see Section 2.3.6). That is expected to cause the average particle diameter of the reheated powder to differ from that of the as-received powder. Data of the average particle diameter for polycarbonate powder in its used form were not available. In the absence of these data, the average particle diameters of the sintered solid and the powder were assumed to be equal to that reported for the as-received powder (90μm).

Yagi-Kunii model also requires the radiation heat transfer coefficients h_{rv} and h_{rs} (see Equations 2-6 and 2-7). The estimation of these coefficients requires the value of emissivity of the solid surfaces of the powder particles ($\in$). That emissivity value was considered equal to 0.95 (see Section 2.3.5.2).

Similar to previous heat transfer models [7], the gas filling the interstitial spaces in the powder bed was assumed to be air. The thermal conductivity of the gas, denoted k_g in Equation 4-24, is defined as a function of the temperature T as follows [7],

$$k_g = 0.004372 + 7.384\times10^{-5}T \quad \text{W/(m.K)} \qquad 4\text{-}27$$

The definition of the conductivity of the solid, signified k_s in Equation 4-24, was based on experimental measurements carried out in a previous study [7]. The conductivity measurements were performed on a polycarbonate solid at temperatures ranging from 27°C to 87°C. The conductivity results were found to conform to a simple linear relationship with temperature (T) as follows,

$$k_s = 0.02504 + 5\times10^{-4}T \qquad \text{W/(m.K)} \qquad 4\text{-}28$$

The conductivity of solid polycarbonate, in the above equation, increases with the increase in temperature. This trend agrees with the increase in conductivity with temperature expected of amorphous polymers at temperatures below T_g. However, at temperatures above T_g, the conductivity of the polymer decreases [21]. Nevertheless, a number of heat transfer models [41,44] have used Equation 4-28 to estimate the conductivity of polycarbonate at temperatures above and below T_g (155°C). In the absence of more complete data, Equation 4-28 was also used in this work to calculate the conductivity of solid polycarbonate over the entire temperature range expected during sintering.

The values of the parameters above-mentioned were substituted in Equation 4-24 to provide the conductivity relationship with temperature for the powder and sintered solid. The conductivity relationships with temperature defined in the model (in tabulated form) are graphically illustrated in Figures 4.25 and 2.26.

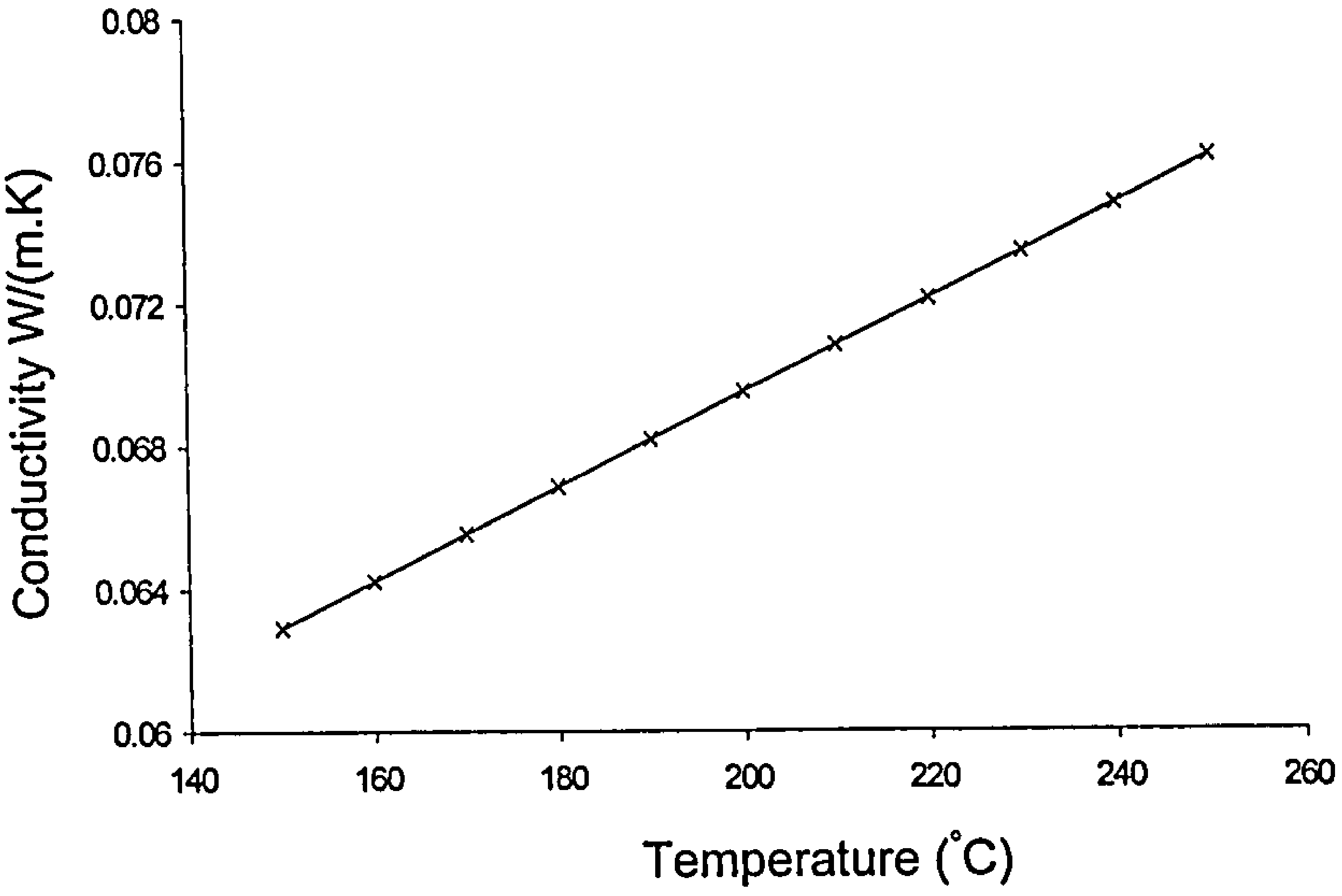

Figure 4.25 Relationship between the thermal conductivity of powder and temperature predicted using the Yagi-Kunii model and defined in the first version of the heat transfer analysis.

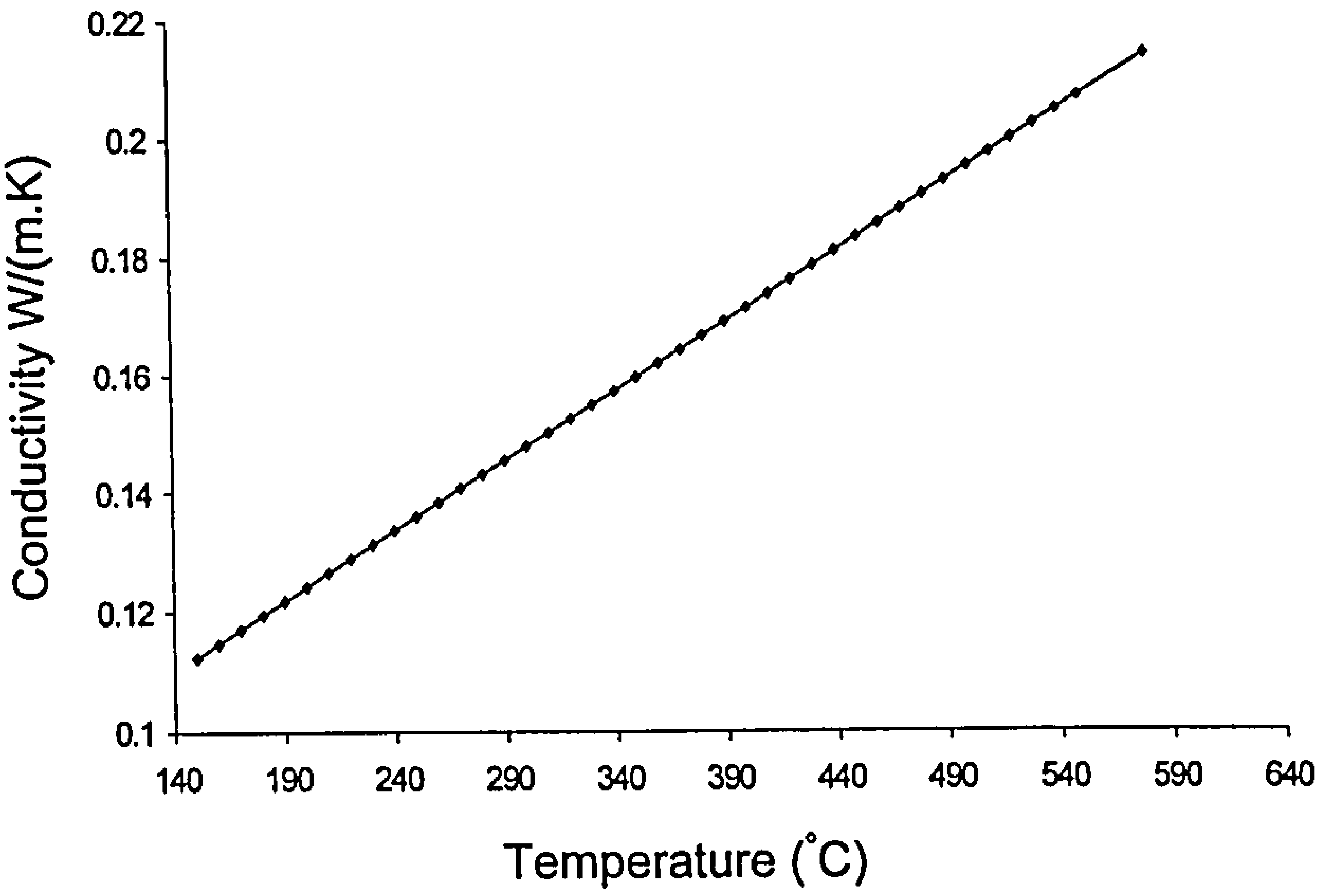

Figure 4.26 Relationship between the thermal conductivity of the sintered part and temperature predicted using the Yagi-Kunii model and defined in the first version of the heat transfer analysis.

4.6.3 Boundary Conditions in Thermal model

The belief held at the start of this work was that curl mainly developed during the building stage in SLS (see Section 4.4). Emphasis was therefore given in the first version of the heat transfer model to simulate thermal effects only occurring through that stage, i.e. thermal effects in the "cooldown" stage were not considered in the analysis. A number of thermal effects occurring in SLS were simulated by applying thermal boundary conditions in the heat transfer model, such as the convection and radiation boundary conditions. Additional boundary conditions used in the model included defining initial temperatures and the enforcing of insulation at certain surfaces. In this section, thermal effects expected to occur in SLS and the corresponding thermal boundary conditions simulating these effects are described.

Prior to adding (fresh) powder on the top surface of a recently sintered layer, the powder is heated in the feed cartridges to the highest possible temperature at which it can still flow freely when spread by the roller. This action is taken to limit cooling of the upper most regions of the sintered layer and therefore reduce its curling (see Section 2.2.5.4.2). Once the powder is spread onto the part bed, the part heater heats the powder to a temperature just below its glass transition temperature, termed the part-heater set point. That is made to reduce additional laser energy required to fuse the powder. In SLS fabrication of the modelled ten-layer parts, the temperature at which the powder was elevated to in the feed cartridges was set at 80°C. The part-heater set point, however, was adjusted to 150°C, based on the understanding that the glass transition temperature of polycarbonate was 155°C.

For simplicity, preheating of powder in the feed cartridges and part bed, prior to its sintering taking place, was not considered in this version of the heat transfer model. Therefore, the initial temperature of layers spread to form the sintered part was assumed equal to 150°C. That (initial) temperature was specified to all nodes attached to elements that together represent the sintered part in the heat transfer mesh (see Figure 4.22). Additionally, due to the lack of powder bed temperature data prior to sintering taking place, the initial temperature of the powder bed was also assumed equal to 150°C. That initial temperature was assigned to all nodes attached to elements together representing the powder bed in the heat transfer analysis mesh.

The boundary conditions of convection and radiation were specified at the edges of elements that together represent the top surface of a recently added (activated) layer. To enforce these boundary conditions in the model, temperatures of the gas filling the build chamber and that of the enclosing walls had to be defined (see Equation

4-2). For simplicity, these temperatures were assumed to be identical. The gas in the SLS chamber is not static; it enters through ducts positioned at the top of the chamber then flows across the surface of the part bed before exiting the chamber. The circulation of the gas allowed us to assume that the temperature of the gas in the chamber is uniform. Heating of the gas was mainly expected to be due to heat emanating from the part heater. This heater switches On/Off to maintain the temperature of the top surface of the part bed (surrounding the sintered region) to that set by the operator. In SLS fabrication of the modelled ten-layer parts, that temperature was set at 150°C. This temperature was assumed to be equal to the temperature of the (circulating) gas contacting the top surface of the part bed used for convection calculations, and that of the enclosing walls used for radiation calculations, all through simulation of the "build" stage in SLS.

For convection and radiation boundary conditions to be taken into account, the values of both emissivity of polycarbonate and the convection coefficient of the gas had to be additionally provided. Based on (previous) experimental measurements, reported in Section 2.3.5.2, the emissivity of polycarbonate was defined in the model equal to 0.95 [7]. In addition, similar to previous SLS thermal models [1], the gas filling the chamber was assumed to be air. Therefore, and for simplicity, the convection coefficient of the circulating nitrogen in the chamber was considered equal to the natural convection of air, 15W/m^{2}°C [46].

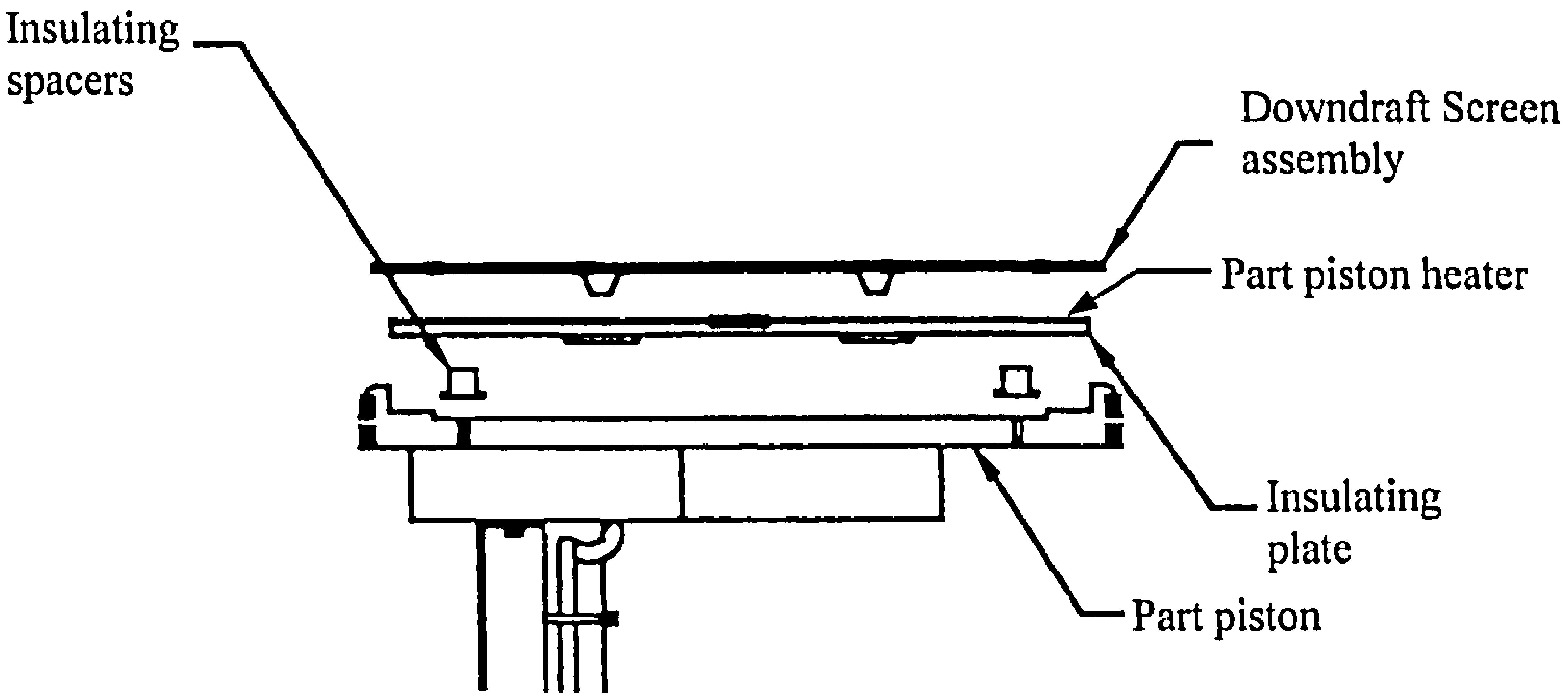

Figure 4.27 Schematic diagram of part piston assembly. From [47].

In the SLS process, the powder bed is supported by the part piston (see Figure 2.13). Thus, in specifying boundary conditions that simulated thermal effects at the bottom surface of the powder bed, the assembly of the part piston was explored. In SLS polycarbonate builds, the first layer of the powder bed is spread onto a down draft screen (see Figure 4.27). The purpose of that screen is to prevent powder from entering the downdraft tubes in the part piston while the downdraft is switched on (see Section 2.2.5.4.2). The downdraft screen is directly positioned on a part piston heater that is bonded to an insulating plate (see Figure 4.27). The design of that plate is most possibly to ensure that heat emanating from the part piston heater is directed upwards towards the powder bed. In SLS fabrication of the modelled ten-layer parts, both downdraft and the part piston heater were switched off. In addition, due to the existence of the insulating plate, it was assumed that the amount of heat imparting from the bottom surface of the powder bed into the part piston was negligible. Therefore, in the heat transfer model, the bottom surface of the powder bed was assumed to be insulated. Insulation does not require the application of any boundary condition at the edges of elements that together represent the bottom surface of the powder bed (see Figure 4.28). In the condition that no boundary conditions are applied, there will be no heat flow, since there is no connecting model underneath the bottom surface of the powder bed.

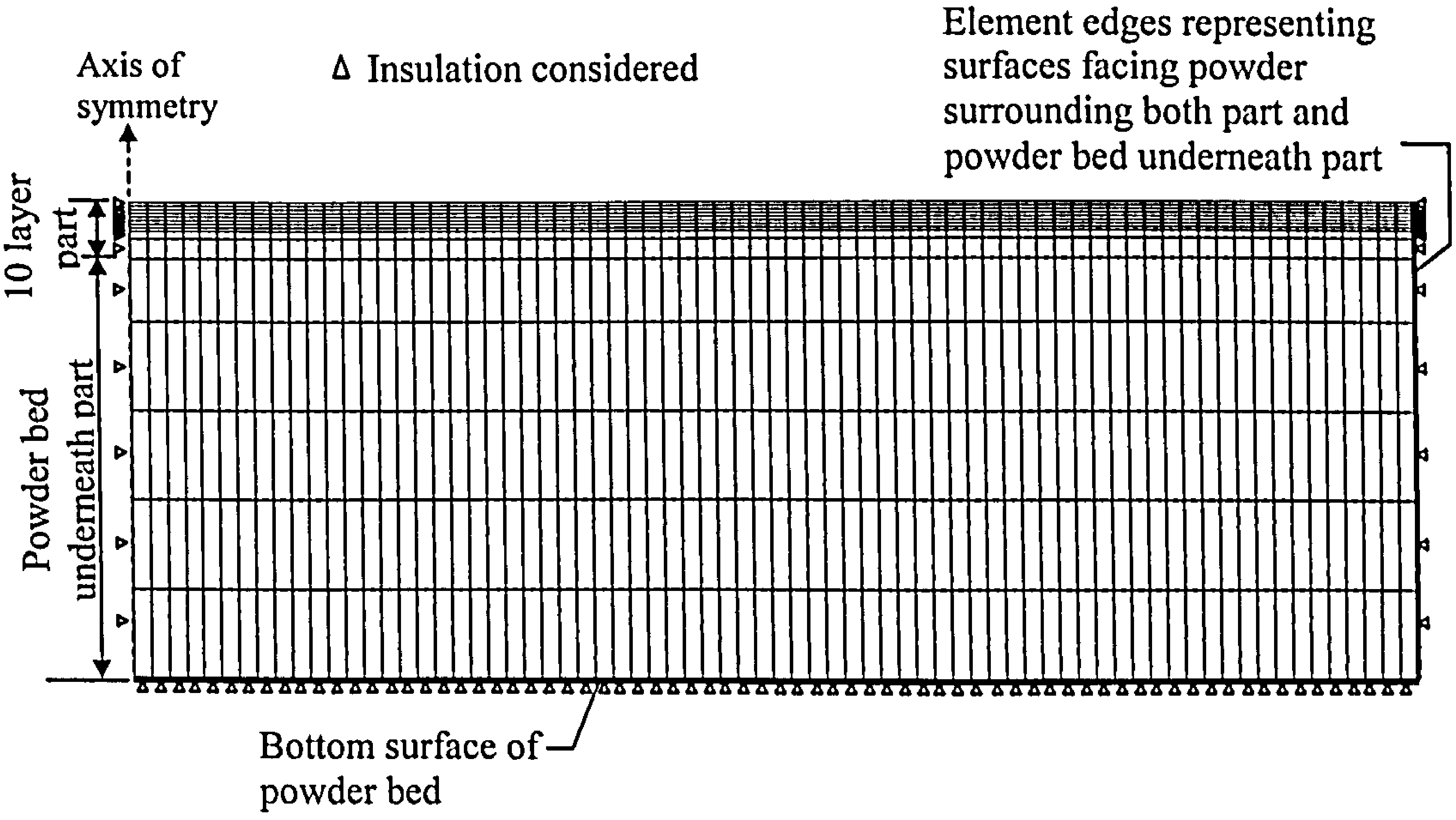

Figure 4.28 First version of heat transfer analysis mesh showing surfaces where insulation was considered.

The symmetry condition in thermal analyses also implies that no heat flows across the line of symmetry, i.e. that line is considered insulated. Therefore, no boundary conditions were applied on the edges of elements located along the line of symmetry. The belief held in developing this version of the heat transfer model was that heat lost from the side walls of sintered layers to the surrounding powder was insignificant (see Section 4.6.1). In addition, heat transferring from the region of the powder bed underneath the part to its surrounding powder was also assumed (for simplicity) to be too small to be considered in the heat analysis. Therefore, the edges of elements (in the part and powder bed meshes) supposed to be facing the surrounding powder were considered insulated. That also did not require the definition of any boundary conditions at these edges, as the surrounding powder was not included in the heat transfer analysis mesh (see Figure 4.28).

4.6.4 Analysis method in Heat model

The aim in this section is to describe the sequence of events defined in the heat transfer model to simulate thermal effects occurring during SLS fabrication of the ten-layer parts. The sequence of events is specified in ABAQUS by a sequence of steps. Each step includes definitions of thermal loads and boundary conditions applied to the model, and the time periods of their application. In this section, an effort is made to describe the main stages of SLS fabrication with the corresponding step(s) defined to simulate thermal effects occurring in each stage.

- First step defined in first version of heat transfer analysis

The SLS building of the ten-layer parts started by spreading the first layer of powder onto the powder bed. The laser beam then raster scanned a region on the top surface of the layer to form the first layer of the part. These initial stages (powder spreading and laser sintering) were simulated in a single step in the heat transfer model. The addition of the first layer of powder was replicated by simultaneously deactivating (removing) the elements signifying the layers from two to ten of the sintered part (see Figure 4.22). Therefore, in this step, the heat transfer analysis mesh was composed of elements representing the powder bed and the first layer of the part.

The SLS (raster) scanning of the layer was simulated by a uniform heat flux (see Sections 4.6.1) simultaneously applied on the edges of elements that together represent the top surface of the sintered layer. The heat flux is calculated by dividing the laser power with the cross sectional area of the laser beam spot. The SLS fabrication of the ten-layer parts was performed at laser power equal to 11W. The diameter of the laser beam spot in SLS is 0.4mm, and therefore the heat flux was 87.5MW/m^2. However, allowing for the reflectivity of polycarbonate that is equal to 5% (see Section 2.3.5.2), the heat flux used in the model was 83.1MW/m^2 (representing the heat flux absorbed by the top surface of the layer in SLS fabrication).

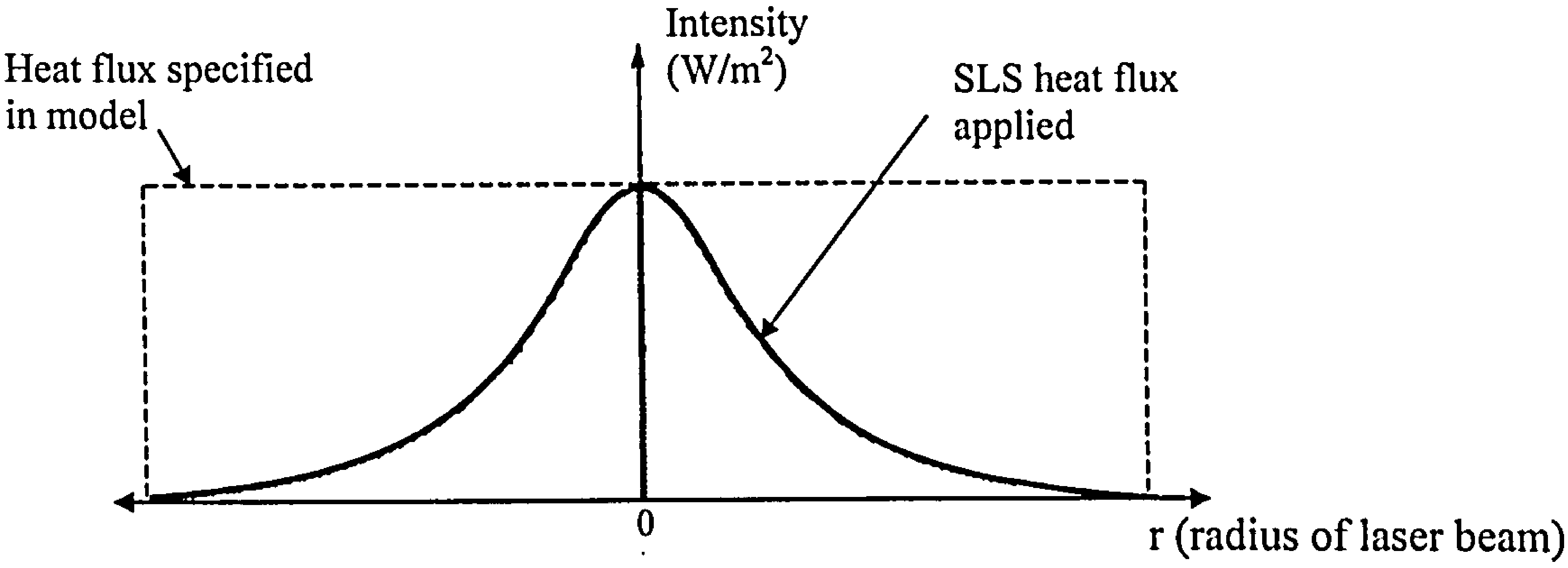

Figure 4.29 Schematic diagram showing actual heat flux applied in SLS and that specified in model.

However, it must be emphasised that the value of heat flux estimated using this (simple) method is not expected to represent the actual heat flux absorbed by a surface during SLS fabrication. The reason being that the power intensity of the laser used in SLS has a Gaussian profile and is not uniform over the entire laser spot area. In this condition, the heat flux specified in the model, assumed to be uniform over the entire area, was greater than that applied during SLS scanning (Figure 4.29). Conversely, a point on the surface of the powder is generally exposed more than once to the laser beam effect during SLS processing. The number of times the point is exposed to the laser beam is dependent on the scan spacing specified. This aspect was not taken into account in the heat transfer analysis, i.e. a point on the surface of the powder was assumed to be exposed only once to the laser beam effect.

The time the heat flux was activated in the model represented the approximate period a point on the top surface of the layer would have been exposed to the moving laser beam during SLS scanning. To simplify calculation of that period, the laser beam spot was imagined to be squared in shape with side length identical to the SLS laser beam spot diameter (D= 0.4mm). Assuming that a point (m') was scanned by that square, then the period the point would have been exposed to the laser beam effect is approximately equal to the time it took the square to travel the distance D (see Figure 4.30). That time (τ) can be expressed in terms of the speed of the laser beam spot (in the direction of scanning) U as $\tau = D/U$. In fabrication of the ten-layer parts, the speed of the laser beam was 1188.87mm/s and therefore, the value of τ specified in the model was equal to 3.36×10^{-4} seconds. That was considered to be the time period of the first step in the heat model. In addition, during that period, both convection and radiation thermal boundary conditions were set to take place from the edges of elements together representing the top surface of the first layer of the sintered part.

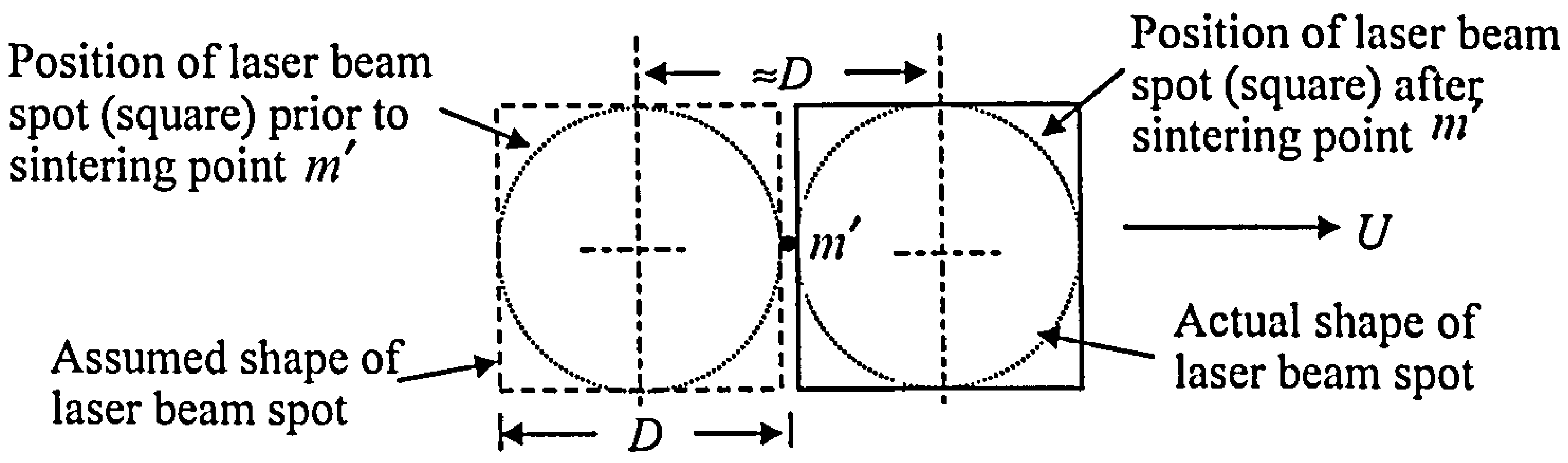

Figure 4.30 Schematic diagram showing the method used in estimating the period of heat flux application in the heat transfer analysis.

- Second step defined in first version of heat transfer analysis

Once SLS raster-scanning of the top surface of the first layer was completed, the roller started transporting and levelling fresh powder from one feed cartridge, then onto the part bed, to the other feed cartridge. In the second step of the heat transfer analysis, thermal effects simulated were those occurring on the first sintered layer just before fresh powder was added on its top surface. The heat transfer analysis mesh in this step still comprised elements representing the first layer of the part and the powder bed underneath that layer. However, the heat flux that was applied in the first step was deactivated in the second step. In the second step, convection and radiation thermal boundary conditions were still applied at the edges of elements together representing the top surface of the first layer of the part. The duration of this step represented the time it took the roller to travel from its starting position to the position just before powder was physically added on the top surface of the sintered layer. That time was assumed (for simplicity) to be the time it would have taken the roller to travel from positions *A* to *B* in Figure 4.31. The modelled ten-layer parts were SLS fabricated at the centre of the part bed in an arrangement shown in Figure 3.1. The roller speed (*RS*) set during fabrication was 110.9mm/sec. The distance between the corresponding points *A* and *B* was approximately equal to 620mm, and therefore the time set for the second step was 5.6 seconds.

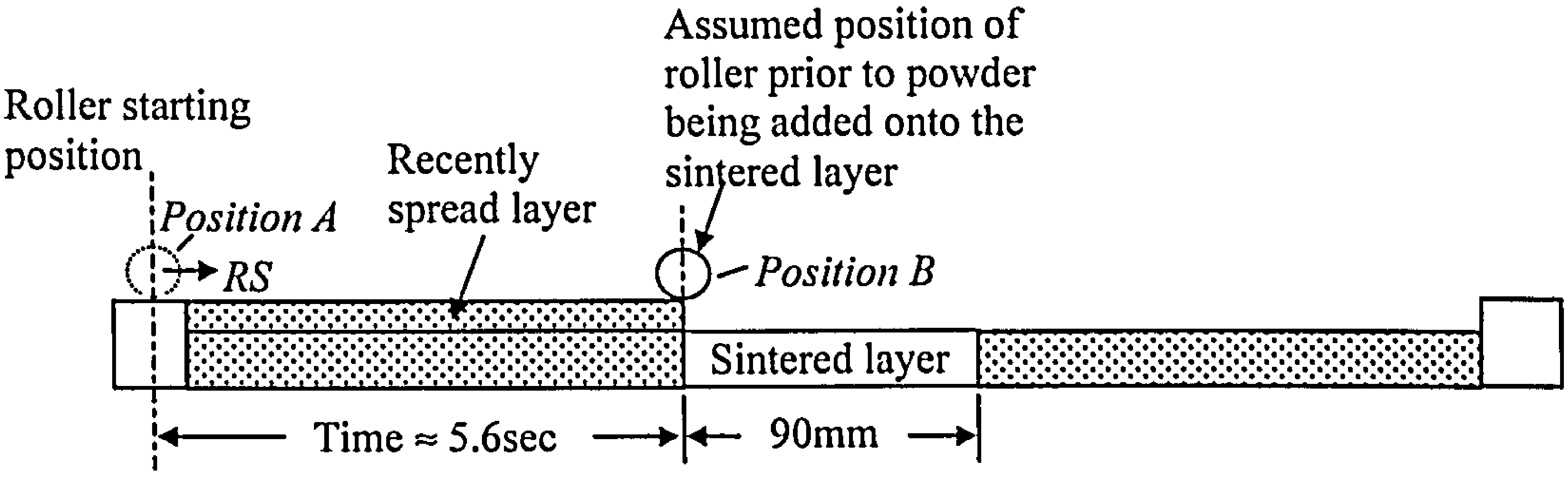

Figure 4.31 Schematic diagram representing the case simulated in the second step of the heat transfer model: convection and radiation from the top surface of the sintered layer during the time it took the roller to travel from positions *A* to *B*

- Third step defined in first version of heat transfer analysis

The next (third) step in the heat transfer analysis simulated thermal effects occurring once powder had been spread onto the first sintered layer to the instant at which the roller had travelled to its final position (position *D* in Figure 4.32). The addition of fresh powder on the top surface of the first sintered layer was simulated by simultaneously activating (adding) the elements signifying the second layer of the part in the heat transfer analysis mesh (see Figure 4.22). Therefore, the heat transfer analysis mesh in this step is composed of elements representing the powder bed, the first and second layers of the sintered part. Thermal effects considered in this step were those occurring while the roller was travelling from positions *C* to *D* (see Figure 4.32). Convection and radiation boundary conditions previously applied on the top surface of the first layer in the second step were deactivated in the third step. Instead, these boundary conditions were applied on the edges of elements together representing the top surface of the recently added layer. The period these boundary conditions were applied in the model was assumed to be identical to the time it took the roller to travel from positions *C* to *D* during SLS fabrication (see Figure 4.32). That time was equal to 5.6 seconds, and was considered to be the time specified for the third step.

In SLS fabrication, the part heater heats the top surface of the recently spread layer to 150°C prior to sintering of the layer taking place. In the heat transfer model, the initial temperature of all layers forming the part was defined equal to 150°C. Therefore, SLS stages in which preheating of layers of powder occurs prior to sintering were not simulated.

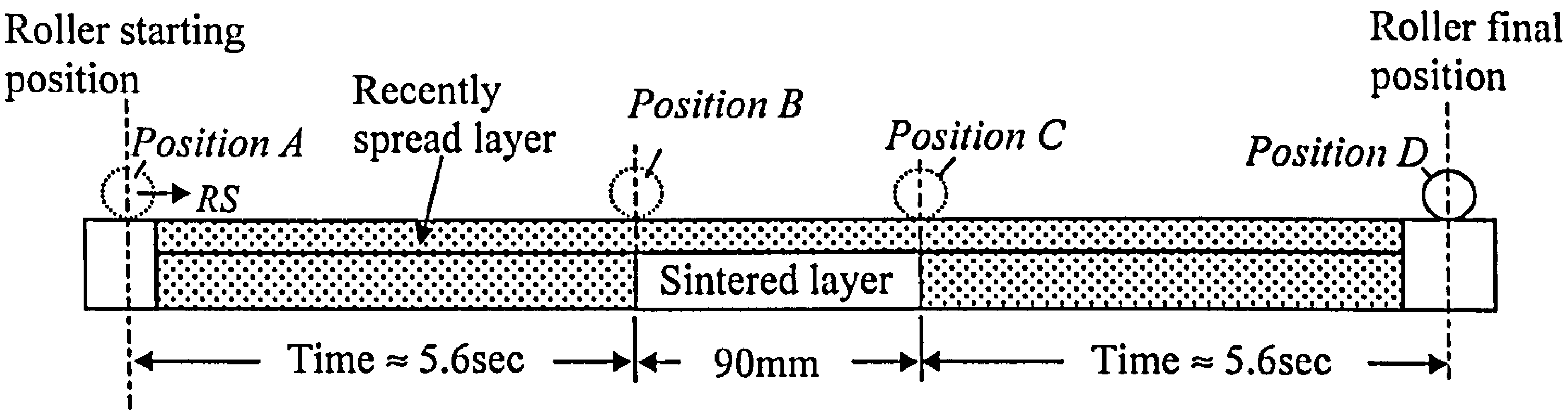

Figure 4.32 Schematic diagram representing the case simulated in the third step of the heat transfer model: convection and radiation from the top surface of the added layer during the time it took the roller to travel from positions *C* to *D*.

- **Fourth step defined in first version of heat transfer analysis**

The fourth step in the heat transfer model simulated thermal effects occurring during sintering of the second layer. The period specified for this step was identical to the time set for the first step through which sintering of the first layer was simulated (3.36×10^{-4} seconds). In addition, the value of heat flux simultaneously applied on the edges of elements representing the top surface of the second layer in the fourth step was identical to that specified in the first step (83.1MW/m^2). Furthermore, convection and radiation boundary conditions applied on the top surface of the first layer in the first step were applied on the top surface of the second layer in the fourth step. Due to the repetitive nature of SLS fabrication stages, steps two, three and four in the heat transfer analysis were repeated on successive layers of elements until sintering of the tenth layer of the part was simulated.

- **Final step defined in first version of heat transfer analysis**

In SLS fabrication of the modelled ten-layer parts, the heaters were switched off immediately after sintering of the tenth layer was completed. The parts were then allowed to cool down in the chamber until the temperature measured by the IR sensor was equal to 100°C (see Section 3.2). However, due to the lack of real temperature data during cooling of the parts, an artificial cooling was simulated. It was understood that insignificant curl developed during cooling of the parts to room temperature. Therefore, the last step of the model simulated the condition in which the part was allowed to cool down to 150°C with the gas and enclosing walls maintained at that temperature. The heat flux activated in the previous step, simulating laser sintering of the tenth layer, was deactivated in this last step. Thermal boundary conditions defined in this step were only convection and radiation applied on the edges of elements together representing the top surface of the tenth layer. An arbitrary time period of 20 minutes was specified for the step, which was believed to be sufficient for cooling of the part to 150°C.

4.6.5 Results

Due to the complexity of placing thermocouples in layers of powder to be sintered, measurements of temperature profiles in the (modelled) ten-layer parts during SLS fabrication were not performed. The complexity was mainly expected to arise due to roller motion during the addition of powder, which was bound to shift wiring connecting the thermocouples to the Data Acquisition system to be placed outside the chamber. Therefore, there were no available means of checking the accuracy of temperature profiles predicted by the heat transfer analysis. In fact, the only method found in validating the outcome of the finite element analyses was to compare deformations predicted by the stress analysis (which are highly influenced by temperature history data calculated in the thermal analysis) with experimental measurements of curl reported in Chapter 3. The criteria selected were therefore to first explore aspects related to finite element modelling for the most accurate solutions from the analyses to be obtained. In the condition that deformation results from the stress analysis were unsatisfactory, assumptions used in the models such as geometrical and material approximations were then to be investigated.

The accuracy of results obtained from a finite element analysis is generally dependent on the mesh density selected in solving the problem. The effect of increasing the number of elements leads to model predictions gradually approaching the exact solution (see Figure 4.33). However, in the generation of a too fine mesh, the cost of the analysis can be out of proportion to the accuracy of the results obtained. For example, doubling the number of elements in some situations can only increase the accuracy by less than 5%, but may require considerable additional amount of computational time and disk space to solve the problem, which is unjustifiable.

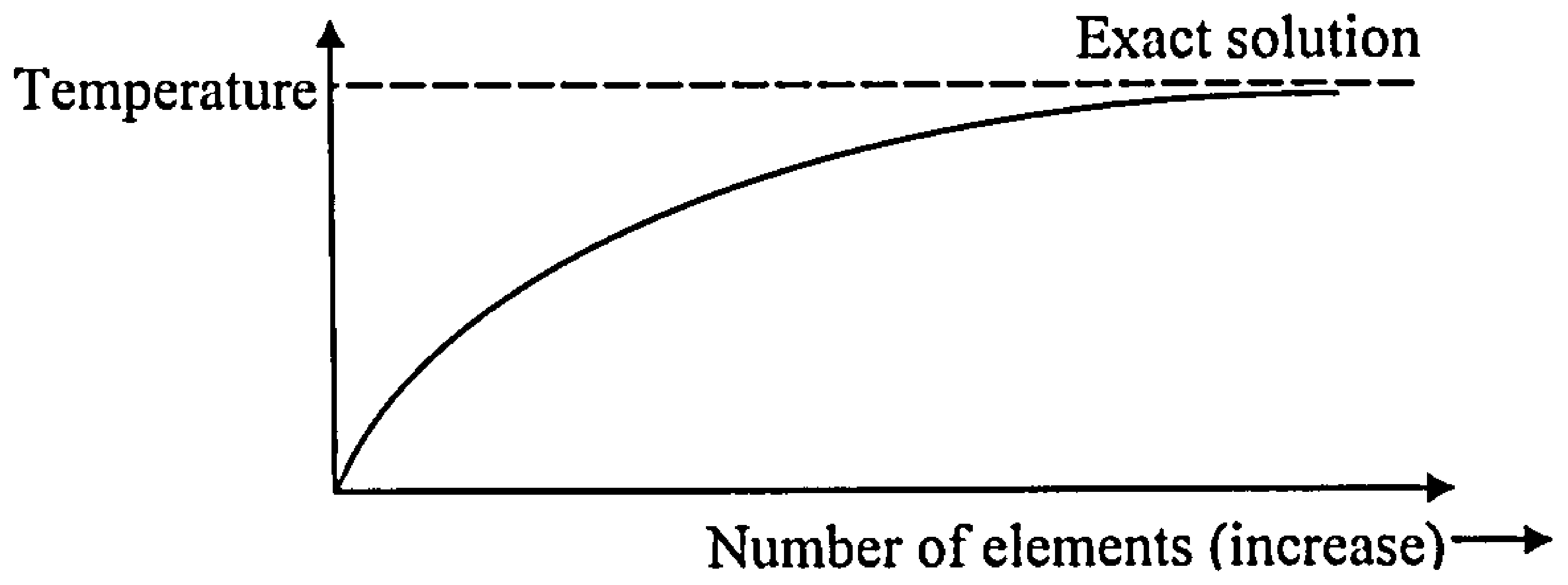

Figure 4.33 Schematic diagram showing the increase in element numbers leading to prediction of the finite element analysis approaching the exact solution.

Generally, a finite element mesh can consist of a fine mesh in some regions and a coarse mesh in other regions. The former is required where high rates of change in temperature (for example) are expected whereas the latter is used in areas of approximately constant temperature. In the present thermal model, high rates of change in temperature are expected in regions close to where the heat flux is applied. However, the further away from the sintered regions, i.e. in the powder bed, changes in temperature are less expected to occur. In this work, refinement of the heat transfer analysis mesh, shown in Figure 4.22, is performed and is described in this section. The method of refinement employed is termed reducible net whereby progressive mesh refinements are made such that all previous meshes are contained in the finer mesh [48], as illustrated in Figure 4.34. The temperature history data predicted using a recently refined mesh was compared with that estimated using the previously refined mesh. The mesh consisting of the least number of elements and giving temperature history data in the range of 5% compared to the additionally refined meshes is the one selected.

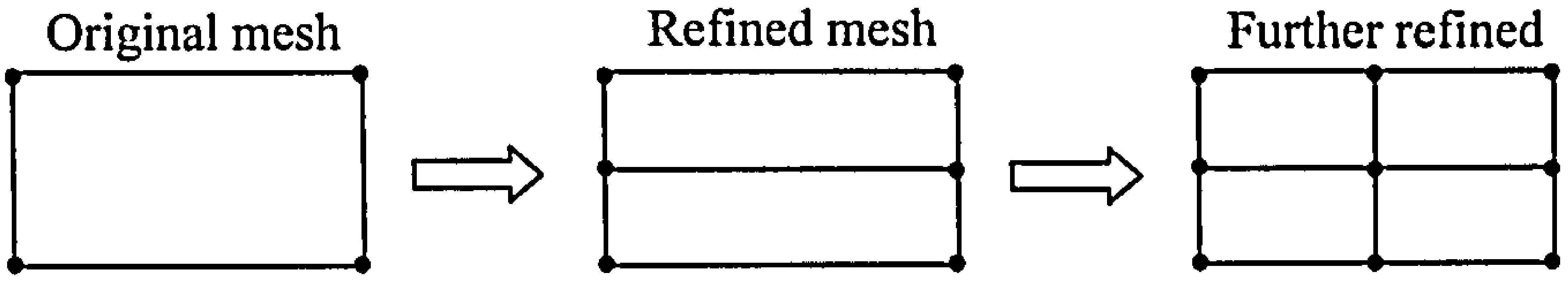

Figure 4.34 Illustration of the reducible net method in mesh refinement.

The heat transfer finite element meshes used in examining solution convergence are described in Table 4-1. The elements used in these meshes were four noded heat transfer linear quadrilateral elements, denoted in ABAQUS (DC2D4). The sequence of analyses implemented in each of the heat transfer models was that described in Section 4.6.4. The term "Original mesh" in Table 4-1 signifies the mesh illustrated in Figure 4.22. Initial refinement of that mesh was made by increasing the mesh density in regions representing the first and second layers of the part. Mesh refinement of the powder bed was also made; a fine mesh was used in regions close to the first layer and a coarser mesh was used in regions further away from the layer. Changes in element sizes from the fine meshed regions to the coarser meshed ones were gradual, i.e. abrupt changes in element sizes were avoided. This mesh is denoted in Table 4-1 as the "Refined mesh" and is shown in Figure 4.35. Additional refinement was made by dividing each element in the "Refined mesh" into 4 equally sized elements. The resulting mesh is termed in Table 4-1 the "Further refined mesh". The aspect ratio of the elements in all three meshes did not exceed a value of 5.

Mesh	Mesh Size (Depth* x Length*)			
	Powder bed	Sintered Part		
		1st layer	2nd layer	Layers from three to ten
Original	5x72	1x72	1x72	1x72
Refined	13x72	5x72	2x72	1x72
Further refined	26x144	10x144	4x144	2x144

Depth*: Number of elements along z direction.
Length*: Number of elements along x direction. (Directions shown in Figure 4.35)

Table 4-1 Description of meshes generated for the mesh convergence study performed on the first version of the heat transfer analysis.

To introduce the results of the convergence study, temperature history data at carefully selected nodes were monitored. These nodes were expected to experience high changes in temperature during the analyses. The nodes examined were located at the top surface of each layer forming the part and at the bottom surface of the first layer. The temperatures of some of these nodes predicted at selected instants using the meshes described earlier are reported in Tables 4-2 to 4-5.

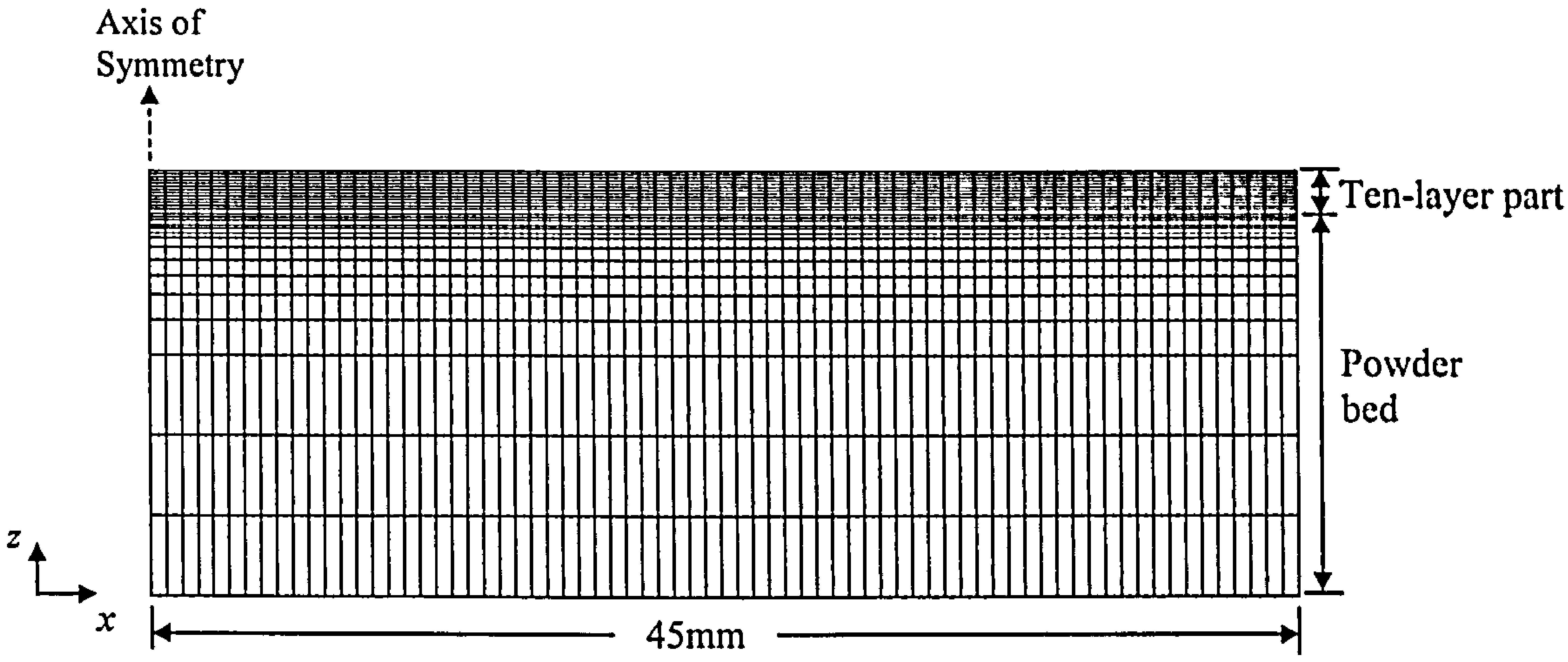

Figure 4.35 "Refined" 2D mesh of first version of heat transfer analysis.

Mesh	Temperature at bottom surface of 1st layer (°C)	Temperature at top surface of 1st layer (°C)
Original	150.7	206.9
Refined	150.2	292.2
Further refined	150.2	289.4

Table 4-2 Temperatures predicted after 0.1 seconds of applying heat flux on the edges of elements together representing the top surface of the first layer.

Table 4-2 shows temperatures predicted after 0.1 seconds of applying heat flux on the top surface of the first layer. Temperatures predicted at that surface using the "Refined" and "Further refined" meshes were approximately identical (differing by less than 1%). However, analysis performed using the "Original" mesh tended to underestimate the temperature at top surface of the layer by approximately 29% compared to temperatures predicted at the surface using the other two meshes. Conversely, temperatures estimated at the bottom surface of the layer using all three meshes were almost identical, and were not significantly varying from the initial temperature specified (150°C). That was expected to be due to the period following the application of heat flux, at which results are presented, being too short for the effect of heat conducted into the layer to be considerably sensed at its bottom surface. However, the underestimation of temperature at the top surface of the layer using the "Original" mesh is believed to be a result of the coarse mesh generated especially in regions close to where heat flux was applied.

Mesh	Temperature at bottom surface of 1st layer (°C)	Temperature at top surface of 1st layer (°C)	Temperature at top surface of 2nd layer (°C)
Original	160	168.1	271
Refined	158.9	171.8	299.7
Further refined	158	169.2	296.1

Table 4-3 Temperatures predicted after 0.1 seconds of applying heat flux on the edges of elements together representing the top surface of the second layer.

Table 4-3 shows temperatures predicted after 0.1 seconds of applying heat flux on the top surface of the second layer. Temperatures predicted at that surface using the "Refined" and "Further refined" meshes were approximately identical (differing by 1.2%). However, analysis performed using the "Original" mesh underestimated the temperature at the top surface of the layer by approximately 9% compared to corresponding predictions made using the other two meshes. That was mainly expected to be caused by the coarse mesh representing the second layer in the "Original" mesh.

Mesh	Temperature at bottom surface of 1st layer (°C)	Temperature at top surface of 1st layer (°C)	Temperature at top surface of 2nd layer (°C)	Temperature at top surface of 5th layer (°C)
Original	172.9	174.1	176.5	310.8
Refined	171.7	173.4	176.4	310.3
Further refined	169.3	170.7	173.1	305.8

Table 4-4 Temperatures predicted after 0.1 seconds of applying heat flux on the edges of elements together representing the top surface of the fifth layer.

Table 4-4 shows temperatures predicted after 0.1 seconds of applying heat flux on the top surface of the fifth layer. Temperatures estimated at that surface using the "Original" and "Refined" meshes were approximately similar (differing by less than 0.2%). That was expected to be a result of the mesh representing the fifth layer in both the “Original” and “Refined” being identical. Conversely, the higher mesh density used in representing the layer in the “Further refined” had an insignificant improvement on the temperature estimated at the top surface of the layer at that instant of the analysis. The temperature predicted at the surface of the layer using the “Further refined” mesh differed by approximately 1.6% compared to corresponding predictions made using both the “Original” and “Refined” meshes.

Table 4-5 shows the influence of mesh refinement on temperatures predicted after 11 seconds of applying heat flux on the top surface of the tenth layer, i.e. during the cooling down stage simulated in the analysis. Predicted temperatures of corresponding nodes in all three meshes were approximately identical at that instant of the analyses.

Mesh	Temperature at bottom surface of 1st layer	Temperature at top surface of 2nd layer	Temperature at top surface of 3rd layer	Temperature at top surface of 5th layer	Temperature at top surface of 10th layer
Original	182.7	185.2	185.5	185.1	181.6
Refined	182	184.7	185.2	185.2	181.9
Further Refined	178.6	181.1	181.7	181.7	178.9

Table 4-5 Temperatures predicted after 11 seconds of applying heat flux on the edges of elements together representing the top surface of the tenth layer.

The overall observation in Tables 4-2 to 4-5 is that temperatures of corresponding nodes predicted using the “Refined” and “Further refined” meshes were approximately identical (differing by less than 2%). However, analysis performed using the “Original mesh” underestimated temperatures at the top surfaces of the first and second layers. Conversely, temperatures predicted at the bottom surface of the first layer using the three meshes were approximately equal at all selected instants.

To illustrate the effect of mesh refinement on temperatures predicted at the bottom surface of the first layer, temperatures estimated at that surface using all three meshes are drawn alongside over the period of the analysis in which the building stage in SLS was simulated (see Figure 4.36). Temperatures estimated using the three meshes were approximately identical in that period (differing by less than 3%).

That observation was also noticed when temperatures predicted at the bottom surface of the layer using the three meshes were compared in the period simulating the cooling down stage.

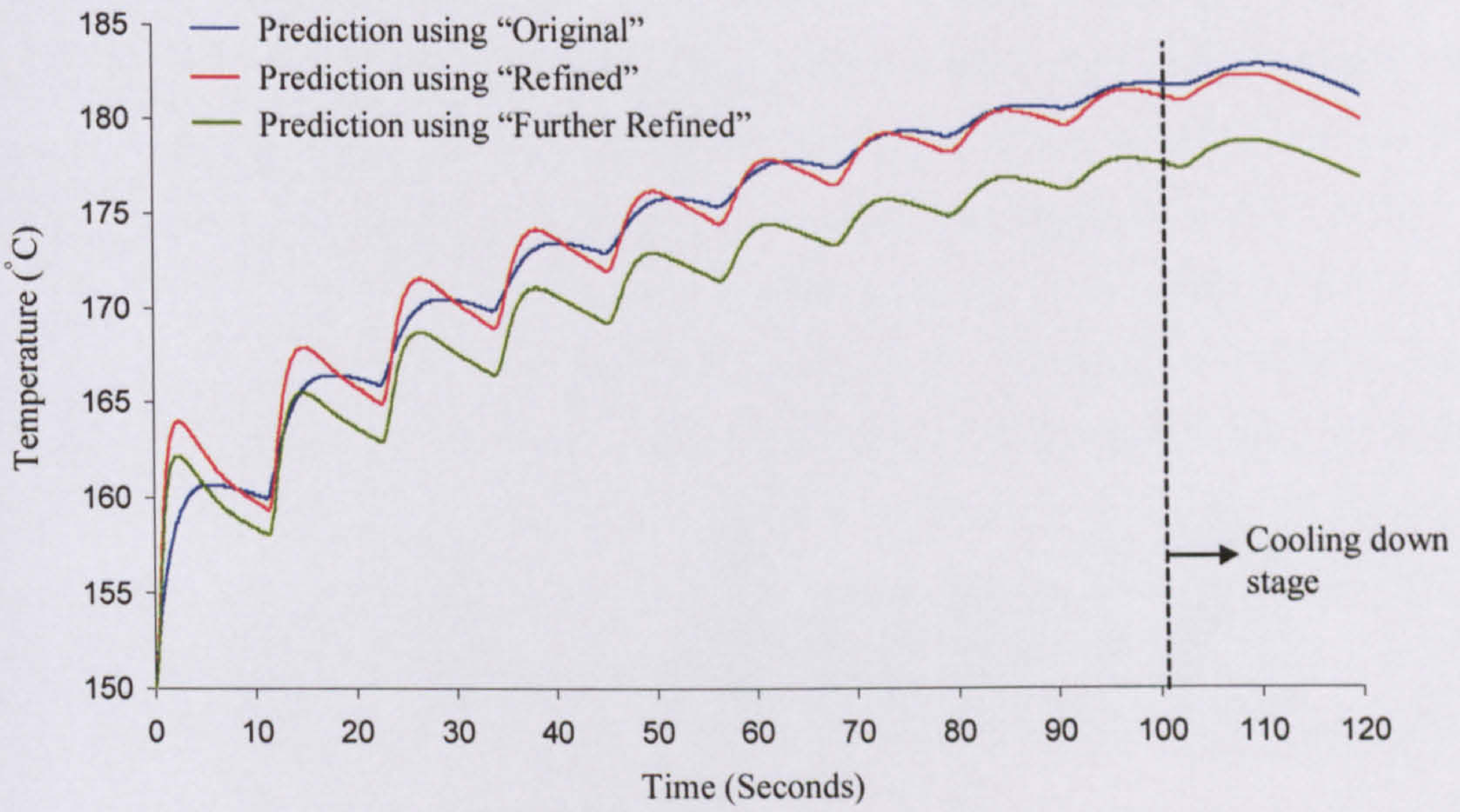

Figure 4.36 Temperatures predicted at bottom surface of first layer using the three meshes generated to examine solution convergence of the first version of the heat transfer analysis, the "Original", "Refined" and "Further refined".

Mesh	Original	Refined	Further Refined
Relative CPU time	1	1.75	7.56

Table 4-6 Relative CPU times required to run the simulations performed using the meshes generated to examine solution convergence of the first version of the heat transfer analysis.

The overall conclusion was that solution convergence was achieved using the "Refined" and "Further refined" meshes. Table 4-6 shows the relative CPU times required to run the simulations performed using each of the three meshes. Relative CPU time was calculated by dividing the CPU time required to solve the analysis using a specific mesh by the CPU time required for solution using the "Original" mesh. It was noticed that the CPU time required to solve the analysis performed using the "Further refined" mesh was 4.3 times that required for solution using the "Refined" mesh. Therefore, the "Refined mesh" was the most efficient mesh and was selected in the remainder of this version of modelling.

Selected nodal temperature histories estimated using the "Refined mesh" are illustrated in Figures 4.37 and 4.38. Figure 4.37 shows temperatures predicted in the first eight steps of the heat transfer analysis. The nodal temperature histories illustrated in Figure 4.37 are also magnified in Figures 4.45 and 4.46. In the first step, sintering of the first layer was simulated. During the period of this step (3.36×10^{-4} seconds), nodes located at the top surface of the layer showed an increase in temperature from the initial temperature set (150°C) to 406.2°C. As the temperature of the surface increased, a fraction of heat absorbed by the surface is expected to be lost from the surface through convection and radiation whilst the remainder is expected to be conducted into the layer. However, the effect of heat conducted is not reflected by a significant increase in the temperatures of nodes located within the layer, which was attributed to the short period of the step. For example, at the end of the step, nodes located at a depth of 0.125mm from the surface showed only a slight increase in temperature from 150°C to 150.6°C. However, nodes located at a larger depth than 0.125mm did not vary in temperature from the initial temperature set (150°C).

In the second step of the analysis, thermal effects occurring following sintering of the first layer and prior to the addition of the second layer were simulated. In this step, convection and radiation from the top surface of the first layer were still set to take place. However, the high rate of reduction in temperature seen at the top surface of the layer in the first 0.1 seconds of this step is mainly expected to occur due to radiation, which has an important effect at high temperatures. Conduction into the layer is also expected to have occurred in this step, exhibited by an increase in the temperatures of nodes located within the layer. For instance, nodes located at a depth of 0.125mm from the top surface of the layer showed an increase in temperature from 150.6°C to a maximum of 201.5°C in 0.2 seconds. Further conduction into the layer with time is displayed by a reduction in temperature of these nodes accompanied by an increase in the temperature of nodes located at a larger depth from the top surface. For example, nodes located at a depth of 0.25mm from the top surface of the first layer increased in temperature from 150°C to a maximum of 179.5°C in 0.5 seconds. However, at that instant of the analysis, nodes located at a (lower) depth of 0.125mm from the surface showed a decrease in temperature to

192.1°C. After 3 seconds of the application of heat flux on the surface and for the remaining period of the second step (2.6 seconds), temperatures of all nodes in the layer are seen to reduce. That was expected to be due to heat lost from the top surface of the layer through convection and radiation and due to the continuous conduction of heat from the layer into the powder bed. At the end of the step (5.6 seconds following the application of heat flux), temperatures in the layer were almost identical differing by less than 0.6%.

In the third step of the analysis, thermal effects expected to occur following the addition of the second layer (in powder form) and prior to its sintering were simulated. In the heat transfer analysis, the predefined initial temperature of all nodes in the mesh is equal to 150°C. However, at the instant of activating the second layer, the temperature at the top surface of the layer is the initial temperature set, whereas the temperature at the bottom surface of the layer is equal to 162.4°C. The latter is the temperature estimated at the top surface of the first layer at the end of the previous (second) step. The reason being that elements representing the first and second layers are connected at the interface by common nodes. In this step, conduction of heat from the first layer to the recently added layer is expected to occur. That is displayed by an increase in the temperature of nodes located at a depth of 0.125mm from the top surface of the second layer, followed by an increase in the temperature of nodes located at the top surface of the layer. Following 1.8 seconds from the start of the step and for the remaining period of the step (3.9 seconds), temperatures of nodes in the first and second layers are approximately identical (differing by 0.6%). During that period, these nodes reduce in temperature, which is expected to be caused by the continuous conduction of heat from the layers into the powder bed and due to convection and radiation from the top surface of the second layer.

In the fourth step of the analysis, sintering of the second layer was simulated. During the period of this step, nodes located at the top surface of the second layer increased in temperature from 159.2°C to 413.7°C. The latter is higher than the temperature predicted at the top surface of the first layer immediately following its sintering (406.2°C). That is probably because the temperature at the top surface of the first layer prior to its sintering was 150°C, whereas that at the top surface of the second layer was 159.2°C.

In the fifth step of the analysis, thermal effects occurring following sintering of the second layer and prior to the addition of the third layer were simulated. The first 0.1 seconds of this step shows a large reduction in temperature at the top surface of the second layer, which is mainly believed to be caused by radiation from that surface. In the first 1.2 seconds of this step, conduction of heat from the recently sintered surface (top surface of the second layer) into the build and powder bed is expected to have occurred. That is displayed by an increase in the temperature of nodes located in the first and second layers. Convection and radiation from the top surface of the second layer are also expected to have taken place. The continuous heat loss from the top surface of the second layer through conduction, convection and radiation had its effect seen at the instant 1.2 seconds from the start of the step. At that instant and for the remaining period of the step (4.5 seconds), the temperature at the top surface of the second layer was less than that at its bottom surface. Consequently, conduction of heat is expected from the build towards that surface. Conduction of heat is also expected from the build into the powder bed. However, in the final 1.3 seconds of the step, temperatures in the first and second layer were seen to continuously reduce. The reduction in temperature at the bottom surface of the build is probably an indication that heat received by that surface from the build is less than that conducted from the surface into the powder bed. At the end of the step, the highest temperature in the build predicted at a depth of 0.125mm from the top surface of the first layer is 169.3°C. However, at that instant of the analysis, temperatures predicted at the top and bottom surfaces of the (2-layer) build were 168.4°C and 167.3°C respectively.

In the sixth step of the analysis, thermal effects occurring following the addition of the third layer and prior to its sintering were simulated. In this step, conduction of heat from the build to the added layer is expected to occur, which is displayed by an increase in temperature at the top surface of the third (added) layer. That was additionally seen, in the first 0.2 seconds of the step, by a slight rise in the temperatures of nodes located at the top surface of the second layer and those at a depth of 0.125mm from that surface. Conversely, in that period, nodes in the first and second layers located at a depth greater than 0.125mm from the top surface of the second layer showed a slight decrease in temperature. After 0.5 seconds of adding the third layer and for the remaining period of the step (5.1 seconds), temperatures of nodes in the added layer and the build were almost identical (differing by 0.3%). In that period, these temperatures reduced which was expected to be due to convection and radiation from the top surface of the third layer and due to the continuos conduction of heat into the powder bed.

In the seventh step of the analysis, sintering of the third layer was simulated. During the period of this step, the top surface of the third layer increased in temperature from 164.8°C to 418.2°C. The latter is higher than temperatures predicted immediately following the application of heat flux on the top surfaces of the previous layers. The observations seen in temperature histories predicted in the first seven steps of the analysis (described earlier) were also noticed in temperatures predicted in the following steps, i.e. from the step in which the fourth layer was added to that simulating sintering of the tenth layer.

Selected nodal temperature histories predicted in the final step of the heat transfer analysis are illustrated in Figure 4.38. The step simulates thermal effects occurring following sintering of the tenth layer. In the first 0.9 seconds of the step, temperatures predicted at the top surface of this layer were the highest in the build. Thus, during this period, conduction of heat from that surface into the build is expected to have taken place. Convection and radiation from that surface to the environment are also believed to have occurred. The large amounts of heat lost from the top surface of the tenth layer through convection, radiation and conduction is expected to be the reason for the high reduction rate in temperatures predicted at that surface. However, following 0.9 seconds from the start of the step and for a duration of 2.1 seconds, the highest temperatures in the build were at the bottom surface of the tenth layer. Thus, in this period, conduction of heat from that surface upwards into the tenth layer, and downwards into the layers underneath are expected to occur. Following that period and for a duration of 2.2 seconds, the temperature at the bottom surface of the ninth layer was the highest in the build. That was then followed with the temperature at the bottom surface of eighth layer being the highest in the build, and after a while, that at the bottom surface of the seventh layer being the highest and so forth. After 76 seconds from the start of this step and for a period of 17 minutes, temperatures at the bottom surface of the first layer were the highest in the build, and reduced in the build the further away nodes were located from that surface. Consequently, in that period, heat is expected to be conducted from the powder bed towards the top surface of the tenth layer, and then lost from that surface to the environment through convection and radiation. However, the continuous reduction in temperatures in the build during that period is probably an indication that heat lost from the surface is higher than that conducted from the powder bed into the build. By the end of the step, temperatures in the build were identical and equal to the temperature of the environment (150°C), and thus the build has reached a thermal equilibrium state.

4.7 Stress model

The aim of the stress model is to predict the development of curl in the ten-layer parts that curl measurements, reported in Chapter 3, had been performed on. In the following, a description of the first version of the stress model is provided. The curl results predicted by the model are then presented.

4.7.1 Geometry

As the sintered part is not bonded to the powder bed underneath, deformation of the latter (if it occurs) is not expected to have a significant effect on curling of the part. Therefore, the powder bed was not represented in the stress analysis mesh. Curling of SLS fabricated parts is genuinely a 3D problem, and thus requires a 3D stress model for solution. The use of a 3D model allows curl seen in both the *x-z* and *y-z* planes to be predicted (Figure 4.39*a*). However, due to the large number of nodes and elements generally needed in a 3D stress model, solution of the analysis can be extremely expensive; requiring long computational times and huge disk space. Additionally, the sequentially coupled thermal-stress analysis approach necessitates that all nodes (connected to elements) in the stress analysis mesh have corresponding nodes in the heat transfer analysis mesh. Consequently, the use of a 3D stress model can also cause solving of its corresponding heat transfer analysis to become expensive, which may result in a huge deficit in computing resources.

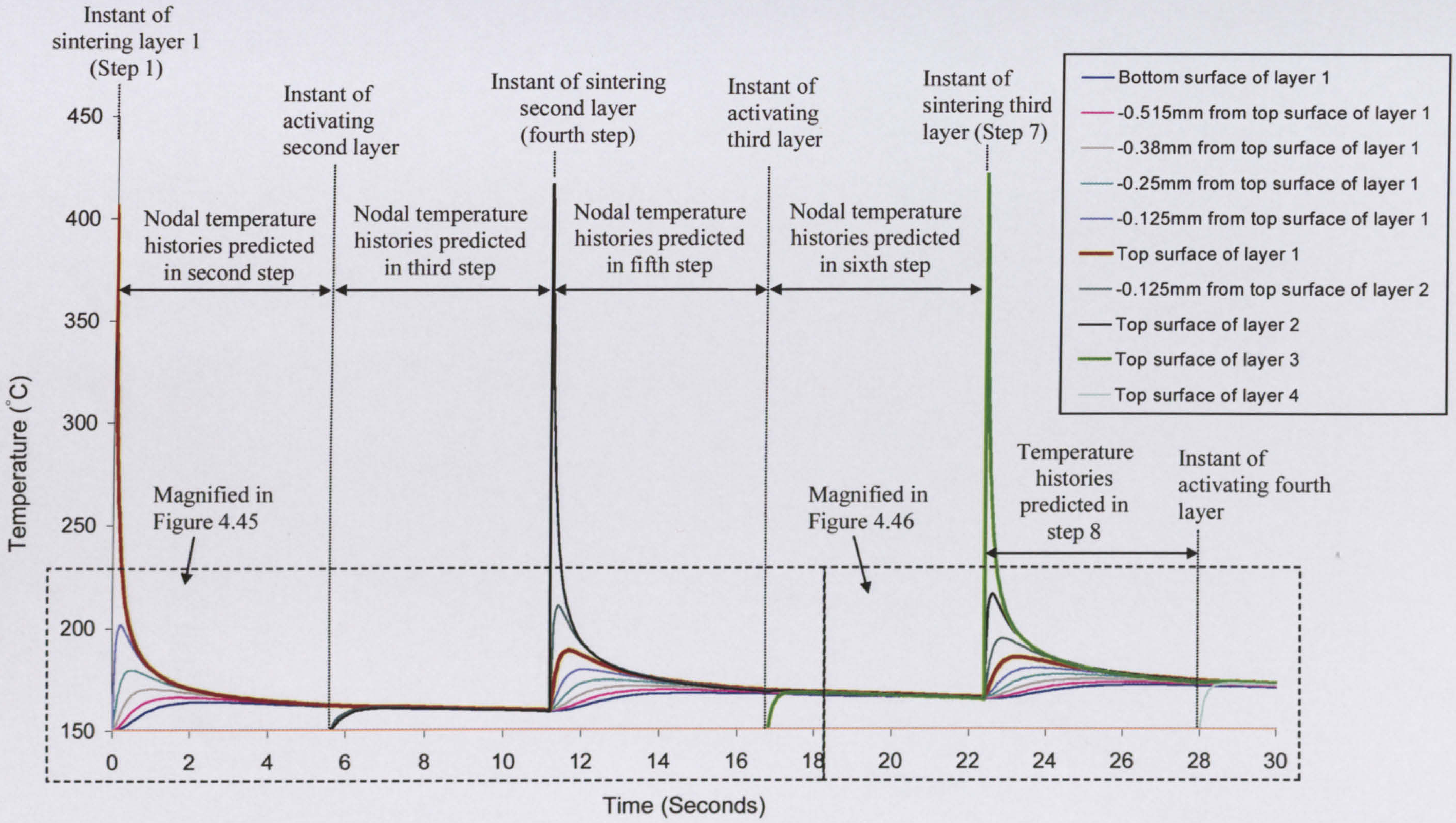

Figure 4.37 Nodal temperatures of interest predicted in the first eight steps of the “refined” first version of the heat transfer model

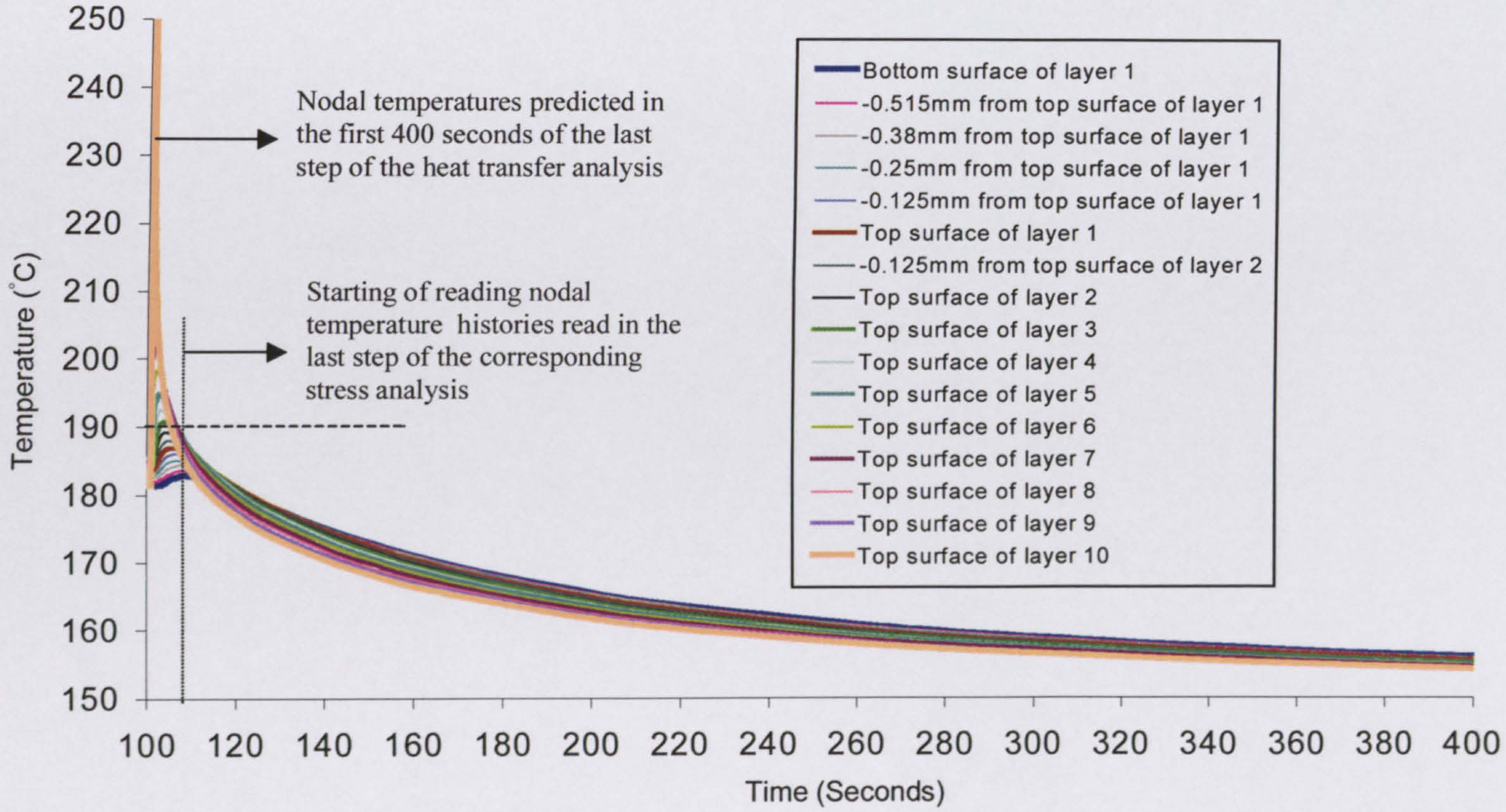

Figure 4.38 Selected nodal temperature histories of interest predicted in the final step of the “refined” first version of the heat transfer analysis

The ultimate goal of this work is to create the simplest finite element models that can guide the design of geometrically acceptable parts. However, due to the high cost expected of solving 3D stress and corresponding thermal models, employing these models to replace the presently used technique of selecting optimal machine parameters by experimental trials can no longer be economically feasible. Therefore, a simplification was made by using a (less expensive) 2D stress model to solve the curl problem rather than a 3D one. A similar simplification was performed in previous studies by Dalgarno et al. [35] (see Section 2.4.2) and Beuth et al. [49]. The latter developed a general model to predict residual stresses that can result in delamination of multi-layer parts.

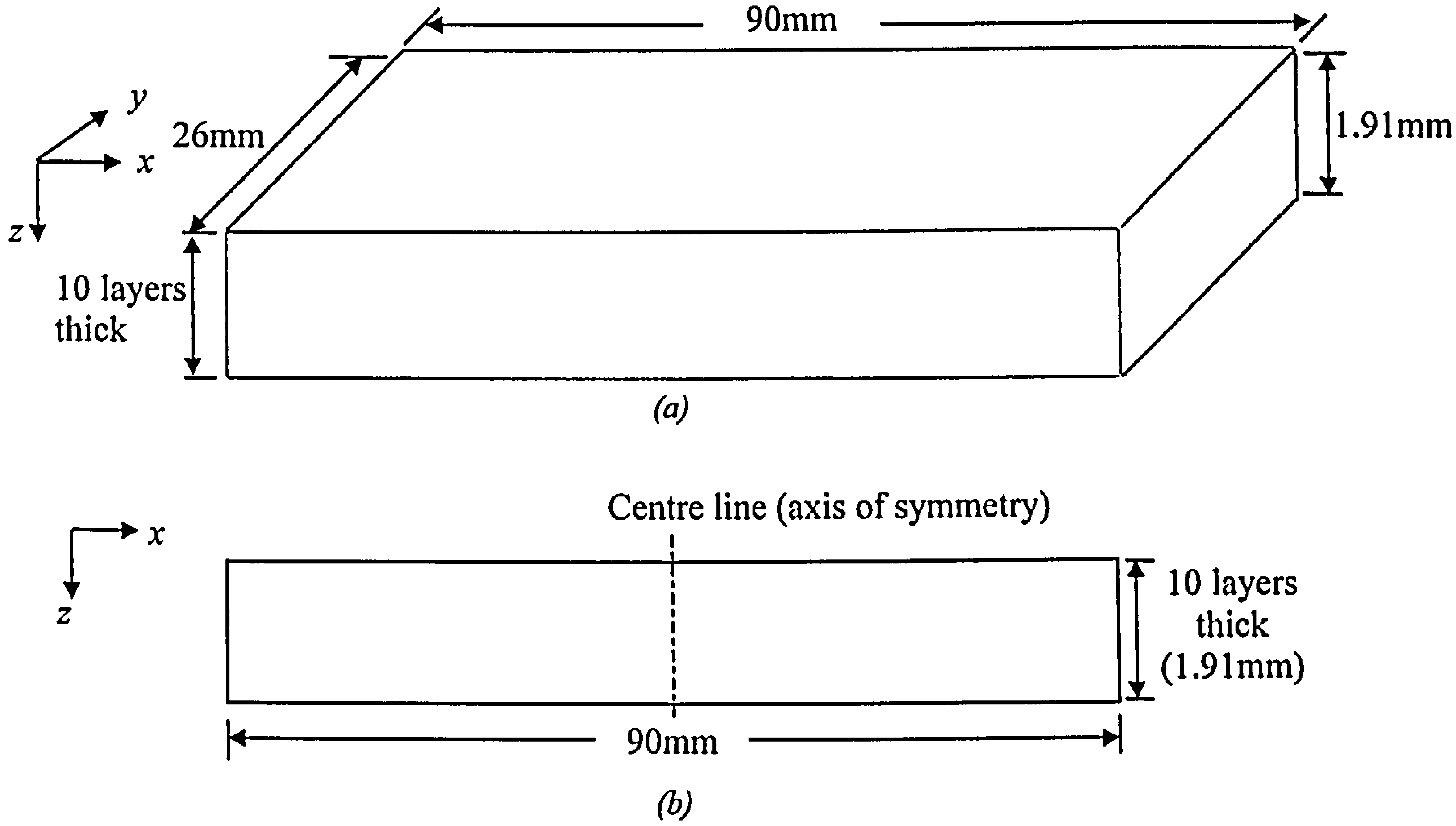

Figure 4.39 (*a*) A 3D representation of the part examined (*b*) A simplified 2D representation of the part modelled.

The 2D representation of the part analysed in the present stress model is schematically shown in Figure 4.39*b*. The 2D stress model was developed using the plane strain assumption. That assumption was made based on that the width of the part (26mm) is approximately 13 times its thickness (1.91mm) (see Figure 4.39). Similar conditions were used as basis for implementing the plane strain assumption by Liu et al. [50]. As the geometry of the 2D representation of the part, in addition to loadings and boundary conditions applied are mirror symmetrical about the centre line (Figure 4.39*b*), only half of that geometry was modelled. The 2D mesh generated in the stress model is shown in Figure 4.40. In the mesh, the ten-layer sintered part was represented using four noded, plane strain quadrilateral elements, denoted in ABAQUS (CPE4). The first and second layers had thicknesses equal to 0.66mm and 0.25mm respectively, while the thickness of layers from three to ten was 0.125mm [35]. The mesh representing the part in the stress model was identical in shape to that representing the part in the "Refined" heat transfer analysis mesh (Figure 4.35). Thus, the first layer of the part was represented in the stress model using a 5×72 element mesh and the second layer was represented using a 2×72 element mesh. The layers from three to ten, however, were represented each using a 1×72 element mesh. The aspect ratio of each element in the mesh did not exceed a value of 5.

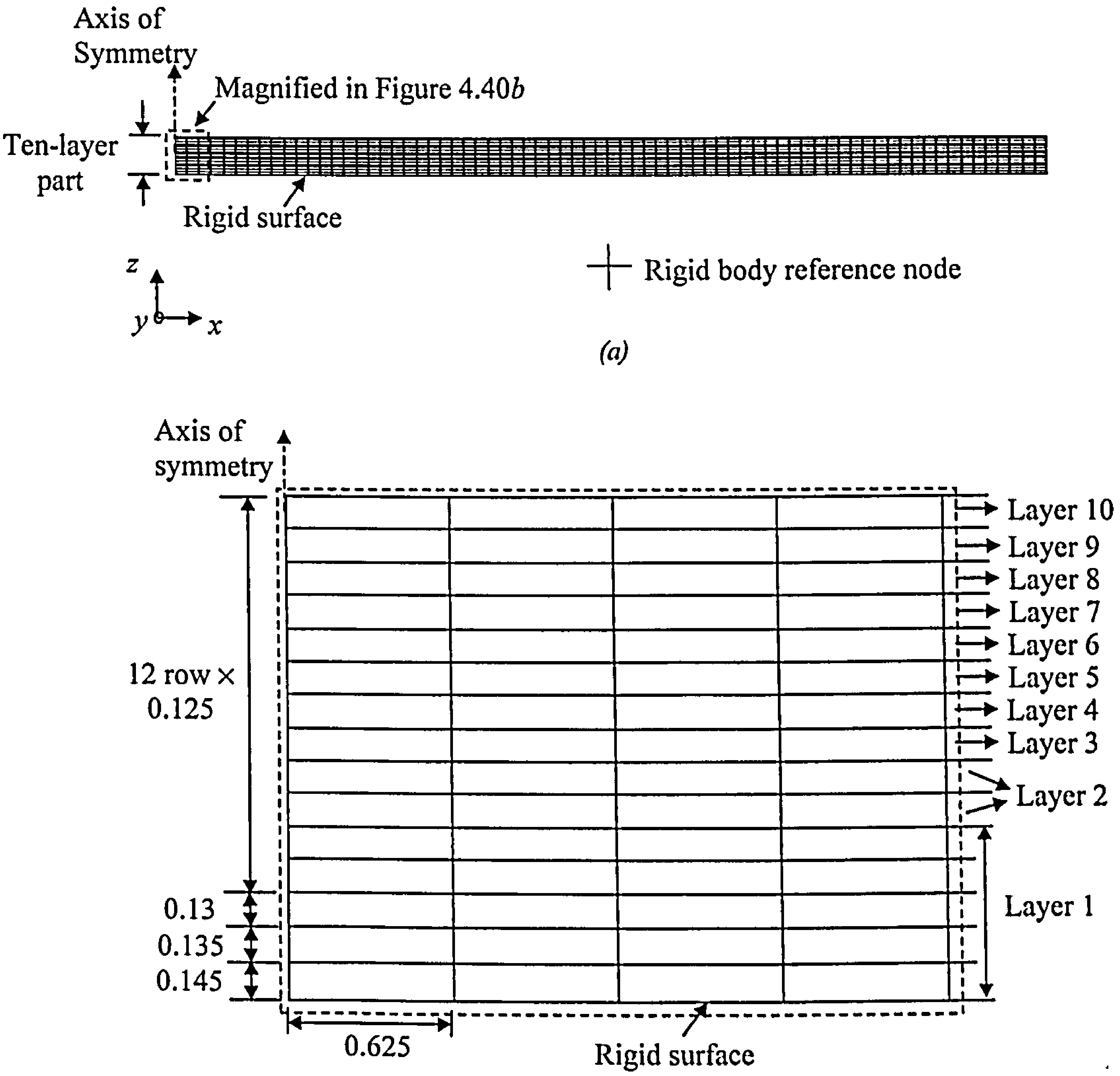

(a)

(b)

Figure 4.40 (*a*) 2D finite element mesh generated in the first version of the stress model (*b*) Magnified region of the ten-layer part mesh.

Due to the lack of mechanical properties of the powder bed, the surface of the powder bed in contact with the bottom surface of the part was represented for simplicity by a rigid surface, which is similar to the assumption considered by Dalgarno et al. [35]. That surface was modelled using 2D rigid surface elements denoted in ABAQUS (IRS21). The motion of that surface (seen as a line in the 2D model) is controlled by the motion of a single node, associated with the rigid surface, termed the "rigid body reference node" [43]. The active degrees of freedom of the node are translational along the x and z directions and rotational about the y-axis of the local co-ordinate of that node.

4.7.2 Material Properties Defined in the Stress Model

The main material properties required as input to the stress analysis were identified in Section 4.4 as the coefficient of thermal expansion and the modulus of elasticity. Additionally, the viscoelastic behaviour of polycarbonate was reported to highly influence curl [36], and thus was taken into account in the stress model. The (dead) weight of each layer forming the part was also assumed to oppose the development of curl, and its effect was therefore considered. However, for the effect of dead weight to be allowed for in the stress analysis, the density of each layer forming the part had to be defined (Weight/ area = density × gravitational acceleration × thickness of layer). Finally, similar to previous curl models [35,36], friction between the bottom surface of the part and the powder bed underneath was also taken into account, which required definition of the coefficient of friction.

Most physical properties of SLS fabricated parts differ from those of zero porosity solids made of the same material. Physical properties of the former are mainly influenced by the amount of fusion (sintering) that occurs between contacting particles during fabrication. The rate of sintering, however, increases with the rise in local temperatures between these particles and vice versa [24]. These temperatures are dependent on the energy absorbed by a surface during sintering, which is mainly determined by the energy density used in fabrication (see Section 2.3.4). An increase in the energy density generally causes the physical density of the fabricated part to increase (see Figure 2.41). In addition, previous experimental measurements found that the higher the physical density of an SLS produced polycarbonate part the higher was its elastic modulus and vice versa [41]. The increase in sintering was also reported to increase dimensional inaccuracies (shrinkage) in fabricated parts [1], i.e. the coefficient of thermal expansion is expected to increase with the amount of fusion between contacting particles. As physical properties are dependent on temperature histories experienced in fabricated layers, these properties are assumed to vary with the depth from the sintered surface (see Figures 4.37 and 4.38). Thus, the elastic modulus, expansion coefficient and density are expected to be higher in regions close to the sintered surface and reduce the further away the region is from that surface. The variation in density with depth from the sintered surface, described earlier, was also predicted analytically in a previous study [34]. In the following, the criteria supported in defining each of the material properties used in the stress model are described.

- **Coefficient of Thermal Expansion**

The inclusion of the expansion coefficient allows thermal strains and resulting stresses that may arise due to changes in temperature to be calculated. In a previous study, significant thermal stresses were reported to develop in a polycarbonate melt at the instant its temperature starts to reduce below 190°C [34]. It was therefore assumed that thermal stresses above that temperature are equal to zero. That condition can be implemented in the stress model by defining the expansion coefficient above 190°C to be equal to zero, or (and) specifying the elastic modulus above that temperature to be equal to zero (see Equation 2-21). However, in the latter, the material cannot support its weight and the weight of subsequently added layers, which leads to numerical solution problems presented in the form of infinite displacements. Thus, the former approach was the one implemented in the stress model.

In the stress model, an element was assumed to be in a melt state provided its average nodal temperatures exceeded 190°C during simulation. Temperature histories predicted by the heat transfer model showed elements representing part layers from two to ten to have satisfied that condition, following the application of heat flux on the top surface of the layer. That was also seen in regions of the first layer represented by elements flanked by nodes located at the top surface of the layer and those located at a depth of 0.125mm from that surface. In the model, all of these elements were assigned an expansion coefficient equal to zero at temperatures equal and above 190°C. Below that temperature, these elements were given a constant expansion coefficient equal to 2×10^{-6} C^{-1}, as assumed by Dalgarno et al. [35].

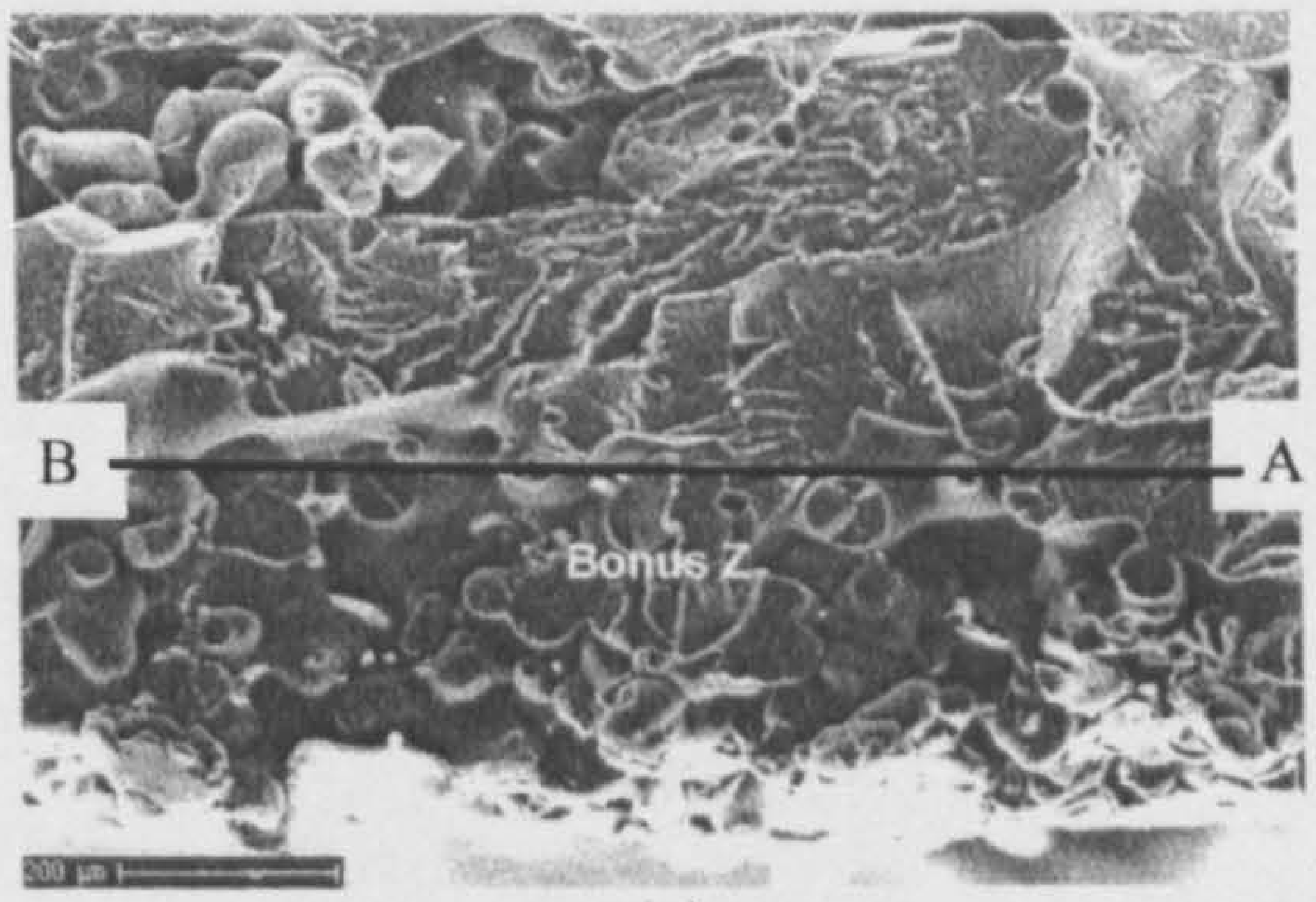

Figure 4.41 Fractured cross-section of the first layer of an SLS fabricated part produced under energy density of 0.094 J/mm^2. From [52].

However, the remaining elements in the first layer did not exceed an average nodal temperature of 190°C through the entire period simulated in the heat transfer model. These elements are flanked by nodes located at the bottom surface of the first layer and those located at a depth of 0.125mm from the top surface of the layer. It is worth mentioning that the intended thickness during fabrication of the first layer was 0.125mm [35], and thus the additional material represented by these elements is in fact bonus Z (see Section 2.2.5.4.1). As nodes in the bonus Z region did not display a considerable rise in temperature compared to those in other regions of the build, bonus Z is believed to be the least sintered region of the build. This phenomenon was observed in a previous study [52] through a microscopic image of a fractured section of the first layer of a polycarbonate part, fabricated under an energy density equal to 0.094 J/mm^2 (see Figure 4.41). In this figure, the line connecting points A and B represents the section of the intended bottom surface of the first layer. Above that surface, the layer shows a high degree of coalescence between the polycarbonate powder particles. The additional material sintered beyond that surface is the bonus Z region. In that region, powder particles are slightly fused at the points of contact, and individual particles can be easily noticed. Because of the low degree of fusion between particles in the bonus Z region, the expansion coefficient of this region is expected to be extremely small compared to that in other regions of the build. Hence, in the present work, due to the lack of the expansion coefficient of the bonus Z region, elements representing that region (identified from predicted nodal temperature histories) were given an expansion coefficient equal to zero over the entire temperature range used in the stress analysis.

- **Density**

The density is defined for the effect of the weight of part layers to be considered in the stress analysis. The weight of a layer remains unchanged regardless of transformations in structure that occur during fabrication, provided that no additional material is bonded to the layer through growth and bonus Z. As the geometry of part layers are defined in the model based on dimensional measurements performed on fabricated layers, the density of each element representing the part was given the density reported for the fabricated part, which is equal to 700kg/m^3 [35]. However, it must be emphasised that defining the density of all elements representing the ten-layer part to be identical is an approximation. That is because it considers a region of certain dimensions in a highly sintered layer to have the same weight of a region with the same dimensions in bonus Z.

- **Mechanical Properties**

Several models were previously developed to explain the mechanical behaviour of viscoelastic polymers. These models consisted basically of a spring to describe the elastic (time-independent) response of the polymer and a dashpot to describe its viscous (time-dependent) response (see Figure 2.26). In the following, the methods employed in defining these responses in the stress model are described.

- **Definition of the Elastic (Time-Independent) response**

Prediction of the elastic (time-independent) response of a polymer requires the knowledge of its instantaneous (immediate) modulus (see Section 2.3.1.2). The instantaneous modulus, however, is understood to be highly influenced by temperature changes, especially in the glass transition region of the polymer (see Figure 2.24), which is expected to be for polycarbonate in the vicinity of 150°C. In a previous study [36], tensile test measurements performed at 100°C on an SLS fabricated polycarbonate specimen gave a value of the instantaneous modulus equal to 319.4MPa. Due to the absence of more complete elastic modulus data, the instantaneous modulus of all elements representing the part was assigned a value of 319.4MPa over the entire temperature range used in the stress analysis. Additionally, based on Dalgarno et al. [35], all elements representing the part were given a constant Poisson's ratio equal to 0.4.

- Time-Dependent Response

The time-dependent response of an SLS fabricated polycarbonate part was examined in a previous study [36] through a stress relaxation test performed at 100°C. Variation in the modulus with the relaxation time, reported in that study, are presented in Table 2-2. In the model, the time-dependent response is specified by defining the values of $g_R(t)$ against the relaxation time (t) in tabulated form. Corresponding values reported in Table 2-2 were assigned to all elements representing the part in the stress analysis mesh. The temperature at which these stress relaxation data apply was also specified in the model (100°C).

The time-dependent response of polycarbonate at temperatures other than 100°C was additionally considered in the stress analysis. The model uses the time-dependent response given at 100°C to estimate that at other temperatures by applying the WLF approximation (see Equation 2-3). Thus, values of the WLF constants C_1 and C_2 had to be provided. The constants C_1 and C_2 were reported for an SLS fabricated part to be equal to 2.778 and 7.389 respectively, estimated with the reference temperature T_s being 100°C [36] (see Equation 2-3). These properties were defined for all elements representing the part in the stress analysis mesh. The method of defining the time-dependent response and the use of the WLF approximation in the stress model is further explained in Section (6.2.2.2).

▪ Friction Coefficient

Finally, based on the previous study by Dalgarno et al. [35], the coefficient of friction between the edges of elements together representing the bottom surface of the part and the rigid surface (Figure 4.40) was given a value of 1.0.

4.7.3 Boundary Conditions and Constraints

In SLS fabrication, the powder bed and sintered part are supported by the part piston. Prior to spreading powder onto the part bed, the piston lowers by a distance equal to the intended thickness of the added layer causing the entire structures of the powder bed and part to lower by that same distance. Lowering of the piston, therefore, is not expected to cause any relative motions between layers forming the part or between these layers and the powder bed. As a consequence, lowering of the stress analysis mesh during simulation of SLS part build was not performed. Instead, the rigid surface supporting the ten-layer part was considered to remain fixed in the (vertical) z-direction (Figure 4.40) through the entire stress analysis. That was simulated by applying a boundary condition on the "rigid body reference node" preventing translational motion of the node in the z direction. However, the use of this boundary condition assumed that the entire surface of the powder bed (represented by a rigid surface) does not displace downwards due to the weight of subsequent layers added to form the part. In addition, it also meant that the surface of the bed does not displace upwards due to powder bed particles changing in shape from oblate to spherical which may occur as a result of increasing temperature (see Section 2.3.6).

In SLS fabrication, the powder bed is contained in the (fixed) part cylinder. Thus, global translational motion in the x direction and rotation of the bed about the y-axis do not occur. That was simulated in the model by applying a zero translational boundary condition in the x direction on the "rigid body reference node" and zero rotational motion applied on that node about the y and z axes of its local co-ordinate.

The simplicity of representing half of the model due to mirror symmetry requires the application of boundary conditions on the nodes located along the axis of symmetry. The boundary conditions applied constrained motions of these nodes in the x direction and prevented rotation of each of the nodes about the y-axis of its local co-ordinate.

In SLS fabrication, deformation of a recently added layer is expected to have an insignificant effect on curling of the build underneath provided that the added layer is in powder form or the layer is sintered but is at temperatures equal or above

190°C. Consequently, SLS stages of powder addition and laser sintering were not simulated. In the model, attempts were made to activate a layer of elements, representing a recently sintered layer, just before its temperature (as predicted by the thermal analysis) starts to reduce below 190°C, i.e. in a stress-free state. Defining the coefficient of thermal expansion as zero at temperatures equal and above 190°C ensures that no thermal stresses generate at these temperatures. Nevertheless, as the elastic modulus was not defined equal to zero at these temperatures, the (ordinary) method of activating elements was bound to generate stresses in these elements. These stresses are expected to effect curl results predicted by the stress model. In the following discussion, a simple example illustrating the (ordinary) method of element activation is presented. The measures undertaken to activate elements in an unstressed condition are then described.

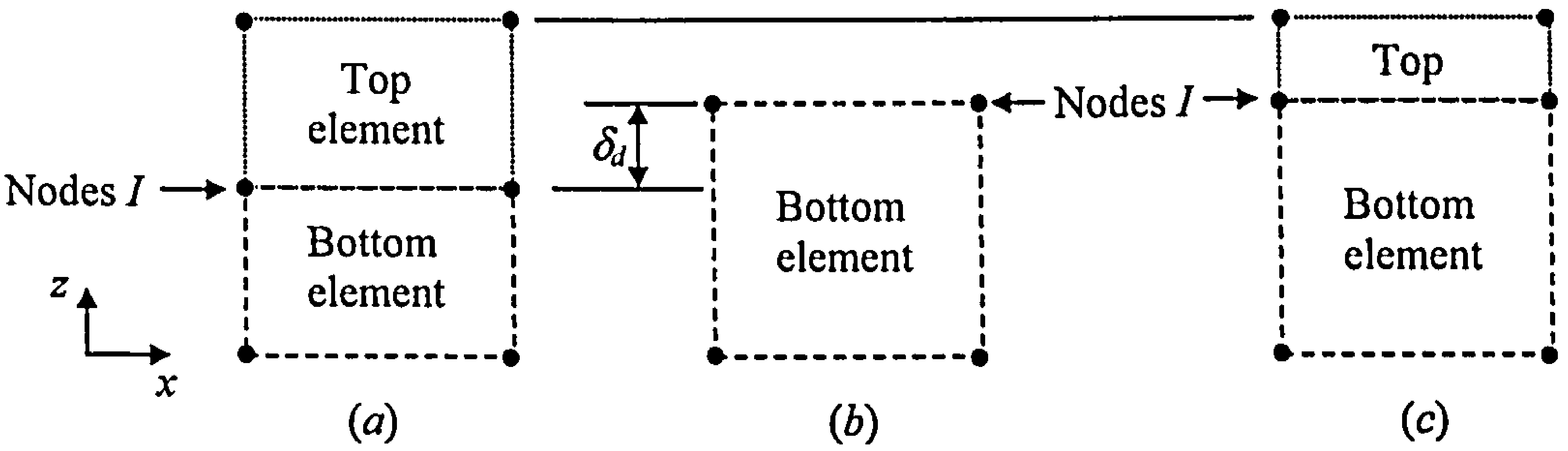

Figure 4.42 A schematic diagram illustrating the (ordinary) method of element activation. (a) initial stress analysis mesh defined prior to analysis. (b) First step of analysis: top element deactivated and bottom element thermally loaded (c) Second step of analysis: top element activated in a stressed and strained condition.

The model analysed in the example is illustrated in Figure 4.42*a*: an element (top element) positioned on top of another element (bottom element). Both elements are connected to common nodes at the interface, termed nodes (*I*). In the first step of the analysis, the top element is (deactivated) removed from the mesh. The bottom element is then thermally loaded causing the element to strain. At the end of the step, that loading is assumed to have displaced nodes (*I*) in the +z direction by a distance equal to δ_d (see Figure 4.42*b*). In the second step of the analysis, the top element is activated. However, due to the common nodes (*I*) displacing in the previous step, the top element would have been strained and stressed once the element is activated (Figure 4.42*c*).

The method of solving such a problem was described by ABAQUS [51]. This method requires definition of separate nodes along the interface where new elements are to be activated during simulation. Thus, in implementing this method, nodes (*I*) located along the interface are only connected to the bottom element. A new set of nodes (*J*) are created at the same locations of nodes (*I*), but are only connected to the top element (see Figure 4.43*a*). Additional nodes (*K*) that are not associated with any element are also defined. These nodes are at a coincident location with nodes (*I*) and (*J*), as illustrated in Figure 4.43*a*. The translational motion components and rotations of these nodes (about the *y*-axis of the local co-ordinate of each of the nodes) are related as follows,

$$u_x^J = u_x^I - u_x^k \qquad 4\text{-}29$$

$$u_z^J = u_z^I - u_z^k \qquad 4\text{-}30$$

$$u_\theta^J = u_\theta^I - u_\theta^k \qquad 4\text{-}31$$

where u_x^J, u_x^I, u_x^K are the translational motions in the x direction of nodes *J*, *I* and *K* respectively. In addition, u_z^J, u_z^I, u_z^K are the translational motions in the z directions of nodes *J*, *I* and *K* respectively, and u_θ^J, u_θ^I, u_θ^K are rotations about the *y*-axis of the local co-ordinates of each of the nodes *J*, *I* and *K* respectively. These equations are applied in all steps defining the analysis. For simplicity, the previous example only assumed motions of nodes to occur in the *z* direction (no rotations were considered). Thus, only Equation 4-30 is referred to in the following description of the method used in activating the top element in an unstressed state.

In the first step of the (new) analysis, a boundary condition is applied to constrain all displacement components and rotations of nodes *J* to zero, i.e. $u_x^J = 0$, $u_z^J = 0$ and $u_\theta^J = 0$. Thus, Equation 4-30 can be expressed during this step as $u_z^I = u_z^k$. In this step, the top element is (deactivated) removed from the mesh. The bottom element is then thermally loaded resulting in the element to strain. At the end of the step, nodes *I* and *K* would have undergone a displacement in the +*z* equal to δ_d (see Figure 4.43*b*), i.e. at the end of this step $u_z^I = u_z^k = \delta_d$.

In the second step of the analysis, a boundary condition is applied to fix all displacement and rotational components of nodes K to the values calculated at the end of the first step ($u_z^k = \delta_d$, $u_x^k = 0$ and $u_\theta^k = 0$) through the rest of the simulation. In addition, the boundary conditions previously applied to fix all displacement components and rotations of nodes J to zero are removed in this step. Thus, Equation 4-30 is expressed through the second and following steps of the analysis as,

$$u_z^J = u_z^I - u_z^k = u_z^I - \delta_d \tag{4-32}$$

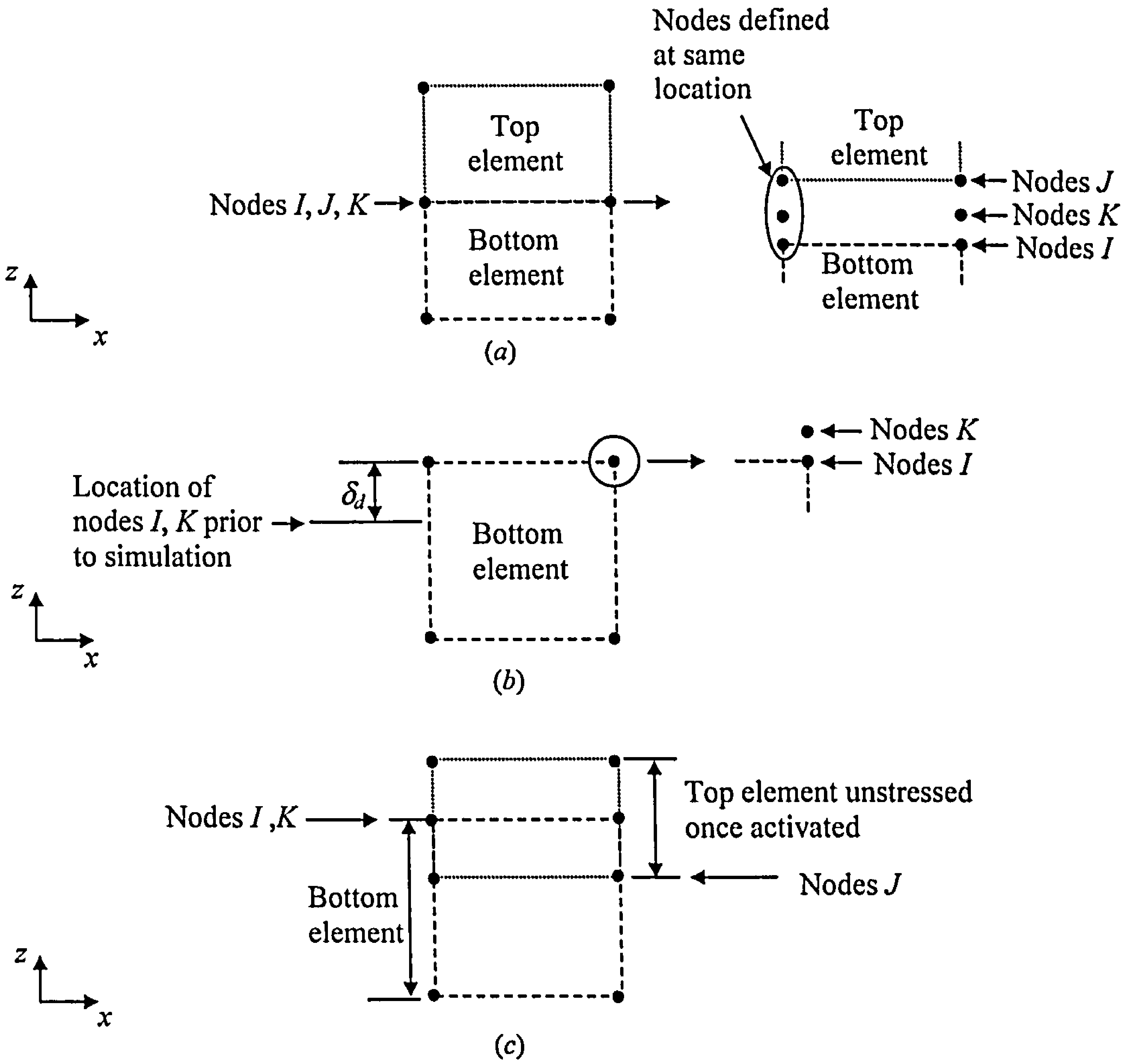

Figure 4.43 Schematic diagram illustrating the method of activating the top element in an unstressed condition. (*a*) Initial stress analysis mesh defined prior to analysis: Nodes J are located at the interface and connected to the top element, nodes I are at the same location of nodes J but connected to the bottom element, nodes K are at same location of nodes I and J but not connected to any element. (*b*) First step of analysis: top element deactivated and bottom layer thermally loaded, $u_z^J = 0$, $u_z^I = u_z^k$ (*c*) Second step: top element activated in an unstressed condition $u_z^J = u_z^I - \delta$

At the instant of activating the top element in the second step $u_z^I = \delta_d$. Thus, displacements of nodes (J) in the z direction (u_z^J) at the instant of activation are equal to zero (see Equation 4-32). Therefore, the top element using this approach is activated in an unstressed condition, as illustrated in Figure 4.43*c*. However, it must be emphasised that the top element is activated in its originally defined configuration (undistorted). Therefore, the assumption considered in using this method is that deformations occurring to the bottom element prior to activating the top element are fairly small.

The above-mentioned method was implemented in the stress model. Consequently, separate nodes were defined along the interfaces between elements together representing the first and second layers of the part, second and third layers and so forth. However, the use of the sequentially coupled thermal-stress analysis technique in this work necessitates that nodes connected to elements in the stress analysis mesh have temperature histories predicted by the heat transfer analysis. Thus, the additional nodes generated along the interfaces and connected to elements in the stress model required the heat transfer analysis (described earlier) to be slightly modified. Figure 4.44*a* shows schematically a number of nodes, generated in the stress analysis mesh, along the interface between elements representing the first and second layers of the part. Nodes (I_s), numbered from 1 to 73, are connected to the edges of elements together representing the top surface of the first layer. Nodes (J_s) numbered from 147 to 219 are defined at the same locations of nodes I_s but are connected to edges of elements together representing the bottom surface of the second layer. Nodes (K_s) numbered from 74 to 146, however, were chosen to be at a coincident location with nodes I_s and J_s but are not associated with any elements. Equations 4-29 to 4-31 were defined in the stress analysis to relate motions and rotations of nodes I_s, J_s and K_s through the entire period of simulation. As nodes I_s and J_s are connected to elements in the stress analysis mesh, temperature histories of these nodes had to be predicted by the heat transfer analysis. The second layer when activated in the stress analysis symbolises the layer in its sintered form; bonding between the first and second layer is assumed to have occurred. Consequently, temperatures at the bottom surface of the second layer and those at the top surface of the first layer are assumed identical, i.e. temperature histories of nodes (I_s) are equal to those of nodes (J_s). To achieve that in the output of the heat transfer analysis, elements representing the first and second layers in the heat transfer analysis mesh were only connected at the interface to one set of common nodes (I_h). These nodes had the same node numbering of nodes I_s (see Figure 4.44). Additional nodes J_h were defined along the interface between the two layers in the heat transfer analysis mesh, but were not associated with any element. These nodes had identical numbering to nodes J_s, which were created in the stress analysis mesh (see Figure 4.44). Equations were then defined in the heat transfer analysis matching the temperature histories of nodes (I_h) with those of nodes (J_h) through the entire period of simulation. Therefore, in the outcome of the thermal analysis, the temperature history of node number 147 is identical to that of node number 1, and that of node number 148 is identical to the temperature history of node number 2 and so forth (Figure 4.44*b*). In this condition, temperature histories of the nodes connected to elements in the stress analysis mesh (such as nodes numbered from 1 to 73 and nodes numbered from 147 to 219) are already predicted by the heat transfer analysis. That procedure was implemented along the interfaces between all layers of elements representing layers forming the part in both the heat and stress models.

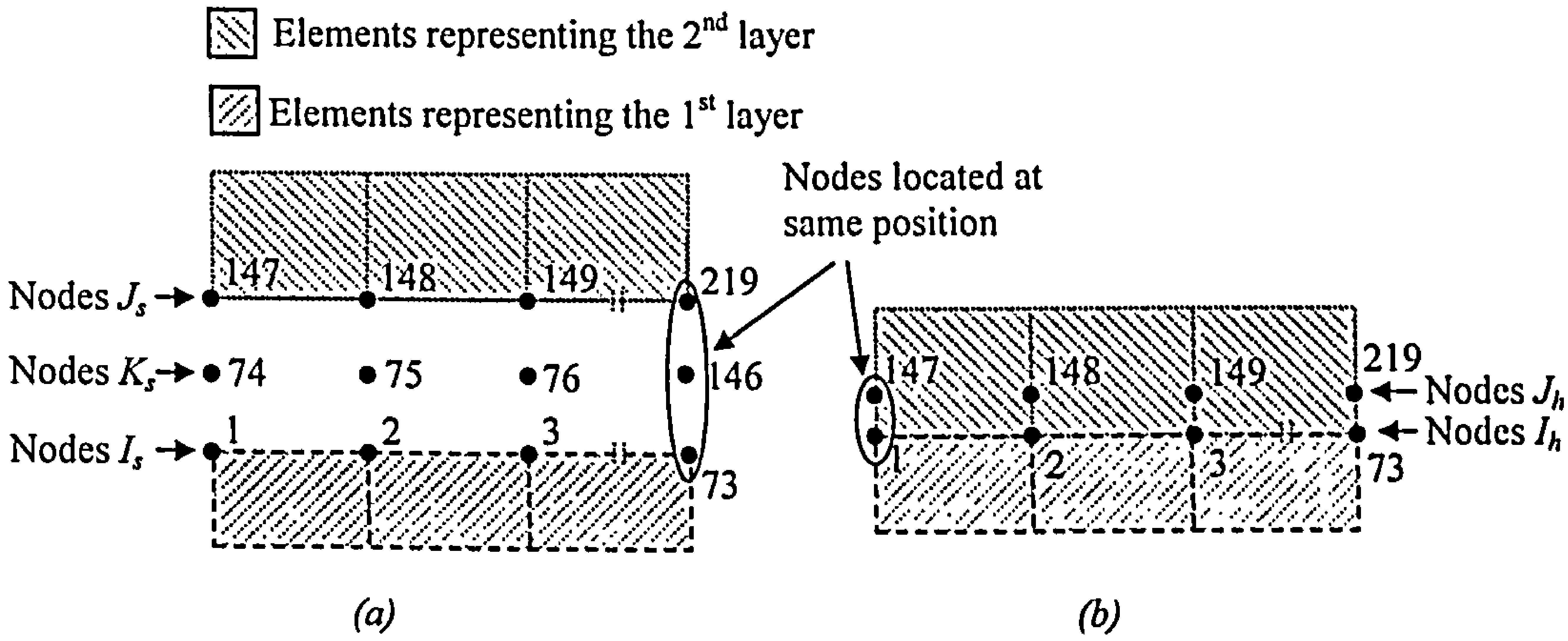

Figure 4.44 Schematic diagram illustrating modifications required in the heat transfer model due to the extra nodes added along the interface between elements representing the first and second layers of the part in the stress analysis (*a*) Stress analysis mesh (*b*) Corresponding heat transfer analysis mesh.

In the stress model, the initial nodal temperature of each element expected to undergo thermal deformation has to be predefined. These initial temperatures represent the nodal temperature of the element at the instant of activation. Deviation in the temperature of these nodes from the initial nodal temperatures causes thermal strains and stresses to generate, provided that the coefficient of thermal expansion in the range of temperature change is not equal to zero. Elements in the first layer, flanked by nodes located at the top surface of the layer and those located at a depth of 0.125mm from that surface, are the only elements in the layer considered to undergo thermal strains. Reading of temperature histories of these nodes starts at the instant nodal temperatures, as predicted by the heat transfer analysis, are about to reduce below 190°C. The initial temperature of these nodes was set equal to 190°C. In this condition, reduction in the temperature of these nodes causes shrinkage in the elements to occur. Nevertheless, an increase in temperatures above 190°C during simulation does not generate any thermal strains as the expansion coefficient at these temperatures is defined equal to zero.

The initial nodal temperatures of elements representing the second layer were also defined. These nodes are those connected to the edges of elements representing the bottom surface of the second layer (nodes J_s in Figure 4.44*a*), nodes located at a depth of 0.125mm from the top surface of the layer and those located at its top surface. The assumption in this version of the stress model was that thermal stresses and strains in an element are zero provided that average nodal temperatures of an element are above or equal to 190°C. However, temperatures predicted at the bottom surface of the second layer surface reached a maximum of 189°C following its sintering. At the instant that temperature was achieved, sintering of the entire second layer is assumed to have taken place. Thus, temperature histories were read from that instant. To ensure that thermal strain and stresses are zero immediately prior to reading, the bottom surface of the second layer was assigned an initial temperature equal to 189°C. At that instant, the temperature of nodes located 0.125mm from the top surface were 200.9°C, whereas that at the top surface of the layer 206.1°C. These were taken as the initial temperature of these nodes. That ensured that the layer upon activation was in a stress and strain free conditions, and that the average nodal temperatures exceed 190°C. Remaining nodal temperatures of elements representing layers from three to ten exceeded 190°C, and thus the initial temperature of these nodes was set equal to 190°C.

4.7.4 Sequence of Analysis Defined in the Stress Model

The aim of the stress model is to predict deformations of the ten-layer parts during SLS fabrication. Similar to the heat transfer model, the complete load history of the stress analysis is divided into a number of steps. Each step is a time period in which the response of the model to a particular set of loads and boundary conditions is calculated. Thus, loads and boundary conditions have to be defined in each step of the analysis. The analysis procedure must also be specified. That was performed in each step using the (*VISCO*) option in ABAQUS. The use of this particular option in all steps of the model indicated the response of the material to be examined is time-dependent (viscoelastic) through the entire period of simulation. In this section, selected steps defined in the stress model are described.

▪ First Step Defined in the Stress Model

The first step of the analysis simulated thermal and mechanical effects expected to occur following sintering of the first layer and prior to the addition of the second layer in powder form. Thus, the part build in that stage of SLS fabrication was only composed of the first layer. That was simulated by deactivating the predefined elements together representing part layers from two to ten. Thus, in this step, the only active elements in the stress analysis mesh were those representing the rigid surface and the first layer of the part. In the following, boundary conditions and loadings defined in this step are presented.

- Boundary Conditions Applied in the First Step

In this step of the analysis, motions and rotations of nodes located along the interface between elements representing the first and second layers of the part were related using Equations 4-29 to 4-31, as described in Section 4.7.3. Implementation of these equations required constraining to zero all the degrees of freedom of nodes located along the interface and connected to the edges of elements representing the bottom surface of the second layer (nodes J_s in Figure 4.44*a*). However, as elements representing the second layer are deactivated in this step, it may be assumed that all motions and rotations of nodes connected to these elements are set by default to zero. Then, in this condition, constraining motions and rotations of the nodes located along the interface and connected to the deactivated second layer is not expected to be necessary. It must be emphasised that all nodes connected to inactive elements in an

ABAQUS simulation are ignored unless constraints (such as displacement boundary conditions) are applied on these nodes. Hence, with no boundary conditions being applied on nodes located along the bottom surface of the inactive second layer, the use of Equations 4-29 to 4-31 in the analysis resulted in solver problem causing the simulation to stop.

Additional boundary conditions were applied to enforce mirror symmetry of the first layer, on nodes located along the axis of symmetry of the layer. Furthermore, all degrees of freedom of the "rigid body reference node" were constrained to zero, as reported in Section 4.7.3.

- Loading Applied in the First Step

The loads applied in this step are gravitational loads specified on each element representing the first layer and thermal loads. The latter are nodal temperature histories predicted previously by the heat transfer analysis. For specific nodal temperature histories to be used in the stress analysis, the instants in the heat transfer analysis output referring to the start and end of the temperature histories to be read by must be defined. In the first active layer, the only elements given an expansion coefficient other than zero were those flanked by nodes located at the top surface of the layer and nodes located at a depth of 0.125mm from that surface. Thus, in defining the time range of temperature histories to read into the stress analysis, the temperature histories of these nodes were the only monitored. In this step, reading of nodal temperatures started at the instant 0.5 seconds (from the start of the thermal analysis) and ended at the instant 5.6 seconds (see Figure 4.45). The former denotes the instant in the heat transfer analysis at which the temperature of nodes located at a depth of 0.125mm from the top surface of the first layer was approximately 190°C. The latter, however, represents the instant at which the second layer was activated in the heat transfer analysis. The period specified for the first step of the stress analysis was equal to the period that nodal temperatures were read, i.e. the difference between these two instants 0.5 seconds and 5.6 seconds, which is equal to 5.1 seconds (Figure 4.45).

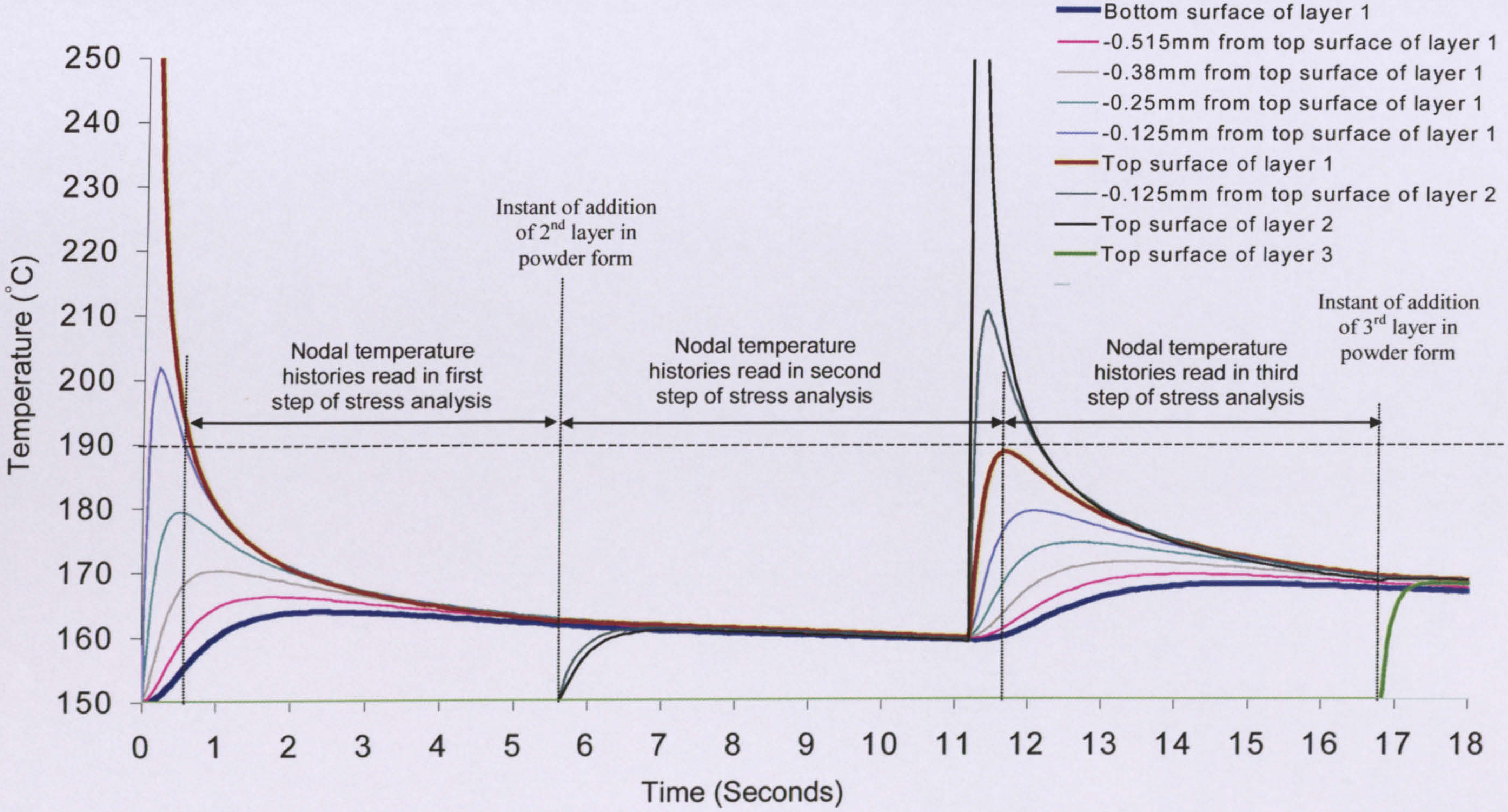

Figure 4.45 Illustration of the nodal temperature histories used as thermal loading in the first three steps of the first version of the stress analysis

Second Step Defined in the Stress Model

The second step simulated thermal and mechanical effects expected to occur in two SLS fabrication stages; addition of the second layer in powder form and sintering of the second layer, whilst temperatures in the layer are above 190°C. In both of these stages, dimensional changes in the second layer (if they occur) are expected to have an insignificant influence on curling of the first layer. Therefore, in this step of the analysis, elements representing the second layer in the (original) stress analysis mesh were not activated. Thus, the active elements in the stress analysis mesh remained those representing the rigid surface and the first layer of the part. In addition, boundary conditions previously applied in the first step remained applied in the second step.

- Loading Applied in the Second Step

The gravitational loads that simulated the weight of the first layer in the first step were kept applied in this step. The weight of the second layer, expected to oppose the development of curl, was additionally allowed for in this step of the analysis. As the second layer is not activated, its weight was simulated by a uniform load simultaneously applied over the edges of elements together representing the top surface of the first layer. To include that effect in the analysis, ABAQUS requires the "pressure" representing the weight per unit area, and the edge of the element on which pressure is applied. The weight is estimated analytically based on the undistorted shape of the second layer as predefined in the stress analysis mesh. The weight (wt) is calculated in terms of the density of the second layer ρ, its volume V, and the gravitational acceleration g as,

$$wt = \rho \times V \times g \qquad \text{4-33}$$

Dividing both sides of the equation by the area gives the pressure in terms of the thickness of the second layer (h_l) as,

$$P = \rho \times t_l \times g \qquad \text{4-34}$$

The density ρ of the second layer is predefined in the stress model as equal to 700kg/m^3, the predefined thickness of the layer is 0.25mm and the gravitational acceleration is 9.81m/s^2. Thus, the pressure using Equation 4-34 is equal to 1.7168N/m^2. In a two dimensional model, the in-plane thickness is assumed to be equal to unity [43], and the value calculated for the pressure (*P*) is therefore considered in the analysis as load per unit length (1.7168N/m).

In this step of the analysis, temperature histories read from the output of the heat transfer analysis were from the instant 5.6 seconds (estimated from the start of the thermal analysis) to the instant 11.7 seconds. The former denotes the instant of the heat transfer analysis at which elements representing the second layer were activated. The latter, however, signifies the instant at which nodes at the bottom surface of the second layer had achieved a maximum temperature (188.7°C) immediately following the application of heat flux on the top surface of the second layer. The second layer at that instant (11.7 seconds) had average nodal temperatures exceeding 190°C, and thus the element was assumed in an unstressed condition. The period specified for the second step of the stress analysis was equal to the period that nodal temperatures were read in that step, i.e. the difference between these two instants 5.6 seconds and 11.7 seconds, which is equal to 6.1 seconds (Figure 4.45).

▪ Third Step Defined in the Stress Model

The third step of the stress analysis simulated thermal and mechanical effects occurring following sintering of the second layer (as temperatures in the layer reduce below 190°C) and prior to the addition of the third layer in powder form. As thermal stresses and strains arising in the second layer at temperatures below 190°C are expected to influence curl of the build, elements representing the second layer are activated in this step. Thus, the elements activate in this step are those representing the rigid surface, first and second layers of the part.

- Boundary Conditions Applied in the Third Step

In this step, Equations 4-29 to 4-31 are applied to relate motions and rotations of all nodes located along the interface between the bottom surface of the second layer and the top surface of the first layer. These equations are also applied in this step on nodes located along the interface between the top surface of the second layer and the bottom surface of the third layer (see Section 4.7.3). Thus, proper implementation of these equations required the following boundary condition to be applied:

- Fixing all displacement components and rotations of nodes located along the interface, but not connected to any element (nodes K_s in Figure 4.44*a*) to the values calculated at the end of the previous (second) step.
- Removing the boundary conditions previously applied in the first step constraining to zero all the degrees of freedom of nodes connected to the edges of elements representing the bottom surface of the second layer (nodes J_s in Figure 4.44*a*).
- Constraining to zero all degrees of freedom of nodes connected to the edges of elements together representing the bottom surface of the third layer.

Due to the removal of boundary conditions in this step, boundary conditions previously applied in the first step on the “rigid body reference node” and on nodes located along the axis of symmetry had to be redefined. Thus, all degrees of freedom of the “rigid body reference node” were constrained to zero. Furthermore, mirror symmetrical boundary conditions are applied on nodes located along the axis of symmetry in the first and second layers.

- Loading Applied in the Third Step

The pressure previously applied on the top surface of the first layer to represent the weight of the second layer in the previous step was removed. Instead, gravitational loads were specified on each element representing the second layer. The gravitational load specified previously on each element of the first layer was also allowed for in this step.

In this step of the analysis, temperature histories read from the output of the heat transfer analysis were from the instant 11.7 seconds (estimated from the start of the thermal analysis) to the instant 16.9 seconds. The former represented the instant at which thermal stresses were expected to develop in the second layer. The latter represented the instant at which the third layer (in powder form) was activated in the heat transfer analysis. The period of this step is the difference between these two instants, which is equal to 5.2 seconds (Figure 4.45).

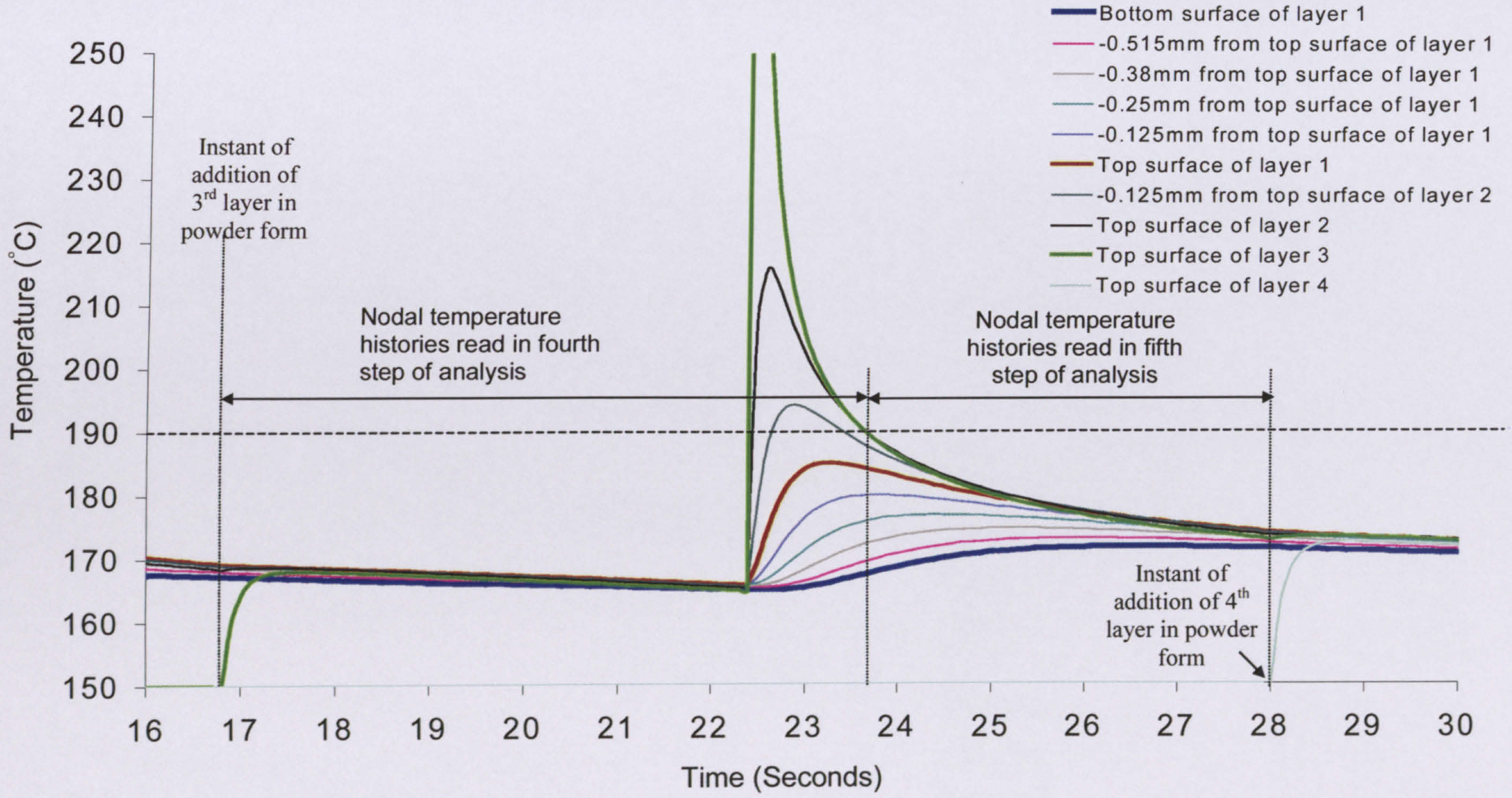

Figure 4.46 Nodal temperature histories used as thermal loading in the fourth and fifth steps of the first version of the stress analysis

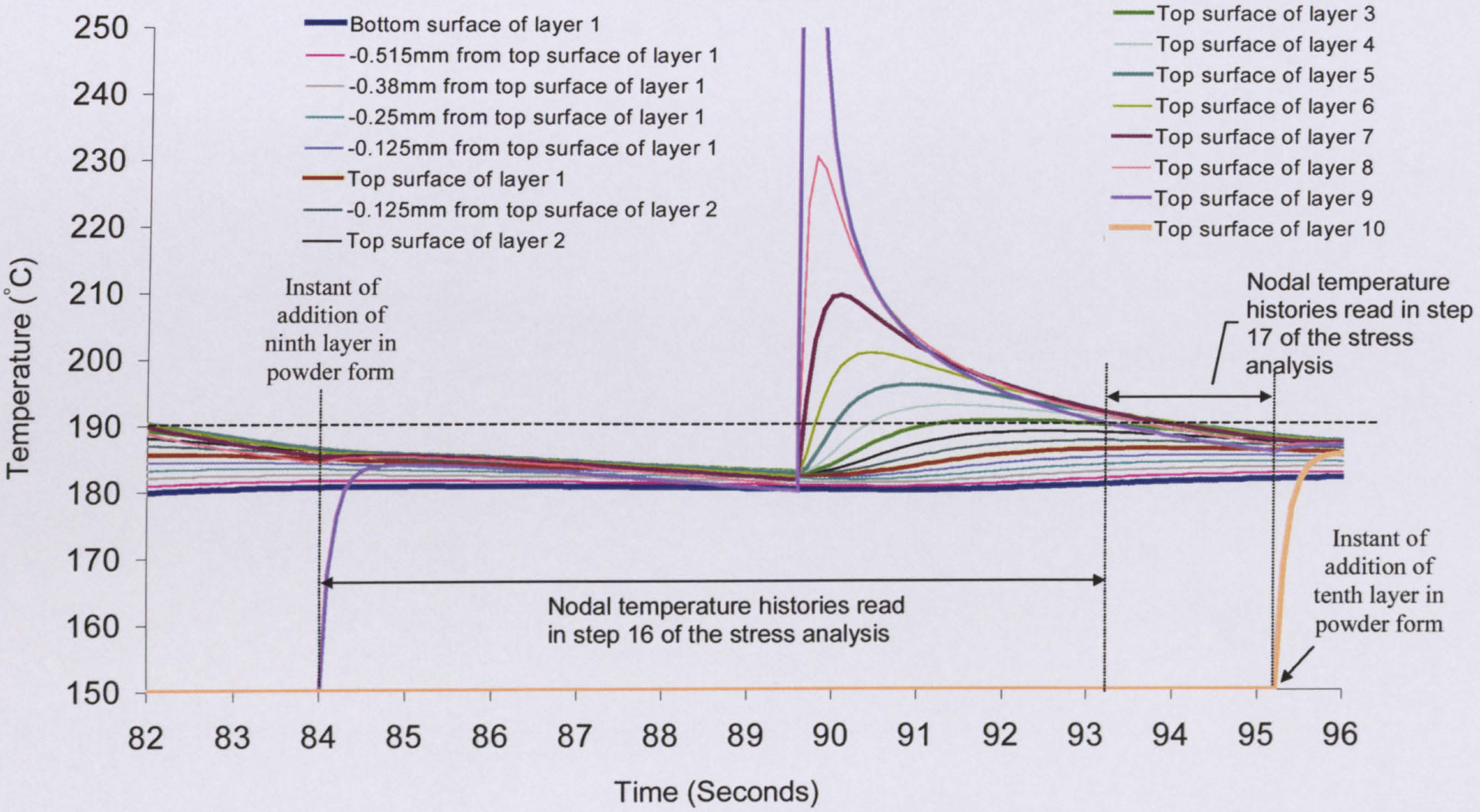

Figure 4.47 Nodal temperature histories used as thermal loading in steps 16 and 17 of the first version of the stress analysis

- **Fourth Step Defined in the Stress Model**

The fourth step simulated thermal and mechanical effects expected to occur in two SLS stages, addition of the third layer in powder form and sintering of the third layer whilst temperatures in the layer are above 190°C. The definition of this step is quite similar to that of the second step. In this step, elements representing the third layer were not activated, and the active elements were therefore those representing the rigid surface, first and second layers of the part. Additionally, boundary conditions applied in the previous step remained applied in this step.

Gravitational loads were applied on each element in the mesh representing first and second layers of the part. The weight of the third layer was simulated by a uniform load simultaneously applied over the edges of elements together representing the top surface of the second layer. That was implemented in the model using the method mentioned in description of the second step. Thermal histories read from the output of the heat transfer analysis were from the instant 16.8 seconds (estimated from the start of the thermal analysis) to the instant 23.6 seconds. The former signifies the instant of the heat transfer analysis at which elements representing the third layer were activated. The latter, however, denotes the instant at which nodes at the top and bottom surfaces of the third layer were at 190°C, following the application of heat flux on the top surface of the layer. Thus, the time period of this step is the difference between the two instants 16.8 seconds and 23.6 seconds, which is equal to 6.8 seconds (Figure 4.46).

The main concepts used in defining steps three and four, described above, were also implemented in the subsequent steps defined to simulate thermal and mechanical effects occurring in fabrication of the layers from three to ten. The final step of the analysis (step 19) simulated thermal and mechanical effects expected to occur following sintering of the tenth layer. In the step, elements representing the tenth layer were activated. Boundary conditions applied on nodes located along the interface between the ninth and tenth layer are similar to those described in the second step. Nodal temperature histories read in the step were those from the instant 104.6 seconds to 1300.8 seconds. The former represents the instant in the heat transfer analysis at which the temperature at the top surface of the tenth layer is

190°C (see Figure 4.38), whereas the latter signifies the instant at which the heat transfer analysis stopped. The time period of this step is the difference between these two instants which is equal to 1196.2 seconds.

4.7.5 Results

To ensure that results predicted by the stress analysis are numerically accurate, a mesh refinement study was performed. The method used in mesh refinement is the reducible net, described in Section 4.6.5. However, refinement of the stress analysis mesh requires the mesh density of the corresponding heat transfer analysis to be also changed, so that densities of the mesh representing the part in both the heat and stress models are identical. Emphasis was also given to ensure that the aspect ratio of elements in the heat transfer and stress models did not exceed a value of 5.

Mesh	Mesh Size of Sintered Part (Depth* x Length*)		
	1st layer	2nd layer	Layers from three to ten
Normal	5x72	2x72	1x72
Fine	5x144	2x144	1x144
Very Fine	10x144	4x144	2x144

Depth*: Number of elements along *z* direction.
Length*: Number of elements along *x* direction. (Directions shown in Figure 4.40)

Table 4-7 Description of meshes generated for the mesh convergence study performed on the first version of the stress analysis.

The stress analyses meshes used in examining solution convergence are described in Table 4-7. The sequence of analyses implemented in all stress models was that described Section 4.7.4. The simulations were initially performed using (first-order) four-noded plane strain elements, denoted in ABAQUS (CPE4). However, these elements were reported by ABAQUS [55] to underpredict deflections in problems involving significant bending due to the inability of the edges of a single element to curve. To examine its significance on curl results, deflections predicted using a specific mesh density with (CPE4) elements were compared with those predicted using the same mesh density but with (higher order) 8-noded plane strain elements, denoted in ABAQUS (CPE8). The use of 8-noded elements was reported by ABAQUS [55] to produce better results in simulations involving considerable amounts of bending due to the ability of the edges of a single 8-noded element to curve. The performance of 4-noded plane strain incompatible elements, denoted in ABAQUS (CPE4I), was additionally investigated. These were reported by ABAQUS [55] to have additional degrees of freedom introduced into the first-order element, which allow these elements to produce results in bending problems that are comparable to 8-noded elements, but at a significantly lower computation cost.

To reduce solution cost, a stress analysis performed using an 8-noded element mesh had a corresponding heat transfer analysis mesh, with the same mesh density representing the part, using 4-noded heat transfer elements (DC2D4), not 8-noded. That was facilitated by the (*MIDSIDE*) option in ABAQUS. The use of this option in the stress analysis allows midside nodal temperatures in the 8-noded element to be linearly interpolated from corner nodal temperatures previously predicted by the (4-noded element) heat transfer analysis (see Figure 4.48). Figure 4.48*a* shows a schematic representation of a 4-noded element used in the heat transfer analysis mesh, whereas the corresponding 8-noded element in the stress analysis mesh is illustrated in Figure 4.48*b*. In the heat transfer analysis, temperature histories are predicted for nodes numbered 1, 2, 3 and 4. In the stress analysis, however, the temperature histories of node number 5 are linearly interpolated from the temperature histories read of nodes numbered 1 and 2. Similarly, temperature histories of node number 6 are linearly interpolated from temperature histories of nodes numbered 2 and 3 and so forth. However, as nodes numbered 5, 6, 7 and 8 are connected to the 8-noded element in the stress model, initial temperatures of these nodes had to be provided. These were estimated by linearly interpolating the corner nodal initial temperatures, which are defined using the method described in Section 4.7.3.

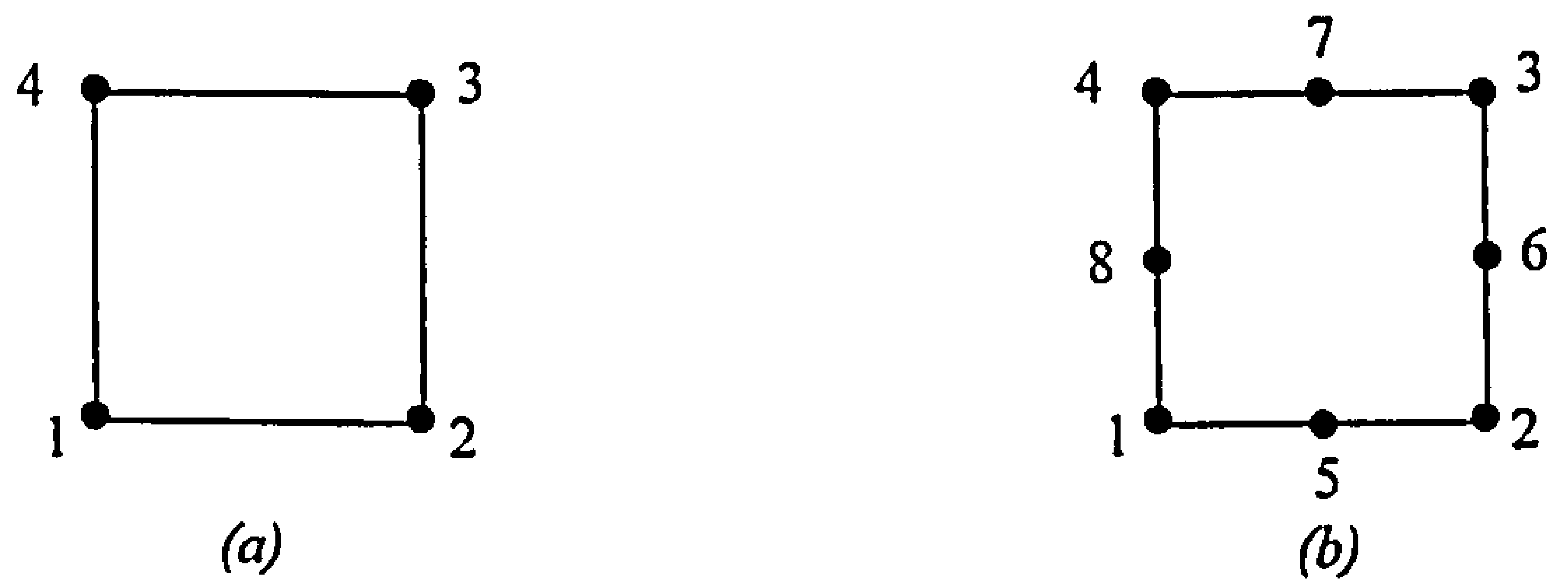

Figure 4.48 (*a*) 4-noded element used in the heat transfer analysis mesh (*b*) 8-noded element used in the corresponding stress analysis mesh

To introduce the results of the convergence study, deformation histories of all nodes located at the bottom surface of the part were monitored. These nodes were expected to undergo continuous deformation due to thermal deformation (expansion and contraction) of subsequently activated layers of elements. The influence of variation in mesh density and element type on the final deformation of the node located at the bottom edge of the part (Figure 4.49) is illustrated in Table 4-8. Deformations examined of that node represent the vertical distance in the *z*-direction of the node from the rigid surface, schematically shown in Figure 4.49.

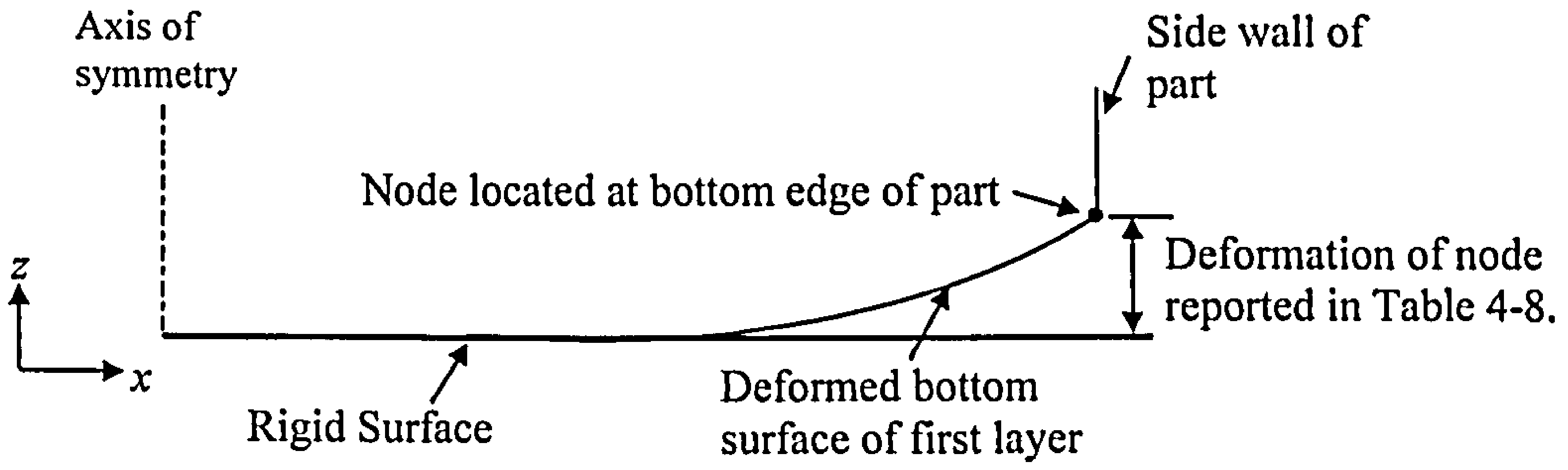

Figure 4.49 Schematic illustration of the deformation of the node located at the bottom edge of the part.

Table 4-8 shows that analyses performed using (linear) CPE4 elements underestimated deflections compared to those predicted using CPE4I and CPE8 elements, with the same mesh density used in comparison. Conversely, for the same mesh density, deformations predicted using CPE4I and CPE8 elements are approximately identical (differing by less than 1%).

Element Type	Mesh (see Table 4-7)		
	Normal	Fine	Very Fine
4-noded (linear) plane strain (CPE4)	5.2728×10^{-5}	5.5601×10^{-5}	5.6495×10^{-5}
4-noded plane strain Incompatible (CPE4I)	5.6542×10^{-5}	5.6770×10^{-5}	5.9516×10^{-5}
8-noded plane strain (CPE8)	5.6735×10^{-5}	5.7298×10^{-5}	5.9544×10^{-5}

Table 4-8 Final deformations (meters) of the node located at the bottom edge of the part used in examining solution convergence of the stress analysis.

The increase in mesh density from "Normal" to "Fine" using CPE4 elements showed a considerable increase in deformation by 5.2%, which indicated that solution convergence was not achieved using the "Normal" mesh with CPE4 elements. However, the increase in mesh density from "Normal" to "Fine" using CPE4I and CPE8 elements showed a slight increase in deformation by 0.4% and 1% respectively. The transformation from "Normal" to "Fine" reduced the aspect ratio of elements in the stress analysis mesh from a maximum value of 5 to a maximum value of 2.5, which is expected to enhance deformation results predicted. Thus, the similarity in deflections predicted using the "Normal" and "Fine" meshes with elements CPE4I and CPE8 is expected to indicate that solution convergence was achieved using these meshes with these type of elements.

The remarkable observation was seen in comparing deflections predicted using the "Fine" mesh with those predicted using the higher density "Very Fine" mesh. The increase in mesh density with CPE4I and CPE8 elements showed deformations to increase by 3.7% and 3.8% respectively, whereas (linear) CPE4 elements showed an increase in deformation by only 1.6%. At first sight, it may be assumed that solution convergence was achieved using the "Fine" and "Very Fine" meshes with all elements examined. However, analysis performed using the "Very Fine" mesh with (linear) CPE4 elements underestimated the final nodal deflection by 5.1% when compared to nodal deflections predicted using that mesh with elements CPE4I and CPE8. In the following, the effect of increasing mesh density from "Fine" to "Very Fine" using CPE4, CPE4I and CPE8 elements on the final nodal deflections presented in Table 4-8 is investigated.

It must be emphasised that besides mesh density and element type, temperatures used in the stress analysis have an important influence on deformations predicted. In this version of modelling, temperatures predicted by the heat transfer analysis only vary in the z-direction; nodal temperature histories predicted along the x-direction at a constant z-position are identical (see Section 4.6.1). Therefore, increasing the number of elements along the x-direction in the heat transfer analysis mesh did not show an alteration in temperatures predicted in the z-direction. Thus, nodal temperature histories read by the stress analyses performed using the "Normal" and "Fine" meshes, with the same type of element used in both meshes, are identical in the z-direction. In this condition, comparing deflections predicted using the "Normal" and "Fine" meshes, with the same type of element used in both meshes, is expected to mainly illustrate the influence of mesh density on results obtained. However, increasing the mesh density from "Fine" to "Very Fine" required, for the latter, increasing the number of elements in the z-direction in the corresponding heat transfer analysis mesh. The increase in the number of elements in that direction caused a slight variation in nodal temperatures predicted. That (slight) variation can be seen by comparing nodal temperatures predicted using the "Refined" and "Further refined" heat transfer analyses meshes (see Tables 4-1 to 4-5). Those predicted using the former mesh have identical nodal temperature histories, at different z positions, to those used in the "Fine" mesh stress analyses, whereas temperatures predicted using the latter are used in the "Very Fine" mesh stress analyses. Thus, comparing nodal deflections produced by the "Fine" and "Very Fine" stress analyses examines the effect of mesh refinement and the slight difference in nodal temperatures used in both analyses, with the same type of element used in comparison. The combined effect has most probably contributed to the difference in deflections predicted using these meshes with elements CPE4I and CPE8. However, that effect was not reflected by a noticeable variation in deformations predicted using the "Fine" and "Very Fine" with (linear) elements CPE4 (1.6%). The reason being that the use of these linear elements can cause the part to become too stiff to bending, as reported by ABAQUS [55]. In this condition, increasing the number of elements along the depth of the part may not show a considerable difference in deflections predicted, ABAQUS [55].

The overall observation in Table 4-8 was that solution convergence was achieved using the "Normal", "Fine" and "Very Fine" meshes with CPE8 and CPE4I elements, whereas these meshes with CPE4 elements were found to be not suitable for predicting curl. Table 4-9 shows the relative CPU times required to produce deflections using the meshes with elements achieving solution convergence. Relative CPU time was estimated as the *total* CPU time required to predict deflections using a specific stress analysis mesh with a specific element type divided by the *total* CPU time required to predict deflections using the "Normal" mesh with CPE4I elements. The *total* CPU time required to predict deflections, however, is estimated as the sum of the CPU times required to solve a stress analysis and that required to solve its corresponding heat transfer analysis.

Element Type	Mesh		
	Normal	Fine	Very Fine
CPE4I	1	2.05	2.77
CPE8	1.35	2.74	3.2

Table 4-9 Relative CPU times required to run the simulations performed using the meshes with element types producing stress analysis solution convergence

Table 4-9 shows that the mesh achieving solution convergence and requiring the least *total* CPU time to produce deformations was the "Normal" mesh with CPE4I elements, and thus this mesh is the most efficient one. Deformations of the bottom surface of the build predicted in selected steps of the stress analysis with the "Normal" CPE4I finite element mesh employed are shown in Figure 4.50 to 4.52. These deformations represent the distances in the *z*-direction of the nodes located along the bottom surface of the part from the rigid surface.

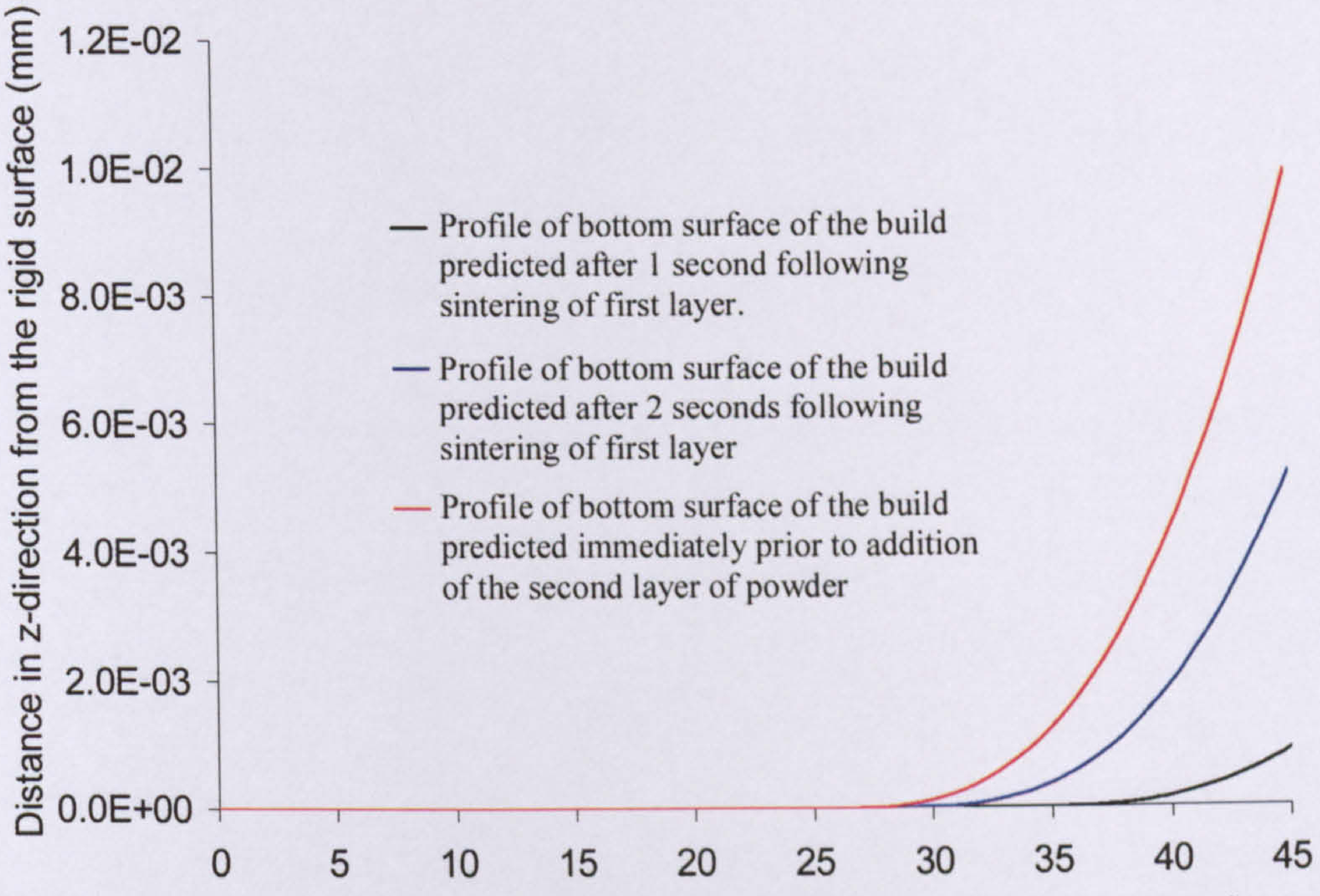

Figure 4.50 Selected profiles of the bottom surface of the build predicted in the first step of the first version of the stress analysis, i.e. following sintering of first layer and prior to addition of second layer.

Figure 4.50 shows deformations of the bottom surface of the build predicted in the first step of the stress analysis. The step simulated thermal and mechanical effects expected to occur following sintering of the first layer and prior to the addition of the second layer in powder form. Temperature histories read in the step are of all nodes connected to elements representing the first layer of the part, illustrated in Figure 4.45. In addition, shrinkages causing the development of curl are only of elements flanked by nodes located at the top surface of the first layer and those located at a depth of 0.125mm from that surface. The continuous reduction in nodal temperatures of these elements (see Figure 4.45) is expected to be the cause of the continuous rise in curl predicted in this step of the stress analysis.

Figure 4.51 shows selected deformations of the bottom surface of the build predicted in the second step of the analysis. The step simulated thermal and mechanical effects expected to occur after addition of the second layer in powder form and prior to thermal stresses developing in the layer following its sintering. In the step, the second layer was not activated, but its weight was simulated by a uniform load simultaneously applied on the top surface of the first layer. Thus, temperature histories read in the step are of nodes connected to elements representing the first layer of the part, illustrated in Figure 4.45. In addition, thermal deformations (contraction and expansion) considered in the step remained those of elements flanked by nodes located at the top surface of the first layer and those located at a depth of 0.125mm from that surface.

In the first 1×10^{-6} seconds of the step, a significant reduction in curl of the bottom surface of the part was predicted. During that period, the maximum distance of the bottom surface of the part from the rigid surface reduced from 9.89×10^{-3}mm to 3.85×10^{-3}mm, i.e. by 61%. That sudden reduction in curl is expected to have occurred due to the effect of load applied on the top surface of the first layer simulating the weight of the second layer. Reduction in curl is also displayed in the following 0.8 seconds of the step; the maximum distance from the rigid surface reduced from 3.85×10^{-3}mm to 3.67×10^{-3} mm, i.e. by 4.67%. It must be emphasised that during that period, nodal temperatures of elements developing thermal strains decrease. Thus, the reduction in curl seen in that period is expected to indicate that shrinkages giving rise to curl were not sufficient to overcome both the weight of the first layer and load applied on its top surface. However, following that period and for the duration of 4.8 seconds, thermal shrinkages of elements in the first layer, caused by reductions in their nodal temperatures, was reflected by a continuous rise in curl. The maximum distance of the bottom surface of the build from the rigid surface increased in that period from 3.67×10^{-3}mm to 4.12×10^{-3}mm, i.e. by 11%. Nodal temperature histories read in the remaining period of the step (0.5 seconds) were those predicted during and following the application of heat flux on the top surface of the second layer. In that period, nodal temperatures of elements developing thermal strains in the first layer increase. That is expected to have caused these (previously shrunken) elements to expand, which is reflected by a considerable reduction in curl of the build. In that period, the maximum distance of the bottom surface of the build from the rigid surface reduced from 4.12×10^{-3}mm to 2.30×10^{-4}mm, i.e. by 94.3%

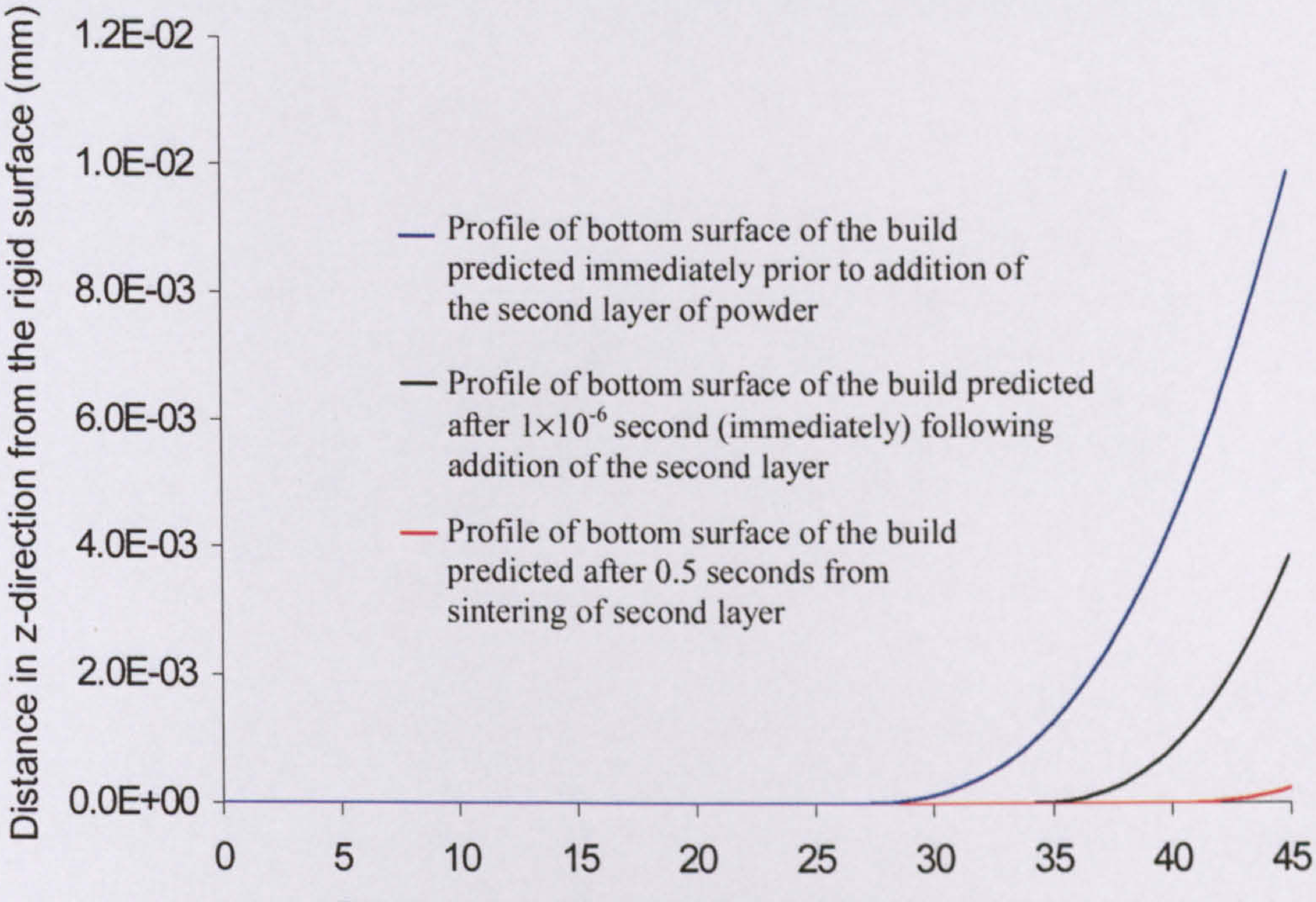

Figure 4.51 Selected profiles of the bottom surface of the build predicted in the second step of the first version of the stress analysis, i.e. following addition of the second layer and prior to stresses developing in the layer after it had been sintered.

The stages of curl development predicted in the first and second steps of the stress analysis were also seen in curl predicted in steps 3 to 15, step 17 and step 19. A description of these steps along with magnitudes of selected maximum deflections of the bottom surface of the build from the rigid surface predicted in these steps are illustrated in Table 4-10. In steps 16 and 18, however, the build displayed a downward curl. In the following, an attempt is made to describe the development of curl in step 16. The same description also applies to the development of curl in step 18.

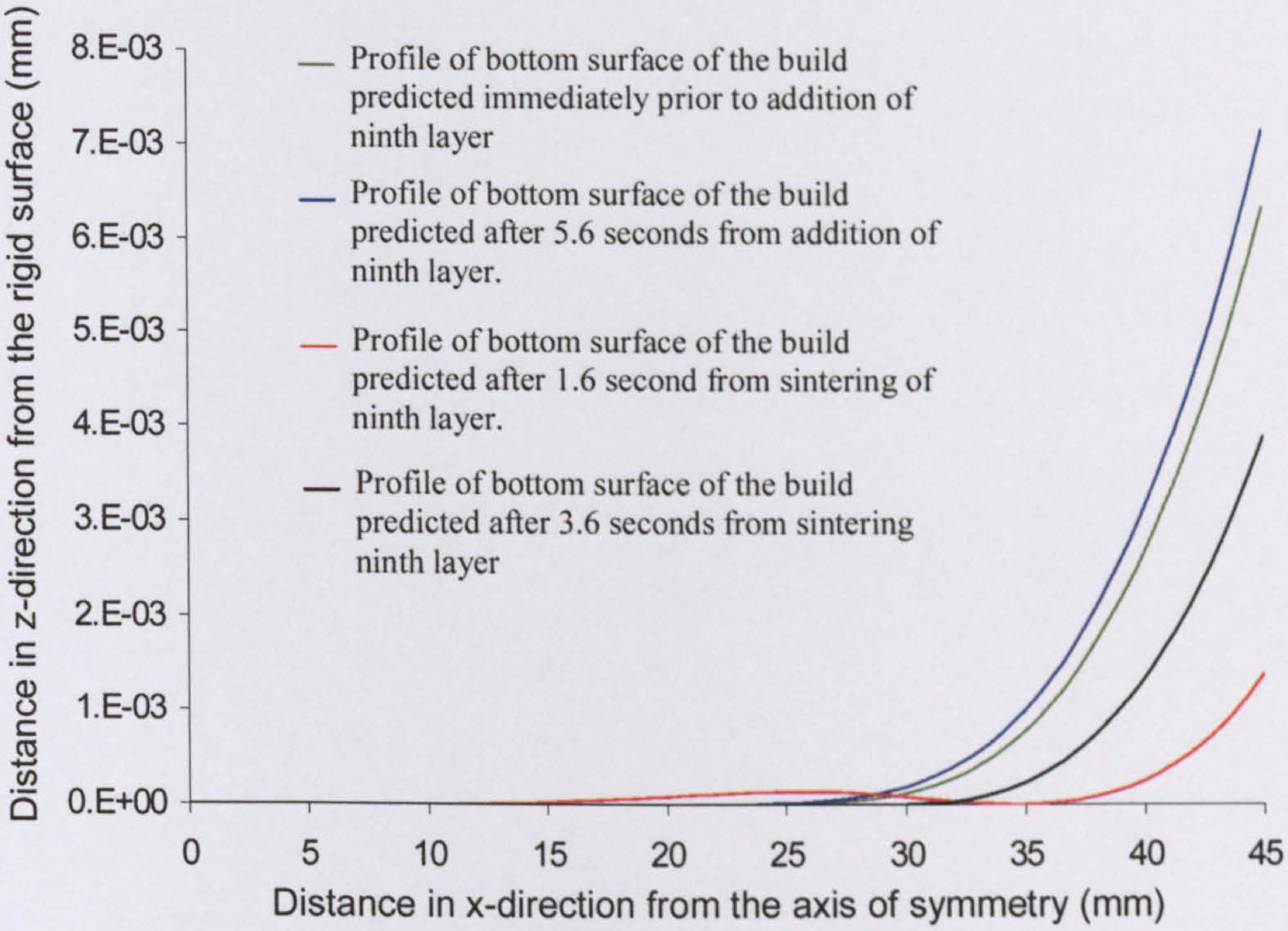

Figure 4.52 Selected profiles of the bottom surface of the build predicted in step 16 of the first version of the stress analysis, i.e. following addition of the ninth layer and prior to stresses developing in the layer after it had been sintered.

Figure 4.52 shows selected deformations of the bottom surface of the part predicted in step 16 of the stress analysis. The step simulated thermal and mechanical effects expected to occur after addition of the ninth layer in powder form and prior to thermal stresses developing in the layer following its sintering. The active elements in the step were those representing the first to the eighth layers of the part. In addition, thermal deformations influencing curl are of elements flanked by nodes located at the top surface of the eighth layer and those located at a depth of 0.125mm from the top surface of the first layer.

In the first 1×10^{-6} seconds of the step, a slight reduction in curl is seen; the maximum distance in the *z*-direction of the bottom surface of the part from the rigid surface reduced from 6.34×10^{-3}mm to 6.18×10^{-3}mm, i.e. by 2.5%. That reduction is expected to have occurred due to the effect of load simulating the weight of the ninth layer. In the following 5.6 seconds, a continuous rise in curl is predicted; the maximum distance from the rigid surface increased from 6.18×10^{-3}mm to 7.15×10^{-3}mm (by 13.6%). Nodal temperature histories read in the remaining period of the step (3.6 seconds) were those predicted during and following the application of heat flux on the top surface of the ninth layer (see Figure 4.47). Upon the application of heat flux, nodes located close to the sintered surface experience a considerable increase in temperature compared to those located at a large depth from the surface. Thus, elements flanked by the former nodes experience a larger expansion than those flanked by the latter resulting in the build to undergo downward curl. However, it must be emphasised that following 1.6 seconds from the application of heat flux, nodal temperatures of elements representing layers four to eight were above 190°C. Thus, curl of the build is influenced by thermal deformations of elements representing part layers one to three. In that period, temperatures of nodes located at a large depth from the top surface of the third layer increase at a higher rate than those located close to that surface. This is expected to have caused the disappearance of the downward curl, followed by a continuous rise in the (upward) curl of the build.

Step number	SLS stage (Viscoelasticity considered)	Maximum distance of bottom surface of build from the rigid surface (mm)		Percentage of change in distance in a stage
		Start of stage	End of stage	
1	Cooling of sintered Layer 1	0	9.89×10^{-3}	
2	2nd layer added in powder form	9.89×10^{-3}	4.12×10^{-3}	-58.34%
	2nd layer in melt state	4.12×10^{-3}	2.30×10^{-4}	-94.4%
3	Cooling of sintered layer 2	2.30×10^{-4}	3.06×10^{-2}	+99.2%
4	3rd layer added in powder form	3.06×10^{-2}	3.08×10^{-2}	+0.6%
	3rd layer in melt state	3.08×10^{-2}	4.07×10^{-3}	-86.7%
5	Cooling of sintered layer 3	4.07×10^{-3}	2.29×10^{-2}	+82.2%
6	4th layer added in powder form	2.29×10^{-2}	2.35×10^{-2}	+2.6%
	4th layer in melt state	2.35×10^{-2}	4.38×10^{-3}	-81.4%
7	Cooling of sintered layer 4	4.38×10^{-3}	1.72×10^{-2}	+74.5%
8	5th layer added in powder form	1.72×10^{-2}	1.82×10^{-2}	+5.5%
	5th layer in melt state	1.82×10^{-2}	4.46×10^{-3}	-75.5%
9	Cooling of sintered layer 5	4.46×10^{-3}	1.3×10^{-2}	+65.7%
10	6th layer added in powder form	1.3×10^{-2}	1.41×10^{-2}	+7.8%
	6th layer in melt state	1.41×10^{-2}	4.36×10^{-3}	-69.1%
11	Cooling of sintered layer 6	4.36×10^{-3}	1×10^{-2}	+56.4%
12	7th layer added in powder form	1×10^{-2}	1.1×10^{-2}	+9%
	7th layer in melt state	1.1×10^{-2}	4.16×10^{-3}	-62.2%
13	Cooling of sintered layer 7	4.16×10^{-3}	7.86×10^{-3}	+47.1%
14	8th layer added in powder form	7.86×10^{-3}	8.8×10^{-3}	+10.7%
	8th layer in melt state	8.8×10^{-3}	4.05×10^{-3}	-54%
15	Cooling of sintered layer 8	4.05×10^{-3}	6.34×10^{-3}	+36%
16	9th layer added in powder form	6.34×10^{-3}	7.15×10^{-3}	+11%
	9th layer in melt state	7.15×10^{-3}	3.89×10^{-3}	-45.6%
17	Cooling of sintered layer 9	3.89×10^{-3}	5.25×10^{-3}	+26%
18	10th layer added in powder form	5.25×10^{-3}	6.85×10^{-3}	+23.3%
	10th layer in melt state	6.85×10^{-3}	1.22×10^{-3}	-82%
19	Cooling of sintered layer 10	1.22×10^{-3}	0.0565	+97%

Table 4-10 Selected magnitudes of the maximum distance in the z-direction of the bottom surface of the build from the rigid surface predicted by the first version of the stress analysis with viscoelasticity considered.

4.7.6 Discussion

To validate the finite element models, the final predicted profiles of the top and bottom surfaces of the part were compared with experimental measurements of curl reported in Chapter 3. Figure 4.53 shows the predicted profiles drawn along side the experimentally obtained results. It must be emphasised that the thicknesses of the modelled part (1.91mm) and the measured one (1.733mm) are not identical. Thus, the predicted profile of the top surface had to be repositioned so that the predicted and measured profiles had the same height from the rigid surface at the points on the profiles intersecting the axis of symmetry.

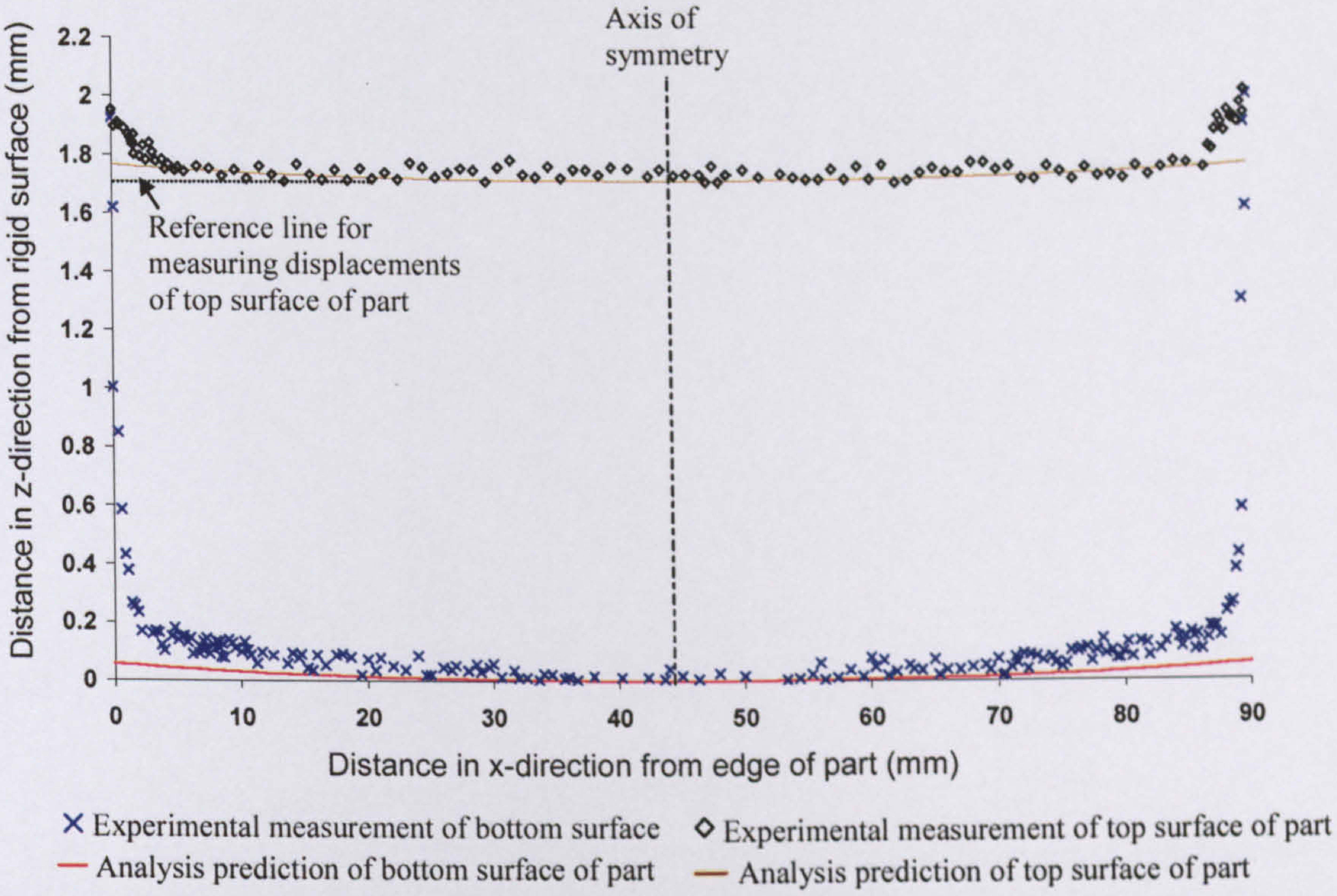

Figure 4.53 Profiles of top and bottom surfaces of the part predicted from the first version of the stress analysis drawn alongside the experimentally obtained profiles

Figure 4.53 shows that the stress model has predicted the top and bottom surfaces of the part to undergo an upward curl, which agrees with the trend of the measured profiles of these surfaces. However, the model underestimated curl in regions of the surfaces close to the side walls of the part. For example, the distance in the *z*-direction between the predicted edge of the top surface and the point at the axis of symmetry (Figure 4.53) differed by 90% compared to the corresponding distance measured from experimentally obtained results. Additionally, the distance in the *z*-

direction between the rigid surface and the predicted profile of the bottom surface, 2.15mm from the bottom edge of the part, differed by 70% compared to the corresponding distance measured from the experimentally obtained profile.

Therefore, the finite element models at this stage of development did not produce satisfactory predictions of curl at the top and bottom surfaces of the part. Nevertheless, predictions made by the stress model (see Table 4-10) can provide an idea of the SLS stages wherein significant variations in curl are expected to occur. These stages are sintering of a recently added layer, and cooling of the layer from its melt state. The former has a reducing effect on the upward development of curl, whereas the latter gives rise to curl. In addition, effects of laser sintering and thermal shrinkage of a recently sintered layer on the development of (upward) curl were seen to reduce with the increase in number of layers forming the build. For example, with the second layer in a melt state following its sintering, the maximum distance from the rigid surface reduced by 94.4%, whereas that distance reduced by 62% with the seventh layer in the melt state. Furthermore, shrinkage of second layer following its sintering increased the maximum distance by 99.2%, whereas shrinkage of the seventh layer increased that distance by only 47%. It may be suggested the one reason of the reduction in the ability of the build to deform as SLS fabrication progresses being the increase in thickness of the build with successive layers added. That finding was additionally recognised in the analytical stress model described in Section 4.4.

The immediate effect of the weight of a recently added layer of powder on curl is illustrated in Table 4-11. The table shows the maximum distances of the bottom surface of the build from the rigid surface immediately prior to applying load simulating the weight of the powder layer and those predicted 1×10^{-6} seconds following load application. In the latter, temperature variations in that short period are assumed negligible, and thus variations in curl are mainly dependent on the weight of the added layer. The effect of weight had the most significant effect in reducing upward curl at the instant the weight of the second layer was added; the maximum distance from the rigid surface reduced by 61%. That is most probably because the weight of the second layer (0.25mm thick) was twice as much the weight simulated of subsequently added layers (0.125mm thick). However, the overall trend seen in Table 4-11 suggests that deformation of the build is less susceptible to the weight of an added layer with increase in thickness of the build.

SLS stage (Viscoelasticity considered)	Maximum distance of bottom surface of build from the rigid surface (mm)		Percentage of change in distance in a stage
	Prior addition of load	Immediately following addition of load	
2nd layer added in powder form	9.89×10^{-3}	3.85×10^{-3}	-61.1%
3rd layer added in powder form	3.06×10^{-2}	2.51×10^{-2}	-18%
4th layer added in powder form	2.29×10^{-2}	2.09×10^{-2}	-8.7%
5th layer added in powder form	1.72×10^{-2}	1.6×10^{-2}	-6.97%
6th layer added in powder form	1.30×10^{-2}	1.22×10^{-2}	-6.15%
7th layer added in powder form	1.0×10^{-2}	9.54×10^{-3}	-4.6%
8th layer added in powder form	7.86×10^{-3}	7.59×10^{-3}	-3.68%
9th layer added in powder form	6.34×10^{-3}	6.18×10^{-3}	-2.52%
10th layer added in powder form	5.25×10^{-3}	5.16×10^{-3}	-1.71%

Table 4-11 Illustration of the immediate effect of the weight of added layers on the maximum distance in the z-direction of the bottom surface of the build from the rigid surface predicted by the first version of the stress model with viscoelasticity not considered.

The effect of the viscoelastic behaviour of polycarbonate was additionally investigated. Table 4-12 illustrates the maximum distances of the bottom surface of the part from the rigid surface predicted without the viscoelasticity considered in the stress analysis. The table shows that SLS stages wherein significant variations in curl occur are those previously identified in Table 4-10. Additionally, comparing distances reported in Table 4-12 with those presented in Table 4-10 reveals that curl predicted at the end of each SLS stage is less with viscoelasticity considered. For example, the final distances from the rigid surface predicted at the end of the stress analyses with viscoelasticity considered and without it being taken into account were 5.65×10^{-2}mm and 6.23×10^{-2} mm respectively (differing by 9.3%).

Step number	SLS stage (Viscoelasticity not considered)	Maximum distance of bottom surface of build from the rigid surface (mm)	
		Start of stage	End of stage
1	Cooling of sintered Layer 1	0	1.17×10^{-2}
2	2nd layer added in powder form	1.17×10^{-2}	4.88×10^{-3}
	2nd layer in melt state	4.88×10^{-3}	2.63×10^{-4}
3	Cooling of sintered layer 2	2.63×10^{-4}	3.63×10^{-2}
4	3rd layer added in powder form	3.63×10^{-2}	3.45×10^{-2}
	3rd layer in melt state	3.45×10^{-2}	4.76×10^{-3}
5	Cooling of sintered layer 3	4.76×10^{-3}	2.69×10^{-2}
6	4th layer added in powder form	2.69×10^{-2}	3.03×10^{-2}
	4th layer in melt state	3.03×10^{-2}	5.11×10^{-3}
7	Cooling of sintered layer 4	5.11×10^{-3}	2.02×10^{-2}
8	5th layer added in powder form	2.02×10^{-2}	2.38×10^{-2}
	5th layer in melt state	2.38×10^{-2}	5.21×10^{-3}
9	Cooling of sintered layer 5	5.21×10^{-3}	1.53×10^{-2}
10	6th layer added in powder form	1.53×10^{-2}	1.86×10^{-2}
	6th layer in melt state	1.86×10^{-2}	5.07×10^{-3}
11	Cooling of sintered layer 6	5.07×10^{-3}	1.17×10^{-2}
12	7th layer added in powder form	1.17×10^{-2}	1.47×10^{-2}
	7th layer in melt state	1.47×10^{-2}	4.85×10^{-3}
13	Cooling of sintered layer 7	4.85×10^{-3}	9.22×10^{-3}
14	8th layer added in powder form	9.22×10^{-3}	1.18×10^{-2}
	8th layer in melt state	1.18×10^{-3}	4.72×10^{-3}
15	Cooling of sintered layer 8	4.72×10^{-3}	7.41×10^{-3}
16	9th layer added in powder form	7.41×10^{-3}	9.56×10^{-3}
	9th layer in melt state	9.56×10^{-3}	4.54×10^{-3}
17	Cooling of sintered layer 9	4.54×10^{-3}	6.12×10^{-3}
18	10th layer added in powder form	6.12×10^{-3}	7.12×10^{-3}
	10th layer in melt state	7.12×10^{-3}	1.41×10^{-3}
19	Cooling of sintered layer 10	1.41×10^{-3}	0.0623

Table 4-12 Selected magnitudes of the maximum distance in the z-direction of the bottom surface of the build from the rigid surface predicted by the first version of the stress model with viscoelasticity not considered.

The overall conclusion has been that the finite element models, at this stage of development, did not produce satisfactory predictions of curl. However, it was possible to use SLS machine parameters, such as laser power and initial temperatures of the powder bed and added layers, as input to the heat transfer model. Additionally, the stress model has predicated the SLS stages wherein significant variations of curl may occur, which previous finite element models failed to do (see Section 2.4.2). However, the inaccurate predictions of curl are believed to be a result of the considerable number of assumptions the present models comprised. These include assumptions made with regard to material properties, boundary conditions and geometrical approximations. Thus, investigation into reducing these assumptions in further developments of the models was required.

Chapter 5

Experimental Measurements

5.1 Introduction

The subject of this chapter is to describe the experimental measurements performed in the present work. The aim of the measurements was to reduce the number of assumptions made in the first versions of the heat and stress finite element models (see Chapter 4) in an attempt to achieve a more accurate prediction of curl. The measurements were focused on two aspects; estimating the thickness of each layer forming the modelled ten-layer parts and obtaining better material property data to be used as input to the models.

5.2 Measurements of Layer Thicknesses

In this section, a description of the method used to estimate the thickness of each layer forming the modelled ten-layer parts is given along with results obtained. Polycarbonate blocks, 90×26mm in area and 1 to 10 layers in thickness, were fabricated using the SLS machine parameters reported in Section 3.2. A number of thickness measurements were then performed on each of the produced blocks with the use of a micrometer. The measurements were taken at regions distant from the curled edges of the blocks. Thickness readings obtained for each block were next averaged. The average thickness of the one-layer block was equal to 0.59mm. That thickness is larger than the nominal thickness of the layer (0.127mm) indicating the development of bonus Z during fabrication. The measured thickness of the one-layer block was considered to be equal to the thickness of the first layer of the modelled ten-layer part. The measured average thickness of the two-layer block, however, was equal to 0.717mm. The thickness of the second layer in the modelled ten-layer part was regarded to be equal to the difference between the average thickness of the fabricated two-layer block and that of the one-layer block, which is equal to 0.127mm. Additionally, the thickness of the third layer in the modelled ten-layer part was assumed to be equal to the difference between the average thickness of the three-layer block (0.844mm) and that of the two-layer block (0.717mm), which is equal to 0.127mm. In a similar way, the thickness of each of the layers from four to ten of the modelled ten-layer part were estimated. The layers had an identical thickness equal to 0.127mm.

5.3 Measurements of Material properties

In following sections, a description of experimental measurements performed to estimate a number of material properties used as input to the heat transfer and stress models is provided along with results obtained.

5.3.1 Material Properties Used as Input to Heat Transfer Analysis

The main material properties required as input to the heat transfer model were identified in Section 4.3 as the specific heat, density and thermal conductivity. In the following, experimental measurements carried out to estimate the specific heat and densities of the powder bed and polycarbonate fabricated parts are described. Thermal conductivities, however, were defined in further developed heat transfer models based on the Yagi-Kunii predictions (Section 4.6.2), using the density values experimentally obtained.

5.3.1.1 Density of Sintered Part

Nine polycarbonate blocks, 90x26mm in area and 10 layers in thickness, were fabricated using the SLS machine parameters reported in Section 3.2. After the blocks were fabricated, their curled edges were cut out resulting in blocks with vertical side walls and flat horizontal surfaces. The weight of each block was measured. The density of a block was calculated by dividing its weight by its volume. The calculated densities of the blocks were then averaged, giving an average density for the produced parts equal to 497±12kg/m^3.

5.3.1.2 Density of the Powder Bed

The density of SLS polycarbonate powder was measured using the method reported by Childs et al. [31]. Nine hollow cylinders with closed bottoms were SLS fabricated in an arrangement in the powder bed illustrated in Figure 5.1. Each of the cylinders had an internal diameter equal to 22mm and an internal height equal to 15mm. After the cylinders were fabricated, they were carefully removed from the powder bed containing within them the unsintered powder. The density of the powder was calculated by dividing the weight of the powder by the volume it had occupied in the cylinder. The densities of the powder in each cylinder were next averaged, giving an average density of the powder bed equal to 439±20kg/m^3.

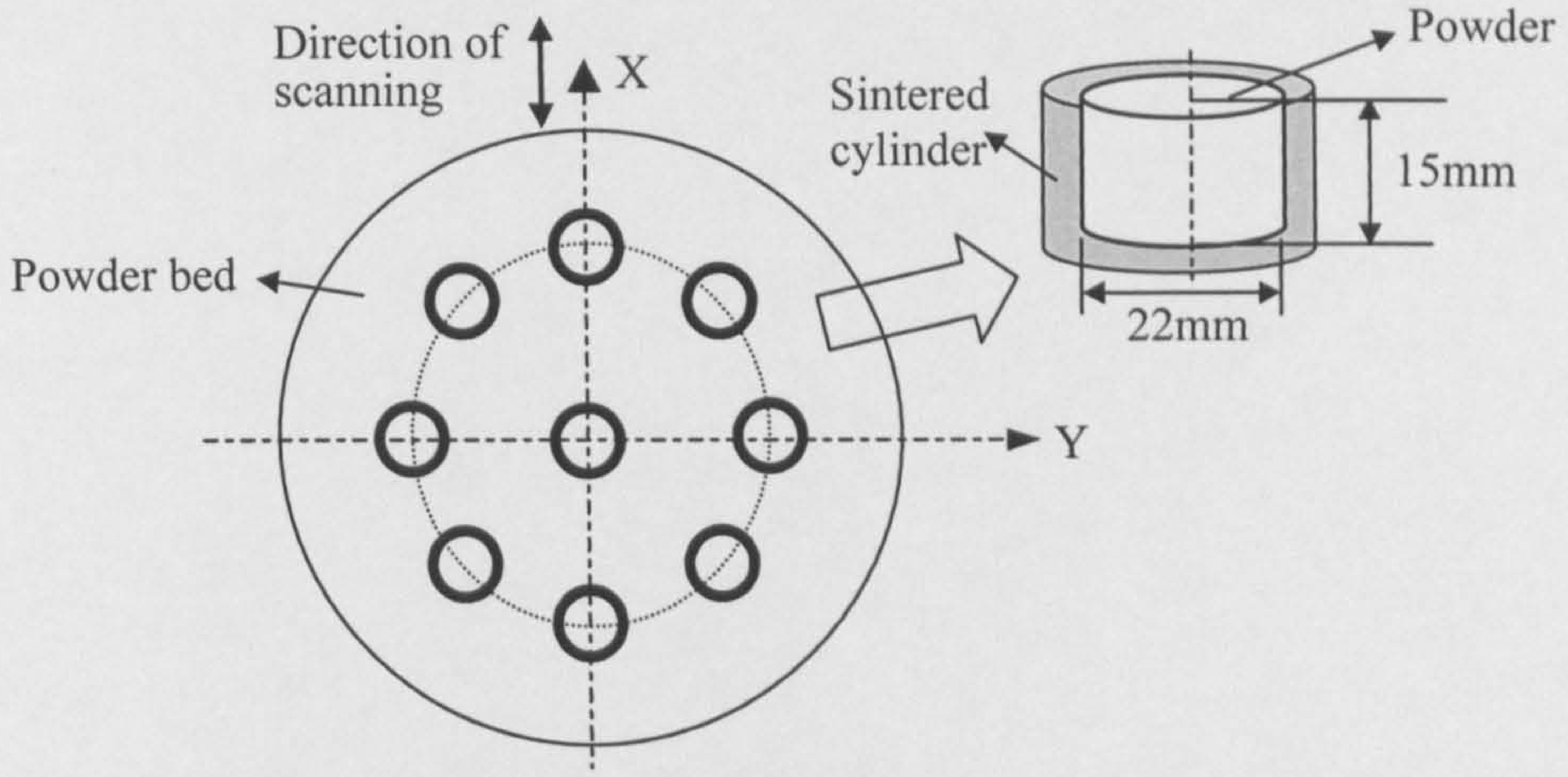

Figure 5.1 Arrangement of cylinders in the powder bed for powder bed density measurements

5.3.1.3 Specific Heat Measurement

Specific heat measurements were carried out on a polycarbonate powder sample. The measurements were performed using a Differential Scanning Calorimeter (DSC); a Perkin Elmer DSC-7. The DSC consists of two identical pans made of the same material. In the test, the powder sample was placed in one pan whilst the other pan was left empty. Each pan was then positioned on top of a heater, as schematically illustrated Figure 5.2.

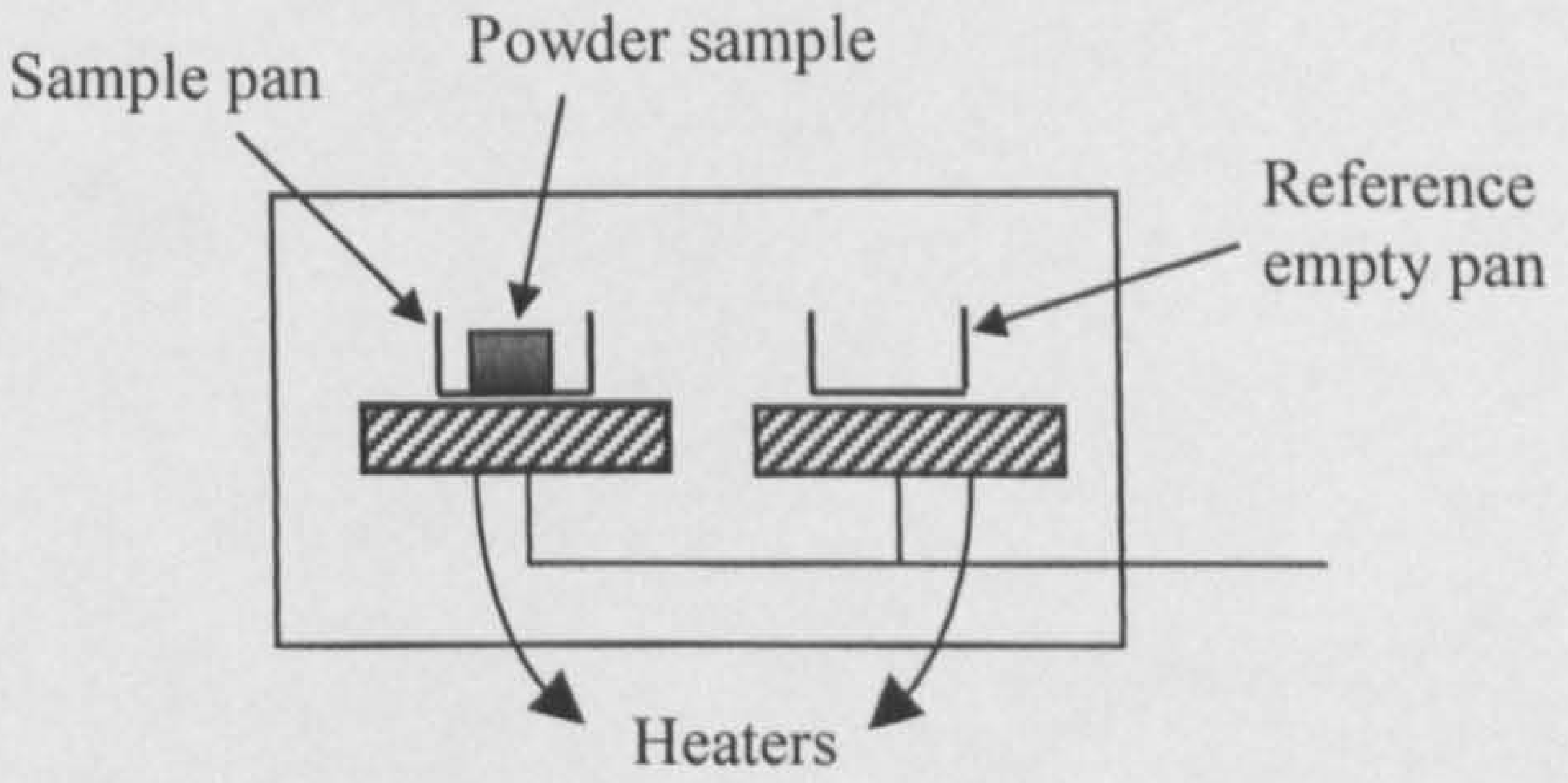

Figure 5.2 A schematic diagram of a DSC arrangement.

In the test, the pans were heated at a rate equal to 40°C/min. The heat supplied to each pan needed to maintain both pans at identical temperatures was recorded. The difference in heat supplied to the pans was also computed as a function of temperature. The heat difference calculated represents the amount of heat absorbed by the powder sample. Based on these data, the DSC calculates the specific heat C_p (J/kg.K) as follows,

$$C_p = \frac{Q}{m_s.\Delta T} \qquad \text{5-1}$$

where Q is the heat absorbed by the powder sample, ΔT is the increase in its temperature and m_s denotes its mass.

The variation in specific heat with temperature generally obtained for an amorphous polymer such as polycarbonate is schematically illustrated in Figure 5.3 [56]. In the figure, the specific heat increases linearly with temperature in both the glassy and rubbery regions. The glass transition region is manifested as a step change in the specific heat curve. The change in the specific heat curve, however, does not occur suddenly but takes place over a range of temperatures. The glass transition temperature (T_g) is selected where the corresponding specific heat is midway between the specific heat measured at the end of the glassy region and that at the start of the rubbery region [56] (see Figure 5.3).

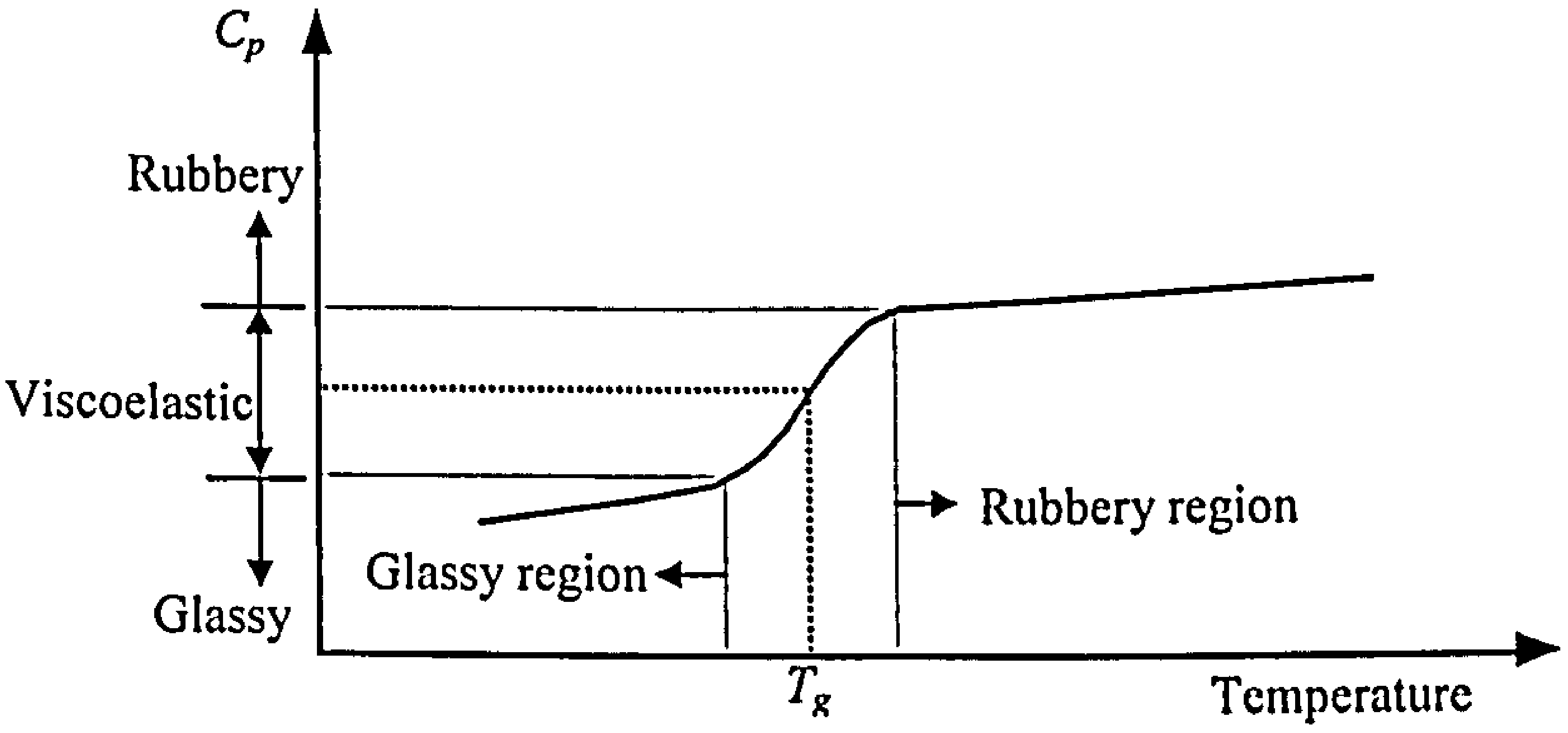

Figure 5.3 Schematic illustration of the specific heat as a function of temperature for a typical amorphous polymer.

The variation in specific heat with temperature measured experimentally for the SLS polycarbonate powder sample used in the present work is illustrated in Figure 5.4. The figure shows a linear increase in the specific heat with temperature in the rubbery region and in the most part of the glassy region. The change in the slope of the specific heat curve seen at approximately 136°C most probably indicates that sample transition (from glassy to viscoelastic) had started. However, further increase in temperature of the sample (above 136°C) shows the specific heat curve to undergo a sharp peak and then decrease to values that are higher than those in the glassy region. The peak in the specific heat curve, however, is not a trend generally expected for a typical amorphous polymer.

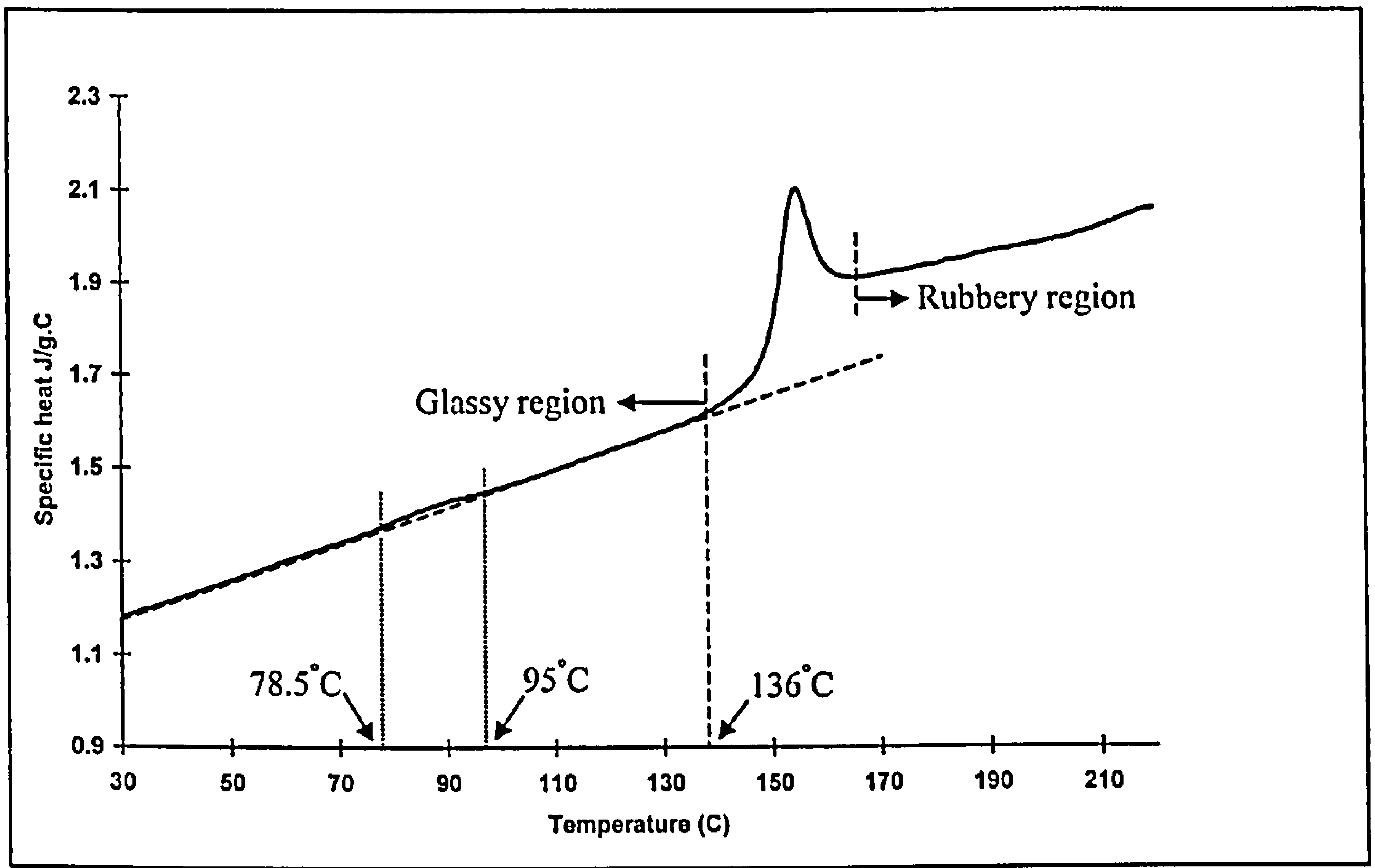

Figure 5.4 Specific heat measured using a DSC during the heating of an SLS polycarbonate powder sample.

It was reported in a previous study by Vick et al. [57] that such a peak is a sign of the physical ageing of the polymer. In the study, the specific heat was measured for as-received and aged SLS polycarbonate powder samples. Ageing of the powder was achieved by maintaining its temperature at 130°C for 200 hours. The specific heat curve for the aged sample showed a peak in the vicinity of T_g, as illustrated by curve (B) in Figure 5.5. However, as the aged sample was cooled and then reheated, the peak was no longer present (see curve (C) in Figure 5.5). In fact, the (reheated) aged polymer exhibited an approximately identical specific heat curve to that measured for the as-received powder sample (see Curve A in Figure 5.5). It must be emphasised that curves (A), (B) and (C) are drawn alongside in Figure 5.5 with a vertical shift for the purpose of clarification. The findings illustrated in Figure 5.5 indicated that physical ageing caused by thermal cycling is totally thermally reversible [57,58].

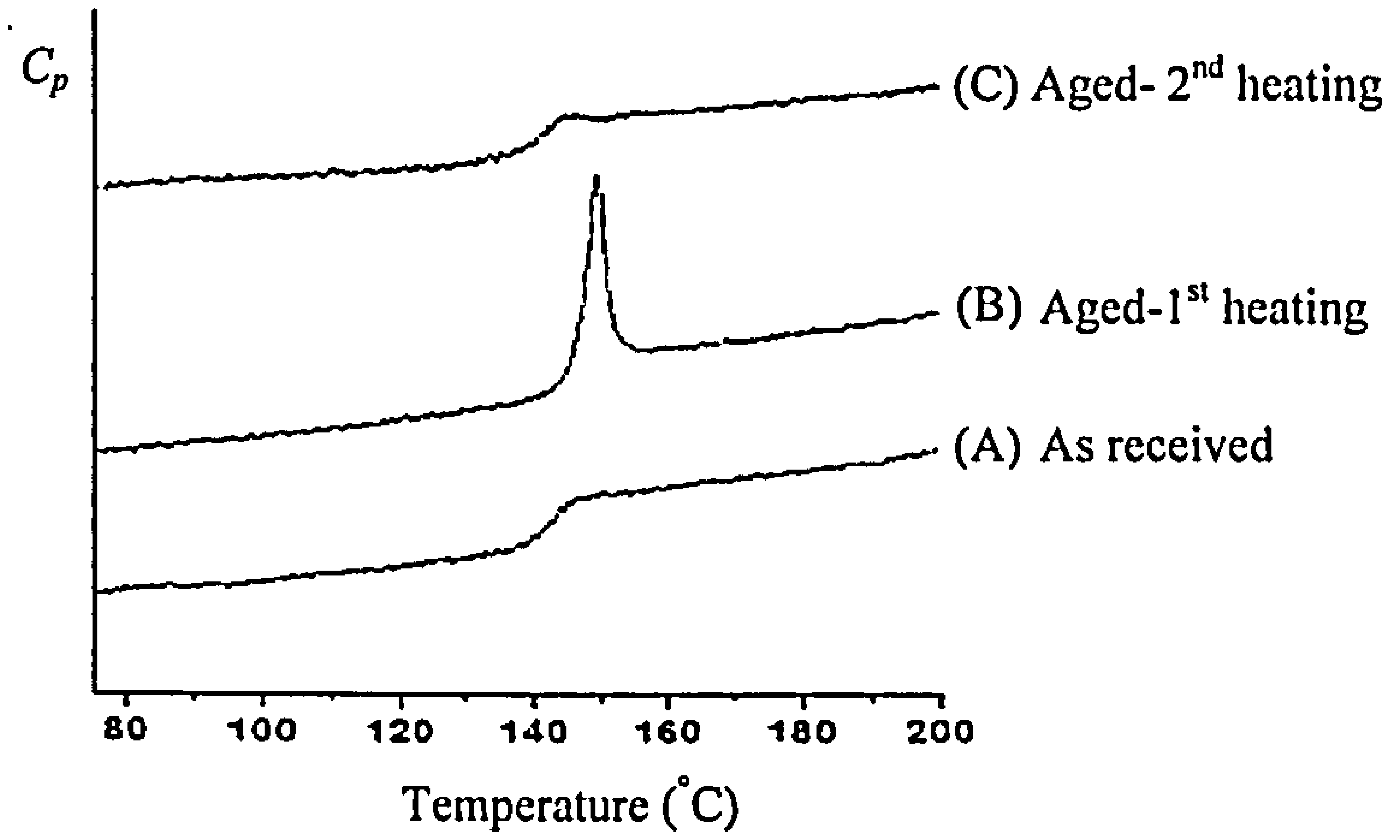

Figure 5.5 Specific heat with temperature for aged and as-received SLS polycarbonate powder sample. From [57].

In the SLS process, the polymer powder is initially heated to a temperature close to its glass transition temperature. After the cooling down stage, the powder surrounding the fabricated parts is stored for further use. The same powder can therefore undergo heating and cooling cycles each time new parts are produced. As (thermal) physical ageing is thermally reversible, it is expected that thermal cycling of the powder during the SLS process is unlikely to have caused the "overshoot" in the specific heat curve seen in Figure 5.4. However, it was also reported by Vick et al. [57] that physical ageing could be introduced by powder handling operations such as drying and long term storage.

Figure 5.4 also shows a slight peak (deviation from a linear slope) in the specific heat curve over the temperature range from 78.5°C to 95°C. The slight peak most probably indicates the existence of a secondary transition region, termed β transition. That transition is a general phenomenon of glassy polymers, and was reported to occur in typical polycarbonate over the temperature range from 47°C to 97°C [59]. The occurrence of the β transition in polycarbonate is attributed to defects in the glassy structure of the polymer [59]. However, β transition was also reported to be influenced by the thermal history of the polymer. In some conditions, the transition is evident when the polymer is quenched from the melt, but was found to reduce or disappear by annealing [59]. Nevertheless, due to the existence of the sharp peak in the specific heat curve (Figure 5.4), measurement of the exact glass transition temperature of the SLS polycarbonate powder was not possible, compelling us to resort to alternative means for measuring that temperature (see Section 5.3.2.1).

5.3.2 Material Properties Used as Input to Stress Analysis

In the following, experimental measurements performed to provide better material property data to be used as input to stress analyses are described. The measurements included estimation of the glass transition temperature, instantaneous modulus, time-dependent response (viscoelastic behaviour) and the coefficient of friction.

5.3.2.1 Measurement of the Glass Transition Temperature

The importance of estimating the glass transition temperature developed as it was experimentally identified, in a previous study [60], as the temperature above which stresses in polymers are negligible. The glass transition temperature of SLS polycarbonate was measured in the present work using a Dynamic Mechanical Analyser (DMA); a Perkin Elmer DMA 7. In a DMA, a polymer sample is subjected to a sinusoidal stress and the resulting (sinusoidal) strain of the sample is measured as temperature is varied. The polymer sample at low temperatures or at short experimental times is in a glassy state; its behaviour is time-independent. In this condition, the stress and measured strain are both in phase. The behaviour of a rubbery polymer is also time-independent, and the stress and measured strain are in phase. However, the polymer in a viscoelastic state has a time-dependent response, and the strain response lags behind the stress by a phase lag (an angle δ), as illustrated in Figure 5.6. In this condition, the modulus of the polymer E^* is made of two components E_1 and E_2, (see Figure 5.7). The modulus E_1 represents the real component of the modulus, which is in phase with the applied stress. This component is termed the storage modulus as it defines the energy stored in the specimen due to the applied stress. The modulus (E_2) is the imaginary component of the modulus (E^*), and is out of phase with the applied stress. This modulus (E_2)

defines the dissipation of energy and is often termed the loss modulus. The ratio E_2/E_1, however, is equal to the tangent of the phase angle ($\tan\delta$) [20,23].

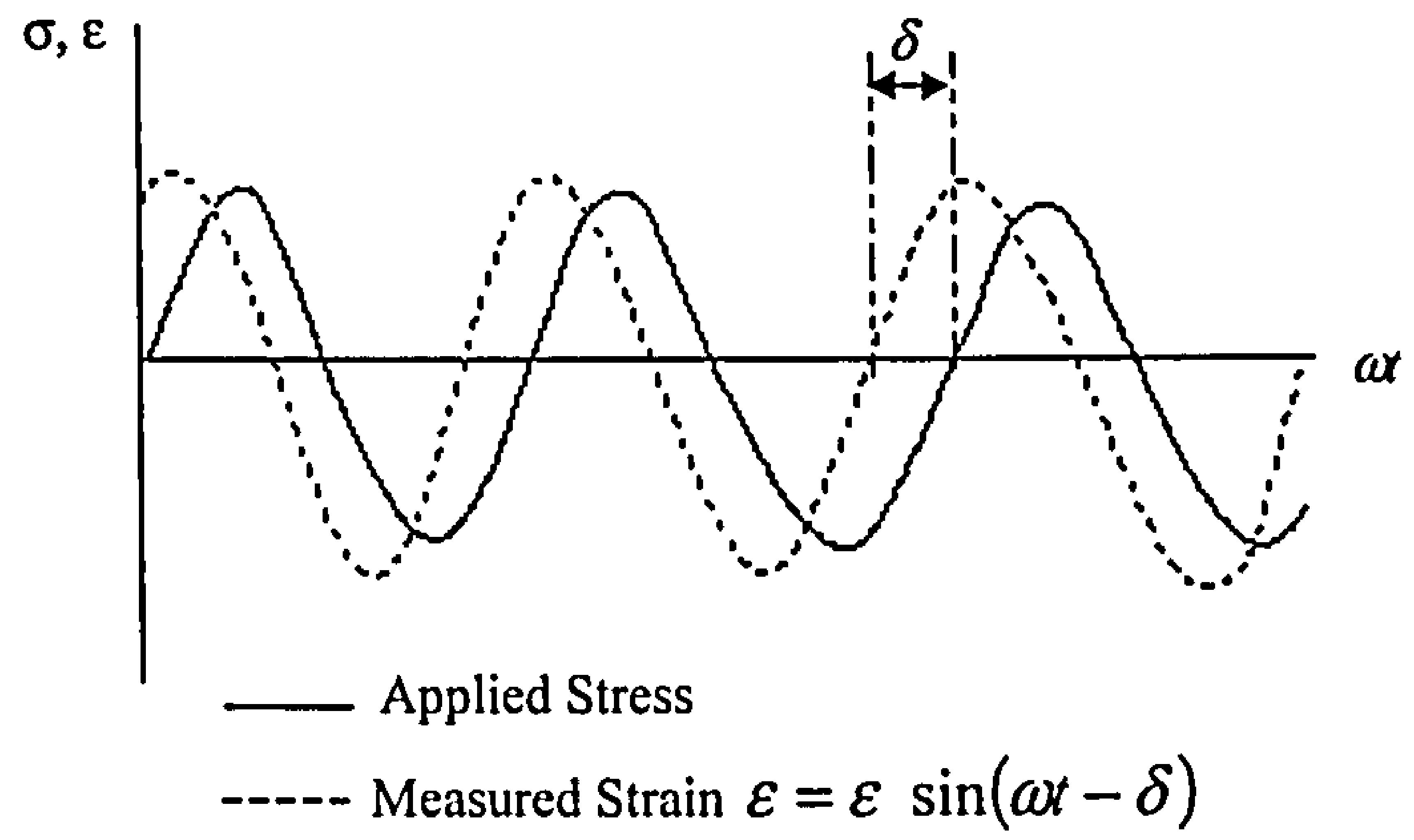

Figure 5.6 Schematic illustration of the stress-strain relationships during application of a sinusoidal stress in DMA testing

When the polymer is in its glassy state, the modulus E_1 is large and the loss modulus E_2 is small. Conversely, when the polymer is rubbery, both the modulus E_1 and loss modulus E_2 are small [20,23]. However, at the glass transition temperature, a sharp drop in the storage modulus E_1 occurs, and the loss modulus attains a maximum value. The glass transition temperature is usually selected from DMA measurements as the temperature at which $\tan\delta$ attains a maximum value [20,61,62].

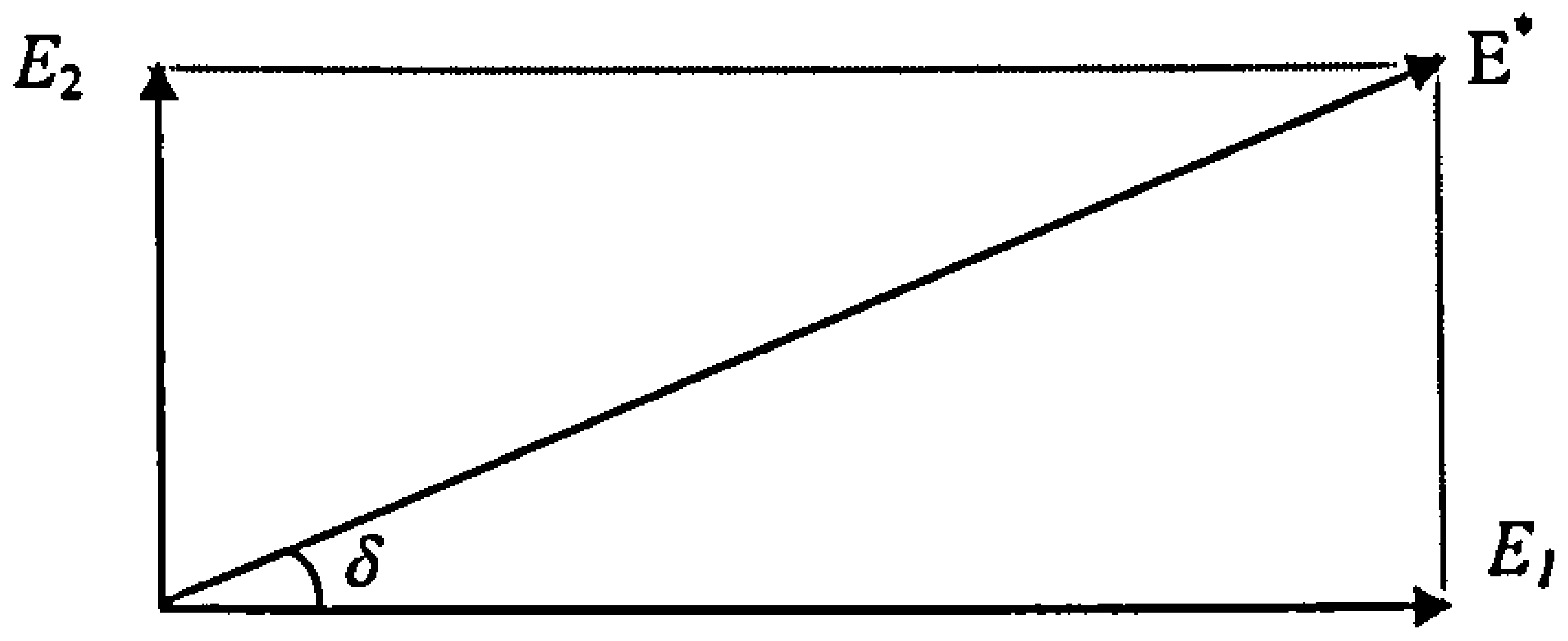

Figure 5.7 The complex modulus $E^*=E_1+iE_2$ and $\tan\delta=E_2/E_1$

The DMA measurements were carried on a cylindrical sample of diameter and height equal to 5mm and 2mm respectively. The sample was machined from a polycarbonate block produced using the SLS machine parameters reported in Section 3.2. In the test, the sample was subjected to a static force equal to 50mN and a dynamic force equal to 20mN at a frequency of 1Hz. The temperature of the specimen was increased during the test from 2°C to 250°C at a rate of 5°C/min. The variation in $\tan\delta$ with temperature, experimentally obtained, is illustrated in Figure 5.8. The figure shows that $\tan\delta$ achieves a maximum value at 175°C. That temperature was considered in further stress models to be the temperature above which thermal stresses are negligible.

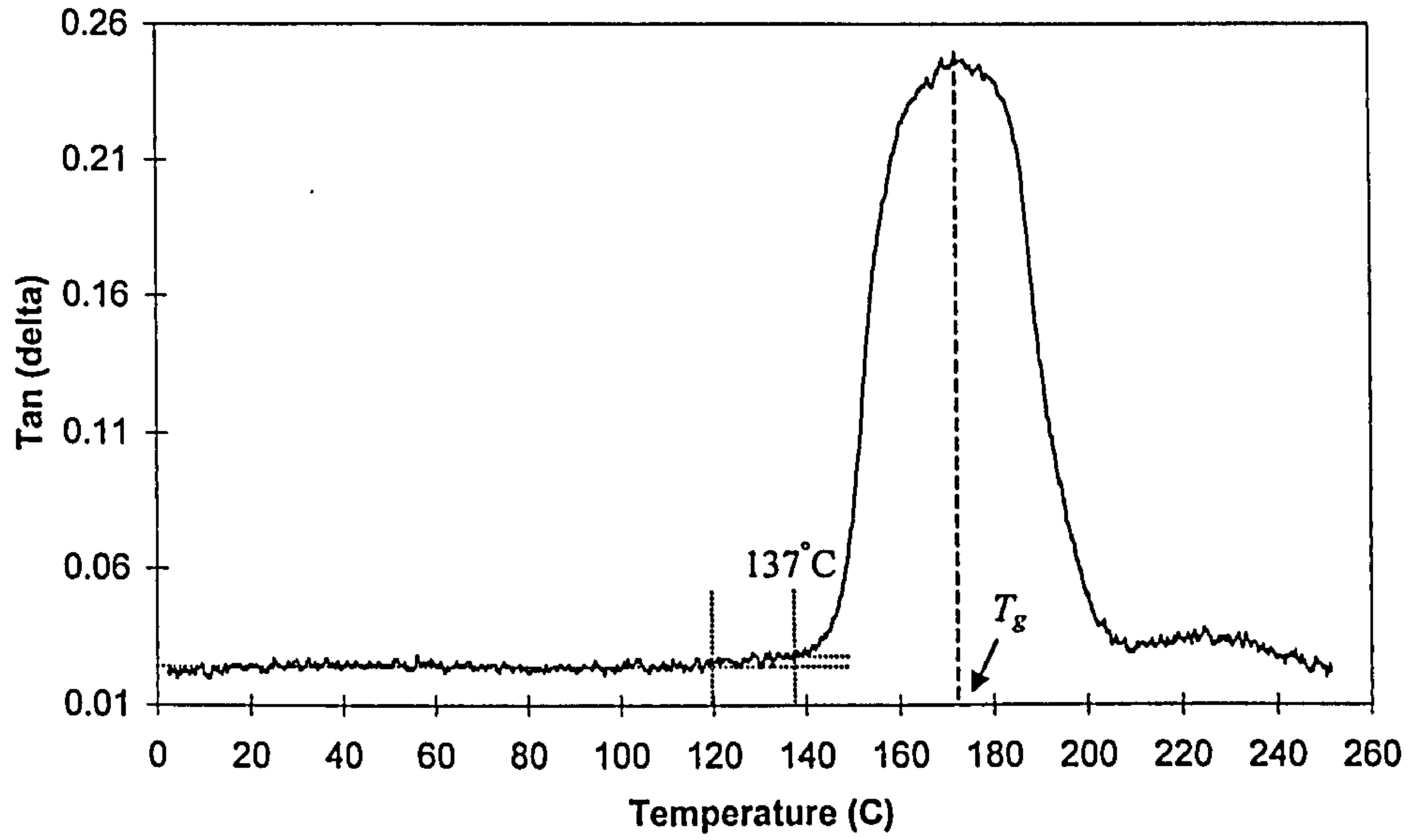

Figure 5.8 *Tan (δ)* against temperature measured using a DMA for an SLS fabricated polycarbonate sample.

The results in Figure 5.8 show an approximately constant value for *tanδ* below 120°C. However, a slight increase in *tanδ* is seen in the temperature range from 120°C to 137°C. In addition, as the temperature exceeded 137°C, a noticeable rise in *tanδ* was displayed. The rise in *tanδ* at 137°C most probably indicates the start of the glass transition region at that temperature. This almost agrees with the DSC measurements illustrated in Figure 5.4, which identified 136°C to be the temperature at which the transition starts. Comparison between DSC and DMA measurements in Figures 5.4 and 5.8 respectively is applicable, as it was reported that 1Hz DMA measurements can correspond to those obtained from a DSC test performed at a heating rate equal to 40°C/min [20]. However, the β transition noticed in the DSC measurements is not clearly visible in Figure 5.8. The reason being that the β transition is very sensitive to the frequency at which the DMA test is carried out, whereas T_g measurements are relatively less sensitive to frequency [59].

5.3.2.2 Instantaneous Modulus of Elasticity Measurements

The "instantaneous" modulus was measured through tensile tests carried out on SLS polycarbonate specimens fabricated using the machine parameters reported in

Section 3.2. However, it must be emphasised that material properties of SLS fabricated parts are generally anisotropic. Tensile tests performed in a previous study [29] showed that the tensile strength along the scanning direction is generally higher than that perpendicular to the scanning direction. The latter was reported to be dependent on the scan spacing selected; the larger the scan spacing, the less bonding between parallel scans occurs resulting in lower tensile strength. Deformation of the ten-layer parts investigated in the 2D stress models is that seen in the *x-z* plane with the laser scanning along the *x*-direction (see Figure 4.16), i.e. the elastic modulus perpendicular to the scanning paths (*y*-direction) was not of interest. The specimens used in the tensile tests were therefore fabricated so that modulus measurements were made parallel to the laser scanning direction, as illustrated in Figure 5.9.

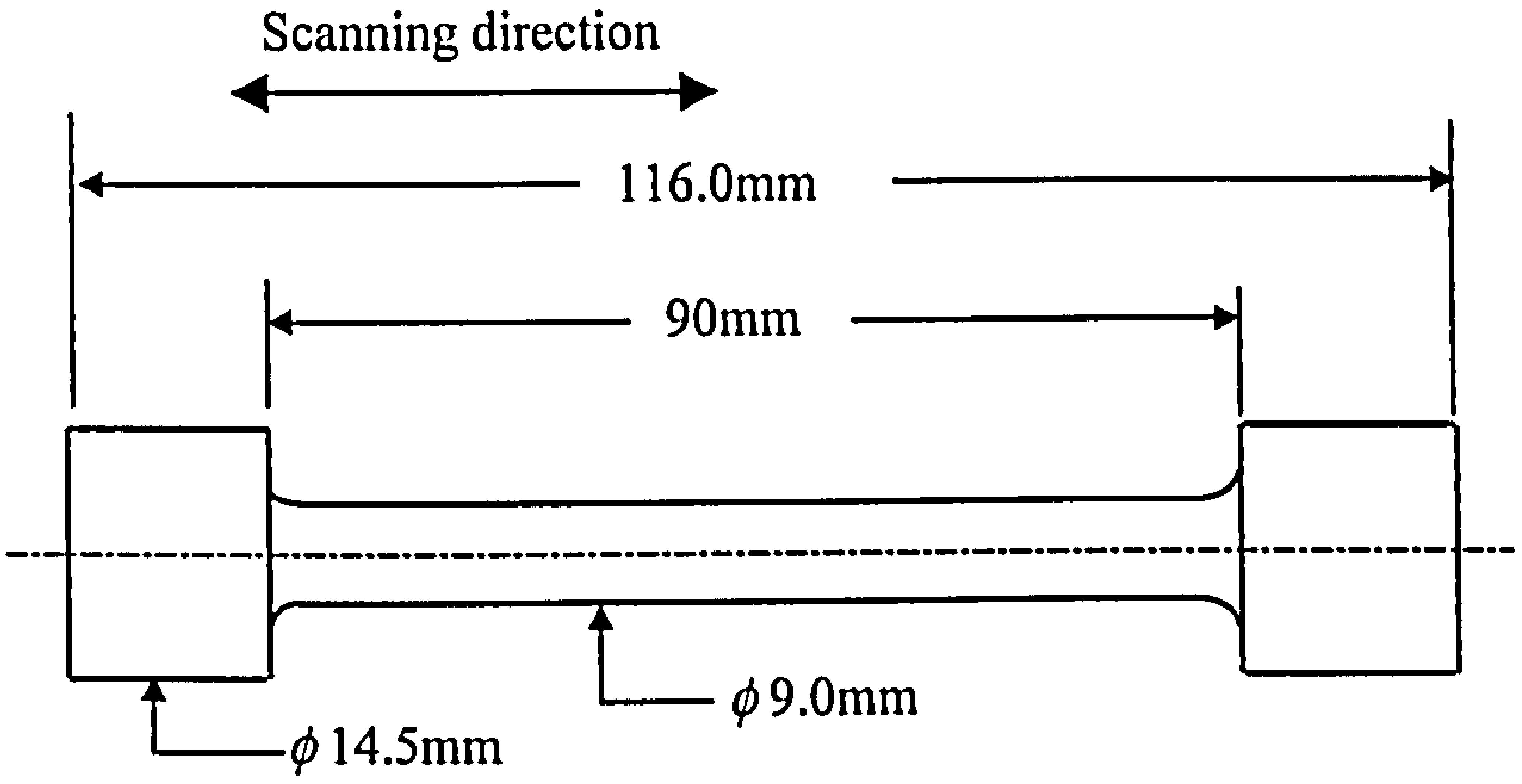

Figure 5.9 Schematic diagram of the SLS polycarbonate specimens produced for the tensile and stress relaxation tests.

The tensile tests were carried out using an Instron 4500. The tests were performed at 20°C, 120°C, 135°C, 140°C, 145°C, 147°C and 150°C. An oven, a Harvard/LTE chamber, was used to heat a specimen to the desired temperature and maintain it at that temperature throughout the test. The oven was positioned at the centre of the tensile test machine in an arrangement illustrated in Figure 5.10. Once the temperature in the oven had reached the desired temperature, the specimen was maintained at that temperature for 30 minutes prior to the tensile test taking place. That was made to ensure that the temperature within the specimen was uniform. In the tensile tests, stretching of the specimens was performed at a constant ramp rate equal to 0.25mm/second.

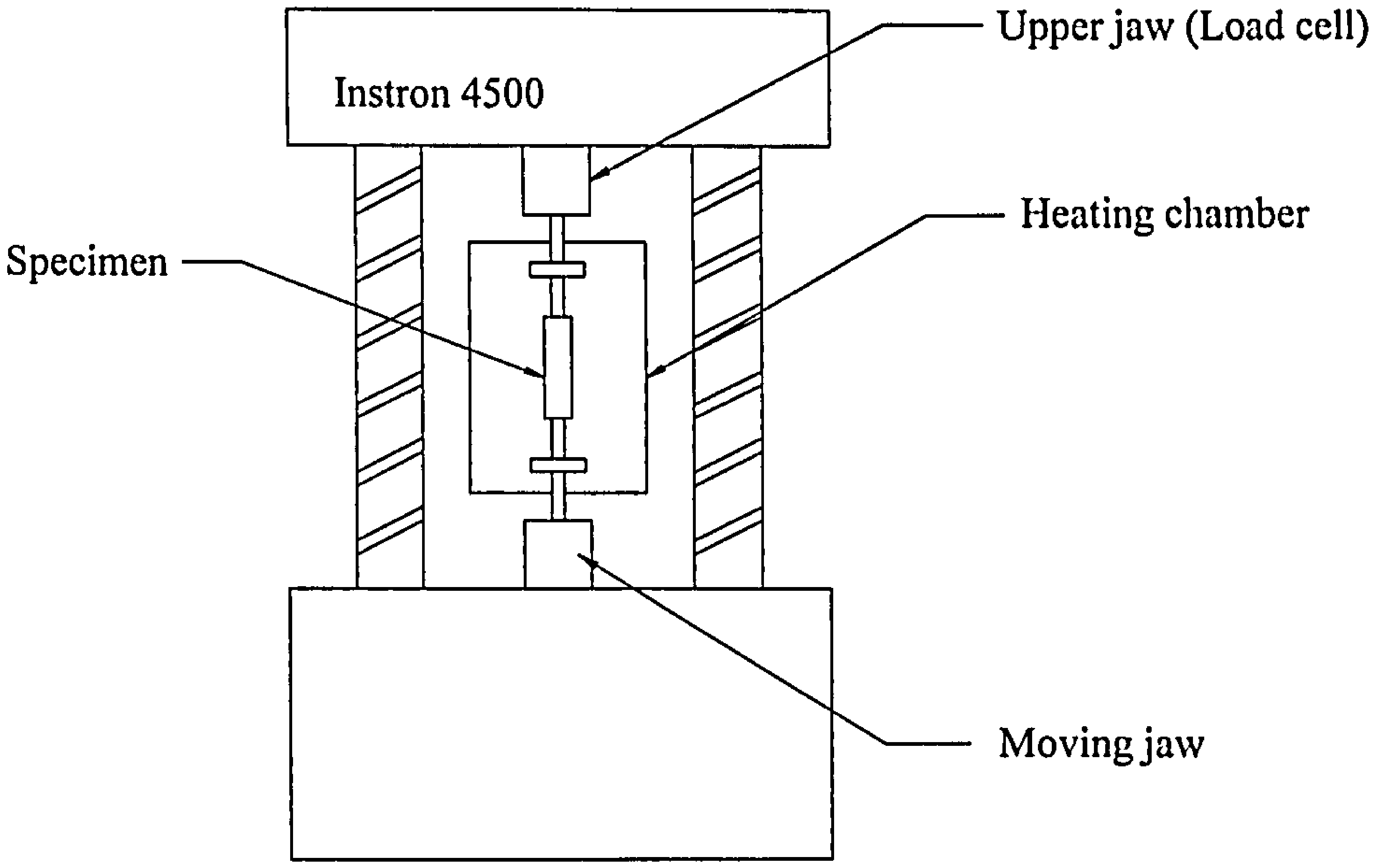

Figure 5.10 Schematic diagram of the tensile test arrangement.

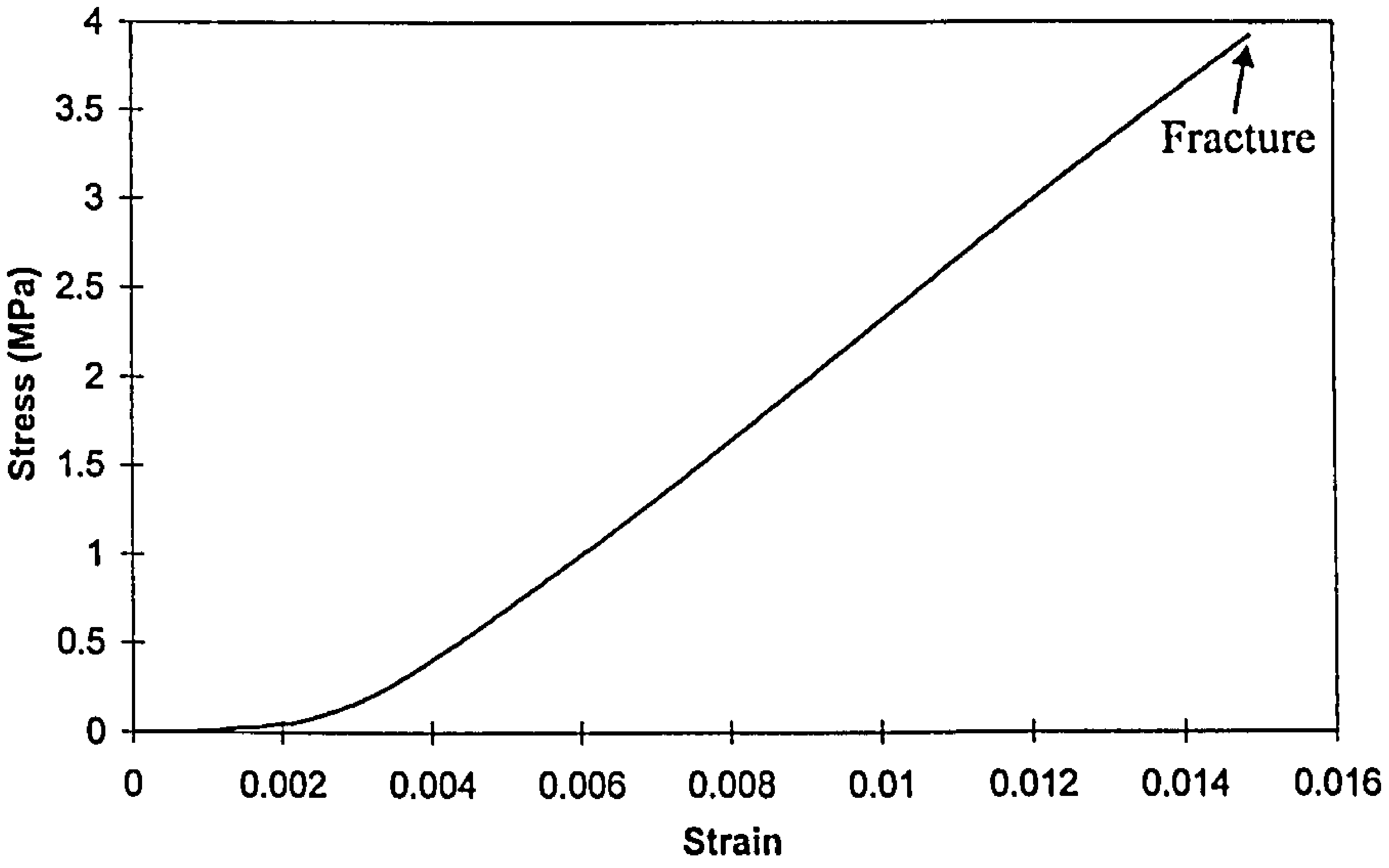

Figure 5.11 Stress-Strain curve for the polycarbonate specimen tested at 20°C.

The stress-strain curve experimentally obtained at 20°C is illustrated in Figure 5.11. The figure shows that an amount of strain was recorded at the early stages of the test with no corresponding stress detected. The reason being that the specimen was not initially preloaded prior to the test starting. The stress-strain curve in Figure 5.11 shows that the polymer specimen had behaved similar to a brittle solid; the stress rises linearly with strain followed by sudden fracture. The "instantaneous" elastic modulus was estimated by measuring the slope of the (linear) stress-strain curve, which gave an elastic modulus equal to 329.3MPa.

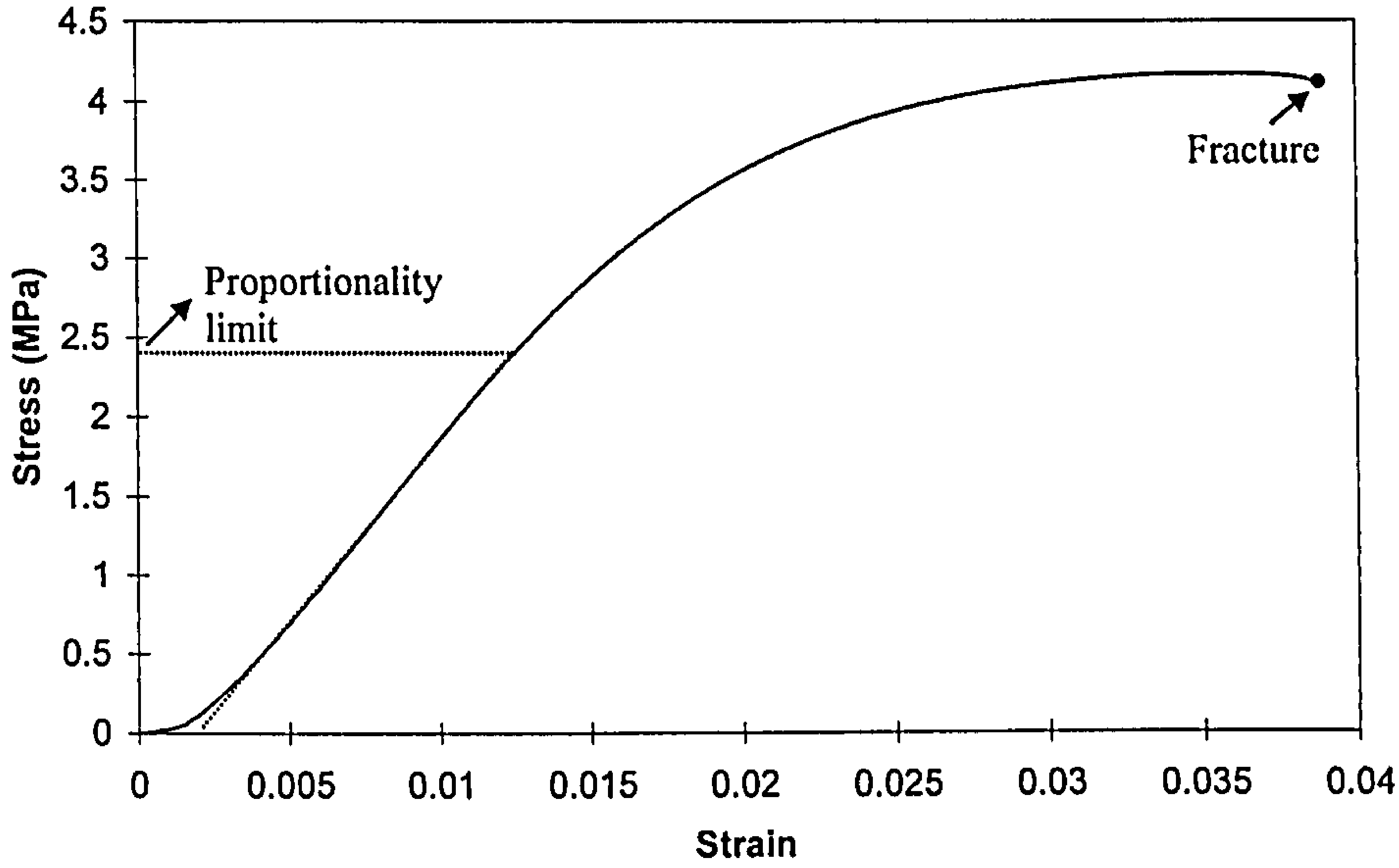

Figure 5.12 Stress-Strain curve for the polycarbonate specimen tested at 120°C

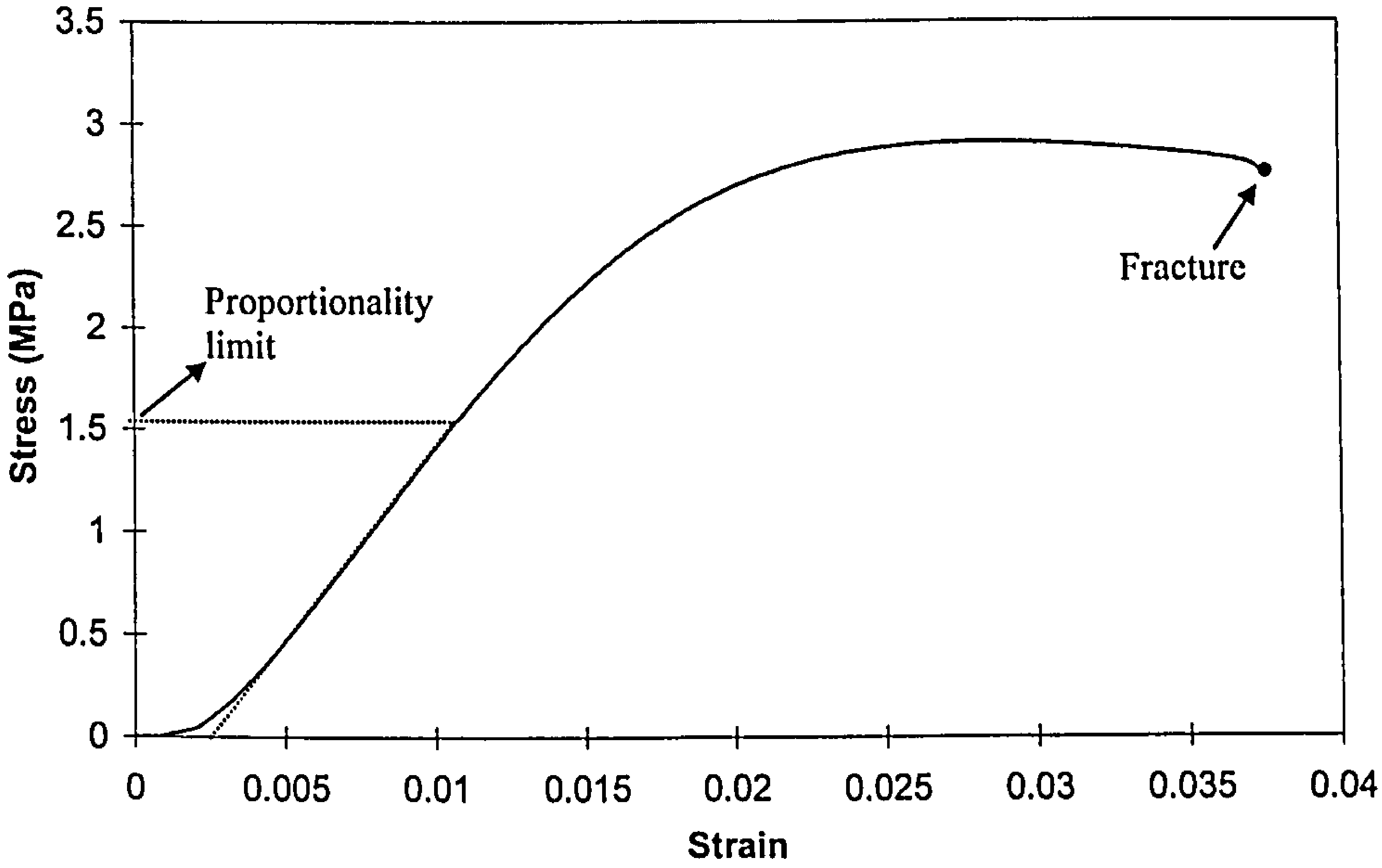

Figure 5.13 Stress-Strain curve for the polycarbonate specimen tested at 135°C

Figures 5.12 and 5.13 show the stress-strain curves experimentally obtained at 120°C and 135°C respectively. The curves reveal a gradual change from a linear to a non-linear region. The yield points in the curves are also not identifiable. The proportionality limit is estimated as the maximum stress, beyond which the relation between the stress and the strain is no longer linear. The "immediate" elastic modulus was calculated as the slope of the linear portion of the stress-strain curve, giving moduli values at 120°C and 135°C equal to 221.2MPa and 204MPa respectively.

Figure 5.14 illustrates the stress-strain curve experimentally obtained at 140°C. On the initial elongation of the specimen, the curve shows an increase in stress with the increase in strain (Points A to B in Figure 5.14). Further elongation of the specimen, however, is accompanied by decline in stress followed by fracture of the specimen at point C. The reduction in stress beyond point B most probably indicates that necking had occurred at a particular cross section of the specimen, and thus lower force was required to continue deformation. The "immediate" elastic modulus at 140°C was estimated by measuring the slope of the linear portion of the stress-strain curve, seen at the initial elongation the specimen, which gave a modulus value equal to 106MPa.

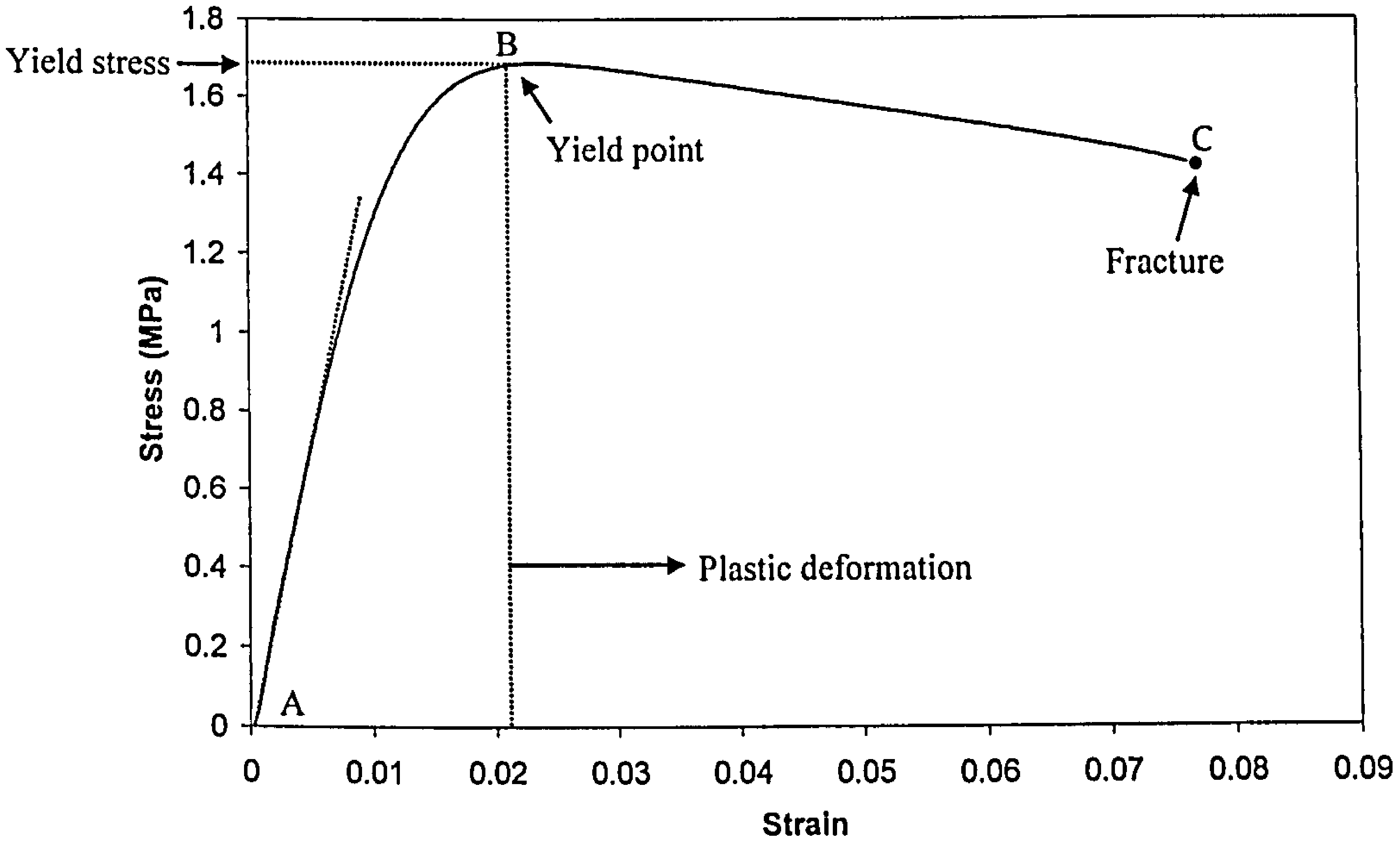

Figure 5.14 Stress-strain curve for the polycarbonate specimen tested at 140°C

Figure 5.15 shows the stress-strain curve experimentally obtained at 145°C. On the initial elongation of the specimen, the polymer behaved similar to an elastic solid; stress rising linearly with strain (Points A to B in Figure 5.15). Further elongation of the specimen, however, showed a slight increase in stress (Points B to C). That is expected to be a sign of uniform plastic deformation of the specimen, which results from polymer chains stretching, rotating, disentangling and sliding past one another under the application of strain [21]. Additional stretching of the specimen (beyond point C) is accompanied by decrease in stress followed by fracture of the specimen at point D. The start of the decrease in stress at point C is expected to indicate that uniform plastic deformation of the specimen had stopped. Further stretching of the specimen is therefore believed to have resulted in the formation of a neck, requiring less load to continue deformation of the specimen. The "immediate" elastic modulus of the specimen at 145°C is calculated by measuring the slope of the linear elastic region of the stress-strain curve, giving a value of the elastic modulus equal to 61MPa.

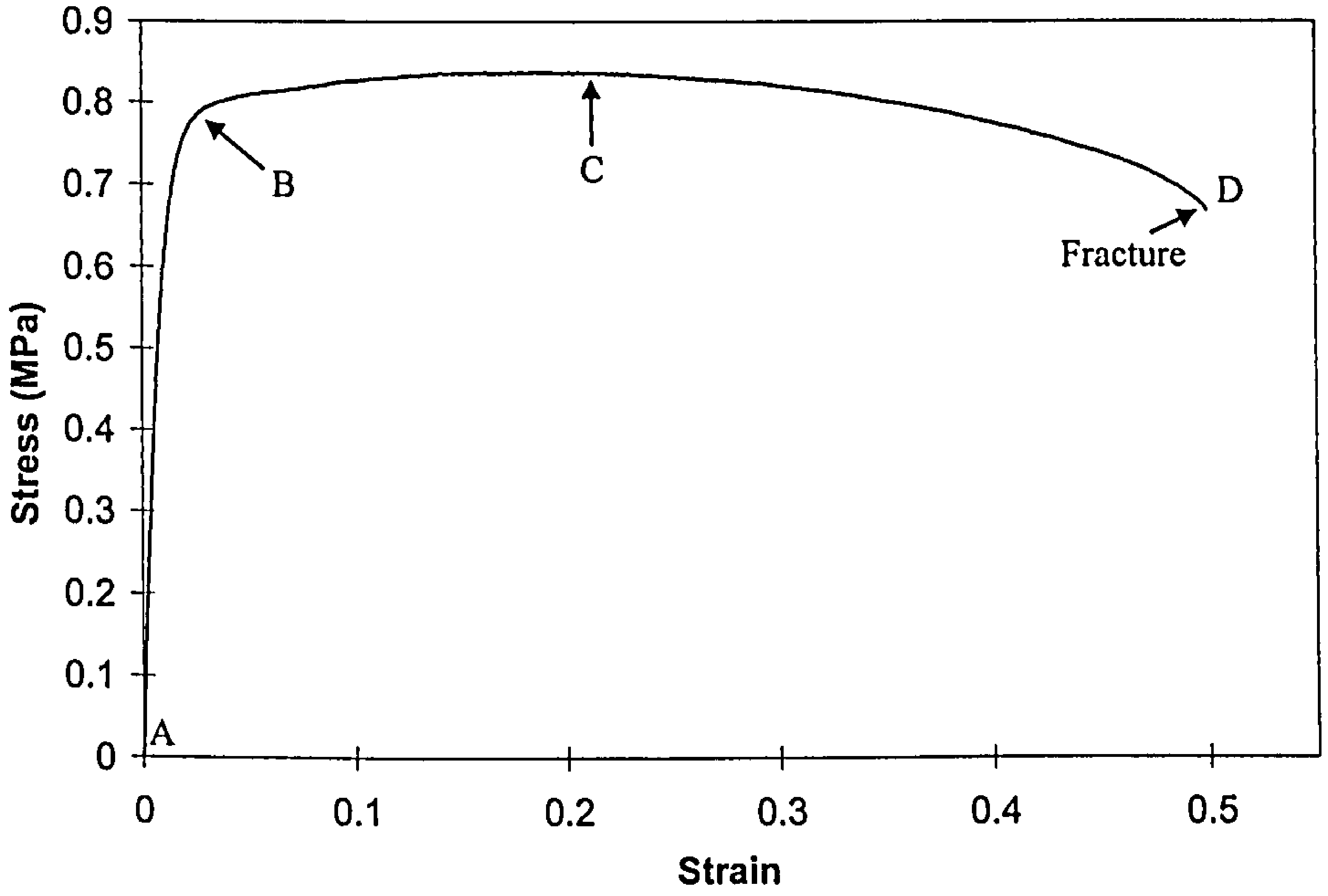

Figure 5.15 Stress-Strain curve for the polycarbonate specimen tested at 145°C.

Figures 5.16 and 5.17 illustrate the stress-strain curves experimentally obtained at 147°C and 150°C respectively. The curves do not show the entire stress-strain results to the point of fracture. The reason being that the specimens were stretched to the maximum elongation allowed by the tensile test machine with no fracture of the specimens occurring. Emphasis was therefore given in Figures 5.16 and 5.17 to illustrate the regions where elastic and initial plastic deformations of the specimens took place. On the initial elongation of the specimens at 147°C and 150°C, the curves displayed a steady increase in stress with strain (points A to B in Figures 5.16 and 5.17). However, further elongation of the specimens, beyond Point B, was also accompanied by an increase in stress. In that region, uniform plastic deformation of the specimens is expected to have occurred. The stretching, rotating, sliding and disentangling of the polymer chains under the application of strain are expected to be facilitated by the high temperatures at which the tests were performed. As the cross-sectional area of the specimens uniformly reduced, the polymer chains are expected to have transformed from being intertwined to becoming almost parallel and close together. In this condition, Van der Waals bonding between the most closely-aligned chains requires higher loads to complete deformation and fracture of the specimens [21]. The "immediate" elastic moduli at these temperature were calculated by measuring the slopes of the linear portions of the stress-strain curves, obtained at the start of elongation, giving immediate moduli values at 147°C and 150°C equal to 38.4MPa and 11.8MPa respectively.

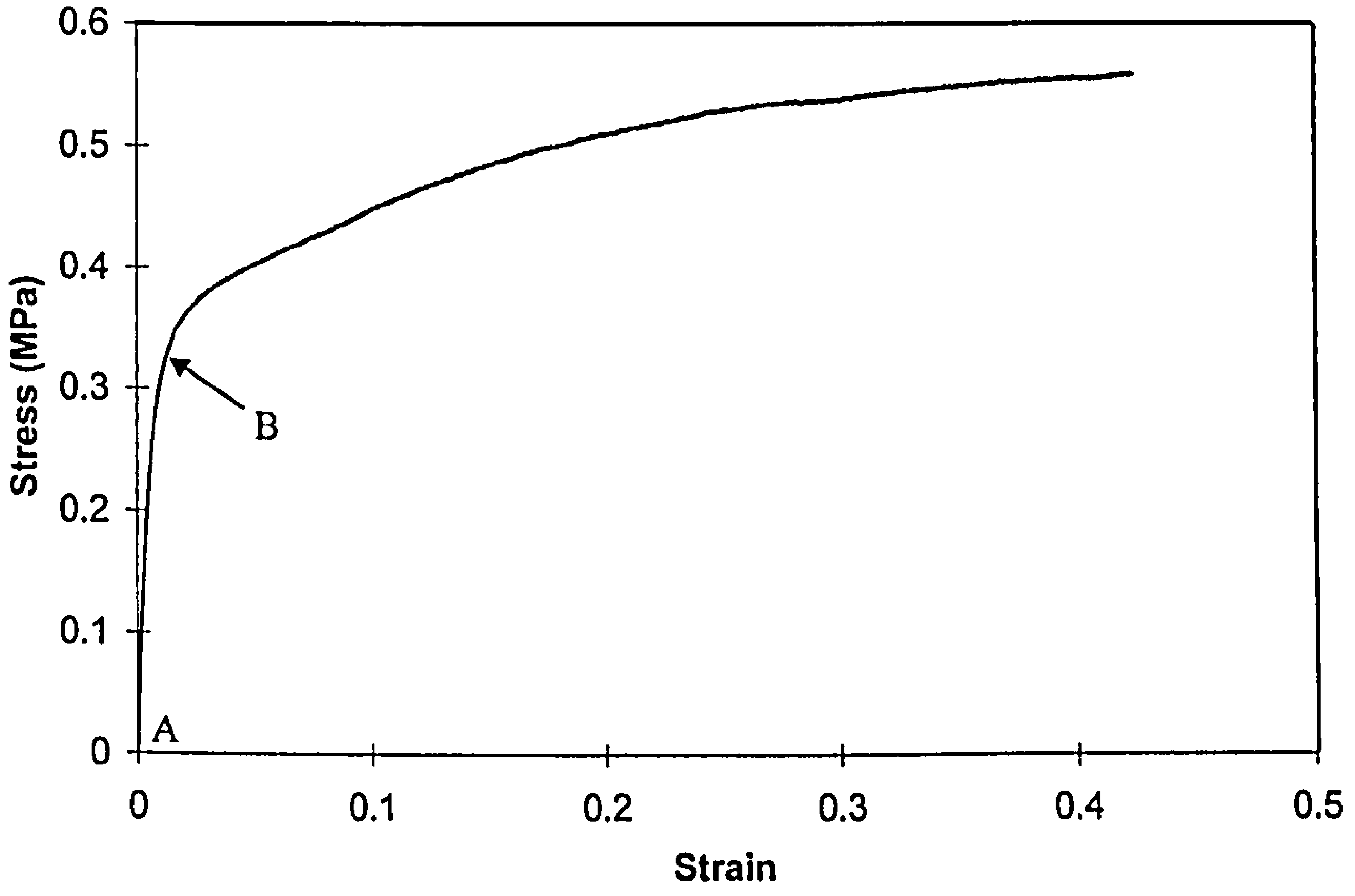

Figure 5.16 Stress-Strain curve for the polycarbonate specimen tested at 147°C.

Additional tensile tests were carried out at 155°C and 160°C. In the tests, the specimens were stretched to the maximum elongation allowed by the tensile test machine with no fracture of the specimens occurring. However, no values of the change in load were recorded during the tests. That was because the loads were too small to be detected by the load cell used on the tensile test machine.

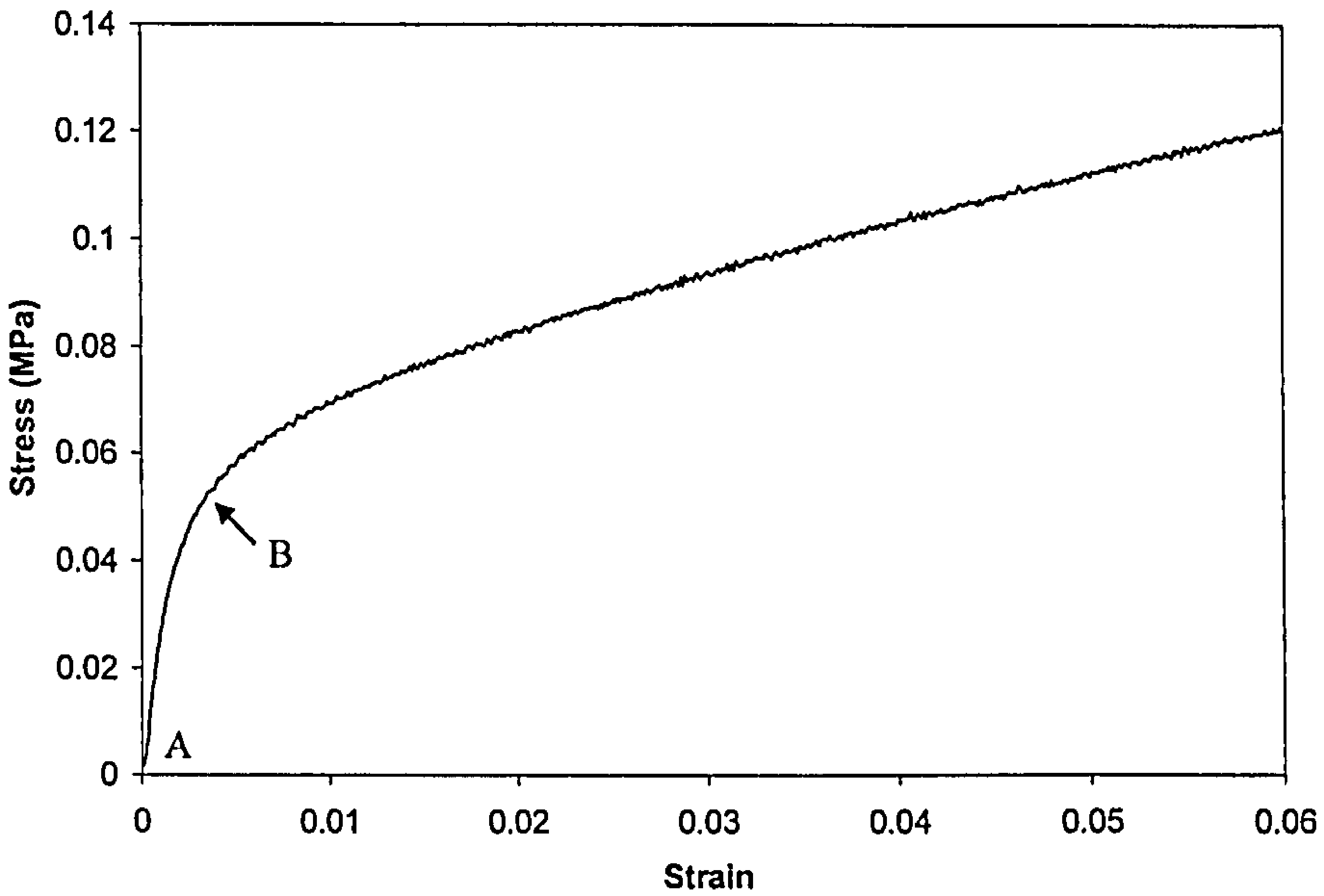

Figure 5.17 Stress-Strain curve for the polycarbonate specimen tested at 150°C

The values of the "instantaneous" elastic modulus obtained experimentally at 20°C, 120°C, 135°C, 140°C, 145°C, 147°C and 150°C are summarised in Table 5-1. The modulus values, in the table, is seen to reduce with the increase in temperature. Based on DSC and DMA measurements, the starting temperature of the glass transition region is approximately equal to 137°C (see Sections 5.3.1.3 and 5.3.2.1), and thus the polymer at 20°C, 120°C and 135°C is initially in a glassy state. Consequently, reduction in the modulus with the increase in temperature, whilst the polymer is in that state, is most probably due to secondary transitions occurring during the heating of the specimen to the desired temperature. However, the polycarbonate specimens at 140°C, 145°C, 147°C and 150°C are in the glass transition region, and the modulus is therefore highly dependent on changes in temperature (see Figure 2.24). For example, moduli values listed in Table 5-1 at 135°C and 140°C differed by approximately 48%, whereas the moduli at 120°C and 135°C (with the polymer in a glassy state) differed by less than 8%. Additionally, the modulus of the polymer in the glass transition region is seen to be more sensitive to changes in temperature as the temperature is increased. For example, an increase in temperature by 5°C, from 140°C to 145°C, showed a reduction in modulus by 42.5%, whereas the increase in temperature from 145°C to 150°C showed the modulus to reduce by 81%.

Temperature (C°)	20	120	135	140	145	147	150
Modulus (MPa)	329.3	221.4	204	106	61	38.4	11.8

Table 5-1 Values of the modulus estimated using the stress-strain curves in Figures 5.11 to 5.17

5.3.2.3 Stress Relaxation Tests

In the following, the stress relaxation tests performed to examine the time-dependent response of SLS fabricated polycarbonate parts are described. In a stress relaxation test, a specimen is subjected to a constant strain and the decay in the load required to maintain that strain is recorded over a period of time. Provided that the strain applied in the test is small, the stress and strain can be directly related using Hooke's law [23]. Consequently, the decay in modulus $E(t)$ during the test can be written in terms of decay in stress $\sigma(t)$ as $E(t)=\sigma(t)/\varepsilon$, where ε is the constant strain applied and t is the relaxation time.

The stress relaxation tests were performed at 135°C, 140°C, 145°C and 147°C. The polycarbonate specimens used in the test (see Figure 5.9) were fabricated using the SLS machine parameters reported in Section 3.2. In the tests, emphasis was given to ensure that the specimens were in an elastic state, immediately following their initial elongation. Thus, the load applied during the initial elongation of the specimen was ramped to a value, selected to correspond to a stress equal to one-third of the proportionality limit estimated from the tensile test measurements performed at that temperature (see Section 5.3.2.2). Once that load was achieved, the corresponding strain was held constant for the remaining period of the stress relaxation test. The initial elongation of the specimens was performed at a ramp rate equal to 0.25mm/second.

Figure 5.18 shows the stress relaxation (modulus-time) curve experimentally obtained at 147°C. In the figure, the modulus is seen to reduce with time in the first 12 seconds of the test. Thus, the behaviour of the polymer was time-dependent during that period, i.e. the polymer was viscoelastic. However, following 12 seconds from the start of the test, the polymer attained a constant modulus. Therefore, the behaviour of the polymer was time-independent during that period, i.e. the polymer was in a rubbery state. The (modulus-time) curves obtained experimentally at 145°C and 140°C, illustrated in Figures 5.19 and 5.20 respectively, also show signs of polymer transformation from viscoelastic to rubbery during stress relaxation. However, the time it took the polymer to transform from viscoelastic to rubbery differed in relation to the temperature that the stress relaxation test was performed. The specimen tested at 145°C, for example, took 30 seconds to relax to a rubber state whereas that tested at 140°C took 20 minutes to relax.

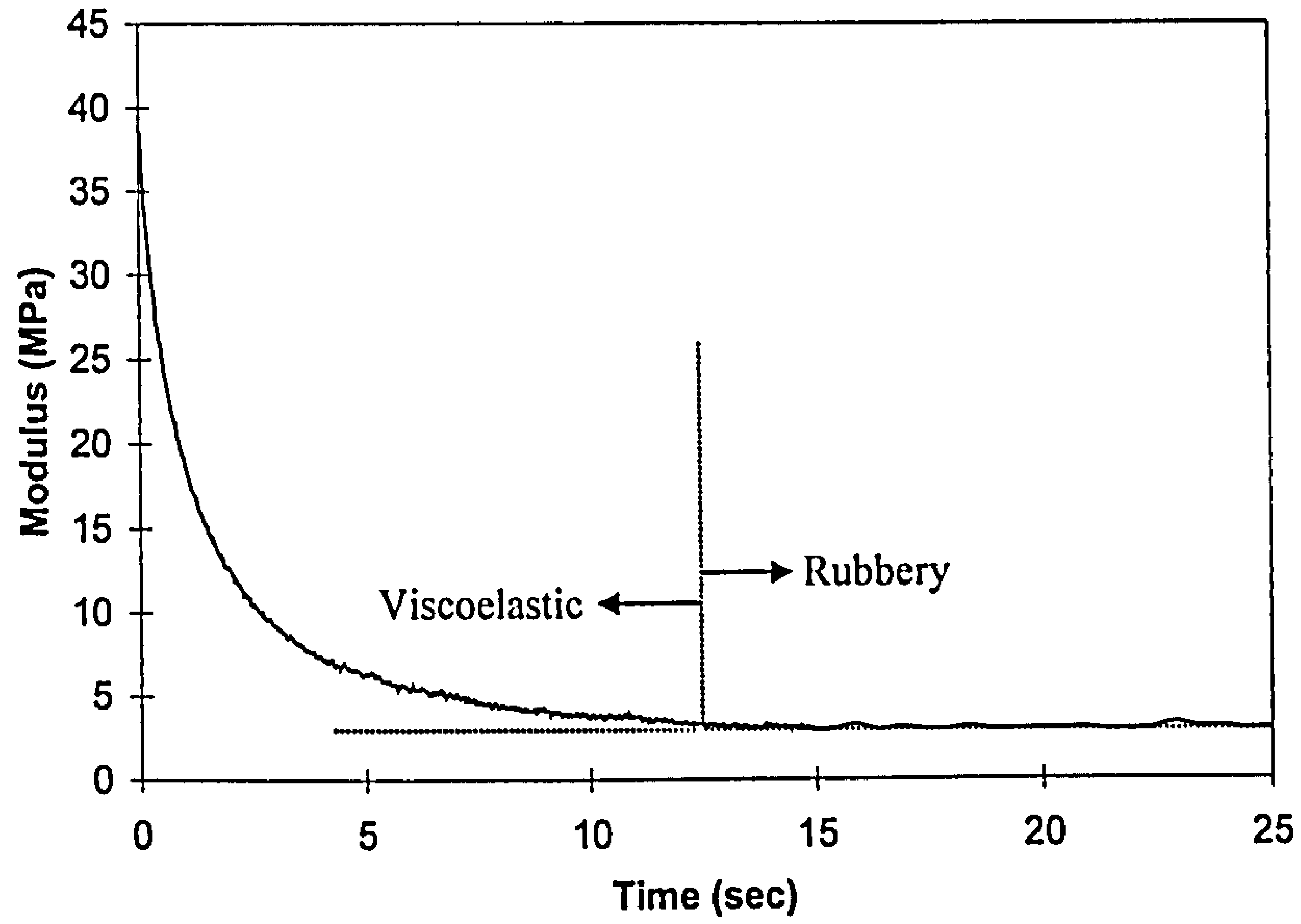

Figure 5.18 Modulus-time stress relaxation curve for the polycarbonate specimen tested at 147°C.

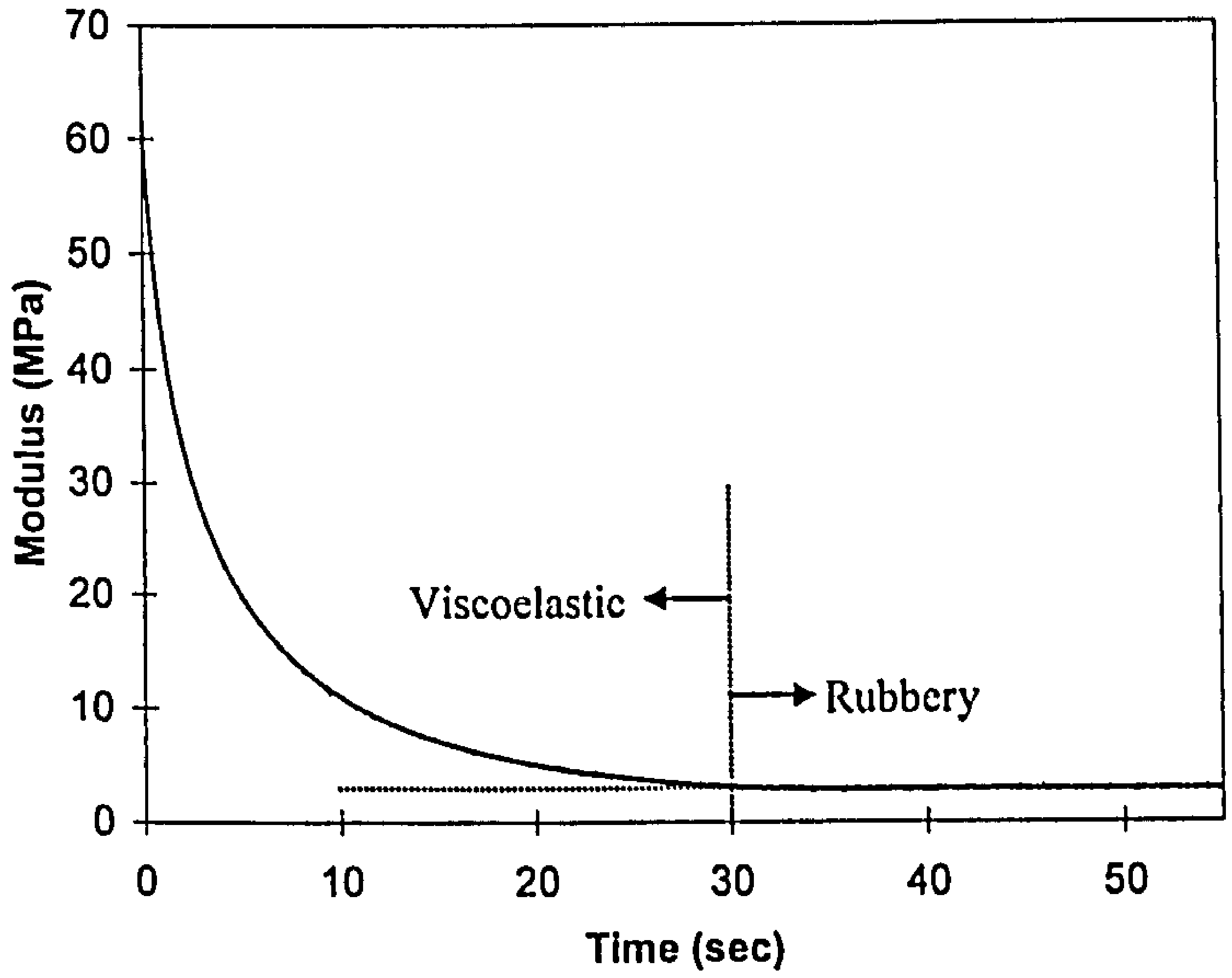

Figure 5.19 Modulus-time stress relaxation curve for the polycarbonate specimen tested at 145°C

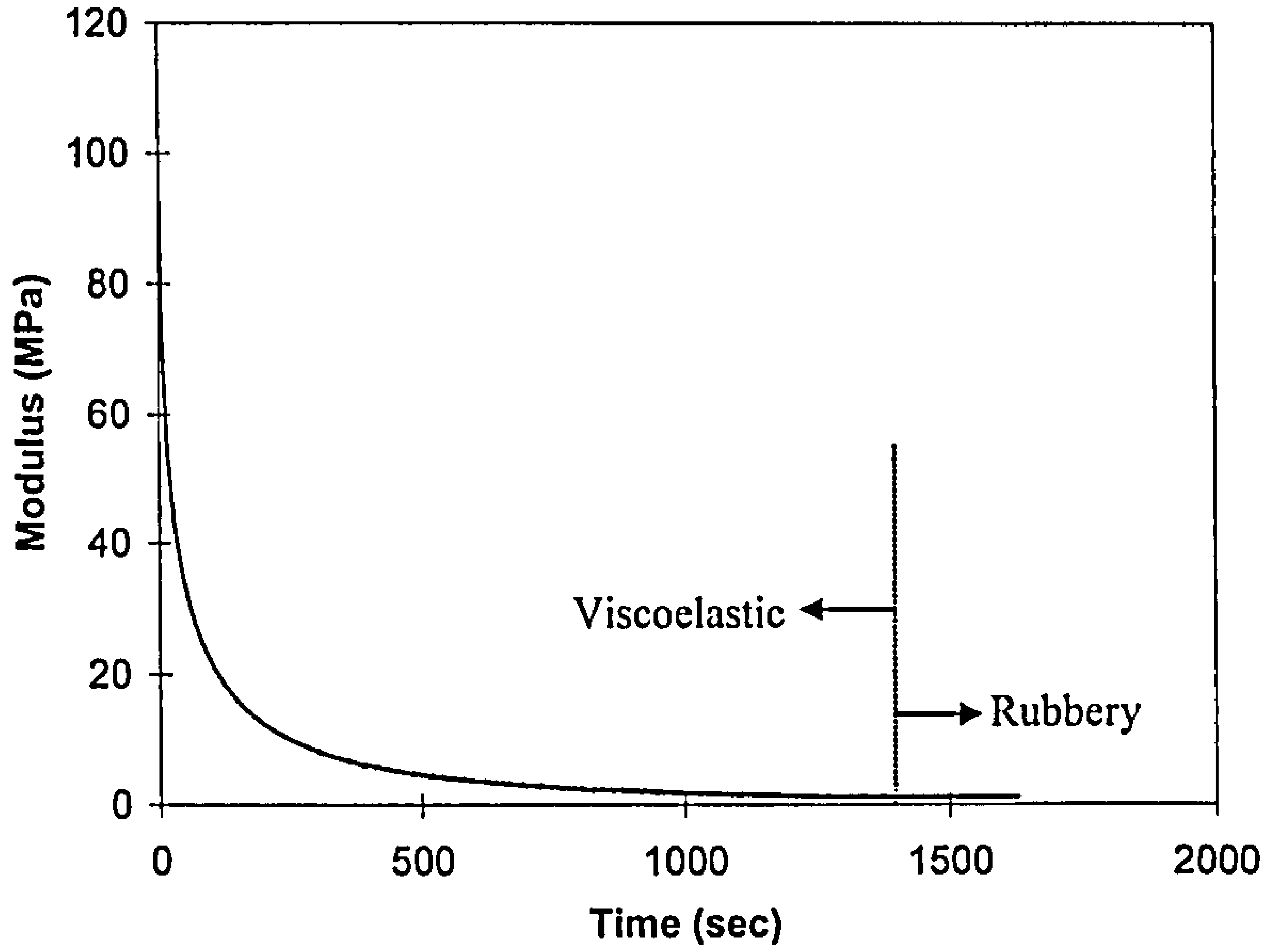

Figure 5.20 Modulus-time curve for the stress relaxation test at 140°C

Figure 5.21 shows the (modulus-time) curve obtained during the stress relaxation test performed at 135°C. The figure shows a continuous decay in modulus even after one hour and 45 minutes from the start of the test i.e. the polymer remained viscoelastic during that period.

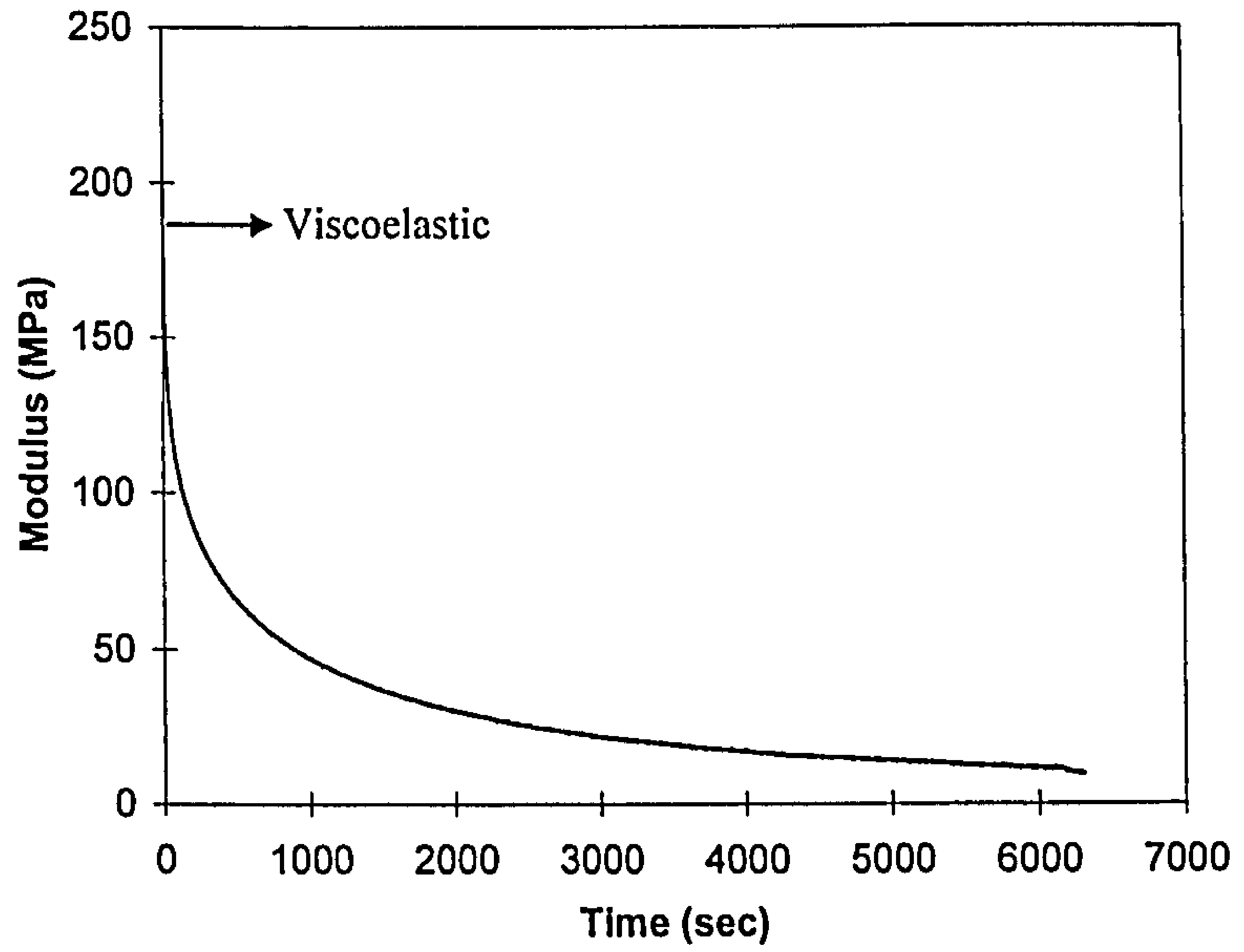

Figure 5.21 Modulus-time curve for the stress relaxation test at 135°C

An additional stress relaxation test was performed at 150°C. However, the decay in load with time was too fast to be recorded. Moreover, the loads during the test were too small to be detected by the load cell used in the stress relaxation test. The periods it took the specimens to transform from a viscoelastic state to rubbery during the stress relaxation tests performed at 147°C, 145°C, 140°C and 135°C are summarised in Table 5-2. The results in the table demonstrate that the period required by the polymer to relax to its viscoelastic state is highly dependent on temperature; the lower the temperature, the longer it takes the polymer to relax and vice versa.

Temperature (°C)	147	145	140	135
Relaxation time from viscoelastic to rubbery (seconds)	12	30	1200	> 6300

Table 5-2 Times required for the polymer to transform from viscoelastic to rubbery in the stress relaxation tests performed at 147°C, 145°C, 140°C. At 135°C the polymer remained viscoelastic even after 6300 seconds.

5.3.2.4 Measurement of the Coefficient of Friction

In the following, the method used to measure the friction coefficient is introduced. The aim of the measurements was to estimate a friction coefficient to be used as input to the stress models at the interface between the bottom surface of the (modelled) ten-layer part and the powder bed underneath. The apparatus employed in friction coefficient measurements is the sliding machine illustrated in Figure 5.22. A cylindrical sample of 3mm in diameter and 5mm in height was used in the measurements. The sample was machined from a polycarbonate block fabricated using the SLS machine parameters reported in Section 3.2. The sample was positioned in a sample holder, which was then loaded underneath an arm as illustrated in Figure 5.22. The arm was attached to a piezoelectric force transducer by which the output voltage can be converted into force using a known calibration factor. A load of 10N was mounted on top of the specimen as shown in Figure 5.22. The polycarbonate powder was placed in a hollow rectangular container with a closed base. The container was reciprocating during the test by a motor at a controlled (constant) sliding speed equal to 4mm/seconds. The force generated at the contact between the sintered polycarbonate sample and the powder was sensed by the transducer attached to the loading arm which prevents motion of the sample whilst the container was reciprocating.

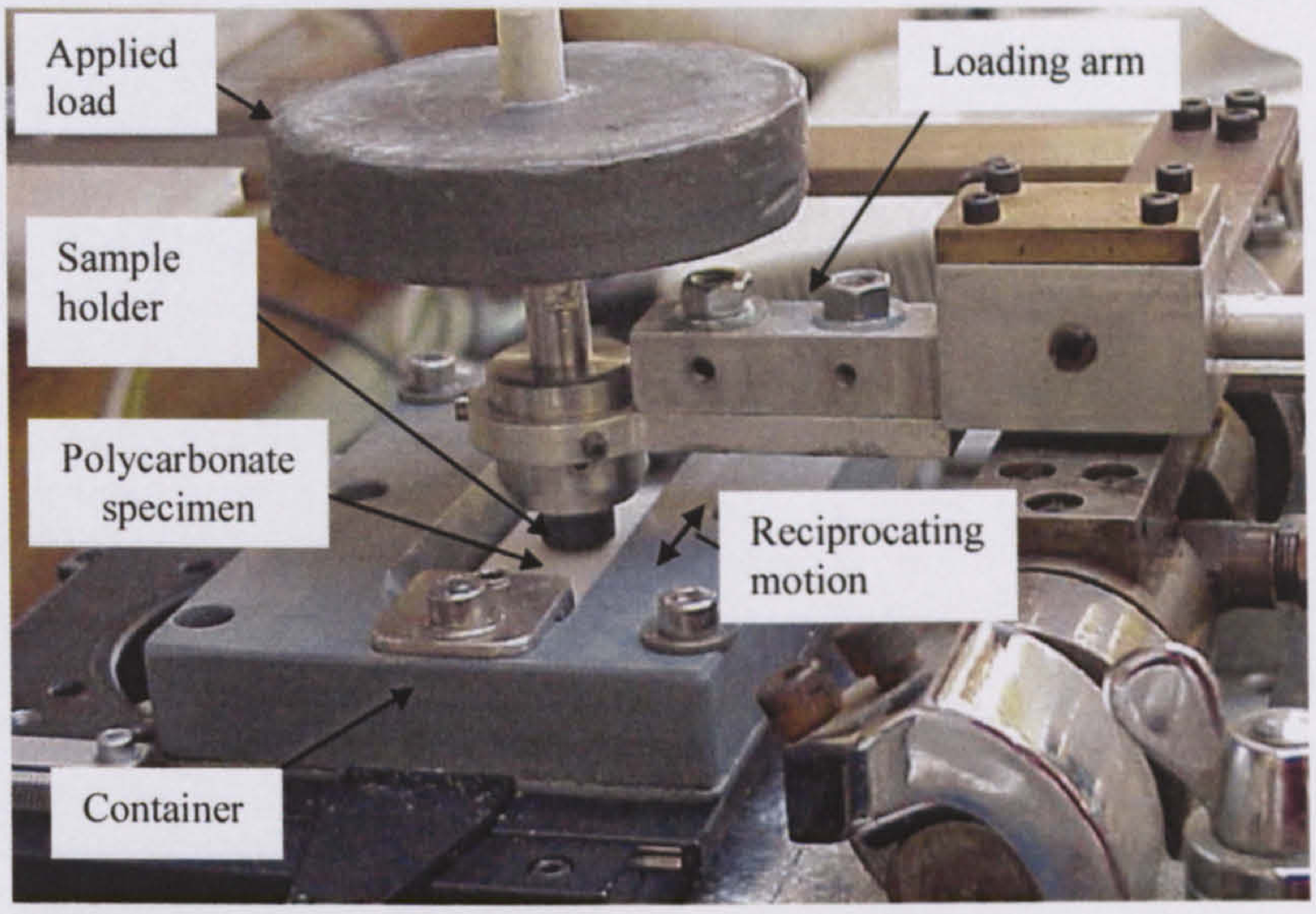

Figure 5.22 Sliding Friction machine used to estimate the friction coefficient of polycarbonate

However, the reciprocating motion of the container resulted in shifting of the powder in the container. Consequently, forces measured by the transducer may have probably included those applied in powder shifting. The alternative approach implemented came with the assumption that the powder particles in the powder bed in contact with the bottom surface of the part do not undergo rolling or sliding during SLS fabrication.

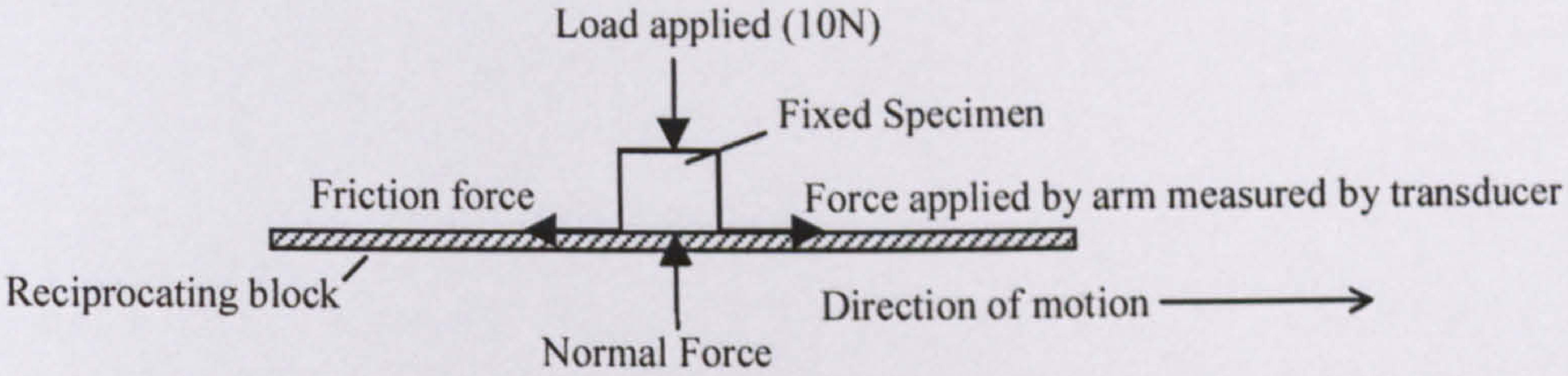

Figure 5.23 Free body diagram of the polycarbonate sample in the sliding friction machine

The powder in the container, used in friction measurements, was therefore replaced with a sintered polycarbonate block, constrained from motion in the container. The block was fabricated using the SLS machine parameters reported in Section 3.2. The force measured by the transducer was that in the middle of the stroke cycle, where the container slides at a constant velocity. A free body diagram of the sample during the test is illustrated in Figure 5.23. As the sample is fixed in position, all forces acting on the specimen must be in equilibrium. Thus, the force applied by the arm (measured by the transducer) is equal to the frictional force, and the normal force applied on the specimen is equal to 10N. The friction coefficient is calculated by dividing the friction force by the normal force giving a friction coefficient equal to 0.38. The value is equal to the reported value of the dynamic friction coefficient of polycarbonate [63]. It must be mentioned that the friction coefficient was measured in the present work at room temperature.

Chapter 6

Further Development of Thermal-Stress Analyses

6.1 Introduction

The initially developed finite element models, described in Chapter 4, focused on the concept of using the sequentially coupled thermal-stress analysis as a method of predicting curl in SLS fabricated parts. However, the models did not produce accurate predictions of curl, presumably as a result of the considerable number of assumptions the models comprised. Attempts were therefore made to further develop the models by considering fewer assumptions for a better prediction of curl to be achieved. The subject of this chapter is to describe the two main stages (second and third) performed to further develop the models. The second stage focused on better simulation of the SLS process with less assumptions made with regard to thermal and mechanical material properties of polycarbonate. The following stage, however, attempted to reduce geometrical assumptions in the heat transfer model by considering thermal effects of the powder bed surrounding the side walls of the sintered part. In the following sections, a detailed description of these stages is given along with results obtained.

6.2 Second Stage of Model Development

The second stage of model development used the sequentially coupled thermal-stress analysis as a method of solution. The most significant development in the second version of the heat transfer model came with the realisation that curl is highly influenced by temperature changes occurring during SLS fabrication (see Section 4.7.5). Therefore, attempts were made in the model to improve simulation of thermal effects occurring during SLS processing. The second version of the stress model, however, focused on better simulation of the viscoelastic behaviour of polycarbonate due to its significant effect expected on part deformation (see Section 4.7.6). In following sections, the second versions of the heat transfer and stress models are described with emphasis given to illustrate the significant improvements performed in these models over the previous ones.

6.2.1 Second Version of Heat Transfer Model

The second version of the heat transfer model focused on improving simulation of thermal effects expected to occur during the "build" and "cooldown" stages in SLS. In this section, improvements made to the model are briefly introduced. In following sections, a detailed description of the model is given with results obtained.

In the "build" stage, layers of powder are added to form the part. During the "build" stage in fabrication of the ten-layer parts, the powder in the feed cartridges was maintained at a temperature equal to 80°C. The top surface of a recently added layer was then heated by the part heater to 150°C prior to sintering of the layer taking place. The improvement made to the second version of the heat transfer model was by defining an initial nodal temperature of elements representing a layer spread during the "build" stage equal to 80°C. Additionally, heating of a recently added layer of powder was simulated by raising the temperature of the nodes located at the top surface of the layer from 80°C to 150°C prior to the application of heat flux on that surface. In the first version of the heat transfer model, however, heating of a recently added layer was not simulated as the initial nodal temperature of elements representing the part was already defined equal to 150°C.

The final stage in SLS is the "cooldown" stage. In that stage, the fabricated ten-layer part was allowed to cool in the chamber until the temperature measured by the IR sensor on the top surface of the part bed was equal to 100°C. The fabricated part was then removed from the chamber and left to cool naturally to room temperature. The second version of the heat transfer model was improved by simulating cooling of the part to room temperature. In the first version of the model, however, the modelled part was only allowed to cool to a final temperature equal to 150°C.

6.2.1.1 Geometry

Geometrical approximations adopted in the first version of the heat transfer model were also implemented in this version of modelling. Thus, the sintered ten-layer part and the portion of the powder bed underneath the part were only modelled. However, the improvement made to the second version of the model was that thicknesses of layers forming the part were defined based on experimental measurements described in Section 5.2. Therefore, the thickness of the first layer of the sintered part was defined in the model equal to 0.59mm. Layers from two to ten, however, were each given a thickness equal to 0.127mm. Additionally, the overall thickness of the powder bed (underneath the part) was defined in the model equal to 14.777mm, estimated using the method illustrated in Figure 6.1.

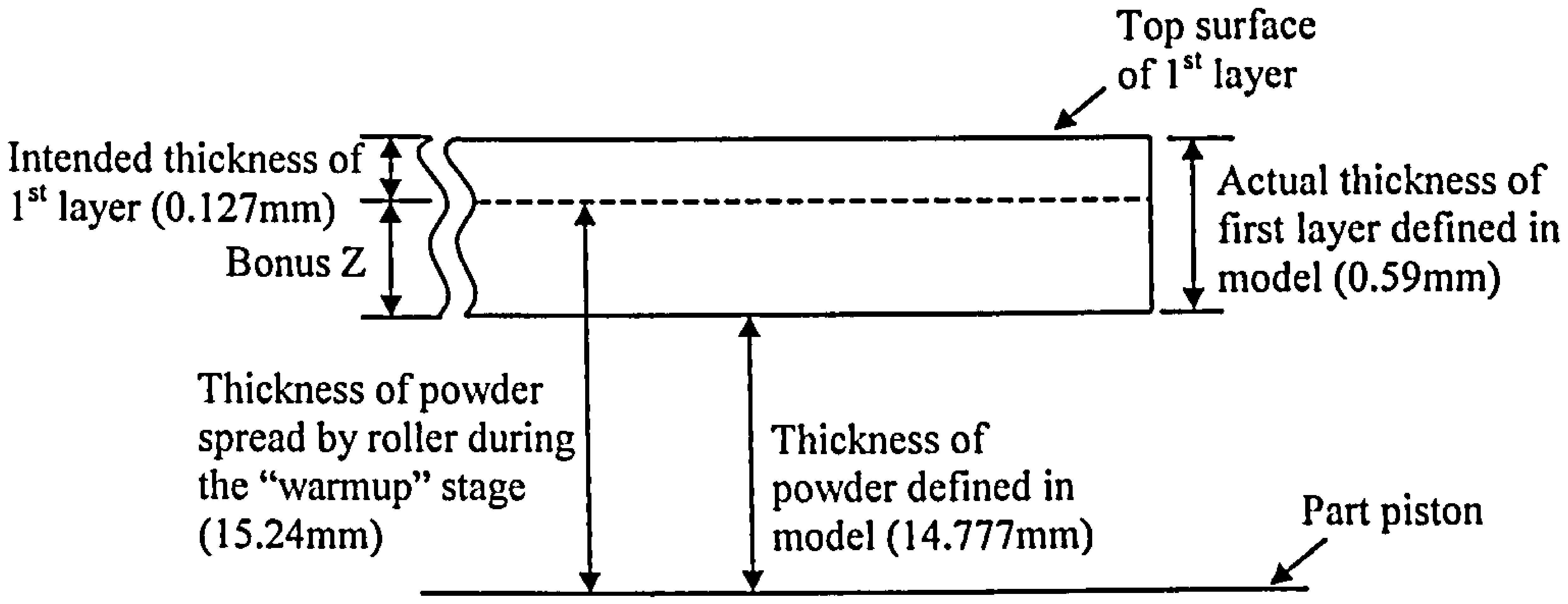

Figure 6.1 Schematic diagram showing the method used to calculate the thickness of powder underneath the part to be defined in the second version of the heat transfer model (not to scale).

The 2D heat transfer finite element mesh representing the part and powder bed in the present heat transfer model is illustrated in Figure 6.2. Elements used in the mesh are of the type four noded heat transfer linear quadrilateral, denoted in ABAQUS (DC2D4). In the model, the powder bed was represented by a 15×144 element mesh. The first layer, however, was represented by a 4×144 element mesh, whereas layers from two to ten were represented each by a 1×144 element mesh. Additionally, similar to the previous heat transfer model, nodes that are not associated with elements were generated along the interfaces between elements representing the layers forming the part (see Section 4.7.3). The heat transfer analysis mesh shown in Figure 6.2 was refined using the method reported in Section 4.6.5. Furthermore, the mesh representing the part was generated allowing solution convergence for the corresponding stress analysis (see Section 4.7.5).

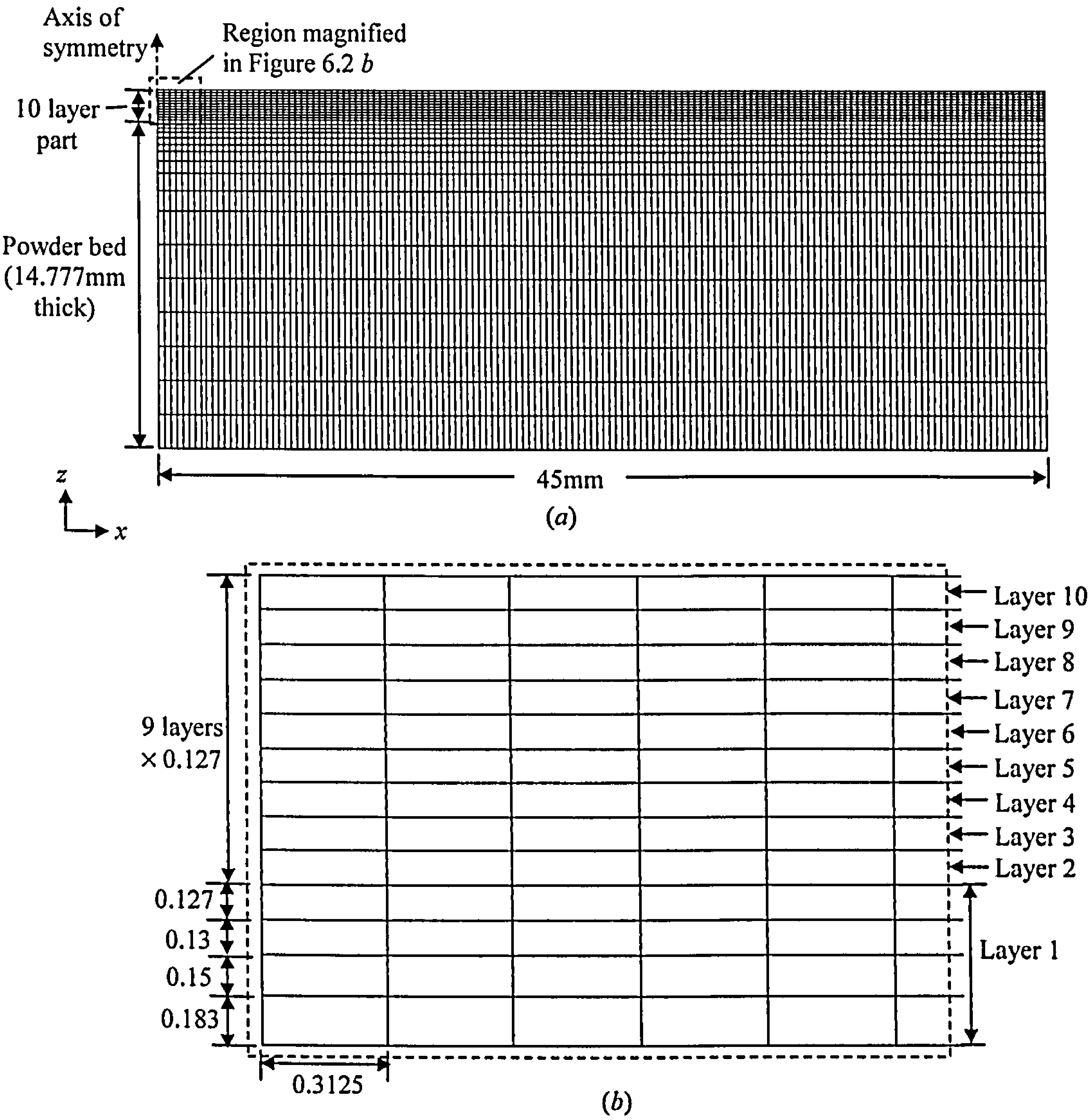

Figure 6.2 (*a*) Second version of 2D heat transfer analysis mesh. (*b*) Magnified view showing dimensions of elements forming a region of the part mesh. (All dimensions are in mm).

6.2.1.2 Material Properties in Heat Model

In this section, thermal material properties defined in the second version of the heat transfer model are introduced. These properties are the density, specific heat, thermal conductivity and emissivity. An improvement made to this version of the heat transfer model over the previous one that the specific heat and densities of the powder bed and sintered part were defined based on experimental measurements reported in Section 5.3.1. Thermal conductivities, however, were calculated using the Yagi-Kunii model with void fractions (used an input to the model) estimated from measured density values. In the following, a more thorough description of the thermal material properties defined in the heat transfer model is provided.

Densities of the powder bed and sintered part were defined in the model based on experimental measurements described in Sections 5.3.1.2 and 5.3.1.1. Thus, elements representing the sintered part were given a constant density equal to 497kg/m^3. Elements representing the powder bed, however, were assigned a constant density value equal to 439kg/m^3. The densities were considered constant in the heat analysis due to limitations in the finite element package used (see Section 4.6.2).

The specific heat was defined in the model based on experimental measurements reported in Section 5.3.1.3. The results obtained, illustrated in Figure 5.4, were defined in the model in tabulated form (specific heat against temperature). These values were assigned to all elements representing the part and powder bed in the heat transfer analysis mesh (see Section 4.6.2). Additionally, based on previous experimental measurements [7], the emissivity was defined in the model equal to 0.95.

Thermal conductivities of elements representing the powder bed and sintered part were defined in the model based on predictions of the high temperature form of the Yagi-Kunii model (see Section 4.6.2). In calculating thermal conductivities, parameters required as input to the Yagi-Kunii model had the values reported in Section 4.6.2, with the exception of void fractions of the powder bed and sintered part. These were calculated using Equation 4-26 based on the density values obtained experimentally. Thus, the void fraction calculated for the powder bed (with density of 439kg/m^3) is equal to 0.634, whereas the void fraction calculated for the sintered part (with density of 497kg/m^3) is equal to 0.586. The conductivity relationships with temperature predicted by the Yagi-Kunii model for the powder and sintered part are illustrated in Figures 6.3 and 6.4 respectively. These were defined in the heat transfer model in tabulated form (thermal conductivity against temperature).

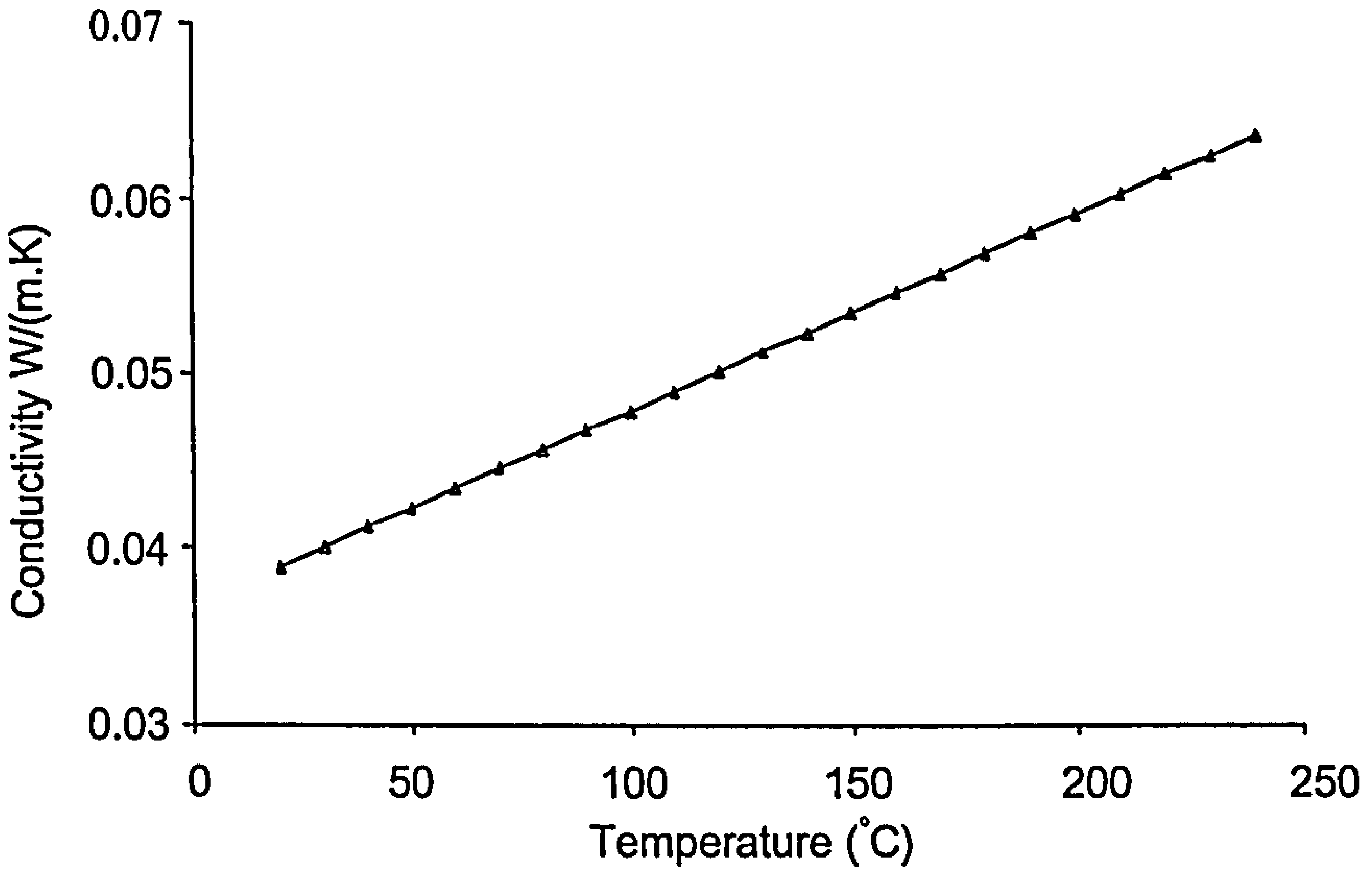

Figure 6.3 Relationship between the thermal conductivity of powder and temperature predicted using the Yagi-Kunii model and defined in the second version of the heat transfer analysis

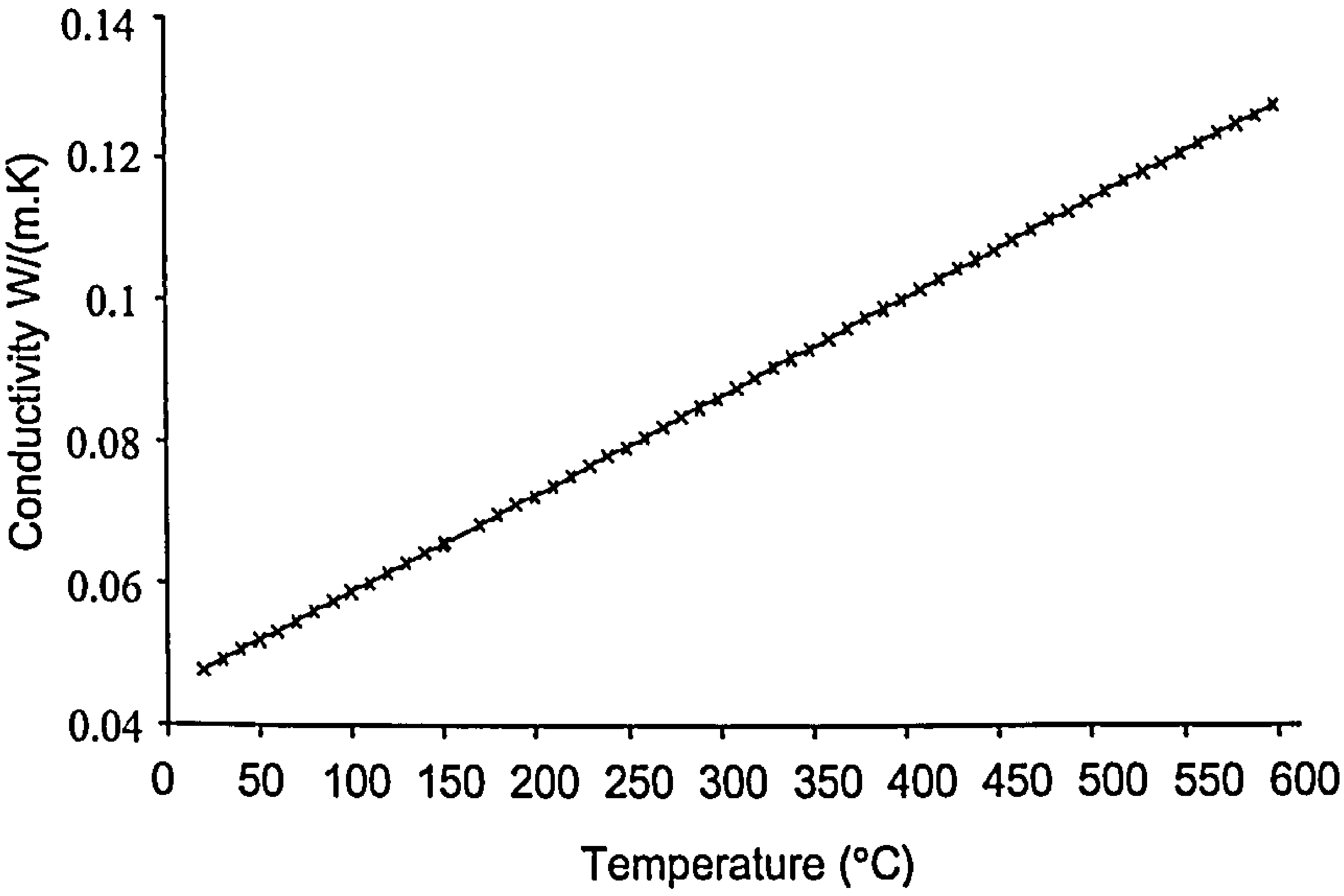

Figure 6.4 Relationship between the thermal conductivity of the sintered part and temperature predicted using the Yagi-Kunii model and defined in the second version of the heat transfer analysis.

6.2.1.3 Boundary Conditions

In this version of the heat transfer model, thermal effects occurring during the "warmup" stage were not simulated. However, similar to the previous heat transfer model, elements representing the powder spread during the "warmup" stage to form the powder bed were given an initial nodal temperature equal to 150°C. These elements are flanked by nodes located at the bottom surface of the powder bed and those located at a depth of 0.127mm from the top surface of the first layer of the part (see Figures 6.1 and 6.2).

However, attempts were made in this version of the heat transfer model to simulate thermal effects expected to occur during the "build" and "cooldown" stages in SLS. A number of these effects were simulated in the model by applying thermal boundary conditions. The boundary conditions applied included definition of initial nodal temperatures, enforcing insulation at certain surfaces and the application of convection and radiation thermal boundary conditions. In the following, an SLS stage is presented along with the boundary conditions applied to simulate thermal effects expected to occur in that stage.

▪ Build Stage

Simulation of thermal effects in the "build" stage requires understanding of the various operations that occur during that stage. The operations were identified by Pham et al. [65] as the addition of a new layer of powder, waiting for the temperature of the part bed to reach the set point, slicing model and loading the scanner, sintering and roller pausing prior to addition of next layer. These operations comprise one cycle of the "build" stage, as illustrated in Figure 6.5. In the figure, the operation of slicing the CAD model and loading the scanner is seen to start during powder addition and end during sintering. However, the period of the operation is difficult to estimate in the SLS machine used in fabrication of the ten-layer parts (DTM Sinterstation 2000). The reason being that the duration of the operation is dependent on the geometrical complexity of the CAD model and on the number of models sliced [65]. In the present work, each of the ten-layer parts was separately fabricated. Additionally, the parts were relatively simple in geometry; rectangular with a cross section of 90×26mm. Therefore, the assumption made was that the operation of slicing model and loading the scanner (operation 3) was completed during heating of the powder bed to the set point (operation 2). Thus, the period between the points (c) and (d) (see Figure 6.5) was considered equal to zero, i.e. sintering of the layer (operation 4) was assumed to start immediately following the layer had reached the set point temperature (operation 2). Furthermore, in SLS fabrication of the ten-layer parts, the time delay between two successive layers was set to zero (operation 5), i.e. the points (e) and (a) in Figure 6.5 coincided. Emphasis was therefore given to simulate thermal effects occurring in the duration of operations 1, 2 and 4. In the following, a description of these operations is given along with the boundary conditions applied to simulate thermal effects in each operation.

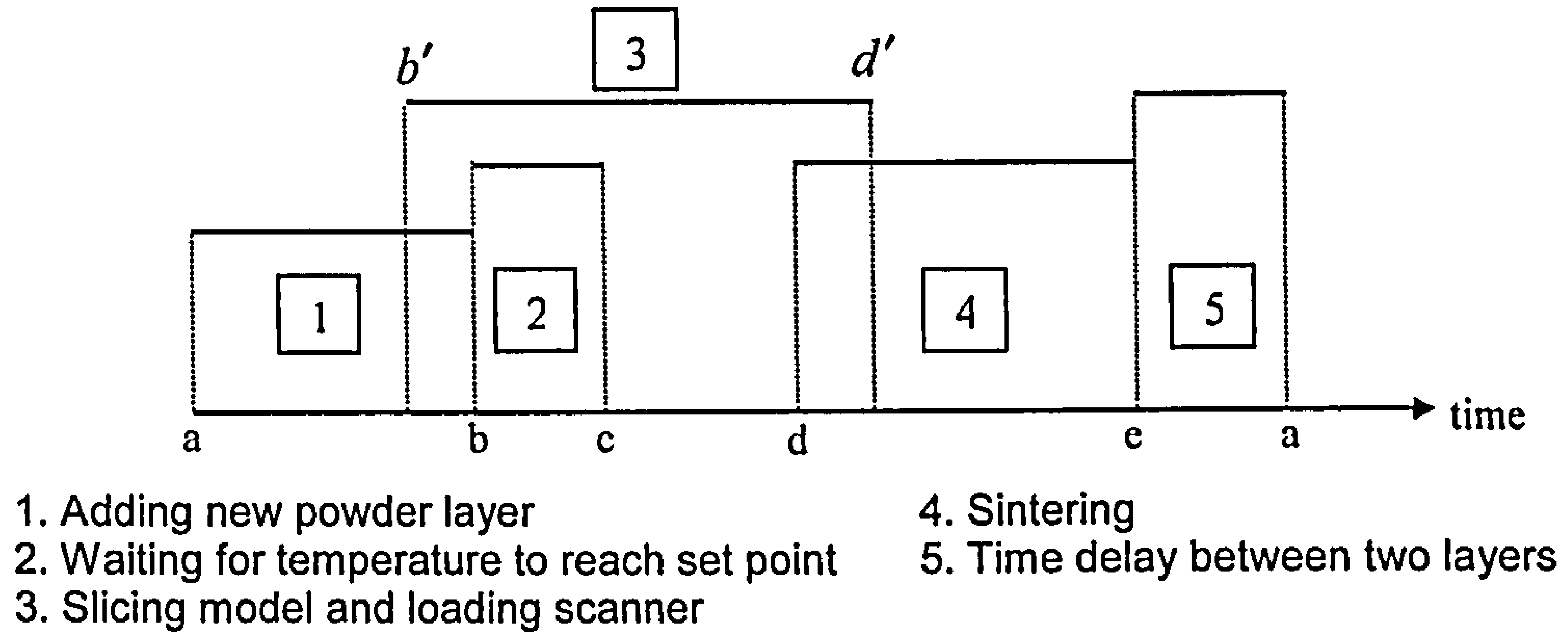

Figure 6.5 One cycle of operations occurring during the SLS "build" stage. Reproduced from [65].

- Adding a New Layer of Powder (Operation 1)

The operation of adding a new layer involves the roller transporting and levelling fresh powder from one feed cartridge, onto the part bed to the other feed cartridge. In the "build" stage in fabrication of the ten-layer parts, the powder in the feed cartridges was maintained at 80°C. However, as a layer of powder was spread by the roller, the part heater is expected to have raised the temperature of the added layer (above 80°C). Due to the lack of the actual temperature of a layer the moment it is spread onto the position where sintering was to occur, which is only of interest in modelling, the temperature of the added layer at that instant was assumed to be 80°C. That was simulated in the model by defining the initial nodal temperature of elements representing part layers from two to ten equal to 80°C. However, the initial nodal temperatures of elements flanked by nodes located at the bottom surface of the first layer of the part and those located at a depth of 0.127mm from its top surface were defined equal to 150°C, as previously reported.

- Waiting for temperature of Part Bed to reach to set point (Operation 2)

During the "build" stage, the IR sensor regularly measures the temperature at the top surface of a recently added layer of powder at a location distant from the regions to be sintered. Based on the IR sensor readings, the part heater switches on and off to maintain the temperature of the top surface of the layer to that set by the operator (150°C). As above-mentioned, the initial temperature of a recently added layer of powder in the "build" stage was assumed to be 80°C. The operation of heating the recently added layer to the set point is assumed therefore to entail raising the temperature of the top surface of the layer from 80°C to 150°C. In principle, the heating operation can be simulated by applying heat flux on the edges of elements together representing the top surface of the recently added layer of powder. The magnitude of heat flux applied would be identical to the fraction of heat emanating from the part heater and absorbed by the top surface of the added layer. The time period of heat flux application would be equal to the time required to raise the temperature of the top surface of the powder surrounding the region to be sintered (measured by the IR sensor) to 150°C. On the basis of user observation of IR sensor readings, the time required to heat up the layer was estimated to be 7 seconds.

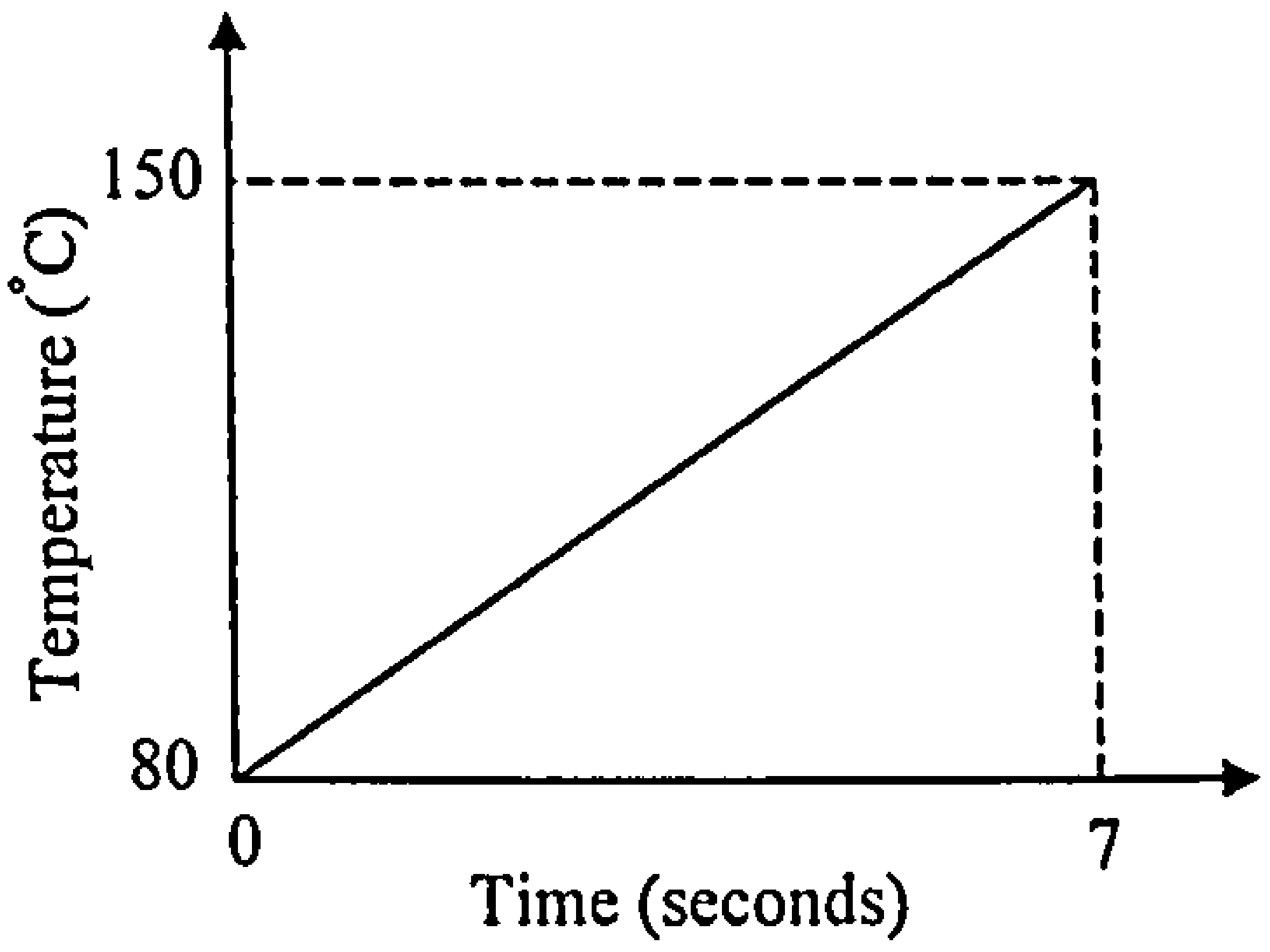

Figure 6.6 Schematic diagram illustrating the boundary condition applied on the nodes located at the top surface of the added powder to simulate the operation of heating the part bed to the set point temperature, operation 2 in Figure 6.5.

However, the amount of heat flux imparting from the part heater and absorbed by the part bed was not known, and cannot be accurately estimated without knowledge of the actual temperatures in the powder bed immediately prior to the heating operation. Thus, simulation of the heating effect using the method above-mentioned was not possible, compelling the author to resort to an alternative approach for simulation. The approach implemented was by applying a boundary condition raising the temperature of the nodes located along the top surface of a recently activated (added) layer from 80°C to 150°C in a period equal to 7 seconds. In simulation, the temperature was assumed to increase linearly with time as illustrated in Figure 6.6. However, the drawback of the assumption is that the temperature of the top surface of the added layer increases according to the boundary condition applied (see Figure 6.6) regardless of changes in temperature expected to actually arise at the surface due to heat conducted from the sintered layers underneath and due to heat lost from the surface through convection and radiation.

- Sintering of an Added Layer (Operation 4)

Boundary conditions applied to simulate thermal effects occurring during sintering of a layer were identical to those specified in the previous version of the model (see Section 4.6.3). These are convection and radiation thermal boundary conditions applied on the edges of elements together representing the top surface of the layer being sintered with the temperature of the gas in the chamber and that of enclosing walls equal to 150°C.

Following sintering of a layer, the roller immediately starts transporting and levelling fresh powder from one feed cartridge onto the part bed to the other feed cartridge. Boundary conditions applied to simulate thermal effects occurring on the recently sintered layer just before fresh powder was added on its top surface were also identical to those defined in the previous model (see Figure 4.31). These are convection and radiation thermal boundary conditions applied on the top surface of the recently sintered layer with the temperature of the gas and enclosing walls assumed to be equal to 150°C.

▪ Cooling of Part to Room Temperature

In the "cooldown" stage, the heaters were switched off, and the parts were allowed to cool in the chamber until the temperature measured by the IR sensor on the top surface of the part bed was equal to 100°C. The part and surrounding powder (part bed) were then removed from the process chamber and left to cool naturally to room temperature. In the following, boundary conditions applied to simulate thermal effects occurring whilst the part bed was in the chamber and following its removal are introduced.

➢ Cooling of the part whilst in the chamber

Boundary conditions defined to simulate thermal effects whilst the part bed was in the chamber were convection and radiation thermal boundary conditions applied on the edges of elements representing the top surface of the last fabricated layer (tenth layer). However, application of these boundary conditions requires changes in temperature of the gas in the chamber and of surrounding walls to be identified. Similar to the previous model, these temperatures were assumed to be equal to the temperature at the top surface of the part bed surrounding the last fabricated region. Estimation of these temperatures was therefore based on IR sensor readings of the temperature at the top surface of the part bed during the SLS "cooldown" stage. Figure 6.7 illustrates a number of IR sensor temperature measurements recorded at different instants during cooling of the top surface of the part bed in the chamber (from 150°C to 100°C). These were defined in the model in tabulated form (time against temperature) to represent changes in temperature of the gas and enclosing walls used in convection and radiation calculations. In the "build" stage and during cooling of the part in the chamber, the bottom surface of the powder bed was assumed to be insulated for the reasons reported in Section 4.6.3.

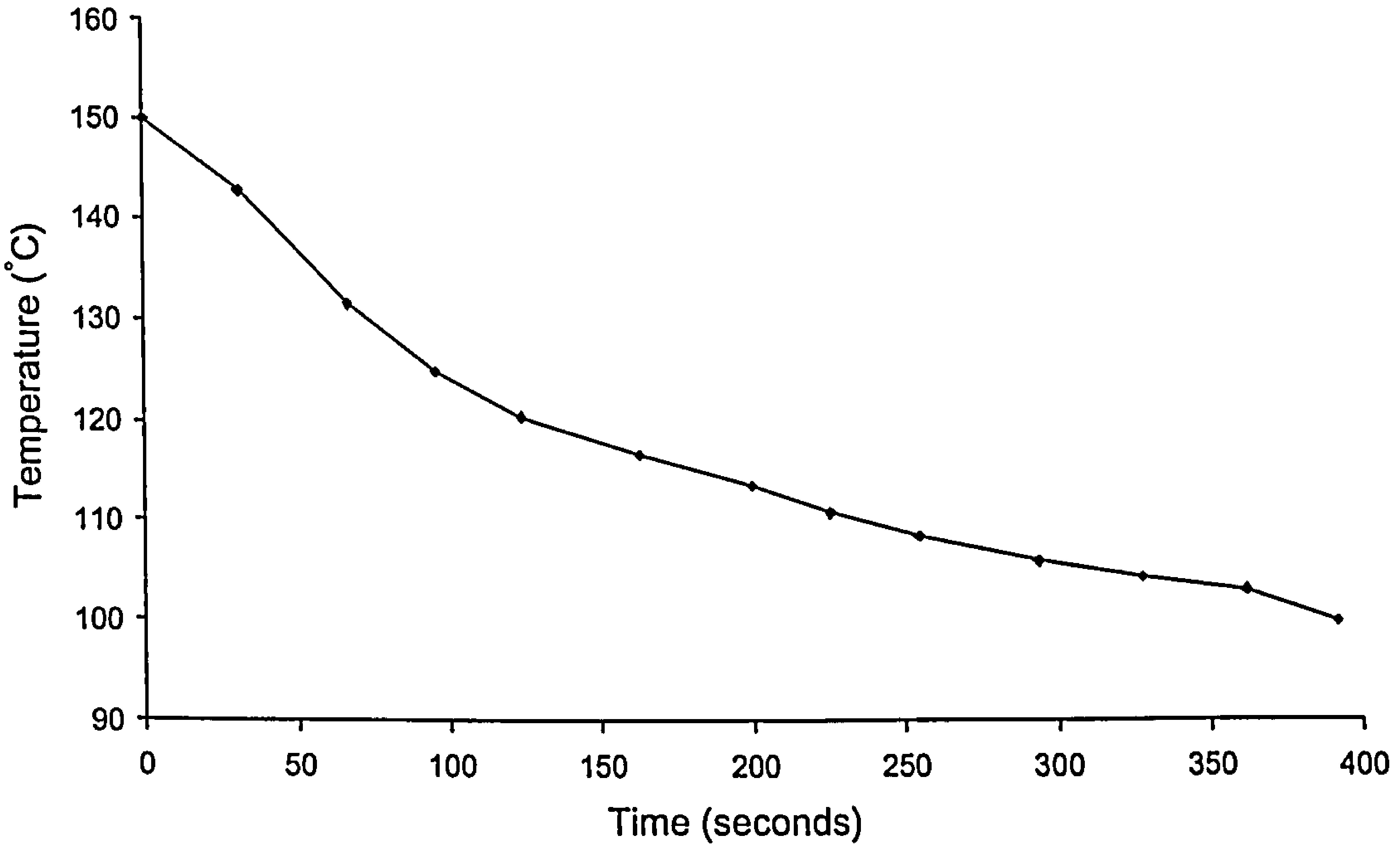

Figure 6.7 Temperatures measured by the IR sensor at the top surface of the part bed during cooling of the part bed in the chamber (following part fabrication).

- Cooling of the part following its removal from the chamber

After the temperature measured by the IR sensor was equal to 100°C, the process chamber was unlocked. A metallic tray was then used to lift the part bed from the chamber. The tray with the part bed on its surface were then positioned on a metallic table (Breakout Station) for part post-processing after the part in the bed had cooled to room temperature (20°C). Simulation of thermal effects occurring in that period was performed by applying convection and radiation thermal boundary conditions on the edges of elements together representing the top surface of the tenth layer of the part. The temperature of the gas and of surrounding walls, used in convection and radiation calculations, was assumed to be equal to room temperature (20°C). Additionally, as the metallic structures (tray and the breakout station) have a large heat capacity, deviation in the temperature of the structures from room temperature due to heat conducted from the part bed was assumed to be negligible. Thus, the bottom surface of the powder bed in contact with the tray was assumed to have the same (constant) temperature as that of the metallic structures (20°C). That was simulated by applying a boundary condition instantly setting the temperature of the nodes located at the bottom surface of the powder bed at 20°C and maintaining it at that temperature.

In the following, boundary conditions applied through the entire period of simulation are presented. The temperature histories of nodes not associated with any element and located along the interfaces between layers forming the part were defined as reported in Section 4.7.3. Additionally, similar to the previous model, the edges of elements in the part and the powder bed mesh supposed to be in contact with surrounding powder were assumed to be insulated. The edges of elements located along the axis of symmetry were also insulated.

6.2.1.4 Sequence of Analysis Defined in the Heat Transfer Analysis

The aim in this section is to describe the sequence of analysis defined in the model to simulate SLS fabrication of the ten-layer part and its cooling to room temperature. As previously reported, the sequence of analysis is defined in an ABAQUS model by a sequence of steps, each representing a time period in which the response of the model to a particular set of thermal loads (such as heat flux) and boundary conditions is calculated. The steps defined in the present heat transfer model were quite similar to those specified in the first version of the model (see Section 4.6.4). However, steps simulating addition of layers of powder at 150°C in the first version of the model were replaced in the present model with steps simulating addition of the layers at 80°C and their heating to the set point temperature (150°C). Additionally, the step specified in the previous model to simulate cooling of the part to 150°C (following its fabrication) was substituted in the present model with steps simulating cooling of the fabricated part to room temperature. In the following, selected steps defined in the present model are introduced with emphasis given to describe the steps differing from those specified in the previous model.

- First step defined in the heat transfer analysis

The "build" stage started by spreading a layer of powder onto the powder bed. The part heater then heated the top surface of the layer to the set point temperature (150°C) prior to sintering of the layer taking place. These operations (powder spreading and heating to set point) were simulated in the first step of the heat model. Similar to the previous model, spreading of the layer of powder was simulated by deactivating the elements in the heat transfer analysis mesh together representing layers from two to ten of the sintered part. Heating of the layer was simulated, however, by applying a boundary condition simultaneously raising the temperature of nodes connected to the edges of elements representing the top surface of the layer from 80°C to 150°C in 7 seconds (see Figure 6.6). That period was considered to be the time period of the first step defined in the model.

- Second step defined in the heat transfer analysis

After the top surface of the layer had reached 150°C, the laser beam was assumed to immediately raster scan a region on the top surface of the added layer to form the first layer of the part. Thermal effects expected to occur during sintering of the layer were simulated in the second step of the analysis. The sintering operation was simulated by applying a uniform heat flux on the edges of elements representing the top surface of the first layer of the part. The amount of heat flux applied and the time period of application were identical to those specified in the first step of the previous heat transfer model, 83.1MW/m^2 and 3.36×10^{-4} second respectively. That period

(3.36×10^{-4} second) was considered as the duration of the second step of the analysis. In that period, convection and radiation boundary conditions were applied on the edges of elements representing the top surface of the first layer of the part, with the temperature of the gas and enclosing walls maintained at 150°C.

- **Third step defined in heat transfer analysis**

After sintering of the layer was completed, the roller immediately started spreading fresh powder from one feed cartridge, onto the part bed to the other feed cartridge. Thermal effects simulated in the third step were those expected to occur just before fresh powder was added on the top surface of the recently sintered layer. Definition of the step was identical to that of the second step in the previous heat transfer model (see Section 4.6.4).

- **Fourth step defined in heat transfer analysis**

The fourth step of the analysis simulated thermal effects expected to occur immediately from the instant powder was spread on the top surface of the first layer of the part and during heating of the added layer to the set point temperature (150°C). Spreading of powder was simulated by simultaneously activating the elements together representing the second layer of the part (see Figure 6.2). In the step, convection and radiation boundary conditions previously applied on the top surface of the first layer of the part were deactivated. Similar to the first step of the analysis, heating of the powder layer was simulated by applying a boundary condition on the nodes (connected to elements) located at the top surface of the second layer raising their temperature from 80°C to 150°C in 7 seconds (see Figure 6.6). That duration was defined in the model to be the time period of the fourth step.

Due to the repetitive nature of operations in the "build" stage, steps two, three and four were repeated in the heat transfer model on successive layers of elements until sintering of the tenth layer of the part was simulated. The following steps (steps 30 and 31) simulated thermal effects expected to occur after fabrication of the part was completed, i.e. during cooling of the part to room temperature. In the following, a description of these steps is given.

- **Simulation of Cooling of the part whilst in the chamber (Step 30)**

Thermal effects expected to occur during cooling of the fabricated part whilst in the chamber were simulated in step 30 of the model. In the step, the heat flux previously applied on the top surface of the tenth layer to simulate its sintering (in the previous step) was removed. Additionally, thermal boundary conditions previously applied on that surface were deactivated. These were replaced with convection and radiation boundary conditions applied on the top surface of the tenth layer with the temperature of the gas and surrounding walls reducing as illustrated in Figure 6.7. Referring to the figure, the time period of the step was defined equal to 392 seconds.

- **Cooling of the part following its removal from the chamber (Step 31)**

Step 31 simulated thermal effects expected to occur following removal of the part bed from the process chamber. In the step, the thermal boundary conditions previously applied in step 30 were deactivated. These were replaced with convection and radiation boundary conditions applied on the top surface of the tenth layer with the temperature of the gas and surrounding walls maintained at room temperature (20°C). Additionally, positioning of the part bed onto the metallic tray and breakout station was simulated by applying a boundary condition setting and maintaining the temperature of nodes located at the bottom surface of the powder bed equal to 20°C. The time period of the step was defined to be equal to 40 minutes, which was sufficient to allow part cooling to room temperature.

6.2.1.5 Results

Figures 6.8 to 6.10 illustrate nodal temperature histories of interest predicted in selected steps of the heat transfer model. The general observation seen was that steps simulating identical thermal effects in both the previous and present versions of the heat transfer model had quite similar temperature profiles predicted. However, these profiles were seen to differ in steps simulating addition of layers of powder and in steps simulating cooling of the fabricated part to room temperature.

Figure 6.8 illustrates the nodal temperature histories of interest predicted in the first step of the heat transfer analysis. The step simulates addition of the first layer of powder in the "build" stage and its heating to the set point temperature. The initial temperature of nodes located at the top surface of the layer was defined equal to 80°C. However, nodes located at a depth of 0.127mm from that surface and those located at a larger depth were given an initial temperature equal to 150°C. Consequently, conduction of heat is expected to have occurred (in the initial period of the step) from the powder bed and first layer towards the top surface of the layer. Heat transfer in that direction is exhibited by reduction in the temperature of nodes located at a depth of 0.127mm from the top surface of the layer, followed by reduction in the temperature of nodes located at a larger depth from that surface. However, it must be remembered that heat conducted to the top surface does not give rise to its temperature, as the increase in temperature of the surface is controlled by the boundary condition applied (see Figure 6.6).

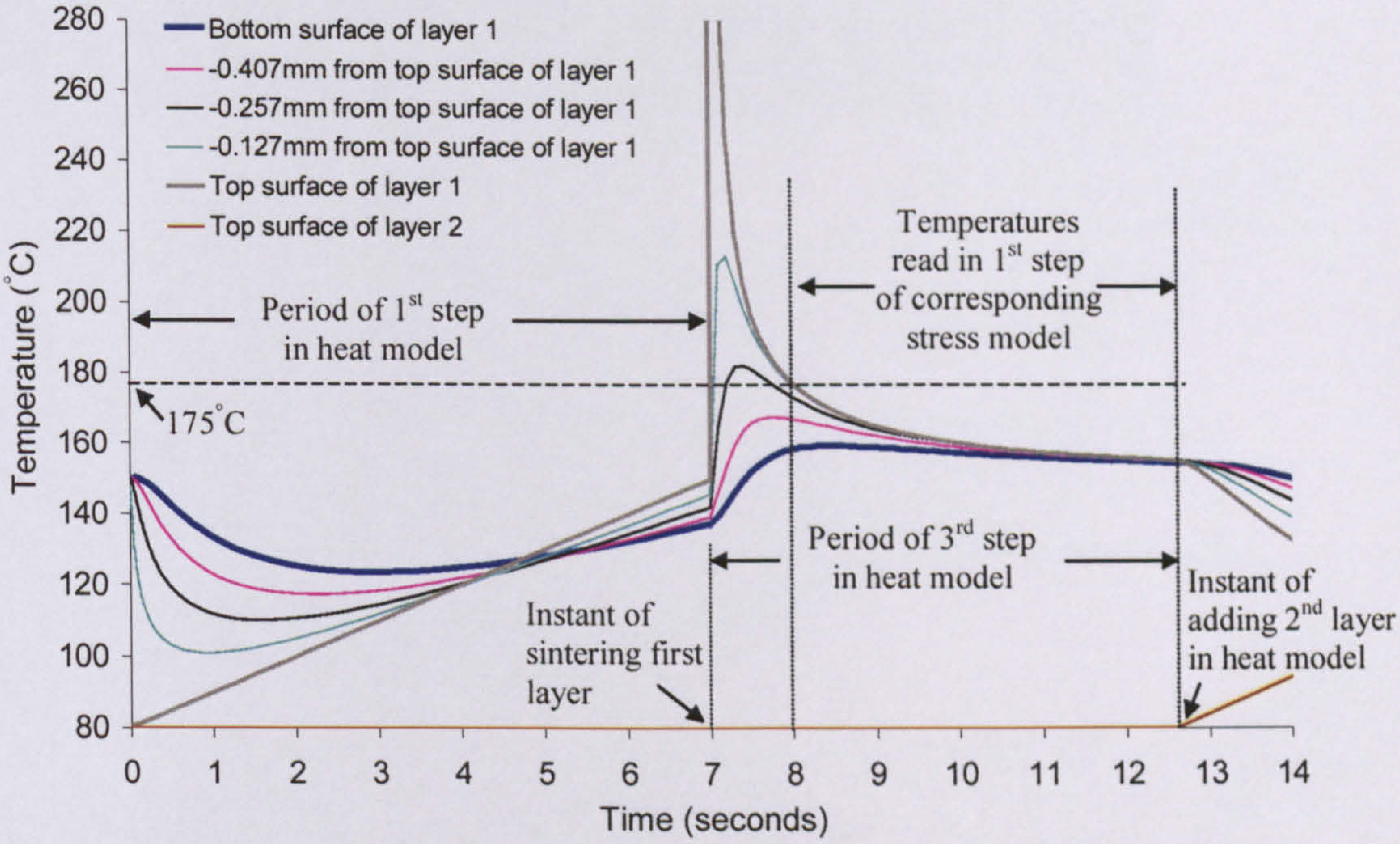

Figure 6.8 Nodal temperature histories (of interest) predicted in the first three steps of the second version of the heat transfer model. The figure also illustrates the nodal temperature histories read in first step of the corresponding stress analysis

Following 0.9 seconds from the start of the step and for a period of 3 seconds, conduction of heat towards the top surface of the first layer from nodes located at a depth of 0.127mm from that surface is believed to have continued to take place. However, heat conducted to the top surface of the layer is expected to have reduced with time as the temperature of surface was raised. Consequently, the increase in the temperature of the nodes located at a depth of 0.127mm, seen in that period, is probably an indication that heat received from regions at a larger depth was greater than that lost from the nodes to the top surface of the layer. The continuous conduction of heat from the powder bed towards the first layer is additionally reflected by gradual reduction in the rate of temperature decrease of nodes located at depth larger than 0.127mm from the top surface of the layer, followed by an increase in the temperature of these nodes.

Following 4.7 seconds from the start of the step and for the remaining period of the step (2.3 seconds), the temperature at the top surface was the highest in the layer. As a consequence, conduction of heat is expected to have taken place from that surface into the layer. At the end of the step, the temperature at the top surface of the layer was equal to 150°C, as defined by the boundary condition applied, whereas the lowest temperature in the layer was that at its bottom surface (137.4°C).

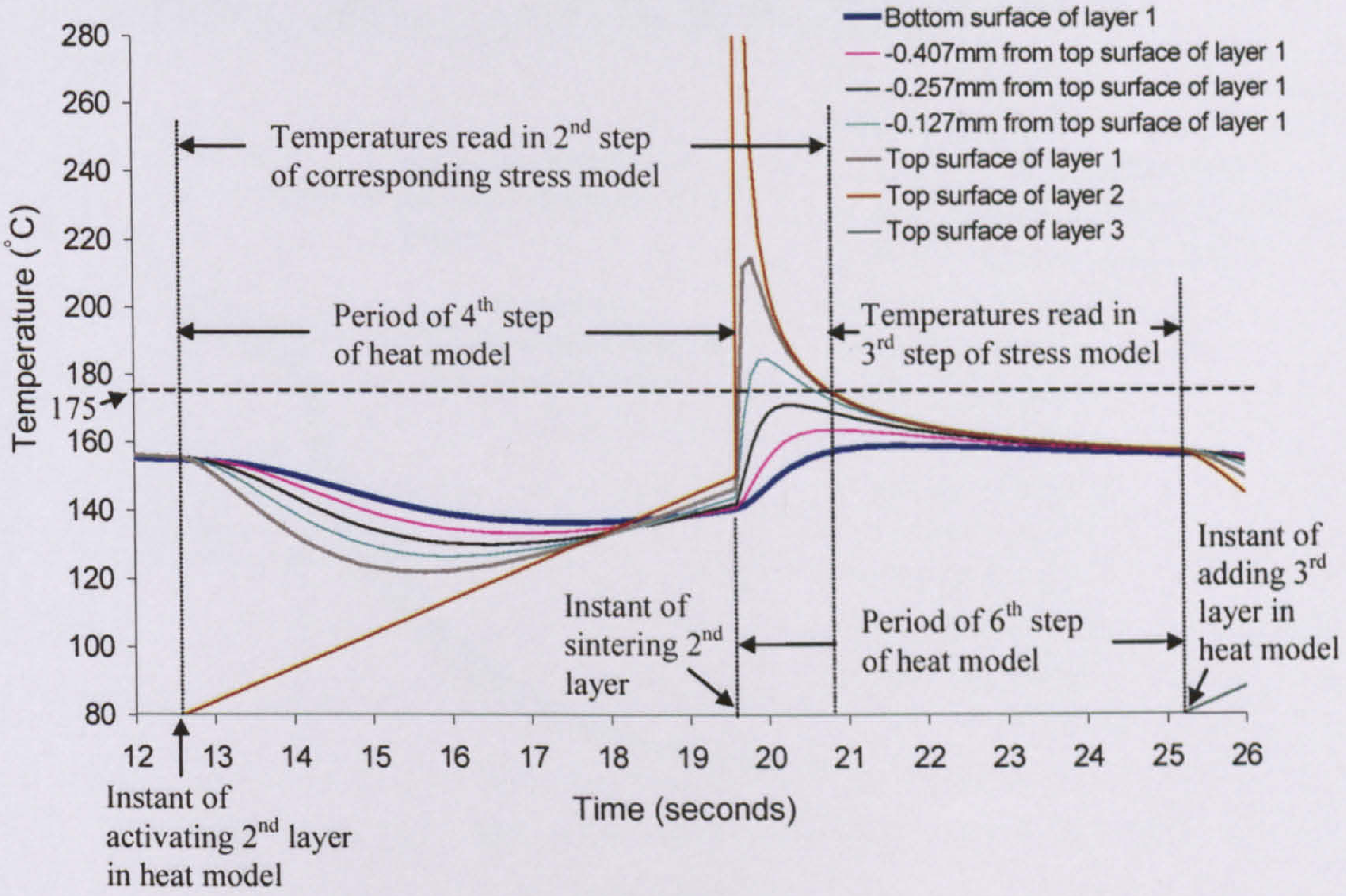

Figure 6.9 Nodal temperature histories (of interest) predicted in step 4, 5 and 6 of the second version of the heat transfer model. The figure also shows the nodal temperatures histories read in the second and third steps of the corresponding stress analysis.

Figure 6.9 illustrates the nodal temperatures predicted in the fourth step of the heat transfer analysis. The step simulates addition of the second layer of powder and its heating to the set point temperature. Temperature profiles predicted in the step were quite similar to those predicted in the first step of the model, i.e. temperatures in the build are seen to reduce in the initial period of adding the second layer but increase during heating of the added layer to the set point temperature. That phenomenon was also observed in all steps simulating identical thermal effects on subsequently added layers of powder.

Figure 6.10 illustrates the nodal temperature histories of interest predicted in the last two steps (step 30 and 31) of the heat transfer model. The steps simulate cooling of the part in the chamber and its cooling to room temperature following removal of the part bed from the chamber. In both stages of cooling, the top surface of the tenth layer was predicted to be the lowest in the build, whereas the highest temperature in the part was seen at its bottom surface. Consequently, conduction of heat is expected to have occurred from the bottom surface of the build towards its top surface, which is then lost from the latter through convection and radiation.

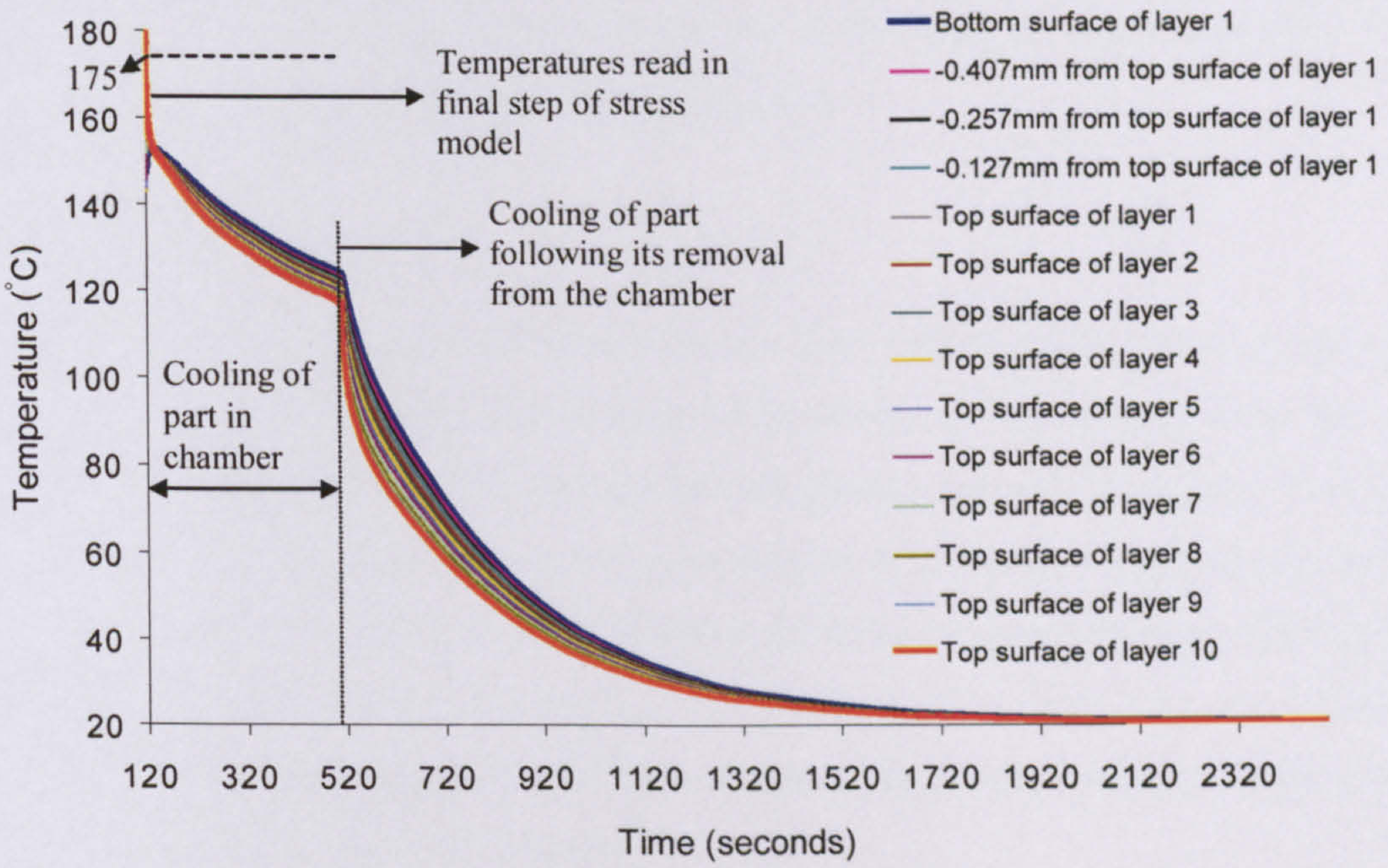

Figure 6.10 Nodal temperature histories predicted in the steps simulating cooling of the part in the chamber and following its removal. The figure also illustrates the nodal histories used as input to the last step of the corresponding analysis.

The large amounts of heat lost from the top surface of the tenth layer through convection and radiation is reflected by large reduction in the temperature in the part following its removal from the chamber (the gas and surrounding walls maintained at

20°C). It must be remembered that the bottom surface of the powder bed was maintained during that period at 20°C. Thus, conduction of heat is expected to have occurred from the bottom regions of the powder bed towards that surface. However, as the temperature at the bottom surface of the first layer was the highest in the build, heat lost from the part through conduction into the powder bed is expected to be less than that lost through convection and radiation. That is probably due to the large thickness of the powder bed compared to that of the part and the low conductivity of the powder making the powder bed a more resistive path for the conduction of heat.

6.2.2 Second version of stress model

The most significant improvement made to this version of the stress model over the previous one that it attempted to provide better simulation of the viscoelastic behaviour of polycarbonate. Additionally, the instantaneous modulus was defined in the model over a (relatively) wide range of temperatures, whereas in the previous model only a single value of the modulus was defined (experimentally obtained at 100°C). In the following, the second version of the stress model is described. Curl results predicted by the model are then presented.

6.2.2.1 Geometry

Geometrical approximations assumed in the first version of the stress model (see Section 4.7.1) were also implemented in this version of the model. Thus, the ten-layer part and surface of the powder bed supporting the part were only modelled. However, the definition of geometry was improved in this version of the model by specifying the thicknesses of layers forming the ten-layer part based on experimental measurements reported in Section 5.2. The thickness of the first layer was therefore defined in the model equal to 0.59mm, whereas layers from two to ten were each given a thickness equal to 0.127mm.

The 2D stress analysis mesh representing the ten-layer part and the surface of the powder bed supporting the part is illustrated in Figure 6.11. The ten-layer part was represented in the mesh using four noded plane strain incompatible elements, denoted in ABAQUS (CPE4I). The mesh representing the part in the stress model was identical to that used to represent the part in the corresponding heat transfer model (see Figure 6.2). Thus, the first layer was represented using a 4×144 mesh whereas layers from two to ten were represented each using a 1×144 mesh. As previously implemented in the first version of the stress model, edges of elements representing the top surface of a layer and those representing the bottom surface of a subsequently added layer were not connected by common nodes (see Section 4.7.3).

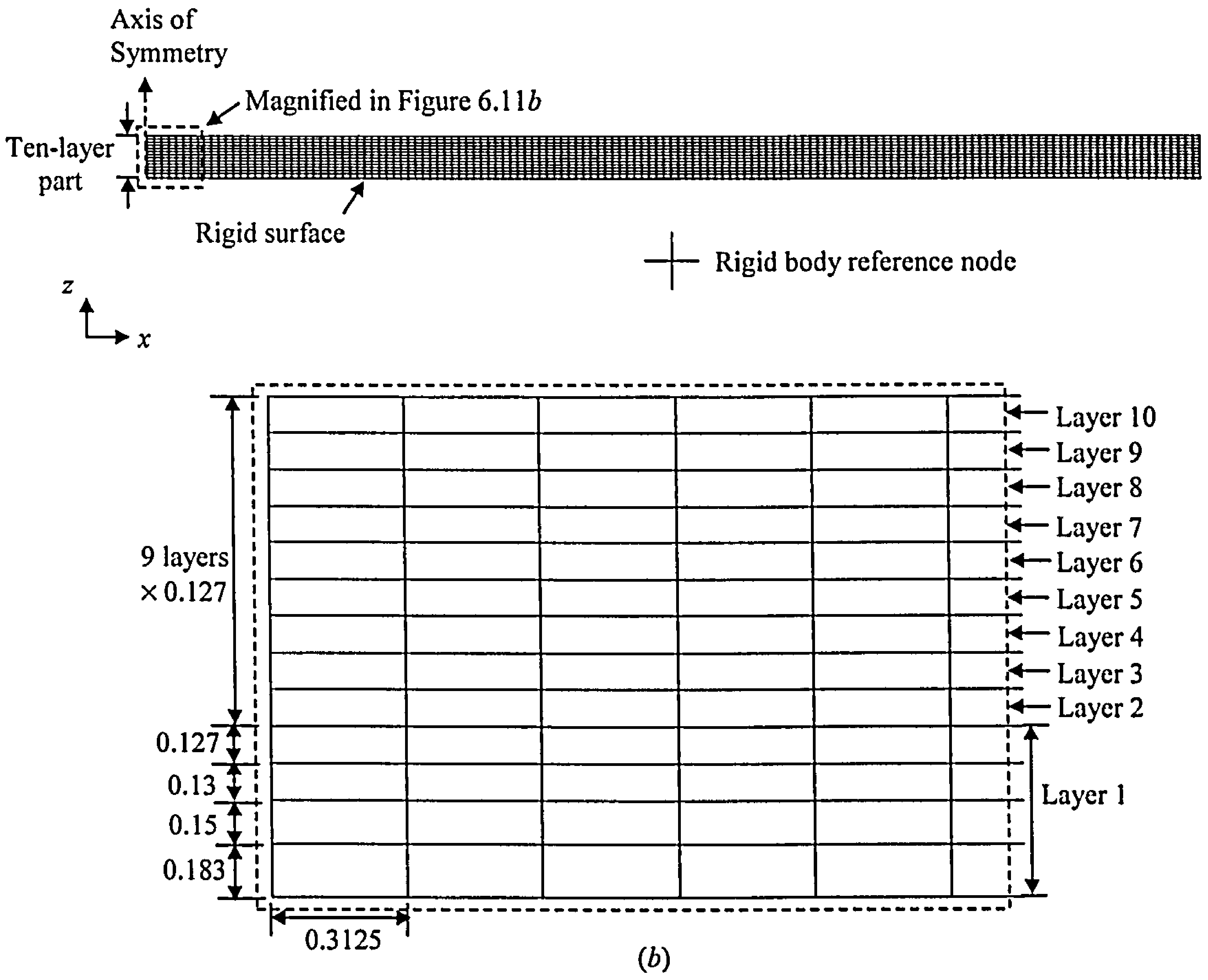

(*b*)

Figure 6.11 (*a*) Second version of the 2D stress analysis mesh. (*b*) Magnified view showing dimensions of elements forming a region of the part mesh. (All dimensions are in mm).

Additionally, similar to the previous model, the surface of the powder bed supporting the ten-layer part was assumed to be rigid. That was represented in the model by 2D rigid surface elements, denoted in ABAQUS (IRS21). The motion of the rigid surface is controlled by the motion of the "rigid body reference node", illustrated in Figure 6.11. The stress analysis mesh illustrated in the figure was refined using the method described in Section 4.7.5.

6.2.2.2 Material Properties

Material properties selected as input to the stress model included the expansion coefficient, density, coefficient of friction, Poisson's ratio and the elastic modulus. In the following, the criteria supported in defining these properties in the stress model are described.

- **Coefficient of Thermal Expansion**

The general method adopted in defining the expansion coefficient in the first version of the stress model was also implemented in this version of the model (see Section 4.7.2). The improvement made to this version, however, was based on DMA measurements that identified 175°C to be the temperature above which thermal stresses in polycarbonate are negligible (see Section 5.3.2.1). An element was therefore assumed not to sustain any thermal stresses provided that its average nodal temperature is equal or exceeds 175°C. Nodal temperature histories predicted by the heat transfer model showed elements representing part layers from two to ten to have satisfied that condition. That was also seen in elements in the first layer flanked by nodes located at the top surface of the layer and those located at a depth of 0.257mm from that surface (see Figure 6.8). In the model, these elements were assigned an expansion coefficient equal to zero at temperatures equal and above 175°C. However, due to the lack of real values for the expansion coefficient below 175°C, the elements were given an assumed expansion coefficient at these temperatures equal to $2\times10^{-6}C^{-1}$; a value identical to that used in the first version of the stress model.

Conversely, elements flanked by nodes located at the bottom surface of the first layer and those located at a height of 0.333mm from that surface did not exceed an average nodal temperature equal to 175°C. Based on the method implemented in the previous model, these elements were given an expansion coefficient equal to zero at all temperatures used in the stress analysis (see Section 4.7.2).

- **Density**

The density was defined in the model for the effects of the weight of each layer forming the part to be included in the stress analysis. Similar to the previous stress model, elements representing the ten-layer part were given the density of the fabricated part. However, the density defined in this version of the model was based on experimental measurements, 497kg/m^3 (see Section 5.3.1.1).

- **Coefficient of Friction**

Based on experimental measurements, the coefficient of friction between the edges of elements representing the bottom surface of the first layer and the rigid surface was defined in the model equal to 0.38 (see Section 5.3.2.4).

- **Mechanical Properties**

Mechanical properties defined in the stress model included the (time-independent) instantaneous modulus of elasticity and the (time-dependent) viscoelastic behaviour of polycarbonate.

– **Instantaneous Elastic modulus and Poisson's Ratio**

The instantaneous modulus was defined in the stress model based on tensile test measurements reported in Section 5.3.2.2. The measurements gave an estimation of the modulus at 20°C, 120°C, 135°C, 140°C, 148°C and 150°C (see Table 5-1). Modulus values estimated at these temperatures were defined in the stress model in tabulated form (modulus, temperature). Thus, the modulus was defined at selected temperatures and was not specified at all temperatures used in the stress analysis. At temperatures that the modulus is not defined, ABAQUS estimates the modulus by linearly interpolating between the (modulus, temperature) data given, provided that temperatures are in the range from 20°C to 150°C [43]. However, it was not experimentally possible to measure the modulus at temperatures exceeding 150°C (see Section 5.3.2.2). Due to the lack of moduli values above that temperature, the modulus above 150°C was assumed in this version of the model equal to that experimentally measured at 150°C, 11.8 MPa.

The Poisson's ratio of polycarbonate at 20°C was reported to be equal to 0.385 [66]. In the absence of high temperature data, the value reported was defined in the model over the entire temperature range used in the stress analysis.

– **Time-Dependent Response (Viscoelasticity)**

The time-dependent response of the polymer was defined in the stress model based on predictions of a (built-in) viscoelastic model. The viscoelastic model initially simulates the time-dependent response of the polymer at a certain (reference) temperature based on stress relaxation data provided at that temperature. Based on that simulation, the model employs the WLF approximation (see Section 2.3.1.3) to predict the time-dependent response of the polymer at all other temperatures used in the stress analysis. In the following, the method implemented by the viscoelastic model to simulate the stress relaxation behaviour at a specific temperature based on stress relaxation data given at that temperature is first described. The use of the WLF approximation in the model is then introduced.

- **Modelling of the Time-Dependent Response at a Single Temperature**

A simple mechanical model generally used to describe the stress relaxation behaviour of polymers is a Maxwell model [1]. The model consists of a spring element and a dashpot connected in series, as illustrated in Figure 6.12*a*. If a Maxwell model is rapidly stretched to a certain elongation and held in that position, the resulting decay in stress (σ) with time (t) can be written as [24],

$$\sigma(t) = \sigma_o \exp(-t/\tau_m) \qquad 6\text{-}1$$

where σ_o is the initial stress at $t = 0$ and τ_m is the relaxation time constant. The relaxation time constant, however, can be expressed in terms of the modulus of the elastic spring E_o and the viscosity of the dashpot η_o (see Figure 6.12) as $\tau_m = \eta_o / E_o$ [1].

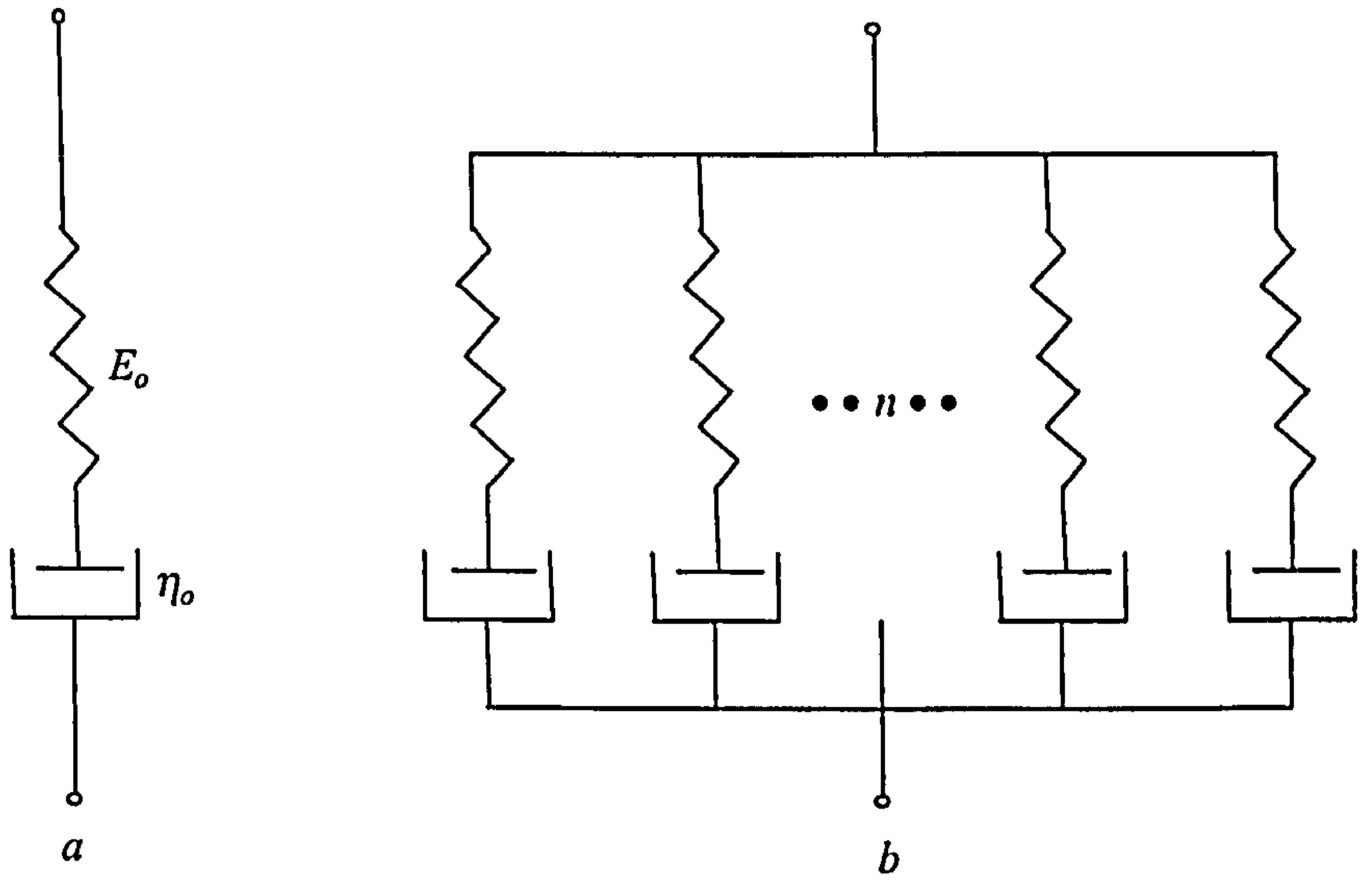

Figure 6.12 (*a*) Maxwell model (*b*) modified model with *n* parallel Maxwell models.

The Maxwell model can also describe the decay in modulus *E(t)* during a stress relaxation test by simply dividing both sides of Equation 6-1 by the constant strain applied, giving,

$$E(t) = E_{\circ} \exp(-t/\tau_m) \qquad 6\text{-}2$$

Equations 6-1 and 6-2 predict the stress and modulus to decay exponentially with time during a stress relaxation test. However, the Maxwell model is too simple to describe the actual time-dependent response of a polymer during stress relaxation [1]. In general, a more complex model that consists of a number of Maxwell elements assembled in parallel (see Figure 6.12*b*) is employed to explain stress relaxation in polymers. Using the (more complex) model, the decay in modulus *E(t)*, during stress relaxation can be expressed as follows [24],

$$E(t) = \sum_{i=1}^{n} E_i \exp(-t/\tau_{mi}) \qquad 6\text{-}3$$

where E_i is the elasticity of the spring element in a Maxwell unit (numbered *i*), τ_{mi} is the relaxation time constant of that unit and *n* is the total number of Maxwell units the model comprises. However, Equation 6-3 implies that the modulus *E(t)* continues to decay during stress relaxation until it attains a zero modulus at extremely long relaxation times ($t = \infty$). Thus, the model contradicts the experimentally obtained stress relaxation modulus data (see Figures 5.18 to 5.21), as these data show that at the end of stress relaxation the modulus decays to a constant value which is higher than zero. Improvement to the model was made by including a term E_∞, as expressed in Equation 6-4, where E_∞ denotes the modulus the polymer attained at extremely long relaxation times ($t = \infty$). The improved form of the model presented by Equation 6-4 is termed the Prony series [67].

$$E(t) = \sum_{i=1}^{n} E_i \exp(-t/\tau_{mi}) + E_\infty \qquad 6\text{-}4$$

At relaxation time ($t = 0$), the modulus measured is the instantaneous modulus of the polymer, i.e. $E(t) = E_o$ and thus Equation 6-4 can be written as,

$$E_\infty = E_o - \sum_{i=1}^{n} E_i \qquad 6\text{-}5$$

Substituting the expression of E_∞ derived in Equation 6-5 into Equation 6-4 gives,

$$E(t) = E_o - \sum_{i=1}^{n} E_i \left(1 - \exp(-t/\tau_{mi})\right) \qquad 6\text{-}6$$

Dividing both sides of Equation 6-6 by E_o gives,

$$\frac{E(t)}{E_o} = 1 - \sum_{i=1}^{n} \frac{E_i}{E_o} \left(1 - \exp(-t/\tau_{mi})\right) \qquad 6\text{-}7$$

Assuming that $g_R(t) = E(t)/E_o$ and $g_i = E_i/E_o$, Equation 6-7 can be rewritten as follows,

$$g_R(t) = 1 - \sum_{i=1}^{n} g_i \left(1 - \exp(-t/\tau_{mi})\right) \qquad 6\text{-}8$$

Equation 6-8 represents the form of the Prony series used in ABAQUS. The equation therefore requires the value of the instantaneous modulus E_o. In addition, selected values of $g_R(t)$ experimentally obtained at different relaxation times (t) need to be provided. Using these data, ABAQUS estimates the values of n, g_i and τ_{mi} (see Equation 6-8) for a best curve fitting of the data given to be achieved. Equation 6-8 can then be used to predict the entire stress relaxation behaviour of the polymer.

In the following, the accuracy of the Prony series in curve fitting experimentally obtained stress relaxation data is investigated. That was performed by simulating the stress relaxation tests described in Section 5.3.2.3, then comparing the predicted (modulus-time) results with those obtained experimentally.

▫ Simulation of the Stress Relaxation Tests in ABAQUS

The stress relaxation tests simulated were those experimentally performed at 135°C, 140°C, 145°C and 148°C. In the following, a description of the models simulating these tests is provided.

➢ Description of Geometry of modelled Specimens

The specimens used in the stress relaxation tests had the dimensions illustrated in Figure 5.9. For simplicity, the elongated portion of the specimen was only considered in the model. The elongated structure is cylindrical in shape with diameter equal to 9mm and length equal to 90mm (see Figure 6.13*a*). The geometry of the structure and loading applied are mirror symmetrical about the *x*-*y* plane, and thus only half of the structure needs to be modelled. Additionally, the geometry and loading are axisymmetric about the *z*-axis. Therefore, the 3D structure can be represented by a 2D plane (the hatched region in Figure 6.13*a*) with axisymmetric elements used in simulation. The finite element mesh used to represent the structure is illustrated in Figure 6.13*b*. Elements used in the mesh are of the type four noded axisymmetric reduced integration elements, denoted in ABAQUS (*CAX4R*).

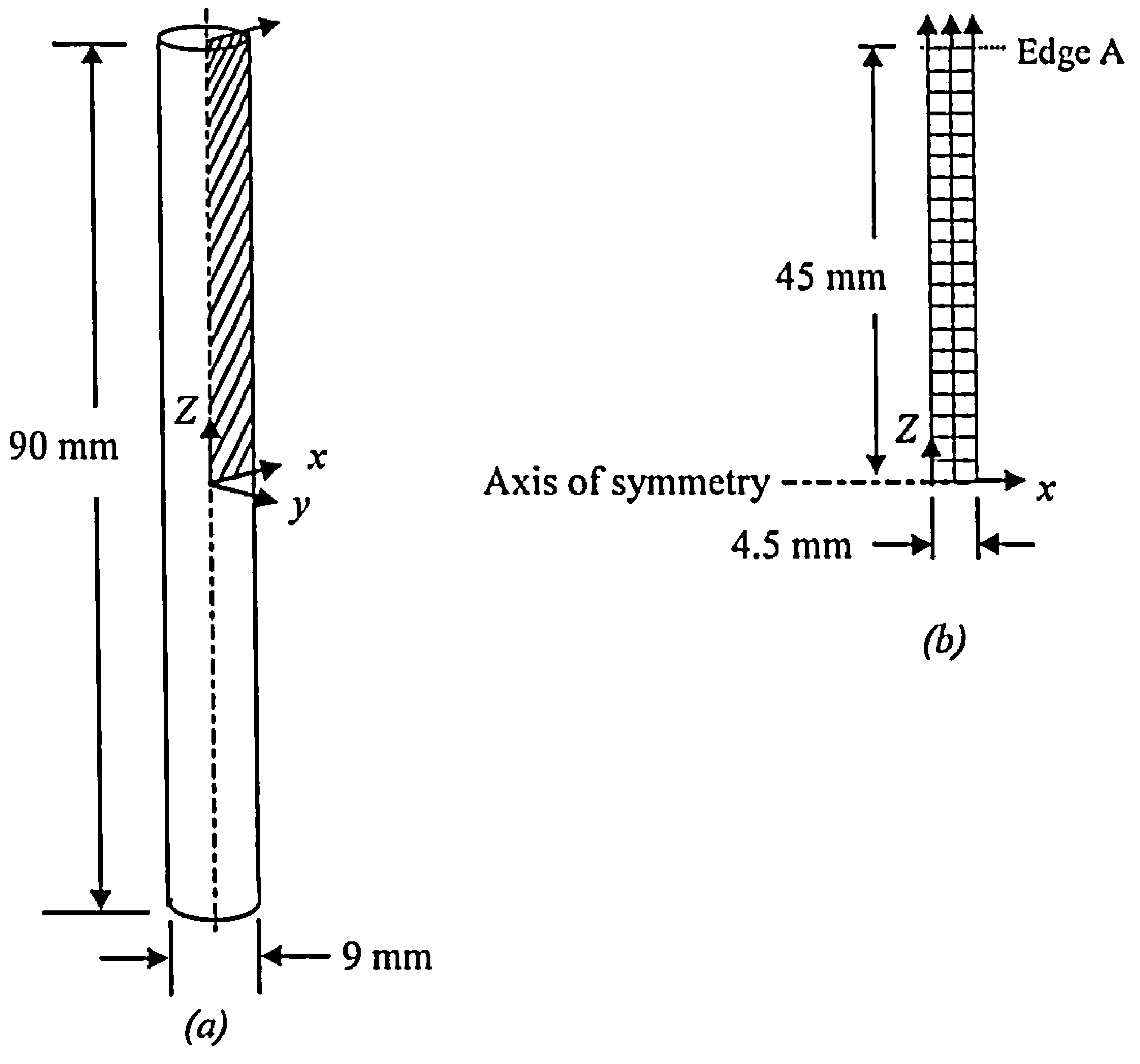

Figure 6.13 (a) Schematic diagram of the specimen considered in the stress relaxation simulations. (b) Simplified 2D finite element mesh representing the specimen using axisymmetric elements.

➢ Material Properties

Each of the models attempted to simulate a stress relaxation test performed at a specific temperature, i.e. simulation of the stress relaxation tests at 135°C, 140°C, 145°C and 148°C required the development of four models. In a model, the instantaneous modulus E at a specific temperature was defined (see Table 5-1). Values of $(t,\ g_R(t))$ experimentally obtained at that temperature were also provided. These were defined in the model in tabulated form, where $g_R(t) = E(t)/E_o$ and $E(t)$ is the modulus calculated at relaxation time (t) (see Figures 5.18 to 5.21).

➢ Boundary Conditions

Boundary conditions applied were those enforcing mirror symmetry of the model about the *x*-*y* plane (see Figure 6.13*b*). These boundary conditions constrained the nodes located along the axis of symmetry from translating in the *z*-direction, and prevented rotations of the nodes about the *x* and *y* axes of the local co-ordinate of each of the nodes. However, application of boundary conditions enforcing axisymmetry of the model was not required. The reason being that the element formulation automatically includes the effects of axial symmetry, preventing rigid body motion of the structure in the radial direction (*x*-direction), as reported by ABAQUS [43].

➢ Sequence of Loadings

In a stress relaxation test the specimen is initially stretched to a certain elongation, and held in that position for a period of time. That was replicated in the model in two steps. In the first step, elongation of the specimen was simulated by applying a boundary condition displacing the nodes located along edge (A) by a distance equal to 1mm in the (+*z*) direction (see Figure 6.13*b*). The time allowed for these nodes to displace was 0.01 seconds, which is set as the time period of the first step. That short period was chosen to allow the instantaneous elastic response of the structure to dominate.

In the second step, nodes located along edge (A) were constrained from translating, i.e. these nodes remained displaced in the step by 1mm in the z-direction from their originally defined (undeformed) structure. The time period specified for the step was equal to 10000 seconds allowing the structure to relax to its long term behaviour. The displacement boundary conditions applied on the nodes located along edge (A) during the analysis are schematically illustrated in Figure 6.14.

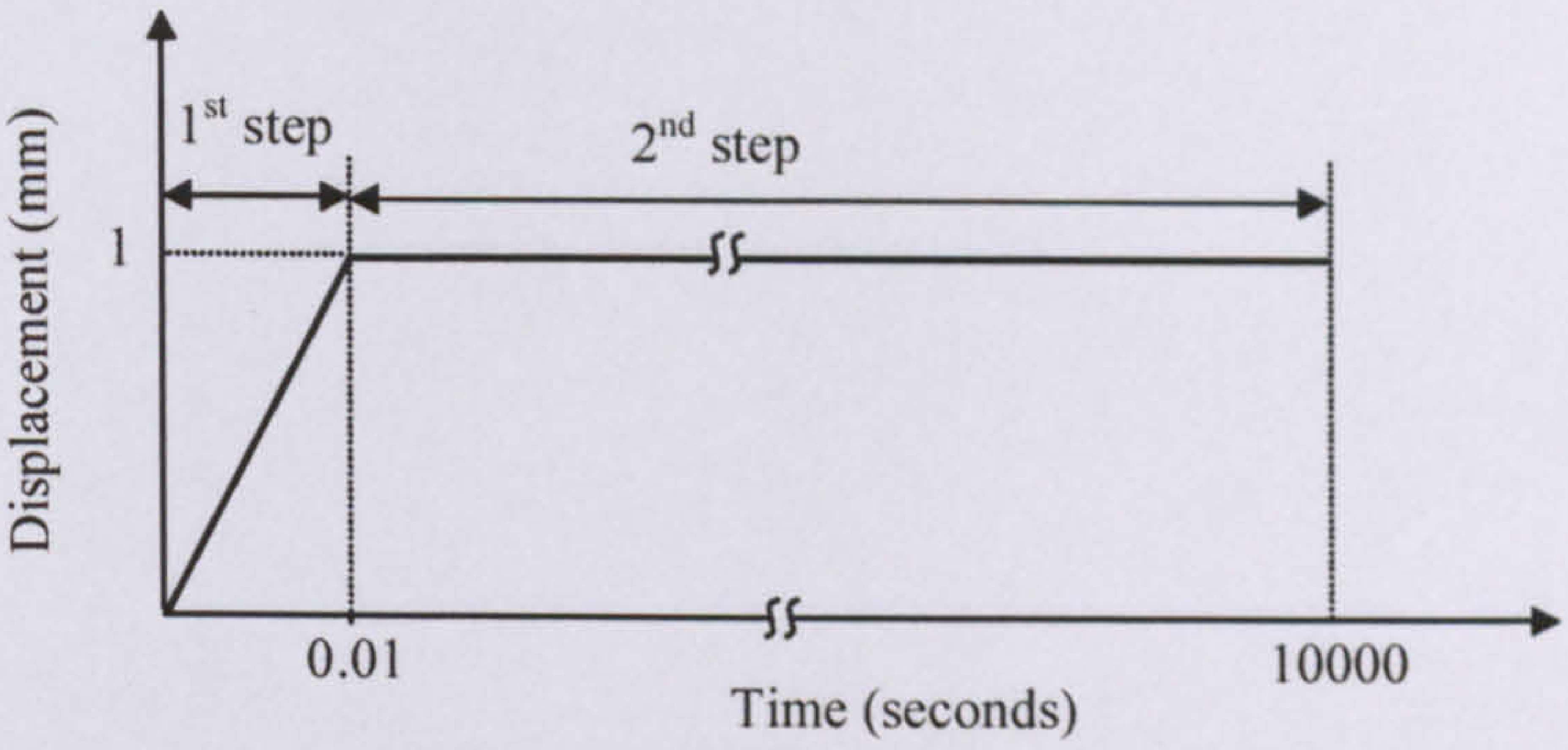

Figure 6.14 Schematic diagram illustrating the boundary conditions applied on the nodes located along edge (A) (see Figure 6.13) in the model investigating the accuracy of the Prony series.

➢ Results

The results predicted by a model are the decay in stress with time of each element in the mesh (see Figure 6.13*b*). Using Hooke's law, the stress in an element was divided by its (constant) strain giving a prediction of the decay in modulus with time. Figures 6.15 to 6.18 show the modulus-time curves predicted at 135°C, 140°C, 145°C and 148°C respectively, with each predicted curve drawn alongside the (modulus-time) data experimentally obtained at a corresponding temperature. The predicted (modulus-time) data show good agreement with the experimentally obtained stress relaxation data. The conclusion was that the Prony series is suitable in curve fitting experimentally stress relaxation obtained data.

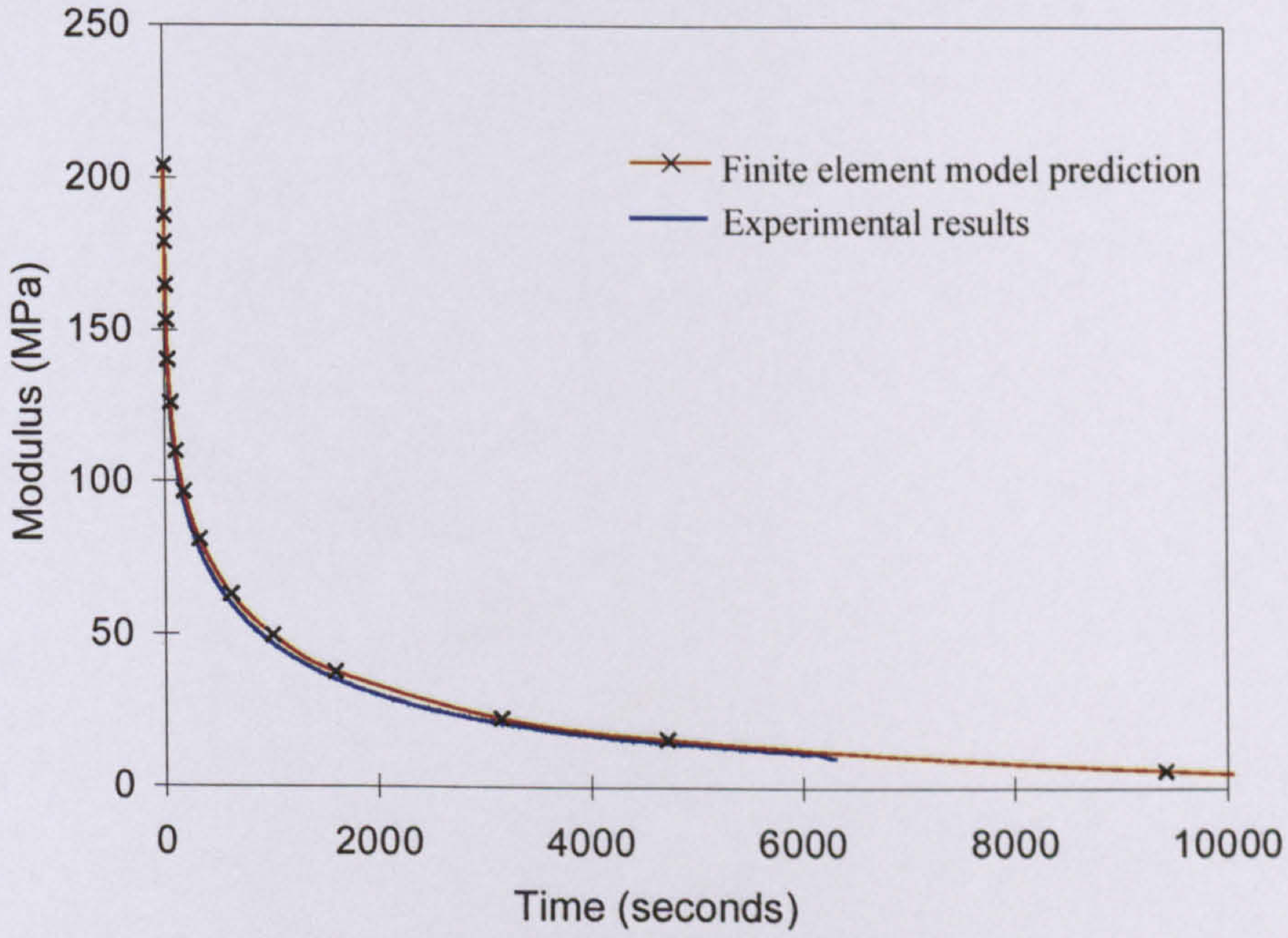

Figure 6.15 Stress relaxation results predicted using the Prony series at 135°C drawn alongside the experimentally obtained data at that temperature

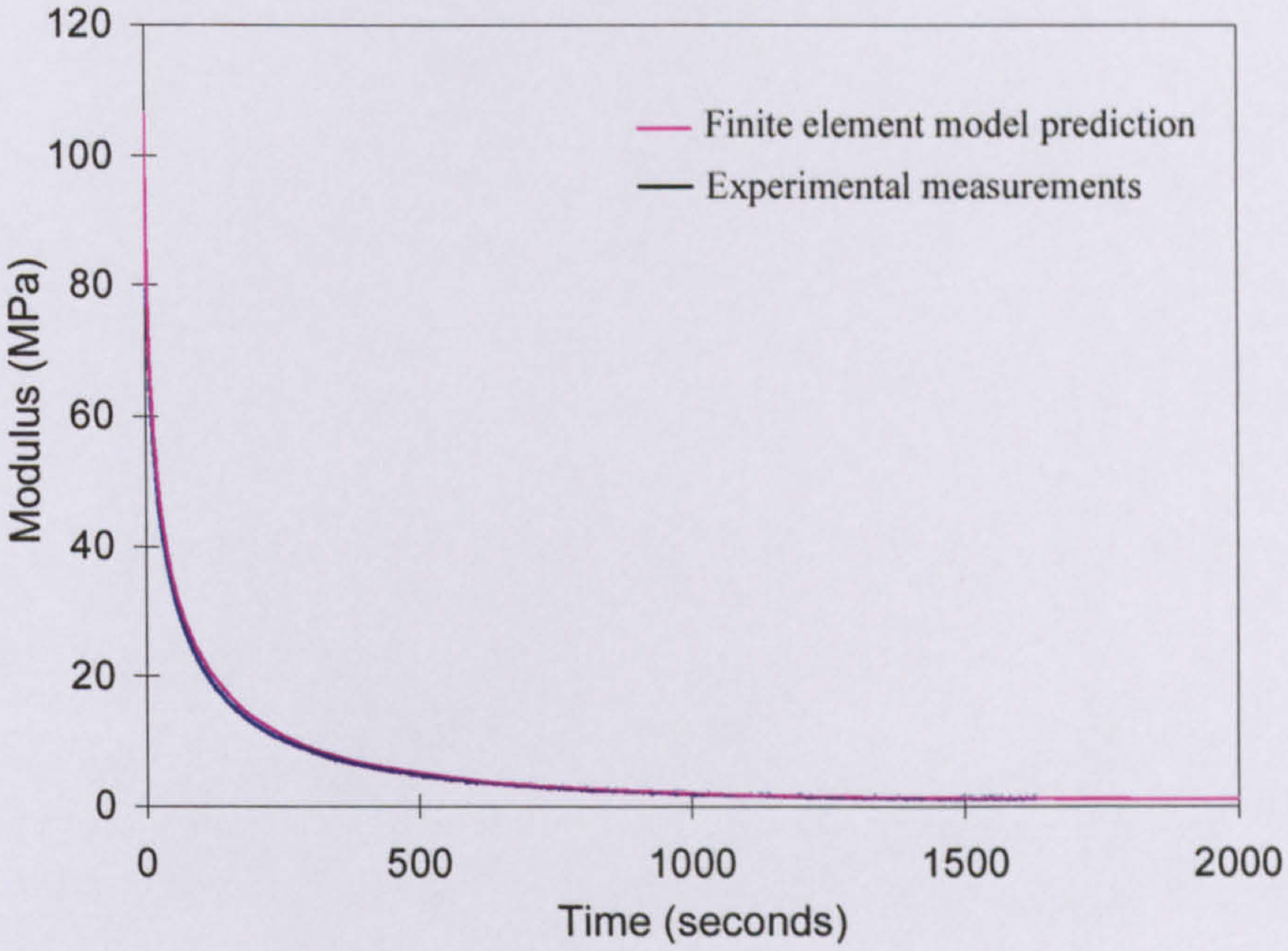

Figure 6.16 Stress relaxation results predicted using the Prony series at 140°C drawn alongside the experimentally obtained results at that temperature.

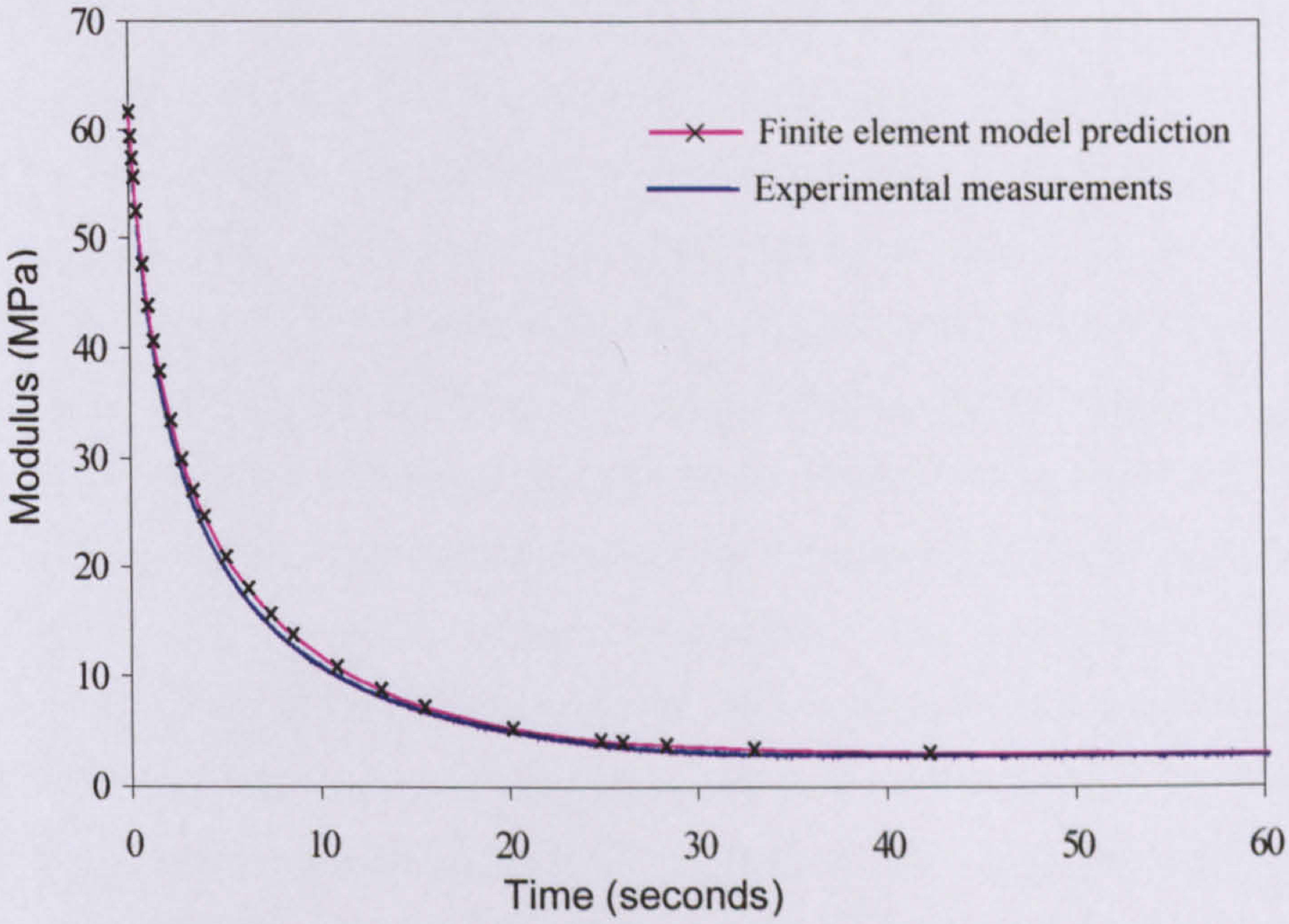

Figure 6.17 Stress relaxation results predicted using the Prony series at 145°C drawn alongside the experimentally obtained results at that temperature.

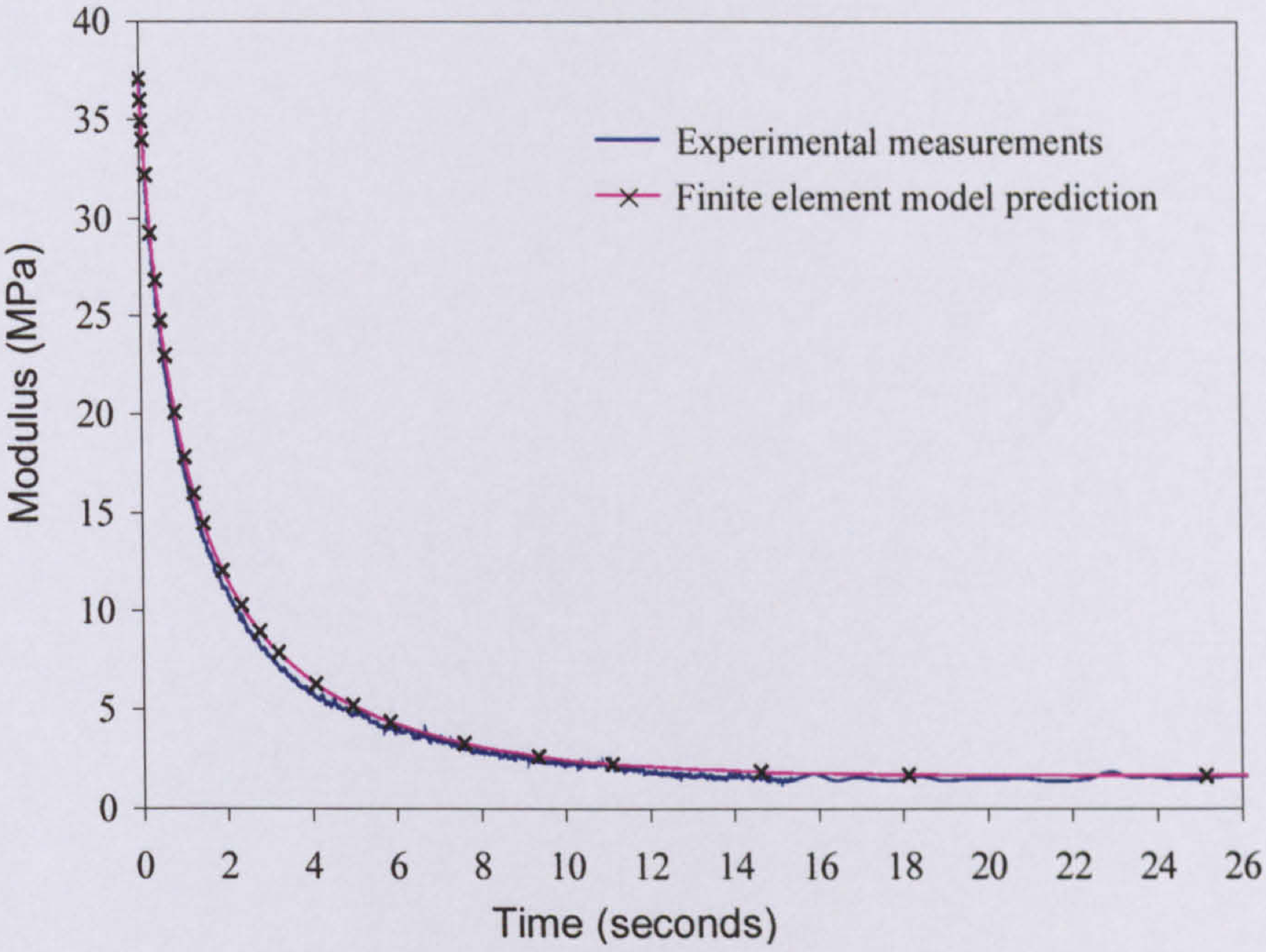

Figure 6.18 Stress relaxation results predicted using the Prony series at 148°C drawn alongside the experimentally obtained results at that temperature.

It has now been established that the Prony series can accurately curve fit stress relaxation data experimentally obtained at a single temperature. However, the (modelled) part in the stress analysis goes through extreme changes in temperature. Thus, a proper investigation into the effect of the viscoelastic behaviour on curl requires the time-dependent response at every temperature used in the stress analysis to be defined. The direct use of the Prony series to predict the time-dependent response at all temperatures used in the stress analysis requires stress relaxation tests to be experimentally performed at these temperatures, which is impracticable. The WLF approximation was therefore used as an alternative approach, whereby the stress relaxation data experimentally obtained at a single (reference) temperature are given along with the WLF constants estimated at that temperature (see Section 2.3.1.3). Based on the data provided, the WLF approximation predicts the time-dependent behaviour at every temperature used in the stress model. In the following, the method used in estimating the WLF constants is described. The accuracy of the WLF approximation in predicting the stress relaxation behaviour at various temperatures is then investigated.

Attempts were made to calculate the WLF constants based on the stress relaxation (modulus-time) data experimentally obtained at 135°C, 140°C, 145°C and 148°C (see Figures 5.18 to 5.21). To estimate the constants, the time scales of these data were first converted into logarithmic time scales, i.e. the resulting data were in the form (modulus-log(time)). The resulting (modulus-log (time)) data at 135°C, 140°C, 145°C and 148°C were then drawn alongside each other on the same logarithmic time scale as illustrated in Figure 6.19. The reference temperature (T_s) at which the WLF constants (C_1 and C_2) were to be calculated was selected to be 145°C (see Equation 2-3).

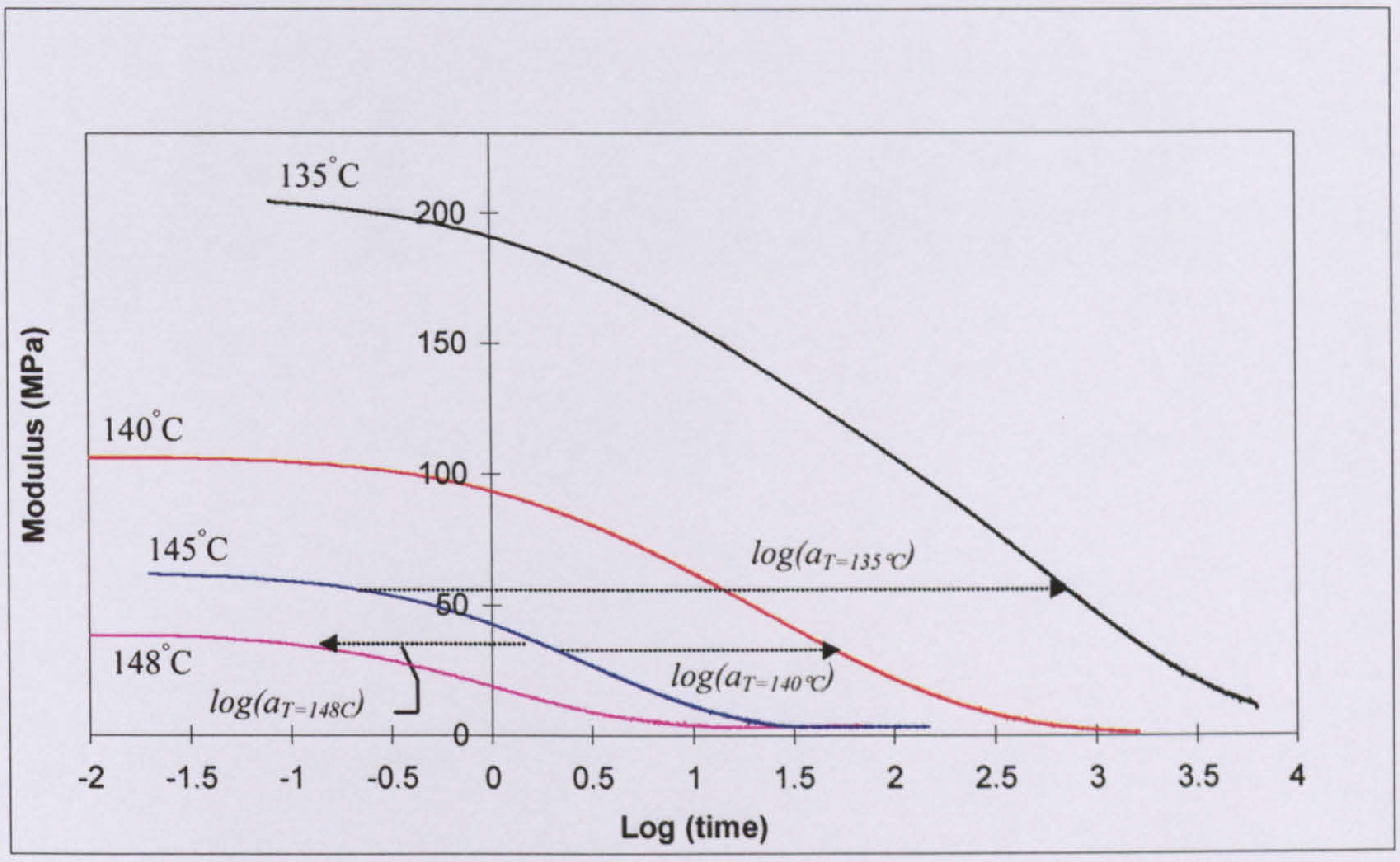

Figure 6.19 Stress relaxation (modulus-log(time)) curves experimentally obtained at 148°C, 145°C, 140°C and 135°C, drawn alongside for estimation of the WLF constants

Referring to Figure 6.19, the WLF approximation implies that the curves drawn at 148°C, 140°C and 135°C can be predicted by separately shifting the curve drawn at 145°C by horizontal shifts (along the logarithmic time scale) equal to $log(a_{T=148})$, $log(a_{T=140})$, $log(a_{T=135})$ respectively. The horizontal shift $log(a_{T=148})$, for instance, can be expressed using the WLF approximation as follows,

$$log(a_{T=148}) = \frac{-C_1(T-T_s)}{C_2+(T-T_s)} = \frac{-C_1(148-145)}{C_2+(148-145)} = \frac{-3C_1}{C_2+3} \qquad 6\text{-}9$$

In a similar way, the horizontal shifts $log(a_{T=140})$ and $log(a_{T=135})$ can be written with (T) in Equation 6-9 substituted with 140°C and 135°C respectively. Conversely, the shifts $log(a_{T=148})$, $log(a_{T=140})$ and $log(a_{T=135})$ can be numerically evaluated by estimating the horizontal distances, along the logarithmic time scale, between the curves drawn in Figure 6.19 at 148°C, 140°C and 135°C and that drawn at 145°C. As the curves drawn in the figure are not parallel, numerical values of the shifts were calculated by averaging several distance measurements made parallel to the logarithmic time scale between the curve drawn at 145°C and the other curves. The averaged values of the shifts $log(a_{T=148})$, $log(a_{T=140})$ and $log(a_{T=135})$ are summarised in Table 6-1. Working backwards by applying the calculated numerical values of the shifts into the corresponding WLF expressions of $log(a_{T=148})$, $log(a_{T=140})$ and $log(a_{T=135})$, the WLF constants C_1 and C_2 can be evaluated (see Equation 6-9). To simplify calculation of the constants, the WLF equation was first rearranged as follows [68],

$$\log(a_T) = \frac{-C_1(T-T_s)}{C_2+(T-T_s)} \tag{6-10}$$

$$\frac{(T-T_s)}{\log(a_T)} = \frac{C_2+(T-T_s)}{-C_1} \tag{6-11}$$

$$\frac{(T-T_s)}{\log(a_T)} = -\frac{1}{C_1}(T-T_s) - \frac{C_2}{C_1} \tag{6-12}$$

Equation 6-12 resembles the equation of a straight line of the form ($y = mx + b$), where m is the slope of the line and b is its intersection with the y-axis. Assuming that the line described by Equation 6-12 is drawn with the x-axis representing $(T-T_s)$ and the y-axis representing $(T-T_s)/\log(a_T)$ then the slope of the line would be equal to $-1/C_1$, whereas the intersection of the line with the y-axis would be equal to $-C_2/C_1$.

The values of $(T-T_s)$ and $(T-T_s)/\log(a_T)$ calculated at temperatures (T) equal to 135°C, 140°C and 148°C with T_s equal to 145°C are summarised in Table 6-1. These data are additionally plotted in Figure 6.20. The equation of the line best fitting the data points is expressed as follows,

$$\frac{(T-T_s)}{\log(a_T)} = -0.03(T-T_s) - 3.7128 \qquad 6\text{-}13$$

Temperature (T)	T-T_s	$Log\ (a_T)$	$(T-T_s)/\log(a_T)$
135°C	-10	2.888	-3.4626
140°C	-5	1.436	-3.4819
148°C	3	-0.7825	-3.8339

Table 6-1 Summary of $Log\ (a_T)$ and $(T-T_s)/\log(a_T)$ values estimated using the stress relaxation modulus curves experimentally obtained at (T) 135°C, 140°C and 148°C with T_s equal to 145°C

Thus, the slope of the line ($-1/C_1$) is equal to –0.03, giving a value of C_1 equal to 33.33. Additionally, the intersection of the line ($-C_2/C_1$) with the $(T-T_s)/\log(a_T)$ axis is equal to –3.7128 giving a value of C_2 equal to 123.76.

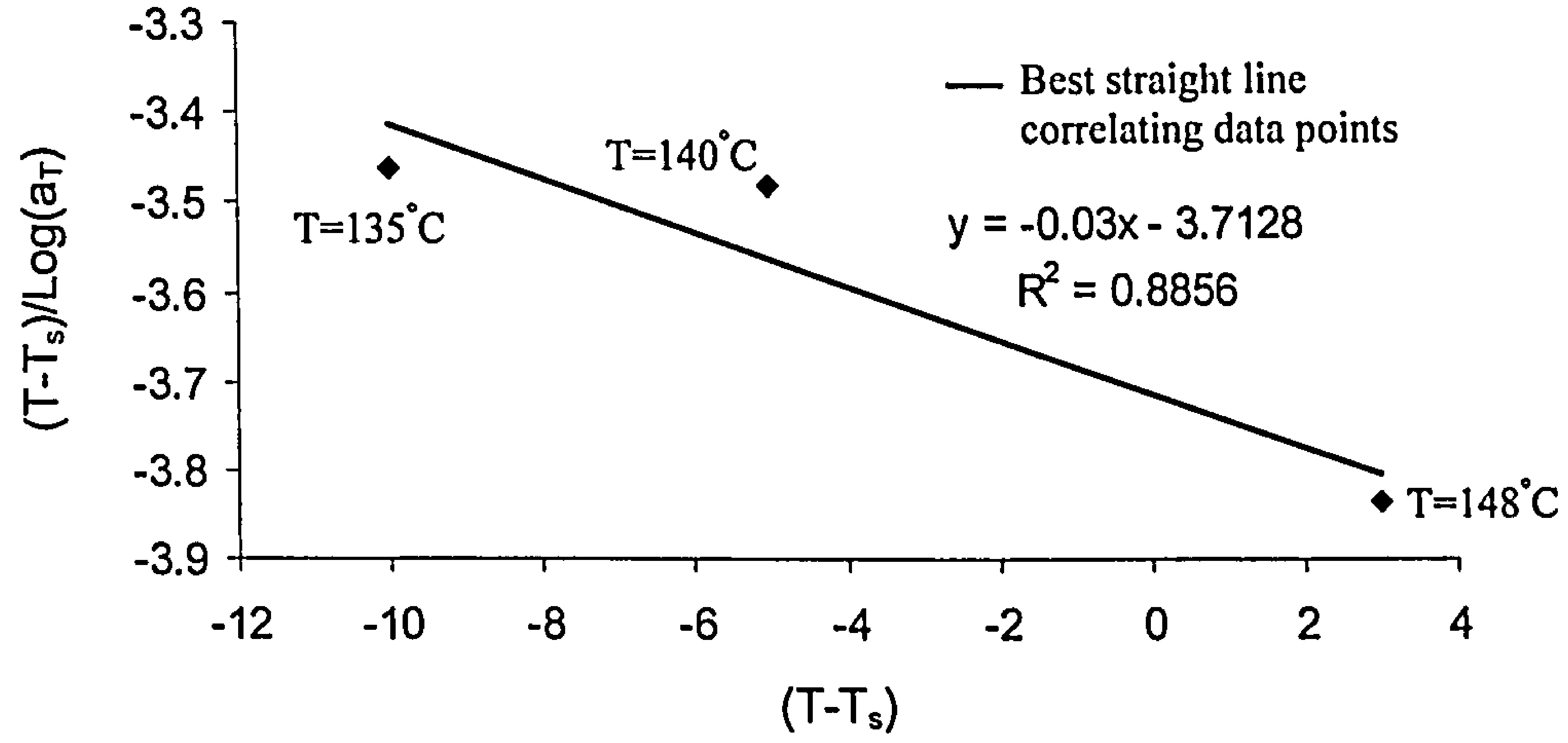

Figure 6.20 Illustration of the straight line best correlating the data points (T-T_s, $(T-T_s)/log(a_T)$) drawn at temperatures (T) equal to 135°C, 140°C and 148°C, T_s=145°C. Log (a_T) is the shift estimated between the curve experimentally obtained at T_s and those obtained at temperatures T. The symbol (R) denotes the coefficient of correlation of the straight line.

□ Investigation of the Accuracy of the WLF approximation in ABAQUS

In the following, the finite element models developed to investigate the accuracy of the WLF approximation are described. The models attempted to predict the stress relaxation behaviours at 135°C, 140°C and 148°C based on the stress relaxation data experimentally obtained at 145°C and WLF constants (C_1 and C_2) estimated at that temperature. The (modulus-time) data predicted at a certain temperature were compared to those obtained experimentally at that temperature.

The models developed were quite similar to those generated to examine the accuracy of the Prony series (described earlier). Aspects of similarity were in representing the geometry of the modelled specimen (see Figure 6.13), boundary conditions and sequence of loading. However, in the models employing the WLF approximation, an additional boundary condition was applied. The boundary condition maintained the nodal temperature of all elements in the mesh (see Figure 6.13*b*), through the entire period of simulation, equal to the temperature at which the stress relaxation behaviour is to be predicted. In the following, material properties defined in the models are described. Emphasis is also given to illustrate the method used by ABAQUS in implementing the WLF approximation.

The main material properties required as input to the models were the stress relaxation data experimentally obtained at the reference temperature (145°C) and the WLF constants estimated at that temperature. Based on Equation 6-13, the WLF constants C_1 and C_2 were defined in the models equal to 33.33 and 123.76 respectively. The stress relaxation data experimentally obtained at 145°C were defined in the model in tabulated form, $(t, g_R(t))$, where (t) is the relaxation time and $g_R(t) = E(t)/E_o$. In calculating values of $g_R(t)$, $E(t)$ was considered to be the decay in modulus estimated at 145°C (see Figure 5.19), whereas E_o is the instantaneous modulus experimentally measured at 145°C, which is equal to 61MPa. The model then uses the $(t, g_R(t))$ data given to estimate the Prony series parameters n, g_i and τ_{mi} (see Equation 6-8) for a best curve fitting of the experimentally obtained data to be achieved. For the (resulting) Prony series expression relating $g_R(t)$ with t to be transformed in ABAQUS into an expression relating $E(t)$ with t, the value of the instantaneous modulus E_o has to be provided, $E(t) = g_R(t) \cdot E_o$. However, the modulus E_o can be defined in the model as a function of temperature. The value of E_o selected to estimate the Prony series expression relating *E(t)* with *t* at 145°C was seen to be that defined at a temperature corresponding to the nodal temperature of the elements during simulation. For example, in the model simulating the stress relaxation behaviour at 135°C, the nodal temperature of all elements was maintained at 135°C. Thus, a single value of E_o was used through the entire simulation, which is equal to 204MPa (see Table 5-1). Similarly, the instantaneous modulus used in the models simulating the stress relaxation behaviours at 140°C and 148°C were equal to 106MPa and 38.4MPa respectively (see Table 5-1). It must be emphasised that the resulting Prony series expressions relating *E(t)* with *t* are considered in the ABAQUS models to describe the time-dependent behaviour at the reference temperature 145°C, regardless of the value of E_o used in estimating these expressions.

Based on the stress relaxation (modulus-time) relation defined by the Prony series at 145°C and the WLF constants provided, the WLF approximation is employed in the analyses to predict the stress relaxation behaviour at the temperature required. Figure 6.21 shows the method seen to be implemented by ABAQUS to predict the stress relaxation behaviour at 135°C. The (modulus-time) data expressed by the Prony series at 145°C, using the value of E_o defined at 135°C, are first converted into (modulus-log(time)) data (see Figure 6.21). The WLF approximation is then employed to estimate the shift $log(a_{T=135})$ required to displace the (modulus-log(time)) curve at 145°C along the logarithmic time scale to give the (modulus-log(time)) curve at 135°C. The shift $log(a_{T=135})$ is calculated as follows,

$$log\,(a_{T=135}) = \frac{-C_1(T-T_s)}{C_2+(T-T_s)} = \frac{-33.33(135-145)}{123.76+(135-145)} = 2.93$$

Using the same method, the (modulus-log(time)) curves at 140°C and at 148°C are predicted in ABAQUS, with $log(a_{T=140})$ and $log(a_{T=148})$ equal to 1.403 and –0.7888 respectively.

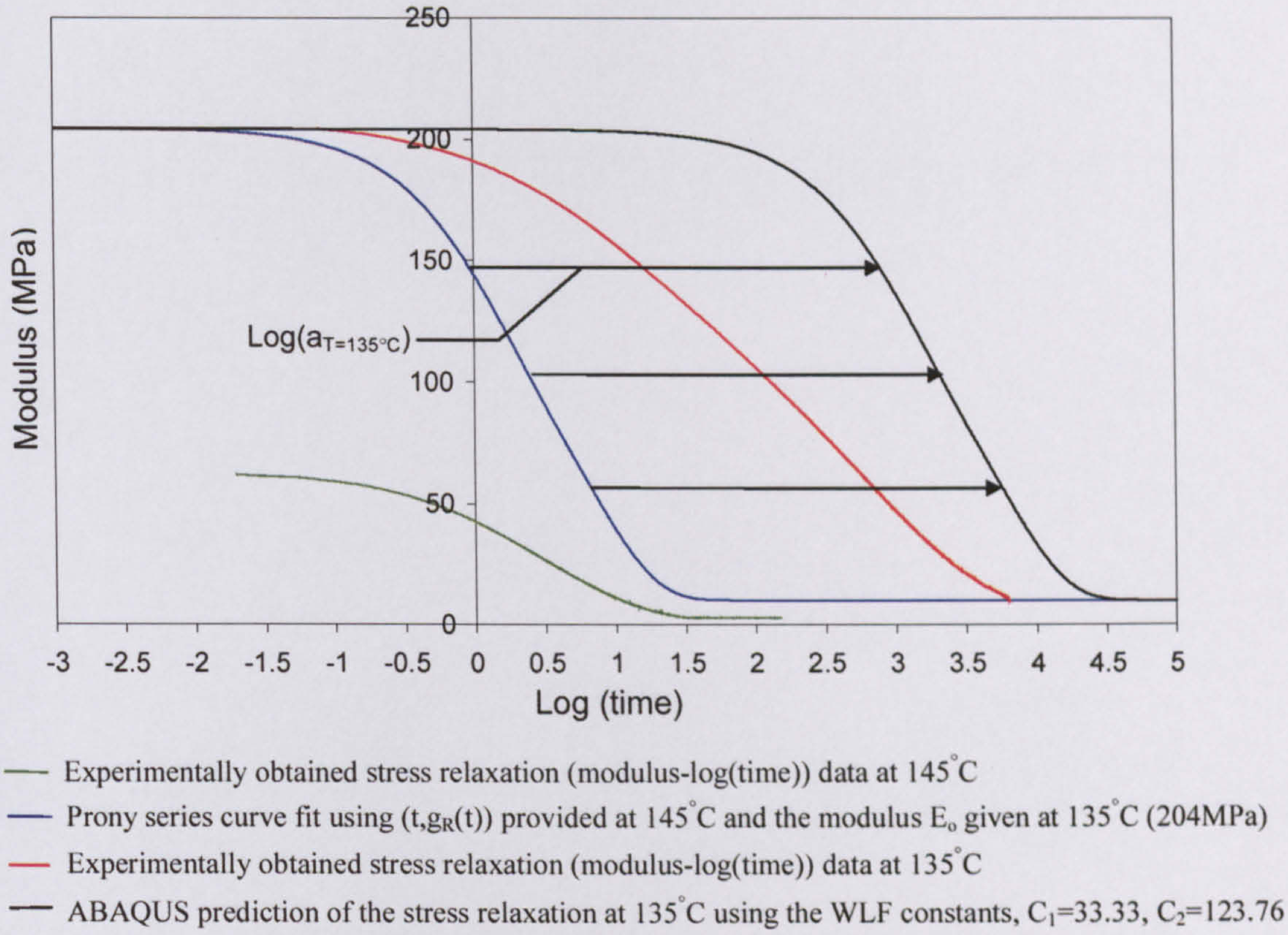

Figure 6.21 Illustration of the method used by ABAQUS to predict the (modulus-log(time) curve at 135°C using the WLF constants C_1=33.33 and C_2=123.76, with the reference temperature T_s= 145°C.

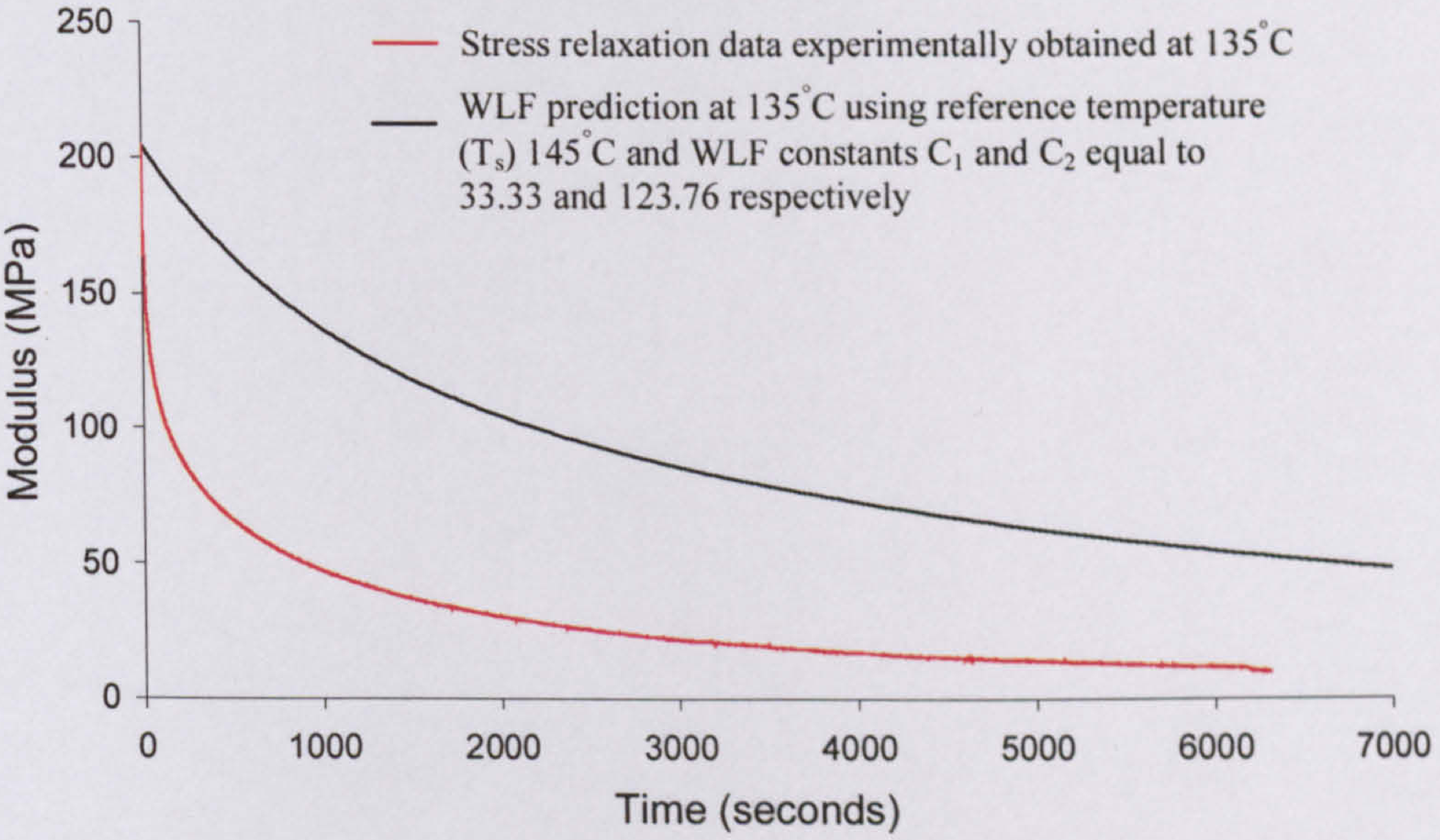

Figure 6.22 Stress relaxation (modulus-time) data predicted at 135°C using the WLF approximation, with C_1=33.33, C_2=123.7 and T_s=145°C, drawn alongside the experimentally obtained (modulus-time) data at 135°C.

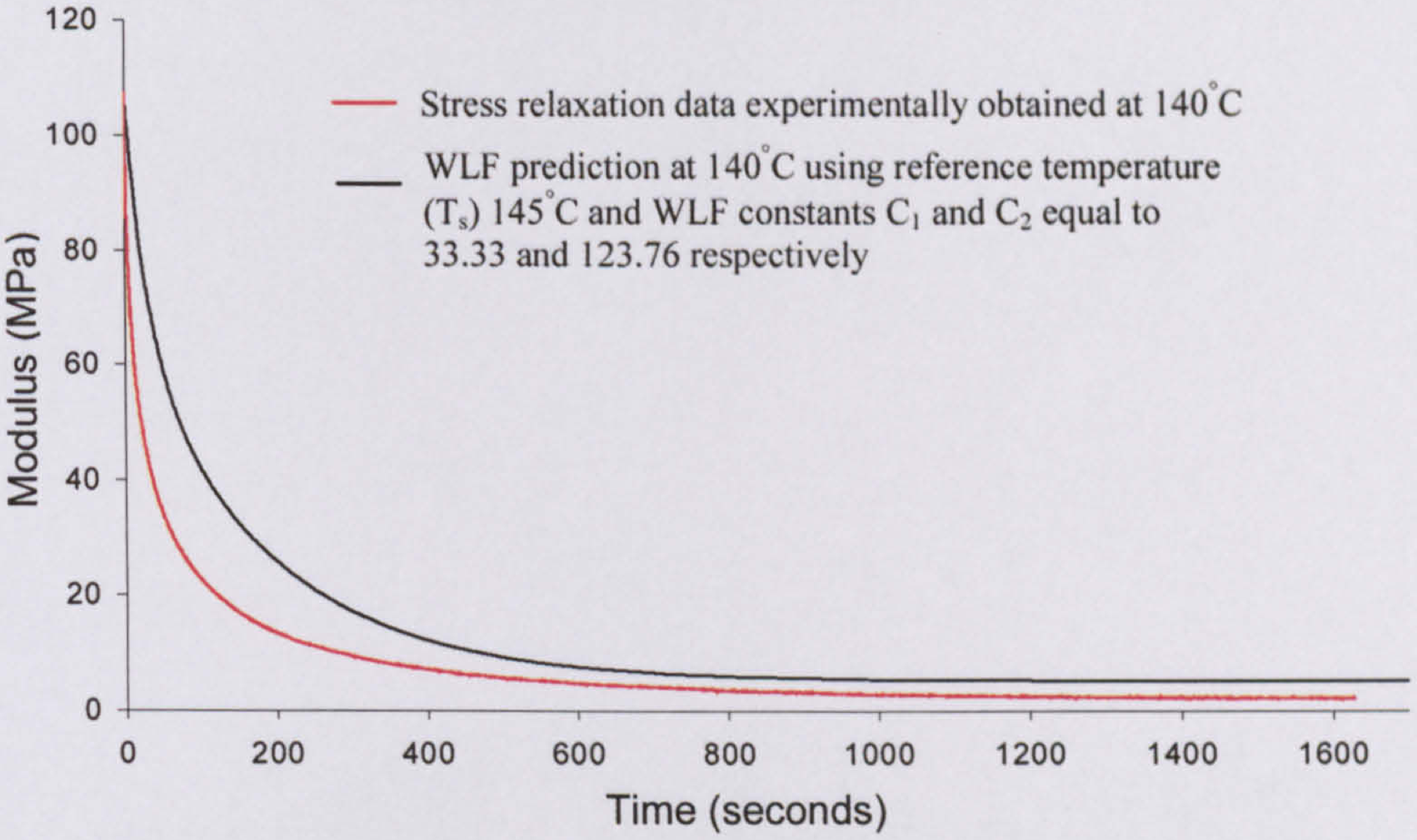

Figure 6.23 Stress relaxation (modulus-time) data predicted at 140°C using the WLF approximation, with C_1=33.33, C_2=123.7 and T_s=145°C, drawn alongside the experimentally obtained (modulus-time) data at 140°C.

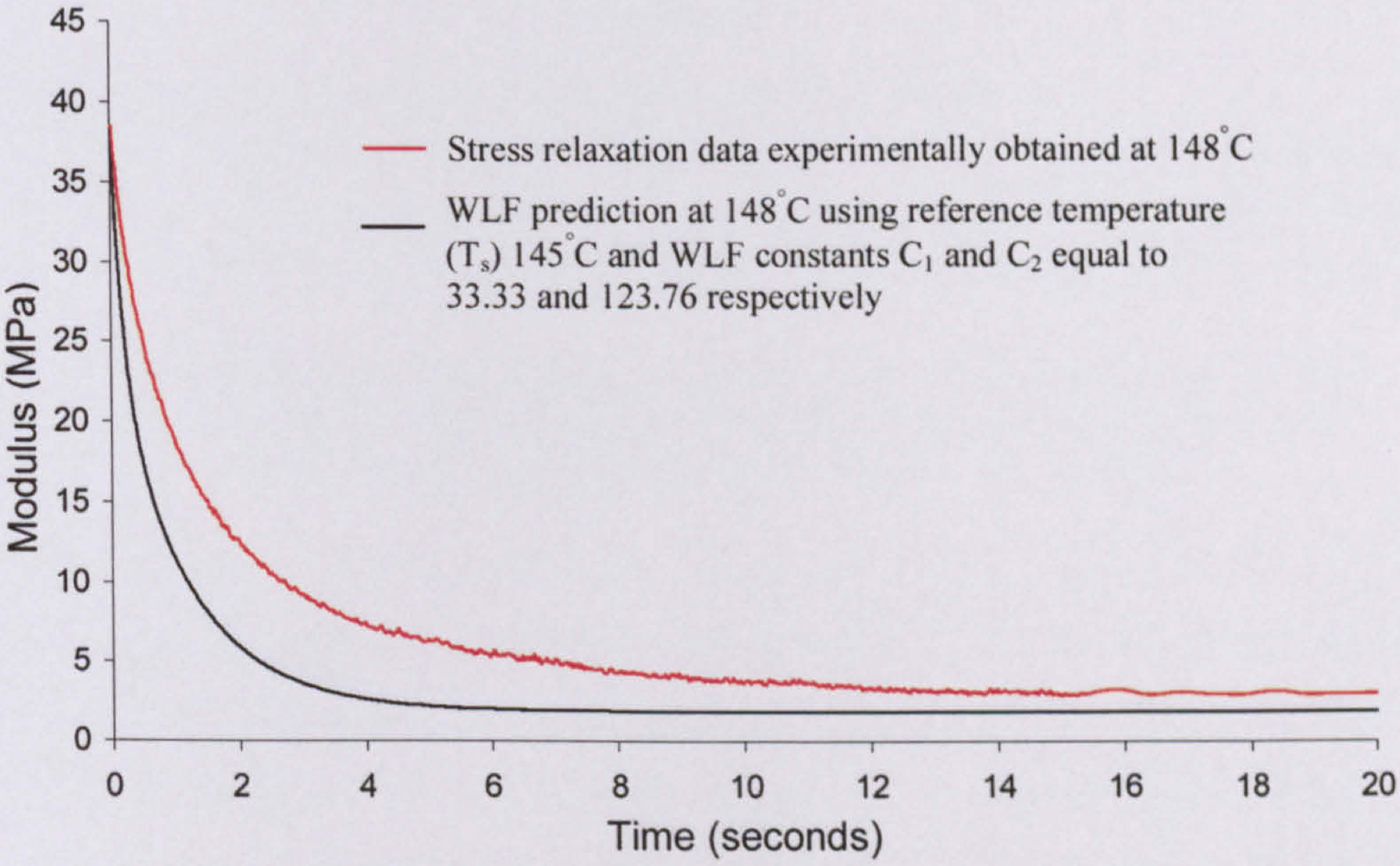

Figure 6.24 Stress relaxation (modulus-time) data predicted at 148°C using the WLF approximation, with C_1=33.33, C_2=123.7 and T_s=145°C, drawn alongside the experimentally obtained (modulus-time) data at that temperature.

Figures 6.22 to 6.24 show the (modulus-time) curves predicted at 135°C, 140°C and 148°C respectively, with each curve drawn alongside the (modulus-time) curve experimentally obtained at a corresponding temperature. The figures show that the (modulus-time) curves predicted using the WLF approximation disagree with the experimentally obtained stress relaxation data. In the following, a possible reason for the inaccurate prediction of the WLF approximation is investigated. Attempts made to reduce the inaccuracy are then described.

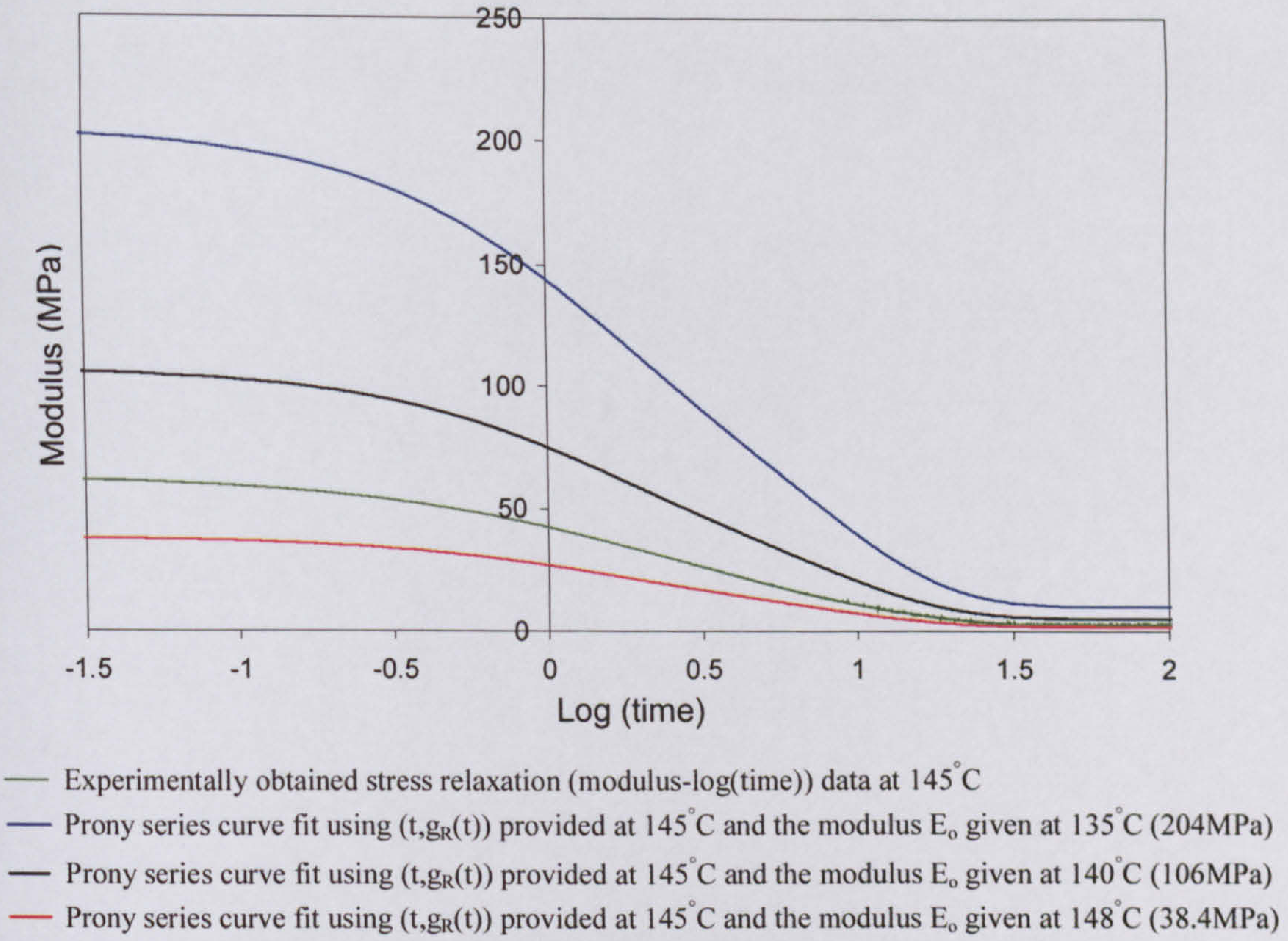

Figure 6.25 Illustration of the (modulus-log(time)) curves predicted using the Prony series at 145°C with E_o used as input the modulus experimentally measured at 135°C, 140°C, 148°C, drawn alongside the experimentally obtained curve at 145°C.

A major source of inaccuracy in the WLF predictions is the method used by ABAQUS in implementing the Prony series to predict the stress relaxation behaviour at the reference temperature selected (T_s). As aforementioned, ABAQUS uses the $(t, g_R(t))$ data given at T_s and the instantaneous modulus E defined at the temperature at which the stress relaxation behaviour is to be predicted to estimate the Prony series (modulus-time) relationship at T_s (see Equation 6-8). However, the instantaneous modulus E defined in the models at 135°C, 140°C and 148°C (204MPa, 106MPa, 38.4MPa) differ from E used in calculating the values of $g_R(t)$ defined in the models at the reference temperature, 145°C (61MPa). As a consequence, the resulting Prony series (modulus-log(time)) curves at 145°C, used in the WLF predictions, differ according to the temperature at which the stress relaxation behaviour is to be predicted (see Figure 6.21). Additionally, these curves disagree with the (modulus-log(time)) curve experimentally obtained at 145°C (see Figure 6.25). As the latter was previously used in estimating the WLF constants, the (modulus-time) curves predicted using the WLF approximation at 135°C, 140°C and 148°C are bound to disagree with the (modulus-time) curves experimentally obtained at these temperatures.

In an attempt to reduce the inaccuracy of WLF predictions performed by ABAQUS, an alternative method was employed in estimating the WLF constants to be used as input to the models. The method was developed based on the author's understanding on how the WLF approximation in ABAQUS is implemented. The reference temperature considered in estimating the WLF constants remained equal to 145°C. However, new values of the shifts $log(a_{T=135})$, $log(a_{T=140})$ and $log(a_{T=148})$ were estimated, resulting in WLF constants that differed from those previously calculated. In the following, the method used in estimating the new shifts are described.

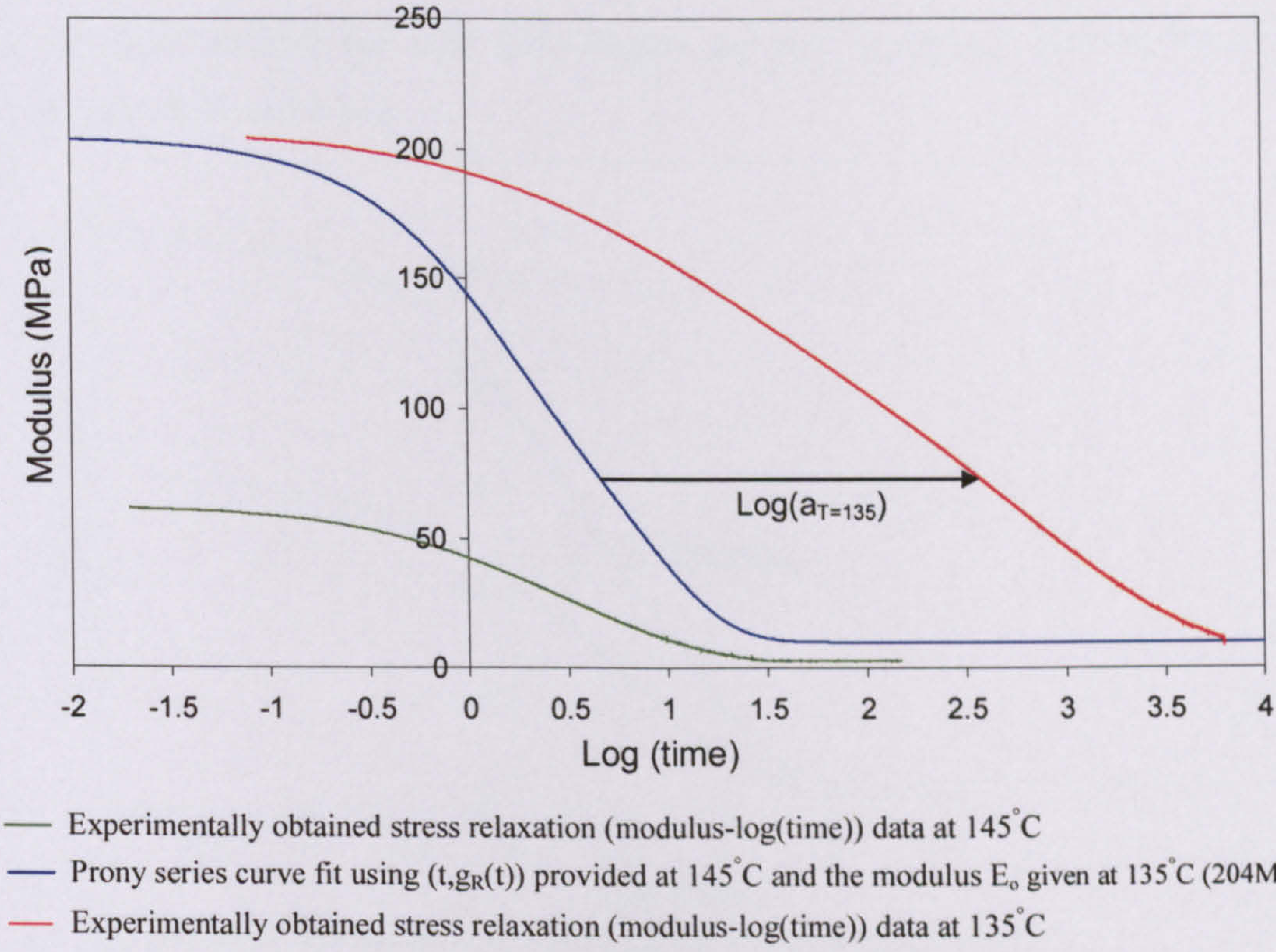

Figure 6.26 Illustration of the method used to estimate the new shift $log(a_{T=135})$, based on stress relaxation data Prony series predicted at 145°C using E_o which is experimentally measured at 135°C

Estimation of the shifts required utilisation of the ABAQUS model previously developed to simulate the stress relaxation test at 145°C (described earlier). To estimate the shift *log(*$a_{T=135}$*)*, for example, material properties selected as input to the model were values of $(t,\ g_R(t))$ calculated based on stress relaxation (modulus-time) data experimentally obtained at 145°C. However, the instantaneous modulus E defined in the model was that experimentally measured at 135°C, which is equal to 204MPa. The (modulus-time) data predicted by the model using the Prony series were then converted into (modulus-log(time)) data. The predicted (modulus-log(time)) data were drawn alongside the stress relaxation (modulus-log(time)) curve experimentally obtained at 135°C, as illustrated in Figure 6.26. It must be emphasised that the Prony series predicted curve, shown in the figure, represents the (modulus-log(time)) curve at the reference temperature (145°C). Consequently, the averaged distances measured parallel to the logarithmic time scale between the predicted (modulus-log(time)) curve at 145°C and that experimentally obtained curve at 135°C represents the new shift *log(*$a_{T=135}$*)* (see Figure 6.26). Using the same method, the new shifts *log(*$a_{T=140}$*)* and *log(*$a_{T=148}$*)* were estimated (see Figures 6.27 and 6.28).

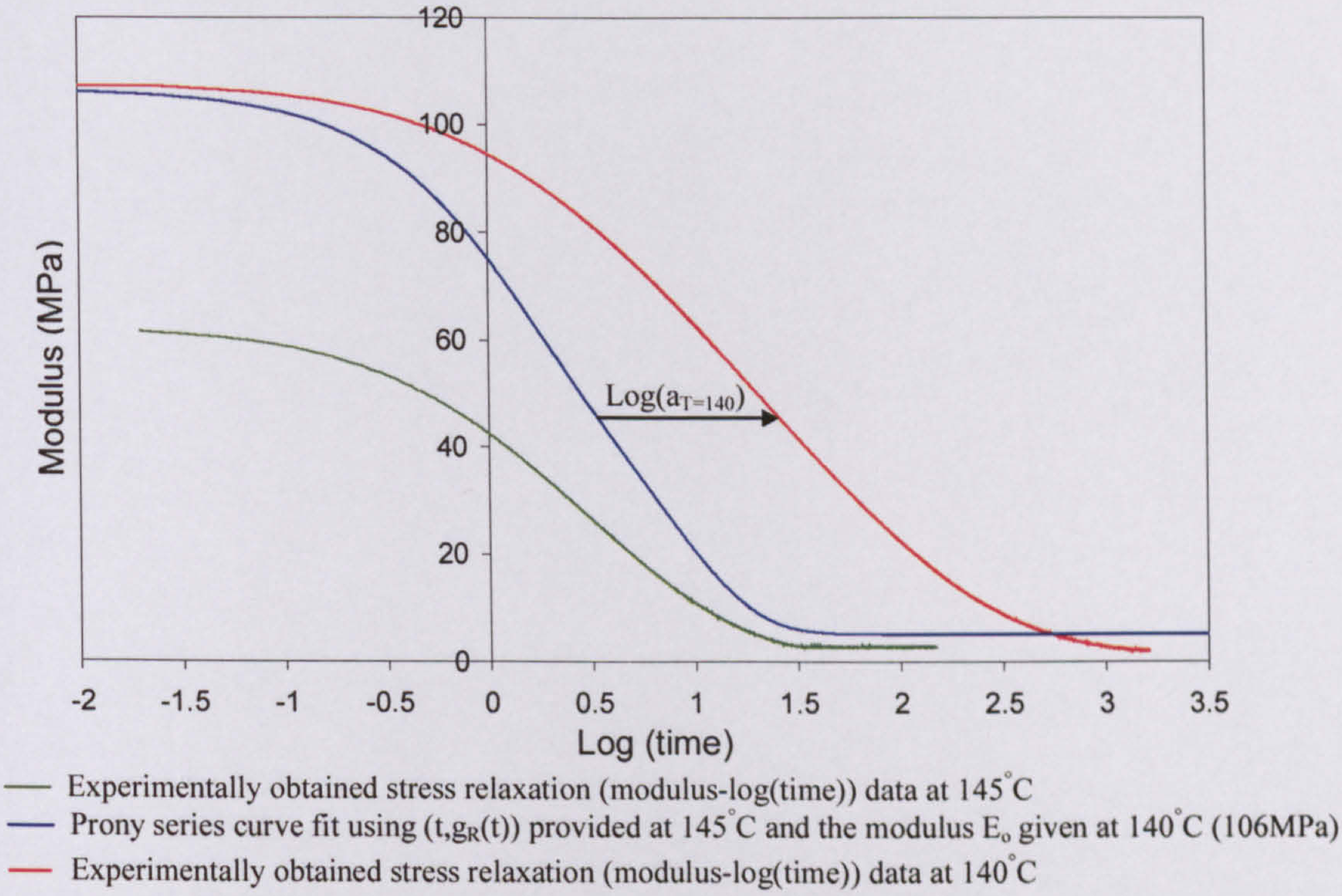

Figure 6.27 Illustration of the method used to estimate the new shift *log(*$a_{T=140}$*)*, based on stress relaxation data Prony series predicted at 145°C using E_o which is experimentally measured at 140°C

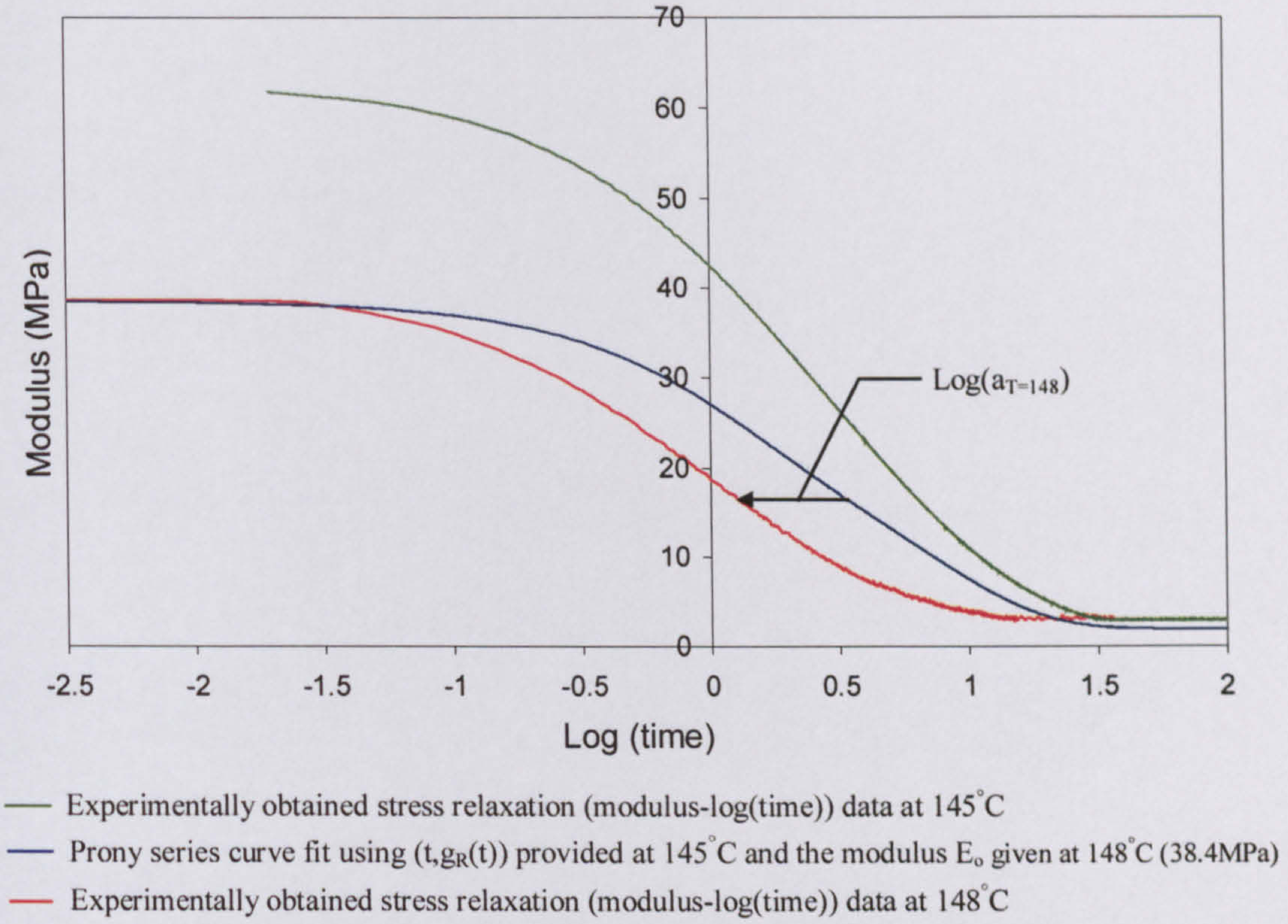

Figure 6.28 Illustration of the method used to estimate the new shift $\log(a_{T=148})$, based on stress relaxation data Prony series predicted at 145°C and using E_o which is experimentally measured at 148°C

The new values of the shifts $log(a_{T=135})$, $log(a_{T=140})$ and $log(a_{T=148})$ estimated using the method above-mentioned are introduced in Table 6-2. The data points plotted with the *x*-axis representing $(T-T_s)$ and the *y*-axis representing $(T-T_s)/\log(a_T)$ at T equal to 135°C, 140°C and 148°C and T_s equal to 145°C are illustrated in Figure 6.29. In the figure, the equation of the line best fitting the data points is expressed as follows,

$$\frac{(T-T_s)}{\log(a_T)} = -0.0607(T-T_s) - 7.0138 \qquad 6\text{-}14$$

Thus, the slope of the line ($-1/C_1$) is equal to –0.0607, giving a new value of C_1 equal to 16.47. Additionally, the intersection of the line ($-C_2/C_1$) with the $(T-T_s)/\log(a_T)$ axis is equal to –7.0138 giving a new value of C_2 equal to 115.549 (see Equation 6-12). Using these constants, the WLF approximation was again employed in ABAQUS to predict the stress relaxation behaviours at 135°C, 140°C and 148°C.

Temperature (T)	T-T_s	$Log\ (a_T)$	$(T-T_s)/\log(a_T)$
135°C	-10	1.5557	-6.4280
140°C	-5	0.7489	-6.6765
148°C	3	-0.41615	-7.20894

Table 6-2 Summary of $Log\ (a_T)$ and $(T-T_s)/\log(a_T)$ values estimated using the stress relaxation modulus curves experimentally obtained at (T) 135°C, 140°C and 148°C and that predicted using the Prony series at 145°C.

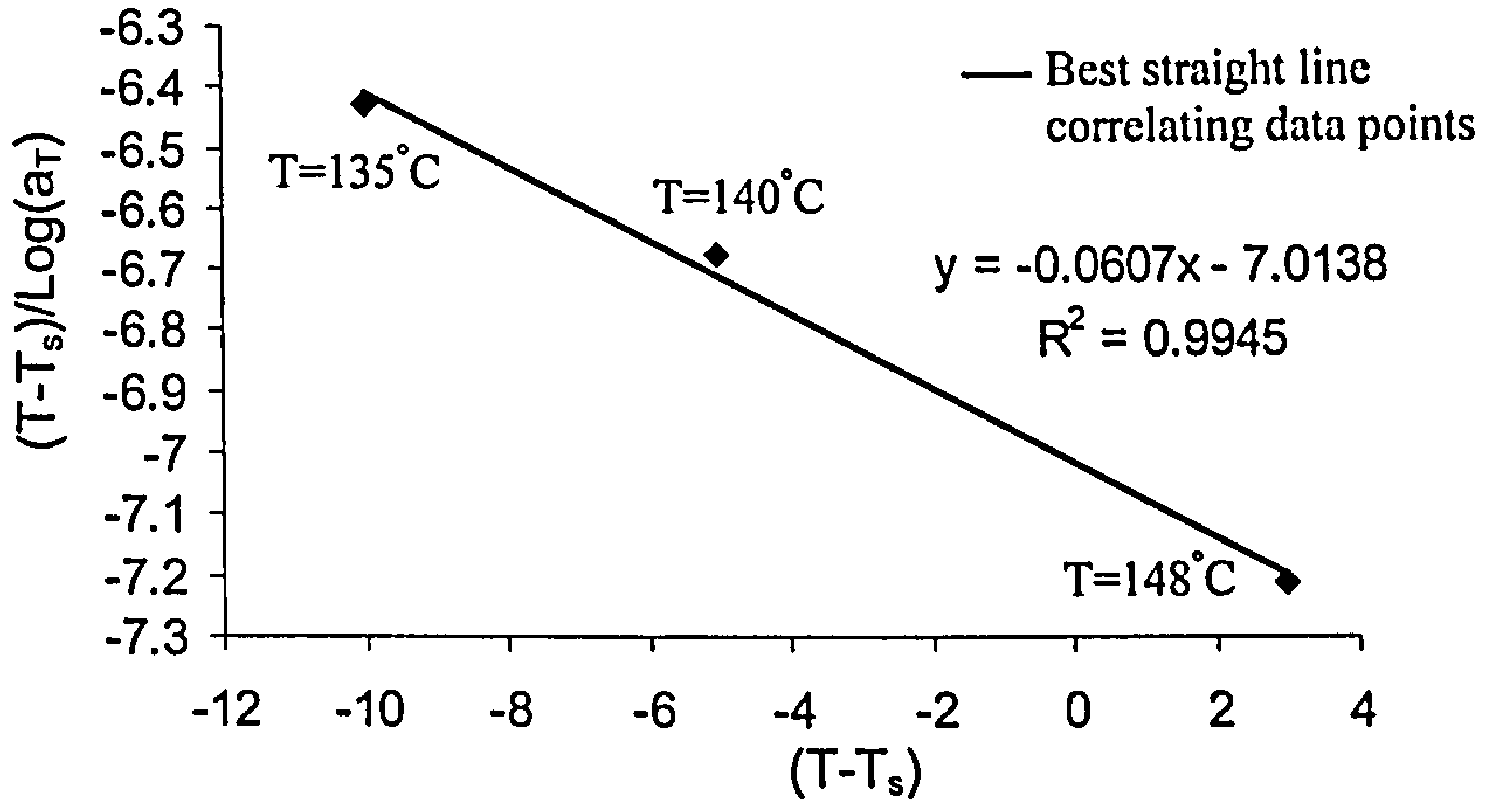

Figure 6.29 Illustration of the straight line best correlating the data points (T-T_s, $(T$-$T_s)/log(a_T)$) drawn at temperatures (T) equal to 135°C, 140°C and 148°C, T_s=145°C (listed in Table 6-2). The symbol (R) denotes the coefficient of correlation of the straight line.

The (modulus-time) curves predicted at 135°C, 140°C and 148°C using the recently calculated WLF constants (C_1=16.47, C_2=115.549) are illustrated in Figures 6.30 to 6.32. Each of the curves is drawn alongside the (modulus-time) curve experimentally obtained at a corresponding and the curve previously predicted using the (old) estimated WLF constants C_1=33, C_2=123.76. The figures show that the recently predicted curve do not agree with those experimentally obtained. However, they remain more accurate than those previously predicted. Due to the lack of better material properties, the newly calculated values C_1=16.47, C_2=115.549 were used as input to the stress model, with the reference temperature equal to 145°C. These data were assigned to all elements together representing the ten-layer part in the stress analysis mesh (see Figure 6.11).

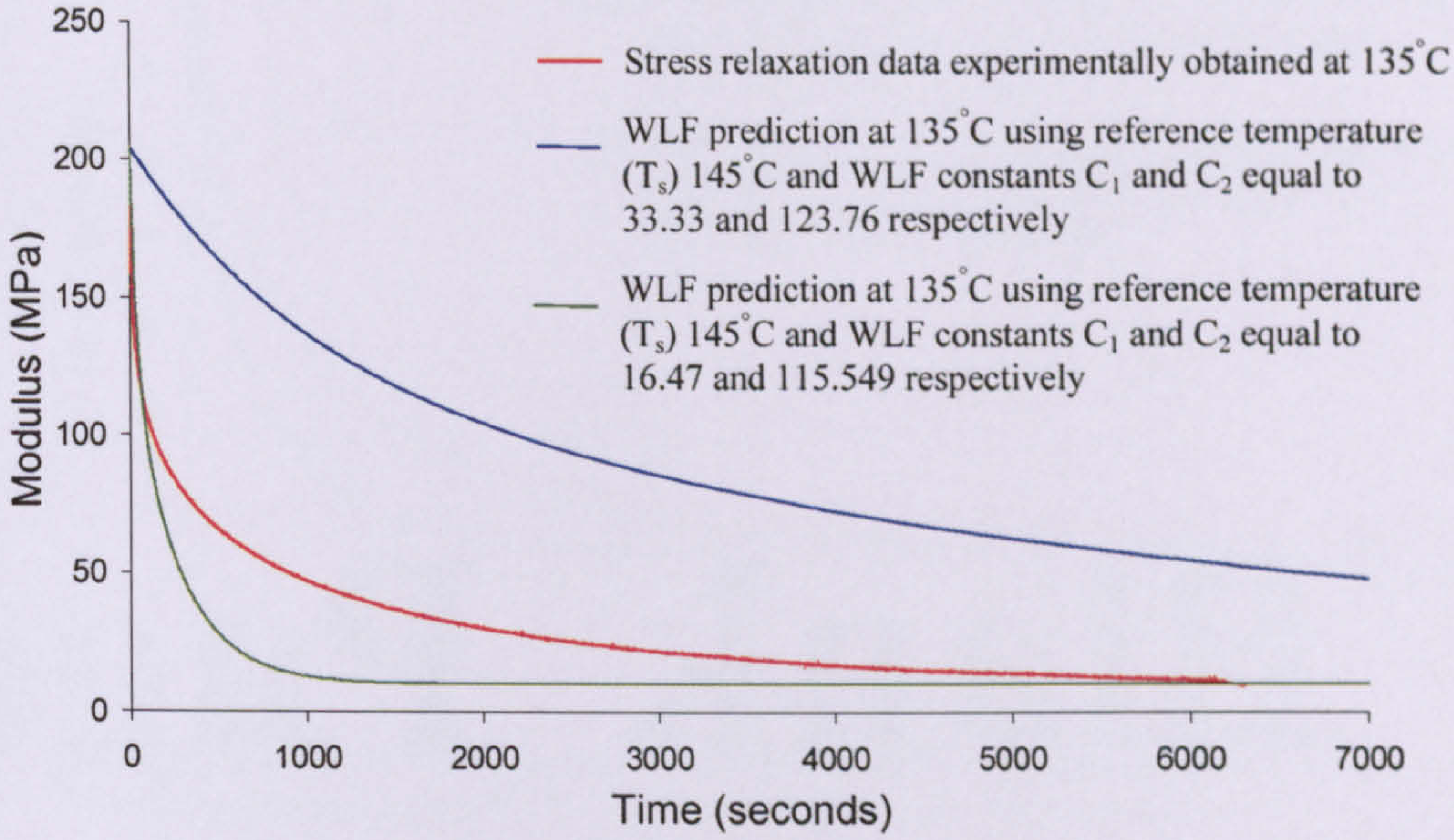

Figure 6.30 Stress relaxation curve experimentally obtained at 135°C drawn alongside the curves WLF predicted using the new constants C_1=16.47, C_2=115.549, and the old ones C_1=33.33 and C_2=123.76, with T_s=145°C.

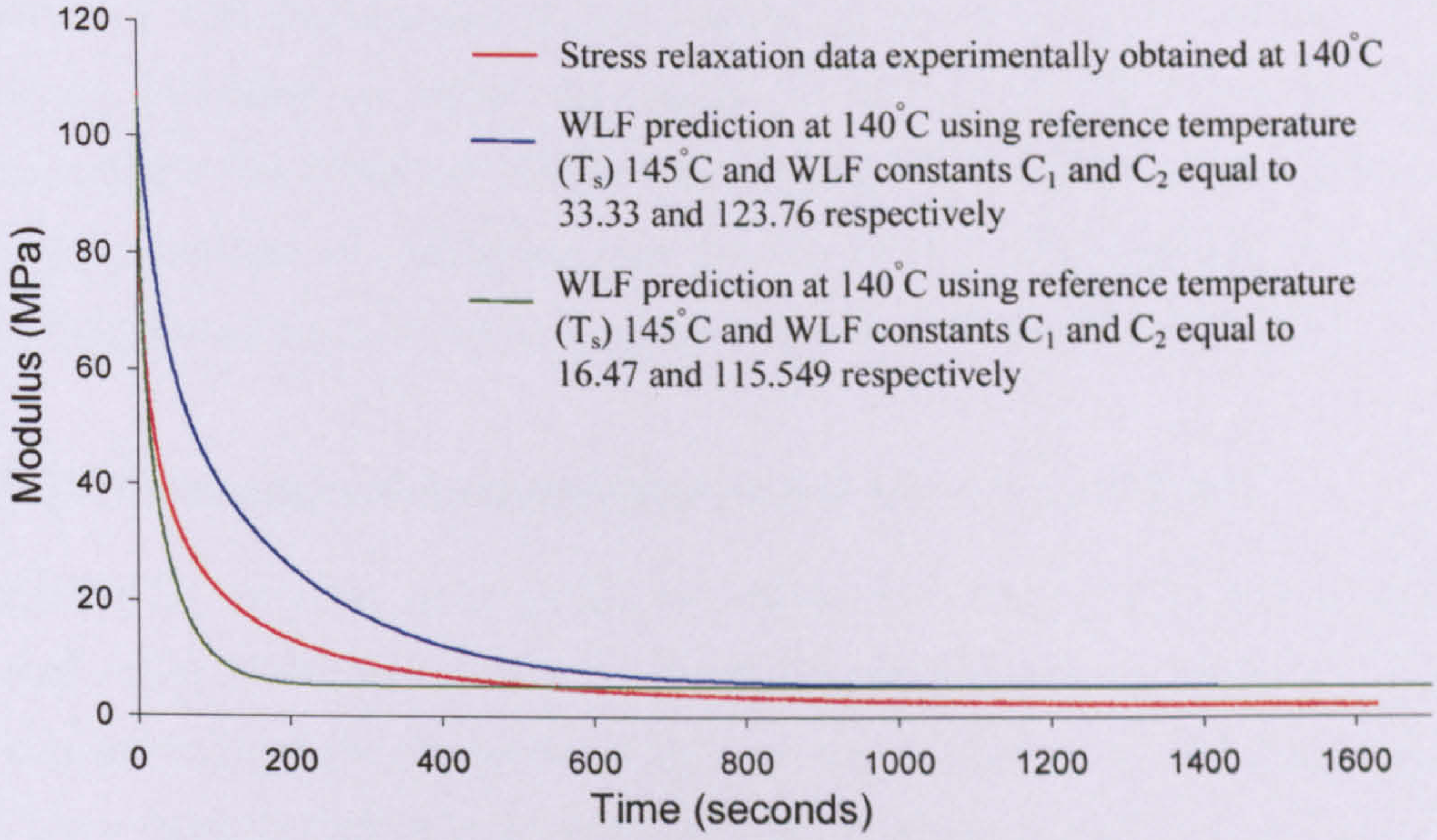

Figure 6.31 Stress relaxation curve experimentally obtained at 140°C drawn alongside the curves WLF predicted using the new constants C_1=16.47, C_2=115.549, and the old ones C_1=33.33 and C_2=123.76, with T_s=145°C.

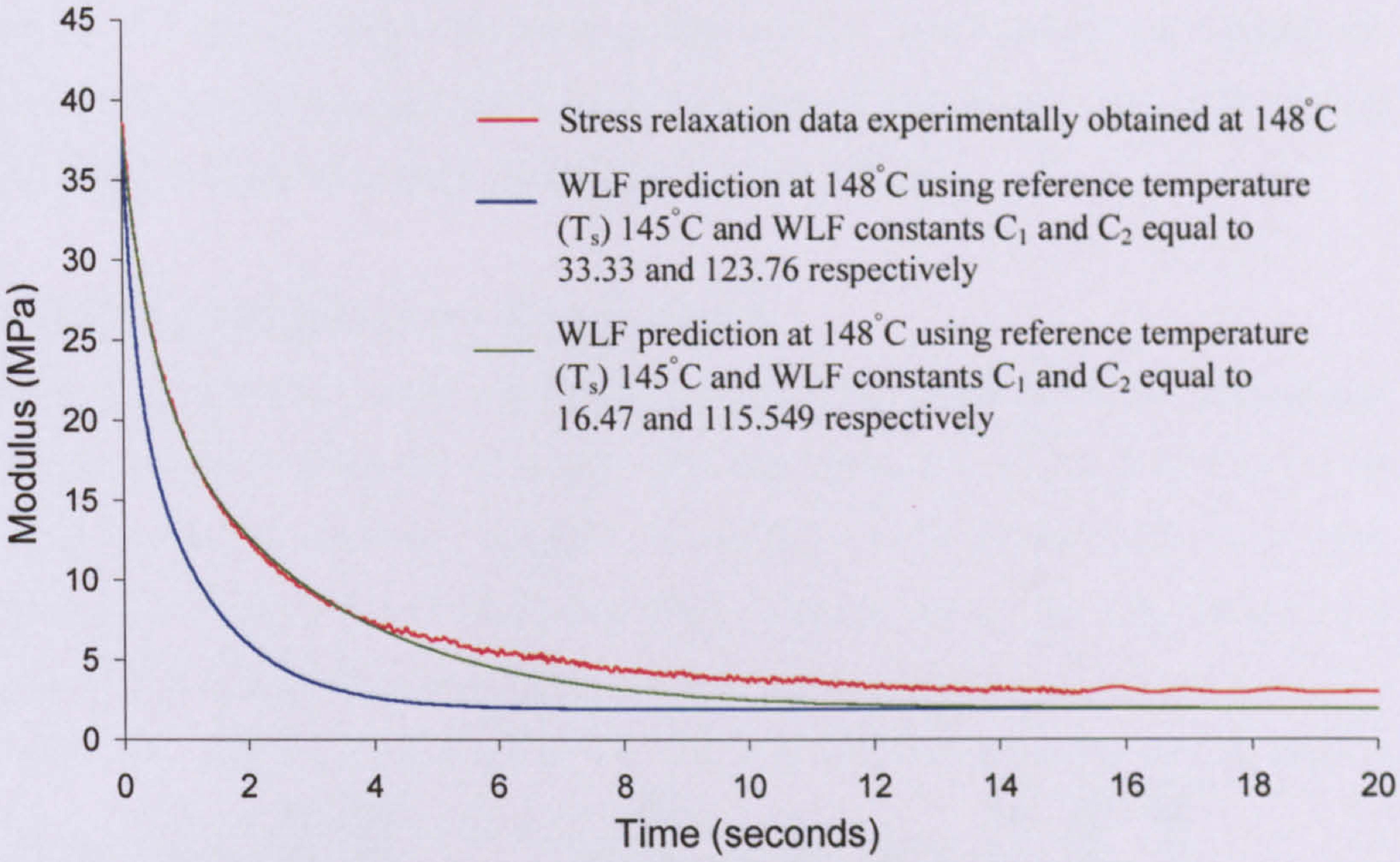

Figure 6.32 Stress relaxation curve experimentally obtained at 148°C drawn alongside the curves WLF predicted using the new constants C_1=16.47, C_2=115.549, and the old ones C_1=33.33 and C_2=123.76, with T_s=145°C.

6.2.2.3 Boundary Conditions

The method adopted in defining boundary conditions in the first version of the stress model was also implemented in this version of the model (see Section 4.7.3). However, definition of initial temperatures in this model was based on DMA measurements that identified 175°C to be the temperature above which stresses in SLS polycarbonate are negligible (see Section 5.3.2.1). Consequently, the initial temperature of all nodes in the stress analysis mesh was defined equal to 175°C.

6.2.2.4 Sequence of Analysis Defined in the Stress Model

Similar to the previous stress model, the sequence of analysis was defined in the present stress model on the basis of nodal temperature histories predicted by the corresponding heat transfer model. However, nodal temperature histories used as thermal loading in various steps of the present stress model were selected based on DMA measurements that identified 175°C to be the temperature below which stresses develop in a recently sintered layer. Additionally, magnitudes of loads corresponding to the weight of layers differed in the present model than those defined in the previous one due to modifications in density definition and in thicknesses of layers forming the ten-layer part. In the following, thermal and mechanical loading defined in selected steps of the stress model are introduced. Boundary conditions applied, however, were identical in corresponding steps of both the previous and present stress models (see Section 4.7.3).

- **First Step Defined in the Stress model**

Similar to the previous model, the first step in the stress model simulates thermal and mechanical effects expected to occur following sintering of the first layer (with thermal stresses developing) and prior to addition of the second layer of powder. Referring to Figure 6.8, the nodal temperature histories read in the step started at the instant 8 seconds (from the start of the thermal analysis) and ended at the instant 12.6 seconds. The duration specified for the first step was therefore the time difference between the two instants, which is equal to 4.6 seconds.

- **Second Step Defined in the Stress model**

The second step simulates thermal and mechanical effects expected to occur after addition of the second layer of powder and prior to stresses developing in the layer (immediately) following its sintering. Similar to the second step of the previous model, elements representing the second layer were not activated. However, the weight per area of the added layer was simulated by uniform pressure simultaneously applied on the top surface of the first layer. The amount of pressure (P) defined in the step was calculated using Equation 4-34, with t_l and ρ substituted with 0.127mm and 497kg/m^3 respectively giving a value of P equal to 0.609Pa. Referring to Figure 6.9, nodal temperatures histories read in the step were from the instant 12.6 seconds (from the start of the thermal analysis) to the instant 20.7 seconds. The time period of the step was specified as the difference between the two instants, which is equal to 8.1 seconds.

The concept used in defining the first two steps of the stress model was also implemented in defining the remaining steps simulating the "build" stage in fabrication of the ten-layer parts. The final step in the stress model simulates effects expected to occur during cooling of the fabricated part to room temperature. Referring to Figure 6.10, nodal temperature histories read in the step were from the instant 121.6 seconds (from the start of the heat transfer analysis) to the instant 2320 seconds. The latter denotes the instant at which the temperature in the part was equal to 20°C. The time period of the step was specified as the difference between the two instants, which is equal to 2198.4 seconds.

6.2.2.5 Results

Effects simulated in all steps of the model along with selected magnitudes of the maximum distance of the bottom surface of the build from the rigid surface are presented in Table 6-3. The table illustrates a rise in curl predicted in steps simulating effects occurring following sintering of a layer (with stresses developing) and prior to addition of the next layer of powder. That was also observed in steps simulating corresponding effects in the first version of the stress model (see Table 4-10). However, the development of curl predicted by both models was seen to differ in steps simulating effects occurring following addition of certain layers of powder and prior to sintering of the layers taking place. In the previous model, addition of the second and third layers of powder resulted in reduction in curl (see Table 4-10), whereas addition of all layers of powder was predicted in the present model to give rise to curl. The development of curl was additionally seen to vary in predictions of both models in steps simulating effects occurring whilst the ninth and tenth layers were in the melt (immediately) following their sintering. In the previous model, sintering of these layers resulted in downward curl of the build, whereas sintering of all layers in the present model was accompanied by reduction in curl with the build exhibiting at all times an upward curl.

Figure 6.33 illustrates selected profiles of the (modelled) bottom surface of the build predicted in the second step of the stress model. In the step, elements representing the second layer were not activated. Additionally, thermal strains influencing the development of curl were of elements flanked by nodes located at the top surface of the first layer and those located at a depth of 0.257mm from that surface. In the first 1×10^{-6} seconds of the step, the load simulating the weight of the second layer had an insignificant effect on reducing curl; the maximum distance of the bottom surface of the build from the rigid surface reduced from 1.73×10^{-4}mm to 1.64×10^{-4}mm, i.e. by 5.2%.

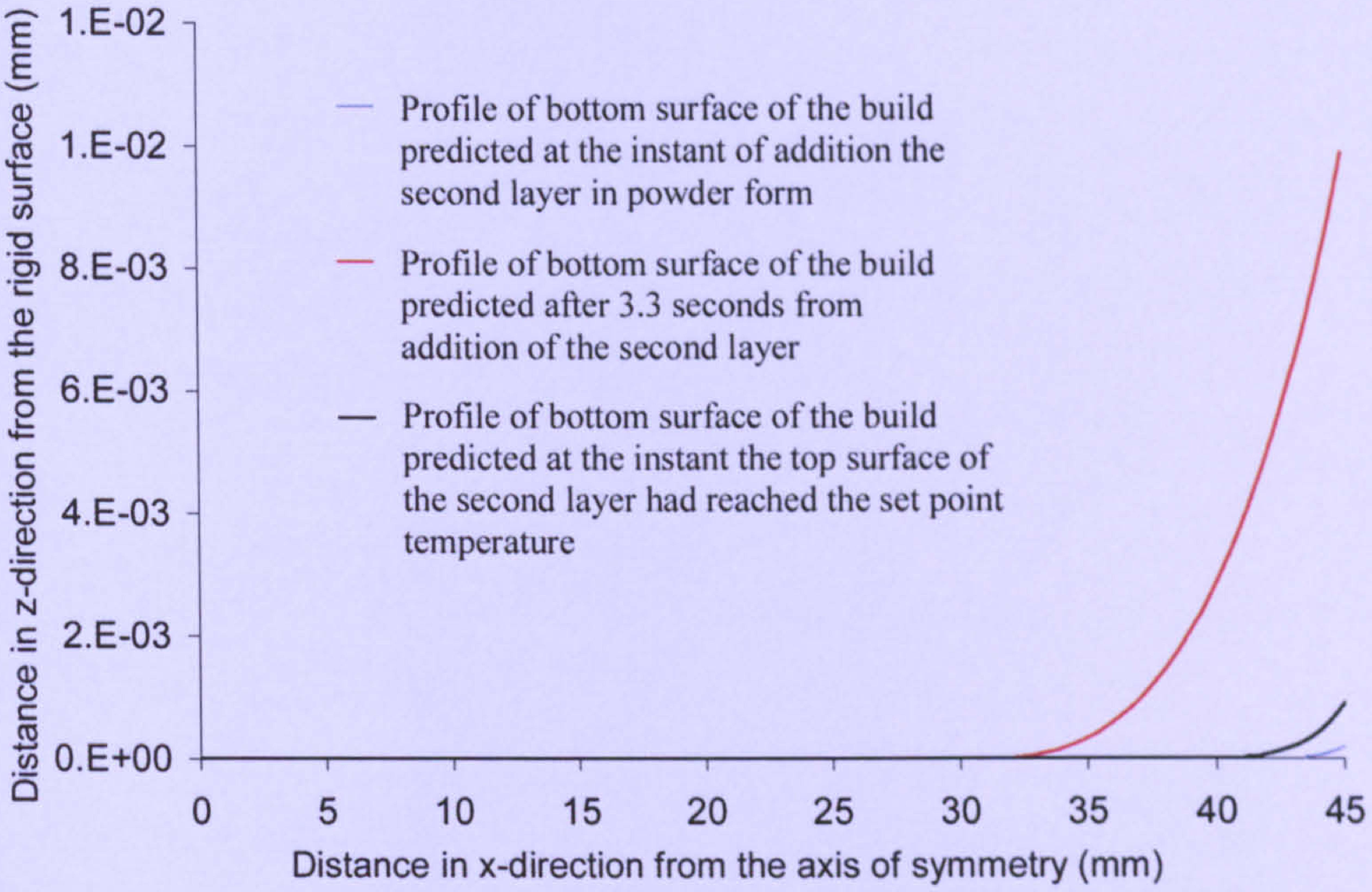

Figure 6.33 Selected profiles of the bottom surface of the build predicted in the second step of the second version of the stress model, i.e. following addition of the second layer of powder and during its heating to the set point temperature.

However, following that period and for a duration of 3.3 seconds, the decrease in the nodal temperature of elements developing thermal strains (see Figure 6.9) was reflected by continuous rise in curl. In that period, the maximum distance of the bottom surface of the build from the rigid surface significantly increased from 1.64×10^{-4}mm to 9.86×10^{-3}mm, i.e. by 98.4%. Following that period, and immediately prior to sintering of the second layer, the increase in the nodal temperature of the previously (thermally) shrunken elements in the first layer is expected to have caused these elements to expand (see Figure 6.9). That was exhibited by a noticeable reduction in curl, with the maximum distance of the bottom surface of the layer from the rigid surface reducing from 9.86×10^{-3}mm to 8.97×10^{-4}mm, i.e. by 91%.

6.2.2.6 Discussion

Figure 6.34 shows the final profiles predicted by the stress model of the top and bottom surfaces of the ten-layer part drawn alongside the experimentally measured ones. Profiles of these surfaces predicted by the first version of the stress model are also illustrated in the figure to demonstrate the effects of enhancements made to the second version of the heat and stress models on the final deformations predicted. The present model appears to have accurately predicted curl at the bottom surface of the part, with the exception of regions extending approximately 1.6mm in the *x*-direction from both edges of that surface. Figure 6.34 also illustrates that the final profile of the bottom surface predicted by the present stress model was more accurate than that estimated by the previous model.

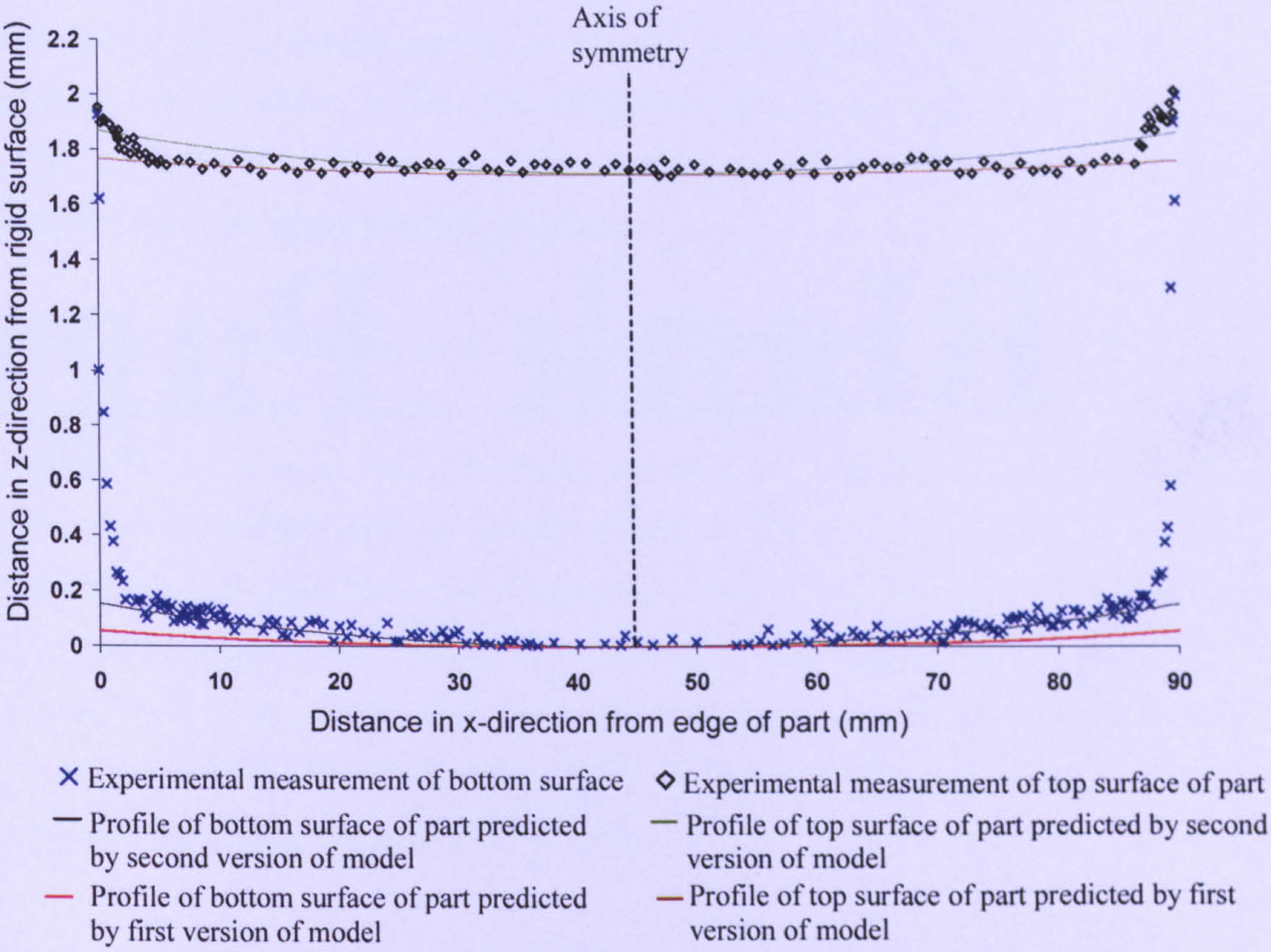

Figure 6.34 Final profiles of the top and bottom surfaces of the part predicted by the first and second versions of the stress model drawn alongside the experimentally obtained profiles

Conversely, the final profile of the top surface of the part predicted by the previous model was more accurate than that predicted by the present model (see Figure 6.34). However, the remarkable observation in the figure is that the final profiles of the bottom and top surfaces predicted by the present stress model were quite similar, which is also noticed in the profiles predicted by the previous stress model. The present stress model, for example, predicts the top surface of the part to have undergone a (final) vertical maximum deflection from its originally defined position of 0.1532mm (seen at the edge of the surface). The (final) maximum deflection of the bottom surface of the part was predicted to be 0.1542mm, i.e. differing from the maximum deflection of the top surface by 0.6%. The curl of the bottom surface of the part being (slightly) higher than that at its top surface is probably due to the former developing during the "build" and "cooldown" stages, whereas the latter mainly developing during the "cooldown" stage. However, as most of the curl was predicted by the models to generate during the "cooldown" stage, the curl developed during the "build" stage was insignificant to be noticed on the final profile (predicted) of the bottom surface of the part. Consequently, curl experimentally measured at the bottom surface of the fabricated ten-layer part being higher than that at its top surface is probably an indication that curl actually developed during the "build" stage was larger than that predicted.

Therefore, the stress model at this stage of development did not provide satisfactory predictions of curl. However, the model suggested the SLS stages wherein significant variations in curl of the build may have occurred. For example, sintering of a recently added layer of powder (whilst in the melt) was predicted to be accompanied by reduction in curl. Conversely, a rise in curl was predicted following sintering of a layer (with stresses developing) and after addition of a new layer of powder prior to its sintering. The rise in curl during these operations indicated by the model also agrees with visual signs of curl development during fabrication of SLS polycarbonate builds reported by DTM [13].

The second version of the stress model (with minor modifications) was additionally implemented to investigate the effect of viscoelasticity on curl. The modifications involved replacing the type of analysis defined in all steps of the stress model using the (VISCOELASTIC) option in ABAQUS with the (STATIC) option. The use of the (STATIC) option implies that the modulus of elasticity is time-independent, but remains dependent on temperature as specified in Table 5-1. However, other definitions in steps of the modified stress model (boundary conditions, loadings and the time period of their application) were identical to those mentioned in the second version of the stress model. Selected maximum distances of the bottom surface of the build from the rigid surface predicted by the modified stress model are illustrated in Table 6-4.

Step number	SLS stage	Maximum distance of bottom surface of build from the rigid surface (mm)		Percentage of change in distance in a stage
		Start of stage	End of stage	
1	Cooling of sintered Layer 1	0	1.73×10^{-4}	
2	Heating of 2nd layer of powder	1.73×10^{-4}	8.97×10^{-4}	+81%
	2nd layer in melt state	8.97×10^{-4}	8.06×10^{-6}	-99%
3	Cooling of sintered layer 2	8.06×10^{-6}	1.65×10^{-4}	+95%
4	Heating of 3rd layer of powder	1.65×10^{-4}	1.11×10^{-3}	+85%
	3rd layer in melt state	1.11×10^{-3}	2.22×10^{-5}	-98%
5	Cooling of sintered layer 3	2.22×10^{-5}	1.855×10^{-4}	+88%
6	Heating 4th layer of powder	1.855×10^{-4}	9.107×10^{-4}	+79.6%
	4th layer in melt state	9.107×10^{-4}	3.478×10^{-5}	-96%
7	Cooling of sintered layer 4	3.478×10^{-5}	2.195×10^{-4}	+84%
8	Heating of 5th layer of powder	2.195×10^{-4}	7.84×10^{-4}	+72%
	5th layer in melt state	7.84×10^{-4}	4.946×10^{-5}	-94%
9	Cooling of sintered layer 5	4.946×10^{-5}	2.515×10^{-4}	+80%
10	Heating of 6th layer of powder	2.515×10^{-4}	7.22×10^{-4}	+65.2%
	6th layer in melt state	7.22×10^{-4}	7.133×10^{-5}	-90%
11	Cooling of sintered layer 6	7.133×10^{-5}	2.830×10^{-4}	+75%
12	Heating of 7th layer of powder	2.830×10^{-4}	7.158×10^{-4}	+60.5%
	7th layer in melt state	7.158×10^{-4}	1.074×10^{-4}	-85%
13	Cooling of sintered layer 7	1.074×10^{-4}	3.19×10^{-4}	+66%
14	Heating of 8th layer of powder	3.19×10^{-4}	7.26×10^{-4}	+56%
	8th layer in melt state	7.26×10^{-4}	1.57×10^{-4}	-78%
15	Cooling of sintered layer 8	1.57×10^{-4}	3.58×10^{-4}	+56%
16	Heating of 9th layer of powder	3.58×10^{-4}	7.4×10^{-4}	+56%
	9th layer in melt state	7.4×10^{-4}	2.15×10^{-4}	-71%
17	Cooling of sintered layer 9	2.15×10^{-4}	4.03×10^{-4}	+47%
18	Heating of 10th layer of powder	4.03×10^{-4}	7.811×10^{-4}	+48%
	10th layer in melt state	7.811×10^{-4}	2.82×10^{-4}	-64%
19	Cooling of sintered layer 10	2.82×10^{-4}	0.1542	+99.8%

Table 6-3 Selected magnitudes of the maximum distance in the z-direction of the bottom surface of the build from the rigid surface predicted by the second version of the stress model with viscoelasticity considered. Heating of a layer of powder denoted in the table implies raising the temperature of its top surface to the set point (150°C)

Step number	SLS stage (viscoelasticity not considered)	Maximum distance of bottom surface of build from the rigid surface (mm)	
		Start of stage	End of stage
1	Cooling of sintered Layer 1	0	2.45×10^{-3}
2	Heating of 2nd layer of powder	2.45×10^{-3}	6.55×10^{-3}
	2nd layer in melt state	6.55×10^{-3}	4.95×10^{-5}
3	Cooling of sintered layer 2	4.95×10^{-5}	2.21×10^{-3}
4	Heating of 3rd layer of powder	2.21×10^{-3}	1.39×10^{-2}
	3rd layer in melt state	1.39×10^{-2}	5.78×10^{-5}
5	Cooling of sintered layer 3	5.78×10^{-5}	2.23×10^{-3}
6	Heating 4th layer of powder	2.23×10^{-3}	1.39×10^{-2}
	4th layer in melt state	1.39×10^{-2}	1.21×10^{-4}
7	Cooling of sintered layer 4	1.21×10^{-4}	2.32×10^{-3}
8	Heating of 5th layer of powder	2.32×10^{-3}	1.31×10^{-2}
	5th layer in melt state	1.31×10^{-2}	1.97×10^{-4}
9	Cooling of sintered layer 5	1.97×10^{-4}	2.49×10^{-3}
10	Heating of 6th layer of powder	2.49×10^{-3}	1.21×10^{-2}
	6th layer in melt state	1.21×10^{-2}	2.87×10^{-4}
11	Cooling of sintered layer 6	2.87×10^{-4}	2.72×10^{-3}
12	Heating of 7th layer of powder	2.72×10^{-3}	1.12×10^{-2}
	7th layer in melt state	1.12×10^{-2}	3.97×10^{-4}
13	Cooling of sintered layer 7	3.97×10^{-4}	3.00×10^{-3}
14	Heating of 8th layer of powder	3.00×10^{-3}	1.00×10^{-2}
	8th layer in melt state	1.00×10^{-2}	5.38×10^{-4}
15	Cooling of sintered layer 8	5.38×10^{-4}	3.31×10^{-3}
16	Heating of 9th layer of powder	3.31×10^{-3}	9.65×10^{-3}
	9th layer in melt state	9.65×10^{-3}	7.17×10^{-4}
17	Cooling of sintered layer 9	7.17×10^{-4}	3.67×10^{-3}
18	Heating of 10th layer of powder	3.67×10^{-3}	9.23×10^{-3}
	10th layer in melt state	9.23×10^{-3}	9.44×10^{-4}
19	Cooling of sintered layer 10	9.44×10^{-4}	0.241

Table 6-4 Selected magnitudes of the maximum distance in the z-direction of the bottom surface of the build from the rigid surface predicted by the second version of the stress model with viscoelasticity not considered. Heating of a layer of powder denoted in the table implies raising the temperature of its top surface to the set point (150°C)

The general observation in table 6-4 is that the development of curl (rise and reduction) predicted in steps of the modified stress model was similar to that predicted in corresponding steps of the second version of the model simulating identical effects (see Table 6-3). However, comparing magnitudes of distances reported in both Tables 6-3 and 6-4 shows the viscoelasticity to have a reducing effect on curl. For example, the (final) maximum distance of the bottom surface of the part from the rigid surface predicted with viscoelasticity considered and without it being taken into account were 0.1542mm and 0.241mm respectively (differing by 36%). Due to the significant effect suggested of the viscoelasticity on curl, its effect remained considered in further developed stress models.

6.3 Third stage of Model development

The finite element models previously developed did not produce satisfactory predictions of curl (see Figure 6.34). Attempts were therefore made in the third stage of model development to further improve simulation of thermal effects occurring during SLS processing for a better prediction of curl to be achieved. Similar to the previous models, the third stage of model development adopted the sequentially coupled thermal-stress analysis as a method of solution. In the following, a description of the third versions of the heat and stress models is provided with emphasis given to illustrate improvements made to the models over the previous ones.

6.3.1 Third Version of Heat Transfer Model

The most significant development in the third version of the heat transfer model came with the observation that the previous stress model underestimated curl of the bottom surface of the part in regions extending 1.6mm (in the x-direction) from both edges of that surface (see Figure 6.34). Additionally, the previous model did not predict a distinct curled profile close to the edges of the top surface of the part as seen by the experimentally measured profile of that surface (see Figure 6.34). The focus in this version of the heat transfer model was therefore to include thermal effects, not previously taken into account, which are expected to cause the development of distinct curled profiles in the regions close to the edges of the top and bottom surfaces of the part.

In the previous heat transfer models, the side walls of layers forming the part were assumed to be insulated through the entire period of simulation. The assumption was based on the understanding that sintering of powder is accompanied by reduction in its volume. Sintering of a region on the top surface of a layer of powder is therefore expected to result in a diminutive gap between the side walls of a sintered layer and its surrounding powder. As the thermal conductivity of the gas filling the gap is expected to be extremely small compared to that of the powder, heat lost from the side walls of the sintered layer through the gap was assumed to be negligible (see Section 4.6.1).

However, following sintering of a layer, the roller spreads the next layer of powder. This action is believed to fill any gaps that may have developed between the side walls of the previously sintered layer and its surrounding powder. Consequently, the side walls of fabricated layers are believed to be in direct contact with powder in different phases of SLS processing. In this condition, conduction of heat is expected to occur from the side walls of sintered layers to the contacting powder. However, due to the low conductivity of polycarbonate, reduction in temperature (due to heat conducted) is most probably localised in regions close to the side walls of sintered layers. That causes (additional) shrinkage in these regions to occur, probably exhibited in additional curl close to the side walls of fabricated layers than that predicted by the previous stress model. However, the amount of heat conducted is dependent on temperature differences between that of the build and its surrounding powder. These differences are expected to be significant during the "build" stage where sintering of subsequently added layers takes place, and thus the development of the distinct edge curl is mainly thought to occur during that stage. Conversely, differences in temperature between the fabricated part and surrounding powder are expected to become less significant in the "cooldown" stage. In that stage, most of heat loss is assumed to occur through convection and radiation from the top surface of the last fabricated layer resulting in an overall bending of the fabricated part (as predicted by the previous stress models).

The aim in the third stage of model development is to investigate the thermal effect of the surrounding powder on curling of the build. For that to be achieved, the surrounding powder has to be represented in the heat transfer analysis mesh. However, it must be remembered that the sequentially coupled thermal-stress analysis method implies that the heat transfer analysis solution is independent of part deformations predicted by the corresponding stress model. Consequently, to investigate the utmost thermal effect of surrounding powder on curl, the powder was assumed in the heat transfer model to be in direct contact with the build through the entire period of simulation. In following sections, a description of the heat transfer model is given with results obtained.

6.3.2 Geometry

Figure 6.35*a* shows the 2D finite element mesh generated for the third version of the heat transfer model. Similar to the previous models, the ten-layer part and the portion of the powder bed underneath the part were represented. However, the present model was improved by additionally representing the powder surrounding these structures, i.e. the entire part bed was represented. During SLS processing, the side wall of the part bed is supported by the part piston cylinder wall. In a previous study [15], parts (physically) fabricated close to the cylinder wall were seen to exhibit additional curl than those fabricated in the centre of the part bed at the same height from the part piston (see Section 2.2.5.4.2). The additional curl was attributed in the study to the large heat conduction from the part to the cylinder wall which is at a temperature lower than that of the powder. In an attempt to investigate the (additional) thermal effect of the cylinder wall on temperatures of fabricated layers, the wall was also represented in the heat transfer analysis mesh (see Figure 6.35*a*). On the basis of mirror symmetry conditions established in Section 4.6.1, only half of the above-mentioned structures were modelled.

Similar to the previous model, the thicknesses of layers forming the part were defined in the model based on experimental measurements described in Section 5.2. Thus, the thickness of the first layer was defined in the model equal to 0.59mm, whereas layers from two to ten were each given a thickness equal to 0.127mm. Additionally, the thickness of the powder bed underneath the fabricated part was specified in the model equal to 14.777mm, estimated using the method illustrated in Figure 6.1. On the basis of experimental measurements, the radius of the part bed (which is equal to the inner radius of the cylinder wall) was defined in the model equal to 165mm. The thickness of the cylinder wall was specified in the model equal to 12mm. The thickness was estimated by subtracting the inner radius of the cylinder wall (165mm) from its measured outer radius (177mm).

The mesh representing the part was identical to that created in the previous heat transfer model (see Figure 6.2*b*). Moreover, nodes that are not associated with elements were generated along the interfaces between the elements representing the layers forming the part. However, simulation of the "build" stage in the present model required the layers of powder surrounding part layers from two to ten to be distinctly represented. That was also required for the portions of the cylinder wall supporting each of these layers of powder. In the model, these powder layers and portions of the cylinder wall were each represented by a single row of elements. The elements had a thickness equal to the nominal thickness of a layer of powder spread during the "build" stage, 0.127mm. Elements used in representing these structures were of the type four-noded heat transfer elements, denoted in ABAQUS (DC2D4). However, using a similar mesh density to represent these structures as that of the (relatively highly meshed) part is expected to result in an enormous number of elements in the heat transfer analysis mesh. To reduce the cost of solving the analysis, a fine mesh was generated in regions of the surrounding powder where high rates of change in temperature are expected (close to the side walls of fabricated layers) with gradual reduction in mesh density the further the region is from the fabricated layers. That was performed by increasing the aspect ratio of elements from 2.5 in highly meshed regions to 24 in elements representing the cylinder wall. The use of an aspect ratio greater than 5 was reported to be acceptable in "non-critical" regions of the model [48], i.e. in regions distant from the fabricated part. Additionally, it was reported that in the use of significantly different sized elements, emphasis needs to be given to ensure that element lengths do not vary by more that 100:1 in the model, i.e. the ratio of areas do not exceed 10000:1 [48]. These conditions are valid in the present heat transfer finite element mesh.

In representing the powder bed and the powder surrounding the first layer of the part, a fine mesh was generated in regions close to the layer boundaries. The mesh density gradually reduced the further the region was from the layer. Elements used in representing the powder bed and the powder surrounding the first layer of the part were of the type four-noded heat transfer elements, denoted in ABAQUS (DC2D4), and three-noded heat transfer elements denoted in ABAQUS (DC2D3). The latter was used in transition regions were variations in mesh density were performed (see

Figure 6.35). However, the portion of the cylinder wall supporting that powder was represented with a coarse (DC2D4) finite element mesh.

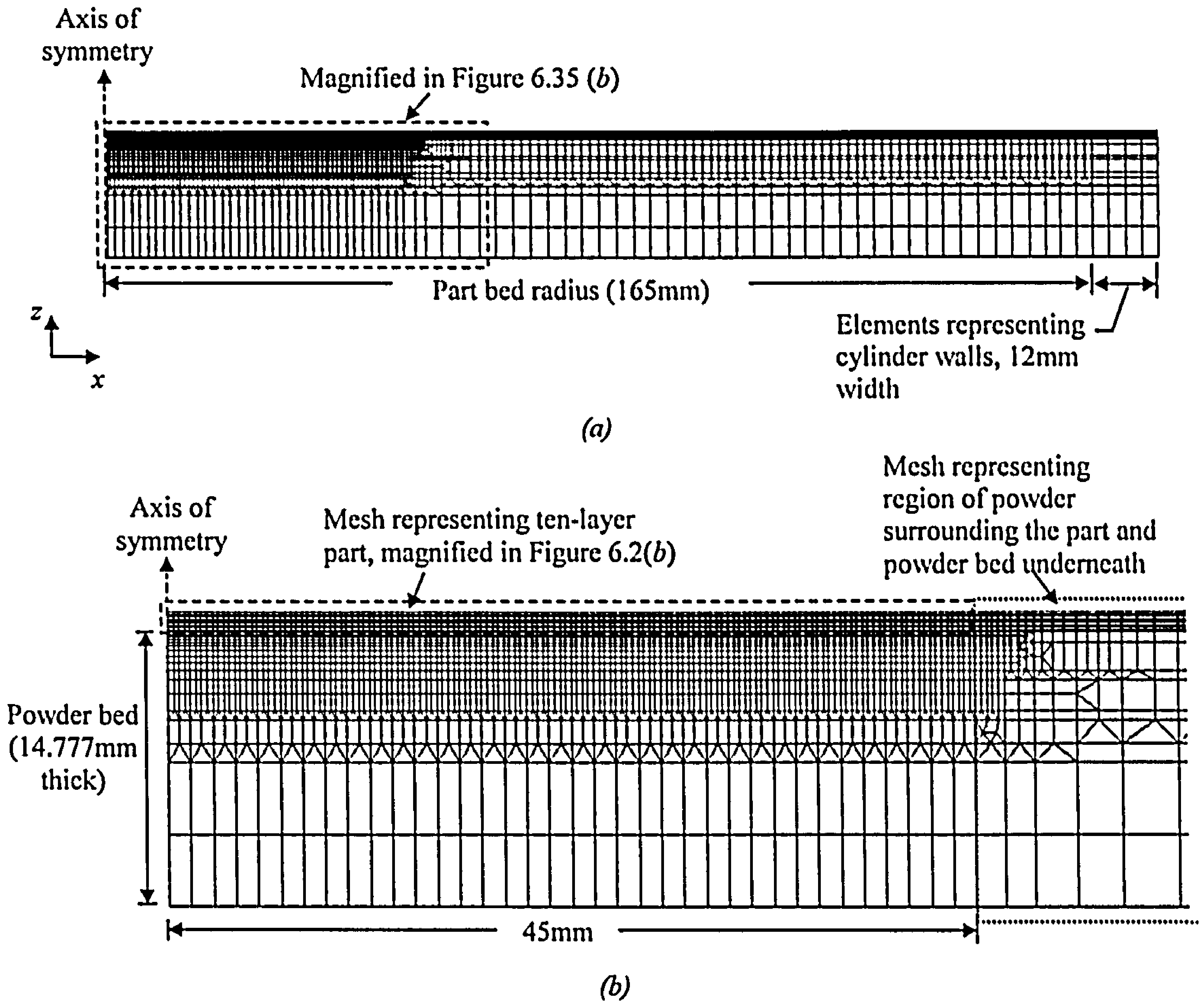

Figure 6.35 *(a)* The 2D finite element mesh used in the third version of the heat transfer model. *(b)* magnified view of the part and the region of the part bed surrounding the boundaries of the part.

6.3.2.1 Material Properties Defined in Heat model

Elements representing the sintered part and the powder in the heat transfer analysis mesh (see Figure 6.35*a*) were given the thermal material properties reported in Section 6.2.1.2. The additional material properties defined in the model were of elements representing the cylinder wall. As properties of the cylinder wall were not available, the wall was assumed to be made of stainless steel. Thus, the thermal conductivity (*k*) of the cylinder wall, its specific heat, density and emissivity were defined in the model equal to 14.9W/m.K, 477J/kg.K, 7900kg/m^3 and 0.21

respectively [46]. These properties were defined in the model to be constants (independent of temperature changes) through the entire period of simulation.

6.3.2.2 Boundary Conditions

In this version of the heat transfer model, thermal effects occurring during the "warmup" stage were not simulated. However, similar to the second version of the heat transfer analysis, layers of powder spread during the "warmup" stage were assumed to be at 150°C, immediately prior to the "build" stage starting. That was simulated in the model by specifying an initial temperature equal to 150°C to nodes in the part bed located between (and inclusive) those at the bottom surface of the part bed and those at a distance of –0.127mm in the *z*-direction from the top surface of the first layer of the part. As elements representing the part bed and cylinder wall are connected by common nodes, the nodes generated along the inner surface of the wall between (and inclusive) the locations aforementioned had an initial temperature equal to 150°C. The temperature of the region of the outer surface of the cylinder wall surrounding the powder spread during the "warmup" stage was not known immediately prior to the "build" stage starting. As that region of the surface is exposed to the environment, which is at room temperature (20°C), an assumption was made by assigning an initial temperature equal to 20°C to the nodes located at that region of the outer surface of the cylinder wall. However, nodes located along the thickness of that region of the wall were given an initial temperature that varied linearly through the thickness, i.e. from 150°C at the inner surface of the wall to 20°C at its outer surface.

Similar to the second version of the heat transfer model, attempts were made in this model to simulate the "build" and "cooldown" stages in SLS. In the following, an SLS stage is presented along with the boundary conditions applied to simulate thermal effects expected to occur in that stage.

- **Build Stage**

For the reason previously reported (see description of build stage in Section 6.2.1.3), thermal effects simulated were those expected to occur in the duration of the operations in the "build" stage denoted 1, 2 and 4 in Figure 6.5. In the following, boundary conditions applied in the model to simulate these operations are introduced.

- Adding a New Layer of Powder (Operation 1)

Similar to the second version of the heat transfer model, layers of powder spread during the "build" stage were assumed to be at 80°C, immediately following deposition. That was simulated in the model by defining the initial nodal temperature of elements representing layers two to ten of the part and their surrounding powder equal to 80°C. Additionally, the initial temperature of nodes located along the region of the outer surface of the cylinder wall surrounding these layers (exposed to the environment) was assumed in the model equal to room temperature (20°C). Nodes located along the thickness of that region of the cylinder wall were given an initial temperature that varied linearly through thickness, i.e. from 80°C at the inner surface of the wall to 20°C at its outer surface.

- Waiting for Temperature of Part Bed to Reach to Set Point (Operation 2)

The method accepted in the second version of the heat transfer analysis in simulating heating of a recently added layer of powder to the set point temperature was also implemented in the present model (see Section 6.2.1.3). Thus, the operation was simulated by applying a boundary condition simultaneously raising the temperature of the nodes connected to the edges of elements representing the top surface of the added layer of powder from 80°C to 150°C in 7 seconds (see Figure 6.6).

- Sintering of an Added Layer (Operation 4)

During the sintering operation, the IR sensor regularly measures the temperature at the top surface of the recently added layer of powder at a location distant from the regions being sintered. Based on the IR sensor readings, the part heater switches on and off to maintain the temperature measured at 150°C. However, due to heat conduction from the surface being sintered, the top surface of the powder neighbouring the sintered region is expected to be at a higher temperature than that measured by the IR sensor (150°C). Conversely, due to the cooling effect of the (part piston) cylinder wall, the top surface of the powder close to the wall is expected to be at a lower temperature than that measured by the IR sensor. For simplicity in simulation, the temperature measured by the IR sensor was assumed to be uniform over the entire top surface of the powder surrounding the region being sintered. That was simulated by applying a boundary condition maintaining at 150°C the temperature of nodes (connected to elements) located at the top surface of the recently added layer of powder (excluding those connected to the edges of elements representing the top surface of the sintered layer). Additionally, convection and radiation boundary conditions are applied on the edges of elements representing the top surface of the layer being sintered, with the temperature of the gas and enclosing walls equal to 150°C.

▪ Cooling of the Part to Room Temperature

Cooling of the part (following its fabrication) occurs in two stages; cooling in the process chamber and cooling following removal of the part bed from the chamber. In the following, boundary conditions defined to simulate both stages of cooling are introduced.

➢ Cooling of the part whilst in the chamber

Figure 6.7 illustrates IR sensor readings recorded at different instants during cooling of the fabricated ten-layer part in the process chamber. The readings represent the temperatures measured at a location on the top surface of the part bed distant from the last sintered region (the top surface of the tenth layer of the part). For simplicity, the assumption made in the model was that the temperature measured by the IR sensor was uniform over the entire top surface of the part bed surrounding that sintered region. That was simulated by applying a boundary condition on the nodes located at the top surface of the part bed (excluding those connected to the edges of elements representing the top surface of the tenth layer of the part) reducing their temperature with time as illustrated in Figure 6.7. On these edges of elements, convection and radiation boundary conditions were applied with the temperature of the gas and surrounding walls reducing with time as shown in Figure 6.7.

In the "build" stage and during cooling of the part in the chamber, convection and radiation boundary conditions were applied on the edges of elements representing the outer surface of the cylinder wall (exposed to the environment). The temperature of the gas and enclosing walls used in the convection and radiation calculations was defined in the model equal to room temperature (20°C). In addition, the bottom surface of the part bed whilst in the chamber was assumed to be insulated for the reasons reported in Section 4.6.3.

➢ Cooling of the part Following its Removal from the Chamber

The concept used in defining boundary conditions to simulate thermal effects occurring whilst the part bed is placed on the breakout station (following its removal from the chamber) was quite similar to that adopted in the second version of the heat transfer analysis (see Section 6.2.1.3). Thus, convection and radiation boundary conditions were applied on the edges of elements representing the entire top surface of the part bed, with the temperature of the gas and enclosing walls maintained at room temperature (20°C). In addition, positioning of the part bed on the breakout station was simulated by setting and maintaining the temperature of nodes located at the bottom surface of the part bed equal to 20°C.

In all steps of the heat transfer analysis, the temperature histories of nodes not associated with any element and located along the interfaces between layers forming the part were defined in the model as reported in Section 4.7.3. Moreover, the edges of elements located in the heat transfer analysis mesh (see Figure 6.35) along the axis of symmetry were considered insulated, i.e. no boundary conditions were applied on these edges.

6.3.2.3 Sequence of Analysis Defined in the Heat Transfer analysis

In the following, the sequence of analysis defined in the third version of the heat transfer model is described. Similar to the previous models, the sequence of analysis was specified by a sequence of steps. In the following, attempts are made to describe the steps defined to simulate SLS fabrication of the ten-layer part and its cooling to room temperature.

- First step defined in heat transfer analysis

The "build" stage in SLS started with the roller spreading a layer of powder onto the powder bed. The part heater then raised the temperature of the top surface of the added layer to the set point temperature (150°C) prior to sintering taking place. The operations of powder spreading and heating to set point were simulated in the first step of the heat transfer analysis. Powder spreading was simulated by deactivating the elements representing layers two to ten of the sintered part, their surrounding powder and the portion of the cylinder wall supporting that powder.

Heating of the layer was simulated by applying a boundary condition simultaneously raising the temperature of nodes connected to the edges of elements representing the top surface of the added layer from 80°C to 150°C in 7 seconds (see Figure 6.6). That duration was considered to be the time period of the first step. In the step, convection and radiation boundary conditions were applied on the edges of "active" elements representing the outer surface of the cylinder wall. The temperature of the gas and surrounding walls used in the convection and radiation calculations was equal to 20°C.

- Second step defined in heat transfer analysis

After the top surface of the added layer of powder had reached 150°C, the laser beam was assumed to immediately start raster scanning a region on the top surface of the layer to form the first layer of the part. During sintering, the part heater was assumed to maintain the entire top surface of the powder surrounding the region being sintered at 150°C. Thermal effects expected to occur during sintering of the layer were simulated in the second step of the analysis. The sintering operation was simulated by a uniform heat flux simultaneously applied on the edges of elements together representing the top surface of the first layer of the part. Similar to the first step defined in the first version of the heat transfer analysis, the amount of heat flux applied and the period of application were specified equal to $83.1 \mathrm{MW/m^2}$ and 3.36×10^{-4} second respectively (see Section 4.6.4). The latter was considered to be the time period of the second step of the analysis. The effect of the part heater was simulated by applying a boundary condition maintaining at 150°C the temperature of the nodes connected to the edges of elements representing the top surface of the recently added layer (excluding those connected to the edges of elements representing the top surface of the first layer of the part). In the step, convection and radiation boundary conditions were applied on the edges of elements representing the top surface of the first layer. Additionally, the boundary conditions applied in the previous step on the edges of elements representing the outer surface of the part bed cylinder wall remained applied in this step.

- Third step defined in heat transfer model

After sintering of the layer was completed, the part piston lowered allowing spreading of fresh powder onto the part bed. The third step simulated thermal effects expected to occur from the instant the roller began moving from its starting position to the instant immediately prior to fresh powder being added on the top surface of the first (sintered) layer of the part. Lowering of the part piston can be simulated by activating the elements representing the portion of the cylinder wall surrounding the layer being added. Additionally, it may be assumed that the portion of the powder added in the duration of interest can be simulated by activating the elements representing the powder surrounding the second layer of the part (see Figure 6.35). However, it must be remembered that the heat transfer model (same as the previous heat transfer models) was developed on the basis of mirror symmetry about the y-z plane (see Figure 4.16). Activation of the elements representing the surrounding powder therefore simulates the condition where powder is added on both sides of the region to be sintered without it being added on the top surface of the recently sintered layer, which is an invalid representation. Consequently, the assumption made in simulation was that the entire layer of powder is simultaneously added onto the part bed at the instant it was physically spread on the top surface of the recently sintered layer. As powder deposition was not simulated in this step, elements representing the added powder and the portion of the cylinder wall surrounding that powder were not activated. However, thermal boundary conditions defined in the second step of the analysis remained applied in this step. Referring to Figure 4.31, the time period specified for the step was equal to 5.6 seconds.

- Fourth step defined in heat transfer model

The fourth step simulated thermal effects expected to occur from the instant the layer being added was spread on the top surface of the first layer of the part to the instant immediately prior to sintering taking place. In that period, the part heater was assumed to have raised the temperature of the top surface of the added layer to 150°C. Powder addition was simulated by simultaneously activating the elements representing the second layer of the part, its surrounding powder and the portion of the cylinder wall supporting the added layer. Thermal boundary conditions applied in the previous step were removed in this step. Similar to the first step of the analysis, heating of the layer was simulated by applying a boundary condition simultaneously raising the temperature of nodes connected to the edges of elements representing the top surface of the added layer from 80°C to 150°C. Referring to Figure 6.6, the time period specified for the step was equal to 7 seconds. In the step, convection and radiation boundary conditions were applied on the edges of (active) elements representing the outer surface of the cylinder wall.

Due to the repetitive nature of operations in the "build" stage, steps two, three and four were repeated on subsequently activated layers of elements until sintering of the tenth layer of the part was simulated. The following steps (steps 30 and 31) simulated thermal effects expected to occur after fabrication of the part was completed, i.e. during cooling of the part to room temperature. In the following, a description of these steps is given.

- Simulation of Cooling of the part whilst in the chamber (Step 30)

Following sintering of the tenth layer of the part, the heaters were switched off. IR sensor readings assumed to represent the temperature over the entire top surface of the part bed surrounding the last sintered layer were seen to reduce with time as illustrated in Figure 6.7. Thermal effects expected to occur during cooling of the part bed in the chamber were simulated in step 30 of the analysis. In the step, the heat flux applied in the previous step on the edges of elements representing the top surface of the tenth layer of the part to simulate its sintering was deactivated. Additionally, boundary conditions applied in the previous step were removed. The IR sensor measurements were simulated by applying a boundary condition reducing with time the temperature (as illustrated in Figure 6.7) of the nodes located at the top surface of the part bed (excluding those connected to the edges of elements representing the top surface of the tenth layer of the part). On these edges of elements, convection and radiation boundary conditions were applied, with the temperature of the gas and surrounding walls reducing as illustrated in Figure 6.7. Referring to the figure, the time period of the step was specified equal to 392 seconds. In that period, convection and radiation boundary conditions were applied on the edges of elements representing the outer surface of the cylinder wall surrounding the part bed, with the temperature of the gas and surrounding walls maintained at 20°C.

- **Cooling of the part following its removal from the chamber (Step 31)**

After the temperature measured by the IR sensor reached 100°C, the process chamber door was unlocked. The part piston then raised the part bed and a plastic hollow cylinder, with an internal diameter slightly larger than that of the part bed, was positioned to support the side wall of the part bed previously supported by the (part piston) cylinder wall. A metallic tray was next slid underneath the part bed and hollow cylinder. The metallic tray with the part bed and the plastic hollow cylinder (supporting the bed side wall) on its top surface was then placed on the breakout station for the fabricated part to cool naturally to room temperature. Thermal effects expected to occur following removal of the part bed from the chamber were simulated in step 31 of the model. In the step, the boundary conditions previously applied in step 30 were removed. The part piston raising the part bed was simulated in step 31 by simultaneously deactivating the elements representing the (part piston) cylinder wall. However, material properties of the plastic cylinder were not known. For simplicity, the plastic hollow cylinder was assumed to be made of an insulating material. Thus, the insulation of the part bed vertical side wall (due to the surrounding plastic cylinder) did not require for simulation the application of any boundary condition on that wall. However, convection and radiation boundary conditions were applied on the edges of elements representing the top surface of the part bed. The temperature of the gas and surrounding wall used in the convection and radiation calculations was considered in the model to be maintained at room temperature (20°C). Additionally, heat lost from the part bed through conduction is assumed to have an insignificant effect on raising the temperature of the metallic tray and breakout station from room temperature (20°C). That was simulated by applying a boundary condition setting and maintaining the temperature of nodes located at the bottom surface of the part bed equal to 20°C. The time period of the step was specified equal to 40 minutes, which was seen in the second version of the heat transfer model to be sufficient for part cooling to room temperature.

6.3.2.4 Results

The temperature history of a node in the part located along the symmetry axis was identical to that predicted by the second version of the heat transfer model of nodes located at a corresponding height from the bottom surface of the part. However, due to heat lost through conduction from the side walls of fabricated layers to surrounding powder, temperatures in regions of the layers close to the side walls were less than those predicted in other regions of the layer.

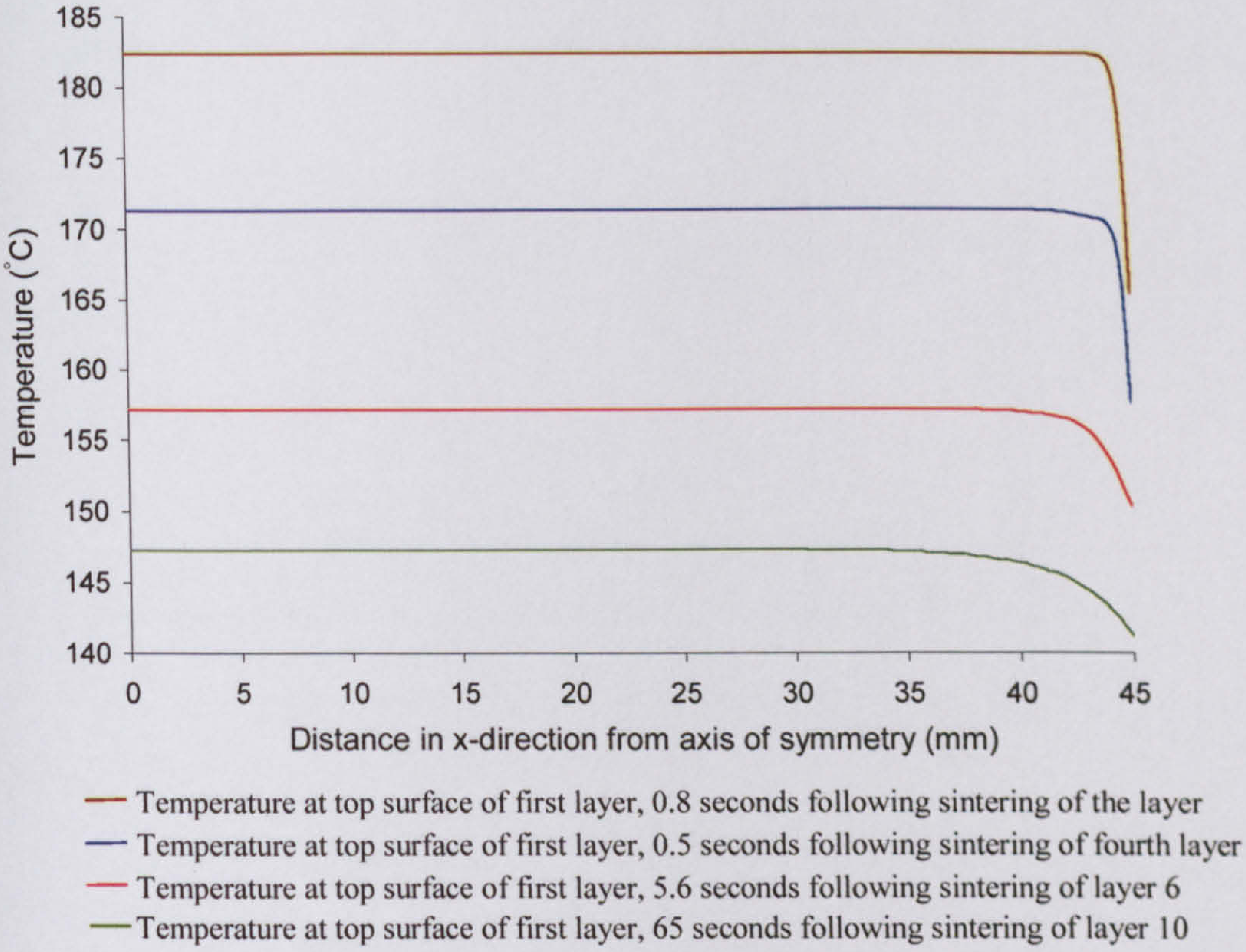

Figure 6.36 Temperatures along the top surface of the first layer of the part predicted at different instants during the "build" and "cooldown" stages.

Figures 6.36 and 6.37 show temperatures at the top surfaces of the first and tenth layer of the part predicted at selected instants in the third version of the heat transfer analysis. The figures show temperature reduction at the surfaces to be localised close to the side walls in the initial period following sintering of a layer. That is probably due to the low conductivity of the surrounding powder causing the rate of heat lost from the part through conduction is to be slow. However, reduction in the temperature of the layer is seen to be accompanied by the region close to the side wall that is at a less temperature extending. Reduction in temperature of the layer probably indicates an increase in the temperature of the neighbouring surrounding powder. As the conductivity of the powder was defined to increase with temperature (see Figure 6.3), an increase in the temperature of neighbouring powder is expected to facilitate heat loss from the side walls of the layer.

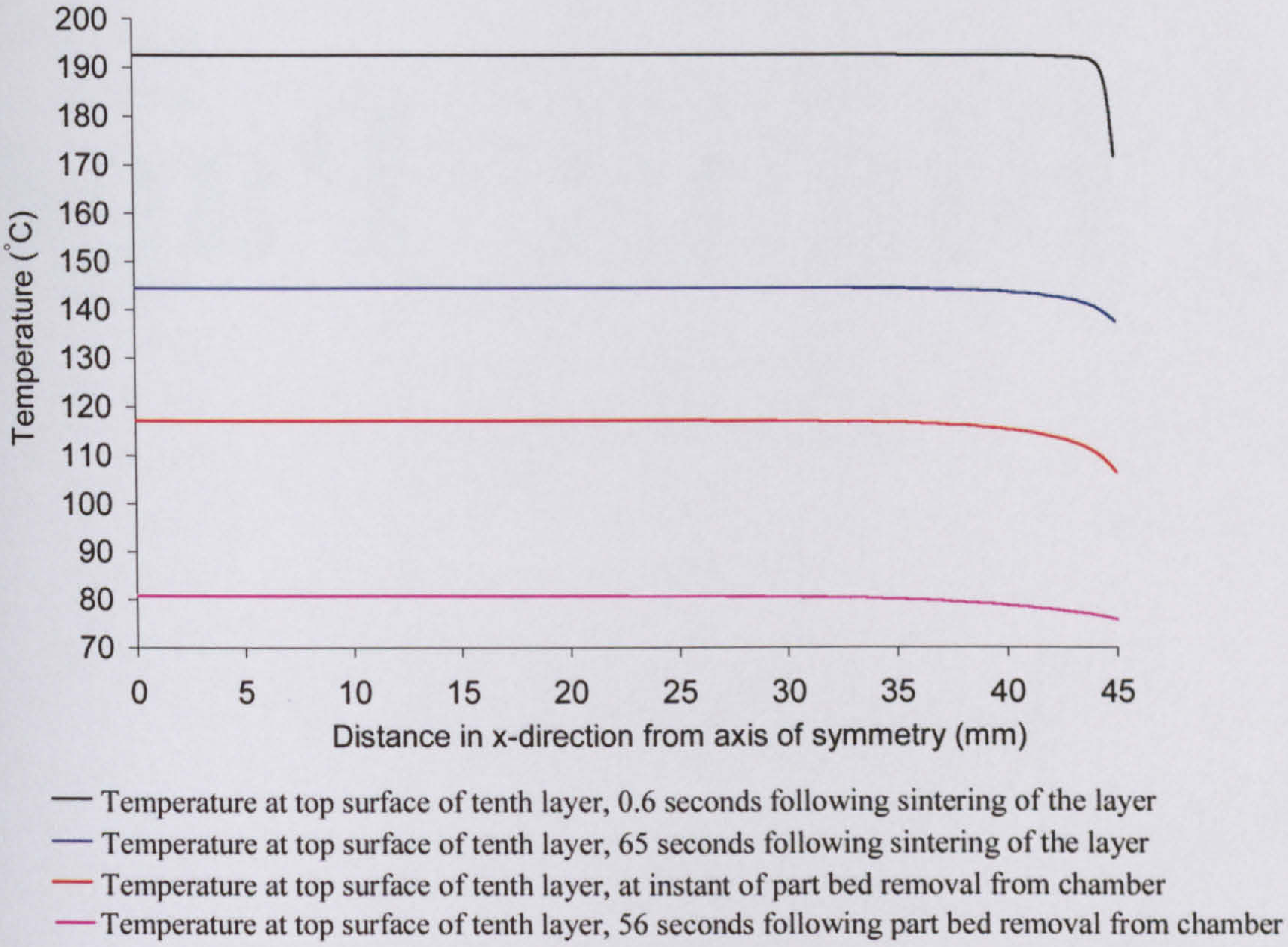

Figure 6.37 Temperatures along the top surface of the tenth layer predicted at different instants during cooling of the fabricated part to room temperature.

6.3.3 Third version of stress model

Improvements in the third version of the heat transfer model did not require the corresponding stress model to significantly differ from the second version of the stress model. Aspects of similarity were in the finite element mesh of both stress models (see Figure 6.11), material properties defined and boundary conditions applied. Additionally, emphasis was given to ensure that elements representing a recently sintered layer were activated in the third version of the stress analysis prior to their nodal temperatures reducing below 175°C, i.e. (immediately) before stresses developing in the layer. However, temperatures (of interest) predicted by the third version of the heat transfer model were seen to be the lowest at the side wall of fabricated layers. Elements in the corresponding stress analysis are therefore activated immediately prior to the temperature at the side wall reducing below 175°C. Thus, upon activation, elements located close to the side wall are expected to shrink first due to the early reduction in their nodal temperature, followed by shrinkage of the other elements in the layer.

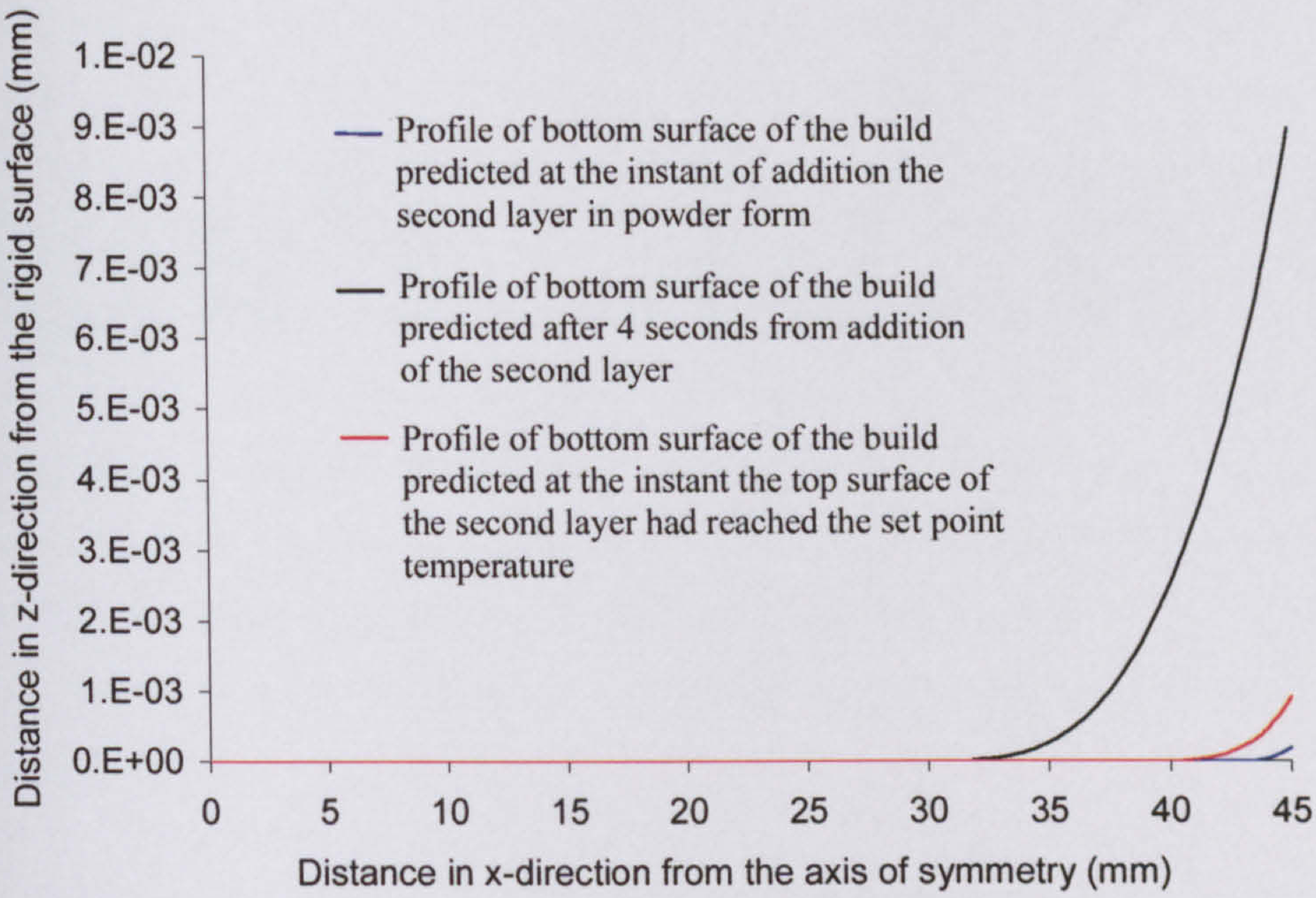

Figure 6.38 Selected profiles of the bottom surface of the build predicted in the second step of the third version of the stress model, following addition of the second layer of powder and during its heating to the set point temperature

The development of curl (rise and reduction) predicted in various steps of the present stress model were similar to those predicted in steps simulating identical effects in the previous stress model. Reduction in curl of the build was exhibited during sintering of a recently added layer of powder and whilst the layer was in the melt (above 175°C). A rise in curl was also predicted following sintering, with thermal stresses developing in all elements together representing the recently sintered layer. Moreover, a rise in curl was initially predicted after addition of a layer of powder, followed by reduction in curl during heating of the added layer to the set point temperature, as illustrated in Figure 6.38. Selected magnitudes of the maximum distance of the bottom surface of the build from the rigid surface predicted by the present and previous stress models at identical instants during SLS fabrication are illustrated in Table 6-5. Comparing the distances predicted by both models at a corresponding instant shows that conduction of heat from the fabricated part to surrounding powder, taken into account in third version of the model, has a rising effect on curl. However, that effect is mainly exhibited during the "build" stage. Heat lost through conduction in that stage is facilitated by the considerable differences in temperature between the build and surrounding powder, which generate mostly due to application of the laser flux. Figure 6.39 shows the final profiles of the top and bottom surfaces of the part predicted by the present stress model drawn alongside the experimentally measured ones. The stress model did not produce a distinct curl close to the edges of the top and bottom surfaces of the part. In fact, profiles of these surfaces predicted by the present model were approximately identical to those predicted by the second version of the stress model. The final maximum distances of the bottom surface of the build from the rigid surface, predicted by the present stress model and the previous one were 0.15694mm and 0.15495mm respectively, i.e. differing by 1.7%. In addition, the edge of the top surface of the part was predicted by the present and previous stress models to have displaced in the z-direction by 0.15495mm and 0.15323mm respectively, i.e. a difference of 1.1%. That seems to suggest that the surrounding powder had an insignificant effect on the final curl of the part.

However, both stress models predict the majority of curl to occur during the "cooldown" stage. For example, the final maximum distance of the bottom surface of the build from the rigid surface predicted by the present stress is (0.15694mm), which is approximately 93 times that predicted immediately prior to sintering of the tenth layer (1.693×10^{-3}mm). Thus, the additional curl predicted in the "build" stage, due to heat lost from the part to surrounding powder, was too small to be visible on the final profiles predicted.

The profiles experimentally measured show the bottom surface of the part to have exhibited additional curl than the top surface (see Figure 6.39). In fact, the top surface of the part appears to be almost flat except in the regions extending (approximately) 5mm from both edges of the surface. If the majority of curl did actually develop following fabrication of the part, one may expect the final curl at the bottom and top surfaces of the part to be quite similar. Thus, the profiles experimentally measured seem to suggest that the majority of curl did not develop during the "cooldown" stage, but in the "build" stage. The stress models therefore appear to over-predict curl in the "cooldown" stage whilst underestimating curl in the "build" stage. Additionally, it was seen from comparing predictions of the previous and present stress models that significant rise in curl occurs in the "build" stage due the thermal effect of the surrounding powder. Thus, if curl developed during the "build" stage is the main cause for the final measured profiles, the rise in curl caused by the thermal effect of the surrounding powder may probably be visible on the final curl of the part.

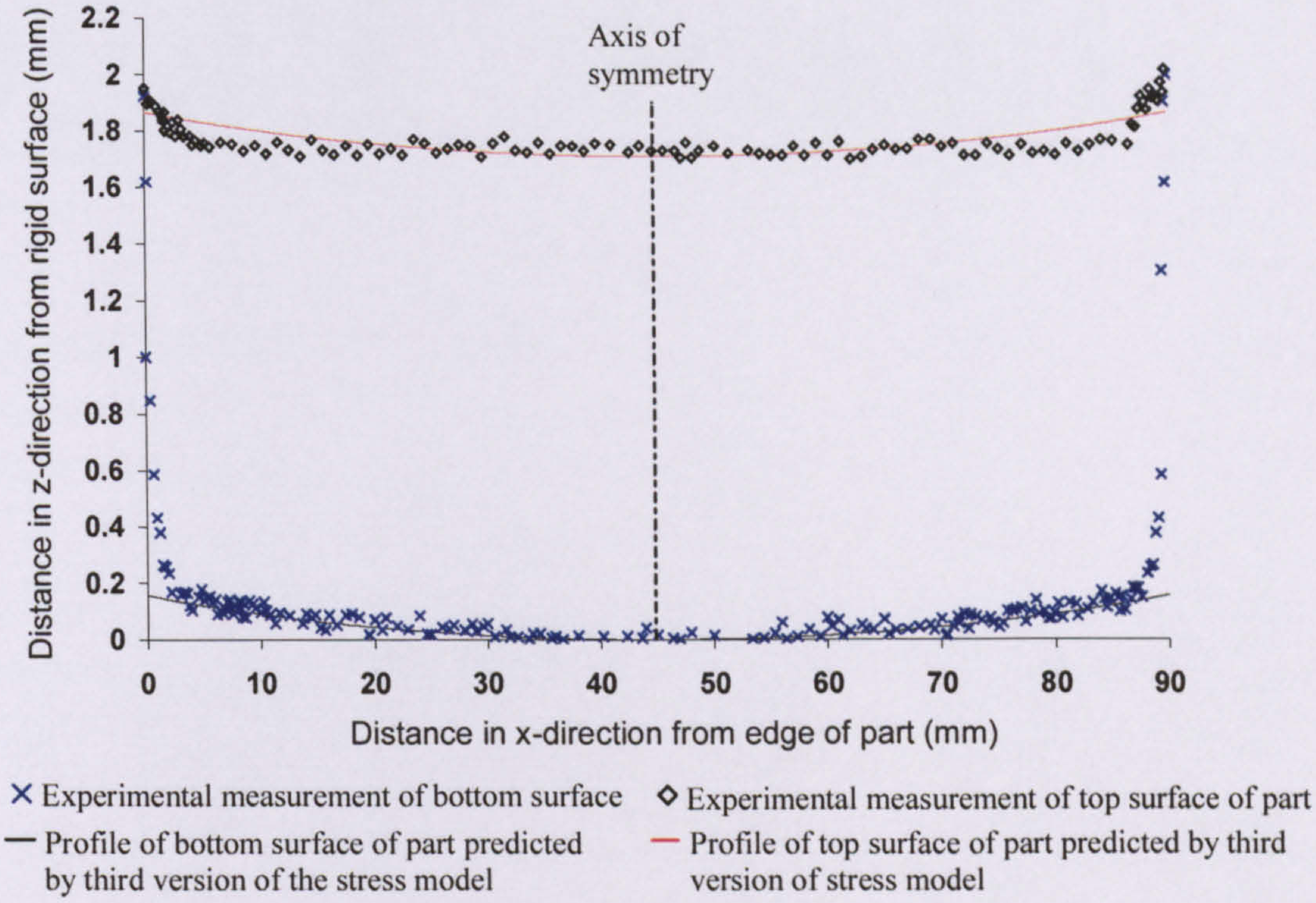

Figure 6.39 Profiles of top and bottom surfaces of the part predicted by the third version of the stress model drawn alongside the experimentally obtained profiles.

The conclusion, therefore, is that despite the stress model suggesting an insignificant influence of surrounding powder, its effect needs to be examined in further developed models. However, emphasis needs to be first given to examine the effects of assumptions considered in the second versions of the heat and stress models that may have resulted in over-prediction of curl in the "cooldown" stage. Additionally, investigation into the assumption that may have resulted in an underestimation of curl in the "build" stage is required. The effects of these assumptions on curl development predicted by the models are discussed in the following chapter.

Step number	SLS stage	Maximum distance of bottom surface of build from the rigid surface (mm) at end of stage		Difference between predictions of the second and third stages of the stress model
		Second version of stress model	Third version of stress model	
1	Cooling of sintered Layer 1	1.73×10^{-4}	1.956×10^{-4}	+11.5%
2	Heating of 2nd layer of powder	8.97×10^{-4}	9.136×10^{-4}	+1.8%
3	Cooling of sintered layer 2	1.65×10^{-4}	2.513×10^{-4}	+34.34%
4	Heating of 3rd layer of powder	1.11×10^{-3}	1.283×10^{-3}	+13.48%
5	Cooling of sintered layer 3	1.855×10^{-4}	3.432×10^{-4}	+45.9%
6	Heating of 4th layer of powder	9.107×10^{-4}	1.125×10^{-3}	+19.04%
7	Cooling of sintered layer 4	2.195×10^{-4}	4.472×10^{-4}	+50.9%
8	Heating of 5th layer of powder	7.84×10^{-4}	1.058×10^{-3}	+25.9%
9	Cooling of sintered layer 5	2.515×10^{-4}	5.769×10^{-4}	+56.4%
10	Heating of 6th layer of powder	7.22×10^{-4}	1.104×10^{-3}	+34.6%
11	Cooling of sintered layer 6	2.830×10^{-4}	7.264×10^{-4}	+61%
12	Heating of 7th layer of powder	7.158×10^{-4}	1.223×10^{-3}	+41.4%
13	Cooling of sintered layer 7	3.19×10^{-4}	8.918×10^{-4}	+64.2%
14	Heating of 8th layer of powder	7.26×10^{-4}	1.363×10^{-3}	+46.7%
15	Cooling of sintered layer 8	3.58×10^{-4}	1.062×10^{-3}	+66.3%
16	Heating of 9th layer of powder	7.4×10^{-4}	1.517×10^{-3}	+51.2%
17	Cooling of sintered layer 9	4.03×10^{-4}	1.23×10^{-3}	+67.2%
18	Heating of 10th layer of powder	7.811×10^{-4}	1.693×10^{-3}	+53.9%
19	Immediately prior to removal of part bed from chamber	9.82×10^{-3}	1.2177×10^{-2}	+19.3%
	Fabricated part at room temperature	0.1542	0.15694	+1.7%

Table 6-5 Selected magnitudes of the maximum distance in the z-direction of the bottom surface of the build from the rigid surface predicted by the second and third versions of the stress model. Heating of a layer of powder denoted in the table implies raising the temperature of its top surface to the set point (150°C)

Chapter 7

Discussion and Conclusion

7.1 Introduction

The second and third versions of the stress model appeared to have accurately predicted the profile of the bottom surface of the ten-layer part, with the exception of regions extending 1.6mm in the x-direction from both edges of the surface (see Figure 6.34). The models, however, did not produce an accurate prediction of the profile of the top surface of the part. On the basis of the experimentally measured profiles, the models are assumed to have over-predicted curl in the "cooldown" stage whilst underestimating curl in the "build" stage (see Section 6.3.3). The aim in this chapter is to review assumptions considered in the models and investigate the sensitivity of curl predicted to variations in the assumed values. The strategy used in the sensitivity investigations is to vary the value of one assumed parameter while holding the other parameters constant. Based on the sensitivity study, a more specified approach into future model development could be suggested.

Improvements made to the third version of the models over the second version did not show considerable enhancement in the final curl predicted. That is probably due to assumptions causing the inaccurate prediction of curl in the second version of the models being also implemented in the third version. As the total CPU time required to produce results in the third version of the models was approximately twice that in the second version, the latter was employed in investigating the sensitivity of curl to variations in assumptions considered.

The topics discussed in this chapter include the following:

- The effect of maintaining the bottom surface of the part bed at 20°C, following its removal from the chamber, on the final curl predicted.
- Sensitivity of curl predicted to values of the expansion coefficient and elastic modulus assumed in the second version of the stress model.

- The sensitivity of curl to assumptions made with regard to the temperature of the powder bed and that of added layers of powder in the "build" stage.
- The effect of the temperature of the gas occupying the process chamber on curl of the part.

7.2 Part Cooling Following Removal of the Part Bed From the Chamber

In the second version of the heat transfer analysis, placing the part bed on the metallic breakout station, following its removal from the chamber, was simulated by applying a boundary condition that maintained the temperature of the nodes located at the bottom surface of the bed at room temperature (20°C). However, heat conducted from the part bed to the metallic structures is expected to have caused a slight rise in the temperature of the metallic surface in contact with the bottom surface of the bed. That rise in temperature is believed to reduce the amount and rate of heat lost through conduction from the part bed to the metallic structures. Thus, assuming the bottom surface of the part bed to be maintained at 20°C may have resulted in the heat transfer analysis to overestimate the amount of heat lost from the bottom surface of the part bed following its removal from the chamber.

To investigate the effect of that assumption on the final curl predicted, an opposite extreme case was simulated whereby the bottom surface of the part bed was assumed to be insulated following its removal from the chamber, i.e. no heat is lost from the bottom surface of the part bed to the metallic structures. Simulation of that case required the final step in the second version of the heat transfer analysis to be slightly modified; the boundary condition applied on the nodes located at the bottom surface of the part bed was removed. However, other definitions in the final step and the definition of remaining steps in the modified heat transfer model were identical to those mentioned in the second version of the heat transfer model. The temperature histories predicted by both heat transfer analyses at the top and bottom surfaces of the part following removal of the part bed from the chamber are illustrated in Figure 7.1. In the figure, the temperatures at the top and bottom surfaces of the part are seen to reduce at a lower rate in the case where the bottom surface of the part assumed to be insulated than that with the bottom surface of the bed maintained at 20°C. Modifications made to the second version of the heat transfer analysis did not require the corresponding stress analysis to differ from the second version of the stress analysis. The final maximum distance of the bottom surface of the part predicted by the stress analysis with the bottom surface of the part bed assumed to be thermally insulated was equal to 0.15414mm. The distance differed by 0.04% compared to that predicted with the bottom surface of the bed maintained at 20°C (0.1542mm). Thus, assuming the bottom surface of the part bed to be maintained at 20°C following its removal from the process chamber had an insignificant effect on the final curl predicted.

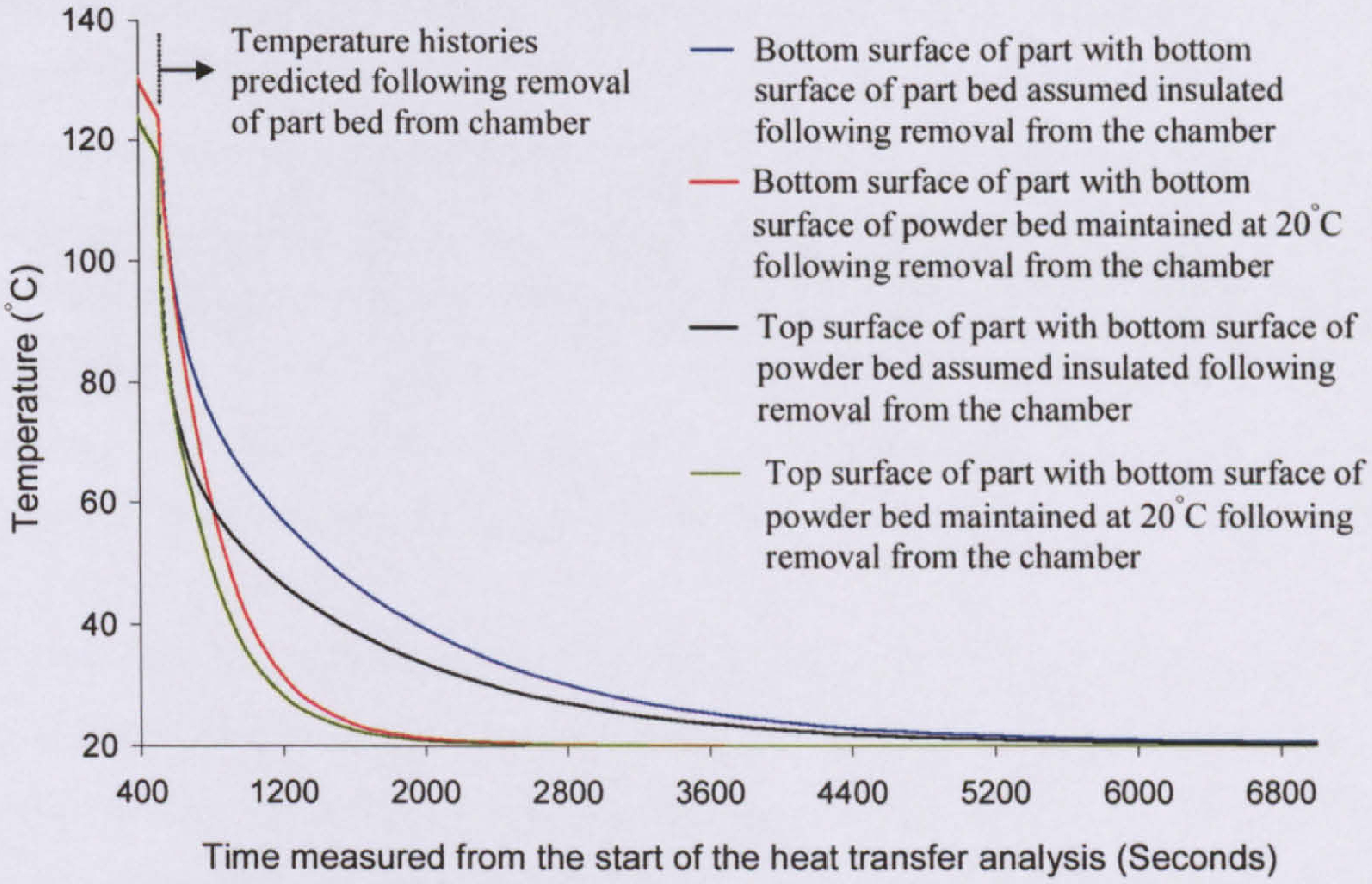

Figure 7.1 Temperature histories at the top and bottom surfaces of the part predicted by the second version of the heat transfer analysis, i.e. with the bottom surface of the part bed maintained at 20°C following its removal from the chamber drawn alongside the temperature histories predicted with the bottom surface of the bed assumed to be thermally insulated.

However, the similarity in the final curl predicted in both the cases above-mentioned is rather surprising. It has been established that viscoelasticity has a reducing effect on curl (see Tables 6-3 and 6-4). Additionally, the time-dependent (viscoelastic) response becomes less apparent as the temperature of the polymer is reduced (see Figures 5.18 to 5.20). Thus, the higher rate at which the temperature in the part decreases with the bottom surface of the part bed maintained at 20°C is expected to minimise the effect of viscoelasticity in reducing curl compared to its effect with the surface being insulated (see Figure 7.1). The similarity in the final curl predicted in both situations prompted an investigation into the effect of viscoelasticity on curl following removal of the part bed from the chamber. The investigation required the second version of the stress analysis to be modified by replacing the final step in the stress analysis with two steps. The first of the steps used as thermal loading the nodal temperature histories predicted by the second version of the heat transfer analysis during cooling of the fabricated ten-layer part in the chamber. The following step (final step), however, used as thermal loading the nodal temperature histories predicted by the heat transfer analysis following removal of the part bed from the chamber. The type of analysis was defined in the final step using the (STATIC) option in ABAQUS, whereas the (VISCOELASTIC) option was used to specify the analysis type in all other steps of the stress model. The (final) maximum distance of the bottom surface of the part from the rigid surface, predicted by the modified stress model, was equal to 0.1546mm. The distance differed from that estimated by the second version of the model (0.1542mm) by 0.25%. That clearly suggested that viscoelasticity had an insignificant effect on the final curl following removal of the part bed from the process chamber, which is probably due to the relatively low temperatures experienced by the part in that period.

However, the insignificant effect of viscoelasticity, following part bed removal from the chamber, is not a sufficient reason to explain the similarity between the final curl predicted with the bottom surface of the part bed maintained at 20°C and that predicted with the surface insulated. That is because the nodal temperature histories predicted in both cases clearly differ (see Figure 7.1). As the instantaneous modulus was defined in the stress analysis to vary with temperature, the similarity in the final curl predicted appears to indicate that changes in modulus, following part bed removal from the chamber, had an insignificant effect on the final curl of the part. To investigate the accuracy of that belief, the second version of the stress analysis was modified. That was made by defining a constant modulus in the temperature range from 123°C to room temperature equal to the modulus previously specified at room temperature, 329.3MPa. The temperature 123°C denotes the highest temperature in the part, seen at its bottom surface, at the instant of part bed removal from the chamber. The final maximum distance predicted by the modified stress model was equal to 0.1545mm, i.e. differing from that predicted by the second version of the stress model (0.1542mm) by 0.19%. Thus, variation in the modulus following part bed removal from the chamber had an insignificant effect on the final curl predicted.

The simulations performed indicate that the part behaves elastically following its removal from the chamber, with changes in modulus with temperature in that period having an insignificant effect on the final curl of the part. Therefore, one may assume that the rise in curl predicted following part bed removal from the chamber is not influenced by the rate at which the temperature in the part reduces, but only on the magnitude of temperature reduction. To validate the assumption, the final step in the second version of the heat transfer analysis, which simulated cooling of the part following its removal from the process chamber, was removed. That was replaced with a step in which a boundary condition was applied to all nodes connected to elements representing the ten-layer part reducing their temperature to 20°C. An arbitrary time period was specified for the step of 0.1 second. The final maximum distance of the bottom surface of the part from the rigid surface predicted by the corresponding stress model was equal to 0.1549mm. The distance differed from that predicted by the second version of the stress model (0.1542mm) by 0.5%.

The results therefore suggest that keeping the part surrounded by the part bed following its removal from the chamber has an insignificant effect on the final curl of the part. Additionally, the findings indicate that the time consuming process of keeping the polycarbonate part bed in the process chamber to cool to room temperature would also have no considerable effect in reducing the final curl. However, the most important conclusion from a modelling point of view that simulating the lengthy period of part cooling to room temperature following its removal from the process chamber is not a necessity. Instead, the temperature in the part can be instantly reduced to room temperature. This new method reduces the CPU time required to solve the heat and corresponding stress analyses, and thus improves the efficiency of the finite element modelling.

7.3 Sensitivity of Curl to Material Properties Assumed in the Stress Analysis

In the context of material properties, the ten-layer part was assumed in the second version of the stress analysis to be formed of two distinct regions. The first region was represented by elements flanked by nodes located at a depth of 0.257mm from the top surface of the first layer and those located at the top surface of the part, whereas the second region was symbolised by the remaining elements in the first layer (see Figure 6.2). The former, termed in the following the highly sintered region of the part, was assigned in the stress analysis an assumed expansion coefficient equal to $2\times10^{-6}{}^{\circ}C^{-1}$. The latter, denoted in the following the slightly sintered region of the first layer, was given an assumed expansion coefficient equal to zero and assumed elastic moduli. As these material properties were assumed and were not defined in the stress analysis based on experimental measurements, investigation into the sensitivity of curl to variation in the assumed values was performed. The investigation was carried out to examine the necessity of accurately defining these properties in future developed stress models. In the following, the sensitivity studies are introduced.

7.3.1 Expansion Coefficient of Highly Sintered Region of the Part

The sensitivity of curl to variation in the assumed expansion coefficient of elements representing the highly sintered region of the part was performed by predicting curl using the second version of the stress analysis, whilst implementing different values of the expansion coefficient. Based on the concept adopted in the second version of the stress analysis, the expansion coefficients implemented were constant at temperatures below 175°C, while equal to zero at temperatures equal and above 175°C. Other parameters and material properties defined in the stress analysis were unchanged. The results of the sensitivity study are illustrated in Figures 7.2 and 7.3. The figures show the maximum distance of the bottom surface of the build from the rigid surface immediately prior to sintering of the tenth layer and that predicted after the ten-layer part had reached room temperature (20°C), at each of the expansion coefficients selected. The results suggest that an increase in the value of the expansion coefficient of the highly sintered regions of the part has a rising effect on curl and vice versa. For example, considering the expansion coefficient of the highly sintered region of the part to be $2.1\times10^{-6}{}^{\circ}C^{-1}$, i.e. differing by 5% from that assumed in the second version of the stress analysis ($2\times10^{-6}{}^{\circ}C^{-1}$), the maximum distance of the bottom surface of the build from the rigid surface, predicted immediately prior to sintering of the tenth layer was equal to 9.31×10^{-4}mm. The distance differed by 16%

compared to the corresponding distance predicted by the second version of the stress analysis (7.811×10^{-4}mm). That suggested that a slight variation in the expansion coefficient had a significant effect on curl developed in the "build" stage. However, variations in the expansion coefficient did not show, to that degree, a considerable effect on curl predicted in the "cooldown" stage. For example, the final maximum distance of the bottom surface of the ten-layer part from the rigid surface, predicted with the expansion coefficient implemented equal to 2.1×10^{-6}°C^{-1} was 0.16397mm. The distance differed by 6% compared to the corresponding distance predicted by the second version of the stress analysis (0.1542mm). Due to the high sensitivity of curl to variations in the expansion coefficient of the highly sintered region of the part, particularly in the "build" stage, a more accurate definition of that expansion is required in future developed stress models.

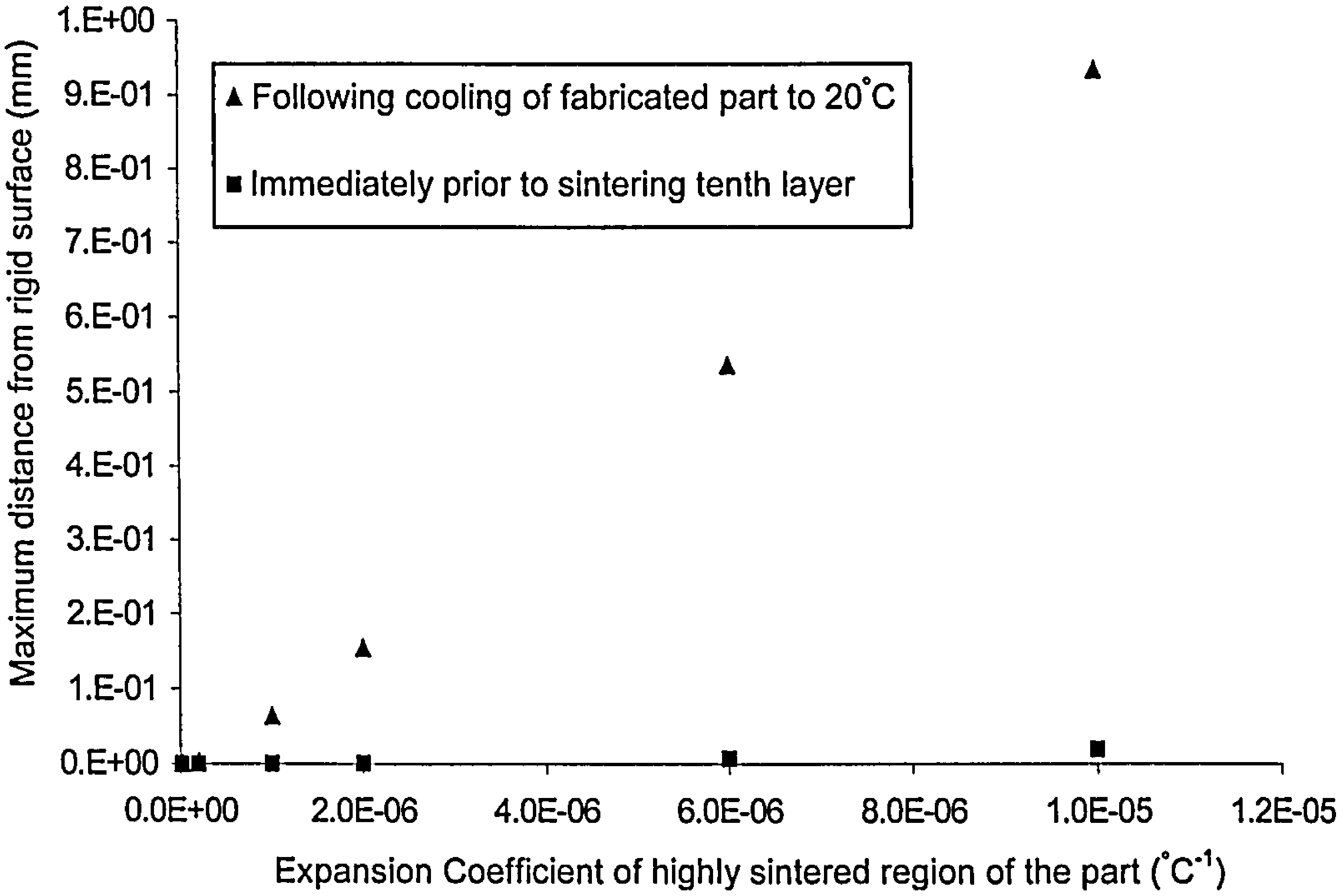

Figure 7.2 Maximum distance of bottom surface of part from rigid surface predicted immediately prior to sintering the tenth layer of powder and that predicted following cooling of the fabricated ten-layer part to room temperature, at each of the expansion coefficients selected for the highly sintered region of the part.

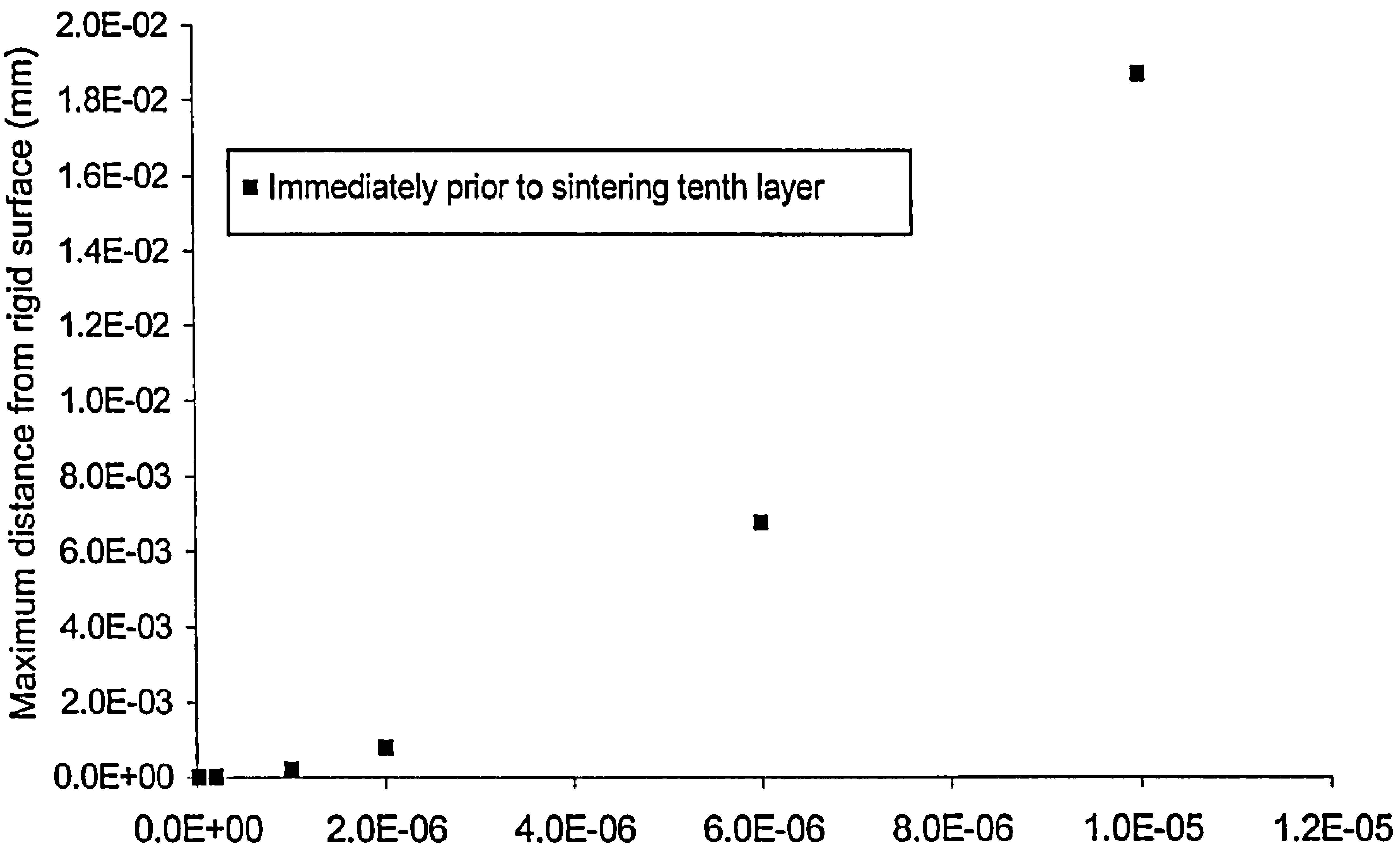

Figure 7.3 Maximum distance of bottom surface of part from rigid surface predicted immediately prior to sintering the tenth layer of powder, at each of the expansion coefficients selected for the highly sintered region of the part.

7.3.2 Expansion Coefficient of Slightly Sintered Region in First Layer

In the second version of the stress analysis, the expansion coefficient of the slightly sintered region in the first layer was assumed to be equal to zero. The assumption was made based on the understanding that shrinkages developed in that region, wherein particles are poorly bonded, is extremely small compared to those generated in the highly sintered regions of the part. As the expansion coefficient of the slightly sintered region in the first layer was assumed and was not defined in the stress analysis on the basis of experimental measurements, sensitivity of curl to variation in that coefficient was investigated. That was performed by predicting curl using the second version of the stress analysis, whilst implementing different values of that coefficient. Based on the understanding that the expansion coefficient of the slightly sintered region is less than that of the highly sintered regions of the ten-layer part, the former was given different values in the sensitivity study that were less than that defined for the latter (2×10^{-6}°C^{-1}). Other parameters and material properties defined in the second version of the stress analysis were unaltered. The results of the sensitivity study are illustrated in Figures 7.4 and 7.5. The figures show the maximum distance of the bottom surface of the build from the rigid surface, immediately prior to sintering the tenth layer of powder and that predicted after the fabricated ten-layer part had reached room temperature (20°C), at each of the expansion coefficients selected. The results suggest that an increase in the value of the expansion coefficient of the slightly sintered region of the part has a reducing effect on curl and vice versa. For example, assuming an expansion coefficient of the slightly sintered region in the first layer to be $1.5\times10^{-6}{}^{\circ}C^{-1}$ instead of zero, the final maximum distance of the bottom surface of the build from the rigid surface, predicted immediately prior to sintering of the tenth layer was equal to 5.725×10^{-4}mm. The distance differed by 27% compared to the corresponding distance predicted by the second version of the stress analysis (7.811×10^{-4}mm). However, the final maximum distance of the bottom surface of the part predicted with the expansion coefficient equal to $1.5\times10^{-6}{}^{\circ}C^{-1}$, was 0.019771mm. The distance differed from that predicted by the second version of the stress analysis (0.1542mm) by 87.2%. The sensitivity of curl is therefore highly influenced by changes in the expansion coefficient of the slightly sintered region of the first layer, particularly in the "cooldown" stage. Due to the significant effect of the expansion coefficient of the slightly sintered region on curl, a more accurate definition of that coefficient is required in future developed stress analyses.

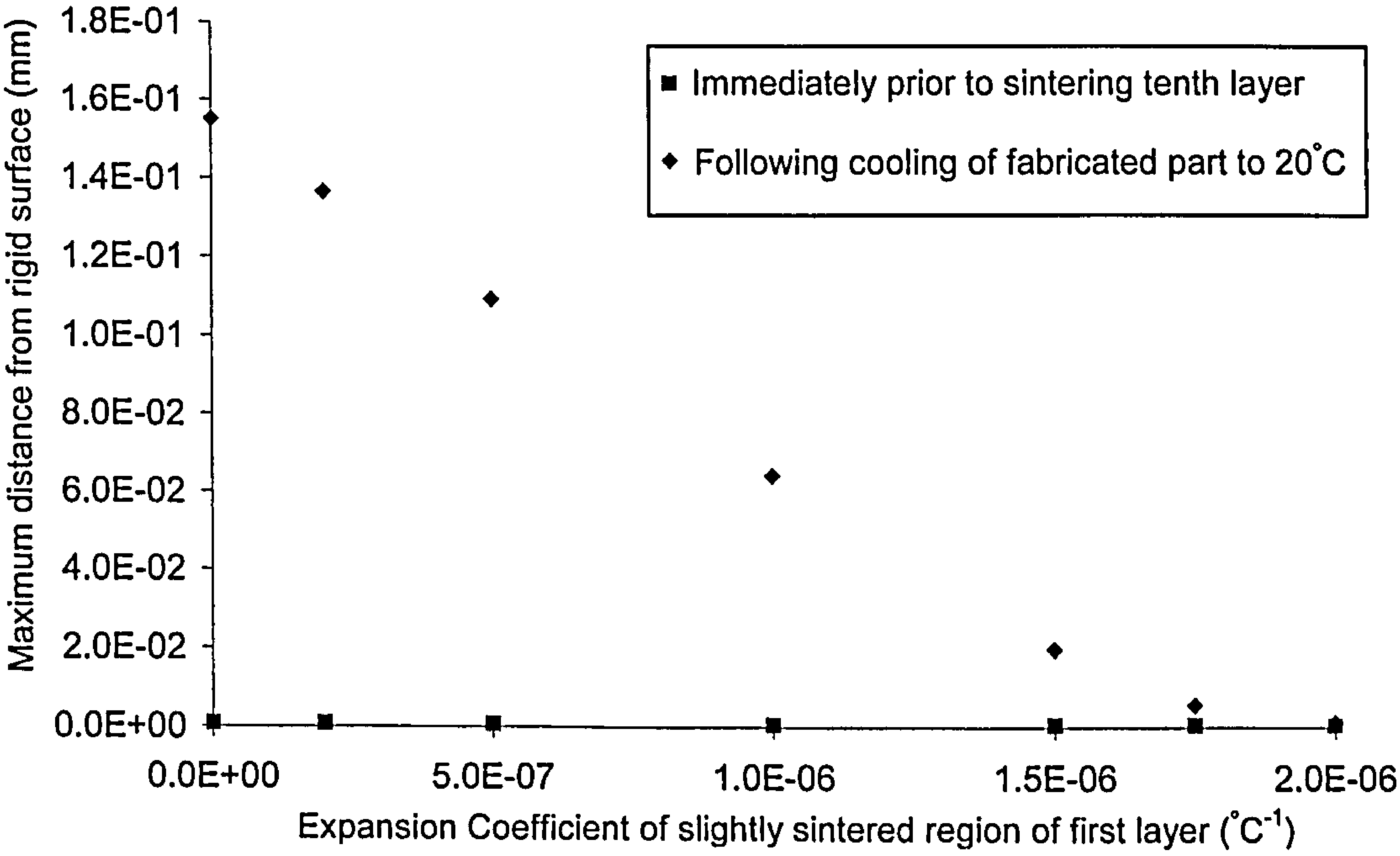

Figure 7.4 Maximum distance of bottom surface of part from rigid surface predicted immediately prior to sintering the tenth layer of powder and that predicted following cooling of the fabricated ten-layer part to room temperature, at each of the expansion coefficients selected for the slightly sintered region of the first layer of the part.

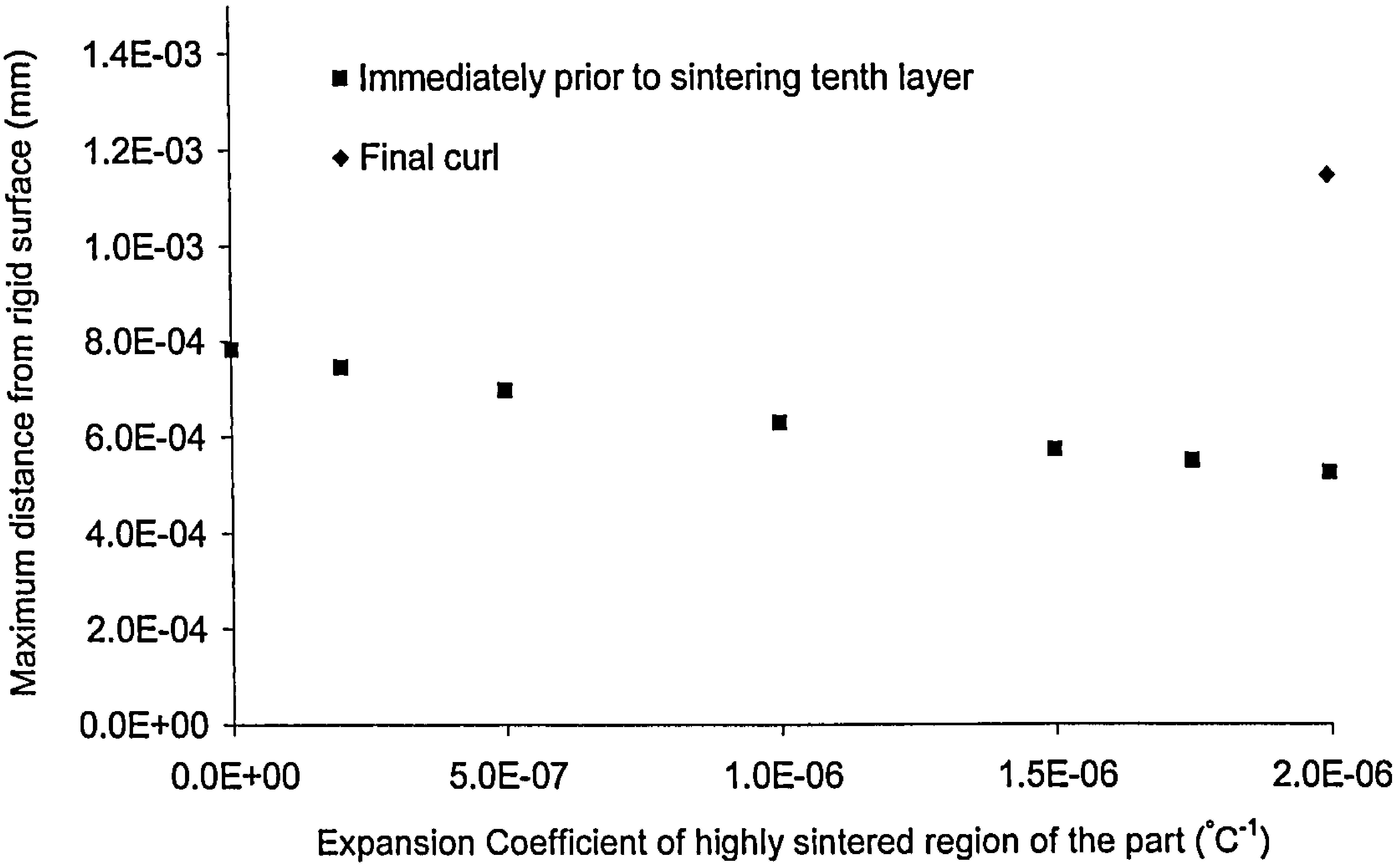

Figure 7.5 Maximum distance of bottom surface of part from rigid surface predicted immediately prior to sintering the tenth layer of powder, at each of the expansion coefficients selected for the slightly sintered region of the first layer of the part.

7.3.3 Elastic Modulus of Slightly Sintered Region in First Layer

In the second version of the stress analysis, the elastic moduli of all elements together representing the ten-layer part were assumed to be identical. The moduli values were defined in the analysis based on tensile test measurements performed on SLS polycarbonate fabricated specimens. The fabricated specimens are also expected to consist of slightly (poorly bonded) and highly sintered regions. However, as the cross-sectional area (perpendicular to the direction of tension) and the elastic modulus of the former region are much less than that of the latter, the elastic modulus measured is expected to correspond mainly to the modulus of the highly sintered region in the specimens. Thus, the elastic moduli defined in the second version of the stress analysis for the slightly sintered region in the first layer is expected to be an overestimation of the actual value. Therefore, the sensitivity of curl to variation in the elastic moduli of the slightly sintered region was investigated. That was performed by defining in the second version of the stress analysis a small constant modulus to the elements representing the slightly sintered region of the first layer equal to 11.9MPa, whilst maintaining other parameters unchanged. The value of modulus selected (11.9 MPa) represents the lowest modulus defined previously in the stress analysis i.e. at temperatures equal and exceeding 150°C (see Table 5-1). However, it must be emphasised that there is no scientific basis for selection of this particular value of modulus. The maximum distance of the bottom surface of the build from the rigid surface predicted immediately prior to sintering of the tenth layer was equal to 7.538×10^{-4}mm. The distance differed by 3.5% compared to the corresponding value predicted by the second version of the stress analysis (7.811×10^{-4}mm). However, the final maximum distance predicted with the modulus of the slightly sintered region in the first layer equal to 11.9MPa was 0.0106mm, i.e. differing by 93% compared to the corresponding distance estimated by the second version of the stress analysis (0.1542mm). Due to the high sensitivity of curl to the variation in the elastic modulus of the slightly sintered region of the first layer, a more accurate definition of the modulus of that region is required in future developed stress analyses.

7.4 Sensitivity of Curl Predicted to Temperature of Powder bed

In the second version of the heat transfer analysis, simulation of the "warmup" stage was not performed. However, the assumption made was that the initial temperature of the layers of powder spread in that stage was uniform, equal to 150°C, immediately prior to the "build" stage starting. As the initial temperature was assumed, and was not defined in the analysis based on experimental measurements, numerical investigations or analytical models, investigation into the sensitivity of curl to variation in the assumed initial temperature was performed. The investigation was carried out to examine the necessity of accurately defining temperatures in the powder bed, immediately prior to the "build" stage starting, in future developed heat transfer models. The sensitivity study was performed by implementing different values of the initial nodal temperature of elements representing the powder spread in the "warmup" stage and employing the stress model to predict curl at each of the temperatures selected. The assumption made in the developed heat transfer models was that the initial temperature of the powder spread in the "warmup" stage was uniform. Other definitions in the heat transfer analyses were identical to those specified in the second version of the heat transfer analysis. The corresponding stress analyses were quite similar to the second version of the stress analysis. However, the only slight variations made were in the nodal temperature histories read in corresponding steps of the stress analyses, and consequently in the time period of the steps. That was made to ensure that elements representing recently sintered layers were activated just before their nodal temperatures reduced below 175°C. The results of the sensitivity investigation are illustrated in Figure 7.6. The figure shows the maximum distance of the bottom surface of the build from the rigid surface predicted at different instances in the "build" stage, at each of the initial temperatures selected. The results suggest that reduction in the temperature of the powder spread in the "warmup" stage has a rising effect on curl and vice versa. For example, considering the initial temperature of the powder spread in the "warmup" stage to be 142.5°C, i.e. differing by 5% from that assumed in the second version of the heat transfer analysis (150°C), the maximum distance of the bottom surface of the build from the rigid surface, immediately prior to the addition of the third layer of powder, is equal to 2.1631×10^{-4}mm. The distance differed from the corresponding value predicted by the second version of the stress analysis (1.65×10^{-4}mm) by 24%. Moreover, prior to addition of the tenth layer of powder, the maximum distance predicted with the initial temperature of the powder equal to 142.5°C was 5.45×10^{-4}mm, i.e. differing by 26% from the corresponding distance predicted by the second version of the stress analysis (4.03×10^{-4}mm). The results therefore suggest that a slight variation in the initial temperature of the powder spread in the "warmup" stage has a significant effect on curl developed in the "build" stage. Consequently, a proper definition of the initial temperature of the powder spread in the "warmup" stage is required in future developed heat transfer models. However, the effect of selecting an initial temperature of 142.5°C instead of 150°C did not show a significant variation in the final curl predicted. The final maximum distance of the bottom surface of the part from the rigid surface was equal to 0.15724mm at 142.5°C whereas equal to 0.1542mm at 150°C, i.e. a difference in distance of 2%. That is most probably due to the overestimation in curl in the "cooldown" stage causing the significant variations in curl seen in the "build" stage not to be clearly exhibited on the final profiles predicted of the top and bottom surface of the part.

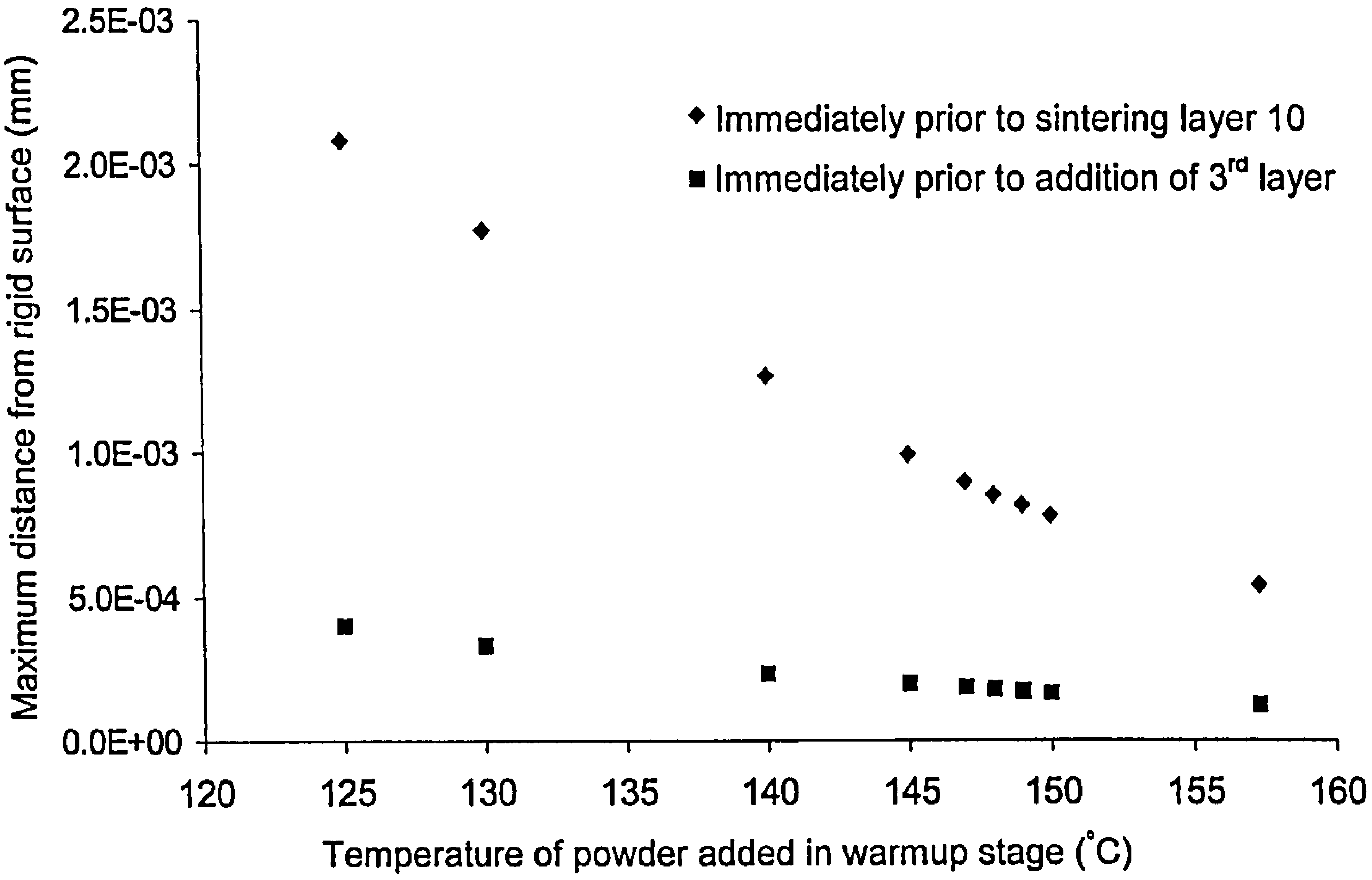

Figure 7.6 Maximum distance of bottom surface of part from rigid surface predicted immediately prior to addition of the 3rd layer of powder and prior to sintering of the 10th layer, at each of the temperatures selected for the powder spread in the "warmup" stage.

7.5 Sensitivity of Curl to Temperature of added layers of powder

In the "build" stage in fabrication of the ten-layer parts, the powder in the feed cartridges was maintained at 80°C. In modelling, the temperature was assumed to be that of a layer of powder the moment it was spread onto the position where sintering was to occur. However, during powder addition, the part heater is expected to have raised the temperature of the layer as it is spread by the roller above 80°C. As the assumed value of the initial nodal temperature of elements representing the layers of powder spread in the "build" stage (80°C) was not based on experimental measurements, numerical investigations or analytical models, sensitivity of curl to variation in the temperature of the added powder was investigated. In the sensitivity study, the concept accepted in the second version of the heat transfer analysis was implemented; the initial temperature of all layers added in the "build" stage was assumed to be identical. Different initial temperatures of layers of powder added in the "build" stage were implemented in the heat transfer model, and the stress model was employed to predict curl at each of the initial temperature selected. However, variation in the initial temperature of added layers required the steps simulating heating of the added layer of powder to the set point temperature (150°C) to differ from corresponding steps in the second version of the heat transfer analysis. In the modified heat transfer analyses, heating of the recently sintered layer was simulated by linearly raising the temperature of the top surface of the added layer from the initial temperature selected to 150°C in 7 seconds. The corresponding stress models were quite similar to the second version of the stress model. However, alteration in the nodal temperature histories used as thermal loading in corresponding steps of the stress models and consequently in the time period of the steps was made to ensure that elements representing recently sintered layers were activated just before their nodal temperatures reduced below 175°C. The results of the sensitivity investigation are illustrated in Figure 7.7. The figure shows the maximum distance of the bottom surface of the build from the rigid surface predicted at different instances in the "build" stage, at each of the initial temperatures implemented. The results suggest that increasing the initial temperature of the added layers has a reducing effect on curl and vice versa. For example, considering the initial temperature of added layers in the "build" stage to be 84°C, i.e. differing by 5% from that assumed in the second version of the heat transfer model (80°C), the maximum distance of the bottom surface of the build from the rigid surface, immediately prior to addition of the third layer of powder, was equal to 1.54816×10^{-4}mm. The distance differed by 6.2% compared to the corresponding distance predicted by the second version of the stress analysis (1.65×10^{-4}mm). That suggested that a slight variation in the initial temperature of added layers did not have a considerable effect on curl developed in the early phases of the "build" stage. However, the effect of the increase in the initial temperature of the added layers became significant as the "build" stage progressed. The maximum distance of the bottom surface of the build from the rigid surface, predicted immediately prior to sintering the tenth layer of powder was equal to 6.8546×10^{-4}mm, i.e. differing by 12% compared to the corresponding distance predicted by the second version of the stress model 7.811×10^{-4}mm. Due to the large effect of the initial temperature of added layers on curl, a more accurate definition of that temperature is required in future developed heat transfer analyses.

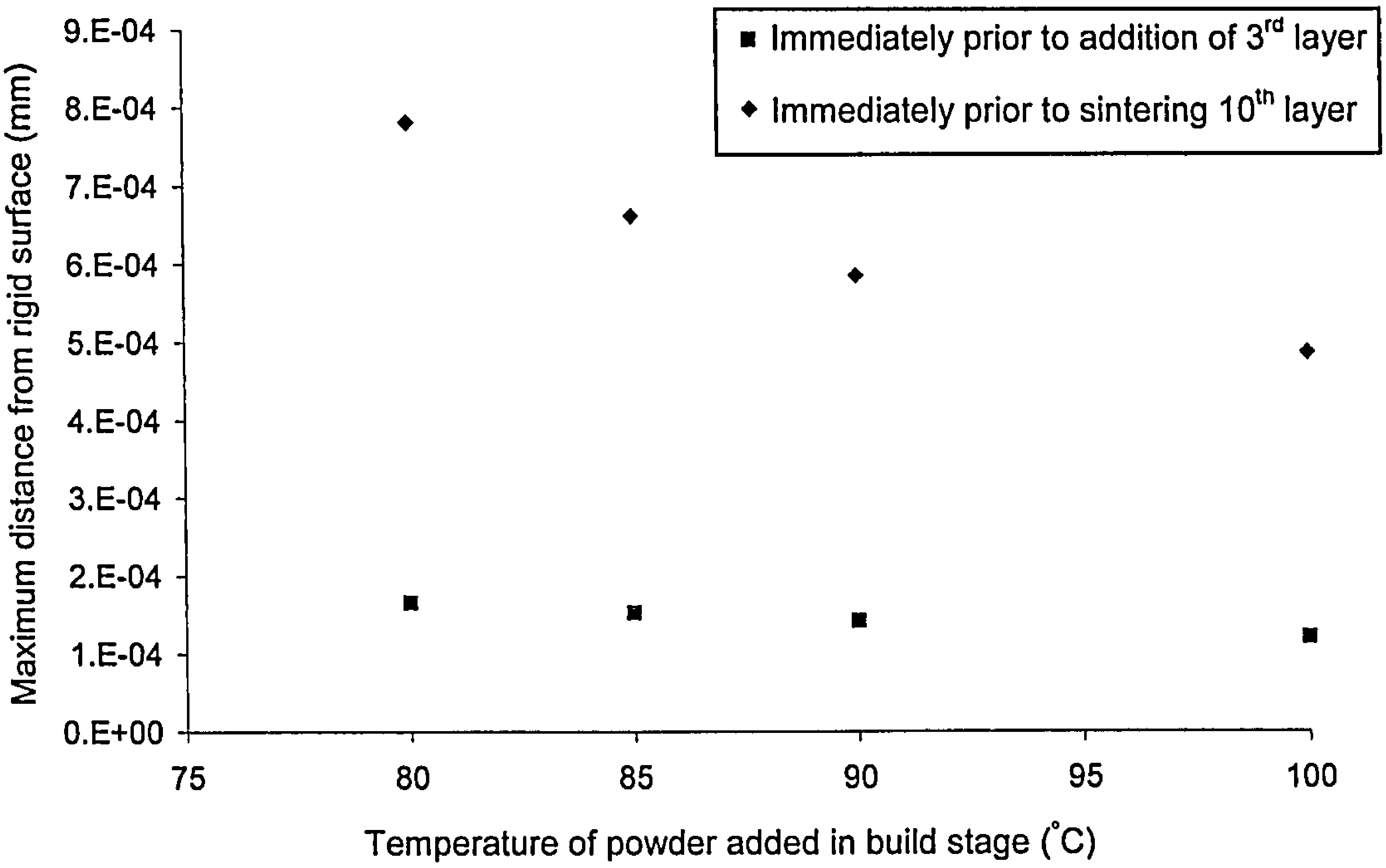

Figure 7.7 Maximum distance of bottom surface of part from rigid surface predicted immediately prior to addition of the 3rd layer of powder and prior to sintering of the 10th layer, at each of the temperatures selected for the powder spread in the "build" stage.

7.6 Sensitivity of Curl to Temperature of Gas in the Chamber

In convection and radiation calculations performed in the second version of the heat transfer analysis, the temperature of the gas in the process chamber and that of surrounding walls were assumed in the "build" stage to be maintained at 150°C. In SLS fabrication, the temperature of the gas circulating the chamber can not be directly controlled, but its mass flow rate as it enters the chamber could be adjusted. Based on the understanding that the gas is mainly heated by heat emanating from the part heater, one may expect that reducing the flow rate of the circulating gas may cause an increase in the temperature of the gas and enclosing walls. As the temperature used in the convection and radiation calculations was assumed, and was defined in the analysis based on experimental measurements, numerical investigations or analytical models, investigation into the sensitivity of curl to variation in the assumed temperature was performed. The investigation was carried out to examine the necessity of defining the accurate temperature of the gas and enclosing walls in future developed heat transfer models. The sensitivity study was performed by implementing different values of the temperatures used in the convection and radiation calculations and employing the stress analysis to estimate curl at each of the temperatures implemented. Other variables and step definitions in the heat transfer models were identical to those mentioned in the second version of the heat transfer analysis. The corresponding stress analyses were quite similar to the second version of the stress analysis. However, alteration in the nodal temperature histories used as thermal loading in corresponding steps of the stress models and consequently in the time period of the steps was performed to ensure that elements representing recently sintered layers were activated just before their nodal temperatures reduced below 175°C.

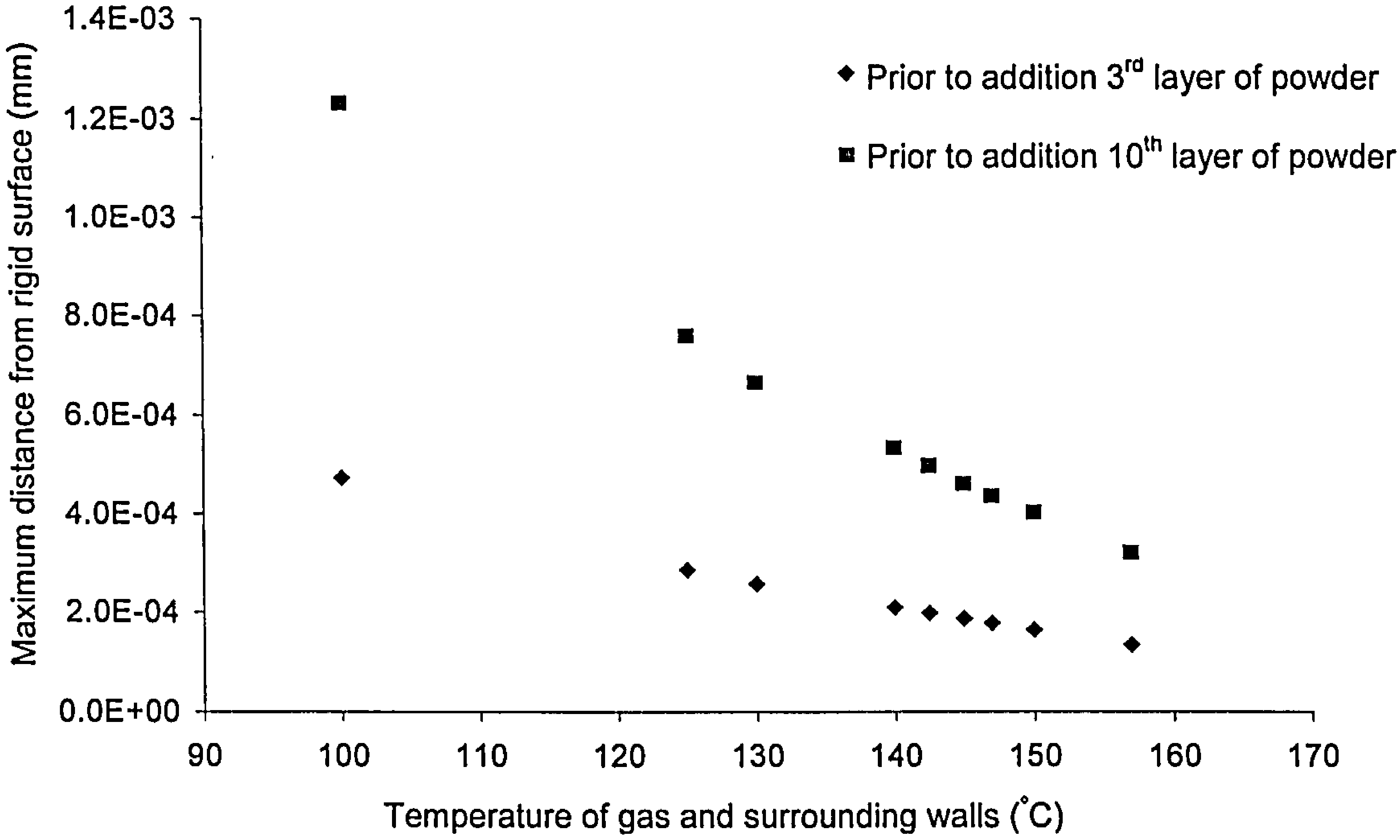

Figure 7.8 Maximum distance of bottom surface of part from rigid surface predicted immediately prior to addition of the 3rd layer of powder and prior to addition of the 10th layer, at each of the temperatures selected for the gas and surrounding walls, used in the convection and radiation calculations in the 2nd version of the heat transfer analysis.

The results of the sensitivity study are shown in Figure 7.8. The figure shows the maximum distance of the bottom surface of the build from the rigid surface, predicted at different instances in the "build" stage, at each of the temperatures implemented. The results indicate that reducing the temperature of the gas and enclosing walls has a rising effect on curl. For example, considering the temperature of the gas and enclosing walls to be 142.5°C, i.e. differing by 5% from that assumed in the second version of the heat transfer analysis (150°C), the maximum distance of the bottom surface of the build from the rigid surface, immediately prior to addition of the third layer of powder was equal to 1.984×10^{-4}mm. The distance differed from the corresponding value predicted by the second version of the stress analysis (1.65×10^{-4}mm) by 17%. Furthermore, immediately prior to addition of the tenth layer of powder, the maximum distance predicted with the temperature assumed to be 142.5°C was equal to 4.97×10^{-4}mm, i.e. differing by 19% compared to that predicted by the second version of the stress model (4.03×10^{-4}mm). Due to the significant effect suggested in the variation in the temperature of the gas and enclosing walls on curl, a proper definition of that temperature is required in future developed heat transfer models.

7.7 Conclusions

The primary objective of this research has been to develop finite element models that can predict curl in SLS fabricated parts. The models consist of a heat transfer and a stress models, which were both coupled using the sequentially coupled thermal-stress analysis technique. The second and third versions of the models provided an (almost) accurate prediction of the curled profile of the bottom surface of a ten-layer SLS fabricated polycarbonate part. However, predictions of the curled profile of the top surface of the part were unsatisfactory. On the basis of the experimentally measured profiles of the part, the models are assumed to have underestimated curl developed in the "build" stage, whilst over-predicted curl in the "cooldown" stage. In an attempt to investigate the effect of assumptions made on curl predicted, a sensitivity study was performed. The method adopted in the study was to predict curl when varying the value of one assumed parameter, whilst holding the other parameters constant. Based on the study, parameters assumed in the models, which have a high influence on curl predicted were identified. These parameters are as follows:

- The expansion coefficient of the slightly sintered region in the first layer: The sensitivity study showed that a rise in the expansion coefficient of the slightly sintered region of the first layer has a considerable effect in reducing curl in the "build" and "cooldown" stages. Thus, future work is required to determine the expansion coefficient of that region prior to future model development.

- The elastic modulus of the slightly sintered region in the first layer: A reduction in the elastic modulus of the slightly sintered region in the first layer was seen to have reducing effect on curl. Consequently, proper estimation of that modulus is essential in future developed models.

- The expansion coefficient of the properly sintered region of the part. An increase in the expansion coefficient of the properly sintered regions of the part has a considerably rising effect on curl. Therefore, finding the actual magnitude of that coefficient is of paramount importance in future developed models.

- Temperature of layers of powder added in the "warmup" stage: Reduction in the temperature of the layers of powder added in the "warmup" stage had a considerable rising effect on curl. Therefore, estimation of actual temperatures in the powder bed, immediately prior to the "build" stage starting, is required in future developed models.

- Temperature of added layers of powder in the "build" stage: An increase in the temperature of the added layers was seen to have a significant reducing effect on curl developed in the "build" stage. Thus, proper estimation of the temperature of the layer, the moment it is added on top of a recently sintered region is important in future developed models.

- Temperature of the gas and walls in the chamber: Reduction in the temperature of the gas in the chamber and enclosing walls was exhibited by considerable rise in curl. Consequently, proper estimation of the temperature is important in future developed models.

7.8 Recommendation For Future Work

Based on the results of the sensitivity study, the following aspects can be suggested in future modelling to predict curl:

- Estimation of the expansion coefficient and modulus of the slightly sintered region in the first layer of the part, the expansion coefficient of the highly sintered region in the part, temperature of the powder added in the "warmup" and "build" stages and the temperature of the gas in the chamber in the "build" stage.

- Implementing the estimated values of the parameters above-mentioned in the second and third versions of the models developed in this research. A comparison between results obtained from these models may provide a better insight into the thermal effect of the powder surrounding the part on the final curl predicted.

Bibliography

[1] J. Beaman, J. Barlow, D. Bourell, R. Crawford, H. Marcus, and K. McAlea. *Solid Freeform Fabrication: A New Direction in Manufacturing.* Kluwer Academic Publishers, Dordrecht, 1997.

[2] B. Palm and J. Lamancusa. *Rapid Prototyping Primer.* Department of Mechanical and Nuclear Engineering, Pennsylvania State University. http://www.me.psu.edu/lamancusa/rapidpro/primer/chapter2.htm, 1998.

[3] S. Au and P.Wright. A. *A Comparative Study of Rapid Prototyping Technology.* Intelligent Concurrent design: Fundamentals, methodology, modelling and practice ASME, DE-Vol. 66, 73-82, 1993

[4] P. Jacobs. *Rapid Prototyping and Manufacturing: Fundamentals of Stereolithography,* Society of Manufacturing Engineers, Dearborn, 1992.

[5] Bremen Institute of Industrial Technology and Applied Work Science at the University of Bremen, *Introduction to Fused Deposition modelling,* http://www.biba.uni-bremen.de/groups/rp/fdm.html, 2001

[6] X. Wang, *Calibration of Shrinkage and Beam Offset in SLS Process,* Rapid Prototyping Journal, vol. 5, No. 3, pp.129-133, 1999

[7] J. Nelson, S. Xue, J. Barlow, J. Beaman, H. Marcus and D. Bourell, *Model of the Selective Laser Sintering of Bisphenol-A Polycarbonate,* Industrial Engineering Chemical Research, vol. 32, No. 10, pp. 2305-2317, 1993.

[8] B. Saleh, M. Teich, *Fundamentals of Photonics,* New York Chichester: Wiley, 1991.

[9] J. Williams and C. Deckard, *Advances in Modelling the Effects of Selected Parameters on the SLS Process,* Rapid Prototyping Journal, vol. 4, No. 2, pp.90-100, 1998.

[10] General Scanning, Inc, 500 Arsenal Street, Massachusetts, *DE Series: 2000, 3000, Digital electronics, User Manual,* 1992.

[11] DTM Corporation, 1611 Headway Circle, Austin, Texas 78754, *DTM Sinterstation system 2000, User's Guide,* 1996.

[12] C. Deckard and J. Beaman, *Process and Control Issues in Selective Laser Sintering,* Sensors and Controls for Manufacturing, ASME PED-Vol. 33, pp.191-197, 1988.

[13] DTM Corporation, 1611 Headway Circle, Austin, Texas 78754, *DTM Sinterstation System 2000, Guide to Materials: Polycarbonate LPC 3000, 1996*

[14] DTM Corporation, 1611 Headway Circle, Austin, Texas 78754, *DTM Sinterstation System 2000, SLS Geometry Tools Guide,* 1996.

[15] P. Forderhase, K. McAlea, M. Michalewicz, M. Ganninger and K. Firestone, *SLS Prototypes from Nylon*, Proceedings of the Solid Freeform Fabrication Symposium, The University of Texas at Austin, Austin, Texas, pp.102-109, 1994.

[16] C. Kai, L. Fai, *Rapid Prototyping: Principles & Applications in Manufacturing*, New York, John Wiley and sons Ltd, 1997.

[17] K. McAlea, R. Booth, P. Forderhase, U. Lakshminarayan, *Materials for Selective Laser Sintering Processing*, 27th International SAMPE Technical Conference, Albuquerque, pp. 949-961, October 9-12, 1995.

[18] F. Billmeyer, *Textbook of Polymer Science*, second edition, New York Chichester: Wiley-Interscience, 1971.

[19] Y. Godovsky, *Thermophysical Properties of Polymers*, Berlin London: Springer, 1992.

[20] A. Turi, *Thermal Characterisation of Polymeric Materials*, New York London Academic Press, 1981

[21] D. Askeland, *The Science and Engineering of Materials*, Third Edition, Monterey, Calif.: Brooks/Cole Engineering Division, 1984.

[22] R. Young, *Introduction to Polymers*, London: Chapman and Hall, 1981.

[23] I. Ward, *Mechanical Properties of Solid Polymers*, second Edition, John Wiley & sons Ltd, 1985.

[24] Z. Tadmor and C. Gogos, *Principles of Polymer Processing*, New York Chichester: Wiley, 1979.

[25] C. Orr, *Particulate Technology*, New York: Macmillan, 1966.

[26] S. Yagi and D. Kunii, *Studies on Effective Thermal Conductivities in Packed Beds*, J. AIChE, vol. 3, No. 3, pp.373-381, 1957.

[27] S. Sih and J. Barlow, *The Prediction of Thermal Conductivity of Powders*, Proceedings of the Solid Freeform Fabrication Symposium, The University of Texas at Austin, Austin, Texas, pp.397-401, 1995.

[28] S. Sih and J. Barlow, *Measurement and Prediction of the Thermal Conductivity of Powders at High Temperatures*, Proceedings of the Solid Freeform Fabrication Symposium, The University of Texas at Austin, Austin, Texas, pp.321-329, 1994.

[29] H. Ho, I. Gibson and W. Cheung, *Effects of Energy Density on Morphology and Properties of Selective Laser Sintered Polycarbonate*, Journal of materials processing technology, vol. 90, pp 204-210, 1999.

[30] B. Briscoe and M. Adams, *Tribology in Particulate Technology*, Bristol : Hilger, 1987.

[31] T. Childs, G.Ryder and M.Berzins, *Experimental and Theoretical Studies of Selective Laser Sintering*, In Rapid Product Development, Edited by N. Kawa et al., Chapman and Hall, pp.132-141, 1997.

[32] J. Gere and S. Timoshenko, *Mechanics of Materials*, 2nd Edition, Van Nostrand Reinhold (UK), 1988.

[33] Editor-in-chief M. Bever, *Encyclopedia of Materials Science and Engineering*, Oxford : Pergamon, 1986

[34] M. Berzin, T.Childs, K. Dalgarno, G. Ryder and G. Stein, *Densification and Distortion in Selective Laser Sintering of Polycarbonate Parts*, Proceedings of the Solid Freeform Fabrication Symposium, The University of Texas at Austin, Austin, Texas, pp.196-203, 1995.

[35] K.Dalgarno, T. Childs, I.Rowntree and L.Rothwell, *Finite Element Analysis of Curl Development in the Selective Laser Sintering Process*, Proceedings of the Solid Freeform Fabrication Symposium, The University of Texas at Austin, Austin, Texas, pp. 559-566, 1996.

[36] N. Jamal, *Finite Element Analysis of Curl Development in the Selective Laser Sintering Process*, Master thesis, University of Leeds, 1997.

[37] S. Timoshenko, *Analysis of Bi-Metal Thermostats*, Journal of Optical Society of America, Vol. 11, pp. 233-255, 1925.

[38] B. Boley and J. Weiner, *Theory of Thermal Stresses*, First Edition, Dover Publications, Inc., Mineola, NY, 1960.

[39] DTM Corporation, 1611 Headway Circle, Austin, Texas 78754, *DTM Sinterstation system 2000, Guide to materials Nylon Compounds: ProtoForm Composites (LNC-7000), LN-4010, and LNF-5000,* 1995.

[40] R. Festa, O. Manca and V. Nalso. *A Comparison Between Models of Thermal Fields in Laser and Electron Beam Surface Processing*, Journal of Heat and Mass Transfer, vol. 31, No. 1, pp99-106, 1988.

[41] T. Childs, M. Berzin, G. Ryder G, A. Tontowi, *Selective Laser Sintering for an Amorphous Polymer-Simulations and Experiments*, Proceedings IMechE, vol. 213, part B, pp 333-349, 1999.

[42] T. Childs, S. Cardie and M. Brown, *Selective Laser Sintering of Polycarbonate at Varying Powers, Scan Speeds and Scan Spacing*, Proceedings of the Solid Freeform Fabrication Symposium, The University of Texas at Austin, Austin, Texas, pp. 356-363, 1994.

[43] Hibbitt, Karlsson and Sorensen, Inc., 1080 Main Street, Pawtucket, RI 02860-4847, *ABAQUS/ Standard User's Manual*, Version 5.8, vol. 3, 1998.

[44] J. Nelson. *Selective Laser Sintering: A Definition of the Process and an Empirical Sintering Model.* Ph.D. Dissertation, University of Texas at Austin, UMI-Dissertation Services, Michigan, pp.6-210, 1993.

[45] Laserite, DTM Corporation, 1611 Headway Circle, Austin, Texas 78754, *Product Information LPC 3000 Polycarbonate Compound*, 1993.

[46] F. Incropera and D. DeWitt, *Fundamentals of Heat and Mass Transfer*, 3rd edition, New York Chichester : Wiley, 1990.

[47] DTM Corporation, 1611 Headway Circle, Austin, *The Sinterstation 2000 System, Selective Laser Sintering, Illustrated Parts Catalogue*, January 1995.

[48] M. Fagan, Finite Element Analysis: Theory and Practice, Longman Group Limited, 1992.

[49] J. Beuth and S. Narayan. *Residual Stress-Driven Delamination in Deposited Multi-Layers*. International Journal of Solids and Structures, vol. 33, No 1, pp. 65-68, 1999.

[50] Liu C. and Guo Y. *Finite Element Analysis of the Effect of Sequential Cuts and Tool-Chip Friction on Residual Stresses on a Machined Layer*, International Journal of Mechanical Sciences. Vol. 42, pp.1069-1086, 2000.

[51] Hibbitt, Karlsson and Sorensen, Inc., 1080 Main Street, Pawtucket, RI 02860-4847, *ABAQUS/ Standard Manual, Example Problems*, Version 5.5, vol. 1, 1995.

[52] H. Ho., I. Gibson and W. Cheung, *Effects of Energy Density on Bonus Z, Surface Roughness and Warpage of Selective Laser Sintered Polycarbonate*, The Eighth International Conference on Rapid Prototyping, Tokyo, Japan, June 12 and 13, pp. 99-103, 2000.

[53] Hibbitt, Karlsson and Sorensen, Inc., 1080 Main Street, Pawtucket, RI 02860-4847, *ABAQUS/ Standard Manual*, Version 5.8, vol. 2, 1998.

[54] G. Ryder, *A Numerical Model of the Selective Laser Sintering Process*, Ph.D. Thesis, University of Leeds, 1998.

[55] Hibbitt, Karlsson and Sorensen, Inc., 1080 Main Street, Pawtucket, RI 02860-4847, *Getting Started with ABAQUS/Standard*, Version 5.8, 1998.

[56] American Society for testing and material, Test method E1356, *Standard Test Method for Assignment of the Glass Transition Temperatures by Differential Scanning Calorimetry or Differential Thermal Analysis*, 1995.

[57] W. Vick, and R. Kander, *Ambient Temperature Compaction of Polycarbonate Powder*, Polymer Engineering and Science, vol.37, No. 1, pp.120-127, 1997.

[58] V. Mathot, L. Benoist, H. Berghmans, W. Hemminger, G. Hohne, J. Jansen, M. Richardson, R. Riesen and A. Schuijff, *Calorimetry and Thermal Analysis of Polymers*, New York Hanser, 1994.

[59] J. Mark, *Physical Properties of Polymers Handbook*, American Institute of Physics, AIP press, 1996.

[60] H. Tong, C. Hu, C. Feger and P. Ho, *Stress Development in Supported Films during Thermal Cycling*, Polymer Engineering and Science, Vol. 26, No 17, pp.1213-1217, 1986.

[61] J. Lange, S. Toll, J. Mansen and A. Hult, *Residual Stress Build Up in Thermoset Films Cured Above their Ultimate Glass transition Temperature*, Polymer Journal, Vol. 36, No.16, pp.3135-3141, 1995.

[62] D. Hill, M. Pera, P. Pomery, H. Toh, Dynamic Mechanical Properties of Networks Prepared from Siloxane Modified Divinyl Benzene Pre-Polymers. Polymer Journal, vol. 41 No. 26, pp. 9131-9137, 2000.

[63] N. Waterman and M. Ashby, *The Materials Selector*, Chapman & Hall, second edition, vol. 3, 1996

[64] DTM Corporation, 1611 Headway Circle, Austin, Texas 78754, *DTM Sinterstation System 2000, Sinterstation System Software Utility Guide*, January 2000.

[65] D. Pham and X Wang, *Prediction and Reduction of Build Times for the Selective Laser Sintering Process*, Proc Instn Mech Engrs, Vol. 214, Part B, pp. 425-430, 2000.

[66] W. Bushko and V. Stokes, *Solidification of Thermoviscoelastic Melts, Part 4: Effects of Boundary Conditions on Shrinkage and Residual Stresses*. Polymer Engineering and Science, Vol. 36, No. 5, pp. 658-675, Mid-March 1996.

[67] R. Taylor, K. Pister and G.Goudreau, *Thermomechanical Analysis of Viscoelastic Solids*, International Journal for Numerical Methods in Engineering, Vol. 2, pp. 45-59, 1970.

[68] J. Ferry, Viscoelastic Properties of Polymers, Wiley, New York, 1961